

**NASA CONTRACTOR
REPORT**



NASA CR-2436

NASA CR-2436

**REDUCTION OF ACOUSTIC DISTURBANCES
IN THE TEST SECTION OF SUPERSONIC
WIND TUNNELS BY LAMINARIZING THEIR
NOZZLE AND TEST SECTION WALL
BOUNDARY LAYERS BY MEANS OF SUCTION**

by W. Pfenninger and J. Syberg

Prepared by

BOEING COMMERCIAL AIRPLANE COMPANY

Seattle, Wash. 98124

for Langley Research Center



NATIONAL AERONAUTICS AND SPACE ADMINISTRATION • WASHINGTON, D. C. • NOVEMBER 1974

1. Report No. NASA CR- 2436		2. Government Accession No.		3. Recipient's Catalog No.	
4. Title and Subtitle REDUCTION OF ACOUSTIC DISTURBANCES IN THE TEST SECTION OF SUPERSONIC WIND TUNNELS BY LAMINARIZING THEIR NOZZLE AND TEST SECTION WALL BOUNDARY LAYERS BY MEANS OF SUCTION				5. Report Date November 1974	
				6. Performing Organization Code	
7. Author(s) W. Pfenninger and J. Syberg				8. Performing Organization Report No. D6-41564	
9. Performing Organization Name and Address Boeing Commercial Airplane Company P.O. Box 3707 Seattle, Washington 98124				10. Work Unit No.	
				11. Contract or Grant No. NASw-2359	
12. Sponsoring Agency Name and Address National Aeronautics and Space Administration Washington, D.C. 20546				13. Type of Report and Period Covered Contractor Report	
				14. Sponsoring Agency Code	
15. Supplementary Notes FINAL REPORT					
16. Abstract <p>The feasibility of quiet, suction laminarized, high Reynolds number (Re) supersonic wind tunnel nozzles was studied. According to nozzle wall boundary layer development and stability studies, relatively weak area suction can prevent amplified nozzle wall TS (Tollmien-Schlichting) boundary layer oscillations. Stronger suction is needed in and shortly upstream of the supersonic concave curvature nozzle area to avoid transition due to amplified TG (Taylor-Goertler) vortices. To control TG instability, moderately rapid and slow expansion nozzles require smaller total suction rates than rapid expansion nozzles, at the cost of larger nozzle length Re and increased TS disturbances. The total suction mass flow ratios for the laminarization of high Re supersonic air nozzles increase from $\dot{m}_s/\dot{m}_c = 0.005$ at $M^* = 3$ (test section) to 0.0105 at $M^* = 9$. Nozzle wall cooling decreases TS oscillations; TG instability in the concave curvature region, though, may be worse. Due to smaller nozzle length Re and Goertler parameters, $M^* = 9$ helium nozzles require half as much suction for their laminarization as $M^* = 9$ air nozzles of the same U^*D^*/ν^* (test section). Boundary layer crossflow instability on the side walls of two-dimensional high Re supersonic nozzles due to streamline curvature requires strong local suction to avoid transition. Nozzle wall surface roughness is critical in the throat area, especially at high M^*, but not in the downstream nozzle region. Allowable surface roughness in the throat area of a $M^* = 9$ helium nozzle is five times larger than for a comparable $M^* = 9$ air nozzle. Test section mean flow irregularities can be minimized with suction through longitudinal or highly swept slots (swept behind local Mach cone) as well as finely perforated surfaces (hole spacing \leq subsonic nozzle wall boundary layer thickness). Longitudinal slot suction is optimized when the suction-induced crossflow velocity increases linearly with surface distance from the slot "attachment line" toward the slot (through suitable slot geometry). Suction in supersonic blowdown tunnels may be operated by one or several individual vacuum spheres.</p>					
17. Key Words (Suggested by Author(s)) Boundary layer instability Laminarization Supersonic wind tunnel Suction				18. Distribution Statement Unclassified—unlimited STAR Category: 01	
19. Security Classif. (of this report) Unclassified	20. Security Classif. (of this page) Unclassified		21. No. of Pages 305	22. Price* \$7.25	

CONTENTS

	Page
SUMMARY	1
INTRODUCTION	6
SYMBOLS AND ABBREVIATIONS	8
FORMULATION OF THE PROBLEMS	14
Tollmien-Schlichting Type Boundary Layer Oscillations	14
Boundary Layer Crossflow on the Side Walls of Two-Dimensional Nozzles	16
Taylor-Goertler Type Boundary Layer Instability	17
Laminarization of Corner Flow in Two-Dimensional Supersonic Nozzles	20
Suction-Induced Disturbances	20
Disturbances at the Nozzle Inlet	27
ANALYTICAL STUDIES	30
Laminar Boundary Layer Development and Stability Analyses With Area Suction	30
Methods and Assumptions	30
Analytical Results	38
Discussion of the Results	40
Taylor-Goertler Type Boundary Layer Instability	40
Tollmien-Schlichting Type Boundary Layer Instability	47
Boundary Layer Crossflow Instability on Two-Dimensional Nozzle Side Walls	50
Unit Length Reynolds Number and Nozzle Wall Surface Roughness Considerations	51
Detailed Considerations of Suction Through Perforated Surfaces	53
Influence of Suction-Induced Disturbances on the Nozzle Wall Boundary Layer	53
Suction-Hole Induced Mean Flow Irregularities in the Test Section	60
SUCTION DRIVE SYSTEM CONSIDERATIONS	64
RECOMMENDATIONS FOR RESEARCH AND DEVELOPMENT	67
Theoretical and Experimental Investigations of Suction-Induced Mean Flow Irregularities	68
Experimental Investigation at High Length Reynolds Numbers With Various Suction Methods	69

CONTENTS—Concluded

	Page
RECOMMENDATIONS FOR RESEARCH AND DEVELOPMENT—Continued	
Subsonic and Supersonic Transition Investigations in the Presence of Taylor-Goertler Disturbance Vortices	70
Investigation of Methods to Minimize Nozzle Inflow Disturbances	72
 APPENDIX A—VERSION OF COMPUTER PROGRAM TEM139 TO CALCULATE LAMINAR BOUNDARY LAYER FLOWS WITH VERY SMALL OR UNIFORM CROSSFLOW	74
 APPENDIX B—POTENTIAL CROSSFLOW IN THE DIRECTION NORMAL TO LONGITUDINAL SUCTION RODS	76
 APPENDIX C—SUMMARY OF RAETZ'S NONLINEAR BOUNDARY LAYER STABILITY THEORY	78
 APPENDIX D—ASYMPTOTIC SUCTION PROFILES	81
 APPENDIX E—TABLES AND FIGURES INDEX	82
 REFERENCES	86
 TABLES	93
 FIGURES	161

REDUCTION OF ACOUSTIC DISTURBANCES IN THE TEST SECTION OF SUPERSONIC WIND TUNNELS BY LAMINARIZING THEIR NOZZLE AND TEST SECTION WALL BOUNDARY LAYERS BY MEANS OF SUCTION

by W. Pfenninger and J. Syberg
Boeing Commercial Airplane Company

SUMMARY

The feasibility of quiet, high Reynolds number, low turbulence supersonic wind tunnels with suction laminarized nozzles and test sections was studied. For axisymmetric tunnels, the test section Mach number ranged from $M^* = 3$ to 9, including two $M^* = 9$ helium nozzles. Slow expansion nozzles with large streamwise nozzle wall surface curvature ratios R/R_{th} in the nozzle throat area as well as moderately rapid and rapid expansion nozzles were studied. A $M^* = 4.6$, two-dimensional JPL wind tunnel nozzle was included. Relatively large supersonic wind tunnels with test section Reynolds numbers $U^*D^*/\nu^* = 26.2 \times 10^6$ were usually assumed.

Turbulent wall boundary layer noise in the test section of supersonic tunnels can, in principle, be avoided by suction laminarized nozzle and test section wall boundary layers. With the high equivalent length Reynolds numbers Re_{Lequ} of larger supersonic wind tunnel nozzles, especially at higher M^* , area suction should be closely approached and aerodynamic, acoustic, and thermal nozzle inlet disturbances minimized. The minimization of such inlet disturbances and the development and stability of the wind tunnel nozzle wall boundary layer with area suction were studied under various conditions with the following objectives in mind:

- Prevention of premature transition on the nozzle walls by: (1) suction-induced disturbances; (2) Taylor-Goertler (TG) type boundary layer instability in the concave nozzle wall curvature region; (3) Tollmien-Schlichting (TS) type boundary layer instability particularly in the upstream high pressure, low supersonic nozzle areas; and (4) boundary layer crossflow instability on the side walls of two-dimensional nozzles.
- Minimization or prevention of suction-induced spatial (mean) flow irregularities as well as timewise flow fluctuations in the test section (the latter might be induced by amplified nozzle wall boundary layer oscillations, especially of the TS type, radiating into the test section) to prevent premature transition on test models. Since suction-induced mean flow irregularities decay relatively slowly in the supersonic flow region of the nozzle, they should be attenuated as much as possible within the subsonic portion of the supersonic

nozzle wall boundary layer (thickness δ_s). Timewise flow fluctuations in the test section, resulting from amplified nozzle wall boundary layer oscillations of the TS type, should be minimized by preventing an excessive growth of such boundary layer oscillations.

According to the nozzle wall boundary layer analysis, premature transition due to amplified TG boundary layer disturbance vortices in the concave curvature region of high Reynolds number supersonic nozzles can be prevented by removing a rather large percentage of the nozzle wall boundary layer by means of area suction in the concave curvature region as well as in the upstream low supersonic Mach number area of the nozzle. Asymptotic suction conditions are then closely approached over most of the nozzle surface. The nozzle wall boundary layer therefore becomes highly stable also with respect to amplified TS-type boundary layer disturbances, obviating the need for a more elaborate TS-type stability analysis. Under otherwise the same conditions, smaller total suction mass flow ratios \dot{m}_s/\dot{m}_0 appear adequate to prevent premature transition due to TG disturbance vortices in slow and moderately slow expansion supersonic nozzles. The \dot{m}_s/\dot{m}_0 ratio needed to avoid transition due to TG disturbance vortices in the concave curvature region of slow expansion supersonic nozzles increases from 0.005 at $M^* = 3$ to 0.0105 at $M^* = 9$ (using air as the working medium). The larger suction mass flow ratios of supersonic nozzles required at higher M^* are explainable by their larger nozzle length to test section diameter ratio and their higher wall surface friction losses in the high pressure, low supersonic Mach number region of the nozzle.

To control TG instability in the concave curvature nozzle region and TS instability in the high pressure, low supersonic nozzle area at higher test section Reynolds numbers U^*D^*/ν^* , a progressively larger percentage of the nozzle wall boundary layer must be removed. However, the total suction mass flow ratio \dot{m}_s/\dot{m}_0 required to control the TG vortices was found to be nearly constant with increasing test section Reynolds number due to a corresponding reduction in boundary layer thickness.

Nozzle wall cooling also affects TG instability. The surface cooling raises Re_θ and $Re_\theta \sqrt{\theta}/r$ to apparently cause a more rapid growth of TG disturbance vortices in the concave curvature region of the nozzle, as compared with the case of insulated nozzle walls.

Compared with shorter, moderately rapid expansion supersonic nozzles, a major disadvantage of slow expansion supersonic nozzles—especially at higher M^* —is the substantially higher Re_{Lequ} (at a given U^*D^*/ν^*) and, as a result, increased sensitivity to amplified TS-type nozzle wall boundary layer oscillations. In addition, the relatively high nozzle wall surface friction losses in the high pressure, low supersonic region of high supersonic Mach number nozzles contribute to an increasing nozzle wall boundary layer momentum loss as the nozzle flow expands over larger streamwise distances in slow expansion nozzles. As a result, the nozzle wall boundary layer Reynolds numbers Re_θ of slow expansion, high supersonic Mach number nozzles are higher than for

moderately rapid expansion nozzles to partially compensate for the smaller streamwise radius of curvature of the latter in the evaluation of the TG vortex growth factor. Slow expansion, high supersonic Mach number nozzles may then lose most of their superiority with respect to TG boundary layer instability (compare, for example, the $M^* = 9$ slow expansion and moderately rapid expansion NASA helium nozzles). With their smaller Re_θ and Re_{Lequ} , moderately rapid expansion high supersonic Mach ($M^* = 9$) and high Reynolds number nozzles appear then as a favorable overall compromise from the standpoint of TG- and TS-type boundary layer instability.

Extremely high unit length Reynolds numbers U/ν_e (at a given U^*/ν^* in the test section) in the nozzle throat region of high supersonic Mach number nozzles are a result of the high pressure and density ratios of such nozzles, requiring very close surface tolerances in the nozzle throat region and raising the Re_{Lequ} of the nozzle for larger U^*D^*/ν^* to values far beyond experimentally observed transition length Reynolds numbers. These problems can be greatly alleviated by using monatomic gases such as helium with $\gamma = 1.66$ (instead of $\gamma = 1.4$ for air) as the working medium of such high supersonic Mach number tunnels. Due to substantially smaller nozzle pressure and density ratios with $\gamma = 1.66$, the values U/ν_e in the low supersonic nozzle region and Re_{Lequ} of $M^* = 9$ axisymmetric helium nozzles are 5.3 and two times smaller, respectively, than the corresponding values for $M^* = 9$ axisymmetric air nozzles under otherwise the same conditions. In addition, the suction mass flow ratio that is needed to control TG-type boundary layer instability in the concave curvature region of $M^* = 9$ axisymmetric helium nozzles is less than half that of $M^* = 9$ axisymmetric air nozzles under otherwise the same conditions. Furthermore, the permissible nozzle wall surface roughness height for laminar flow in the throat region of $M^* = 9$ axisymmetric nozzles is about five times larger for helium than for air nozzles under otherwise the same conditions. Thus, the use of helium as the working medium in supersonic, quiet, high Reynolds number, low turbulence wind tunnels with suction laminarized nozzles will enable substantially higher test section Mach numbers before considerations of unit length and equivalent nozzle length Reynolds number set limits to U^*D^*/ν^* and U^*/ν^* in the test section.

At a given U^*/ν^* ($26.2 \times 10^6/m$ in most cases studied), the permissible wall surface roughness in the nozzle throat region for laminar flow decreases substantially with increasing M^* to rather impractically small values for the $M^* = 7$ and particularly $M^* = 9$ air nozzles. Over a large percentage of the downstream region of the nozzle, however, the permissible nozzle wall surface roughness for laminar flow is surprisingly large, especially at higher M^* and particularly for axisymmetric $M^* = 9$ helium nozzles.

According to the boundary layer analysis with area suction on the walls of the axisymmetric $M^* = 5$ LARC Q-nozzle and the floor and ceiling walls of the $M^* = 4.6$ two-dimensional JPL nozzle, the total suction mass flow ratios \dot{m}_s/\dot{m}_0 at $U^*D^*/\nu^* = U^*H^*/\nu^* = 26 \times 10^6$ that are required to control TG instability in the concave nozzle wall curvature region are practically the same.

However, to avoid premature transition due to boundary layer crossflow instability on the side walls of two-dimensional supersonic wind tunnel nozzles, much stronger suction is required, particularly in the low supersonic Mach number region of the side walls as compared to the floor and ceiling walls. With the resulting extremely thin wall boundary layers and low Re_θ on the side walls, the surface roughness in the nozzle throat region becomes extremely critical, limiting the maximum permissible test section unit length Reynolds number to perhaps $U^*/\nu^* \leq 10^7/\text{m}$ at $M^* = 5$. Furthermore, premature transition in the corners between the side walls and the floor and ceiling walls of two-dimensional supersonic nozzles must be prevented by longitudinal corner suction slots and, possibly, locally increased suction rates in the immediate vicinity of these corners.

Aerodynamic nozzle inflow turbulence can be strongly damped by inlet screens with relatively wide open area ($\geq 60\%$) and very fine screens, maintaining if at all possible viscous screen wakes and a clean initial laminar inlet wall boundary layer downstream of the screens. To minimize thermally induced turbulence and thermal convection currents in the nozzle, the temperature distribution at the nozzle inlet should be extremely uniform. This would probably require a cooler or heat exchanger system in the inlet section with a highly sophisticated temperature control, as well as thermal insulation of the inlet wall surfaces. Acoustic disturbances, originating from the tunnel drive system in closed-return supersonic tunnels or blowdown valves in supersonic blowdown tunnels, must be strongly attenuated (by perhaps 80 dB or more) by suitable techniques. Mechanical vibrations, originating from the tunnel drive system, the blowdown valve, and possibly the exit diffuser downstream of the test section, must be prevented from entering the wind tunnel nozzle and test section by suitable vibration isolation techniques.

Porous, finely perforated suction surfaces with very closely spaced electron-beam-drilled small suction holes closely approach the aerodynamic ideal of area suction without introducing major flow disturbances in the test section. The suction-hole-induced mean flow irregularities in the test section are greatly reduced when the suction hole spacing is equal to or preferably smaller than the thickness δ_s of the subsonic portion of the local boundary layer. For a given total number of suction holes, suction-induced mean flow irregularities in the test section can be minimized with suction hole rows swept behind the local Mach angle. The hole spacings ($\leq \delta_s$) within the individual hole rows should be particularly small, while the spacing between the hole rows could be much larger. With this arrangement, the suction-induced disturbance flow field in the direction normal to the highly swept hole rows decays rapidly to insignificant values in the test section. Extremely closely spaced suction holes are required in the low supersonic region of the nozzle, where δ_s is particularly small, especially at higher M^* (at a given U^*/ν^*). In contrast, δ_s is substantially larger in the downstream nozzle areas; therefore, larger suction hole spacings appear to be permissible in these regions.

For laminarization of the nozzle walls by means of suction through finely perforated surfaces, especially of high supersonic Mach number nozzles at high Re_{Lequ} , the suction-induced streamwise disturbance vortices must be very weak and should be kept within the slowest boundary layer wall region by minimizing the suction rates per hole, i.e., using an extremely large number of very closely spaced, small diameter suction holes applied, for example, by electron-beam drilling techniques. This requirement is compatible with the above requirement to minimize suction-hole-induced mean flow irregularities in the test section.

In contrast to perforated suction surfaces, slotted suction surfaces with longitudinal as well as highly swept slots,[†] swept behind the local Mach angle, automatically avoid suction-induced mean flow irregularities in the test section, at least as long as streamwise suction discontinuities are prevented. This latter requirement dictates a relatively large number of individual suction chambers and a careful layout of the internal throttling design within each suction chamber, such that the streamwise suction mass flow distribution is continuous. For this purpose a separate second suction skin, containing additional throttling holes, located underneath the external suction skin and separated from it by small plenum chambers (in the form of small grooves or cells), must be provided. To minimize or preferably avoid mean flow irregularities in the test section induced by streamwise suction discontinuities, the structural elements located in the inner second suction skin and supporting the suction surface should be swept behind the Mach angle of the local nozzle flow wherever possible. In this manner, external flow disturbances induced by blockage from such supports propagate in the direction normal to them at subsonic speeds and thus decay rapidly spatially. Similarly, streamwise supports would avoid such disturbances. Suction, however, might be partially blocked by such supports to cause suction variations in the direction normal to the mean flow. In contrast, the structural elements in the suction chambers supporting the second suction skin may be aligned in any direction without necessarily introducing mean flow disturbances in the test section.

Flush spanwise (i.e., perpendicular to the flow direction) or moderately swept suction slots swept ahead of the local Mach angle generate weak shock waves at each slot, which radiate into the test section to possibly cause premature transition on test models. Therefore, suction surfaces with flush spanwise slots probably are not acceptable.

To accomplish uniform suction over longitudinally slotted suction surfaces, the suction-slot-induced potential crossflow velocity should increase linearly from the centerline or "attachment line"^{††} between adjacent slots toward the slots themselves. According to appendix B, this appears to

[†]With such highly swept slots, the suction-induced disturbance flow field in the direction normal to the slots is subsonic and thus decays rapidly to negligible values in the test section.

^{††}With the suction-induced flow normal to the suction surface, the flow on the longitudinal suction rods is then similar to the flow in the front attachment line region of a very highly swept wing.

be possible within a limited range of slot width/slot spacings with specially contoured longitudinal suction rods.

Disadvantages of longitudinally slotted suction surfaces are larger surface wetted areas with correspondingly higher suction rates, as well as increased difficulties to control TG instability in the concave curvature region of the nozzle. Ideal area suction pulls TG disturbance vortices closer toward the surface, where they are more quickly dissipated by the stronger viscous forces in the inner layers, thus alleviating TG instability. This alleviating effect may not exist to the same degree in the "attachment line" region between adjacent longitudinal slots, requiring accordingly larger suction mass flow rates to sufficiently reduce Re_θ , $Re_\theta \sqrt{\theta/r}$, and $\int \beta dx$.

Highly swept slots pull TG vortices closer to the surface at each slot location. Thus they appear to be more effective than longitudinal slots in raising the TG stability limit, as long as the suction slot spacing is very small.

The suction power, which is needed to recompress the suction medium to tunnel stagnation pressure, can be minimized by individually recompressing the suction medium of the individual suction chambers and by approaching isothermal compression. The resulting suction power (on the order of 2% to 3% of the kinetic energy of the flow in the test section) contributes in a particularly efficient manner to the drive power in closed-return continuous supersonic tunnels. With the thin, suction laminarized tunnel walls, friction losses as well as diffuser losses (downstream of the test section) are greatly reduced. In suction laminarized supersonic blowdown tunnels, suction may instead be provided by one or several individual suction vacuum spheres.

The feasibility of supersonic, quiet, high Reynolds number supersonic tunnels of low turbulence with suction laminarized nozzles and test sections hinges on several critical factors: the stabilizing influence of area suction on the TG-type boundary layer instability and its dependence on Mach number up to high supersonic M ; the laminarization of the tunnel nozzle walls at extremely high Re_{Lequ} ; the minimization or preferably elimination of suction-induced spatial as well as timewise flow fluctuations in the test section; the drastic reduction of aerodynamic, acoustic, and thermal nozzle inlet disturbances; and the manufacturing and technological development of suitable suction surfaces and structures. Research and development to verify these particularly critical items and establish the necessary technology are therefore strongly recommended.

INTRODUCTION

Premature transition on supersonic wind tunnel test models has often resulted from acoustic disturbances, presumably originating from the tunnel drive system of closed-return tunnels, the

valves in blowdown tunnels, and especially the turbulent wall boundary layers in the tunnel test section and its upstream nozzle. In flight, such acoustic disturbances are usually absent. Therefore, to improve the wind tunnel model simulation of supersonic vehicles at atmospheric flight conditions, the acoustic disturbances in supersonic tunnels need to be minimized.

Acoustic disturbances and mechanical vibrations originating from the tunnel drive system in supersonic closed-return tunnels and the valves in blowdown tunnels can be largely eliminated through acoustic and mechanical vibration isolation of the test section, as verified by the closed-return supersonic tunnel of the Institute for Statistical Mechanics in Marseilles, France, and one of the supersonic blowdown tunnels of the Institute of Theoretical and Applied Mechanics (ITAM) in Akademgorodok, Novosibirsk, USSR. Since practically identical transition results were obtained at high supersonic Mach numbers at ITAM both with and without attenuation of the noise from the blowdown valve, the acoustic disturbances originating from the nozzle and test section wall boundary layers apparently dominated and controlled transition on the test models. Therefore, to properly simulate flight conditions on supersonic test models, especially at higher Reynolds numbers, the acoustic disturbances that radiate from the turbulent wall boundary layers of supersonic tunnels into the test sections should be minimized or preferably eliminated.[†] In principle, this should be possible by maintaining clean and undisturbed laminar boundary layers on the nozzle and test section walls of supersonic tunnels within the test rhombus, accomplished for example by means of boundary layer suction.

This report discusses the feasibility of maintaining laminar wall boundary layers in supersonic wind tunnels through suction. A detailed analytical investigation of the laminarization of axisymmetric and two-dimensional tunnels in the Mach number range of 3 to 9 is also presented.

As an aid to readability, appendix E contains a listing that describes the figures and tables presented in this report. The reader's attention is also directed to tables E-1 and E-2, which cross-reference nozzle type and suction configurations with figure and table numbers.

The boundary layer crossflow calculations on the side walls of two-dimensional nozzles (appendix A) were programmed by Dr. T. Reyhner for the CDC 6600 computer. The authors wish to express their appreciation for his contribution and for his valuable advice during the boundary layer development calculations.

[†]In the intermittency region of turbulence, boundary layer eddies alternate with potential flow regions. The outer edge of the turbulent boundary layer is then highly irregular. At supersonic speeds, pressure waves then radiate from the intermittency region of the turbulent boundary layer along Mach lines at 75% to 80% local freestream Mach number into the test section of supersonic tunnels to often cause premature transition on test models (refs. 1 and 2).

SYMBOLS AND ABBREVIATIONS

a, b	major and minor axis of longitudinal suction rods (appendix B)
c_f	surface friction coefficient
d	wire diameter of damping screens
dA	nozzle wall surface element
$d\dot{m}_s/dA$	suction mass flow per unit nozzle wall surface area
g	width of longitudinal slots (appendix B)
\bar{h}	mean height of sucked layer per row of suction holes
k	height of three-dimensional surface roughness
\dot{m}_O	wind tunnel test section mass flow per unit time
\dot{m}_s	suction mass flow per unit time
p	absolute pressure
p'	absolute pressure at suction compressor exit
r	(circumferential) nozzle radius at station X (in the Taylor-Goertler stability analysis, r is the streamwise radius of curvature of the nozzle walls)
s	surface distance, or slot width for spanwise or highly swept slots
u, v, w	nozzle wall boundary layer velocities in x, y, and z directions
\bar{u}	mean boundary layer velocity in sucked layer per row of suction holes
\bar{v}	mean velocity normal to the suction surface through spanwise and highly swept suction slots

v_o	fictitious area suction velocity, as if suction medium is removed at $\rho = \rho_e$
v_{\perp}	disturbance velocity in y direction induced by sinks of spacing λ at $y = h$ from the wall (fig. 37b)
w_n	boundary layer crossflow velocity component in the direction normal to the potential flow streamline
x	streamwise coordinate ($x = 0$ at nozzle throat $M = 1$)
$x' \equiv \frac{x}{R_{th}}$	nondimensional streamwise coordinate
y	coordinate normal to surface
y_{crit}	critical height of three-dimensional surface roughness with $Re_k = \frac{u_k y_{crit}}{\nu_k} = 200$
z	spanwise coordinate
$B = \beta \theta Re_{\theta}$	growth parameter of Taylor-Goertler disturbance vortices
D^*	nozzle exit and test section diameter
$G \equiv Re_{\theta} \sqrt{\frac{\theta}{r}}$	Goertler parameter for growth of Taylor-Goertler vortices
H	height coordinate of two-dimensional supersonic nozzle at station X
H_i	$\delta^*_{incompress} / \theta_{incompress}$
$KE_{test\ section}$	kinetic energy of flow in tunnel test section
$L_{suct\ isoth}$	isothermal suction power
LFC	laminar flow control
M	Mach number, or honeycomb mesh size

M^*	test section Mach number
R	gas constant, or streamwise radius of curvature of nozzle wall surface in the throat area
R_{th}	nozzle throat radius (circumferential)
Re	Reynolds number
Re_c	wing chord Reynolds number
$Re_k \equiv \frac{u_k k}{\nu_e}$	roughness Reynolds number
$Re_L = \frac{UL}{\nu}$	length Reynolds number
$Re_{Lequ} = \int \frac{U}{\nu_e} ds$	equivalent length Reynolds number
$Re_n \equiv \frac{w_{nmax}(\delta_{0.1})}{\nu_e}$	boundary layer crossflow Reynolds number based on the maximum crossflow velocity w_{nmax} and boundary layer thickness $\delta_{0.1}$ where $w_n = 0.1 w_{nmax}$
$Re_{ref} = U^* D^* / \nu^*$	reference Reynolds number
$Re_\theta \equiv \frac{U\theta}{\nu_e}$	boundary layer momentum thickness Reynolds number
$Re_{\theta_{al}}$	Re_θ for spanwise boundary layer profile at front attachment line of swept wings
RF	nozzle wall temperature recovery factor
S	entropy
T	absolute temperature, $T_E \equiv \frac{T}{M^{*2}(\gamma - 1)T^*}$
T^*	test section freestream absolute temperature

T_k	boundary layer absolute temperature at edge of roughness element at $y = k$
TG	Taylor-Goertler
TS	Tollmien-Schlichting
U	potential flow velocity in x direction
U^*/ν^*	test section unit length Reynolds number
U/ν_e	local nozzle unit length Reynolds number
U/ν_k	nozzle unit length Reynolds number based on U and the kinematic viscosity ν_k at the edge of the roughness
W	potential crossflow velocity on longitudinal suction rods (appendix B)
W_∞	potential flow velocity at infinity normal to longitudinally slotted suction surface (appendix B)
$\alpha = \frac{2\pi}{\lambda}$	wave number of amplified boundary layer oscillations (in fig. 32, α is the suction hole spacing)
$\beta' \equiv \beta R_{th}$	Taylor-Goertler vortex growth parameter
$\int \beta dx$	exponent in Smith's linearized Taylor-Goertler vortex growth factor
$\gamma \equiv \frac{c_p}{c_v}$	c_p and c_v are specific heats at constant pressure and volume
δ	total boundary layer thickness (in this report, $\delta = \delta_{0.99}$ where $u = 0.99U$)
$\delta^* \equiv \int_0^\delta \left(1 - \frac{\rho U}{\rho_e U}\right) dy$	boundary layer displacement thickness
δ_s	thickness of subsonic boundary layer region
$\Delta x, \Delta z$	distances between suction holes in x and z directions

ϵ $L_{\text{suct isotherm}}/KE_{\text{test section}}$

$$\theta \equiv \int_0^{\delta} \frac{\rho U}{\rho_e U} \left(1 - \frac{u}{U}\right) dy$$

boundary layer momentum loss thickness

 λ

wavelength of amplified boundary layer oscillations

 μ

absolute viscosity

$$\nu \equiv \frac{\mu}{\rho}$$

kinematic viscosity

 ρ

density in boundary layer

$$\frac{\rho_e v_o}{\rho^* U^*}$$

local suction mass flow rate

 τ_o

wall surface friction

 $\omega_x, \omega_y, \omega_z$

vorticity in x, y, and z directions

$$\chi \equiv \left[\frac{w_{n\max}^{(\delta_{0.1})}}{v_e} \right]_{\text{stab limit}}$$

boundary layer crossflow stability limit Reynolds number

$$\left(\frac{\partial U}{\partial s} \right)_{\text{al}}$$

chordwise potential flow velocity gradient at front attachment line of swept wing (normal to wing leading edge)

Superscripts and subscripts:

ad

adiabatic condition

al

attachment line

compr

compression condition

crit

critical condition

e

outer edge of boundary layer

k	condition at edge of three-dimensional surface roughness ($y = k$)
max	maximum
o	wall condition
s	suction
stag	stagnation condition
th	nozzle throat
tr	transition
*	test section
∞	infinity

FORMULATION OF THE PROBLEMS

The question arises as to how to laminarize the nozzle and test section walls of large supersonic tunnels with two-dimensional and axisymmetric inlet nozzles by means of boundary layer suction.

Since the purpose of quiet supersonic tunnels with laminarized nozzle and test section walls is the simulation of atmospheric flight conditions, the length Reynolds numbers are necessarily high on the models in the tunnel test section, and particularly in the upstream portions of the tunnel nozzle. Under such conditions the artificially laminarized boundary layers on the nozzle and test section walls can then become unstable in various ways. Different types of amplified laminar boundary layer oscillations can develop, leading to increasingly more complicated boundary layer flows and finally transition, as discussed in the following sections.

TOLLMIE-SCHLICHTING TYPE BOUNDARY LAYER OSCILLATIONS

Various kinds of external disturbances, such as aerodynamically, acoustically, and thermally induced flow turbulence at the nozzle inlet, mechanical vibrations, as well as suction-induced aerodynamic and acoustic disturbances introduce initial fluctuations into the boundary layer. These fluctuations can induce strongly amplified Tollmien-Schlichting (TS) and other types of boundary layer oscillations, which finally cause transition. The maximum laminar length Reynolds number Re_L in the presence of amplified laminar boundary layer oscillation under the action of such finite initial boundary layer disturbances critically depends on the magnitude of these initial disturbances.

Experiments on various low drag suction wings and bodies of revolution in different wind tunnels at subsonic speeds have shown that the maximum laminar Re_L of such low drag suction surfaces varies approximately inversely proportional to the turbulence level u'/U_∞ of the external flow (fig. 1, refs. 3-8). In these experiments, area suction usually had been closely approached by using a large number of fine suction slots, located over the entire length of the model. In other words, extremely high laminar flow length Reynolds numbers appear possible in supersonic nozzles and test sections if it should prove feasible to drastically decrease external disturbances. When mechanical vibrations of the nozzle and test section walls can be prevented and noise from the turbulent nozzle and test section wall boundary layers eliminated by laminarizing them through boundary layer suction, the remaining disturbances that control transition will consist of nozzle inflow disturbances, such as aerodynamically and thermally induced inflow turbulence and inlet noise. Therefore, to maximize the laminar flow length Reynolds number of supersonic nozzles and test sections and to alleviate the problems involved with the laminarization of the nozzle and test section, the above nozzle inflow disturbances should be minimized as much as possible.

In compressible flow, according to Squire (ref. 9), two-dimensional normal TS waves (i.e., with their wave fronts normal to the potential flow direction) are less stable than oblique TS waves traveling at an oblique angle to the mean flow. However, according to Brown's supersonic TS stability analysis on an insulated supersonic flat plate (ref. 10) using the full disturbance equations (i.e., including terms containing the normal velocity of the mean flow), oblique two-dimensional TS waves become more unstable at higher supersonic Mach numbers ($M \geq 5$) than normal TS waves. Brown obtained still somewhat lower TS stability limit Reynolds numbers as well as a closer agreement with experimental results by Demetriades (California Institute of Technology, 1958) at $M = 5.8$ by assuming three-dimensional TS-type disturbances varying periodically both in the x and z directions and growing exponentially with time, using Dunn's expressions for the disturbance velocities (ref. 11):

$$\begin{aligned} u &= u_0 + f(y) e^{i(\alpha_1 x + \alpha_3 z - \alpha_1 c t)} \\ v &= v_0 + \alpha_1 \phi(y) e^{i(\alpha_1 x + \alpha_3 z - \alpha_1 c t)} \\ w &= h(y) e^{i(\alpha_1 x + \alpha_3 z - \alpha_1 c t)} \end{aligned}$$

where:

$$\begin{aligned} u, v, w &= \text{TS disturbance velocities in the } x, y, \text{ and } z \text{ directions} \\ u_0, v_0 &= \text{mean boundary layer velocities in the } x \text{ and } y \text{ directions} \\ c &= c_r + ic_i, \text{ the complex wave velocity} \end{aligned}$$

Since the most critical TS disturbance waves are usually swept ahead of the local Mach angle, amplified TS waves can propagate along Mach lines with only minor attenuation into the test section of supersonic tunnels to induce local flow fluctuations there. When the amplitude of the TS oscillations in the wall boundary layers becomes excessively large, the flow fluctuations induced by the oscillations in the test section may cause premature transition on test models. Therefore, strongly amplified boundary layer oscillations—especially of the TS type—must be avoided on the nozzle and test section walls of supersonic tunnels, even though they would not necessarily cause transition on these walls. At the high length Reynolds numbers of large supersonic tunnels, this requirement dictates an even more stringent minimization of the initial disturbances at the nozzle inlet than for the mere prevention of transition on the tunnel walls. Methods to reduce such nozzle inflow disturbances are discussed later. Furthermore, to avoid an excessive growth of the wall boundary layer oscillations and the resulting flow fluctuations in the test section of supersonic

tunnels, the tunnel wall boundary layer must be stabilized to a higher degree than that needed for transition prevention. In this connection, it should not be overlooked that other more complicated boundary layer oscillations may often couple with the TS waves to increase the growth rate of the boundary layer oscillations, thus further aggravating the laminarization problems of large supersonic tunnels at higher Reynolds numbers. As the nozzle length and test section diameter Reynolds number are raised, the aerodynamic ideal of area suction must be approached to an increasingly higher degree.

For the same reason, an undisturbed initial laminar wall boundary layer at the nozzle inlet shortly downstream of the inlet damping screens is highly desirable although not absolutely mandatory. An otherwise turbulent initial nozzle wall boundary layer immediately downstream of the inlet damping screens may, if necessary, be completely removed by means of suction, thus reestablishing an undisturbed "clean" new laminar boundary layer (refs. 12-15).

BOUNDARY LAYER CROSSFLOW ON THE SIDE WALLS OF TWO-DIMENSIONAL NOZZLES

On the side walls of two-dimensional supersonic nozzles, streamline curvature induces spanwise pressure gradients and a resultant boundary layer crossflow in the direction normal to the potential flow streamlines in a manner similar to that of swept low drag suction wings (see, for example, refs. 16-19). The resulting boundary layer crossflow profiles show inflection points and are thus dynamically highly unstable. In contrast, the TS instability is generated by the presence of friction forces, which are relatively weak. As a result, the TS instability is a rather mild instability as compared with the dynamic instability of the boundary layer crossflow. Beyond the crossflow stability limit Reynolds number, longitudinal crossflow disturbance vortices develop, which rotate in the same direction and eventually become sufficiently unstable at higher crossflow Reynolds numbers to break up and cause transition.

At higher supersonic speeds, laminar boundary layers become increasingly sensitive to spanwise pressure gradients, at least for insulated walls. First, the boundary layer thickness usually increases substantially with increasing supersonic Mach number. Furthermore, the boundary layer temperature close to the insulated wall surface is substantially higher than the freestream static temperature; accordingly, the boundary layer density close to the surface is considerably smaller than the freestream density. As a result, the kinetic energy of the slowest boundary layer particles in the vicinity of the wall decreases to very low values at higher supersonic Mach numbers. These slowest boundary layer particles are then more strongly deflected from the potential flow direction by spanwise pressure gradients, inducing a correspondingly more severe boundary layer crossflow as the Mach number is raised to higher supersonic values. This increased sensitivity of laminar boundary layers on insulated walls to spanwise pressure gradients has been verified experimentally through

investigations by the Northrop boundary layer research group on swept supersonic low drag suction wings (refs. 20-22). Thus, under otherwise the same conditions, the boundary layer crossflow Reynolds number $w_{n_{\max}} \delta/\nu$ increases substantially with M , at least for insulated surfaces. Unfortunately, according to Brown's supersonic crossflow stability calculations, the boundary layer crossflow stability limit Reynolds number for the same boundary layer crossflow velocity distribution at zero wall heat transfer does not increase significantly with M , at least at lower supersonic M (ref. 23). (No theoretical results are available on the crossflow instability at higher supersonic M .) Thus, control of boundary layer crossflow instability on insulated surfaces in the presence of lateral pressure gradients $\partial p/\partial z$ will become increasingly difficult at higher supersonic speeds. Laminar boundary layers of two-dimensional supersonic wind tunnel nozzles, supersonic airplanes, or hypersonic vehicles therefore become particularly sensitive to boundary layer crossflow induced by spanwise pressure gradients at higher M . With wall surface cooling, on the other hand, the temperature, density, and kinetic energy of the boundary layer in the vicinity of the wall increase. As a result, boundary layer crossflow induced by pressure gradients $\partial p/\partial z$ should be strongly alleviated by surface cooling.

Since boundary layer crossflow disturbance vortices develop essentially in the streamwise direction, their disturbance flow field decays rapidly spatially even at high supersonic freestream Mach numbers. Thus, in contrast to TS disturbances, relatively strongly amplified boundary layer crossflow disturbance vortices appear permissible without affecting the flow quality in the test section, provided they do not cause premature transition in the wall boundary layer.

In contrast to the flow in two-dimensional nozzles, the flow in axisymmetric nozzles is axisymmetric, and circumferential pressure gradients and resulting boundary layer crossflows are therefore absent, thus alleviating the laminarization problems. Axisymmetric nozzles, though, have some disadvantages over the two-dimensional type, such as reduced operational flexibility; furthermore, disturbances from the tunnel walls are focused on the tunnel axis, requiring a particularly careful nozzle design and minimization of suction-induced disturbances in the artificially laminarized tunnel wall boundary layers.

TAYLOR-GOERTLER TYPE BOUNDARY LAYER INSTABILITY

In the concave wall curvature region of axisymmetric and two-dimensional supersonic nozzles,[†] Taylor-Goertler (TG) type boundary layer instability (refs. 24-30) can generate

[†]In principle, concave wall surface curvature can be avoided in the subsonic portion of the nozzle by means of a suitable nozzle geometry. Concave nozzle wall curvature, however, cannot be avoided in the downstream region of the supersonic portion of the nozzle.

longitudinal disturbance vortices rotating in the opposite direction. They can become sufficiently unstable to break up and cause premature transition when the exponent $\int \beta dx$ in the growth factor of TG vortices exceeds a value of 10 (according to a linearized analysis by A. M. O. Smith on the growth of TG disturbance vortices from transition experiments on concave surfaces [ref. 26]).

Thus, TG-type boundary layer instability in the concave curvature region of supersonic nozzles may become particularly critical at higher tunnel Reynolds numbers, based for example on test section diameter, flow velocity, and kinematic viscosity in the test section. Since TG vortices are oriented essentially streamwise, their disturbance flow field decays rapidly even at high supersonic Mach numbers. Thus, in contrast to TS disturbances, rather strongly amplified TG disturbance vortices appear permissible without affecting the flow quality in the test section of supersonic tunnels as long as they do not cause premature transition in the nozzle wall boundary layers.

The TG-type boundary layer instability on concave surfaces (or in the presence of Coriolis forces in turbomachines) results essentially from the difference between the centrifugal forces acting on the faster boundary layer particles toward the outer edge of the boundary layer and the slower ones close to the wall. In other words, the TG instability depends primarily on the velocity difference between the inner and outer region of the boundary layer and not on the shape of the boundary layer profile as in the case of the TS-type instability (refs. 25-30), at least in the absence of boundary layer suction. For this reason TG boundary layer instability is substantially more difficult to influence and control than TS or boundary layer crossflow instability.

In general, for a given change in flow direction, transition due to TG vortices is delayed (i.e., $\int \beta dx$ is smaller) when this change in flow direction is accomplished over a shorter streamwise distance, even though the local values of the Goertler number $G \equiv Re_\theta \sqrt{\theta/r}$ and thus β (refs. 25-30) are larger as a result of the smaller radius of surface curvature r (according to calculation of TG vortex growth factors). In supersonic nozzles, however, a rapid change in flow direction can produce a nonuniform Mach number distribution with shock waves in the test section and therefore is not permissible.

According to Smith's (linearized) stability diagram (ref. 26) of $Re_\theta \sqrt{\theta/r} = f(\alpha\theta)$ (where the wave number $\alpha = 2\pi/\lambda$) for different amplification factors $B \equiv \beta\theta Re_\theta$, the locus for the minimum values of B for different $Re_\theta \sqrt{\theta/r}$ closely coincides with curves for constant wave numbers, α , i.e., constant lateral vortex spacings, λ . Therefore, as θ increases, maximum growth of TG vortices is closely approached for constant λ . This case is to be expected on the top and bottom walls of two-dimensional supersonic nozzles. On the other hand, when the potential flow streamlines and the TG disturbance vortices diverge in the downstream direction, as for the case of axisymmetric supersonic nozzles, λ increases in the downstream direction. The locus of $Re_\theta \sqrt{\theta/r} = f(\alpha\theta)$ then deviates substantially from the locus for maximum amplification of TG vortices. Thus, TG vortices

may be somewhat less amplified in axisymmetric nozzles as compared to two-dimensional ones. According to TG stability calculations in axisymmetric and two-dimensional supersonic nozzles, this effect is relatively minor and was therefore usually neglected in the TG stability analysis.

The question arises concerning the possibility of alleviating TG boundary layer instability by means of boundary layer suction. According to Kobayashi's linearized analysis (ref. 27) of the TG instability with laminar asymptotic area suction boundary layer profiles, the stability limit Goertler number for zero growth of TG disturbance vortices is substantially higher and the amplification factor $\beta\theta Re_\theta$ therefore lower than they are without suction (fig. 2). The growth of TG vortices would thus be substantially reduced. A previous linearized analysis of the TG stability limit with the same asymptotic suction profile, but assuming $v_o = 0$ as the wall boundary condition, has shown essentially the same TG stability limit as the Blasius profile (refs. 27 and 30). The substantially higher stability limit of the asymptotic suction profile, with the wall boundary condition $v_o \neq 0$ properly satisfied, is explained by Kobayashi by the fact that area suction pulls the TG vortices closer toward the wall where the stronger viscous forces may damp the TG vortices to a higher degree than in the case of impervious walls.

In addition, relatively strong area suction generates a streamline curvature within the boundary layer that is opposite to the concave wall surface curvature. The curvature of the streamlines in the vicinity of the wall thus becomes less concave and TG boundary layer instability is alleviated accordingly. According to calculations of the streamline curvature in an asymptotic suction boundary layer, this effect might be significant in the lower range of Goertler parameters G . With increasing G , however, its influence seems to become increasingly less significant, as compared to the stabilizing effect by pulling the TG vortices closer to the surface through area suction. At very large G values, i.e., small surface radii r at a given Re_θ and θ , the streamline curvature induced by area suction becomes negligible compared to the surface curvature and does not substantially affect the growth of TG vortices. The stabilizing influence of area suction on TG instability is then essentially a result of the TG vortices being pulled closer toward the surface by suction.

If Kobayashi's theoretical results (ref. 27) on the stabilizing influence of relatively strong area suction on TG boundary layer instability should prove to be correct, the laminarization problems of supersonic nozzles at higher Reynolds numbers would, indeed, be greatly alleviated. This conclusion, however, may be valid only with area suction or when area suction is very closely approached. It should not necessarily be generalized for the cases of suction through spanwise slots with larger chordwise spacings or longitudinal slots. Unpublished low drag suction experiments by K. Rogers (Northrop boundary layer research group) on a two-dimensional concave suction surface with relatively coarsely spaced suction holes at practically zero streamwise pressure gradient have shown only slightly higher TG transition values $\int \beta dx$ than those for nonsuction surfaces, using Smith's TG

vortex growth factors for impervious surfaces. Suction through relatively coarsely spaced spanwise slots pulls TG vortices closer to the surface only in the immediate vicinity of the slots, not in the region between them. Suction through such slots induces a concave streamline curvature in the rear slot stagnation region immediately downstream of the slots, which may partially compensate for the stabilizing effect when suction pulls the TG vortices closer to the surface in the vicinity of the slots. To substantially alleviate TG instability by suction through spanwise or swept slots, very small suction slot spacings and a correspondingly very close approach toward area suction thus appear desirable.

LAMINARIZATION OF CORNER FLOW IN TWO-DIMENSIONAL SUPERSONIC NOZZLES

Flow disturbances in the corners of two-dimensional nozzles may lead to premature transition. These disturbances can be avoided by thinning the corner boundary layer by means of suction through longitudinal corner slots connected to several individual suction chambers, as verified experimentally by Feifel (ref. 31) and Goldsmith (refs. 32-34).

SUCTION-INDUCED DISTURBANCES

Undisturbed "clean" laminar boundary layers must be maintained by means of suction on the nozzle and test section walls at the high length Reynolds numbers of large supersonic tunnels without introducing flow disturbances into the test section, which might otherwise induce premature transition on test models. Various suction methods will be evaluated in this respect.

Laminarization of the tunnel nozzle and test section walls at high length Reynolds numbers requires a very close approach toward area suction, especially in view of the fact that different types of boundary layer oscillations may adversely superimpose and couple. The minimization or preferably elimination of suction-induced flow disturbances in the test section severely restricts the choice of suitable suction methods. For example, with suction applied through many fine spanwise slots, weak shock waves are generated at each slot and radiate into the test section (see, for example, ref. 35). Therefore, suction through many fine flush spanwise slots (front and rear slot edges not displaced) does not appear satisfactory from the standpoint of suction-induced disturbances in the test section, even though laminar flow has thus been maintained up to 60×10^6 length Reynolds number both at subsonic and supersonic speeds (refs. 4 and 36). In principle, local shock waves radiating from spanwise slots at supersonic speeds might be avoided by eliminating the sink effect around the slots and the resulting suction-induced waviness of the streamlines at the outer edge of the boundary layer in the vicinity of the slots. This can be accomplished by stepping up the rear slot edges with respect to the slot inlet. Such an approach, however, may be too delicate

in practice. Suction through closely spaced flush spanwise slots is acceptable in the subsonic part of the nozzle, except possibly in its transonic region where the slot sink effect may be excessively aggravated by compressibility (in the transonic region of the nozzle, the pressure distribution and flow are extremely sensitive to weak streamline waviness at the outer edge of the boundary layer, induced by suction through flush spanwise slots).

In contrast to spanwise slots, longitudinal suction slots[†] avoid streamwise discontinuities of the streamlines at the outer edge of the boundary layer and thus suction-induced mean flow irregularities in the test section. Of course, suction must be continuous in the streamwise direction across adjacent suction chambers; otherwise, streamwise discontinuities in the boundary layer thickness may result at the juncture of adjacent suction chambers to possibly cause weak shock waves in the test section. The question arises as to how to maximize the effectiveness of suction through longitudinal slots in laminarizing the nozzle wall boundary layers. In this respect suction appears optimum if the boundary layer thickness were uniform in the region between the slot "attachment line" (in the center between adjacent slots) and the slots themselves. If this were possible, the wall surface friction would be essentially constant in the region between the attachment line and the slots (the crossflow induced by suction through longitudinal slots is too weak to significantly influence the local wall surface friction). According to boundary layer momentum considerations, the boundary layer thickness (for example, θ) would remain constant in the area between the slot attachment line and the slots if the boundary layer momentum removed by the suction-induced crossflow in the direction normal to the potential flow direction is constant between the slot attachment line and the slot, i.e., $\partial(\int \rho u w dy)/\partial z = \text{constant}$ between the slot and the slot attachment line. This is the case when W is proportional to z (assuming constant streamwise boundary layer profiles in the region between the slot attachment line and the slots).

The same result follows from the superposition of the streamwise boundary layer flow with the suction-induced boundary layer crossflow. The boundary layer development in the slot attachment line region can then be evaluated in a manner similar to that of the front attachment line of a highly swept wing, where the chordwise velocity normal to the attachment line increases proportionally to the surface distance in this direction. The boundary layer thickness is then constant (see, for example, Schlichting), at least for the case of the infinitely long yawing wing. Similarly, the boundary layer thickness should remain practically constant in the region between the slot attachment line and the slots as long as the crossflow velocity W_1 , induced by suction through longitudinal slots, increases linearly with surface distance z from the slot attachment line toward the slots. This result is strictly correct only when the spacing of the longitudinal slots is considerably larger than the boundary layer thickness. This is usually the case in the upstream part of the concave curvature region of supersonic nozzles, which generally contributes a particularly

[†] As used by Klebanoff and Spangenberg in unpublished experiment

large percentage to the growth of TG vortices. Toward the downstream end of supersonic nozzles, the boundary layer is usually considerably thicker, and the slot spacing is then not necessarily much larger than the local boundary layer thickness. In this case, to achieve uniform boundary layer removal between the slot attachment line and the slots by suction through longitudinal slots, the condition $\partial(\int \rho u w dy)/\partial z = \text{constant}$ should be satisfied.

The requirement that W be proportional to the spanwise distance from the slot attachment line calls for special contouring of the surface between the slots in the spanwise direction. Flush longitudinal slots do not generate such a linear spanwise increase of W ; cylindrical rods and especially low fineness ratio ellipses are already much better. Detailed crossflow calculations across the longitudinal suction rods, with the purpose of establishing optimum rod shapes with a linear spanwise increase of W from the slot attachment line toward the slots, are presented in appendix B.

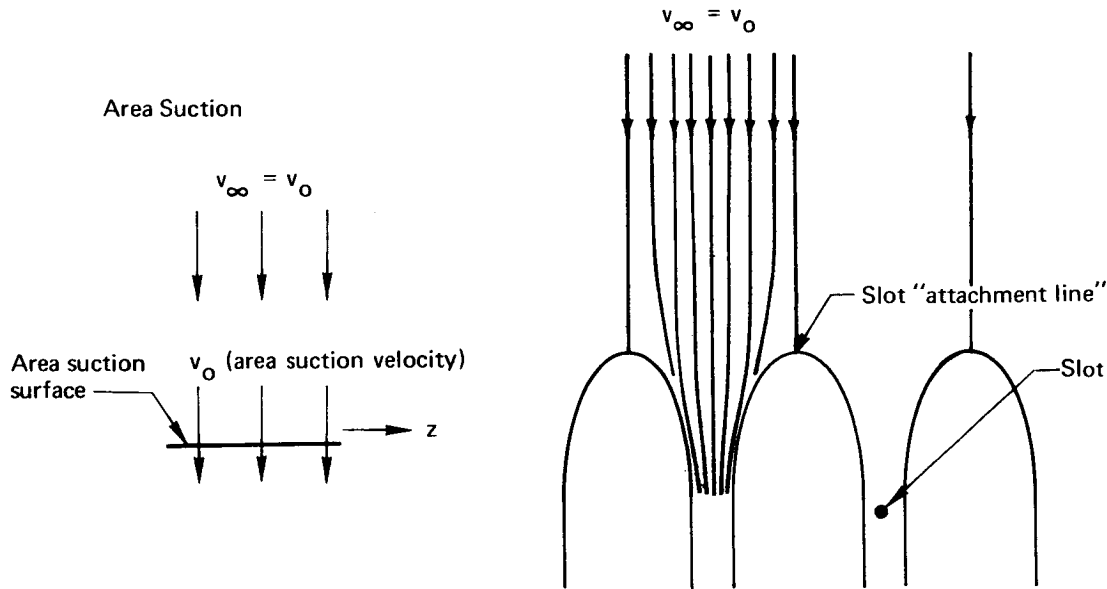
Longitudinal slots should preferably run along potential flow streamlines. To avoid any shock waves originating from suction flow discontinuities in the supersonic region of the nozzle that would penetrate into the test section, suction must be continuous along the length of the slot and should start very gradually at the upstream end of the slots, as demonstrated by Spangenberg.

Suction through longitudinal slots, though advantageous from the standpoint of suction-induced disturbances in the test section, has certain disadvantages. To closely approach a linear spanwise increase of W from the slot attachment line toward the slots, the wetted surface area of the nozzle and test section may substantially increase, requiring accordingly higher suction rates for the laminarization of this larger wetted area. Furthermore, a weak boundary layer crossflow will develop from the slot attachment line toward the slots due to spanwise pressure gradients. This boundary layer crossflow may adversely interact with the TG vortices to cause earlier transition.[†] Somewhat higher suction rates may therefore be necessary to compensate for this interaction.

Perhaps the most serious disadvantage of suction through longitudinal slots in the concave curvature region of supersonic nozzles may arise from the fact that suction does not pull TG disturbance vortices in the slot attachment line region as close to the wall surface as does ideal area suction. This is obvious by considering the suction-induced flow normal to the suction surface for the two cases shown on the following page.

[†]Similar observations have been made by the first author on a swept laminar flow nonsuction wing in the presence of three-dimensional surface roughness elements located in the front part of the wing. The weak longitudinal disturbance vortices, trailing downstream from each roughness element, adversely superimposed with the crossflow disturbance vortices resulting from spanwise pressure gradients to cause premature transition, even though the surface roughness alone would have been far too weak to induce transition. However, when the boundary layer crossflow due to wing sweep had been sufficiently stabilized by suction, three-dimensional surface roughness on swept low drag suction wings behaved essentially in the same manner as in the absence of crossflow.

Suction Through Longitudinal Slots



With suction through longitudinal slots, the normal velocity v in the vicinity of the slot attachment line is much smaller than the suction velocity v_0 for ideal area suction (assuming the same suction rates for area suction and suction through longitudinal slots). Hence, TG vortices are not pulled as strongly toward the surface in the slot attachment line region as they are in the case of ideal area suction, while they are pulled much stronger toward the slots in their immediate vicinity where v is much larger. As a result, TG vortices may grow substantially more rapidly in the slot attachment line region, unless the spanwise slot spacing is smaller than the lateral spacing of the TG vortices. This condition, however, can be seldom met with the thin laminar suction boundary layers at higher test section unit length Reynolds numbers, at least in the upstream portion of the supersonic concave curvature region of supersonic nozzles.

A promising suction method, which avoids suction-induced disturbances in the test section and closely approaches the aerodynamic ideal of area suction, is offered by suction through very closely spaced suction slots swept behind the local Mach angle. As long as the slot spacing is very small, TG vortices are pulled alternately closer to the surface by each slot. As long as the slot spacing is very small, TG instability may be better controlled with these slots than with longitudinal slots, although not quite as well as with ideal area suction. Such highly swept suction slots have been used by the Northrop boundary layer research group on a 72° swept low drag suction wing (ref. 21); A. L. Nagel (NASA) has independently suggested the use of such highly swept slots. The flow component in the direction normal to the slots is then subsonic, and the slot-induced flow field is therefore shock free

and decays rapidly. For this reason, suction-induced disturbances do not propagate into the test section. Very closely spaced flush suction slots are then feasible, using essentially the same standard slot-cutting methods developed by the Northrop boundary layer research group. Local shock waves resulting from suction discontinuities must be carefully avoided by maintaining a smooth streamwise variation of the suction distribution along the length of the slots, as in the case of suction through longitudinal slots. In the presence of a decreasing static pressure in the streamwise direction, this can be accomplished by subdividing the suction area, providing a sufficiently large number of individual suction chambers, and using an additional structural inner skin with throttling holes located underneath the slots and separated from them by small plenum chambers. To avoid trailing disturbance vortices at the slot ends in the corners of two-dimensional nozzles, the ends of the side wall slots should be matched with those of the floor and ceiling wall slots. In this manner the highly swept slots, combined with the longitudinal corner slots, act like a continuous slot without three-dimensional slot end disturbance vortices.

Slot wake fluctuations in the small plenum chambers underneath the slots may cause premature transition at high length Reynolds numbers when the slot wake flow ceases to be purely viscous and steady at higher slot flow Reynolds numbers $\bar{v}s/\nu$. Such slot wake fluctuations should therefore be avoided by maintaining a purely viscous slot wake flow, keeping $\bar{v}s/\nu \leq 100$ with ordinary suction plenum chambers, or ≤ 200 with special shallow plenum chambers containing two rows of suction holes (drilled into the inner skin) located symmetrically with respect to the slot (refs. 37 and 38).

The aerodynamically ideal area suction may be particularly closely approached by means of suction through porous surfaces, provided they can be designed and built for the theoretically required suction distributions and the tight nozzle surface waviness and contour tolerances, which are required to ensure a highly uniform flow in the test section. Suction through improperly designed porous suction surfaces may produce an excessive equivalent aerodynamic roughness, which can generate weak shock waves in the supersonic region of the nozzle. These waves will radiate into the test section to generate mean flow irregularities with longitudinal disturbance vorticity and correspondingly increased turbulence in the test section. As verified by the National Bureau of Standards (NBS), such disturbances can cause premature transition on test models and should therefore be minimized or avoided. Similar considerations apply to finely perforated suction surfaces. To minimize suction-induced aerodynamic roughness, porous suction surfaces with very small mesh sizes or perforated suction surfaces with very closely spaced, extremely small circular or preferably elliptical holes must be used.

The question arises concerning suction hole patterns that for a given total number of holes will minimize suction-induced mean flow irregularities in the test section. From this standpoint, closely spaced suction hole rows swept behind the local Mach angle appear especially promising. The hole

spacing λ_1 within each row of holes would be particularly small, while the spacing λ_2 of the hole rows could be substantially larger. With the rows of holes swept behind the local Mach cone, the flow component in the direction normal to the hole rows is subsonic. Thus, the suction-hole-induced disturbance velocities of this flow component decrease rapidly and do not radiate into the test section. In contrast, the flow component in the direction of the rows of holes is supersonic. Therefore, its suction-hole-induced disturbance velocities decay practically only within the subsonic part of the boundary layer; in the supersonic boundary layer and potential flow region, they propagate along Mach lines and thus decay rather slowly. To minimize flow irregularities in the test section, the suction-hole-induced disturbance velocities of the flow component in the direction of the row of holes therefore must be strongly attenuated within the subsonic wall boundary layer region. This requirement leads to suction hole spacings λ_1 in the direction of the hole rows that are equal to or smaller than the thickness δ_s of the subsonic portion of the local wall boundary layer. The suction-hole-induced disturbance velocities at the edge of the subsonic layer are then practically uniform along a row of holes, and suction-hole-induced disturbances radiated along Mach lines into the test section should then become insignificant. This is not valid when λ_1 is substantially larger than δ_s . To satisfy the requirement $\lambda_1 \leq \delta_s$, extremely small suction holes and hole spacings λ_1 are required especially at higher M^* in the upstream low supersonic regions of the nozzles. For a given test section diameter Reynolds number, the permissible mesh size of porous suction surfaces or suction hole diameter and spacing of perforated suction surfaces decreases inversely proportional to the test section unit length Reynolds number U^*/ν^* , requiring increasingly finer and more closely spaced suction holes as U^*/ν^* is raised.

Steigerwald's technique of electron-beam drilling very small, closely spaced holes appears to be highly attractive in closely approaching the aerodynamically ideal area suction. Laser-beam hole drilling presents another alternate for manufacturing finely perforated, low drag suction surfaces for laminarization. Structurally, a finely perforated suction surface usually is superior to a porous one; furthermore, as compared with a porous surface, the required close nozzle contour tolerances can easily be met. Reference 38 discusses various suction methods and problems associated with laminarization in the presence of the aerodynamic roughness induced by suction through finely perforated surfaces.

The test section unit length Reynolds numbers should be chosen such that excessively close suction surface tolerances are avoided, especially in the initial phases during the testing of experimental laminarized supersonic pilot tunnels.

Streamwise boundary layer disturbance vortices resulting from surface or aerodynamic flow imperfections can easily cause premature transition on the tunnel walls, especially when coupled with streamwise boundary layer crossflow and TG-type disturbance vortices. Therefore, such additional disturbance vortices should be minimized or avoided, especially at higher nozzle and test

section Reynolds numbers. They can be generated in many different ways—for example, by three-dimensional surface roughness, by imperfect suction slots with chipped or damaged slot edges, in the presence of abrupt spanwise variations of the streamwise boundary layer profile, and, more generally, whenever the spanwise boundary layer vorticity component changes rapidly in the spanwise direction. Longitudinal disturbance vortices are also generated by suction through perforated and improperly laid out area suction surfaces (see, for example, refs. 39-48), by blockage of the suction flow through the suction surface in the presence of incorrectly designed support structures underneath the external suction skin, etc. Furthermore, such suction flow blockage can generate discontinuities in the streamwise boundary layer development with resulting weak local shock waves, which in turn radiate into the test section to possibly cause premature transition on test models even though they would not necessarily trip the nozzle wall boundary layer.

To control the suction distribution over the nozzle surfaces, a separate second suction skin containing additional throttling holes, located underneath the thin external suction skin and separated from it by small plenum chambers in the form of small grooves or cells, must be provided. Without this separation the suction flow in the external suction skin would be strongly blocked in the areas of the support structure located underneath the external skin.

To minimize streamwise suction discontinuities, a relatively large number of individual suction chambers should be chosen, especially at the high pressure ratios of higher supersonic Mach number nozzles. A reasonably continuous suction distribution must be maintained across adjacent suction chambers by means of the throttling holes in the inner second suction skin. To further minimize or preferably avoid mean flow irregularities in the test section induced by streamwise suction discontinuities, it appears preferable to sweep the structural elements, which are located in the inner second suction skin and support the outer suction skin, whenever possible, behind the Mach angle of the local nozzle flow. In this manner, external flow disturbances induced by the blockage from such supports propagate in the direction normal to these supports at subsonic speeds and thus decay rapidly and do not propagate into the test section. Similarly, streamwise structural supports in the inner skin underneath the external suction skin would avoid suction-induced mean flow irregularities in the test section. Blockage of the suction airflow in the region of these streamwise supports, however, can easily lead to spanwise variations of the suction mass flow rates and, as a result, of the nozzle wall boundary layer and should therefore be minimized or avoided. In contrast, using a careful design, the structural elements in the suction chambers supporting the structural inner second suction skin may be aligned in any direction without necessarily introducing suction-induced mean flow disturbances in the test section.

The above considerations apply to suction surfaces with small, closely spaced electron-beam- or laser-beam-drilled suction holes as well as very closely spaced suction slots swept behind the local Mach angle. With such closely spaced, highly swept continuous suction slots, streamwise disturbance

vortices are largely absent, allowing possibly higher test section unit length Reynolds numbers, until surface roughness considerations in the nozzle throat area set an upper limit to U^*/ν^* . On the other hand, ideal area suction may not be as closely approached with the streamwise spacing of highly swept slots as with a practically porous suction surface with very closely spaced electron-beam- or laser-beam-drilled suction holes, requiring probably somewhat higher suction rates at higher Re_L or limiting perhaps the maximum Re_L with laminar flow.

DISTURBANCES AT THE NOZZLE INLET

Aerodynamic turbulence at the nozzle inlet can be minimized by placing fine mesh honeycombs and/or damping screens in the inlet section upstream of the nozzle inlet. Purely viscous steady and turbulence-free screen wake flow and at the same time an undisturbed initial laminar wall boundary layer would result at screen Reynolds numbers $\bar{u}d/\nu \leq 40$ (ref. 49). However, this ideal condition can be achieved only with screens of very small wire diameters at low flow velocities through the screens and relatively low stagnation pressures upstream of the nozzle. To avoid erratic behavior of the screens in damping inflow turbulence, an open screen area ratio of 60% or more is preferable (ref. 49). At higher test section unit length Reynolds numbers and especially at higher tunnel Mach numbers, i.e., higher tunnel stagnation pressures, extremely low screen velocities would be required if laminar screen wakes are to be maintained. Very high nozzle area contraction ratios would then be necessary, which eventually would become unacceptable in view of increased difficulties with thermally induced turbulence. Thermal eddies resulting from temperature variations in the inlet section are strongly contracted and stretched, in a manner similar to bathtub vortices, as they pass through the nozzle into the sonic throat region, thereby increasing their kinetic energy and vorticity to generate thermally induced turbulence. Thermal eddies induced by temperature gradients in the low-speed region of the nozzle must be minimized or preferably avoided by maintaining a highly uniform air temperature distribution at the nozzle inlet. As shown by Spangenberg at the NBS, this can be accomplished by placing a series of heat exchangers, such as water radiators, upstream of the screens, with the temperature of the water or heat exchanger medium accurately controlled, combined with a highly efficient thermal insulation of the tunnel walls around and upstream of the nozzle.

Even with these precautions, an upper limit probably exists for the permissible nozzle contraction ratios. In the NBS experiments with laminarized supersonic suction nozzles, Klebanoff and Spangenberg used a nozzle area contraction ratio between the screens and the sonic throat of 100. No difficulties were experienced with thermal convection currents at the inlet when two water radiators were installed upstream of the inlet screens, in contrast to considerable difficulties with thermal inlet convection currents prior to installation of these radiators.

To further increase the tunnel Mach and unit length Reynolds number in the test section while still maintaining laminar screen wakes, the question arises as to how to further increase the nozzle contraction ratio between the screens and the sonic throat without aggravating the thermal convection problems at the inlet. For this purpose one might, for example, install the screens in a section of extremely low local velocity and sharply accelerate the flow immediately downstream of the screens in a first nozzle to a substantially higher (although still low) velocity, followed by a much more gradual flow acceleration over a long streamwise distance into the sonic throat area and the supersonic region of the nozzle. With the rapid flow acceleration in such a first nozzle immediately downstream of the screens, thermal convection currents may have insufficient time to develop before the inlet flow has been contracted to a substantially smaller diameter.

At still higher tunnel stagnation pressures, it may eventually become impossible to maintain laminar screen wakes. Other means must then be sought to minimize the screen wake turbulence and establish an undisturbed laminar wall boundary layer at the nozzle inlet. In principle, the screen or honeycomb wake turbulence $u'/U \sim (X/M)^{-0.5^\dagger}$ (see, for example, ref. 50) for constant axial velocity is minimized by increasing X/M , i.e., increasing X and decreasing M as much as possible. In addition, the reestablishment of an undisturbed initial laminar wall boundary layer requires probably the complete removal of the turbulent wall boundary layer by means of suction (area suction, discrete slots, or scoops) shortly downstream of the last screen or honeycomb. To avoid premature transition, it is essential to remove all the turbulent eddies that intermittently penetrate at times rather far into the potential flow region. Distributed suction further downstream on the inlet walls continuously stabilizes the wall boundary layer in the presence of the screen turbulence, thus maintaining undisturbed laminar flow on the nozzle inlet walls. Since the screen turbulence decreases in the downstream direction, suction may be progressively reduced. In addition to suction, it may be desirable to further stabilize the inlet wall boundary layer and reduce at the same time the screen or honeycomb turbulence in the inlet by continuously accelerating the flow downstream of the screens, resulting in a rather long and slowly converging subsonic inlet nozzle.

Instead of screens, very fine mesh honeycombs may be used at lower tunnel stagnation pressures. Fine mesh honeycombs may also precede the damping screens, with the purpose of minimizing crossflow disturbances in the inlet.

To reduce wake interferences between adjacent screens, which might lead to velocity variations in the test section, relatively large axial screen spacings should be chosen. The individual screens should be oriented at different angles with respect to each other to minimize wake interference.

[†] X = distance downstream from the screens or honeycomb, M = screen or mesh size

Taylor-Goertler type wall boundary layer disturbance vortices in the nozzle inlet should, if possible, be prevented by minimizing or preferably avoiding concave wall surface curvature in the subsonic region of the inlet nozzle between the last screen and the sonic throat.

Upstream acoustic disturbances from the tunnel drive system in closed-return tunnels or the valves in blowdown supersonic tunnels must be sufficiently attenuated in the low-velocity region upstream of the radiators or heat exchanger surfaces. As an example, in one of the supersonic tunnels of the Institute for Theoretical and Applied Mechanics in Novosibirsk, the valve noise has been attenuated by means of acoustic linings by 50 dB (verbal information by associates of this institute). In very low turbulence tunnels, acoustic disturbances often dominate over aerodynamically induced turbulence, especially at higher tunnel speeds. Therefore, to laminarize the nozzle wall boundary layers of supersonic tunnels at further increased Reynolds numbers U^*D^*/ν^* , particular emphasis probably must be given to attenuate still further the upstream noise from the drive system or the blowdown valve, requiring an upstream noise attenuation of perhaps 80 dB or more at very high nozzle and test section length Reynolds numbers. In addition, emphasis should be given to the development of quieter blowdown valves (NASA Langley developments).

Mechanical vibrations from the tunnel drive system, blowdown valve, and tunnel exit diffuser should be prevented from entering the nozzle and test section by means of suitable vibration isolation techniques. In addition, aerodynamic and acoustic disturbances from the exit diffuser should not pass into the test section.

To optimize the design of quiet supersonic tunnels with laminarized nozzles and test sections, the overall development and stability of the laminar boundary layer on the tunnel walls must first be analyzed. In view of the critical importance of inlet disturbances at high nozzle and test section length Reynolds numbers, such disturbances should be minimized as much as possible. To arrive at the most promising suction method, the influence of suction-induced disturbances on the laminarization of the tunnel wall boundary layers and the flow uniformity in the tunnel test section must be evaluated. Special emphasis should be given to a careful overall and detail design of the suction ducting and drive system, minimizing any further suction-induced disturbances that may adversely affect the laminarized tunnel wall boundary layers and the flow in the test area.

The next sections of this report are therefore concerned with analytical investigations of the tunnel wall boundary layer development and stability with area and slot suction. Included are studies of some suction-induced disturbances that may affect the laminarization of the tunnel wall boundary layer and the flow uniformity in the test section.

ANALYTICAL STUDIES

The following analytical studies were conducted:

- Laminar boundary layer development and stability analysis with area suction on the walls of various axisymmetric and two-dimensional supersonic wind tunnel nozzles and test sections for different conditions, including evaluation of the critical height of three-dimensional surface roughness for laminar flow on the suction laminarized nozzle and test section walls of supersonic tunnels
- Detailed studies of various suction methods for the laminarization of the nozzle and test section walls of supersonic tunnels
 - Suction through finely perforated nozzle wall surfaces
 - Study of mean flow irregularities induced in the test section of supersonic tunnels by suction through perforated nozzle walls and the minimization of such flow irregularities by suitable suction hole patterns
 - Determination of thickness δ_s of the subsonic part of the suction laminarized nozzle wall boundary layer (affecting the suction hole spacing) at different streamwise nozzle stations for various conditions
 - Suction through longitudinal slots
 - Analysis of the potential crossflow in the direction normal to the slots for various slot configurations, with the purpose of ensuring uniform boundary layer removal on the nozzle wall surfaces
 - Brief study of the local boundary layer crossflow on longitudinal suction rods

LAMINAR BOUNDARY LAYER DEVELOPMENT AND STABILITY ANALYSES WITH AREA SUCTION

Methods and Assumptions

To determine the overall suction rates and the streamwise suction distributions required for the establishment of clean laminar nozzle wall boundary layers along the entire nozzle length, the

stability limit and growth of various kinds of amplified nozzle wall boundary layer oscillations must be evaluated. These depend strongly on the development of the nozzle wall boundary layer, which in turn is controlled by the external pressure field and streamwise suction distribution. Therefore, the laminar boundary layer development with area suction on the walls of different axisymmetric and two-dimensional supersonic wind tunnel nozzles was analyzed for different test section Mach numbers M^* and test section unit length Reynolds numbers. For a given test section Mach number, the streamwise nozzle surface radius of curvature R in the nozzle throat area was varied from low ratios R/R_{throat} (rapid expansion nozzles) to very high values for long, slender, slow expansion nozzles. The nozzle geometry and streamwise Mach number variation were established from existing nozzles[†] as well as with Farwick's method (ref. 51). Figures 3a-d and tables 1a-g present the radius ratio R/R_{throat} and wall Mach number M at various streamwise stations for the axisymmetric supersonic air nozzles investigated. Tunnel test section Mach numbers $M^* = 3, 5, 7$, and 9 were chosen. A long, shallow, slow expansion $M^* = 9$ axisymmetric helium nozzle ($R/R_{th} = 250$) as well as a moderately rapid expansion axisymmetric $M^* = 9$ NASA helium nozzle[†] are included for comparison (figs. 3e and 3f and tables 1h and 1i). Figure 3g and table 1j show the height ratio H/H_{throat} and wall Mach number at various streamwise stations for the $M^* = 4.6$ JPL two-dimensional nozzle.

For the nozzle wall boundary layer calculations with area suction, T. Reyhner's method was applied (ref. 52). Sutherland's law was used for the variation of the viscosity μ of air with the absolute temperature T . For helium, the power law $\mu \sim T^n$ appears more accurate and was used with $n = 0.675$ (according to refs. 53-55, $n = 0.645$ would have been slightly better).

In view of the high nozzle length Reynolds numbers of large supersonic tunnels, area suction must be very closely approached for the laminarization of their nozzles. Therefore, area suction was assumed for the analysis of the overall boundary layer development. For different test section Mach numbers M^* , nozzle geometries (i.e., throat radius ratios R/R_{th}), and test section unit length Reynolds numbers U^*/ν^* , various streamwise suction distributions $\rho_e v_o / \rho^* U^*$ [or $d(\dot{m}_s / \dot{m}_o) / d(x/R_{th})$] and total suction rates \dot{m}_s / \dot{m}_o were chosen so as to prevent premature transition due to Tollmien-Schlichting, Taylor-Goertler, and crossflow disturbance vortices. In addition, to minimize flow irregularities in the test section induced by amplified TS-type nozzle wall boundary layer oscillations,^{††} the streamwise suction distribution was selected such as to avoid excessively amplified TS oscillations on the nozzle walls. Zero nozzle wall heat transfer was usually

[†]The coordinates and Mach number distribution of these nozzles were furnished by NASA Langley.

^{††}In contrast to TS waves (which are usually swept ahead of the local Mach angle) amplified streamwise TG as well as boundary layer crossflow disturbance vortices do not propagate into the test section and therefore do not induce flow irregularities in the test section.

assumed; for a few cases the effect of moderate wall cooling on TS and TG boundary layer instability was studied. If not otherwise indicated, the data presented apply to insulated nozzle walls.

The boundary layer crossflow induced by streamline curvature on the side walls of two-dimensional supersonic nozzles was evaluated from the boundary layer equation in the crossflow direction, assuming that the boundary layer crossflow velocity w is very much smaller than the chordwise boundary layer velocity component u ($w \ll u$) (see appendix A). The boundary layer velocities u, v can then be calculated to a first approximation by neglecting w . The terms u and v thus evaluated can then be used in the boundary layer crossflow equation to obtain a first approximation for w . For the case of two-dimensional supersonic nozzles without suction, w is not necessarily small compared to u , and the above assumption that u, v do not significantly depend on w is not justifiable. A simultaneous integration of all boundary layer equations and energy and continuity equations would then be required, as developed by Raetz (ref. 56). The boundary layers on the side walls of two-dimensional nozzles are very thin because of the relatively strong area suction necessary to prevent premature transition due to boundary layer crossflow. The kinetic energy of the slowest nozzle wall boundary layer particles in the vicinity of the surface is thus sufficiently large for the nozzle side wall boundary layer to withstand spanwise pressure gradients $\partial p / \partial z$ (in the direction normal to the potential flow direction) without excessive streamline curvature in the boundary layer close to the surface. As a result, as on swept laminar flow control (LFC) wings, the boundary layer crossflow velocity w on the side walls of two-dimensional supersonic nozzles will decrease rapidly with decreasing side wall boundary layer thickness, which results from larger nondimensional suction rates $(\rho_e v_o / \rho^* U^*) \sqrt{Re_{ref}}$. The reference Reynolds number can be based, for example, on U^*, D^*, ν^* in the test section. The assumption $w \ll u$ thus appears to be usually well justified, and further iteration for w is not necessary.

In connection with the boundary layer crossflow calculations on the side walls of two-dimensional supersonic nozzles, the question arises concerning the boundary values of w in the corners between the nozzle side walls and the walls of the nozzle floor and ceiling. As in curved bends, the secondary boundary layer crossflow on the nozzle side walls extends beyond these corners to the nozzle floor and ceiling walls, where it gradually dies out. Thus, $w = 0$ in these corners does not appear correct. On the other hand, the assumption of fully developed boundary layer crossflow in the nozzle corners probably overestimates the local boundary layer crossflow somewhat.

The question arises as to how close to the floor and ceiling walls practically fully developed boundary layer crossflow exists on the side walls of two-dimensional suction laminarized supersonic nozzles. The boundary layer crossflow is considered fully developed when at a given location all the particles within the side wall boundary layer from the surface to the outer edge of the boundary layer originate from upstream areas of the side walls and not from the floor and ceiling walls of the

nozzle, where the boundary conditions for the nozzle wall boundary layer differ from those on the side walls.[†] Thus, in the concave curvature region of the nozzle, where the boundary layer crossflow on the side walls is directed from the nozzle corners toward the nozzle axis, the area with practically fully developed boundary layer crossflow is given by the limiting boundary layer streamlines adjacent to the side wall surface and originating from the nozzle wall corners close to the downstream end of the supersonic convex curvature region of the nozzle where the boundary layer crossflow changes its direction. In the convex curvature region of the nozzle, on the other hand, where the boundary layer crossflow is directed outwards toward the nozzle corners, practically fully developed boundary layer crossflow should exist over the entire height of the nozzle side walls. Since the boundary layer crossflow velocity $w \ll u$ when a relatively large percentage of the side wall boundary layer is sucked away to control boundary layer crossflow instability on the side walls, the angle between the limiting boundary layer side wall surface streamline and the local potential flow streamline is very small. The assumption of practically fully developed boundary layer crossflow on the side walls of suction laminarized two-dimensional supersonic nozzles then appears justifiable over a large percentage of the height of the nozzle side walls.

The fully developed boundary layer crossflow on the side walls of supersonic nozzles, assuming $w \ll u$, was calculated using T. Reyhner's method (appendix A).

From the boundary layer development analysis, attempts were made to evaluate or estimate the boundary layer stability limit, growth of amplified laminar boundary layer oscillations, and transition on the nozzle and test section walls in the presence of various types of disturbances. These include amplified Tollmien-Schlichting boundary layer oscillations, Taylor-Goertler boundary layer disturbance vortices in regions of concave nozzle wall surface curvature, and boundary layer crossflow disturbance vortices on the side walls of two-dimensional supersonic nozzles.

The following assumptions were made:

- a) Aerodynamic, thermal, and acoustic nozzle inlet disturbances: Minimized as much as possible.
- b) Tollmien-Schlichting type boundary layer oscillations on the walls of laminarized supersonic nozzles and test sections: According to theoretical results of Brown (ref. 10), Mack (ref. 57), and transition experiments on cones, etc. at various supersonic Mach numbers without suction and in the absence of strong flow acceleration, the TS stability limit and transition length Reynolds number in the absence of boundary layer crossflow instability increases substantially at higher supersonic Mach numbers, as compared to the

[†] Similar considerations have been applied to swept low drag suction wings.

corresponding values of subsonic and low supersonic Mach numbers, at least for zero wall heat transfer and moderate wall cooling. The question then arises as to the stabilizing influence of area suction and strong flow acceleration on the TS-type boundary layer instability at higher supersonic Mach numbers. Thus far, theory has not provided conclusive answers. Even for the simplest case of the insulated supersonic flat plate with zero pressure gradient and without suction, the theoretical investigations on the TS instability at higher supersonic speeds still appear controversial. Brown's TS stability calculations on an insulated flat plate at $M = 5.8$ (ref. 10) indicate that the mean normal boundary layer velocity apparently cannot be neglected at higher supersonic Mach numbers in a TS stability analysis. Gunness has shown that even further additional terms may have to be included in such an analysis at higher supersonic M (ref. 58). According to Brown (ref. 10), it appears that oblique two- and three-dimensional TS disturbances, usually less important in subsonic flow, will have to be considered in a TS stability analysis at higher supersonic M .

The stabilizing influence of distributed suction on a laminar boundary layer at moderately high supersonic Mach numbers has been demonstrated during low drag suction experiments on a supersonic flat plate and body of revolution in the Tullahoma A-tunnel (refs. 36 and 59). In spite of the substantial acoustic disturbances radiated from the turbulent nozzle and test section wall boundary layers, full length laminar flow was observed on an ogive supersonic suction body of revolution up to $Re_L = 51 \times 10^6$ length Reynolds number—the test limit of the tunnel (ref. 36)—as compared to about 10 times lower values without suction. Distributed suction was approached by means of suction through a very large number of closely spaced circumferential slots. In other words, the stabilizing influence of distributed suction on a supersonic laminar boundary layer in the absence of boundary layer crossflow has been demonstrated at least at $M = 3$. However, it has not been sufficiently verified how far the stabilizing influence of area suction can be extended to higher Mach numbers.

Since the low supersonic Mach number nozzle region of high pressure contributes a large percentage to the "equivalent" nozzle length Reynolds number, especially for high supersonic Mach number nozzles, the transition results of references 36 and 59 with distributed suction at moderately high supersonic speeds appear particularly important and promising in connection with the laminarization of supersonic Mach number nozzles up to high test section Mach numbers. One might then speculate on the laminar flow length Reynolds numbers when nozzle inlet aerodynamic, acoustic, and thermal disturbances are minimized and when acoustic disturbances from the turbulent nozzle wall boundary layer are eliminated by laminarizing them through suction. Assuming $Re_{L_{laminar}}$ of low drag suction surfaces being inversely proportional to the external

disturbance velocity ratio u'/U , "equivalent" nozzle length Reynolds numbers of several times 10^8 might eventually become possible, if the nozzle wall boundary layers were stabilized to the same or preferably somewhat higher degree as those on the suction body of revolution of reference 36. The overall suction rates and streamwise suction distribution on the nozzle walls were therefore chosen for this analysis to be at least as stable with respect to TS oscillations as those of reference 36; i.e., the suction distribution and overall suction rate were varied until the boundary layer profiles on the nozzle walls closely approached asymptotic suction profiles. In general, somewhat higher local suction rates were required anyhow to control the growth of TG boundary layer disturbance vortices in the supersonic concave curvature region of the nozzle such as to avoid transition due to TG instability. Therefore, control of TS instability appeared of secondary importance in this region.

In the supersonic region of axisymmetric supersonic nozzles, TS-type disturbance vortices are stretched in the circumferential direction as the nozzle radius increases in the streamwise direction, lowering accordingly the TS stability limit Reynolds number in this region. Vice versa, they are compressed in the subsonic part of the nozzle to raise the TS stability limit. With the small percentage change of the nozzle radius over a streamwise distance equal to a TS wavelength, these effects usually appear small for the nozzles investigated and were therefore neglected.

c) Taylor-Goertler type boundary layer instability in the concave surface curvature region of supersonic nozzles:

- 1) Compressibility effects on the stability limit Goertler number $(Re_\theta \sqrt{\theta/r})_{stab}$ limit and the growth of Taylor-Goertler vortices were neglected, due to lack of TG stability calculations at higher Mach numbers. TG stability calculations by Hammerlin (ref. 28) at $M = 0.5$ showed practically the same minimum value of $Re_\theta \sqrt{\theta/r}$ at the stability limit as that for the incompressible case. Thus, TG instability seems to be hardly affected by compressibility effects within the low subsonic speed range. To what extent this is true at higher M is uncertain and should be verified theoretically and experimentally. According to Aihara (ref. 29), the minimum value $Re_\theta \sqrt{\theta/r}$ at the stability limit of TG vortices decreases somewhat at higher supersonic M . Aihara's calculations, however, do not furnish results about the growth of TG vortices at higher supersonic M .
- 2) In the supersonic region of axisymmetric nozzles, the lateral spacing and thus the diameter of TG disturbance vortices will increase in the downstream direction, thus reducing their kinetic energy and vorticity to raise somewhat the stability limit

Goertler number, as compared to the case of parallel potential flow streamlines. However, since the spreading angle of the TG vortices is very small, this favorable effect is probably minor and was therefore neglected.

- 3) The flow acceleration in the nozzle causes a longitudinal stretching of the streamwise TG and boundary layer crossflow disturbance vortices, lowering accordingly their stability limit. Again, since the chordwise change of the mean flow over a length equal to the lateral wave spacing is small, this unfavorable effect is probably minor and was therefore neglected.
 - 4) Based on A. M. O. Smith's evaluation of subsonic TG transition experiments (ref. 26), a linearized Taylor-Goertler growth factor $\int \beta dx = 10$ was assumed at transition. This assumption implies no unfavorable coupling with amplified oblique Tollmien-Schlichting type boundary layer oscillations, which would lower the linearized TG disturbance vortex growth factor below 10. Amplified oblique TS waves would distort the streamwise TG disturbance vortices three-dimensionally, thereby stretching them longitudinally and thus increasing their vorticity and kinetic energy to cause transition at lower values of the linearized TG disturbance vortex growth factor. A similar unfavorable coupling between streamwise boundary layer crossflow disturbance vortices and amplified oblique TS waves, induced by external as well as internal acoustic disturbances, has been observed on swept low drag suction wings (refs. 17 and 60). Since, however, even moderately strongly amplified TS-type oscillations must be avoided to minimize the resulting flow fluctuations in the test section, the adverse coupling between such weakly amplified oblique TS waves and streamwise disturbance vortices of the TG or boundary layer crossflow instability type does not appear too critical and was therefore neglected.
 - 5) Kobayashi's stability results (ref. 27) for the asymptotic suction profile were assumed in the analysis of the linearized TG disturbance vortex growth factor. Since the suction velocities required for the laminarization of the nozzle wall boundary layers in the concave surface curvature region of the nozzles did not differ too much from the asymptotic suction rates, this assumption seems justifiable.
- d) Boundary layer crossflow instability on the side walls of two-dimensional subsonic nozzles:
- 1) Based on Brown's theoretical results (ref. 23) on a highly swept supersonic suction wing at $M = 1.8$, according to which the crossflow stability limit Reynolds number of a given boundary layer crossflow profile is only insignificantly higher than in

incompressible flow, the effect of Mach number on the crossflow stability limit Reynolds number and the growth of crossflow disturbance vortices were neglected. Subsonic theoretical and experimental results on the crossflow stability limit Reynolds number, growth of crossflow disturbance vortices, and the resulting transition, gained from previous investigations on swept low drag suction wings (ref. 16), were applied to analyze the boundary layer behavior on the side walls of suction laminarized two-dimensional supersonic nozzles. In general, it was assumed that the minimum crossflow stability limit Reynolds number χ_{\min} on the side walls could be exceeded by a factor of about 2 as on swept low drag suction wings. Since the boundary layer crossflow on the nozzle side walls is critical only over limited regions, in contrast to swept low drag suction wings where the boundary layer crossflow at high wing chord Reynolds numbers is critical over the entire chord, χ_{\min} might be exceeded safely by a somewhat larger factor than 2. χ_{\min} is a function of the shape of the boundary layer crossflow profile and was evaluated for different crossflow profiles according to Brown's incompressible stability calculations for different boundary layer crossflow profiles (ref. 61).

- 2) Similar to the streamwise TG boundary layer disturbance vortices in axisymmetric nozzles, the streamwise boundary layer crossflow disturbance vortices on the side walls of two-dimensional supersonic nozzles will diverge and grow in diameter as the flow passes downstream through the supersonic region of the nozzle. As a result, the kinetic energy and vorticity of these disturbance vortices will be lower than for the case of practically parallel potential flow, raising accordingly the crossflow stability limit and transition Reynolds number. This is apparently the case on a rotating disc where the boundary layer crossflow disturbance vortices, induced by centrifugal forces, diverge rather rapidly. The experimentally observed boundary layer crossflow stability limit and transition Reynolds numbers on a rotating disc have been substantially higher than Brown's theoretical values (ref. 61), which neglect the divergence of the boundary layer crossflow disturbance vortices and the radial variation of the mean boundary layer velocities. Again, since the lateral spread of the crossflow disturbance vortices on the side walls of supersonic two-dimensional nozzles is rather small over a chordwise length equal to the lateral vortex spacing, this favorable effect is probably minor and was therefore neglected.

The question arises concerning the choice of test section size, D or H , and unit length Reynolds number, U^*/ν^* . Since the purpose of quiet supersonic wind tunnels with laminarized nozzles and test sections is the simulation of supersonic flight conditions on test models, preferably at flight Reynolds numbers, it is desirable to obtain rather high test section Reynolds numbers. As a starting point, the test section height and unit length Reynolds number of the Tullahoma

A-supersonic tunnel at $M = 3$ and maximum tunnel pressure was chosen, i.e., $U^*/\nu^* = 26.22 \times 10^6/\text{m}$ and $D = H = 1 \text{ m}$ were assumed for the nozzle test sections. At this U^*/ν^* value, surface roughness should not yet cause premature transition on test models, especially at higher M^* .

With the Taylor-Goertler type boundary layer instability in the concave curvature region of the nozzle being particularly critical, the question arose as to how far the growth of TG disturbance vortices and the resulting transition might be controlled by the nozzle geometry. To determine if long, shallow, supersonic nozzles with a large throat surface radius ratio R/R_{th} are preferable to shorter rapid expansion nozzles with much smaller R/R_{th} ratios with respect to TG disturbances, R/R_{th} of the $M^* = 3, 5$, and 7 nozzles was varied over a wide range.

In view of the absence of boundary layer crossflow in axisymmetric nozzles and the resultant simpler analysis, emphasis was first given to these nozzles, starting at $M^* = 3$ and increasing M^* to $5, 7$, and 9 . After experience was gained on the laminarization problems of axisymmetric supersonic nozzles, the laminar boundary layer development and stability with area suction were analyzed on the floor, ceiling, and side walls of a $M^* = 4.6$ two-dimensional JPL supersonic nozzle for different conditions.

As a result of the high pressures in and shortly upstream and downstream of the throat region of high supersonic Mach number nozzles, the local unit length Reynolds numbers in this region become extremely high. Severe difficulties from surface roughness and suction-induced disturbances would thus be expected in this area. Furthermore, extremely high equivalent nozzle length Reynolds numbers, $\int (u/\nu) dx$, far beyond experimentally observed transition values would then result. These problems might be greatly alleviated by selecting, instead of air, a monatomic gas such as helium as the working medium. With $\gamma \equiv c_p/c_v = 1.66$ for helium, the nozzle pressure and density ratios between stagnation and the test section are substantially smaller than those for air, drastically reducing the local U/ν_e values in the sonic and low supersonic region of the nozzle. Accordingly, the nozzle wall boundary layer development and stability were analyzed for a slow expansion as well as a moderately rapid expansion $M^* = 9$ NASA helium axisymmetric nozzle ($U^*/\nu^* = 26.22 \times 10^6/\text{m}$, $D^* = 1 \text{ m}$). Of course, to properly simulate the flow on test models in such helium tunnels, the models should be modified according to the supersonic or hypersonic similarity law $t/l \sim \gamma^{0.5}$ at higher supersonic Mach numbers (ref. 62).

Analytical Results

Results of the overall boundary layer development with area suction on the nozzle walls of axisymmetric and two-dimensional supersonic tunnels are presented in tables 2 and 3 and figures 4-20 for various conditions. The stagnation temperature was chosen such as to avoid liquefaction of the working medium in the test section. (The geometry and the streamwise variation of the Mach

number M and potential flow velocity ratio U/U^* on the walls of the investigated nozzles are shown in table 1 and fig. 3.) Tables 2 and 3 present the following data for different streamwise stations of the investigated nozzles: the boundary layer momentum, displacement, and total thickness $\theta, \delta^*, \delta \equiv \delta_{u=0.99U}$; the boundary layer momentum thickness Reynolds number $Re_\theta \equiv U\theta/\nu_e$; the local suction mass flow rate $\rho_e v_o/\rho^* U^*$; the laminar friction coefficient c_f ; the temperature recovery factor RF ; and the thickness δ_s of the subsonic portion of the boundary layer. In some typical cases, the critical height y_{crit} of three-dimensional surface roughness (assuming a critical roughness Reynolds number $Re_k \equiv U_k y_{crit}/\nu_k = 200$) and the roughness unit length Reynolds number U/ν_k are presented. The corresponding test section unit length Reynolds number U^*/ν^* and test section diameter D^* in tables 2 and 3 were $26.22 \times 10^6/m$ and 1 m, respectively, except for the $M^* = 5$ rapid expansion and Q-nozzles without suction, for which $U^*/\nu^* = 6.9 \times 10^6/m$ and $R_{th} = 0.01007$ m ($D^* = 0.113$ m).

For aerodynamically similar boundary layers with the same nondimensional streamwise suction mass flow distribution $(\rho_e v_o/\rho^* U^*)\sqrt{Re_{ref}}$ at different nozzle reference Reynolds numbers Re_{ref} (for example, $Re_{ref} = U^* D^*/\nu^*$), the results of the boundary layer development analysis obtained at $U^* D^*/\nu^* = 26.22 \times 10^6$ ($D^* = 1$ m) can be converted to other $U^* D^*/\nu^*$ values by multiplying $\rho_e v_o/\rho^* U^*$, θ/R_{th} , δ^*/R_{th} , δ/R_{th} , δ_s/R_{th} with the factor $(26.22 \times 10^6/[U^* D^*/\nu^*])^{0.5}$ and Re_θ with $(26.22 \times 10^6/[U^* D^*/\nu^*])^{-0.5}$. The growth factor $\int \beta dx$ of Taylor-Goertler type disturbance vortices and the critical roughness height y_{crit} can thus be evaluated for other test section Reynolds numbers.

Figures 5-11 show the nondimensional boundary layer velocity and temperature profiles $u/U = f(y/\delta_{0.99})$ and $T_E = f(y/\delta_{0.99})$ at various streamwise stations x/R_{th} of the $M^* = 3, 5, 7, 9$ axisymmetric nozzles and the $M^* = 4.6$ JPL two-dimensional nozzle for different streamwise suction mass flow distributions (tables 2 and 3, fig. 4). For the total boundary layer thickness $\delta = \delta_{0.99}$, see tables 2 and 3. T_E is the nondimensional temperature ratio $T_E = T/M^{*2}(\gamma-1)T^*$, where T is the absolute temperature in the nozzle wall boundary layer at the nondimensional station $X' = x/R_{th}$ and T^* is the freestream absolute temperature in the test section.

The streamwise variation of the nondimensional TG vortex growth factor $\beta' \equiv \beta R_{th}$ as well as the integrated TG vortex growth factor $\int \beta dx$ is shown in figures 12-17 and tables 4-11 for the various axisymmetric nozzles and the $M^* = 4.6$ two-dimensional JPL nozzle (floor and ceiling walls) for different streamwise suction mass flow distributions.

The boundary layer crossflow profiles $w_n/U = f(y/\delta)$ on the side walls of the $M^* = 4.6$ two-dimensional JPL nozzle, induced by spanwise pressure gradients $\partial p/\partial z$ on the nozzle side walls (fig. 18), are shown in figure 20 and table 12 at the 75%, 50%, and 25% streamline height for different streamwise suction mass flow distributions (fig. 19). The corresponding values for U^*/ν^*

and H^* are $26.22 \times 10^6/\text{m}$ and 1 m, respectively. From these boundary layer crossflow profiles, the boundary layer crossflow Reynolds number $Re_n \equiv w_{n\max} \delta_{0.1}/\nu_e$ has been evaluated at various nozzle stations x/R_{th} for different streamwise suction mass flow distributions at the 75%, 50%, and 25% streamline height (figs. 21 and 22). ($\delta_{0.1}$ is the boundary layer thickness where the boundary layer crossflow velocity w_n is 10% of the maximum crossflow velocity $w_{n\max}$.) The maximum values of the boundary layer crossflow Reynolds number are tabulated in table 13.

Discussion of the Results

The suction system design of the nozzles and test sections of laminarized high Reynolds number supersonic tunnels is influenced by several closely interrelated and often conflicting requirements. For example, long shallow supersonic nozzles usually appear favorable for stabilization of the nozzle wall boundary layer against TG vortices in the concave curvature region of the nozzle. However, with the higher equivalent length Reynolds number of these nozzles, TS-type boundary layer instability is more difficult to control. Problems with surface roughness and certain suction-induced disturbances appear usually less difficult because of the thicker boundary layers of longer shallower nozzles. Therefore, the boundary layer development and stability analysis on the suction laminarized nozzle walls must be evaluated and discussed from the standpoint of TG- and TS-type boundary layer instability, surface roughness, and suction-induced flow disturbances with different suction methods, which may affect both the nozzle wall laminarization as well as the flow quality in the test section. In two-dimensional supersonic nozzles, boundary layer crossflow instability on the side walls and the resulting implications with respect to surface roughness and suction-induced disturbances must be considered. To arrive at a satisfactory compromise solution for suction laminarized supersonic nozzles of high Reynolds numbers, the above aspects must eventually be integrated. The individual problems are discussed separately below.

Taylor-Goertler Type Boundary Layer Instability

To avoid transition from excessively amplified TG vortices (i.e., to keep the exponent $\int \beta dx$ of the linearized TG vortex growth factor below the (subsonic) transition value of 10) in the concave curvature region of suction laminarized supersonic nozzles up to $M^* = 9$ at high U^*D^*/ν^* (up to 5×10^7),[†] the local TG vortex growth factor $B \equiv \beta \theta Re_\theta$ must be kept sufficiently small. This is accomplished by lowering the Goertler parameter $Re_\theta \sqrt{\theta/r}$ in the concave curvature region of the nozzle by removing a considerable percentage of the nozzle wall boundary layer by means of area suction at relatively high nondimensional suction mass flow rates $(\rho_e v_o / \rho^* U^*) \sqrt{Re_{ref}}$ (fig. 4,

[†]In contrast, TG boundary layer instability leads to strongly amplified TG vortices and transition (i.e., $\int \beta dx > 10$) at rather low $U^*D^*/\nu^* \approx 0.8 \times 10^6$ if suction is not applied (according to boundary layer development and TG stability calculations on $M^* = 5$ LARC rapid expansion and Q-nozzles; see tables 2l and 2m and figs. 13a and 13c). NASA Langley transition experiments on an $M^* = 5$ nozzle apparently confirm the existence of amplified TG disturbance vortices. The value $\int \beta dx$ for the start of transition at the downstream end of the nozzle seems to correlate closely with the experimental subsonic transition value of 10.

tables 2 and 3). In addition, to start with a sufficiently thin boundary layer and a correspondingly low Re_θ and $Re_\theta \sqrt{\theta}/r$ at the beginning of the concave curvature region, relatively strong suction must be used in the downstream area of the convex curvature region of the nozzle.

As compared to the low local suction rates required for the laminarization of low drag suction wings and bodies at high length Reynolds numbers in the absence of chordwise pressure gradients and TG boundary layer instability ($-v_o/U \sim 10^{-4}$ to 1.5×10^{-4}), the equivalent suction velocities v_o/U required for the stabilization of the supersonic nozzle wall boundary layer against TG vortices in the concave curvature nozzle area are often considerably larger. For example, $-v_o/U = 2.1 \times 10^{-4}$ in the upstream portion and 4×10^{-4} in the downstream portion of the concave curvature region of the $M^* = 5$ LARC Q-nozzle.

In spite of these relatively high nondimensional suction mass flow rates in the concave curvature region and the downstream areas of the convex curvature region, the absolute local suction mass flow rates and the total suction mass flow ratios that are required for the nozzle wall laminarization in the presence of TG instability at $U^*D^*/\nu^* = 2.6 \times 10^6$ are still surprisingly small. This can be explained by the very thin laminar nozzle wall boundary layers with suction at high U^*D^*/ν^* . For long, shallow, supersonic air nozzles, the total suction mass flow ratio for $\int \beta dx = 10$ varies from $\dot{m}_s/\dot{m}_o \cong 0.005$ at $M^* = 3$ to ~ 0.0105 at $M^* = 9$ (figs. 12-17 and tables 8-11). At constant U^*D^*/ν^* , $\int \beta dx$ decreases approximately linearly with increasing \dot{m}_s/\dot{m}_o ratios (fig. 17).

For the $M^* = 3$ nozzle ($R/R_{th} = 12$), the Taylor-Goertler vortex growth factor $\int \beta dx$ in the concave nozzle region was evaluated for different U^*/ν^* and with $D^* = 1$ m, i.e., for different $Re_{ref} = U^*D^*/\nu^*$. Various nondimensional suction mass flow distributions $(\rho_e v_o/\rho^* U^*) \sqrt{Re_{ref}}$ were chosen. The suction mass flow rates $\rho_e v_o/\rho^* U^*$ are then proportional to $Re_{ref}^{-0.5}$ and were chosen such that they corresponded with suction configurations 5, 8, and 9 at $U^*/\nu^* = 26.22 \times 10^6/\text{m}$ and $D^* = 1$ m.

According to figures 12h-j and tables 4b-g, 4j-o, and 8-11, $\beta' \equiv \beta R_{th}$ and $\int \beta dx$ increased with increasing U^*D^*/ν^* at a given $(\rho_e v_o/\rho^* U^*) \sqrt{Re_{ref}}$. Higher $(\rho_e v_o/\rho^* U^*) \sqrt{Re_{ref}}$ rates are then required to control TG boundary layer instability in the concave nozzle region, i.e., to keep $\int \beta dx \leq 10$ (fig. 12k). A larger percentage of the nozzle wall boundary layer must then be removed by suction. However, since the boundary layer thickness is inversely proportional to $\sqrt{U^*D^*/\nu^*}$, the total suction mass flow ratio \dot{m}_s/\dot{m}_o necessary to control TG boundary layer instability in the concave nozzle region was found to be nearly constant with increasing U^*D^*/ν^* ; see figure 12k. Similar calculations with the $M^* = 5$ Q-nozzle confirmed this result at higher M^* .

The high values for the adiabatic nozzle wall temperature recovery factor RF —especially in the downstream nozzle area—as well as the rapidly decreasing Re_θ in the downstream direction

(particularly in the local medium supersonic Mach number range of the nozzles) further indicate that a relatively large percentage of the nozzle wall boundary layer has been removed by area suction. Figure 11 shows nondimensional nozzle wall boundary layer temperature profiles $T_E = f(y/\delta)$ with area suction for various conditions. Tables 2 and 3 present the adiabatic nozzle wall temperature recovery factors RF for a series of cases. The boundary layer particles located further away from the wall, whose total temperatures are particularly high, are moved progressively closer toward the wall by relatively strong suction at high $(\rho_e v_o / \rho^* U^*) \sqrt{Re_{ref}}$ values, thus raising the adiabatic wall temperature recovery factor eventually to values slightly above 1 in the downstream nozzle areas. In contrast, the adiabatic wall temperature recovery factor of laminar supersonic nozzles without suction decreases from 0.84 in the throat region to a minimum value of 0.82 in the downstream nozzle area (tables 2l and 2m).

The streamwise variation of Re_θ is shown for different cases in figure 23 and tables 2 and 3. Re_θ increases usually to a maximum value at $M_{local} \cong 1.5$ to 2 and then decreases rather rapidly in the medium supersonic Mach number range of the nozzle as a result of the local flow acceleration and relatively strong suction. Toward the downstream end of the nozzle, the local surface friction coefficient c_f (see tables 2 and 3) generally increases considerably.[†] As the downstream end of the nozzle is approached, the pressure decreases at a slower rate, and Re_θ decreases then progressively slower (fig. 23, tables 2 and 3). In contrast, in supersonic nozzles without suction, Re_θ increases continuously in the downstream direction (see figs. 23c and 23d and tables 2l and 2m for $M^* = 5$ rapid expansion and Q-nozzles without suction).

The $Re_{\theta_{max}}$ values at the $M_{local} = 1.5$ to 2 nozzle station for $U^* D^* / \nu^* = 26.2 \times 10^6 / m$, $D^* = 1$ m, and $\int \beta dx \cong 10$ are:

M^*	3 (air)	5 (air)	7 (air)	9 (air)	9 (He)	9 (He)
r/R_{th}	12	Q-nozzle	75	200	250	NASA nozzle
$Re_{\theta_{max}}$	1660	2820	3500	5300	4160	2500

For comparison, laminar Re_θ values of 2500 to 3000 have been observed in the flat pressure region of an 8:1 fineness ratio low-drag-suction Reichardt body of revolution in the Ames 12-ft pressure tunnel at $Re_L = 57.8 \times 10^6$ body length Reynolds number (ref. 4).^{††} With the higher

[†]With the rapidly decreasing density in the downstream direction, the shear stress on the nozzle walls decreases substantially from a maximum in the high-pressure region of the nozzle throat to much lower values in the downstream nozzle areas, especially for the high supersonic Mach number nozzles (see, for example, table 2x).

^{††}Still higher $Re_{\theta_{laminar}}$ values of 5000 to 5500 were observed toward the rear end of this body. These high values can presumably be explained by the lateral compression of TS disturbance vortices when the body diameter decreases rapidly toward the rear end of the body. This lateral compression of the TS vortices reduces their kinetic energy and vorticity, thus raising the TS stability limit Reynolds number.

stability of supersonic laminar boundary layers with respect to TS disturbances, Re_θ values of 3000 to 4000 appear probably permissible, provided tunnel noise and nozzle inflow and suction-induced disturbances are drastically reduced.

To avoid excessively strong amplified boundary layer oscillations especially of the TS type in the low supersonic region of the $M^* = 7$ and 9 axisymmetric nozzles, the high $Re_{\theta_{\max}}$ values in this region may have to be reduced by further increasing the suction mass flow rates in the high subsonic, sonic, and low supersonic regions of the nozzles.

In general, the local Taylor-Goertler vortex growth factors $\beta' \equiv \beta R_{th}$ are especially large at the beginning of the concave surface curvature region of the nozzle, where the streamwise nozzle surface radius of curvature is minimum (figs. 12-17). Particularly high suction rates in and shortly upstream of this region appear advantageous to minimize the local growth of TG vortices in the most critical region. The $M^* = 9$ axisymmetric NASA helium nozzle has been particularly optimized in this respect, using the experience gained from the preceding analysis. Surprisingly small $\int \beta dx$ values are shown for this moderately rapid expansion $M^* = 9$ NASA helium nozzle (fig. 17).

Since Kobayashi's theoretical results (ref. 27) on the growth of TG vortices for the asymptotic suction profile with area suction were used for the analysis of the TG vortex growth factor in the suction laminarized supersonic nozzles, the question arises as to how closely asymptotic area suction has been approached in the concave curvature region of these nozzles. The calculated nozzle wall boundary layer profiles at various nozzle locations x/R_{th} for different cases (figs. 5-10) usually closely resemble the asymptotic area suction profiles on a flat plate at the same local supersonic Mach number (see fig. D-1 and table D-1 of appendix D). Therefore, asymptotic suction conditions are usually closely approached, at least in the downstream part of the nozzle. Furthermore, at the downstream end of the nozzles, the sum $c_f + 2\rho_e v_o / \rho_e U_{local} = 2(\partial\theta/\partial x)^\dagger \cong 0$, indicating that asymptotic suction conditions are closely approached at the downstream end of the nozzle. Boundary layer calculations in the test section downstream of the $M^* = 5$ axisymmetric LARC Q-nozzle—with $U^*/\nu^* = 26.2 \times 10^6/m$, $D^* = 1$ m, $T_{stag} = 400^\circ K$, $T_{wall_{ad}}$, and with suction configuration 5.3 continued in the test section at the same rate as at the downstream end of the nozzle—showed that Re_θ remained, indeed, practically constant along the test section wall, where the freestream velocity is constant. In other words, asymptotic suction conditions were again confirmed at the downstream end of the nozzle.

Further upstream in the concave nozzle wall curvature region, the local suction rates are approximately 10% to 20% lower than the asymptotic suction values. Therefore, Kobayashi's TG vortex growth factors (ref. 27) for the asymptotic suction profile might underestimate slightly the

[†]The pressure gradient term in the momentum equation vanishes at the downstream end of the nozzle.

TG vortex growth in suction laminarized supersonic nozzles. On the other hand, the use of the maximum local TG vortex growth factor $(\beta \theta \text{Re}_\theta)_{\max}$ at a given Goertler parameter $\text{Re}_\theta \sqrt{\theta/r}$ for the evaluation of $\int \beta dx$ in axisymmetric nozzles would partially compensate for the above-mentioned faster growth of TG vortices when suction is slightly weaker than asymptotic area suction. As mentioned previously, the locus $\beta \theta \text{Re}_\theta$ versus $\text{Re}_\theta \sqrt{\theta/r}$ does not follow the locus $(\beta \theta \text{Re}_\theta)_{\max}$ when the TG vortex spacing in axisymmetric nozzles varies in the downstream direction proportional to the local nozzle diameter. Both these effects are of minor importance and compensate each other. Therefore, the use of Kobayashi's results to evaluate the growth of TG vortices on the suction laminarized supersonic nozzle walls appears reasonably well justifiable, at least for axisymmetric nozzles at higher nozzle Reynolds numbers.

Since the nozzle wall boundary layer profiles closely approach asymptotic area suction profiles, they are highly stable against TS-type disturbances. Excessively amplified TS-type nozzle wall boundary layer oscillations then appear unlikely, provided tunnel noise and nozzle inflow and suction-induced disturbances are minimized. Therefore, with TS oscillations relatively weak, the coupling of amplified oblique TS waves with longitudinal TG vortices in the concave curvature region of the nozzles appears sufficiently weak to not significantly reduce the linearized TG growth factor exponent $\int \beta dx$ at transition.

Long, shallow, slow expansion supersonic nozzles with large throat surface curvature ratios R/R_{th} and correspondingly larger surface curvature radii in the concave region of the nozzle usually showed lower values for $\text{Re}_\theta \sqrt{\theta/r}$, βR_{th} and $\int \beta dx$ at a given total suction air mass flow ratio \dot{m}_s/\dot{m}_0 (or smaller \dot{m}_s/\dot{m}_0 ratios for a given value of $\int \beta dx$) as compared to shorter rapid expansion supersonic nozzles with small R/R_{th} (see fig. 17 and tables 8-11). Therefore, from the standpoint of TG instability in the concave nozzle areas, suction laminarized slow and moderately rapid expansion supersonic nozzles appear superior over rapid expansion nozzles, at least at moderately high M^* . Little is gained in this respect with the use of extremely slow expansion nozzles; the relatively high surface friction losses in the extensive low supersonic high-pressure region of such nozzles raises Re_θ and $\text{Re}_\theta \sqrt{\theta/r}$ to compensate for their larger surface radius of curvature. Furthermore, with their larger Re_{Lequ} and Re_θ , the nozzle wall boundary layers of long, slow expansion supersonic nozzles become more sensitive to Tollmien-Schlichting type boundary layer oscillations, particularly at high M^* and U^*D^*/ν^* , taking into account the fact that the flow acceleration (favorable for laminarization in the absence of boundary layer crossflow) is weaker as the nozzle length is increased. Suction laminarized high supersonic Mach number nozzles of high Reynolds numbers may then have to be designed as a compromise between the conflicting requirements to control the growth of TG- and TS-type disturbance vortices (see, for example, the $M^* = 9$ NASA helium nozzle). Moderately rapid expansion nozzles may therefore be the best overall design.

Influence of test section Mach number on TG instability.—According to figure 17 and tables 8-10, the suction mass flow ratios that are required to control TG boundary layer instability in the concave curvature region of the nozzle (i.e., $\int \beta dx \leq 10$) increase substantially with M^* from $\dot{m}_s/\dot{m}_0 = 0.005$ for $M^* = 3$ nozzles ($R/R_{th} = 6$ to 12) to 0.0105 for $M^* = 9$ nozzles ($R/R_{th} = 200$) over a wide range of $U^*D^*/\nu^* = 6 \times 10^6$ to 5×10^7 . The increase in \dot{m}_s/\dot{m}_0 with M^* is largely explainable by the rapidly increasing nozzle pressure and density ratios at higher test section Mach numbers M^* . As M^* increases, the local wall surface friction $c_f(\rho_e/2)U^2 2\pi r dx$ in the upstream low supersonic region of the nozzle—where the local density ρ_e and $\rho_e r U^2$ (see fig. 24) are particularly large—contributes an increasingly larger momentum loss to the nozzle wall boundary layers. Taylor-Goertler instability in high supersonic Mach number nozzles is further aggravated by the fact that the flow in the region of the convex nozzle surface curvature expands to higher velocities as M^* increases. The flow in the vicinity of the nozzle wall is therefore more strongly deflected from the axial direction and must then be returned to axial (parallel) flow in the test section over an increasingly larger streamwise distance at higher M^* . Indeed, the supersonic nozzle length $X_{supersonic}$ increases substantially with increasing M^* :

M^*	3 (air)	5 (air)	7 (air)	9 (air)	9 (He)	9 (He)
R/R_{th}	12	Q-nozzle	75	200	250	NASA nozzle
$X_{supersonic}/D^*$	2.8267	4.6917	5.619	7.214	8.683	7.024

With the longer nozzles and larger streamwise distances X at higher M^* , TG vortices grow to larger amplitudes, requiring further increased suction mass flow ratios to control TG instability in high supersonic Mach number nozzles.

Influence of moderate nozzle wall cooling on TG instability.—Boundary layer development calculations for the $M^* = 5$ LARC Q-nozzle without and with moderate surface cooling ($T_{stag} = 400^\circ K$, $T_{wall} = 300^\circ K$) for the same streamwise suction mass flow distribution (suction configuration 5.3) at $U^*D^*/\nu^* = 26.22 \times 10^6$ indicate higher Re_θ values and correspondingly increased values for the TG vortex growth exponent $\int \beta dx$ for the case of moderate surface cooling (tables 2h and 2i and fig. 13f). The larger θ and Re_θ values with nozzle wall cooling in strongly accelerated nozzle flow may be explained by the smaller ratio of boundary layer displacement to momentum thickness and the correspondingly lower pressure gradient term in the boundary layer momentum equation for $d\theta/dx$, which is negative for accelerated flow. Therefore, somewhat higher suction rates would be required with nozzle wall cooling to stabilize the supersonic nozzle wall boundary layer in the concave curvature region against TG-type instability. On the other hand, moderately cooled nozzle wall boundary layers should be considerably more stable with respect to Tollmien-Schlichting type boundary layer disturbances to enable substantially increased equivalent nozzle length Reynolds numbers with laminar flow. To minimize the suction mass flow rates

required for the laminarization especially of high supersonic Mach number nozzles at high U^*D^*/ν^* , it may be beneficial to moderately cool the upstream nozzle walls in the sonic and low supersonic region of the nozzle, where the nozzle wall has convex surface curvature and the local unit length Reynolds numbers are particularly high (as a result of the high local pressure and density). The stabilization of the nozzle wall boundary layer against TS-type disturbances in this particularly critical region would thus be optimized. Zero heat transfer or perhaps modest heating on the downstream concave nozzle wall surfaces might optimize the stabilization of the nozzle wall boundary layers against TG-type disturbances in this region.

Comparison of suction laminarized axisymmetric and two-dimensional supersonic nozzles with respect to TG-type instability.—According to boundary layer calculations with area suction on the walls of the axisymmetric $M^* = 5$ Q-nozzle and the floor and ceiling walls of the $M^* = 4.6$ two-dimensional JPL nozzle, the total suction mass flow ratios at $U^*D^*/\nu^* = U^*H^*/\nu^* = 2.6 \times 10^6$ that are required to avoid premature transition due to amplified TG vortices in the concave curvature region of these nozzles (i.e., to keep $\int \beta dx \leq 10$) were practically the same (fig. 17 and tables 9 and 13). Therefore, from the standpoint of TG instability on the floor and ceiling walls of two-dimensional supersonic nozzles, there is little to choose between two-dimensional and axisymmetric nozzles. The situation, however, will be completely different on the side walls of two-dimensional nozzles, where boundary layer crossflow considerations dominate.

Taylor-Goertler type boundary layer instability in axisymmetric high Mach number helium nozzles.—To substantially reduce the large nozzle wall boundary layer momentum loss and to thus minimize the suction mass flow ratios \dot{m}_s/\dot{m}_0 that are required for control of TG instability in the concave curvature region of the nozzle, monatomic gases such as helium appear highly attractive as the working medium. With the high ratio $\gamma = c_p/c_v = 1.66$ for helium, the nozzle pressure and density ratios between nozzle inlet and the test section are substantially smaller than those for air ($\gamma = 1.4$). Thus, the nozzle wall boundary layer momentum loss, contributed by the friction losses in the low supersonic, high pressure region of the nozzle and proportional to $\rho_e r U^2$ (fig. 24), is substantially reduced. Furthermore, due to the higher $\gamma_{He} = 1.66$, the temperature ratio between the wall and the potential flow region of the wall boundary layers is substantially larger than that for supersonic air nozzles, and the density ratio between the wall and the outer edge of the boundary layer decreases accordingly. As a result, the boundary layer thickness increases, reducing in turn the nozzle wall surface friction. Both effects substantially decrease the \dot{m}_s/\dot{m}_0 ratios that are required to avoid transition due to Taylor-Goertler disturbance vortices in the concave curvature region of the nozzle. Figures 9, 11i, and 17 and tables 2u-x and 6f-i show pertinent results of the nozzle wall boundary layer development and stability analysis for an axisymmetric slow expansion $M^* = 9$ helium nozzle ($R/R_{th} = 250$) as well as for a shorter, moderately rapid expansion $M^* = 9$ NASA helium axisymmetric nozzle. Both nozzles require practically the same \dot{m}_s/\dot{m}_0 ratios to control TG-type boundary layer instability. The equivalent length Reynolds number of the shorter NASA $M^* = 9$ helium nozzle, however, is about 40% smaller than that for the slow expansion nozzle.

Of course, the present analytical results on TG instability in supersonic area suction nozzles and the attendant basic feasibility of suction laminarized supersonic high Reynolds number nozzles and test sections critically depend on Kobayashi's results (ref. 27) on the stabilizing effect of area suction on the growth of TG disturbance vortices (fig. 2). If the TG stability results for solid walls (i.e., $v_0 = 0$) would have to be used, it is by no means certain that supersonic nozzles with high U^*D^*/ν^* can be laminarized by suction. $Re_\theta \sqrt{\theta}/r$ and Re_θ would have to be reduced to a much higher degree by drastically increasing suction to keep $\int \beta dx \leq 10$. For this reason, an experimental verification of Kobayashi's results on the stabilizing influence of area suction on TG instability appears crucially important.

Tollmien-Schlichting Type Boundary Layer Instability

As mentioned previously, the relatively high nondimensional suction rates required to control TG boundary layer instability in the concave curvature region of laminarized supersonic nozzles, combined with a moderately strong flow acceleration especially in the concave region, lead to nozzle wall boundary layer profiles in this region that closely resemble asymptotic suction profiles at high nozzle Reynolds numbers. Furthermore, Re_θ is relatively low over a large part of the concave curvature region of the nozzle and reaches higher values only in the low supersonic nozzle area. With the strong local flow acceleration in the sonic and low supersonic convex curvature region of the nozzle, much lower suction rates $-v_0/U \cong 10^{-4}$ to 2×10^{-4} appear to be adequate to stabilize the nozzle wall boundary layer in this region against amplified TS oscillations. The corresponding boundary layer profiles resemble asymptotic suction profiles also in the upstream sonic and low supersonic nozzle areas, where the local densities and unit length Reynolds numbers are particularly high and TS oscillations may be most strongly amplified. As a result, it does not appear too difficult to avoid excessively amplified TS nozzle wall boundary layer oscillations up to rather high U^*D^*/ν^* , at least at moderately high M^* , as long as nozzle inflow and suction-induced disturbances are drastically reduced.[†] Therefore, a detailed Tollmien-Schlichting stability analysis of the laminar nozzle wall boundary layer with area suction probably does not appear necessary up to moderately high M^* .

At very high supersonic M^* values, the equivalent nozzle length Reynolds numbers become very large as a result of the extremely high local unit length Reynolds numbers U/ν_e in the sonic and low supersonic nozzle region, where the pressure and density are particularly high. Figure 25 shows the variation of U/ν_e with M_{local} in supersonic air nozzles; indeed, U/ν_e increases to impractically high values in the low supersonic region of the $M^* = 7$ and 9 air nozzles. U^*/ν^* would therefore have to be reduced to avoid such excessively high local U/ν_e values in the high-pressure throat region of the nozzle.

[†]The minimum TS stability limit Reynolds number of the incompressible asymptotic area suction profile is $Re_{\theta \text{ stab limit}} = 35\,000$ (ref. 63) or 20 000 (C.C.Lin).

The corresponding equivalent nozzle length Reynolds numbers $Re_{L^{equ}}$ for $U^*D^*/\nu^* = 26.2 \times 10^6$ are plotted in figure 26, indicating extremely high $Re_{L^{equ}}$ of several 10^8 for the $M^* = 7$ and especially $M^* = 9$ slow expansion air nozzles. The fundamental question then arises concerning the maximum laminar flow length Reynolds number in subsonic and supersonic laminar flow that might be possible with drastically reduced external and suction-induced disturbances, with the boundary layer carefully stabilized by means of area suction such that the boundary layer stability limit Reynolds number for TS and other types of boundary layer oscillations is not appreciably exceeded. This question and suggestions for fundamental research in this direction, with the purpose of experimentally verifying laminar flow length Reynolds numbers up to several 10^8 , are discussed in more detail in reference 64.

With the present state of knowledge, one might speculate as follows about the maximum possible laminar flow length Reynolds numbers. In the Ames 12-ft tunnel, at 5 atmospheres tunnel pressure and a turbulence level $u'/U_\infty \cong 2 \times 10^{-4}$ (resulting primarily from acoustic tunnel disturbances), full length laminar flow was observed on an 8:1 fineness ratio low-drag-suction Reichardt body of revolution up to $Re_L = 57.8 \times 10^6$ by means of suction through closely spaced fine slots (ref. 4). At higher Re_L , laminar flow was abruptly lost, and transition jumped immediately to the front of the body, presumably due to a roughness speck located in the front of the model. Somewhat higher transition Re_L values might have been possible in the absence of such roughness. The body drag, though, already started leveling out somewhat at 57.8×10^6 , indicating that the upper Re_L limit might have been closely approached. Therefore, one might speculate that an upper limit on this model in the Ames 12-ft tunnel would be $Re_L = 65 \times 10^6$ in the absence of such roughness. At further reduced external disturbance levels, such as under atmospheric flight conditions, $Re_L = 10^8$ might be possible with a similar suction model.

A still closer approach toward the aerodynamically ideal area suction and a progressively more sophisticated and careful suction design with correspondingly weaker suction-induced disturbances might push $Re_{L^{laminar}}$ to 2×10^8 and perhaps 3×10^8 under ideal conditions in subsonic flow. With the higher boundary layer stability limit Reynolds numbers at supersonic speeds in the absence of boundary layer crossflow disturbance vortices, etc., still higher transition length Reynolds numbers appear feasible under ideal conditions, at least in the absence of boundary layer crossflow and TG-type disturbance vortices.

How far $Re_{L^{laminar}}$ may eventually be pushed by suction, etc. may be a mute question. According to theory, the upper laminar flow length Reynolds number limit can, in principle, be pushed to increasingly higher values by avoiding an excessive growth of all possible kinds of laminar boundary layer oscillations that may develop in that Reynolds number range and cause transition. In principle, this can be accomplished by drastically reducing or eliminating external and suction-induced disturbances, by stabilizing the boundary layer progressively more carefully, and by

approaching the aerodynamic ideal of area suction increasingly closer at higher Re_L . Low drag suction experiments, indeed, have verified substantial jumps in $Re_{L_{laminar}}$ whenever critical external disturbances were reduced or when suction was further refined and laid out such as to cope with newly discovered and hitherto unknown boundary layer instabilities (such as the boundary layer crossflow instability or the flow instability at the front attachment line of swept wings), which had not been experienced at lower Re_L and had been discovered only at further increased Re_L .

Similarly, in the pursuit of laminarization at increasingly higher Re_L , one should be prepared for other new and hitherto unknown types of boundary layer instabilities that may eventually limit $Re_{L_{laminar}}$ or require further refinements to push $Re_{L_{laminar}}$ again higher. Only careful transition experiments with distributed suction and minimized disturbances at very high length Reynolds numbers can lead to the discovery of such new and as yet unknown boundary layer instabilities. One might perhaps speculate in this respect that distributed surface roughness or aerodynamic roughness induced, for example, by suction through finely perforated surfaces generates weak streamwise boundary layer vorticity. This vorticity may couple for example with amplified oblique Tollmien-Schlichting waves, etc. to eventually lead to a more rapid growth of laminar boundary layer oscillations and finally transition. The corresponding roughness Reynolds number $Re_k \equiv u_k k / \nu_k$ —based on roughness height k , and the velocity u_k and kinematic viscosity ν_k at the height of the roughness—may then be far too small to induce transition directly by the breakup of horseshoe disturbance vortices immediately downstream of the roughness elements. Raetz's nonlinear boundary layer stability theory (see appendix C) may serve as a guide to anticipate such hitherto unknown more complicated boundary layer instabilities.

With the much lower pressure and density ratios of high supersonic Mach number nozzles using helium instead of air as the working medium, the local unit length Reynolds numbers U/ν_e in the nozzle sonic and low supersonic region are considerably reduced (see fig. 27 for $M^* = 7$ and 9 helium nozzles at $U^*/\nu^* = 26.22 \times 10^6/m$ at the nozzle exit). The corresponding equivalent length Reynolds number of a $M^* = 9$ helium nozzle is about half as large as for $M^* = 9$ air nozzles (fig. 26). At the same time, as a result of the much lower U/ν_e values in the sonic and low supersonic region of helium nozzles, surface roughness is much less critical than that for high supersonic air nozzles. Furthermore, with the much thicker subsonic layer δ_s in helium nozzles, test section flow irregularities induced by suction through perforated surfaces become substantially less critical than those for high M^* air nozzles of the same U^*/ν^* and D^* . These aspects are discussed in more detail in the following sections. For these reasons, suction laminarized helium nozzles appear particularly attractive for quiet high supersonic Mach number tunnels with high test section Reynolds numbers.

The streamwise suction mass flow distribution at different streamline heights h on the side walls of the $M^* = 4.6$ JPL two-dimensional nozzle, operating at $U^*D^*/\nu^* = 26.22 \times 10^6$ (see fig. 19 and table 3), were chosen such as to prevent premature transition due to boundary layer crossflow instability. This instability is caused by spanwise pressure gradients normal to the potential flow streamlines (fig. 18) induced by streamline curvature. The boundary layer crossflow profiles $w_n/U = f(y/\delta)$ are shown in figure 20 at various nozzle stations x/R_{th} for different suction distributions at the 75%, 50%, and 25% streamline height. They usually resemble the boundary layer crossflow profiles in the leading edge and flat pressure region of swept low drag suction wings (ref. 16), whose minimum crossflow stability limit Reynolds number X_{min} in this region is about 100 (refs. 16 and 61). Assuming that X_{min} can be exceeded by a factor of 1.8 to 2 (as on swept low drag suction wings [ref. 16]) and perhaps 3, the maximum permissible crossflow Reynolds number for laminar two-dimensional nozzle side wall boundary layers would then be $Re_n = 200$ to perhaps 300. These crossflow Reynolds number limitations require relatively high suction mass flow rates on the nozzle side walls at the 75%, 50%, and even 25% streamline height (fig. 19 and table 12). These suction rates are substantially larger than those required to control TG- and TS-type boundary layer instability on the floor and ceiling walls of this two-dimensional JPL nozzle.

In the upstream convex curvature region of the JPL two-dimensional nozzle, the static pressure decreases from the nozzle axis toward the nozzle corners. The resulting boundary layer crossflow is then directed toward these corners. In the downstream concave curvature region, the spanwise (i.e., normal to the streamlines) pressure gradients and the resulting boundary layer crossflow are directed in the opposite direction.

With the high suction rates on the two-dimensional nozzle side walls, the streamwise boundary layer profiles are highly stable with respect to TS-type disturbances; furthermore, Re_θ on the side walls is rather small along the entire nozzle length and substantially lower than on the nozzle floor and ceiling walls (fig. 23h and table 12). No difficulties should therefore be expected from amplified TS-type oscillations. However, with the extremely thin nozzle side wall boundary layers (table 12), resulting from the high suction rates to control boundary layer crossflow, surface roughness and disturbances induced, for example, by suction through finely perforated surfaces on the nozzle side walls may become critical, especially at higher test section unit length Reynolds numbers U^*/ν^* .

In view of the severe boundary layer crossflow problems on the nozzle side walls of two-dimensional supersonic nozzles and their corner laminarization problems, two-dimensional suction laminarized high Reynolds number supersonic nozzles and test sections may be limited to test section Mach numbers $M^* \leq 5$ and relatively low test section unit length Reynolds numbers $U^*/\nu^* \leq 10^7/m$.

The question arises concerning the critical height y_{crit} of three-dimensional roughness particles located at various streamwise locations of suction laminarized supersonic wind tunnel nozzles. These particles might cause transition directly immediately downstream of the roughness elements as a result of the breakup of horseshoe vortices, which are shed periodically from the roughness elements. Therefore, y_{crit} was evaluated for axisymmetric suction laminarized $M^* = 3, 5$, and 9 slow expansion supersonic nozzles, using air as the working medium, as well as for a slow expansion and moderately rapid expansion NASA $M^* = 9$ helium nozzle at $U^*/\nu^* = 26.22 \times 10^6/\text{m}$ and $D^* = 1$ m. The suction rates were chosen so that transition due to TG vortices would be avoided (i.e., $\int \beta dx \leq 10$). Insulated nozzle walls were assumed. A critical roughness height Reynolds number $Re_k = 200$ was specified for transition, assuming flat cylindrical roughness particles (see, for example, refs. 65-70). Re_k is based on local conditions at the height $k = y_{crit}$ of the roughness element: $Re_k = u_k k / \nu_k$.

Figures 28-30 (see also table 14) show plots of $y_{crit} = f(M_{local})$ for the $M^* = 3, 5$, and 9 supersonic air nozzles and for the $M^* = 9$ helium nozzles. In the high subsonic, sonic, and low supersonic throat region particularly of the higher supersonic Mach number nozzles, y_{crit} is very small because of the very thin nozzle wall boundary layers and the high local unit length Reynolds numbers U/ν_e in this region. (Under otherwise the same conditions, the boundary layer thickness and y_{crit} vary inversely proportional to U/ν_e .) The minimum values for y_{crit} in the nozzle throat region at $U^*/\nu^* = 26.22 \times 10^6/\text{m}$ and $D^* = 1$ m are:

M^*	3 (air)	5 (air)	9 (air)	9 (He)
y_{crit} , mm	0.017	0.008	0.0015	0.008

The value $y_{crit} = 0.0015$ mm for supersonic $M^* = 9$ air nozzles is extremely small. It is obvious that the respective $(U/\nu_e)_{max}$ values of $4 \times 10^8/\text{m}$ and $9 \times 10^8/\text{m}$ at the $M_{local} = 1.2$ station of the $M^* = 7$ and 9 air nozzles (fig. 25) appear impractically high for nozzle laminarization by means of distributed suction; the extremely small surface roughness tolerances at such high U/ν_e values would require nearly mirrorlike surface finishes. The question therefore arises as to how far to push U/ν_e with laminarized suction surfaces. In this respect, the experience gained from transition experiments in ballistic ranges, where extremely high unit length Reynolds numbers are encountered, is valuable. On one hand, though, the supersonic test Mach numbers in these experiments were rather high; the model surfaces, on the other hand, were usually strongly cooled. On some of these ballistic models, extensive laminar flow had been observed at length and unit length Reynolds numbers $Re_L \cong 10^7$ and $U_\infty/\nu_\infty = 1.6 \times 10^8/\text{m}$, respectively. Accepting tentatively

this limitation for U/ν_e at the $M = 1.2$ nozzle station, the test section unit length Reynolds number and permissible surface roughness height in the nozzle throat area would thus be limited to the following values for a test section Reynolds number $U^*D^*/\nu^* = 26 \times 10^6$:

M^*	3 (air)	5 (air)	7 (air)	9 (air)	7 (He)	9 (He)
$10^{-6}(U^*/\nu^*)/m$	50-55	27.7	10.4	4.6	35.2	24.2
y_{crit}, mm	0.008	0.008		0.0085		0.0085

The maximum permissible U^*/ν^* from the standpoint of surface roughness in the nozzle throat region thus decreases rapidly with increasing M^* to rather low values for the $M^* = 9$ air nozzle. Correspondingly larger tunnel dimensions are then necessary to achieve a given U^*D^*/ν^* at higher M^* .

The use of helium instead of air as the working medium in laminarized supersonic tunnels enables substantially higher U^*/ν^* and correspondingly smaller test section and tunnel dimensions at a given U^*D^*/ν^* before wall surface roughness in the nozzle throat region becomes critical.

At $M^* \leq 5$, wall surface roughness in the throat region of axisymmetric supersonic air nozzles does not appear excessively critical at $U^*/\nu^* \leq 25 \times 10^6/m$. The use of helium and the resulting complications in properly designing and evaluating supersonic experiments at $\gamma = 1.66$ thus does not appear justifiable at Mach numbers less than 5.

Figures 29 and 31 and tables 2u, 2x, and 14 show the unit length Reynolds number U/ν_k (based on ν_k at the height of the roughness particle and U) at various nozzle stations. A very rapid decrease of U/ν_k from the nozzle throat area toward the nozzle exit is indicated.

With the very thin side wall boundary layers in the throat region of laminarized two-dimensional supersonic wind tunnel nozzles, resulting from the high suction rates to control boundary layer crossflow on the nozzle side walls, surface roughness becomes much more critical. Thus, U^*/ν^* may have to be limited to considerably lower values ($U^*/\nu^* \leq 10^7/m$ at $M^* = 5$).

As compared to the nozzle throat area, substantially increased surface roughness appears permissible in the medium and particularly high supersonic Mach number regions (figs. 28-30) because of the rapidly decreasing roughness unit length Reynolds number U/ν_k at higher local M values in the downstream nozzle areas (figs. 29 and 31), at least for insulated nozzle walls. With $\nu_k = \mu_k/\rho_k = \mu_k(T) R T_k/p$, ν_k grows rapidly at higher local M as a result of the decreasing pressure at increasing M . The boundary layer temperature T_k at the top of the roughness element for insulated nozzle walls with area suction is usually somewhat lower than the nozzle stagnation

temperature. Therefore, surprisingly large surface roughness heights appear permissible in the downstream high Mach number regions of the nozzles and test sections of laminarized high supersonic Mach number tunnels, at least for insulated nozzle walls.

It might be cautioned that the above evaluation of the permissible nozzle wall roughness applies to isolated three-dimensional surface roughness in the absence of strongly amplified boundary layer oscillations. Streamwise boundary layer disturbance vortices, shed by subcritical three-dimensional surface roughness elements, may get distorted three-dimensionally for example by amplified oblique Tollmien-Schlichting waves. During this process they are stretched and thus increase their kinetic energy and vorticity. As a result, they can develop into highly unstable hairpin-type vortices, which break up and thus cause transition at Re_k values lower than those found in the absence of such amplified TS oscillations. If this hypothesis should prove correct, increased difficulties should be expected with three-dimensional surface roughness in the presence of amplified TS and possibly other types of boundary layer oscillations. This hypothesis seems to be confirmed by the fact that substantially fewer difficulties have usually been experienced with three-dimensional surface roughness in flight (where atmospheric turbulence has only an insignificant influence on amplified boundary layer oscillations and transition) as compared to low-turbulence wind tunnel experience.

Furthermore, the above evaluation of the permissible surface roughness does not necessarily apply to distributed three-dimensional roughness, either in the form of actual surface roughness or aerodynamic roughness induced by suction through perforated surfaces. The roughness-induced disturbance vorticity may adversely couple with various types of amplified boundary layer oscillations. Some of these problems will be discussed in more detail in the next section.

DETAILED CONSIDERATIONS OF SUCTION THROUGH PERFORATED SURFACES

Influence of Suction-Induced Disturbances on the Nozzle Wall Boundary Layer

Disturbance vortices originating from the suction holes of the perforated suction surfaces of laminarized supersonic wind tunnel nozzles can influence the laminar boundary layers on the nozzle walls in several ways (see, for example, refs. 38 and 64). In contrast to suction through uniform spanwise slots, the boundary layer profile downstream of a suction hole and the spanwise boundary layer vorticity component $\omega_z = 0.5 (\partial v / \partial x - \partial u / \partial y)$ vary in the spanwise direction, thus generating streamwise boundary layer disturbance vorticity ω_x . Boundary layer suction through holes then affects a laminar boundary layer in a manner similar to three-dimensional surface roughness. Longitudinal and horseshoe-type vortices originate from the holes and often cause premature transition (refs. 39-48). Full-length laminar flow on perforated LFC surfaces is therefore possible

only as long as these suction-hole-induced disturbance vortices, combined possibly with streamwise boundary layer crossflow and/or Taylor-Goertler disturbance vortices, are sufficiently weak to avoid premature transition.

Three-dimensional surface roughness elements or aerodynamic roughness induced by suction holes, arranged in one or only a few spanwise rows, generally cause transition directly without the intermediate mechanism of amplified boundary layer oscillations (see, for example, refs. 39-45).[†] With coarsely spaced suction holes or at low suction rates per hole, streamwise disturbance vortices originate from the holes and trail in the downstream direction. They become unstable at higher suction rates per hole and start oscillating, until they disintegrate or "explode" to start transition. At smaller spanwise hole spacings and higher suction rates per hole, horseshoe-type disturbance vortices are shed periodically between adjacent suction holes. As they move downstream they are pulled away from the wall and at the same time stretched in the streamwise direction, thereby rapidly increasing their kinetic energy and vorticity, until they become unstable and disintegrate to start transition in the same manner as that downstream of three-dimensional surface roughness elements. With closely spaced holes at low suction rates, these horseshoe vortices may be dissipated by viscosity without causing transition.

Substantially higher critical suction flow rates per hole have been observed with very small spanwise hole spacings when the suction forces in the holes are sufficiently large to prevent the shedding of horseshoe vortices. Standing vortices are then formed between adjacent suction holes. Such rows of very closely spaced holes with standing vortices (without trailing vortices) act like suction slots (ref. 44). When a particular suction hole was plugged, however, unstable horseshoe vortices originated between the holes adjacent to this hole and lowered the critical suction rate per row of holes by a factor of 20. Such rows of very closely spaced suction holes are therefore very sensitive to surface clogging.

For a single spanwise row of circular suction holes, figure 32 shows the variation of the critical suction flow Reynolds number $(\bar{u}\bar{h}/\nu)_{\text{crit}}$ (where \bar{u} = average velocity in the sucked layer, \bar{h} = average height of the sucked layer) versus the ratio of spanwise hole spacing α to h , as measured and explained by Goldsmith, Meyer, and Pfenninger (refs. 39-45). The $(\bar{u}\bar{h}/\nu)_{\text{crit}}$ of a single row of suction holes varies from 40 to 70 over a wide range of α/h . These critical suction hole flow Reynolds numbers correlate reasonably closely with the critical roughness Reynolds numbers of a spanwise row of three-dimensional roughness particles, if the maximum height of the sucked layer and the corresponding boundary layer velocity at this location are chosen for the evaluation of the critical suction flow Reynolds number.

[†]Similar results have been obtained at the NPL in Teddington, England, at Wortmann's Institute in Stuttgart, Germany, and at the Institute for Theoretical and Applied Mechanics, Akademgorodok, Novosibirsk, USSR.

For larger chordwise suction distances, the question arises concerning the critical suction hole Reynolds number $(\bar{u}h/\nu)_{\text{crit}}$ when suction is applied through a series of spanwise rows of holes instead of a single one. Since the suction-hole-induced streamwise boundary layer disturbance vortices decay relatively slowly in the downstream direction except at very low Reynolds numbers $\bar{u}h/\nu$ (according to smoke and naphthalene spray observations as well as boundary layer crossflow calculations at zero pressure gradient without suction), boundary layer disturbance vortices originating from the suction holes of different rows often superimpose to increase the suction-hole-induced streamwise boundary layer disturbance vorticity ω_x . As a result, the critical suction rate per hole and the critical hole flow Reynolds number often decrease substantially with increasing number of spanwise rows of holes, depending on the stagger angle and the geometry of the suction hole pattern. For example, for 10 rows of relatively coarsely spaced suction holes, with each row of holes displaced spanwise against each other by half the spanwise hole spacing, Goldsmith (ref. 41) obtained only half as high a critical suction rate and $(\bar{u}h/\nu)_{\text{crit}}$ per row as with a single row of holes. The analysis of M. Head's flight LFC experiments (unpublished) on a perforated Vampire wing glove with randomly spaced holes also shows substantially lower $(\bar{u}h/\nu)_{\text{crit}}$ per row of holes. Even lower values were often observed by Head on the same Vampire wing glove when regular instead of random suction hole spacings were chosen. With certain suction hole patterns, transition could be delayed to much higher length Reynolds numbers than for others, and the transition location was critically influenced when the test surface was yawed by small amounts.

Very similar results were obtained by Raspet and Carmichael on a perforated low drag suction glider wing up to $Re_c \leq 5 \times 10^6$ (refs. 46 and 47), as well as by Wortmann and Feifel (Stuttgart) on a 19% thick perforated low drag suction wing of 6% camber up to $Re_c \leq 4 \times 10^6$ (ref. 48). In these experiments, suction has been applied through spanwise rows of closely spaced suction holes. On the Stuttgart suction wing, full chord laminar flow was maintained uniformly along the entire model span at lower Re_c , while turbulent wedges started often far upstream at higher Re_c (4 to 5×10^6) presumably as a result of the breakup of the suction-hole-induced streamwise disturbance vortices. Yet, compared for example to low drag suction experiments in the Northrop 7- by 10-ft tunnel, with suction applied through closely spaced spanwise slots when suction-induced streamwise disturbance vortices were essentially absent, the very low turbulence level of the Stuttgart tunnel could have enabled laminarization up to $Re_c \cong 2 \times 10^7$. Therefore, the suction-hole-induced boundary layer disturbance vortices rather than wind tunnel or atmospheric turbulence must have caused transition at the relatively low wing chord Reynolds numbers of Raspet's as well as Wortmann's and Feifel's experiments.

During further suction experiments by Wortmann and Feifel on a perforated laminar flat plate, transition could be shifted over considerable chordwise distances by varying the yaw angle of the plate by surprisingly small amounts, confirming Head's experience. Transition presumably started

when the resultant streamwise boundary layer disturbance vorticity, intensified by the various rows of suction holes, increased until the suction-hole-induced streamwise vortices became unstable and started oscillating to distort finally into highly unstable hairpin vortices, which disintegrated to cause transition. Amplified Tollmien-Schlichting waves cannot explain the observed sudden shift of transition at small yaw angles. Therefore, they do not appear responsible for transition in the above-described experiments.

To avoid premature transition due to the breakup of the suction-hole-induced streamwise disturbance vortices, the Reynolds number of the boundary layer crossflow generated by these streamwise disturbance vortices should be kept below its corresponding boundary layer crossflow stability limit Reynolds number. At increasingly higher Re_L , this requirement dictates much smaller mean suction flow Reynolds numbers $\bar{u}h/\nu$ per row of holes than for a single row of suction holes, leading to perforated suction surfaces with an extremely large number of very closely spaced suction holes. This may become possible with advanced hole-drilling techniques, using for example electron-beam or laser-beam drilling. With such closely spaced small suction holes, the suction-induced streamwise disturbance vortices would be confined to the slowest part of the boundary layer. The "crossflow Reynolds number" of the suction-hole-induced streamwise disturbance vortices is then sufficiently low so that the viscous forces can dominate over the corresponding pressure and inertia forces to thus dissipate these vortices more rapidly. It would be ideal if the generation of suction-hole-induced new streamwise disturbance vorticity could be just compensated by viscous dissipation at particularly low vortex "crossflow Reynolds numbers" and suction flow rates per hole using a correspondingly large number of closely spaced holes. The suction-induced streamwise disturbance vorticity would then remain insignificant along the entire length of the suction region.

The laminarization of the nozzle wall boundary layers by means of suction through finely perforated surfaces appears more complicated when the suction-hole-induced streamwise disturbance vortices interact with various kinds of amplified boundary layer oscillations. For example, amplified Taylor-Goertler type disturbance vortices in the concave curvature region of supersonic nozzles or boundary layer crossflow disturbance vortices on the side walls of two-dimensional supersonic nozzles (and on swept wings) may superimpose the suction-hole-induced streamwise disturbance vortices to cause premature transition. It may then be necessary to further reduce the suction-hole-induced streamwise disturbance vorticity by using a correspondingly larger number of still finer and more closely spaced suction holes.

For the same purpose, the growth of TG vortices (in the concave curvature regions of the nozzle) and boundary layer crossflow vortices (in regions of spanwise pressure gradients) may have to be restricted by increasing the local suction rates, as compared to the case of ideal area suction without suction-hole-induced streamwise disturbance vortices. Admittedly, with an extremely large

number of very closely spaced suction holes and correspondingly small suction rates per hole, the suction-induced streamwise disturbance vortices are confined to the innermost, slowest boundary layer region, while the disturbance velocities induced by TG and boundary layer crossflow disturbance vortices are usually largest at relatively large wall distances for many cases of practical interest (refs. 26 and 61). Therefore, the interaction of amplified TG and boundary layer crossflow disturbance vortices with suction-hole-induced streamwise vortices may often be insignificant with thicker boundary layers, as long as area suction is very closely approached with perforated surfaces having an extremely large number of very closely spaced electron-beam-drilled suction holes.

Suction-hole-induced streamwise disturbance vortices may couple with various kinds of amplified boundary layer oscillations to substantially lower the "crossflow transition Reynolds number" of the suction-induced streamwise vortices by nonlinear cross-coupling with these boundary layer oscillations. Nonlinear boundary layer stability must then describe the resulting boundary layer disturbance growth (see, for example, appendix C). In particular, amplified oblique Tollmien-Schlichting type boundary layer oscillations, excited by external disturbances such as turbulence, noise, etc., will distort the suction-hole-induced streamwise disturbance vortices three-dimensionally, thereby stretching them and thus increasing their kinetic energy and vorticity. As a result, their "crossflow" stability limit and transition Reynolds numbers decrease below the values found in the absence of such TS oscillations. This destabilizing influence of amplified oblique Tollmien-Schlichting waves on boundary layer crossflow disturbance vortices has, indeed, been verified on swept low drag suction wings in the presence of external and internal sound (refs. 17 and 60). In other words, if amplified TS wall boundary layer oscillations in laminarized supersonic wind tunnel nozzles cannot be avoided, the suction-hole-induced streamwise boundary layer disturbance vorticity may have to be still further reduced by using perforated nozzle wall suction surfaces with a correspondingly larger number of finer and more closely spaced suction holes.

When the streamwise spacing of the suction hole rows coincides with the wavelength of strongly amplified TS oscillations and the suction-hole-induced disturbance vortices are located in the critical boundary layer region where the TS disturbance velocities are particularly large, suction-hole-induced streamwise disturbance vortices may drive amplified TS oscillations very rapidly to large amplitudes—even at very low mean suction flow Reynolds numbers $\bar{u}h/\nu$ per row of suction holes—to cause premature transition. This condition exists with thin boundary layers and relatively large streamwise suction hole row spacings, as confirmed by transition experiments (ref. 71) at the front attachment line of a 45° swept blunt-nosed wing, with suction applied along the attachment line through chordwise rows of 0.15-mm i.d. suction holes (3.00-mm spacing in and 0.70-mm spacing normal to the flow direction). Comparison experiments (ref. 72) on the same model, with suction applied in the front wing attachment line region through 0.05-mm-wide chordwise nose slots of 6.00-mm spacing, have shown drastically the destabilizing influence of suction-hole-induced disturbance vortices on transition at the front wing attachment line. With

suction through chordwise rows of suction holes, substantially lower attachment line boundary layer Reynolds numbers $Re_{\theta_{al, tr}}$ at the beginning of transition were observed even at very low suction velocities, as compared to suction through chordwise slots (fig. 33). For example, at $v_O^* \equiv v_O (\nu [\partial U / \partial s]_{al})^{-0.5} = -0.25$, $Re_{\theta_{al, tr}} = 250$ with suction through holes, as compared to $Re_{\theta_{al, tr}} = 350$ at $v_O^* = -0.10$ with suction through slots (both at a spanwise length Reynolds number $Wz/\nu = 5 \times 10^6$ along the attachment line), as measured in the 7- by 10-ft Northrop low-turbulence tunnel. At $v_O^* = -0.25$, the corresponding critical suction hole Reynolds number $(\bar{u}h/\nu)_{crit} \cong 2$ to 3 is very much lower than Goldsmith's critical values for a single row or several rows of suction holes. Even at lower suction rates ($v_O^* = -0.1$) and $\bar{u}h/\nu = 1$, transition at the attachment line still seemed to be adversely affected by the suction-hole-induced streamwise disturbance vortices. Such disturbance vortices, originating from the suction holes, were indeed observed on the perforated attachment line suction strip by means of naphthalene sublimation techniques over a wide suction range (fig. 34). At the above low mean suction flow Reynolds numbers per row of holes, the longitudinal disturbance vortices originating from the suction holes should have been much too weak to cause transition directly, unless they could have induced amplified attachment line boundary layer oscillations. The presence of increasingly stronger attachment line boundary layer oscillations at higher suction rates in the perforated wing attachment line suction strip was verified by boundary layer stethoscope and hot-wire observations. At a given suction velocity v_O^* and tunnel speed, the suction-hole-induced boundary layer oscillations grew rapidly with increasing attachment line length. For comparison, practically no amplified boundary layer oscillations were observed at the same condition with suction through slots, indicating that the suction-hole-induced disturbance vortices rather than tunnel turbulence and noise must have caused transition on the perforated attachment line. Suction through closely spaced chordwise nose slots was therefore superior to suction through chordwise rows of closely spaced holes in stabilizing the attachment line boundary layer.

Admittedly, due to the stretching of TS vortices in the diverging attachment line flow field of swept wings, its front attachment line boundary layer is particularly sensitive to external turbulence, noise, or suction-hole-induced disturbance vortices. Furthermore, the 3.00-mm suction hole row spacing in the direction of the attachment line flow closely coincided with the wavelength of the most strongly amplified attachment line boundary layer oscillations, causing particularly strongly amplified boundary layer oscillations under the action of such suction-hole-induced disturbance vortices.

The destabilizing nonlinear coupling between suction-hole-induced streamwise boundary layer disturbance vortices with amplified boundary layer oscillations of, for example, the TS type appears far less critical when the streamwise spacing of the suction holes is very much smaller than the wavelength of such boundary layer oscillations ($\lambda_{TS} \cong 75\delta^* \cong 150\theta$ for the incompressible asymptotic suction profile) and when the suction-hole-induced vortices are confined to the

innermost wall boundary layer region, where TS disturbance velocities are much smaller. Again, this requirement dictates very small ratios of suction hole size and spacing to boundary layer thickness, leading to an extremely large number of very fine and closely spaced suction holes. Therefore, in suction laminarized supersonic wind tunnel nozzles, particularly small and closely spaced suction holes appear necessary in the sonic and low supersonic nozzle region, where the nozzle wall boundary layers are particularly thin. In contrast, substantially larger suction holes of larger spacing appear permissible in the downstream nozzle region, where the nozzle wall boundary layers are much thicker, especially at higher supersonic test section Mach numbers.

In addition to laminarized supersonic wind tunnel nozzles, the approach of ideal area suction through perforated surfaces with very small, closely spaced (electron-beam drilled) suction holes may be of more general interest to future boundary layer suction airplanes and turbomachines. If it should prove possible to approach area suction more closely, laminarization by means of suction may be feasible at further increased length Reynolds numbers.

The following values are presented for incompressible asymptotic flat plate boundary layer suction profiles when suction is applied through very fine perforated suction surfaces:

$\frac{U}{\nu} \times 10^6/m$	10	100	1	10	10
$-10^4 \frac{v_o}{U}$	1	1.5	2.5	2.5	2.5
Re_θ^\dagger	5000	3333	2000	2000	2000
θ , mm	0.5	0.033	2.0	0.2	
Suction hole spacing, mm	0.5	0.2	1.0	0.1	0.5
$\frac{-v_o \Delta X}{\nu} \equiv \frac{\bar{u} \bar{h}}{\nu}$	0.5	2	0.25	0.25	1.25
u/U (two-dimensional)	0.0049	0.0119	0.0055	0.0055	0.0122
\bar{h} , mm	0.0102	0.00168	0.0459	0.00459	0.0102
$\frac{u_{\max}^{\dagger\dagger}}{U}$	~ 0.03	~ 0.072	~ 0.033	~ 0.033	~ 0.075
λ_{TS} , mm	~ 75	~ 4.5	~ 300	~ 30	~ 30

$^\dagger Re_\theta = 1/(-2v_o/U)$ for incompressible asymptotic suction profile

$^{\dagger\dagger} u_{\max}$ at edge of sucked layer above suction hole

For comparison, shown below are the corresponding experimental values for the 45° swept blunt-nosed wing of reference 71 with suction applied through chordwise rows of closely spaced suction holes at the attachment line:

$$\frac{W}{\nu} = 1.86 \times 10^6 / \text{m} \quad (w = 27.77 \text{ m/s} = \text{spanwise potential flow velocity along attachment line})$$

$$\text{Re}_{\theta_{al}} \equiv \frac{w\theta}{\nu} = 240$$

$$\theta_{al} = 0.129 \text{ mm}$$

$$v_o \left(\nu [\partial U / \partial s]_{al} \right)^{-0.5} = -0.1 \text{ with } [\partial U / \partial s]_{al} = 136 / \text{sec}$$

$$v_o = -0.0045 \text{ m/s (equivalent area suction velocity)}$$

$$\frac{v_o}{w} = -1.62 \times 10^{-4}$$

$$\frac{v_o \Delta x}{\nu} = -0.9 \quad (\Delta X = 3 \text{ mm} = \text{suction hole row spacing})$$

$$\bar{h} = 0.0228 \text{ mm (two-dimensional)}$$

$$\bar{w} = 0.595 \text{ m/s (two-dimensional)}$$

$$\frac{w_{\max}}{w} \cong 0.12 \text{ to } 0.16 \text{ at edge of sucked layer over suction hole (estimated)}$$

$$\lambda_{TS} \cong 5 \text{ mm}$$

Suction-Hole-Induced Mean Flow Irregularities in the Test Section

As discussed previously, suction-hole-induced disturbances decay rapidly within the subsonic portion of the nozzle and test section wall boundary layer region. In the supersonic wall boundary layer and potential flow region of the nozzle and test section, they propagate along Mach lines and thus decay much slower. Therefore, the question arises concerning the decay of the suction-hole-induced mean flow disturbances within the subsonic portion of the boundary layer in laminarized supersonic wind tunnel nozzles and the minimization of such disturbances at the outer edge of the subsonic layer ($y = \delta_s$).

The suction-hole-induced mean flow disturbance velocities at $y = \delta_s$ may be evaluated approximately by replacing the suction holes by sinks and calculating the velocity v_\perp (in the direction normal to the suction surface) induced by these sinks, at $y = \delta_s$ for different locations, assuming incompressible flow. Since the average Mach number in the subsonic layer is ≈ 0.5 , the error caused by this assumption should be small. The ratio λ/δ_s (λ = suction hole spacing) critically affects the spatial variation of the suction-hole-induced disturbance velocity ratio $\Delta v_\perp / v_\perp$ at $y = \delta_s$. The ratio λ/δ_s was varied from 0.5 to 2, and v_\perp at $y = \delta_s$ was calculated for a large number of line (two-dimensional) sinks of spacing λ , representing suction slots of spacing λ . The velocity v_\perp was further calculated above a straight-line row of point (three-dimensional) sinks of spacing $\lambda = \lambda_1$, approximating suction hole rows of relatively large spacing λ_2 , with the hole spacing λ_1 within each hole row very much smaller than λ_2 . This case is of interest for suction hole rows (spacing λ_2) that are swept behind the local Mach angle, with particularly small suction hole spacings $\lambda_1 \ll \lambda_2$ within each individual suction hole row (fig. 35). Suction-hole-induced mean flow irregularities in the test section are thus minimized. Figure 36 and table 15 show for different ratios λ/δ_s ($\delta_s \equiv h$) the ratio of the maximum induced velocity difference $\Delta v_\perp = v_{\perp \max} - v_{\perp \min}$ to the maximum velocity $v_{\perp \max}$ induced at $y = \delta_s$ by a very large number of two-dimensional sinks as well as three-dimensional sinks located along a straight line. With decreasing λ/δ_s ratios, $\Delta v_\perp / v_{\perp \max}$ decreases very rapidly to insignificant values for $\lambda/\delta_s < 1$. For point sinks $\Delta v \sim 1/r^2$, as compared to $\Delta v \sim 1/r$ for line sinks. Therefore, the more distant point sinks contribute a smaller percentage to Δv_\perp as compared to line sinks, while the more closely located point sinks contribute particularly strongly to Δv_\perp . Thus, at the same λ/δ_s ratios, $\Delta v_\perp / v_\perp$ should be larger for straight-line point sinks than for line sinks, as confirmed by figure 36. For the case of perforated suction surfaces with equal suction hole spacings in the x and z directions, the locus of $\Delta v_\perp / v_\perp$ is probably located between the limiting cases of line and point sinks.

In summary, to avoid excessive suction-hole-induced disturbance velocities at the outer edge of the subsonic nozzle wall boundary layer region and thus in the test section of laminarized supersonic wind tunnels, the suction hole spacing should be equal to or preferably smaller than the subsonic thickness δ_s of the nozzle wall boundary layer. For the evaluation of δ_s , the Mach number component in the direction normal to the rows of holes must be used. Thus, for circumferential rows of suction holes, the full local potential flow Mach number must be used to evaluate δ_s . For suction hole rows swept behind the local Mach angle, the suction hole spacing λ_1 within each individual blade row should be equal to or preferably smaller than δ_s , using the Mach number component in the direction of the hole rows. Since the flow component normal to these highly swept suction hole rows is subsonic, flow disturbances in this direction decay very rapidly to insignificant values, thus allowing relatively large spacings $\lambda_2 \gg \lambda_1$ of these rows from the standpoint of suction-hole-induced mean flow irregularities in the test section. Row spacing λ_2 may then be determined by the necessity to closely approach area suction for the laminarization of the nozzle wall boundary layers up to high length Reynolds numbers at minimum suction flow rates, as discussed in the preceding section.

To evaluate the suction hole spacings permissible from the standpoint of suction-hole-induced mean flow irregularities in the tunnel test section, δ_s was determined for several cases, using the full local potential flow Mach number in the nozzle (fig. 37 and tables 2p, 2t, 2u, 2x, 3b-i, and 16). With the thin wall boundary layers in the low supersonic Mach number areas of the nozzle, δ_s and thus the permissible suction hole spacing λ are quite small, especially at higher test section Mach numbers M^* at a given test section unit length Reynolds number U^*/ν^* and diameter D^* . Under otherwise the same conditions, the use of helium as the working medium in high supersonic Mach number nozzles allows substantially larger suction hole spacings due to the larger δ_s in the low supersonic nozzle areas (fig. 37b and tables 2u and 2x).

With the thicker wall boundary layers in the low supersonic region of slow expansion supersonic nozzles, δ_s and λ in this region are somewhat larger than they are for moderately rapid expansion supersonic nozzles (compare the $M^* = 9$ slow expansion helium nozzle ($R/R_{th} = 250$) with the $M^* = 9$ NASA helium nozzle). For such more rapid expansion nozzles, either the suction hole spacing in the particularly critical low supersonic nozzle area or the U^*/ν^* may have to be reduced if suction-hole-induced mean flow irregularities in the test section are to be avoided.

Under otherwise the same conditions, the minimum δ_s and λ values in the low supersonic nozzle area are practically the same for axisymmetric $M^* = 5$ and two-dimensional $M^* = 4.6$ supersonic nozzles on their floor and ceiling walls (fig. 37a and tables 3b, 3c, and 16b). With the very thin boundary layers on the side walls of suction laminarized two-dimensional supersonic wind tunnel nozzles, resulting from control of boundary layer crossflow instability, δ_s on these side walls is substantially smaller than on the nozzle floor and ceiling walls (fig. 37a and tables 3b-i). Extremely small suction hole spacings would be required in the low supersonic region on the side walls of the two-dimensional JPL nozzle at $U^*/\nu^* = 26.2 \times 10^6/\text{m}$ and $H^* = 1$ m. To avoid such close suction hole spacings, U^*/ν^* may have to be reduced and H^* correspondingly increased.

With increasing local Mach number toward the downstream end of the nozzle, δ_s increases rapidly, especially for high supersonic Mach number nozzles (fig. 37 and tables 2p, 2t, 2u, 2x, and 16b). In fact, δ_s and the permissible suction hole spacing are rather large over a considerable percentage of the nozzle length, while the small δ_s and suction hole spacings are restricted to a short region of the low supersonic part of the nozzle (see, for example, fig. 37c and tables 2p, 2t, 2u, 2x, and 16b).

In the above evaluation of $\Delta v_{\perp \max}/v_{\perp \max}$, equal sink strength was assumed. Considerably stronger variations in v_{\perp} might result at $y = \delta_s$ if the suction hole flow rates vary spatially. However, since such suction irregularities usually will be local and three-dimensional, the resulting disturbances should still decay substantially in the supersonic flow field of the nozzle like a three-dimensional shock wave, in contrast to the much slower decay of two-dimensional shock

waves. Thus, the mean flow irregularities in the test section, resulting from very local three-dimensional suction irregularities, may not be quite as critical as the two-dimensional disturbances from the outer edge of the subsonic boundary layer region. Despite this alleviating effect, a uniform suction distribution through the individual suction holes should still be the objective, even though such a high standard would not be required merely for the laminarization of the nozzle wall boundary layers.

The question arises concerning the suction drive systems for suction laminarized supersonic wind tunnel nozzles. The sucked nozzle and test section wall boundary layers may be recompressed to the undisturbed total pressure p' at the aft end of the test section exit diffuser by suction compressors. From this station the suction medium would be further compressed to tunnel stagnation pressure by the main tunnel drive compressors. Alternately, the sucked nozzle and test section wall boundary layers may be recompressed directly in the suction compressors to tunnel stagnation pressure. To minimize suction power and avoid excessively high temperatures in the suction compressors, isothermal compression of the sucked boundary layer, approached with various suction compressor spools and interspool cooling, is preferable over isentropic compression (fig. 38). The high nozzle pressure ratios—especially at higher test section Mach numbers—lead to correspondingly high suction compressor pressure ratios, requiring a large number of compressor stages, mounted on several individual spools with interspool coolers. Such individual suction compressor spools enable the establishment of the desired suction distribution in the nozzle with minimum suction duct pressure losses; furthermore, suction compressor surge during starting can be much better controlled with individually driven suction compressor spools. These general considerations apply both to continuously running closed-return as well as blowdown supersonic wind tunnels with test section exit diffusers.

The ratio ϵ of the suction power L_{suct} to the kinetic energy KE of the flow in the wind tunnel test section is a good parameter for the evaluation and comparison of the suction requirements in different nozzles. A lower bound for ϵ can be given, assuming ideal isothermal compression of each individual sucked boundary layer particle without losses to p' or p_{stag} at constant temperature $T_{\text{compr}} = T_{\text{stag}}$ (or $T_{\text{compr}} = T_{\text{cooling medium}}$, if $T_{\text{stag}} > T_{\text{cooling medium}}$) (fig. 39).

This assumption implies 100% suction compressor efficiency (or $\eta_{\text{suct compr}} = \eta_{\text{tunnel drive compr}}$), an infinite number of individual suction chambers, and zero pressure losses in the suction skin and ducts. Assuming $T_{\text{compr}} = T_{\text{cooling medium}} = T_{\text{stag}}$, the ideal isothermal suction compressor/power necessary to compress the sucked nozzle wall boundary layer at T_{stag} from the suction chamber pressure to the diffuser exit total pressure p' is:

$$dL_{\text{suct isoth}} = g \, d\dot{m}_s \cdot R \cdot T_{\text{stag}} \cdot \ln \left(\frac{p'}{p} \right),$$

$$L_{\text{suct isoth}} = \dot{m}_o \cdot g \cdot R \cdot T_{\text{stag}} \int \left[\ln \left(\frac{p'}{p} \right) \right] \frac{d(\dot{m}_s/\dot{m}_o)}{d(x/R_{\text{th}})} d \left(\frac{x}{R_{\text{th}}} \right)$$

where \dot{m}_0 - test section mass flow rate per unit time.

The kinetic energy of the test section flow is:

$$KE_{\text{test section}} = \frac{\dot{m}_0}{2} \cdot U^2 = \frac{\dot{m}_0}{2} \cdot M^{*2} a^{*2} = \frac{\dot{m}_0}{2} \cdot g \cdot \gamma \cdot RT^* \cdot M^{*2}$$

The ratio ϵ is:

$$\epsilon = \frac{L_{\text{suct isoth}}}{KE_{\text{test section}}} = \frac{2}{\gamma} \cdot \frac{T_{\text{stag}}}{T^* M^{*2}} \int \left[\ln \left(\frac{p'}{p} \right) \right] \frac{d(\dot{m}_s/\dot{m}_0)}{d(x/R_{\text{th}})} d \left(\frac{x}{R_{\text{th}}} \right)$$

$$\text{With } \frac{T_{\text{stag}}}{T^*} = 1 + \frac{\gamma - 1}{2} \cdot M^{*2}:$$

$$\epsilon = \frac{2}{\gamma} \left(\frac{1 + \frac{\gamma - 1}{2} M^{*2}}{M^{*2}} \right) \int_{\text{nozzle and test section}} \left[\ln \left(\frac{p'}{p} \right) \right] \frac{d(\dot{m}_s/\dot{m}_0)}{d(x/R_{\text{th}})} d \left(\frac{x}{R_{\text{th}}} \right),$$

where the nozzle pressure p and the suction mass flow rates $d(\dot{m}_s/\dot{m}_0)$ are functions of x/R_{th} .

In the above analysis, the temperature of the sucked boundary layer was assumed equal to T_{stag} , i.e., the boundary layer temperature recovery factor $RF = 1$. According to the nozzle wall boundary layer analysis, this assumption is usually closely approached with the relatively strong area suction required for stabilization of the nozzle wall boundary layers at high Reynolds numbers, particularly in the downstream nozzle areas.

When $T_{\text{stag}} > T_{\text{cooling medium}}$, the sucked boundary layer could, in principle, be compressed isothermally at $T = T_{\text{cooling medium}} + \Delta T$ (ΔT = temperature loss between cooling medium and sucked boundary layer). The ratio $\epsilon = L_{\text{suct isoth}}/KE_{\text{test section}}$ could then be reduced by the temperature ratio $(T_{\text{cooling medium}} + \Delta T)/T_{\text{stag}}$. Tables 17a-c give values of ϵ for the above ideal isothermal compression of the sucked nozzle wall boundary layer to p_{stag} at $T = T_{\text{stag}}$ for the $M^* = 5.115$ LARC Q-axisymmetric air nozzle as well as for the $M^* = 9$ slow expansion and NASA helium axisymmetric nozzles. These ϵ ratios ($\epsilon = 0.0126$ for the $M^* = 5.115$ Q-nozzle and 0.016 for the $M^* = 9$ helium nozzles) appear remarkably small. Admittedly, such ideal isothermal compression of the sucked nozzle wall boundary layer can be only approached. Suction compressor losses, suction skin and duct pressure losses, interspool cooler temperature and pressure losses must be taken into account. Additional suction skin throttling pressure losses result from the fact that a finite number of suction chambers must be used. Even so, the ratio of suction power to the kinetic energy of the test section flow still appears small.

Considerable ingenuity and care in the detail design of the suction compressor drive and suction ducting system is necessary to establish the desired suction distribution on the nozzle and test section walls without suction and boundary layer discontinuities, which might cause flow irregularities in the supersonic test section.

As with low drag suction airplanes, where the suction drive system is part of the propulsion system to contribute a substantial percentage to the propulsive thrust, the suction compressor drive system of a laminarized supersonic wind tunnel contributes an appreciable percentage to the tunnel drive power. Boundary layer suction on the tunnel nozzle and test section walls strongly thins the tunnel wall boundary layer at the inlet to the exit diffuser to reduce accordingly the resulting diffuser pressure drag losses and tunnel drive power.

Table 17d shows the reduction of the suction power ratio ϵ for the $M^* = 9$ NASA helium tunnel nozzle when the sucked nozzle wall boundary layer is compressed to $p'_{stag} < p_{stag}$ at the aft end of the exit diffuser. The overall suction compressor pressure ratio is influenced to a much higher degree than ϵ as the sucked nozzle wall boundary layer is compressed to a progressively lower diffuser exit pressure p .

Instead of providing suction compressors in supersonic blowdown tunnels to operate continuously during the test runs, suction could be operated in a relatively simple manner by connecting the various suction chambers to one or preferably several separate individual suction vacuum spheres. The suction rates of the individual suction chambers could then be controlled by Laval nozzles, located between the suction ducts and these suction vacuum spheres. With the relatively long time available between test runs to recompress the suction medium to tunnel stagnation pressure, the suction power could be substantially reduced, allowing at the same time a much less sophisticated suction compressor system.

RECOMMENDATIONS FOR RESEARCH AND DEVELOPMENT

To proceed with the development of large quiet supersonic wind tunnels with laminarized nozzles and test sections, initial experience should be gained from quiet laminarized supersonic pilot tunnels. To minimize the risk of setbacks and failures, a cautious and conservative approach both in the overall layout as well as in the detail design should be adopted throughout; preparations should be made for all kinds of problems, adequate margins and operational flexibility should be provided to cover unforeseen difficulties, and unnecessary gambles should be avoided. Careful consideration should be given to how large a step to take with such pilot tunnels. To learn sufficiently from the experimentation with laminarized supersonic pilot tunnels, the step should be sufficiently bold, with the chances of success classically of the order of 80% for such type of development (to quote Ackeret). If the step were substantially smaller and thus the chances of success very close to 100%, too many small steps and an excessive development time would be needed. Too bold a step might rapidly decrease the chances of success and is therefore not recommended either.

To minimize difficulties with surface roughness as well as suction-induced disturbances in the nozzle wall boundary layers and test section, one should design laminarized supersonic pilot tunnels for relatively modest tunnel pressures and accept the larger tunnel dimensions to achieve a given test section Reynolds number. As the experimental investigation of such pilot tunnels progresses, the tunnel stagnation pressure and test section Reynolds number can be slowly raised, until difficulties and limitations emerge that must be gradually eliminated. To enable high laminar flow length Reynolds numbers, no effort should be spared to minimize nozzle inflow disturbances and approach area suction as closely as possible. As in any low drag suction experiment at high Reynolds numbers, such laminarized experimental supersonic pilot tunnels should be designed with a particularly high experimental flexibility to meet unexpected and unforeseen difficulties during the experimentation. For example, the suction surface and suction ducting system should preferably be laid out such that the overall suction rates as well as the streamwise suction distribution can be varied over a wide range without inducing critical suction discontinuities in the streamwise direction. For this purpose, a rather large number of individually controlled suction chambers may be needed.

To learn about the behavior of the suction laminarized nozzle and test section wall boundary layers of supersonic pilot tunnels over a wide range of operating conditions, it will be necessary to subdivide their suction chambers much more extensively than will be necessary for future operational laminarized supersonic tunnels. After gaining sufficient experience from such pilot tunnels, larger quiet supersonic tunnels with suction laminarized nozzles and test sections, operating at further increased length Reynolds numbers, can then be developed without necessarily requiring the extensive experimental flexibility built into laminarized supersonic pilot tunnels.

Since the development of laminarized supersonic tunnels represents a major undertaking, substantial theoretical and experimental research and development as well as efforts to develop the necessary technological basis are highly recommended. Research investigations would be concerned with: verification of laminarization through distributed suction with different suction methods at further increased length Reynolds numbers; suction-induced boundary layer oscillations in the nozzle and test section wall boundary layers as well as mean flow irregularities in the test section; transition investigations on concave surfaces with and without distributed suction in the presence of Taylor-Goertler disturbance vortices from low subsonic to high supersonic speeds; and investigations to minimize nozzle inflow disturbances as much as possible.

THEORETICAL AND EXPERIMENTAL INVESTIGATIONS OF SUCTION-INDUCED MEAN FLOW IRREGULARITIES

Investigations of suction-induced mean flow irregularities in the test section of supersonic tunnels are recommended with the following configurations:

- Suction through a perforated surface with very closely spaced small suction holes, with emphasis given to suction hole patterns that minimize suction-induced flow irregularities in the test section (for example, closely spaced rows of extremely small and very closely spaced electron-beam-drilled suction holes, with the rows of holes swept behind the local Mach angle)
- Suction through closely spaced fine slots swept behind the local Mach angle
- Suction through longitudinal slots

The experimental investigations of suction-induced mean flow irregularities in the test section may be conducted initially on a supersonic flat plate, simulating the conditions in two-dimensional nozzles. To simulate the flow conditions in axisymmetric supersonic nozzles and test sections, these experiments should eventually be extended to the axisymmetric case, using the flow in supersonic tubes. With suction through holes, the ratio of hole spacing to the thickness of the subsonic portion of the nozzle wall boundary layer critically affects the suction-induced disturbance velocities at the sonic line of the boundary layer and thus in the test section of supersonic tunnels; therefore, this parameter must be properly matched. For the investigation of suction-hole-induced mean flow disturbances in the test section, the length Reynolds number does not appear too important, i.e., considerable knowledge can be expediently gained in this respect from low Reynolds number experiments at correspondingly lower tunnel pressures.

At a particular chordwise location, the suction-hole-induced mean flow disturbances are affected primarily by the local suction holes, while the contribution of the more remote suction holes becomes insignificant. In the subsonic portion of the boundary layer, the suction-hole-induced mean disturbances decay rapidly, while they propagate along Mach lines through the supersonic part of the boundary layer and the potential flow region into the test section. As a result, the suction-hole-induced mean flow disturbances depend essentially on local conditions of the suction surface, i.e., for initial preliminary investigations of suction-hole-induced mean flow irregularities in the test section, it appears permissible to apply suction over a relatively short streamwise extent.

Of course, suction-induced mean flow irregularities in the test section will develop at the upstream and downstream end of the suction region. These irregularities can be minimized by tapering out suction in the streamwise direction at both ends of the suction area; by extending suction into the subsonic part of the nozzle, they can be eliminated at the start of suction.

With continuous suction without discontinuities along the length of longitudinal and highly swept slots (swept behind the local Mach angle), suction-induced mean flow irregularities in the test section should be practically absent. However, suction discontinuities caused, for example, by local suction flow blockage in the support structure underneath the slots can generate weak shock waves, which can propagate into the test section to induce mean flow irregularities there. Preliminary supersonic experiments with suction through longitudinal as well as very closely spaced slots, swept behind the local Mach angle, are therefore recommended to establish a proper suction layout without suction-induced mean flow irregularities in the test section.

EXPERIMENTAL INVESTIGATION AT HIGH LENGTH REYNOLDS NUMBERS WITH VARIOUS SUCTION METHODS

The question arises concerning the influence of suction-induced disturbances on laminarization at high Reynolds numbers in the absence of boundary layer crossflow and Taylor-Goertler type boundary layer instability, using different suction methods (suction through longitudinal and very closely spaced, highly swept slots as well as perforated surfaces with very closely spaced small suction holes). With suction applied through perforated surfaces, streamwise and horseshoe disturbance vortices at higher suction rates eventually originate from the suction holes. These disturbance vortices can induce premature transition either directly or as a result of amplified boundary layer oscillations. Such oscillations, induced by suction through perforated surfaces, become increasingly less critical by weakening the suction-hole-induced streamwise disturbance vortices and confining them to the innermost slowest boundary layer region. This can be accomplished by using an extremely large number of very closely spaced electron-beam-drilled, or

possibly laser-beam-drilled, very fine suction holes. In this case, area suction might be particularly closely approached to enable laminarization at further increased length Reynolds numbers.

The question then turns to how small the suction hole spacing and diameter must be in relation to the boundary layer thickness to minimize or preferably avoid suction-induced amplified boundary layer oscillations under various conditions. This question can be answered by subsonic as well as supersonic low drag suction experiments with electron-beam- or laser-beam-drilled perforated suction surfaces at high length Reynolds numbers and low external disturbance levels, using Raetz's nonlinear boundary layer stability analysis as a guideline (appendix C). To simplify the experiment, chordwise pressure gradients as well as boundary layer crossflow due to spanwise pressure gradients should be avoided initially, working with flat suction plates (or thin airfoils), suction bodies of revolution, or laminar flow suction tubes in the laminar inlet region.

For comparison, similar experiments are recommended with other suction methods, using for example longitudinal as well as highly swept slots. Experimental results with closely spaced spanwise slots are available up to 58×10^6 length Reynolds number (ref. 4).

SUBSONIC AND SUPERSONIC TRANSITION INVESTIGATIONS IN THE PRESENCE OF TAYLOR-GOERTLER DISTURBANCE VORTICES

In concave surface curvature regions, streamwise Taylor-Goertler type disturbance vortices can develop to cause premature transition beyond a critical amplification factor of these disturbance vortices. According to A. M. O. Smith's linearized analysis of subsonic transition experiments on two-dimensional concave surfaces without suction, transition starts when the exponent $\int \beta dx$ in the growth factor of amplified Taylor-Goertler disturbance vortices exceeds a value of 10 (ref. 26). A first critical question arises concerning the variation of this transition value for $\int \beta dx$ with Mach number up to higher supersonic speeds on two-dimensional surfaces without suction. Furthermore, since the suction laminarization of the nozzles and test sections of supersonic tunnels critically depends on the stabilizing influence of area suction on TG vortices, a second crucial question arises regarding experimental verification of Kobayashi's (ref. 27) theoretical result, according to which an asymptotic suction boundary layer with area suction is substantially less unstable with respect to TG disturbances than nonsuction boundary layers. Since Kobayashi's result applies to the asymptotic area suction profile, and the suction rates for the laminarization of supersonic nozzles may differ from the asymptotic suction rates, a third question arises concerning the TG stability limit and the transition value for $\int \beta dx$ for suction conditions different from those of the asymptotic case. The aerodynamically ideal area suction, of course, can be approached only to various degrees. Therefore, a fourth question arises as to how far Kobayashi's results for ideal area suction are applicable to suction surfaces with many very fine holes and longitudinal as well as highly swept slots.

Since the variation with θ of the locus for the local growth factor $\beta\theta Re_\theta$ of Taylor-Goertler disturbance vortices versus $\alpha\theta$ (α = wave number) may differ for two-dimensional and axisymmetric flow, a fifth question arises concerning the growth of Taylor-Goertler disturbance vortices and the transition value for $\int\beta dx$ in axisymmetric flow.

Above all, the two most crucial questions—the influence of Mach number and area suction on the Taylor-Goertler type boundary layer instability—must be answered.

The following theoretical investigations are recommended:

- a) Kobayashi's incompressible Taylor-Goertler stability analysis should be repeated with different amounts of suction for area suction boundary layer profiles, which differ from the asymptotic suction profile.
- b) Taylor-Goertler boundary layer stability analysis is recommended for nonsuction and area suction boundary layer profiles at various Mach numbers and different suction rates up to higher supersonic Mach numbers.
- c) Of lesser importance is a Taylor-Goertler boundary layer stability analysis in axisymmetric flow for nonsuction as well as area suction boundary layer profiles from low subsonic to high supersonic speeds.

The following experimental investigations are recommended:

- a) To investigate the growth of TG disturbance vortices and their growth factor $\int\beta dx$ for transition at different supersonic Mach numbers both without and with distributed suction, transition experiments in supersonic nozzles are recommended at different Mach numbers without as well as with distributed suction. Nozzle inflow disturbances should be minimized as much as possible. Area suction should be approached in various degrees.
- b) To verify Kobayashi's critically important theoretical expectations about the stabilizing influence of area suction on TG instability, particular emphasis should be given to transition experiments on two-dimensional concave surfaces with area suction at low subsonic speeds as well as increasingly higher supersonic Mach numbers later.
- c) Less important than items a and b are experimental investigations to establish the difference in the growth of TG disturbance vortices and the resulting transition in axisymmetric and two-dimensional low turbulence supersonic nozzles.

In these experiments, ideal area suction surfaces, perforated suction surfaces with very closely spaced electron-beam-drilled holes, and slotted suction surfaces with longitudinal and highly swept slots (swept behind Mach cone) should be investigated.

INVESTIGATION OF METHODS TO MINIMIZE NOZZLE INFLOW DISTURBANCES

Aerodynamic inflow turbulence would be most ideally reduced through damping screens with laminar turbulence-free wakes and an undisturbed laminar annulus wall boundary layer downstream of the screen section. At larger test section unit length Reynolds numbers and tunnel total pressures, this requirement leads to extremely fine special seamless screens (possibly with wire diameters down to 0.075 mm and open area ratios of at least 60%) and very high nozzle contraction ratios. Thermal convection currents downstream of the screens cause thermally induced inflow turbulence, especially at very high nozzle contraction ratios; they must therefore be minimized by equalizing the temperature upstream of the screens. Furthermore, accelerating the flow immediately downstream of the screens rapidly decreases the inlet section diameter and the contraction ratio between the screen section and the sonic throat before substantial thermal convection currents can develop. Concave wall surface curvature in the inlet section between the screens and the sonic throat may induce amplified Taylor-Goertler disturbance vortices in the inlet wall boundary layer at higher test section Reynolds numbers and should therefore be avoided.

At substantially higher test section unit length Reynolds numbers and total pressures, it may eventually become impossible to maintain laminar screen wakes and a laminar inlet wall boundary layer immediately downstream of the screens. To reestablish a laminar inlet wall boundary layer, the entire turbulent wall boundary layer, including all the turbulent eddies that intermittently penetrate far out into the potential flow region, must then be removed locally downstream of the screens by means of strong suction. The newly established laminar inlet wall boundary layer must then be sufficiently stabilized further downstream in the presence of the screen wake turbulence by means of relatively weak distributed suction and flow acceleration, until an undisturbed laminar inlet wall boundary layer finally is established further downstream.

Since the minimization of nozzle inflow disturbances appears mandatory for the laminarization of supersonic nozzles and test sections at higher Reynolds numbers, preliminary experiments are recommended to reduce as much as possible the aerodynamic, acoustic, and thermal inflow disturbances discussed above.

In the subsonic region of the nozzle, the wall boundary layer should be stabilized by suction such as to minimize or avoid amplified boundary layer oscillations in this region. Suction may be required primarily in the higher subsonic Mach number region while much less or no suction may be

sed in the low subsonic part of the nozzle. Since suction-induced disturbances in the subsonic portion of the nozzle decay rapidly and do not generate mean flow irregularities in the test section, different suction methods appear adequate for the stabilization of the nozzle wall boundary layer in the subsonic part of the nozzle, e.g., suction through closely spaced spanwise slots, a finely perforated or porous suction surface, a few scoop-type suction slots. From the standpoint of subsonic nozzle wall boundary layer stabilization at higher Reynolds numbers, area suction should preferably be closely approached. Excessively thin nozzle wall boundary layers shortly upstream of the throat are sensitive to wall surface roughness and should therefore be avoided. In this respect, area suction closely approached by different methods appears superior over suction through one or a few scoop-type suction slots located shortly upstream of the throat.

Boeing Commercial Airplane Company

P. O. Box 3707

Seattle, Washington 98124, March 1974.

VERSION OF COMPUTER PROGRAM TEM139 TO CALCULATE LAMINAR BOUNDARY LAYER FLOWS WITH VERY SMALL OR UNIFORM CROSSFLOW

SUMMARY

A modification of the finite-difference boundary layer computation program TEM139 (ref. 52) has been developed that allows computation of laminar three-dimensional boundary layers with small crossflow or uniform crossflow. The computational method of the resulting computer program is discussed below.

DISCUSSION

This version of TEM139 solves the same two-dimensional or axisymmetric compressible boundary layer equations as TEM139. In addition, the equation:

$$\rho u \frac{\partial w}{\partial x} + \rho v \frac{\partial w}{\partial y} = -\frac{\partial p}{\partial z} + \frac{1}{Re} \frac{\partial}{\partial y} \left(\mu \frac{\partial w}{\partial y} \right) \quad (A-1)$$

is solved for the crossflow velocity w , with $\partial p / \partial z$ a program input.

Equation (A-1) is an approximation to the laminar boundary layer crossflow equation:

$$\rho u \frac{\partial w}{\partial x} + \rho v \frac{\partial w}{\partial y} + \rho w \frac{\partial w}{\partial z} = -\frac{\partial p}{\partial z} + \frac{1}{Re} \frac{\partial}{\partial y} \left(\mu \frac{\partial w}{\partial y} \right) \quad (A-2)$$

Equation (A-1) is valid when w is very small (small crossflow) or when the crossflow is uniform ($\partial w / \partial z = 0$). These assumptions are also consistent with the use of the procedure of TEM139 to find ρ , T , u , and v .

The complete solution of laminar three-dimensional boundary layers in general requires solving the following equations as well as the crossflow equation (A-2):

[†]This phase of the work was developed by T. A. Reyhner.

Continuity

$$\frac{\partial(\rho u)}{\partial x} + \frac{\partial(\rho v)}{\partial y} + \frac{\partial(\rho w)}{\partial z} = 0 \quad (\text{A-3})$$

X-momentum

$$\rho u \frac{\partial u}{\partial x} + \rho v \frac{\partial u}{\partial y} + \rho w \frac{\partial u}{\partial z} = -\frac{\partial p}{\partial x} + \frac{1}{\text{Re}} \frac{\partial}{\partial y} \left(\mu \frac{\partial u}{\partial y} \right) \quad (\text{A-4})$$

The two-dimensional or axisymmetric equations are the same as these equations less the terms $\partial(\rho w)/\partial z$ in equation (A-3) and $\rho w(\partial u/\partial z)$ in equation (A-4). It thus can be seen that the two-dimensional equations are identical to equations (A-3) and (A-4) if the crossflow is uniform (all z derivatives zero) and a good approximation locally if the crossflow is small ($w \ll u$).

Large errors may be incurred by using the two-dimensional equations even when w is very small if computations are carried out for a long streamwise distance. The effects of the crossflow velocity w on equations (A-3) and (A-4) can be safely neglected locally, but for a calculation over a large distance, the cumulative error can be quite large if there is significant streamline convergence or divergence. An example of this effect is the difference between using two-dimensional and axisymmetric boundary layer equations for boundary layer computations on an axisymmetric body. If the radius of the body does not change much in the region calculated, the results will be similar, but if there is a large change of radius, the axisymmetric equations must be used. This problem can be compensated for in crossflow calculations by defining an axisymmetric body with equivalent streamline convergence and divergence and using the axisymmetric option of TEM139.

POTENTIAL CROSSFLOW IN THE DIRECTION NORMAL TO LONGITUDINAL SUCTION RODS

To stabilize the wall boundary layers of longitudinally slotted laminarized supersonic wind tunnel nozzles in a particularly efficient manner against Tollmien-Schlichting type disturbances, the streamwise nozzle wall boundary layer profiles should preferably not vary in spanwise direction in the region between the slot "attachment" lines (in the middle between adjacent slots) and the slots themselves. This is the case when the potential crossflow velocity component W , induced by suction through longitudinal slots, increases linearly from the slot attachment line toward the slots, accomplished by specially contoured longitudinal suction rods. To develop longitudinally slotted suction surfaces with such a linear increase of W from the slot attachment line toward the slots, incompressible potential crossflow calculations across longitudinal suction rods of different cross sections were conducted, using Omar's method (ref. 73). Elliptical suction rods of different fineness ratios a/b and slot width g were first investigated. The term $2b$ is the thickness of the suction rods in the crossflow direction; $2b + g$ is the slot centerline spacing.

Figures B-1 and B-2 show plots of the crossflow velocity ratio W/W_∞ versus the surface distance $(s/b)_{stag}$, measured from the slot attachment line, for circular and elliptical suction rods of fineness ratio $a/b = 1, 1.5, 2$, and 3 and slot width ratios $g/2b = 1, 0.4, 0.2, 0.1$, and 0.05 . W_∞ is the undisturbed crossflow potential velocity normal to the suction surface at infinity. For circular suction rods ($a = b$), W increases approximately linearly with s_{stag} for rather large slot width ratios $g/2b = 0.4$. For narrower slots with circular suction rods, however, W grows increasingly more rapidly toward the slots. As a result, the boundary layer thickness increases substantially from the slot toward the slot attachment line. Suction may then not be sufficiently effective to adequately stabilize the resulting thicker slot attachment line boundary layer. For elliptical suction rods of fineness ratio $a/b = 1.5$, W increases approximately linearly with s_{stag} for a slot width ratio $g/2b = 0.2$. Again, W grows increasingly more rapidly toward the slots for smaller slot widths, resulting in an increasing boundary layer thickness from the slot toward the slot attachment line and possibly an insufficient boundary layer stabilization in the slot attachment line region. At higher fineness ratios of the elliptical suction rods, the potential crossflow velocity gradient $\partial W/\partial s$ starts from a maximum at the slot attachment line, decreases for some distance and increases again, and decreases finally to zero in the slot.

Elliptical suction rods of low fineness ratio ($a/b = 1.5$) thus appear superior to circular suction rods for relatively wide slots ($g/2b = 0.2$). For narrower slots, however, elliptical suction rods of various fineness ratios failed to provide a perfect linear increase of W with s_{stag} . Therefore,

attempts were made to develop longitudinal suction rods with a more linear increase of W with s_{stag} . Figure B-3 shows the cross section of longitudinal suction rod (d) ($a/b = 1.5$) with a nearly perfect linear increase of W with s_{stag} for a slot width ratio $g/2b = 0.2$ (fig. B-4). Within a considerable distance in the narrow cross section between the suction rods close to the slot inlet, one-dimensional potential crossflow calculations are adequate to design the suction rod contour with a linear increase of W versus s_{stag} in this region.

For narrower slots ($g/2b = 0.1$), however, it became increasingly more difficult to design the suction rods for a linear increase of W with s_{stag} , unless the suction rod fineness ratio was substantially raised. Figure B-5 shows the cross section of suction rods (a), (b), and (c) with fineness ratios $a/b = 2$. Table B-1 shows the coordinates of these rods.

Figure B-6 presents the corresponding potential crossflow velocity distributions $W/W_\infty = f(s/b)_{stag}$ for a slot width ratio $g/2b = 0.1$. A linear increase of W with s_{stag} is only partially approached. Better results were obtained by extending the rod leading edge region and raising the rod fineness ratio somewhat (rod (e), $a/b = 2.15$; fig. B-7, table B-1). The corresponding potential crossflow velocity distribution $W/W_\infty = f(s/b)_{stag}$ is shown in figure B-8 for a slot width ratio $g/2b = 0.1$. In principle, a more perfect linear increase of W with s_{stag} for $g/2b = 0.1$ could be achieved by starting with rod (d) ($a/b = 1.5$, $g/2b = 0.2$) and doubling the surface distance s , using essentially one-dimensional potential crossflow calculations in the slot channel, where its width is between $0.2b$ to $0.4b$. Whether the resulting high fineness ratio suction rods and deep longitudinal suction slots are necessary or desirable is not certain.

Other considerations may favor a deviation from a constant boundary layer thickness in the spanwise direction and a linear increase of W with s_{stag} from the slot attachment line toward the slots. For example, in the presence of Taylor-Goertler type boundary layer instability in the concave curvature region of laminarized supersonic nozzles, suction through longitudinal slots probably does not pull the streamwise Taylor-Goertler type disturbance vortices in the slot attachment line region as close to the wall surface as ideal area suction would, at least as long as the TG vortex spacing is appreciably smaller than the spanwise slots spacing. Particularly thin boundary layers may then have to be maintained in the slot attachment line region, requiring correspondingly larger potential crossflow velocity gradients $\partial W/\partial s$ in this region as compared to the areas located closer to the slots. Correspondingly sharper rod leading edges in the slot attachment line region would then be needed.

SUMMARY OF RAETZ'S NONLINEAR BOUNDARY LAYER STABILITY THEORY

In his nonlinear theory of three-dimensional boundary layer oscillations (ref. 74), Raetz uses a perturbation series for the velocities and pressure:

$$\begin{aligned}
 u = & u_0 \text{ (mean flow)} \\
 & + \epsilon u_1 \text{ (surface and/or external disturbances)} \\
 & + \epsilon^2 u_2 \text{ (second perturbation)} \\
 & + \epsilon^3 u_3 + \epsilon^4 u_4 + \dots \text{ (higher order perturbations)}
 \end{aligned}$$

Each perturbation is expressed as a complex Fourier series. Introducing these perturbation series into the Navier-Stokes and continuity equations leads to the stationary Navier-Stokes equations, including the Reynolds stress terms, and a series of equations of forced boundary layer oscillations driven by the quadratic nonlinear Reynolds stress terms of the lower order perturbations:

$$\begin{aligned}
 \text{pressure} + \text{inertia} + \text{viscous forces} = & \text{sum of the nonlinear Reynolds} \\
 & \text{stress terms of lower} \\
 & \text{perturbations}
 \end{aligned}$$

In linearized disturbance theory, the nonlinear term on the right side of the above equation is zero, leading for example to the Orr-Sommerfeld equation for the second perturbation.

The first-order perturbation is given by external disturbances, such as turbulence and noise, and surface disturbances, such as actual surface roughness, equivalent aerodynamic surface roughness due to suction-hole-induced disturbance vortices, etc., which are equally as important as the external disturbances. The second-order perturbation, representing the amplified boundary layer oscillation of lowest order, is driven by the nonlinear Reynolds stress terms (forcing functions) of one or several of the first-order perturbations (surface and external disturbances). Higher order perturbations (i.e., amplified boundary layer oscillations of the next higher order) can be driven by the nonlinear Reynolds stress terms of two or more of the lower order perturbations. Among these

lower order perturbations, an amplified boundary layer oscillation plus an external disturbance or two amplified boundary layer oscillations may combine to drive a higher order perturbation or boundary layer oscillation.

According to Raetz (refs. 74 through 78) and as summarized by Stuart (ref. 79), the nonlinear interaction of two three-dimensional disturbances $A e^{-i[\alpha_1 x + \beta_1 z - \alpha_1 \tilde{c}_1 t]}$ and $B e^{i[\alpha_2 x + \beta_2 z - \alpha_2 c_2 t]}$ can produce a third driven interaction oscillation, $C e^{i[\alpha_3 x + \beta_3 z - \alpha_3 c_3 t]}$, with $\alpha_3 = \alpha_2 - \alpha_1$, $\beta_3 = \beta_2 - \beta_1$, $c_3 = (\alpha_2 c_2 - \alpha_1 \tilde{c}_1)/\alpha_3$. The terms x and z denote stream and spanwise coordinates; A , B , and C are oscillation amplitudes; α and β denote wave numbers; and the c 's are the complex wave velocities. In general, the parameters α_3 , β_3 , c_3 , and Re of the third oscillation do not form a set of eigenvalues, and the third oscillation then grows with time t as $\phi_3 = e^{-i\alpha_3 c_3 t} \psi_3(z)$, where ψ_3 is a characteristic function of this oscillation. However, under certain conditions α_3 , β_3 , c_3 , and Re do form a set of eigenvalues, i.e., solutions satisfying the disturbance differential equation, and the corresponding boundary conditions exist only for certain sets of α_3 , β_3 , c_3 , and Re . The third driven oscillation then grows in a resonance-like manner with time as $\phi_3 = e^{-i\alpha_3 c_3 t} (\psi_{31}(y) + t \psi_{32}(y))$, where the characteristic functions ψ_{31} and ψ_{32} of this oscillation close to resonance are usually much larger than ψ_3 (see above) in the absence of resonance.

To describe the resonance-like growth of laminar boundary layer oscillations close to transition, as observed by Schubauer and Klebanoff (ref. 80), Raetz expresses the disturbance velocity and pressure as a function of surface distance normal to the wall multiplied with a spatial (or timewise) growth of the boundary layer oscillations, which are expressed by exponential and resonance functions. Resonance-like growths of boundary layer oscillations, observed experimentally prior to transition, were found by Raetz especially for the case when standing or traveling disturbance vortices—inclined at a small angle to the main flow—superimposed certain other boundary layer oscillations, such as oblique Tollmien-Schlichting waves (traveling at an oblique angle to the potential flow). Physically, this result may be explainable by the three-dimensional distortion and the resultant stretching and convection of the above-mentioned nearly longitudinal disturbance vortices in the boundary layer under the action of oblique Tollmien-Schlichting waves, thereby increasing their vorticity and kinetic energy. As a result of this vortex stretching, they eventually develop into unstable hairpin-type vortices, whose vorticity increases proportionally to (distance)ⁿ or (time)ⁿ, multiplied with an exponential growth with distance and/or time.

According to Raetz, the growth of the higher order perturbations, i.e., amplified boundary layer oscillations of different order, critically depends on the magnitude of the first-order perturbations, namely, of external disturbances (turbulence, noise, etc.) as well as surface disturbances in the form of three-dimensional surface roughness or equivalent aerodynamic roughness from suction-hole-induced disturbance vortices, etc. In Raetz's context, suction-hole-induced disturbances may thus affect the growth of laminar boundary layer oscillations and transition under certain conditions in a manner similar to external turbulence.

Practically longitudinal disturbance vortices are generated for example by three-dimensional surface roughness or suction-induced aerodynamic roughness, as well as by boundary layer crossflow instability due to spanwise pressure gradients and Taylor-Goertler type boundary layer instability on concave surfaces. Amplified Tollmien-Schlichting type boundary layer oscillations can be induced by external disturbances, such as turbulence and sound. With such external disturbances practically absent—corresponding, for example, to ideal flight conditions on quiet low drag suction airplanes—Tollmien-Schlichting type boundary layer oscillations remain weak, and the above longitudinal disturbance vortices are not significantly deformed three-dimensionally. In Raetz's theory, the critical driving term—the nonlinear Reynolds stress cross term formed by the disturbance velocities from the roughness-induced streamwise disturbance vortices and the oblique Tollmien-Schlichting waves—becomes zero. Likewise, if it should prove possible to avoid or minimize amplified Tollmien-Schlichting waves by sufficiently stabilizing the boundary layer through suction, the critical nonlinear Reynolds stress cross term is again insignificant. Transition then develops when the streamwise disturbance vortices become sufficiently unstable to become deformed three-dimensionally and break up into highly unstable horseshoe-type vortices.

APPENDIX D

ASYMPTOTIC SUCTION PROFILES

The adiabatic wall asymptotic suction profiles at Mach 2, 3, and 5 for air and at Mach 5 and 9 for helium are shown in figure D-1. The air boundary layer profiles were obtained using Sutherland's viscosity law, while the helium profiles are based on the power law with the exponent $n = 0.675$. The values for y/δ , u/U_e , and H_i are tabulated in table D-1.

APPENDIX E

TABLES AND FIGURES INDEX

Tables E-1 and E-2 provide an index to the tables and figures presented in this report. A description of the tables and figures is given below.

DESCRIPTION OF TABLES

- 1 Coordinates and streamwise Mach number variation for axisymmetric supersonic nozzles and a $M^* = 4.6$ two-dimensional JPL nozzle
- 2 Data from analysis of the nozzle wall boundary layer development in axisymmetric supersonic nozzles
- 3 Data from analysis of the nozzle wall boundary layer development in the $M^* = 4.6$ two-dimensional JPL nozzle
- 4-7 Evaluation of the linearized Taylor-Goertler vortex growth factor in the concave curvature region of supersonic nozzles
 - 4: $M^* = 3$ axisymmetric nozzles
 - 5: $M^* = 5$ axisymmetric nozzles
 - 6: High Mach number axisymmetric nozzles
 - 7: $M^* = 4.6$ two-dimensional JPL nozzles
- 8-10 Summary data on the exponent $\int \beta dx$ of the linearized Taylor-Goertler vortex growth factor in the concave curvature region of suction laminarized supersonic nozzles
 - 8: $M^* = 3$ axisymmetric nozzles
 - 9: $M^* = 5$ axisymmetric nozzles
 - 10: High Mach number axisymmetric air nozzles
- 11 Variation of $\int \beta dx$ with U^*/ν^* for $M^* = 3$ slow expansion axisymmetric air nozzle ($D^* = 1$ m)
- 12 Data from boundary layer crossflow analysis on the side walls of the $M^* = 4.6$ two-dimensional JPL supersonic nozzle

- 13 $\int \beta dx$ on the nozzle floor and ceiling walls and maximum crossflow Reynolds number $Re_{n_{max}}$ on the nozzle side walls of the $M^* = 4.6$ two-dimensional JPL air nozzle
- 14 Critical height y_{crit} of three-dimensional surface roughness
- 15 Ratio $\Delta v_{\perp_{max}}/v_{\perp_{max}} = f(\lambda/h)$ for line and point sinks
- 16 Sonic boundary layer thickness δ_s for $M^* = 3$ and 5 axisymmetric nozzles
- 17 Ideal isothermal compression for sucked nozzle wall boundary layer at $T = T_{stag}$
- B-1 Coordinates of longitudinal slot rods
- D-1 Asymptotic suction profiles (adiabatic wall)
- E-1 Table index
- E-2 Figure index

DESCRIPTION OF FIGURES

- 1 Maximum length Reynolds number Re_L on low drag suction surfaces versus external turbulence level u'/U_{∞} (without and with turbulence wires)
- 2 Linearized maximum local growth factor $B \equiv \beta \theta Re_{\theta}$ of Taylor-Goertler vortices versus $Re_{\theta} \sqrt{\theta/r}$ for the incompressible flat plate Blasius and asymptotic area suction profiles
- 3 Coordinates and Mach number variation for axisymmetric and two-dimensional supersonic nozzles
- 4 Streamwise suction mass flow distributions for axisymmetric supersonic nozzles and the $M^* = 4.6$ two-dimensional JPL nozzle
- 5-10 Nozzle wall boundary layer velocity profiles $u/U = f(y/\delta)$ at various streamwise locations of suction laminarized supersonic wind tunnel nozzles
 - 5: $M^* = 3$ axisymmetric air nozzles
 - 6: $M^* = 5$ axisymmetric air nozzles
 - 7: $M^* = 7$ axisymmetric air nozzles

- 8: $M^* = 9$ axisymmetric air nozzles
- 9: $M^* = 9$ NASA axisymmetric helium nozzle
- 10: $M^* = 4.6$ two-dimensional JPL nozzle

- 11 Nozzle wall boundary layer temperature profiles $T_E = f(y/\delta)$ at various streamwise locations of suction laminarized supersonic wind tunnel nozzles

- 12-17 Analysis of $\int \beta dx$ of the linearized Taylor-Goertler vortex growth factor in the concave curvature region of various suction laminarized supersonic nozzles under different conditions
 - 12: $M^* = 3$ axisymmetric air nozzles
 - 13: $M^* = 5$ axisymmetric air nozzles
 - 14: $M^* = 7$ axisymmetric air nozzles
 - 15: $M^* = 9$ axisymmetric air nozzle
 - 16: $M^* = 4.6$ two-dimensional JPL nozzle
 - 17: Taylor-Goertler instability summary

- 18 Pressure distribution on the side walls of the $M^* = 4.6$ two-dimensional JPL supersonic nozzle

- 19 Suction mass flow distributions on the side walls of the $M^* = 4.6$ two-dimensional JPL supersonic nozzle

- 20 Boundary layer crossflow velocity profiles $w_n/U = (f(y/\delta))$ on the side walls of the $M^* = 4.6$ two-dimensional JPL supersonic nozzle for different conditions

- 21-22 Boundary layer crossflow Reynolds number $Re_n \equiv w_{n\max}(\delta_{0.1})/\nu_e$ and $(y/\delta)_{w_{n\max}}$ on the side walls of the $M^* = 4.6$ two-dimensional JPL supersonic nozzle for different conditions

- 23 Variations of Re_θ versus x/R_{th} for the different suction laminarized supersonic wind tunnel nozzles

- 24 Variation of $\rho_e r U^2$ with the local nozzle Mach number M

- 25 Variation of local nozzle unit length Reynolds number U/ν_e with M_{local} for supersonic air nozzles

- 26 Equivalent length Reynolds number Re_{Lequ} for different suction laminarized supersonic air and helium wind tunnel nozzles
- 27 Variation of the local nozzle unit length Reynolds number U/ν_e with M_{local} for $M^* = 7$ and 9 helium nozzles
- 28-30 Critical roughness height $k = y_{crit}$ and unit length Reynolds number U/ν_k versus M_{local} in various suction laminarized supersonic nozzles (assuming $Re_{k_{crit}} \equiv U_k y_{crit}/\nu_k = 200$)
- 31 Unit length Reynolds number U/ν_k versus M_{local} in $M^* = 9$ axisymmetric helium nozzles
- 32 Goldsmith's critical suction parameter for a single row of suction holes
- 33 $Re_{\theta_{al}}$ at the front attachment line of a 45° swept blunt-nosed wing with suction through chordwise rows of holes and slots located at the attachment line
- 34 Naphthalene spray sublimation at the front attachment line of a 45° swept blunt-nosed wing with suction through chordwise rows of holes located at the attachment line
- 35 Perforated suction surface with suction hole rows swept behind the local Mach angle
- 36 Spatial variation of the vertical disturbance velocity v_\perp induced by a large number of line and point sinks at the distance h from the surface for different λ/h ratios (λ = sink spacing)
- 37 Thickness δ_s of the subsonic part of the nozzle wall boundary layer in various suction laminarized supersonic wind tunnel nozzles versus x/R_{th} and M_{local}
- 38-39 Entropy diagrams (TS) for suction medium
- B1-8 Cross sections and potential crossflow velocity distributions for longitudinal suction rods
- D-1 Asymptotic suction boundary layer profiles for air and helium

REFERENCES

1. Laufer, J.: Aerodynamic Noise in Supersonic Wind Tunnels. JAS, vol. 28, no. 9, September 1961, pp. 685-692.
2. Laufer, J.: Some Statistical Properties of the Pressure Field Radiated by a Turbulent Boundary Layer. The Physics of Fluids, vol. 7, no. 8, August 1964, pp. 1191-1197.
3. Gross, L. W.: Investigation of a Reichardt Body of Revolution With Low Drag Suction in the Norair 7 x 10 Ft Wind Tunnel. Northrop report BLC-143, NOR 62-126, December 1962.
4. Gross, L. W.: Experimental and Theoretical Investigation of a Reichardt Body of Revolution With Low Drag Suction in the NASA Ames 12 Ft Pressure Wind Tunnel. Northrop report BLC-148, NOR 63-46, July 1963.
5. Gross, L. W.: Influence of Turbulent Wakes on a Suction Body. Northrop report NCL-68-46R, July 1968.
6. Gross, L. W.: Investigation of a Laminar Suction Reichardt Body of Revolution in the Ordnance Research Laboratory 4 Ft Water Tunnel. Northrop report BLC-167, NOR 65-311, November 1965.
7. Gross, L. W.: Experimental Investigation of a 4% Thick Straight Laminar Suction Wing of 17 Ft Chord in the Norair 7 x 10 Ft Wind Tunnel. Northrop report BLC-139, NOR 62-45, May 1962.
8. Pfenninger, W.: Untersuchungen ueber Reibungsverminderungen an Tragfluegeln, insbesondere mit Hilfe von Grenzschichtabsaugung. Mittg. no. 13, Institute for Aerodyn., ETH, Zurich, 1946.
9. Squire, H. B.: On the Stability of Three-Dimensional Distribution of Viscous Fluid Between Parallel Walls. Proc. Royal Soc. (London), A 142, 1933.
10. Brown, W. B.: Stability of Compressible Boundary Layers. AIAA, vol. 5, no. 10, 1967, p. 1753.
11. Dunn, D. W.: and Lin, C. C.: On the Stability of the Laminar Boundary Layer in a Compressible Fluid. Jour. Aero. Sci., vol. 22, pp. 455-477, 1955. (See also Jour. Aero. Sci., vol. 20, 577, 1953, and vol. 19, 491, 1952.)

12. Beckwith, I. E.; Harvey, W. D.; Harris, J. E.; and Holley, B. B.: Control of Supersonic Wind Tunnel Noise by Laminarization of Nozzle-Wall Boundary Layers. NASA TMX-2879, December 1973.
13. Bertram, M.; and Beckwith, I.: Survey on NASA Langley Studies on High Speed Transition and the Quiet Tunnel. NASA TMX-2566, July 1972.
14. Pfenninger, W.; and Bacon, J. W.: Investigation of Methods for Reestablishment of a Laminar Boundary Layer From Turbulent Flow. Northrop report BLC-161, NOR 65-48, February 1965.
15. Pfenninger, W.: Flow Phenomena at the Leading Edge of Swept Wings. Agardograph 97, Recent Developments in Boundary Layer Research, part IV, May 1965.
16. Pfenninger, W.; and Bacon, J. W.: About the Development of Swept Laminar Suction Wings With Full Chord Laminar Flow. Northrop report BLC-130, NOR 60-299, September 1960.
17. Pfenninger, W.: Flow Problems of Swept Low Drag Suction Wings of Practical Construction at High Reynolds Numbers. Annals of the New York Academy of Sciences, vol. 154, art. 2, November 22, 1968, pp. 672-703.
18. Owen, P. R.; and Randall, D. J.: Boundary Layer Transition on the Sweptback Wing. RAE TM Aero. 277, May 1952.
19. Gregory, N.; Stuart, J. T.; and Walker, W. S.: On the Stability of Three-Dimensional Boundary Layers With Application to the Flow Due to a Rotating Disc. Phil. Trans. Roy. Soc., A 248, 1955.
20. Groth, E. E.: Low Drag Boundary Layer Suction Experiments on a 36° Swept Wing at Mach Numbers 2.5, 3, and 3.5. Northrop report BLC-150, NOR 63-54, September 1963.
21. Goldsmith, J.: Low Drag Boundary Layer Suction Experiments on a 72° Swept Wing Model at $M = 2$ and 2.25. Vol. II, Summary of Laminar Boundary Layer Control Research, Air Force report ASD-TDR-63-554, March 1964.
22. Groth, E. E.: Low Drag Boundary Layer Suction Experiments on a Three-Dimensional Supersonic Leading Edge Suction Wing. Air Force report AFFDL-TR-65-158, September 1965.

23. Brown, W. B.: Crossflow Stability Calculations of Highly Swept (65° Sweep) Supersonic Low Drag BLC Wing (Mach Number 1.8) With and Without Cooling. Northrop report BLC-138, NOR 61-263, February 1962.
24. Taylor, G. I.: Stability of a Viscous Liquid Contained Between Two Rotating Cylinders. Phil. Trans. Roy. Soc. (London), A 223, 1923, pp. 289-343.
25. Goertler, H.: Ueber eine 3-dimensionale Instabilitaet laminarer Grenzschichten an konkaven Waenden. Ges. d. Wiss. Goettingen, Nachrichten a.d. Math, 2, no. 1, 1940.
26. Smith, A. M. O.: On the Growth of Taylor-Goertler Vortices Along Highly Concave Walls. Douglas report ES 17110, March 1953; Quart. Appl. Math., 13, 1955, pp. 233-262.
27. Kobayashi, R.: Note on the Stability of a Boundary Layer on a Concave Wall With Suction. J. Fluid Mech., vol. 52, part 2, 1972, pp. 269-272.
28. Haemmerlin, G.: Ueber die Stabilitaet einer kompressiblen Stroemung laengs einer konkaven Wand bei verschiedenen Wandtemperaturver-haeltnissen. DVL report no. 176, November 1961.
29. Aihara, Y.: Stability of the Compressible Boundary Layer Along a Curved Wall Under Goertler-Type Disturbances. Report no. 362, Aeronautical Research Institute, University of Tokyo, 1961.
30. Haemmerlin, G.: Ueber das Eigenwertproblem der 3-dimensionalen Instabilitaet laminarer Grenzschichten an konkaven Waenden. Journal Rat. Mech. Anal. 4, 1955, pp. 279-321.
31. Feifel, W.: Experimentelle Untersuchung, uber die Laminarhaltung der Grenzschicht beim Fluegel-Rumpf-uebergang. Diplom-thesis, Inst. f. Aerodynamics and Gasdynamics, TH, Stuttgart, July 1964.
32. Goldsmith, J.: Laminar Flow at the Juncture of Two Aeroplane Components. Vol. 2 of Boundary Layer and Flow Control, G. V. Lachmann, editor, 1961, p. 1000.
33. Goldsmith, J.: Preliminary Experiments on the Maintenance of Laminar Flow by Means of Suction in the Region of a Wing Leading Edge and Fuselage Junction. Northrop report BLC-106, NAI-58-249, April 1958.
34. Goldsmith, J.: Experiments With Laminar Flow Near the Juncture of a Fuselage and Wing Trailing Edge. Northrop report BLC-120, NOR 59-306, June 1959.

35. Groth, E. E.: Investigation of the Flow Field Around a Suction Slot at Supersonic Speeds. Northrop report BLC-116, NAI-59-4, January 1959.
36. Groth, E. E.: Low Drag Boundary Layer Suction Experiments on a Pointed Body of Revolution of 9.2 Inch Maximum Diameter at High Length Reynolds Numbers and Mach Numbers Between 2.5 and 3.5. Air Force report AFFL-TR-66-65, July 1966.
37. Pfenninger, W.; Bacon, J.; and Goldsmith, J.: Flow Disturbances Induced by Low Drag Boundary Layer Suction Through Slots. The Physics of Fluid Supplement, 1967, p. S112.
38. Bacon, J. W.: Study of Slot Flow Induced Disturbances. Northrop report NCL-68-46R, July 1968.
39. Meyer, W. A.; Goldsmith, J.; and Pfenninger, W.: Note on Preliminary Laminar Suction Experiments Through Round Holes at High Reynolds Numbers and Low Turbulence. Northrop report BLC 12, September 1953.
40. Goldsmith, J.; and Meyer, W. A.: Preliminary Experiments on Laminar Boundary Layer Suction Through Circular Holes at High Reynolds Numbers and Low Turbulence. Northrop report BLC 23, November 1953.
41. Goldsmith, J.: Additional Experiments on Laminar Boundary Layer Suction Through Circular Holes at High Reynolds Numbers and Low Turbulence. Northrop report BLC 28, February 1954.
42. Goldsmith, J.: Experiments With Laminar Boundary Layer Suction Through Rows of Closely Space Circular Holes at High Reynolds Number and Low Turbulence. Northrop report BLC 36, March 1954.
43. Meyer, W. A.: Preliminary Report on the Flow Field Due to Low Drag Suction Through Holes. Northrop report BLC 75, NAI-55-457, April 1955.
44. Goldsmith, J.: Investigation of the Flow in a Tube With Laminar Suction Through 80 Rows of Closely-Spaced Holes. Northrop report BLC 86, NAI-56-293, March 1956.
45. Goldsmith, J.: Critical Laminar Suction Parameters for Suction Into an Isolated Hole or a Single Row of Holes. Northrop report BLC 95, NAI-57-529, February 1957.
46. Raspet, A.: Boundary Layer Studies on a Sailplane. Aeron. Eng. Review, vol. 11, no. 6, 1952, pp. 52-60.

47. Carmichael, B. H.: Flight Observations of Suction Stabilized Boundary Layers. Aeron. Eng. Review, vol. 13, no. 2, 1954, pp. 36-41.
48. Wortmann, F. X.; Feifel, W.: Low Drag Suction Experiments in the Stuttgart Low Turbulence Tunnel on a 19% Thick Highly Cambered Low Drag Suction Airfoil With Suction Through Spanwise Rows of Suction Holes. Inst. f. Aerodyn. report, TH, Stuttgart.
49. Schubauer, G. B.; Spangenberg, W. G.; and Klebanoff, P. S.: Aerodynamic Characteristics of Damping Screens. NACA TN 2001, 1950.
50. Townsend, A. A.: The Structure of Turbulent Shear Flow. Cambridge Univ. Press, 1956.
51. Farwick, C. A.: Design of Perfect Supersonic Nozzles LAB 306. Boeing document D6-29880TN, January 1969.
52. Reyhner, T. A.: A Computer Program for Finite-Difference Calculation of Compressible Turbulent Boundary Layers. Boeing document D6-23236, 1970 (includes also the laminar case).
53. Simmons, J. T.: The Physical and Thermodynamic Properties of Helium. W. R. Whittaker Co. Ltd. report D-9027, July 1, 1957.
54. Akin, S. W.: The Thermodynamic Properties of Helium. Trans. ASME, August 1950, pp. 751-757.
55. Johnston, H. L.; and Grilly, E. R.: Viscosities of Carbon Monoxide, Helium, Neon, and Argon Between 80° and 300° K. Coefficients of Viscosity. Journal Phys. Chem., vol. 46, 1942, pp. 948-963.
56. Raetz, G. S.: A Method of Calculating Three-Dimensional Laminar Boundary Layers of Steady Compressible Flows. Northrop report BLC-114, NAI-58-73, December 1957.
57. Mack, L.: Computation of the Stability of the Laminar Compressible Boundary Layer. Methods in Computational Physics, vol. 4, 1965, p. 247.
58. Gunness, R. C.: The Stability Equations for High Mach Number Boundary Layer Flow. Boeing document D6-20652, 1968.

59. Groth, E. E.: Low Drag Boundary Layer Suction Experiments on a Flat Plate at Mach Numbers 3 and 3.5. Northrop report BLC-135, NOR-61-251, October 1961.
60. Bacon, J. W.; and Pfenninger, W.: Influence of Acoustical Disturbances on the Behavior of a Swept Laminar Suction Wing. Northrop report BLC-141, NOR 62-124, October 1962.
61. Brown, W. B.: Numerical Calculation of the Stability of Crossflow Profiles in Laminar Boundary Layers on a Rotating Disc and on a Sweptback Wing. Northrop report BLC-117, NAI-59-5, January 1959. (See also Boundary Layer and Flow Control, vol. II, G. V. Lachmann, editor, 1961, pp. 913-923.)
62. Hayes, W. D.; and Probstein, R. F.: Hypersonic Flow Theory. Academic Press, New York and London, 1959.
63. Bussmann, K.; and Muenz, H.: Die Stabilitaet der laminaren Reibungsschicht mit Absaugung. Jahrbuch d. deutsch Luftfahrtforschung I, 36, 1942.
64. Pfenninger, W.: Studies to Verify Laminar Flow at Very High Length Reynolds Numbers by Means of Distributed Suction in the Presence of Minimum Disturbances. Boeing document D6-40281, February 1972.
65. von Doenhoff, A. E.; and Braslow, A. L.: The Effect of Distributed Surface Roughness on Laminar Flow. Vol. II of Boundary Layer and Flow Control, G. V. Lachmann, editor, 1961, pp. 657-681.
66. Tani, Itiro: Effect of Two-Dimensional and Isolated Roughness on Laminar Flow. Vol. II of Boundary Layer and Flow Control, G. V. Lachmann, editor, 1961, pp. 637-656.
67. Carmichael, B. H.; Whites, R. C.; and Pfenninger, W.: Low Drag Boundary Layer Suction Experiments in Flight on the Wing Glove of an F-94A Airplane. Phase III, Laminar Suction Airfoil Tolerances. Northrop report BLC-101, NAI-57-1163, August 1957.
68. Carmichael, B. H.: Prediction of Critical Reynolds Numbers for Single Three-Dimensional Roughness Elements. Northrop report BLC-109, NAI-58-412, May 1958.
69. Carmichael, B. H.: Critical Roughness Reynolds Numbers for Multiple Three-Dimensional Roughness Elements. Northrop report BLC-112, NAI-58-589, July 1958.

70. Gregory, N.; and Walker, W. S.: The Effect on Transition of Isolated Surface Excrescences in the Boundary Layer. A.R.C., 13436, 1950.
71. Bacon, J. W.; and Pfenninger, W.: Transition Experiments at the Front Attachment Line of a 45° Swept Wing With a Blunt Leading Edge. Air Force report AFFDL-TR-67-33, April 1967. (See also ref. 17.)
72. Pfenninger, W.; and Bacon, J. W.: Amplified Laminar Boundary Layer Oscillations and Transition at the Front Attachment Line of a 45° Swept Flat-Nosed Wing With and Without Boundary Layer Suction. Northrop report NCL-68-40R, July 1968. (Published also in Viscous Drag Reduction, C. S. Wells, editor, Plenum Press, 1969, pp. 85-105.)
73. Omar, M. E.: Two-Dimensional Potential Flow Solutions for an Infinite Cascade of Airfoils. Boeing document D6-20658, 1969.
74. Raetz, G. S.: A New Theory of the Cause of Transition in Fluid Flows. Northrop report BLC-121, NOR 59-383, June 1959.
75. Raetz, G. S.: Calculation of Precise Proper Solutions for the Resonance Theory of Transition. Air Force report AFFDL-TR-64-185, October 1964.
76. Raetz, G. S.: Current Status of Resonance Theory of Transition. Air Force report ASD-TDR-63-554, March 1964.
77. Raetz, G. S.: A Further Development of the Resonance Theory of Transition Including a Correlation With an Experiment. Air Force report AFFDL-TR-66-192, November 1966.
78. Raetz, G. S.: A Hypothetical Model of a Transitional Boundary Layer. Air Force report AFFDL-TR-70-123, November 1970.
79. Stuart, J. T.: Nonlinear Effects in Hydrodynamic Stability. Proceedings of the Xth International Congress for Theoretical and Applied Mechanics, Stresa, 1960; Applied Mechanics, Elsevier Publish. Co., 1962, pp. 63-97.
80. Schubauer, G. B.; and Klebanoff, P. S.: Contributions on the Mechanics of Boundary Layer Transition. NACA TN 3489, 1955; NACA technical report 1289, 1956. (See also Proceedings of the Symposium on Boundary Layer Theory, NPL, England, 1955.)

**TABLE 1.—COORDINATES AND STREAMWISE
MACH NUMBER VARIATION**

a) $M^* = 3$, $R = 6 R_{th}$, axisymmetric air nozzle

$\frac{x}{R_{th}}$	M	$\frac{x}{R_{th}}$	$\frac{r}{R_{th}}$
— 17.634	0.00815	— 17.634	8.4258
— 12.6387	.01017	— 12.6387	7.545
— 11.2344	.01088	— 11.2344	7.2921
— 9.8301	.012	— 9.8301	6.945
— 8.4258	.0138	— 8.4258	6.4654
— 7.0215	.017	— 7.0215	5.8395
— 5.6172	.0227	— 5.6172	5.0493
— 4.915	.0275	— 4.2129	4.0646
— 4.2129	.03505	— 3.5107	3.5048
— 3.5107	.0471	— 2.8086	2.943
— 2.8086	.0668	— 2.2469	2.4936
— 2.4575	.0817	— 1.6852	2.0442
— 2.1064	.103	— 1.1234	1.5949
— 1.7554	.133	— 0.8426	1.3702
— 1.4043	.178	— .5617	1.1599
— 1.0532	.254	— .4213	1.0854
— 0.7021	.403	— .2809	1.0345
— .3511	.66	— .1404	1.007
0	1.0	0	1.0
.49	1.301	.1526	1.0019
.96	1.577	.3249	1.0088
1.48	1.864	.6	1.0301
2.01	2.03	.9097	1.0694
3.02	2.273	1.2605	1.1339
4.03	2.457	1.8921	1.2763
5.13	2.616	2.6208	1.4336
7.04	2.818	3.7327	1.637
8.92	2.945	4.9716	1.8076
10.26	2.991	6.3232	1.9335
		7.7762	2.0115
		9.1185	2.043
		10.26	2.0489

$$\frac{R_{th}}{D^*} = 0.244$$

TABLE 1.—COORDINATES AND STREAMWISE
MACH NUMBER VARIATION (Continued)

b) $M^* = 3$, $R = 12 R_{th}$, axisymmetric air nozzle

$\frac{x}{R_{th}}$	M	$\frac{x}{R_{th}}$	$\frac{r}{R_{th}}$
— 17.634	0.00815	— 17.634	8.4258
— 12.6387	.01017	— 12.6387	7.545
— 11.2344	.01088	— 11.2344	7.2921
— 9.8301	.012	— 9.8301	6.945
— 8.4258	.0138	— 8.4258	6.4654
— 7.0215	.017	— 7.0215	5.8395
— 5.6172	.0227	— 5.6172	5.0493
— 4.915	.0275	— 4.2129	4.0646
— 4.2129	.03505	— 3.5107	3.5048
— 3.5107	.0471	— 2.8086	2.943
— 2.8086	.0668	— 2.2469	2.4936
— 2.4575	.0817	— 1.6852	2.0442
— 2.1064	.103	— 1.1234	1.5949
— 1.7554	.133	— 0.8426	1.3702
— 1.4043	.178	— .5617	1.1599
— 1.0532	.254	— .4213	1.0854
— 0.7021	.403	— .2809	1.0345
— .3511	.66	— .1404	1.007
0	1.0	0	1.0
.498	1.193	.3049	1.0039
.956	1.372	.6119	1.0156
1.456	1.564	.9562	1.0382
1.872	1.737	1.2032	1.0605
2.271	1.922	1.5942	1.1064
2.972	2.128	1.9064	1.1524
4.034	2.343	2.2708	1.2168
5.07	2.506	2.636	1.2888
6.025	2.629	3.2268	1.404
7.036	2.737	3.8938	1.5249
8.281	2.845	4.6151	1.6413
9.401	2.92	5.3818	1.7474
10.562	2.978	6.1895	1.84
11.684	3.009	7.0357	1.9172
		8.0991	1.988
		9.211	2.035
		10.3655	2.0598
		11.684	2.0667

$$\frac{R_{th}}{D^*} = 0.242$$

TABLE 1.—COORDINATES AND STREAMWISE
MACH NUMBER VARIATION (Continued)

c) $M^* = 5$ Q-nozzle (with test section) axisymmetric air nozzle

$\frac{x}{R_{th}}$	M	$\frac{x}{R_{th}}$	$\frac{r}{R_{th}}$
— 11.112	0.012	— 11.112	6.9204
— 10.281	.013	— 10.2805	6.575
— 9.424	.017	— 9.4241	5.857
— 8.568	.027	— 8.5677	4.6049
— 7.724	.042	— 7.7237	3.698
— 6.83	.066	— 6.8295	2.9701
— 6.036	.098	— 6.036	2.441
— 5.192	.142	— 5.1919	2.033
— 4.285	.205	— 4.2851	1.7004
— 3.486	.293	— 3.4864	1.4407
— 2.648	.407	— 2.6475	1.2521
— 1.796	.581	— 1.7962	1.101
— 0.95	.783	— 0.9448	1.02267
— .103	1.0	0	1.0
— .078	1.0	.1587	1.00272
0	1.0	.315	1.00514
.315	1.0826	.4737	1.01028
.6297	1.1637	.6297	1.01511
.9447	1.2001	.9447	1.02781
1.5744	1.2757	1.5744	1.0656
2.8265	1.5943	2.2016	1.11608
3.4538	1.7589	2.8265	1.18138
4.7007	2.0826	3.4538	1.25695
5.9426	2.3881	4.7007	1.44105
7.1847	2.6661	5.9426	1.64752
8.4265	2.9161	7.1847	1.86669
9.666	3.1421	8.4265	2.08827
10.908	3.3496	9.666	2.31499
13.392	3.7086	10.9078	2.54172
15.883	3.9936	12.1472	2.759
18.382	4.2226	13.3918	2.97249
22.138	4.4891	14.6363	3.1717
25.905	4.6851	15.8833	3.35792
30.935	4.8696	17.1327	3.53174
36.598	5.0031	18.3821	3.689
49.1914	5.1151	20.2591	3.91475
		22.1382	4.11366
		24.02	4.29262
		25.9045	4.45133
		28.4184	4.62757
		30.935	4.78144
		33.351	4.90719
		36.5983	5.02811
		39.1173	5.10127
		42.2663	5.1717
		45.4126	5.2122
		49.1914	5.24244

$$\frac{R_{th}}{D^*} = 0.0954$$

TABLE 1.—COORDINATES AND STREAMWISE
MACH NUMBER VARIATION (Continued)

d) $M^* = 5$ rapid expansion axisymmetric air nozzle

$\frac{x}{R_{th}}$	M	$\frac{x}{R_{th}}$	$\frac{r}{R_{th}}$
— 5.6001	0.0121	— 5.6001	6.9302
— 4.4967	.0125	— 4.4967	6.8017
— 3.5496	.0141	— 3.5496	6.4012
— 2.6049	.0185	— 2.6049	5.6001
— 2.0154	.0251	— 2.0154	4.8014
— 1.4779	.0399	— 1.4779	3.8083
— 0.9855	.0782	— 0.9855	2.7249
— .7276	.1324	— .7276	2.1013
— .5399	.2236	— .5399	1.633
— .4105	.3485	— .4105	1.3359
— .315	.4804	— .315	1.1744
— .2303	.6067	— .2303	1.0865
— .1511	.7035	— .1511	1.0363
— .0774	.8542	— .0774	1.0097
— .0085	.9732	— .0085	1.0003
0	1.0	0	1.0
.0166	1.0404	.0166	1.0
.1049	1.1133	.1049	1.0051
.2403	1.2296	.2403	1.0197
.3440	1.3151	.3440	1.0358
.4562	1.4036	.4562	1.0568
.6680	1.5718	.6680	1.1081
.9492	1.7401	.9492	1.189
1.2322	1.9023	1.2322	1.279
1.5166	2.1423	1.5166	1.369
1.8945	2.3118	1.8945	1.4888
2.2672	2.4678	2.2672	1.602
2.834	2.6783	2.834	1.769
3.2421	2.8178	3.2421	1.8869
4.4565	3.1616	4.4565	2.2219
5.6657	3.4321	5.6657	2.5242
7.0713	3.6856	7.0713	2.8391
8.6859	3.9186	8.6859	3.1566
9.8223	4.0551	9.8223	3.3555
11.7116	4.2468	11.7116	3.6502
13.7597	4.4136	13.7597	3.9223
15.9538	4.5558	15.9538	4.1666
18.279	4.6756	18.279	4.3809
20.584	4.7683	20.584	4.552
23.1106	4.8486	23.1106	4.7031
25.7128	4.9098	25.7128	4.8216
29.3706	4.9676	29.3706	4.935
33.9882	5.0056	33.9882	5.0106
38.6765	5.0156	38.6765	5.0308

$$\frac{R_{th}}{D^*} = 0.0994$$

**TABLE 1.—COORDINATES AND STREAMWISE
MACH NUMBER VARIATION (Continued)**

e) $M^* = 7$, $R = 30 R_{th}$, axisymmetric air nozzle

$\frac{x}{R_{th}}$	M	$\frac{x}{R_{th}}$	M	$\frac{x}{R_{th}}$	$\frac{r}{R_{th}}$
11.112	0.012	70.644	6.67	31.694	6.987
10.281	.013	77.889	6.785	34.155	7.3
9.424	.017	85.384	6.882	39.354	7.883
8.568	.027	93.113	6.959	44.921	8.403
7.724	.042	102.425	7.016	50.847	8.855
6.83	.066	$\frac{x}{R_{th}}$	$\frac{r}{R_{th}}$	57.123	9.239
6.036	.098			63.734	9.553
5.192	.142	—		70.664	9.798
4.285	.205			77.889	9.978
3.486	.293			85.384	10.097
2.648	.407			93.113	10.161
1.796	.581			102.425	10.181
0.95	.783				
.103	1.0				
.078	1.0				
0	1.0				
.485	1.1				
.649	1.146				
.851	1.194				
1.364	1.307				
2.149	1.498				
3.61	1.874	0	1.0		
4.567	2.138	.485	1.004		
5.541	2.422	.649	1.007		
6.929	2.841	.851	1.012		
8.245	3.263	1.364	1.031		
9.942	3.683	2.149	1.077		
11.186	3.733	3.61	1.218		
12.538	3.957	4.567	1.35		
13.999	4.151	5.541	1.516		
15.57	4.333	6.929	1.811		
17.243	4.505	8.245	2.155		
19.015	4.668	8.88	2.338		
20.884	4.823	9.942	2.633		
22.849	4.97	11.186	2.975		
24.911	5.11	12.538	3.343		
27.071	5.245	13.998	3.717		
29.329	5.373	15.57	4.099		
31.694	5.503	17.243	4.481		
34.155	5.615	19.015	4.862		
39.354	5.835	20.884	5.238		
44.921	6.037	22.849	5.607		
50.87	6.221	24.911	5.968		
57.123	6.388	27.071	6.319		
63.734	6.538	29.329	6.659		

$$\frac{R_{th}}{D^*} = 0.0491$$

TABLE 1.—COORDINATES AND STREAMWISE
MACH NUMBER VARIATION (Continued)

f) $M^* = 7$, $R = 75 R_{th}$, axisymmetric air nozzle

$\frac{x}{R_{th}}$	M	$\frac{x}{R_{th}}$	M	$\frac{x}{R_{th}}$	$\frac{r}{R_{th}}$
— 11.112	0.012	75.78	6.531	42.116	7.139
— 10.281	.013	82.91	6.647	46.115	7.563
— 9.424	.017	90.308	6.747	50.307	7.955
— 8.568	.027	99.888	6.846	56.191	8.421
— 7.724	.042	111.334	6.916	62.405	8.823
— 6.830	.066			68.939	9.158
— 6.036	.098			75.78	9.427
— 5.192	.142			82.91	9.631
— 4.285	.205	— 11.112	6.902	90.308	9.774
— 3.486	.293	— 10.281	6.575	97.946	9.861
— 2.648	.407	— 9.424	5.857	103.809	9.894
— 1.796	.581	— 8.568	4.605	111.334	9.906
— 0.95	.783	— 7.724	3.698		
— .103	1.0	— 6.830	2.970		
— .078	1.0	— 6.036	2.441		
0	1.0	— 5.192	2.033		
.769	1.1	— 4.285	1.7		
1.104	1.151	— 3.486	1.441		
1.455	1.199	— 2.648	1.252		
2.112	1.293	— 1.796	1.101		
3.026	1.427	— 0.95	1.023		
4.07	1.59	0	1.0		
5.041	1.743	.769	1.004		
6.074	1.914	1.104	1.008		
7.092	2.087	1.455	1.014		
8.225	2.282	2.112	1.030		
9.49	2.504	3.026	1.061		
11.003	2.777	4.07	1.111		
12.731	3.095	5.041	1.17		
14.26	3.383	6.074	1.246		
16.214	3.76	7.092	1.336		
17.723	4.003	8.225	1.452		
19.88	4.231	9.49	1.603		
22.36	4.455	11.003	1.812		
25.109	4.681	12.731	2.088		
28.094	4.892	14.26	2.368		
31.296	5.09	16.214	2.774		
34.703	5.275	17.723	3.111		
38.311	5.449	19.88	3.575		
42.116	5.619	22.36	4.092		
46.115	5.765	25.109	4.629		
50.307	5.91	28.094	5.166		
56.191	6.088	31.296	5.692		
62.405	6.251	34.703	6.2		
68.939	6.399	38.311	6.684		

$$\frac{R_{th}}{D^*} = 0.0504$$

TABLE 1.—COORDINATES AND STREAMWISE
MACH NUMBER VARIATION (Continued)

g) $M^* = 9$, $R = 200 R_{th}$, axisymmetric air nozzle

$\frac{x}{R_{th}}$	M	$\frac{x}{R_{th}}$	$\frac{r}{R_{th}}$
— 11.112	0.012	— 11.112	6.9024
— 10.281	.013	— 10.2805	6.575
— 9.424	.017	— 9.424	5.857
— 8.568	.027	— 8.568	4.605
— 7.724	.042	— 7.724	3.698
— 6.83	.066	— 6.83	2.97
— 6.036	.098	— 6.036	2.441
— 5.192	.142	— 5.192	2.033
— 4.285	.205	— 4.285	1.7
— 3.486	.293	— 3.486	1.441
— 2.648	.407	— 2.648	1.252
— 1.796	.581	— 1.796	1.101
— 0.95	.783	— 0.95	1.023
— .103	1.0	0	1.0
— .078	1.0	1.257	1.004
0	1.0	2.432	1.015
1.257	1.1	3.632	1.033
2.432	1.2	5.112	1.065
3.632	1.304	7.559	1.143
5.112	1.438	10.049	1.253
7.559	1.67	12.682	1.402
10.049	1.917	14.911	1.557
12.682	2.187	17.403	1.759
14.911	2.421	20.441	2.047
17.403	2.686	24.207	2.47
20.441	3.013	28.447	3.033
24.207	3.423	32.384	3.639
28.447	3.89	37.119	4.475
32.384	4.33	40.944	5.201
37.119	4.868	50.336	6.897
40.944	5.184	60.026	8.463
50.336	5.755	70.992	10.014
60.026	6.203	80.835	11.229
70.992	6.604	90.231	12.249
80.835	6.909	100.221	13.203
90.231	7.161	110.798	14.084
100.221	7.396	120.531	14.791
110.798	7.613	130.703	15.435
120.531	7.792	139.768	15.935
130.703	7.961	150.740	16.458
139.768	8.097	160.476	16.852
150.74	8.245	170.511	17.198
160.476	8.364	180.836	17.496
170.511	8.475	191.438	17.746
236.340	8.969	205.985	18.008
265.088	9.066	220.967	18.193
		236.340	18.308
		265.088	18.373

$$\frac{R_{th}}{D^*} = 0.0272$$

TABLE 1.—COORDINATES AND STREAMWISE
MACH NUMBER VARIATION (Continued)

h) $M^* = 8.93$, $R = 250 R_{th}$, axisymmetric helium nozzle

$\frac{x}{R_{th}}$	M	$\frac{x}{R_{th}}$	$\frac{r}{R_{th}}$
— 11.112	0.012	— 11.112	6.902
— 10.281	.013	— 10.281	6.575
— 9.424	.017	— 9.424	5.857
— 8.568	.027	— 8.568	4.605
— 7.724	.042	— 7.724	3.698
— 6.83	.066	— 6.83	2.97
— 6.036	.098	— 6.036	2.441
— 5.192	.142	— 5.192	2.033
— 4.285	.205	— 4.285	1.7
— 3.486	.293	— 3.486	1.441
— 2.648	.407	— 2.648	1.252
— 1.796	.581	— 1.796	1.101
— 0.95	.783	— 0.95	1.023
— .103	1.0	0	1.0
— .078	1.0	1.328	1.004
0	1.0	2.563	1.013
1.328	1.1	4.321	1.037
2.563	1.201	7.011	1.098
4.321	1.350	10.873	1.237
7.011	1.6	15.166	1.46
10.873	2.001	19.115	1.732
15.166	2.502	22.732	2.036
19.115	3.012	25.925	2.348
22.732	3.521	30.691	2.891
25.925	4.001	40.163	4.003
30.691	4.779	50.704	4.985
40.163	5.817	60.141	5.646
50.704	6.621	70.601	6.185
60.141	7.182	80.347	6.54
70.601	7.68	90.773	6.793
80.347	8.057	101.819	6.95
90.773	8.382	111.431	7.014
101.819	8.649	122.119	7.032
111.431	8.819		
122.119	8.93		

$$\frac{R_{th}}{D^*} = 0.0711$$

TABLE 1.—COORDINATES AND STREAMWISE
MACH NUMBER VARIATION (Continued)

i) $M^* = 9$ NASA axisymmetric helium nozzle

$\frac{x}{R_{th}}$	$\frac{y}{R_{th}}$	M	Wall slope
0	1.0000	1.0000	0
0.1554	1.0040	1.1000	
.322	1.0111	1.1813	0.03462
.589	1.0228	1.2774	.05326
1.021	1.0515	1.4353	.07857
1.604	1.1059	1.6520	.1066
2.571	1.2277	2.0120	.1407
3.912	1.4345	2.4696	.1621
5.036	1.6231	2.8225	.1693
6.642	1.9013	3.2899	.1732
8.577	2.2414	3.8091	.1743
10.541	2.5870	4.2811	.1724
13.583	3.0907	4.8204	.1555
16.754	3.5592	5.2717	.1381
20.560	4.0521	5.7222	.1200
24.433	4.4876	6.1106	.1044
30.016	5.0181	6.5829	.08576
35.039	5.4141	6.9426	.07200
40.568	5.7766	7.2846	.05931
46.546	6.0961	7.6035	.04782
52.376	6.3467	7.8728	.03836
58.538	6.5562	8.1194	.02985
63.487	6.6890	8.2928	.02396
69.187	6.8084	8.4679	.01805
75.036	6.8983	8.66224	.01286
80.918	6.9606	8.7538	.00843
86.702	6.9986	8.8602	.00483
91.540	7.0159	8.9314	.00239
95.472	7.0221	8.9758	.00085
98.667	7.0234	8.9991	.00032

$$\frac{R_{th}}{D^*} = 0.0712$$

TABLE 1.—COORDINATES AND STREAMWISE
MACH NUMBER VARIATION (Concluded)

j) $M^* = 4.6$ two-dimensional JPL nozzle

$\frac{x}{0.5 H_{th}}$	M	$\frac{x}{0.5 H_{th}}$	$\frac{H}{H_{th}}$
— 50.27	0.0387	— 50.27	14.956
— 39.639	.0667	— 39.639	8.698
— 34.234	.0886	— 34.234	6.564
— 28.828	.1212	— 28.828	4.82
— 23.423	.1713	— 23.423	3.438
— 18.017	.2510	— 18.017	2.394
— 14.413	.33	— 14.413	1.871
— 10.811	.4384	— 10.811	1.478
— 7.207	.5846	— 7.207	1.207
— 3.602	.7726	— 3.602	1.051
— 1.801	.8819	— 1.801	1.013
0	1.0	0	1.0
1.803	1.1243	1.803	1.012
3.604	1.2529	3.604	1.048
5.405	1.3838	5.405	1.106
7.209	1.5147	7.209	1.186
10.811	1.7702	10.811	1.407
14.415	2.0107	14.415	1.703
19.821	2.3371	19.821	2.268
25.226	2.6234	25.226	2.96
30.631	2.8717	30.631	3.747
36.037	3.0879	36.037	4.603
41.442	3.2762	41.442	5.505
46.318	3.4259	46.318	6.335
52.38	3.5867	52.38	7.358
57.766	3.7099	57.766	8.242
63.983	3.8322	63.983	9.217
71.139	3.9529	71.139	10.275
79.358	4.0682	79.358	11.39
88.75	4.1764	88.75	12.528
95.73	4.2427	95.73	13.28
107.395	4.3334	107.395	14.365
120.685	4.4132	120.685	15.38
135.762	4.4794	135.762	16.275
151.723	4.5287	151.723	16.969
168.011	4.5624	168.011	17.457
184.268	4.5832	184.268	17.764
200.201	4.5944	200.201	17.933
215.49	4.5992	215.49	18.002
229.898	4.6	229.898	18.017

$$\frac{H_{th}}{H^*} = 0.0555$$

TABLE 2.—BOUNDARY LAYER DEVELOPMENT ANALYSIS DATA—AXISYMMETRIC NOZZLES

a) $M^* = 3$, $R = 6 R_{th}$, suction 6 and 5, $T_{stag} = 300^\circ K$, T_{wallad}

$$\frac{U^*}{\nu} = 8 \cdot 10^6 / ft = 26.22 \cdot 10^6 / m, D^* = 1m$$

$\frac{x}{R_{th}}$	$10^3 \cdot \frac{\delta^*}{R_{th}}$	$10^3 \cdot \frac{\theta}{R_{th}}$	$10^3 \cdot \frac{\delta}{R_{th}}$	Re_θ	M	$\frac{r}{R_{th}}$	$\frac{U}{U^*}$	$-10^3 \cdot \frac{\rho_{e/o}}{\rho^* U^*}$	$10^3 \cdot cf$	RF
Suction 6										
-10	6.25	2.93	23.6	653	0.0118	6.993	0.0066	0		
-5	2.49	1.27	12.9	643	.0268	4.641	.0149	0		
-3								0		
-2.5	0.937	0.477	4.69	713	.0796	2.696	.0444	0.080	1.415	0.863
0	.241	.0908	0.872	1140	.990	0.9998	.505	.480	0.738	.8697
0.5	.347	.109	1.063	1412	1.3167	1.0209	.633	.472	.567	.8755
1	.457	.125	1.292	1522	1.6076	1.0844	.728	.463	.548	.8951
2	.719	.1526	1.739	1583	2.0371	1.3006	.840	.447	.521	.9151
4	1.119	.1843	2.371	1565	2.4533	1.6785	.922	.397	.554	.9505
6	1.518	.2120	2.980	1569	2.7215	1.9085	.964	.330	.565	.9759
8	1.842	.2318	3.469	1568	2.893	2.0189	.987	.310	.588	.9814
10.26	2.068	.2437	3.801	1567	2.991	2.0489	.999	.300	.602	
Suction 5										
-10 to 0	As suction 6, $R = 6 R_{th}$									
0.5	0.3450	0.1090	1.060	1406				0.493	0.573	0.8702
1	.4498	.1232	1.278	1501				.507	.564	.8777
2	.6815	.1450	1.672	1504				.533	.571	.9028
4	.9368	.1529	2.038	1299				.573	.726	.9525
6	1.057	.1430	2.124	1058				.600	.928	.9853
8	1.105	.1323	2.079	895				.600	1.084	1.0016
10.26	1.108	.1250	2.008	804				.600	1.187	1.0054

TABLE 2.—BOUNDARY LAYER DEVELOPMENT ANALYSIS DATA—AXISYMMETRIC NOZZLES (Continued)

b) $M^* = 3$, $R = 3 R_{th}$, section 5, $T_{stag} = 300^\circ K$, $T_{wall ad}$

$$\frac{U^*}{p^*} = 8 \cdot 10^6 / ft = 26.22 \cdot 10^6 / m, D^* = 1m$$

$\frac{x}{R_{th}}$	$10^3 \cdot \frac{\delta^*}{R_{th}}$	$10^3 \cdot \frac{\theta}{R_{th}}$	$10^3 \cdot \frac{\delta}{R_{th}}$	Re θ	M	$\frac{r}{R_{th}}$	$\frac{U}{U^*}$	$-10^3 \cdot \frac{\rho_{e v o}}{\rho^* U^*}$	$10^3 \cdot c_f$	RF
-3	0.937	0.477	4.69	713	0.0796	2.696	0.0444	0	0.080	0.862
-2.5	.233	.0877	0.854	1108	1.010	0.9998	.513	.480	.641	.8679
0	.355	.103	1.056	1289	1.503	1.0422	.696	.493	.573	.8811
0.5	.514	.124	1.338	1407	1.8185	1.1562	.787	.507	.588	.9104
1	.729	.146	1.705	1450	2.1320	1.4009	.8607	.533	.772	.9586
2	.977	.152	2.079	1237	2.5348	1.7672	.9353	.573	.984	.9901
4	1.083	.140	2.132	1002	2.7898	1.9694	.9732	.600	1.141	1.0040
6	1.118	.129	2.066	850	2.9492	2.0533	.9939	.600	1.210	1.0060
8	1.113	.124	2.008	790	3.0114	2.0666	1.0013	.600		

c) $M^* = 3$, $R = 12 R_{th}$, section 5, $T_{stag} = 300^\circ K$, $T_{wall ad}$

$$\frac{U^*}{p^*} = 8 \cdot 10^6 / ft = 26.22 \cdot 10^6 / m, D^* = 1m$$

$\frac{x}{R_{th}}$	$10^3 \cdot \frac{\delta^*}{R_{th}}$	$10^3 \cdot \frac{\theta}{R_{th}}$	$10^3 \cdot \frac{\delta}{R_{th}}$	Re θ	M	$\frac{r}{R_{th}}$	$\frac{U}{U^*}$	$-10^3 \cdot \frac{\rho_{e v o}}{\rho^* U^*}$	$10^3 \cdot c_f$	RF
-3	0.937	0.477	4.69	713	0.0796	2.696	0.0444	0	1.415	0.867
-2.5	.332	.163	1.587	808	.271	1.4964	.1500	.320	1.200	.8630
-1	.230	.105	1.000	948	.546	1.124	.2958	.400	0.974	.8627
-0.5	.244	.0912	0.8736	1146	.990	0.9998	.5049	.480	.719	.8794
0	.425	.130	1.264	1662	1.381	1.0418	.6554	.507	.499	.8933
1	.585	.145	1.593	1653	1.799	1.1682	.7819	.533	.544	.9174
2	.770	.154	1.872	1522	2.1452	1.3602	.8634	.560	.602	.9431
3	.889	.155	2.008	1390	2.3475	1.5428	.9031	.573	.672	.9780
4	1.016	.146	2.098	1136	2.6255	1.8200	.9495	.600	.856	.9977
6	1.085	.136	2.083	952	2.823	1.9825	.9777	.600	1.019	1.0050
8	1.111	.128	2.038	838	2.953	2.0541	.9943	.600	1.147	1.0054
10	1.105	.1236	1.990	787	3.009	2.0667	1.0011	.600	1.208	

TABLE 2.—BOUNDARY LAYER DEVELOPMENT ANALYSIS DATA
AXISYMMETRIC NOZZLES (Continued)

d) $M^* = 3$, $R = 12 R_{th}$, suction 6 and 7, $T_{stag} = 300^\circ K$, $T_{wall,ad}$

$U^* = 8 \cdot 10^6 / ft$ $26.22 \cdot 10^6 / m$, $D^* = 1m$

x R_{th}	$10^3 \cdot \frac{\delta^*}{R_{th}}$	$10^3 \cdot \frac{\eta}{R_{th}}$	$10^3 \cdot \frac{\delta}{R_{th}}$	$Re\eta$	$-10^3 \cdot \frac{\rho_e v_o}{\rho^* U^*}$	$10^3 \cdot c_f$	RF
Suction 6							
-3 to 0	As suction 5, $R = 12 R_{th}$						
1	0.431	0.1316	1.276	1684	0.463	0.485	0.8776
2	.612	.1510	1.646	1726	.447	.505	.8875
3	.847	.1697	2.020	1676	.430	.516	.9042
4	1.048	.1841	2.306	1649	.397	.520	.9218
6	1.428	.2111	2.872	1642	.330	.531	.9425
8	1.763	.2317	3.379	1626	.310	.561	.9596
10	2.014	.2440	3.746	1600	.300	.589	.9741
11.68	2.120	.2466	3.892	1571	.300	.607	.9850
Suction 7							
-3 to 3	As suction 5, $R = 12 R_{th}$						
4	0.907	0.1580	2.036	1416	0.540	0.647	0.9409
6	1.127	.1630	2.298	1268	.500	.737	.9687
8	1.312	.1666	2.509	1169	.467	.809	.9862
10	1.515	.1769	2.756	1160	.394	.786	.9925
11.68	1.817	.2061	3.202	1313	.300	.651	.9874

TABLE 2.—BOUNDARY LAYER DEVELOPMENT ANALYSIS DATA—
AXISYMMETRIC NOZZLES (Continued)

e) $M^* = 3$, $R = 12 R_{th}$, suction 8 and 9, $T_{stag} = 300^\circ K$, $T_{wall_{ad}}$

$$\frac{U^*}{\nu^*} = 8 \cdot 10^6 / ft = 26.22 \cdot 10^6 / m, D^* = 1m$$

$\frac{x}{R_{th}}$	$10^3 \cdot \frac{\delta^*}{R_{th}}$	$10^3 \cdot \frac{\theta}{R_{th}}$	$10^3 \cdot \frac{\delta}{R_{th}}$	Re_θ	$-10^3 \cdot \frac{\rho_e v_o}{\rho^* U^*}$	$10^3 \cdot c_f$
Suction 8						
-3					0	
-2.5	0.952	0.482	4.720	721	0.056	1.375
-1	.348	.1714	1.663	847	.224	1.139
-0.5	.239	.1091	1.044	988	.280	0.932
0	.255	.0953	0.912	1197	.336	.678
1	.459	.1400	1.346	1792	.355	.446
2	.649	.1613	1.744	1845	.373	.468
3	.891	.1806	2.137	1784	.392	.485
4	1.073	.1914	2.397	1714	.401	.515
6	1.313	.1961	2.723	1525	.420	.623
8	1.479	.1923	2.900	1350	.420	.723
10	1.573	.1860	2.949	1220	.420	.804
11.68	1.596	.1806	2.918	1150	.420	.843
Suction 9						
-3					0	
-2.5	0.922	0.471	4.662	706	0.104	1.456
-1	.316	.1553	1.492	768	.416	1.264
-0.5	.2203	.1001	0.949	906	.520	1.019
0	.2335	.0874	.839	1098	.624	0.762
1	.3938	.1208	1.192	1546	.659	.554
2	.5287	.1300	1.457	1487	.693	.625
3	.6696	.1321	1.640	1304	.728	.729
4	.7459	.1271	1.686	1139	.745	.842
6	.8094	.1128	1.644	877	.780	1.104
8	.8369	.1027	1.581	721	.780	1.325
10	.8436	.0968	1.536	634	.780	1.495
11.68	.8378	.0939	1.505	598	.780	1.576

f) $M^* = 3$, $R = 12 R_{th}$, suction 10, $T_{stag} = 300^\circ K$, $T_{wall_{ad}}$

$$\frac{U^*}{\nu^*} = 8 \cdot 10^6 / ft = 26.22 \cdot 10^6 / m, D^* = 1m$$

$\frac{x}{R_{th}}$	$10^3 \cdot \frac{\delta^*}{R_{th}}$	$10^3 \cdot \frac{\theta}{R_{th}}$	$10^3 \cdot \frac{\delta}{R_{th}}$	Re_θ	$-10^3 \cdot \frac{\rho_e v_o}{\rho^* U^*}$	$10^3 \cdot c_f$	RF
-3					0		
-2.5	0.8881	0.4596	4.596	688	0.160	1.554	
-1	.2827	.1390	1.334	687	.640	1.420	
-0.5	.2008	.0911	0.859	824	.800	1.126	0.881
0	.2111	.0790	.757	993	.960	0.867	.883
1	.3489	.1063	1.064	1360	.873	.643	.9083
2	.4848	.1169	1.317	1337	.787	.685	.9238
3	.6544	.1264	1.554	1249	.700	.725	.9450
4	.7874	.1330	1.724	1191	.643	.758	.9627
6	1.038	.1472	2.069	1145	.530	.791	.9796
8	1.218	.1535	2.318	1077	.507	.875	.9931
10	1.329	.1541	2.433	1011	.484	.937	1.0024
11.68	1.389	.1557	2.492	992	.465	.945	1.0056

TABLE 2.—BOUNDARY LAYER DEVELOPMENT ANALYSIS DATA—
AXISYMMETRIC NOZZLES (Continued)

g) $M^* = 5$ LARC Q-nozzle, suction 5.2, $T_{stag} = 300^\circ \text{ K}$, $T_{wall_{ad}}$

$$\frac{U^*}{\nu^*} = 8 \cdot 10^6 / \text{ft} = 26.22 \cdot 10^6 / \text{m}, D^* = 1 \text{ m}$$

$\frac{x}{R_{th}}$	$103 \cdot \frac{\delta^*}{R_{th}}$	$103 \cdot \frac{\theta}{R_{th}}$	$103 \cdot \frac{\delta}{R_{th}}$	Re_θ	$-103 \cdot \frac{\rho e v_o}{\rho^* U^*}$	$103 \cdot c_f$	RF
-7					0		
-5	0.6964	0.3362	3.058	1002	0.286	0.882	0.85
-3.5					.500		
0	.5346	.1871	1.720	2467	1.000	.269	.855
2	.6954	.2150	2.056	2884	0.912	.279	.857
4	1.026	.2422	2.662	2778	.824	.295	.8563
6	1.666	.3005	3.704	2741	.730	.299	.8617
8	2.556	.3670	5.044	2679	.630	.313	.8694
10	3.638	.4324	6.570	2608	.530	.328	.8781
15	6.642	.5595	10.49	2381	.442	.395	.9068
20	9.575	.6443	13.96	2228	.354	.434	.9325
25	11.90	.6931	16.56	2106	.328	.480	.9539
30	13.65	.7189	18.43	2009	.303	.509	.9705
40	15.92	.7570	20.78	1949	.272	.523	.9878
49.19	16.87	.7758	21.82	1942	.262	.531	.9960
-7.0					0		

h) $M^* = 5$ LARC Q-nozzle, suction 5.3, $T_{stag} = 400^\circ \text{ K}$, $T_{wall} = 300^\circ \text{ K}$

$$\frac{U^*}{\nu^*} = 8 \cdot 10^6 / \text{ft} = 26.22 \cdot 10^6 / \text{m}, D^* = 1 \text{ m}$$

$\frac{x}{R_{th}}$	$103 \cdot \frac{\delta^*}{R_{th}}$	$103 \cdot \frac{\theta}{R_{th}}$	$103 \cdot \frac{\delta}{R_{th}}$	Re_θ	$-103 \cdot \frac{\rho e v_o}{\rho^* U^*}$	$103 \cdot c_f$
-7					0	
-5	0.3380	0.4558	4.194	1533	0.429	0.751
-3.5					.750	
0	.2852	.2539	2.601	3743	1.500	.251
2	.4057	.2719	2.779	4045	1.368	.261
4	.6386	.3070	3.478	3851	1.236	.283
6	1.074	.3686	4.580	3621	1.096	.304
8	1.660	.4338	5.930	3364	0.948	.336
10	2.350	.4919	7.334	3117	.800	.368
15	4.072	.5772	10.35	2530	.665	.496
20	5.588	.6052	12.25	2129	.530	.576
25	6.617	.5956	12.93	1829	.492	.667
30	7.314	.5732	12.91	1612	.453	.725
40	8.217	.5442	12.57	1403	.407	.767
49.19	8.562	.5256	12.42	1315	.393	.785

**TABLE 2.—BOUNDARY LAYER DEVELOPMENT ANALYSIS DATA—
AXISYMMETRIC NOZZLES (Continued)**

i) $M^* = 5$ LARC Q-nozzle, suction 5.3, $T_{stag} = 400^\circ K$, $T_{wall_{ad}}$

$$\frac{U^*}{\nu^*} = 8 \cdot 10^6 / ft = 26.22 \cdot 10^6 / m, D^* = 1m$$

$\frac{x}{R_{th}}$	$10^3 \cdot \frac{\delta^*}{R_{th}}$	$10^3 \cdot \frac{\theta}{R_{th}}$	$10^3 \cdot \frac{\delta}{R_{th}}$	Re_θ	$-10^3 \cdot \frac{\rho_e v_o}{\rho^* U^*}$	$10^3 \cdot c_f$	RF
-7					0		
-5	0.6413	0.3106	2.838	1045	0.429	0.854	0.857
-3.5					.750		
0	.4750	.1677	1.548	2472	1.500	.279	.863
2	.6118	.1895	1.832	2820	1.368	.289	.8682
4	.8960	.2105	2.346	2640	1.236	.312	.8703
6	1.423	.2541	3.184	2496	1.096	.331	.8796
8	2.132	.3006	4.242	2331	0.948	.362	.8929
10	2.965	.3427	5.380	2172	.800	.395	.9078
15	5.063	.4040	7.961	1770	.665	.523	.9468
20	6.942	.4350	9.952	1531	.530	.600	.9756
25	8.231	.4453	11.22	1367	.492	.687	.9928
30	9.102	.4486	12.03	1261	.453	.741	1.0026
40	10.21	.4658	13.17	1195	.407	.782	1.0065
49.19	10.41	.4703	13.41	1177	.393	.790	1.0048
53	10.40	.4725	13.43	1182	.393	.788	1.0036
56	10.38	.4734	13.43	1185	.393	.788	1.0022

TABLE 2.—BOUNDARY LAYER DEVELOPMENT ANALYSIS DATA—AXISYMMETRIC NOZZLES (Continued)

j) $M^* = 5$ LARC Q-nozzle, section 5.3, $T_{stag} = 300^\circ K$, $T_{wall,ad}$

$$\frac{U^*}{\nu^*} = 8 \cdot 10^6 / ft = 26.22 \cdot 10^6 / m, D^* = 1m$$

$\frac{x}{R_{th}}$	$10^3 \cdot \frac{\delta^*}{R_{th}}$	$10^3 \cdot \frac{\theta}{R_{th}}$	$10^3 \cdot \frac{\delta}{R_{th}}$	Re θ	M	$\frac{r}{R_{th}}$	$\frac{U}{U^*}$	$-10^3 \cdot \frac{\rho_{eVo}}{\rho^* U^*}$	$10^3 \cdot cf$	RF
-7	0.6838	0.3310	3.021	986	0.153	1.957	0.0744	0	0.904	0.85
-5								0.429		
-3.5								.750		
0	.5089	.1794	1.654	2365	1.0046	1.0002	.4473	1.500	.291	.861
2	.6560	.2030	1.958	2723	1.3644	1.0984	.5685	1.368	.302	.8657
4	.9609	.2257	2.506	2589	1.9050	1.3331	.7078	1.236	.324	.8679
6	1.531	.2733	3.415	2493	2.4002	1.6576	.7985	1.096	.342	.8777
8	2.297	.3240	4.548	2365	2.8332	2.0118	.8567	0.948	.372	.8905
10	3.199	.3702	5.772	2233	3.2001	2.3766	.8946	.800	.403	.9040
15	5.497	.4401	8.612	1873	3.8998	3.2274	.9468	.665	.528	.9431
20	7.559	.4757	10.79	1644	4.3491	3.8847	.9706	.530	.603	.9720
25	9.001	.4887	12.23	1485	4.6443	4.3780	.9833	.492	.689	.9907
30	9.969	.4922	13.10	1376	4.8426	4.7268	.9909	.453	.742	1.0020
40	11.12	.5092	14.27	1311	5.0445	5.1240	.9977	.407	.776	1.0060
49.19	11.48	.5184	14.75	1298	5.1150	5.2424	1.000	.393	.791	1.0056

k) $M^* = 5$ LARC Q-nozzle, section 5.1, $T_{stag} = 300^\circ K$, $T_{wall,ad}$

$$\frac{U^*}{\nu^*} = 8 \cdot 10^6 / ft = 26.22 \cdot 10^6 / m, D^* = 1m$$

$\frac{x}{R_{th}}$	$10^3 \cdot \frac{\delta^*}{R_{th}}$	$10^3 \cdot \frac{\theta}{R_{th}}$	$10^3 \cdot \frac{\delta}{R_{th}}$	Re θ	$-10^3 \cdot \frac{\rho_{eVo}}{\rho^* U^*}$	$10^3 \cdot cf$	RF
-7					0	0.882	0.85
-5	0.6964	0.3362	3.058	1002	0.286	.269	.855
0	.5346	.1871	1.720	2467	1.000	.283	.8577
2	.6903	.2138	2.047	2868	1.000	.306	.8591
4	1.004	.2375	2.623	2725	1.000	.328	.8692
6	1.586	.2865	3.561	2613	1.000	.375	.8850
8	2.318	.3321	4.662	2424	1.000	.448	.9058
10	3.064	.3601	5.671	2172	1.000	.725	.9681
15	4.491	.3511	7.158	1494	1.000	1.058	1.0104
20	4.945	.2903	6.960	1004	1.000	1.256	1.0168
25	5.151	.2631	6.790	800	0.914	1.344	1.0102
30	5.464	.2658	7.107	743	.829	1.260	0.9978
40	6.548	.3087	8.512	795	.657	1.023	.9920
49.19	8.318	.3885	10.80	972	.500		

TABLE 2.—BOUNDARY LAYER DEVELOPMENT ANALYSIS DATA
AXISYMMETRIC NOZZLES (Continued)

ℓ) $M^* = 5$ LARC Q-nozzle, no suction, $T_{\text{stag}} = 378^\circ \text{K}$, $T_{\text{wall ad}}$

$$R_{\text{th}} = 0.03308 \text{ ft} = 0.01007 \text{ m}$$

$$\frac{U^*}{\nu^*} = 2.1 \cdot 10^6/\text{ft} = 6.90 \cdot 10^6/\text{m}$$

$\frac{x}{R_{\text{th}}}$	$\frac{\delta^*}{R_{\text{th}}}$	$\frac{\theta}{R_{\text{th}}}$	$\frac{\delta}{R_{\text{th}}}$	Re_θ	$10^3 \cdot c_f$	RF
-5	0.004129	0.001983	0.01792	181	4.803	0.85
0	.003381	.001165	.01063	466	1.298	.842
2	.004483	.001382	.01299	559	1.355	.8379
4	.006718	.001600	.01724	547	1.380	.8319
6	.01138	.002087	.02497	561	1.285	.8275
8	.01832	.002707	.03569	575	1.220	.8237
10	.02732	.003392	.04885	591	1.171	.8206
15	.05758	.005250	.08984	635	1.056	.8162
20	.09416	.007135	.1373	694	0.935	.8153
25	.1320	.008864	.1840	754	.830	.8155
30	.1696	.01052	.2305	820	.735	.8165
40	.2369	.01335	.3115	955	.558	.8191
49.19	.2862	.01559	.3708	1083	.493	.8228

m) $M^* = 5$ rapid expansion nozzle, no suction, $T_{\text{stag}} = 378^\circ \text{K}$, $T_{\text{wall ad}}$

$$R_{\text{th}} = 0.03308 \text{ ft} = 0.01007 \text{ m}$$

$$\frac{U^*}{\nu^*} = 2.1 \cdot 10^6/\text{ft} = 6.90 \cdot 10^6/\text{m}$$

$\frac{x}{R_{\text{th}}}$	$\frac{\delta^*}{R_{\text{th}}}$	$\frac{\theta}{R_{\text{th}}}$	$\frac{\delta}{R_{\text{th}}}$	Re_θ	$10^3 \cdot c_f$	RF
-5	0.01504	0.00588	0.04371	43	10.65	
-0.25	.001239	.00056	.005346	160	5.68	0.841
0	.001115	.00044	.004352	167	5.59	.839
1	.003563	.00088	.008846	305	2.20	.8356
2	.007411	.00134	.01557	353	1.80	.8302
4	.01758	.00229	.03129	417	1.54	.8255
6	.03051	.00324	.04967	461	1.37	.8226
10	.06049	.00502	.08939	534	1.15	.8207
15	.1009	.00706	.1412	615	0.974	.8205
20	.1405	.00889	.1900	693	.831	.8213
25	.1775	.01055	.2360	771	.712	.8228
30	.2109	.01204	.2768	850	.608	.8246
38.68	.2600	.01427	.3353	991	.464	.8280

TABLE 2.—BOUNDARY LAYER DEVELOPMENT ANALYSIS DATA—AXISYMMETRIC NOZZLES (Continued)

n) $M^* = 5$ rapid expansion nozzle, section 5.1 $T_{stag} = 300^\circ K$, T_{wallad}

$$\frac{U^*}{V_\infty} = 8.106/t_t = 26.22 \cdot 10^6/m, D^* = 1m$$

$\frac{x}{R_{th}}$	$10^3 \cdot \frac{\delta^*}{R_{th}}$	$10^3 \cdot \frac{\theta}{R_{th}}$	$10^3 \cdot \frac{\delta}{R_{th}}$	Re θ	M	$\frac{r}{R_{th}}$	$\frac{U}{U^*}$	$-10^3 \cdot \frac{\rho_{evo}}{\rho^* U^*}$	$10^3 \cdot c_f$	RF
-5	2.576	1.007	7.4E4	251	0.0126	6.886	0.0062	0	1.824	
-1								0		
-.25	0.2049	0.0929	0.8E5	908	.569	1.103	.270	0.750	1.012	0.844
0	.1841	.0718	.718	947	.999	1.000	.446	1.0	0.997	.845
1	.5544	.1373	1.4E2	1664	1.764	1.205	.678	1.0	.438	.851
2	1.075	.1949	2.3E1	1814	2.363	1.521	.795	1.0	.414	.8580
4	2.158	.2761	4.0E4	1807	3.045	2.100	.883	1.0	.481	.8855
6	3.092	.3106	5.2E0	1611	3.499	2.602	.923	1.0	.601	.9201
8	3.744	.3112	6.013	1374	3.826	3.027	.945	1.0	.750	.9537
10	4.134	.2949	6.2E6	1157	4.0755	3.385	.960	1.0	.912	.9796
12	4.327	.2731	6.2E3	978	4.273	3.691	.970	1.0	1.076	.9985
15	4.381	.2440	6.012	791	4.498	4.066	.980	1.0	1.305	1.0121
20	4.247	.2162	5.6E0	630	4.747	4.512	.9905	1.0	1.610	1.0104
25	4.632	.2299	6.112	630	4.895	4.7925	.996	0.866	1.588	0.9996
30	5.355	.2611	7.0E9	692	4.975	4.9495	.9987	.732	1.438	.9950
38.68	7.372	.3589	9.6E2	936	5.0155	5.0308	1.000	.500	1.032	.9874

TABLE 2.—BOUNDARY LAYER DEVELOPMENT ANALYSIS DATA—AXISYMMETRIC NOZZLES (Continued)

o) $M^* = 7$, $R = 75 R_{th}$, suction 7.1a

$$\frac{U^*}{v^*} = 26.22 \cdot 10^6 / m, D^* = 1 \text{ m}, T_{stag} = 700^\circ K, T_{wallad}$$

$\frac{x}{R_{th}}$	$10^3 \cdot \frac{\delta^*}{R_{th}}$	$10^3 \cdot \frac{\theta}{R_{th}}$	$10^3 \cdot \frac{\delta}{R_{th}}$	Re θ	M	$\frac{r}{R_{th}}$	$\frac{U}{U^*}$	$-10^3 \cdot \frac{\rho v_0}{\rho^* U^*}$	$10^3 \cdot cf$	RF
-2	0.3611	0.1617	1.476	2267	0.528	1.132	0.2414	0	0.376	0.842
0	.4896	.1664	1.522	3272	1.000	1.000	.4298	0	.167	.8409
8	1.450	.3030	3.586	4092	2.243	1.428	.7443	3.092	.220	.8433
16	4.303	.4063	7.527	2282	3.718	2.727	.9008	1.794	.378	.9011
25	8.560	.4952	12.01	1672	4.670	4.608	.9480	1.083	.463	.9490
40	15.53	.6216	19.46	1410	5.526	6.892	.9745	0.640	.531	.9810
60	23.01	.7283	27.42	1258	6.190	8.678	.9885	.510	.644	1.000
80	26.22	.7197	30.39	1066	6.602	9.556	.9955	.487	.793	1.0123
111.33	27.56	.7022	31.57	930	6.916	9.906	1.000	.450	.901	1.0096

p) $M^* = 7$, $R = 30 R_{th}$, suction 7.1

$$\frac{U^*}{v^*} = 26.22 \cdot 10^6 / m, D^* = 1 \text{ m}, T_{stag} = 700^\circ K, T_{wallad}$$

$\frac{x}{R_{th}}$	$10^3 \cdot \frac{\delta^*}{R_{th}}$	$10^3 \cdot \frac{\theta}{R_{th}}$	$10^3 \cdot \frac{\delta}{R_{th}}$	Re θ	δ_s , mm	$-10^3 \cdot \frac{\rho v_0}{\rho^* U^*}$	$10^3 \cdot cf$	RF
-7						0		
-3.5						2.08		
-2	0.3289	0.1481	1.363	2087		3.289	0.420	0.856
0	.4122	.1451	1.341	2868		4.900	.231	.8626
4	.8400	.1907	2.166	2981	0.0276	3.740	.268	.8683
8.5	2.697	.2988	4.911	2090	.0501	2.386	.388	.8901
15	5.826	.3999	8.552	1662		1.455	.445	.9362
20	8.766	.4850	11.96	1580	.139	0.980	.453	.9514
30	13.84	.5873	17.70	1407		.800	.557	.9773
40	18.52	.6607	22.67	1309	.252	.620	.599	.9900
60	24.90	.7209	29.16	1132	.316	.520	.733	1.0065
80	27.08	.6990	31.02	964	.333	.501	.883	1.0139
102.45	27.45	.6807	31.30	875	.342	.480	.964	1.0100

TABLE 2.—BOUNDARY LAYER DEVELOPMENT ANALYSIS DATA—AXISYMMETRIC NOZZLES (Continued)

q) $M^* = 7$, $R = 75 R_{th}$, section 7.1

$$\frac{U^*}{\nu^*} = 8 \cdot 10^6 / ft = 26.22 \cdot 10^6 / m, D^* = 1m, T_{stag} = 700^\circ K, T_{wall,ad}$$

$\frac{x}{R_{th}}$	$10^3 \cdot \frac{\delta^*}{R_{th}}$	$10^3 \cdot \frac{\theta}{R_{th}}$	$10^3 \cdot \frac{\delta}{R_{th}}$	$Re\theta$	$-10^3 \cdot \frac{\rho_e \nu_o}{\rho^* U^*}$	$10^3 \cdot c_f$
-7					0	
-3.5					2.08	
-2	0.3294	0.1483	1.364	2079	3.083	0.421
0	.4195	.1466	1.353	2883	4.420	.221
8	1.271	.2480	3.007	3349	3.092	.237
16	4.229	.3817	7.065	2143	1.794	.381
25	8.523	.4809	11.73	1623	1.083	.465
40	15.52	.6158	19.34	1397	0.640	.532
60	22.99	.7264	27.38	1255	.510	.644
80	26.21	.7194	30.38	1065	.487	.793
111.33	27.55	.7024	31.56	930	.450	.901

TABLE 2.—BOUNDARY LAYER DEVELOPMENT ANALYSIS DATA—AXISYMMETRIC NOZZLES (Continued)

r) $M^* = 7$, $R = 30 R_{th}$, suction 7.2

$$\frac{U^*}{\nu^*} = 26.22 \cdot 10^6 / m, D^* = 1m, T_{stag} = 700^\circ K, T_{wall,ad}$$

$\frac{x}{R_{th}}$	$10^3 \cdot \frac{\delta^*}{R_{th}}$	$10^3 \cdot \frac{\theta}{R_{th}}$	$10^3 \cdot \frac{\delta}{R_{th}}$	Re θ	M	$\frac{r}{R_{th}}$	$\frac{U}{U^*}$	$-10^3 \cdot \frac{\rho_e \nu_o}{\rho^* U^*}$	$10^3 \cdot c_f$	RF
-7								0		
-3.5	0.3142	0.1419	1.311	1999	0.528	1.1320	0.2411	3.12	0.444	0.859
-2	.3815	.1357	1.263	2683	1.003	1.000	.4297	4.954	.262	.8723
0	.7604	.1708	1.970	2671	1.980	1.268	.6959	5.616	.308	.8856
4	2.313	.2447	4.160	1712	3.351	2.228	.8731	3.504	.487	.9226
15	4.704	.3057	6.807	1270	4.274	3.963	.9301	2.130	.603	.9695
20	6.857	.3608	9.231	1175	4.752	5.063	.9500	1.470	.628	.9816
30	10.09	.4103	12.75	983	5.412	6.755	.9702	1.200	.809	1.000
40	13.04	.4555	15.87	902	5.860	7.949	.9807	0.930	.876	1.0033
60	16.53	.4824	19.46	757	6.456	9.386	.9919	.780	1.093	1.0075
80	17.38	.4618	20.16	637	6.815	10.018	.9973	.752	1.326	1.0062
102.45	17.79	.4539	20.55	584	7.016	10.181	1.000	.720	1.447	1.0026

s) $M^* = 9$ air nozzle, $R = 200 R_{th}$, suction 9.2

$$\frac{U^*}{\nu^*} = 26.22 \cdot 10^6 / m, D^* = 1m, T_{stag} = 1000^\circ K, T_{wall,ad}$$

$\frac{x}{R_{th}}$	$10^3 \cdot \frac{\delta^*}{R_{th}}$	$10^3 \cdot \frac{\theta}{R_{th}}$	$10^3 \cdot \frac{\delta}{R_{th}}$	Re θ	M	$\frac{r}{R_{th}}$	$\frac{U}{U^*}$	$-10^3 \cdot \frac{\rho_e \nu_o}{\rho^* U^*}$	$10^3 \cdot c_f$	RF
-7								0		
-3.5	0.4088	0.1405	1.291	3451	1.000	1.000	0.4209	2.50	0.166	0.852
0	1.182	.2776	3.025	5484	1.912	1.250	.6694	6.25	.136	.8577
10	3.148	.4296	6.159	4497	2.965	2.002	.8224	5.00	.159	.8636
20	7.605	.6231	12.13	3321	4.066	3.262	.9027	3.05	.220	.8797
30	15.85	.8259	21.65	2510	5.118	5.021	.9441	2.12	.272	.9023
40	31.61	1.084	38.17	2022	6.201	8.459	.9693	1.20	.322	.9393
60	48.03	1.315	55.48	1878	6.885	11.132	.9800	0.740	.360	.9596
80	63.17	1.477	70.98	1761	7.391	13.183	.9861	.560	.402	.9749
100	87.71	1.657	95.19	1568	8.100	15.947	.9930	.390	.478	.9966
140	102.6	1.692	109.0	1389	8.571	17.47	.9968	.363	.562	1.0103
180	107.5	1.690	113.3	1320	8.743	17.91	.9980	.350	.593	1.0137
200	110.5	1.622	115.8	1158	9.066	18.37	1.000	.340	.679	1.0158
265.09										

TABLE 2.—BOUNDARY LAYER DEVELOPMENT ANALYSIS DATA—AXISYMMETRIC NOZZLES (Continued)

t) $M^* = 9$ air nozzle, $R = 200 R_{th}$, suction 9.1

$\frac{U^*}{\nu^*} = 26.22 \cdot 10^6/m$, $D^* = 1m$, $T_{stag} = 1000^\circ K$, $T_{wall,ad}$

$\frac{x}{R_{th}}$	$10^3 \cdot \frac{\delta^*}{R_{th}}$	$10^3 \cdot \frac{\theta}{R_{th}}$	$10^3 \cdot \frac{\delta}{R_{th}}$	$Re\theta$	$-10^3 \cdot \frac{\rho v_0}{\rho^* U^*}$	$10^3 \cdot c_f$	δ_s' mm	RF
-7					0			
-3.5	0.3918	0.1358	1.251	3334	4.0	0.179		0.851
0	1.087	.2540	2.810	5018	10.0	.154	0.0217	.8724
10	2.806	.3735	5.484	3909	8.0	.190	.0334	.8876
20	6.458	.5002	10.17	2666	4.88	.286	.0558	.9163
30	12.91	.6135	17.07	1865	3.40	.372	.100	.9479
40	24.18	.7562	28.42	1411	1.92	.469	.177	.9827
60	35.28	.8973	39.93	1282	1.18	.537	.245	.9948
80	44.54	.9827	49.36	1172	0.89	.613	.297	1.0033
100	56.78	1.044	61.32	987	.76	.757	.364	1.0110
140	62.61	1.042	66.98	855	.63	.901	.397	1.0117
180	64.67	1.045	69.12	816	.583	.949	.411	1.0098
200	64.77	1.045	69.12	816	.56			
265.09		1.000	69.40	714	.55	1.100	.416	1.0050

TABLE 2.—BOUNDARY LAYER DEVELOPMENT ANALYSIS DATA—AXISYMMETRIC NOZZLES (Continued)

u) $M^* = 8.93$ helium nozzle, $R = 250 R_{th}$, suction 9.4 He, $\dot{m}_s/\dot{m}_o = 0.00625$, $R_{th} = 0.0711m$

$\frac{U^*}{\nu^*} = 26.22 \cdot 10^6/m$, $D^* = 1m$, $T_{stag} = 300^\circ K$, $T_{wall,ad}$; $\mu \sim T^{0.675}$

$\frac{x}{R_{th}}$	$10^3 \cdot \frac{\delta^*}{R_{th}}$	$10^3 \cdot \frac{\theta}{R_{th}}$	$10^3 \cdot \frac{\delta}{R_{th}}$	Re_θ	M	$10^3 \cdot c_f$	$-10^3 \cdot \frac{\rho_e \nu_o}{\rho^* U^*}$	RF	δ_s' mm	γ_{crit} mm	$\frac{U}{\nu_k} \cdot 10^{-6}/m$	H_i
-7							0					
-3.5							0.536					
-2	0.4761	0.2045	1.898	1687	0.528	0.510	.842	0.8273		0.0085	103.5	2.085
0	.6684	.2027	1.947	2433	1.000	.232	1.250			.0104	114.5	2.367
10	2.006	.3569	4.380	4163	1.904	.175	1.042	.8352	0.107	.0213	52.3	2.249
20	5.311	.4478	8.419	3563	3.131	.187	0.695	.8417	.171	.0625	13.23	2.301
30	12.99	.5070	16.23	2491	4.661	.239	.504	.8679	.314	.194	2.94	2.316
40	23.23	.5368	25.59	1929	5.816	.239	.312	.9322		.464	1.108	2.412
50		.5782		1734								
60	43.17	.6055	43.80	1589	7.176	.267	.222	.9541	.943	.910	0.431	2.377
80	59.51	.6212	57.67	1366	8.046	.305	.197	.9861	1.195	1.31	.279	2.335
100	71.00	.6148	66.88	1215	8.611	.334	.183	1.0066	1.365			2.317
122.19	74.03	.6027	69.16	1152	8.930	.348	.181	1.0188	1.436	1.87	.170	2.313

TABLE 2.—BOUNDARY LAYER DEVELOPMENT ANALYSIS DATA—AXISYMMETRIC NOZZLES (Continued)

v) $M^* = 8.93$ helium nozzle, $R = 250 R_{th}$, suction 9.3 He, $\dot{m}_s/\dot{m}_0 = 0.0125$

$\frac{U^*}{\nu} = 26.22 \cdot 10^6/m$, $D^* = 1m$, $T_{stag} = 300^\circ K$, $T_{wall,ad}$; $\mu \sim T^{0.675}$

$\frac{x}{R_{th}}$	$10^3 \cdot \frac{\delta^*}{R_{th}}$	$10^3 \cdot \frac{\theta}{R_{th}}$	$10^3 \cdot \frac{\delta}{R_{th}}$	Re_θ	$10^3 \cdot cf$	$-10^3 \cdot \frac{\rho_e v_0}{\rho^* U^*}$	M	$\frac{U}{U^*}$	$\frac{r}{R_{th}}$
0	0.626	0.1916	1.852	2300	0.264	2.500	1.001	0.508	1.000
10	1.754	.3050	3.852	3558	.216	2.084	1.904	.752	1.200
20	4.407	.3420	6.819	2721	.255	1.389	3.131	.8905	1.802
30	9.811	.3139	11.44	1541	.381	1.007	4.661	.955	2.809
40	16.19	.2936	16.55	1055	.415	0.625	5.816	.977	3.985
60	26.81	.3159	25.87	829	.495	.443	7.176	.991	5.637
80	32.81	.3123	31.06	687	.592	.394	8.046	.996	6.530
100	35.88	.3117	34.04	616	.660	.365	8.611	.999	6.931
122.19	36.00	.3079	34.64	575	.712	1.072	8.930	1.000	7.032
-3.5						0.000			
-7									

w) $M^* = 9$ NASA helium nozzle, suction 9.5 He, $\dot{m}_s/\dot{m}_0 = 0.00847$, $R_{th} = 0.0711m$

$\frac{U^*}{\nu} = 26.22 \cdot 10^6/m$, $D^* = 1m$, $T_{stag} = 300^\circ K$, $T_{wall,ad}$; $\mu \sim T^{0.675}$, $\beta dx = 0.86$, $Re_{Lequ} = 3.145 \cdot 10^8$

$\frac{x}{R_{th}}$	$10^3 \cdot \frac{\delta^*}{R_{th}}$	$10^3 \cdot \frac{\theta}{R_{th}}$	$10^3 \cdot \frac{\delta}{R_{th}}$	Re_θ	M	$\frac{U}{U^*}$	$\frac{r}{R_{th}}$	$10^3 \cdot cf$	$-10^3 \cdot \frac{\rho_e v_0}{\rho^* U^*}$
-3.5	0.4663	0.2004	1.863	1674	0.5278	0.2955	1.1319	0.5165	0.772
-2	.6095	.1922	1.850	2342	1.000	.5111	1.000	.319	1.213
0	.8707	.1861	2.156	2315	1.649	.7004	1.1058	.326	1.800
1.604	2.451	.2454	4.151	2191	2.823	.867	1.6228	.312	1.762
5.036	6.142	.2684	7.959	1499	4.271	.9432	2.587	.424	1.680
10.541	9.841	.2500	11.03	1046	5.278	.9673	3.559	.513	1.405
16.754	15.16	.2774	15.89	939	6.111	.9796	4.488	.501	1.055
24.433	24.75	.3586	25.22	1002	6.943	.9880	5.414	.438	0.693
35.039	34.78	.4224	34.73	1026	7.604	.9929	6.096	.410	.428
46.546	41.21	.4711	40.96	1085	7.873	.9945	6.347	.372	.310
52.376	50.74	.5250	50.05	1114	8.293	.9968	6.689	.371	.250
63.487	58.94	.5611	57.51	1120	8.622	.9984	6.898	.366	.225
75.036	65.08	.5841	63.09	1117	8.860	.9994	6.999	.370	.200
86.702	69.25	.6021	66.99	1124	8.999	1.000	7.024	.364	.19
98.667									.18

TABLE 2.—BOUNDARY LAYER DEVELOPMENT ANALYSIS DATA—AXISYMMETRIC NOZZLES (Concluded)

x) $M^* = 9$ NASA helium nozzle, suction 9.6 He, $\dot{m}_s/\dot{m}_o = 0.0060$, $R_{th} = 0.0711m$ $\frac{U^*}{\nu^*} = 26.22 \cdot 10^6/m$, $D^* = 1m$, $T_{stag} = 300^\circ K$, $T_{wall,ad}; \mu \sim T^{0.675}$, $\beta \delta x = 5.7$, $Re_{Lequ} = 3.145 \cdot 10^8$

$\frac{x}{R_{th}}$	$10^3 \cdot \frac{\delta^*}{R_{th}}$	$10^3 \cdot \frac{\theta}{R_{th}}$	$10^3 \cdot \frac{\delta}{R_{th}}$	Re_θ	M	$\frac{U}{U^*}$	$10^3 \cdot cf$	Shear $\cdot 10^3$	$-10^3 \cdot \frac{\rho_e v_o}{\rho^* U^*}$	RF	δ_s' mm	y_{crit} , mm ($Re_k=200$)	$\frac{r}{R_{th}}$	$\frac{U}{\nu_k} \cdot 10^{-6}/m$	H_i
-7															
-3.5	0.4737	0.2035	1.888	1700	0.528	0.295	0.506	2.97	U 0.540	0.826		0.0086	1.1319	104	2.086
-2	.6256	.1968	1.889	2398	1.000	.511	.307	3.96	.849	.826		.0094	1.000	113.7	2.253
0	.8974	.1924	2.217	2394	1.649	.700	.311	4.44	1.260	.821		.0128	1.1058	71.6	2.224
5.036	2.611	.2658	4.422	2374	2.823	.867	.277	2.264	1.235	.824	0.057	.038	1.6228	19.4	2.320
10.541	7.042	.3291	9.262	1837	4.271	.943	.333	1.187	1.180	.8759	.0946	.122	2.587	4.29	2.319
16.754	12.05	.3395	13.95	1421	5.278	.967	.380	0.810	0.984	.9307	.185	.244	3.559	1.75	2.336
24.433	19.05	.3778	20.48	1278	6.111	.980	.369	.537	.738	.9585	.285	.420	4.488	0.948	2.367
35.039	31.38	.4779	32.34	1335	6.943	.988	.323	.333	.485	.9658	.711	1.05	5.414		2.385
46.546	44.59	.5598	44.88	1360	7.604	.993	.301	.242	.300	.9736	.988		6.096	.350	2.386
52.376	52.57	.6152	52.52	1416	7.873	.9945	.275	.200	.217	.9731	1.180		6.347	.239	2.406
63.487	65.89	.6984	65.04	1483	8.293	.9968	.270	.170	.158	.9767	1.415	1.54	6.689		2.374
75.036	77.73	.7568	76.06	1511	8.622	.9984	.264	.149	.140	.9825	1.635		6.898		2.363
86.702	87.11	.7976	84.74	1526	8.860	.9994	.264	.138	.133	.9886	1.785		6.999		2.347
98.667	93.92	.8296	91.19	1549	8.999	1.000	.258	.129	.126	.9936	1.927	2.15	7.024	.165	2.346

TABLE 3.—BOUNDARY LAYER DEVELOPMENT ANALYSIS DATA—
 $M^* = 4.6$ TWO-DIMENSIONAL JPL NOZZLES

a) Suction 2D-3, $T_{stag} = 300^\circ \text{ K}$, $T_{wall ad}$, floor and ceiling walls

$$\frac{U^*}{\nu^*} = 8 \cdot 10^6 / ft = 26.22 \cdot 10^6 / m, H^* = 1m$$

$\frac{x}{H_{th}/2}$	$\frac{\delta^*}{H_{th}/2}$	$\frac{\theta}{H_{th}/2}$	$\frac{\delta}{H_{th}/2}$	$10^3 \cdot c_f$	Re_θ	$-10^3 \cdot \frac{\rho_e v_o}{\rho^* U^*}$	RF
-10						0	
-4						0.342	
0	0.001929	0.000720	0.00670	0.370	2230	.570	0.8485
10	.003646	.000968	.01034	.304	2806	.570	.8513
20	.007466	.001436	.01803	.297	3163	.570	.8577
40	.01839	.002258	.03736	.378	3156	.570	.8932
60	.02717	.002474	.05070	.527	2655	.570	
80	.03085	.002227	.05344	.690	2051	.570	1.0019
100	.03100	.001864	.04877	.836	1564	.570	
140	.02762	.001353	.03428	1.034	1031	.570	1.0325
180	.02433	.001158	.02982	1.123	851	.570	1.0230
229.9	.02220	.001111	.02817	1.149	810	.570	1.0116

b) Suction 2D-3, $T_{stag} = 400^\circ \text{ K}$, $T_{wall ad}$, floor and ceiling walls

$$\frac{U^*}{\nu^*} = 8 \cdot 10^6 / ft = 26.22 \cdot 10^6 / m, H^* = 1m$$

$\frac{x}{H_{th}/2}$	$10^3 \cdot \frac{\delta^*}{H_{th}/2}$	$10^3 \cdot \frac{\theta}{H_{th}/2}$	$10^3 \cdot \frac{\delta}{H_{th}/2}$	$10^3 \cdot c_f$	Re_θ	M	$\frac{h}{H_{th}}$	$\frac{U}{U^*}$	δ_s , mm	$-10^3 \cdot \frac{\rho_e v_o}{\rho^* U^*}$	RF
-10										0	
-4	1.688	0.692	6.205	0.384	2107	0.750	1.0629	0.3536		0.342	0.8464
0	1.821	.680	6.345	.353	2329	1.000	1.000	.4539		.570	.8485
10	3.437	.914	9.780	.291	2878	1.713	1.3505	.6762	0.083	.570	.8517
20	7.023	1.352	17.02	.287	3177	2.347	2.289	.8050	.106	.570	.8590
40	17.16	2.104	35.05	.373	3053	3.229	5.2615	.9141	.153	.570	.8961
60	25.10	2.269	47.00	.526	2488	3.756	8.598	.9667	.166	.570	
80	28.30	2.016	48.90	.692	1881	4.077	11.47	.9749	.164	.570	.9939
100	28.27	1.673	43.88	.839	1415	4.279	13.70	.9858	.162	.570	
140	25.08	1.217	31.22	1.036	930	4.495	16.48	.9955	.154	.570	1.0315
180	22.23	1.056	27.24	1.124	777	4.579	17.70	.9990		.570	1.0214
229.9	20.37	1.023	26.11	1.148	745	4.600	18.02	1.000	.150	.570	1.0104

TABLE 3.—BOUNDARY LAYER DEVELOPMENT ANALYSIS DATA—
 $M^* = 4.6$ TWO-DIMENSIONAL JPL NOZZLES (Continued)

c) Suction 2D-1 and 2D-2, $T_{stag} = 300^\circ \text{ K}$, $T_{wall,ad}$: floor and ceiling walls

$$\frac{U^*}{\nu^*} = 8 \cdot 10^6 / ft = 26.22 \cdot 10^6 / m, H^* = 1m$$

Suction 2D-1							
$\frac{x}{H_{th}/2}$	$\frac{\delta^*}{H_{th}/2}$	$\frac{\theta}{H_{th}/2}$	$\frac{\delta}{H_{th}/2}$	$10^3 \cdot c_f$	$Re\theta$	$-10^3 \cdot \frac{\rho e v_o}{\rho^* U^*}$	RF
-10						0	
-4	0.001769	0.000726	0.00652	0.411	1991	0.450	
0	.001893	.000708	.006620	.381	2194	.750	0.8505
10	.003524	.000935	.01005	.320	2711	.750	.8565
20	.007054	.001351	.01715	.325	2975	.750	.8676
40	.01629	.001956	.03344	.459	2734	.750	.9169
60	.02217	.001889	.04094	.685	2026	.750	
80	.02337	.001517	.03767	.923	1397	.750	1.0202
100	.02208	.001185	.02868	1.123	995	.750	
140	.01863	.000890	.02283	1.377	678	.750	1.0246
180	.01680	.000838	.02154	1.484	616	.750	1.0100
229.9	.01596	.000848	.02121	1.512	618	.750	1.0024
Suction 2D-2							
$\frac{x}{H_{th}/2}$	$\frac{\delta^*}{H_{th}/2}$	$\frac{\theta}{H_{th}/2}$	$\frac{\delta}{H_{th}/2}$	$10^3 \cdot c_f$	$Re\theta$	$-10^3 \cdot \frac{\rho e v_o}{\rho^* U^*}$	RF
-10						0	
0	0.001969	0.000733	0.006793	0.359	2270	0.380	0.845
10	.003780	.001004	.01065	.288	2909	.380	.8456
20	.007932	.001531	.01898	.269	3373	.380	.8472
40	.02103	.002641	.04215	.301	3692	.380	.8676
60	.03386	.003281	.06273	.376	3519	.380	.279
80	.04182	.003367	.07377	.463	3101	.380	.308
100	.04536	.003161	.07661	.546	2653	.380	
140	.04497	.002552	.06847	.670	1946	.380	1.011
180	.04115	.002096	.05367	.735	1540	.380	1.0234
229.9	.03674	.001816	.04615	.759	1322	.380	1.021
							.302

TABLE 3.—BOUNDARY LAYER DEVELOPMENT ANALYSIS DATA—
 $M^* = 4.6$ TWO-DIMENSIONAL JPL NOZZLES (Continued)

d) Suction 2D-9, $T_{stag} = 400^\circ \text{ K}$, $T_{wall,ad}$; 50% streamline, side walls

$$\frac{U^*}{\nu^*} = 8 \cdot 10^6 / ft = 26.22 \cdot 10^6 / m, H^* = 1 m$$

$\frac{x}{H_{th}/2}$	$10^3 \cdot \frac{\delta^*}{H_{th}/2}$	$10^3 \cdot \frac{\theta}{H_{th}/2}$	$10^3 \cdot \frac{\delta}{H_{th}/2}$	Re θ	$10^3 \cdot cf$	$-10^3 \cdot \frac{\rho v_o}{\rho^* U^*}$	RF	δ_s' mm
-10	1.737	0.8849	10.023	1945	0.618	2.227	0.876	
-5	1.341	.6229	6.887	1817	.629	3.553	.899	
0	1.173	.4627	4.975	1584	.677	4.880	.9209	
5	1.281	.4000	4.228	1386	.689	4.690	.9379	0.043
10	1.527	.3772	4.200	1188	.767	4.500	.9549	.0344
20	2.460	.4068	5.265	956	.889	3.180	.9741	.038
30	3.516	.4370	6.510	783	1.093	2.557	.9877	
40	4.828	.4913	8.114	713	1.186	1.933	.9904	.055
60	8.602	.6894	13.31	756	1.146	1.160	.9904	.088
80	11.78	.8199	17.33	765	1.134	0.860	.9918	.114
100	14.18	.9063	20.38	767	1.163	.750	.9953	.133
120	16.59	1.0075	23.43	801	1.111	.640	.9945	.153
140	18.54	1.089	25.96	832	1.084	.584	.9956	.169
160	20.45	1.178	28.45	878	1.025	.528	.9952	.189
200	23.85	1.347	32.92	983	0.917	.455	.9960	.216
229.9	26.25	1.482	36.24	1079	.832	.410	.9950	

TABLE 3.—BOUNDARY LAYER DEVELOPMENT ANALYSIS DATA—
 $M^* = 4.6$ TWO-DIMENSIONAL JPL NOZZLES (Continued)

e) Suction 2D-10, $T_{\text{stag}} = 400^\circ \text{K}$, $T_{\text{wall, ad}} = 25\%$ streamline, side walls

$$\frac{U^*}{\nu^*} = 8 \cdot 10^6 / t_t = 26.22 \cdot 10^6 / m, H^* = 1m$$

$\frac{x}{H_{th}/2}$	$\frac{\delta^*}{H_{th}/2}$	$\frac{\theta}{H_{th}/2}$	$\frac{\delta}{H_{th}/2}$	Re θ	$10^3 \cdot c_f$	δ_s' mm	$-10^3 \cdot \frac{\rho_e \nu_o}{\rho^* U^*}$	RF	M	$\frac{U}{U^*}$
-10	0.001896	0.000953	0.01053	2095	0.548		1.483	0.865	0.4684	0.2279
-5	.001543	.000711	.00775	2074	.529		2.367	.8805	.6952	.3300
0	.001423	.000563	.00601	1927	.539		3.250	.8961	1.000	.4539
5	.001592	.000505	.00537	1751	.534	0.0533	3.125	.9101	1.3542	.5760
10	.001946	.000493	.00545	1552	.573	.0444	3.000	.9252	1.7132	.6762
20	.003215	.000546	.00689	1282	.643	.0505	2.120	.9485	2.347	.8050
30	.004765	.000607	.00890	1087	.766	.0624	1.703	.9670	2.8446	.8741
40	.006648	.000688	.01127	998	.825	.0771	1.287	.9758	3.229	.9141
60	.01186	.000966	.01831	1059	.789	.124	0.770	.9759	3.756	.9554
80	.01645	.001160	.02417	1082	.776	.164	.570	.9806	4.077	.9749
100	.02011	.001302	.02889	1101	.790	.192	.500	.9856	4.279	.9854
120	.02348	.001436	.03306	1142	.761	.221	.430	.9876	4.410	.9917
140	.02642	.001563	.03685	1195	.736	.246	.390	.9889	4.495	.9955
160	.02930	.001700	.04063	1268	.691	.272	.350	.9869	4.548	.9978
200	.03454	.001976	.04774	1443	.611	.319	.300	.9864	4.5944	.9998
229.9	.03803	.002173	.05253	1583	.554		.270	.9860	4.600	1.0000

TABLE 3.—BOUNDARY LAYER DEVELOPMENT ANALYSIS DATA—
M* = 4.6 TWO-DIMENSIONAL JPL NOZZLES (Continued)

f) Suction 2D-8, T_{stag} = 400° K, T_{wall,ad}; 75% streamline, side walls

$$\frac{U^*}{\nu} = 8 \cdot 10^6/\text{ft} = 26.22 \cdot 10^6/\text{m}, H^* = 1\text{m}$$

$\frac{x}{H_{th}/2}$	$10^3 \cdot \frac{\delta^*}{H_{th}/2}$	$10^3 \cdot \frac{\theta}{H_{th}/2}$	$10^3 \cdot \frac{\delta}{H_{th}/2}$	Re θ	$10^3 \cdot c_f$	$-10^3 \cdot \frac{\rho e V_0}{\rho^* U^*}$	M	$\frac{h}{H_{th}}$	$\frac{U}{U^*}$	δ_s' mm	RF
-10	1.5933	0.821	9.537	1805	0.694	2.967	0.4684	1.4066	0.2279		0.888
-5	1.1709	.5458	6.141	1592	.736	4.733	.6952	1.0985	.3300		.9154
0	0.9791	.3831	4.083	1311	.826	6.500	1.000	1.000	.4539		.9408
5	1.053	.3235	3.400	1121	.855	6.250	1.3542	1.0911	.5760	0.0350	.9578
10	1.234	.2993	3.353	943	.973	6.000	1.7132	1.3505	.6762	.0275	.9733
20	1.962	.3210	4.163	754	1.144	4.240	2.3471	2.2892	.8050	.0297	.9855
30	2.742	.3386	5.118	607	1.428	3.407	2.8446	3.6509	.8741	.0341	.9948
40	3.748	.3806	6.331	552	1.551	2.573	3.2287	5.2615	.9141	.0422	.9945
60	6.687	.5301	10.33	581	1.503	1.540	3.7561	8.5981	.9554	.0672	.9969
80	9.145	.6327	13.43	590	1.485	1.140	4.0766	11.472	.9749	.088	.9962
100	10.89	.6918	15.62	585	1.532	0.995	4.2789	13.701	.9854	.101	.9990
120	12.75	.7705	18.00	613	1.466	.850	4.4097	15.333	.9917	.114	.9976
140	14.20	.8304	19.86	635	1.429	.774	4.4946	16.483	.9955	.129	.9984
160	15.72	.9015	21.86	672	1.349	.698	4.5478	17.242	.9978	.142	.9976
200	18.41	1.039	25.50	758	1.203	.600	4.5944	17.931	.9998	.165	.9976
229.9	20.33	1.146	28.15	835	1.089	.540	4.6000	18.017	1.0000		.9966

TABLE 3.—BOUNDARY LAYER DEVELOPMENT ANALYSIS DATA—
 $M^* = 4.6$ TWO-DIMENSIONAL JPL NOZZLES (Continued)

g) Suction 2D-7, $T_{stag} = 400^\circ \text{ K}$, $T_{wall,ad}$; 75% streamline, side walls

$$\frac{U^*}{\nu^*} = 8 \cdot 10^6 / ft = 26.22 \cdot 10^6 / m, H^* = 1m$$

$\frac{x}{H_{th}/2}$	$10^3 \cdot \frac{\delta^*}{H_{th}/2}$	$10^3 \cdot \frac{\theta}{H_{th}/2}$	$10^3 \cdot \frac{\delta}{H_{th}/2}$	Re θ	$10^3 \cdot cf$	$-10^3 \cdot \frac{\rho_e v_o}{\rho^* U^*}$	RF	δ_s' mm
-10	1.124	0.5845	7.198	1285	1.008	5.527	0.9305	
-5	0.8173	.3714	3.893	1083	1.042	7.633	.9559	
0	.6886	.2594	2.637	888	1.158	9.740	.9757	
5	.7851	.2350	2.450	814	1.146	8.785	.9795	0.0266
10	.9695	.2319	2.615	730	1.240	7.830	.9860	.0219
20	1.660	.2712	3.509	637	1.358	5.090	.9895	.0244
30	2.352	.2895	4.356	519	1.679	4.033	.9979	
40	3.298	.3348	5.620	486	1.784	2.977	.9971	.0325
60	6.022	.4793	9.379	525	1.693	1.748	.9980	.0597
80	7.651	.5298	11.32	494	1.810	1.404	.9983	.0727
100	10.05	.6436	14.45	544	1.638	1.060	.9953	.0940
120	11.23	.6756	15.83	537	1.688	0.984	1.0006	.102
140	12.21	.7110	17.04	543	1.673	.908	1.0002	.110
160	13.00	.7416	18.07	553	1.657	.862	1.0012	.117
180	13.27	.7476	18.37	550	1.671	.847	1.0014	.118

TABLE 3.—BOUNDARY LAYER DEVELOPMENT ANALYSIS DATA—
 $M^* = 4.6$ TWO-DIMENSIONAL JPL NOZZLES (Continued)

h) Suction 2D-9, $T_{stag} = 400^\circ \text{ K}$, $T_{wall,ad}$; 25% streamline, side walls

$$\frac{U^*}{\nu^*} = 8 \cdot 10^6 / ft = 26.22 \cdot 10^6 / m, H^* = 1m$$

$\frac{x}{H_{th}/2}$	$10^3 \cdot \frac{\delta^*}{H_{th}/2}$	$10^3 \cdot \frac{\theta}{H_{th}/2}$	$10^3 \cdot \frac{\delta}{H_{th}/2}$	Re θ	$10^3 \cdot cf$	$-10^3 \cdot \frac{\rho v_0}{\rho^* U^*}$	RF	δ_s' mm
-10	1.737	0.8849	10.02	1945	0.618	2.227	0.899	
-5	1.341	.6229	6.887	1817	.629	3.553	.9204	
0	1.173	.4627	4.975	1584	.677	4.880	.9379	0.0427
5	1.281	.4000	4.228	1386	.689	4.690	.9549	.0344
10	1.527	.3772	4.200	1188	.767	4.500	.9741	.0377
20	2.460	.4068	5.265	956	.889	3.180	.9877	.0438
30	3.515	.4370	6.510	783	1.093	2.557	.9904	.0547
40	4.828	.4913	8.114	713	1.186	1.933	.9904	.0877
60	8.602	.6894	13.31	756	1.146	1.160	.9918	.115
80	11.78	.8199	17.33	765	1.134	0.860	.9953	.133
100	14.18	.9063	20.38	767	1.163	.750	.9945	.153
120	16.59	1.0075	23.43	801	1.112	.640	.9956	.169
140	18.54	1.089	25.96	832	1.084	.584	.9952	.185
160	20.45	1.178	28.45	878	1.025	.528	.9960	
200	23.85	1.347	32.92	983	0.917	.455	.9950	
229.9	26.25	1.482	36.24	1079	.832	.410		

TABLE 3.—BOUNDARY LAYER DEVELOPMENT ANALYSIS DATA—
 $M^* = 4.6$ TWO-DIMENSIONAL JPL NOZZLES (Concluded)

i) Suction 2D-11, $T_{stag} = 400^\circ \text{K}$, $T_{wall_{ad}}$; 50% streamline, side walls

$$\frac{U^*}{V^*} = 8 \cdot 10^6 / ft = 26.22 \cdot 10^6 / m, H^* = 1 \text{ m}$$

$\frac{x}{H_{th}/2}$	$10^3 \cdot \frac{\delta^*}{H_{th}/2}$	$10^3 \cdot \frac{\theta}{H_{th}/2}$	$10^3 \cdot \frac{\delta}{H_{th}/2}$	Re θ	$10^3 \cdot cf$	$-10^3 \cdot \frac{\rho_e v_o}{\rho^* U^*}$	RF	δ_s' mm
-10	1.649	0.8461	9.725	1860	0.663	2.670	0.884	
-5	1.236	.5753	6.447	1678	.692	4.260	.908	
0	1.051	.4128	4.435	1413	.765	5.850	.933	
5	1.136	.3512	3.699	1217	.787	5.625	.9511	0.038
10	1.339	.3269	3.645	1030	.890	5.400	.9672	.030
20	2.137	.3506	4.568	824	1.042	3.820	.9821	.032
30	3.008	.3720	5.584	667	1.294	3.070	.9927	.037
40	4.115	.4179	6.889	606	1.406	2.320	.9933	.047
60	7.343	.5844	11.34	641	1.361	1.390	.9950	.074
80	10.04	.6958	14.75	649	1.347	1.030	.9947	.097
100	11.99	.7627	17.19	645	1.389	0.900	.9979	.111
120	14.00	.8473	19.76	674	1.331	.770	.9967	.129
140	15.60	.9132	21.84	698	1.298	.702	.9976	.142
160	17.23	.9895	23.96	738	1.227	.634	.9970	.144
200	20.175	1.140	27.95	832	1.094	.545	.9968	
229.9	22.23	1.252	30.70	912	0.991	.490	.9966	

TABLE 4.—EVALUATION OF $\int \beta dx - M^* = 3$ AXISYMMETRIC NOZZLES

a) $R = 12 R_{th}$, working medium: air, suction 10, $T_{stag} = 300^\circ K$, $T_{wall_{ad}}$

$$\frac{U^*}{\nu^*} = 26.22 \cdot 10^6/m, D^* = 1m$$

$\frac{x}{R_{th}}$	$103 \cdot \frac{\theta}{R_{th}}$	Re_θ	$\frac{r}{R_{th}}$	$Re_\theta \sqrt{\frac{\theta}{r}}$	$\beta \theta Re_\theta$	$\beta R_{th} \equiv \beta'$
2.5			convex		< 0	< 0
3	0.127	1249	59.2	1.829	0.103	0.649
4	.133	1191	35.7	2.299	.198	1.250
6	.147	1145	34.0	2.381	.214	1.271
8	.154	1077	44.1	2.013	.140	0.844
10	.154	1011	65.0	1.556	.057	.366
11.68	.156	992	149	1.015	< 0	< 0

b) $R = 12 R_{th}$, working medium: air, suction 9, $T_{stag} = 300^\circ K$, $T_{wall_{ad}}$

$$\frac{U^*}{\nu^*} = 6.55 \cdot 10^6/m, D^* = 1m$$

$\frac{x}{R_{th}}$	$103 \cdot \frac{\theta}{R_{th}}$	Re_θ	$\frac{r}{R_{th}}$	$Re_\theta \sqrt{\frac{\theta}{r}}$	$\beta \theta Re_\theta$	$\beta R_{th} \equiv \beta'$
2.5			convex		< 0	< 0
3	0.264	652	59.2	1.377	0.030	0.174
4	.254	570	35.7	1.520	.052	.359
6	.226	439	34	1.06	< 0	< 0
8	.206	361	44.1	0.78	< 0	< 0
10	.194	318	65	.55	< 0	< 0
11.68	.188	299	149	.34	< 0	< 0

c) $R = 12 R_{th}$, working medium: air, suction 9, $T_{stag} = 300^\circ K$, $T_{wall_{ad}}$

$$\frac{U^*}{\nu^*} = 104.88 \cdot 10^6/m, D^* = 1m$$

$\frac{x}{R_{th}}$	$103 \cdot \frac{\theta}{R_{th}}$	Re_θ	$\frac{r}{R_{th}}$	$Re_\theta \sqrt{\frac{\theta}{r}}$	$\beta \theta Re_\theta$	$\beta R_{th} \equiv \beta'$
2.5			convex		< 0	< 0
3	0.066	2608	59.2	2.75	0.295	1.714
4	.064	2278	35.7	3.04	.360	2.469
6	.057	1754	34	2.26	.190	1.900
8	.052	1442	44.1	1.56	.058	0.773
10	.049	1270	65	1.10	< 0	< 0
11.68	.047	1196	149	0.67	< 0	< 0

TABLE 4.—EVALUATION OF $\int \beta dx - M^* = 3$ AXISYMMETRIC NOZZLES (Continued)d) $R = 12 R_{th}$, working medium: air, suction 9, $T_{stag} = 300^\circ \text{ K}$, $T_{wall_{ad}}$

$$\frac{U^*}{\nu^*} = 26.22 \cdot 10^6/\text{m}, D^* = 1\text{m}$$

$\frac{x}{R_{th}}$	$10^3 \cdot \frac{\theta}{R_{th}}$	Re_θ	$\frac{r}{R_{th}}$	$Re_\theta \sqrt{\frac{\theta}{r}}$	$\beta \theta Re_\theta$	$\beta R_{th} \equiv \beta'$
2.5			convex			< 0
3	0.132	1304	59.2	1.947	0.127	0.738
4	.127	1139	35.7	2.148	.167	1.154
6	.113	877	34	1.599	.066	0.666
8	.103	721	44.1	1.102	< 0	< 0
10	.097	635	65	0.776	< 0	< 0
11.68	.094	598	149	.475	< 0	< 0

e) $R = 12 R_{th}$, working medium: air, suction 8, $T_{stag} = 300^\circ \text{ K}$, $T_{wall_{ad}}$

$$\frac{U^*}{\nu^*} = 104.88 \cdot 10^6/\text{m}, D^* = 1\text{m}$$

$\frac{x}{R_{th}}$	$10^3 \cdot \frac{\theta}{R_{th}}$	Re_θ	$\frac{r}{R_{th}}$	$Re_\theta \sqrt{\frac{\theta}{r}}$	$\beta \theta Re_\theta$	$\beta R_{th} \equiv \beta'$
2.5			convex			< 0
3	0.091	3568	59.2	4.40	0.710	2.187
4	.096	3428	35.7	5.61	1.06	3.221
6	.098	3050	34	5.18	0.935	3.128
8	.096	2700	44.1	3.98	.60	2.315
10	.093	2440	65	2.92	.333	1.467
11.68	.091	2300	149	1.79	.099	0.473

f) $R = 12 R_{th}$, working medium: air, suction 8, $T_{stag} = 300^\circ \text{ K}$, $T_{wall_{ad}}$

$$\frac{U^*}{\nu^*} = 6.55 \cdot 10^6/\text{m}, D^* = 1\text{m}$$

$\frac{x}{R_{th}}$	$10^3 \cdot \frac{\theta}{R_{th}}$	Re_θ	$\frac{r}{R_{th}}$	$Re_\theta \sqrt{\frac{\theta}{r}}$	$\beta \theta Re_\theta$	$\beta R_{th} \equiv \beta'$
2.5			convex			< 0
3	0.362	892	59.2	2.2	0.178	0.551
4	.382	857	35.7	2.8	.307	.938
6	.392	763	34	2.59	.260	.869
8	.384	675	44.1	1.99	.135	.521
10	.372	610	65	1.46	.043	.189
11.68	.362	575	149	0.9	< 0	< 0

TABLE 4.—EVALUATION OF $\int \beta dx - M^* = 3$ AXISYMMETRIC NOZZLES (Continued)

g) $R = 12 R_{th}$, working medium: air, suction 8, $T_{stag} = 300^\circ K$, T_{wallad}

$$\frac{U^*}{\nu^*} = 26.22 \cdot 10^6/m, D^* = 1m$$

$\frac{x}{R_{th}}$	$10^3 \cdot \frac{\theta}{R_{th}}$	Re_θ	$\frac{r}{R_{th}}$	$Re_\theta \sqrt{\frac{\theta}{r}}$	$\beta \theta Re_\theta$	$\beta R_{th} \equiv \beta'$
2.5			convex			< 0
3	0.181	1784	59.2	3.119	0.38	1.177
4	.191	1714	35.7	3.965	.59	1.802
6	.196	1525	34	3.661	.511	1.71
8	.192	1350	44.1	2.817	.309	1.192
10	.186	1220	65	2.064	.150	0.661
11.68	.181	1150	149	1.268	.013	.062

h) $R = 12 R_{th}$, working medium: air, suction 7, $T_{stag} = 300^\circ K$, T_{wallad}

$$\frac{U^*}{\nu^*} = 26.22 \cdot 10^6/m, D^* = 1m$$

$\frac{x}{R_{th}}$	$10^3 \cdot \frac{\theta}{R_{th}}$	Re_θ	$\frac{r}{R_{th}}$	$Re_\theta \sqrt{\frac{\theta}{r}}$	$\beta \theta Re_\theta$	$\beta R_{th} \equiv \beta'$
2.5			convex			< 0
3	0.1541	1522	59.2	2.456	0.230	0.981
4	.1580	1416	35.7	2.979	.345	1.542
6	.1630	1268	34	2.776	.300	1.451
8	.1666	1170	44.1	2.274	.193	0.990
10	.1769	1160	65	1.914	.120	.585
11.68	.2061	1313	149	1.544	.056	.207

i) $R = 12 R_{th}$, working medium: air, suction 6, $T_{stag} = 300^\circ K$, T_{wallad}

$$\frac{U^*}{\nu^*} = 26.22 \cdot 10^6/m, D^* = 1m$$

$\frac{x}{R_{th}}$	$10^3 \cdot \frac{\theta}{R_{th}}$	Re_θ	$\frac{r}{R_{th}}$	$Re_\theta \sqrt{\frac{\theta}{r}}$	$\beta \theta Re_\theta$	$\beta R_{th} \equiv \beta'$
2.5			convex			< 0
3	0.1697	1676	59.2	2.838	0.306	1.076
4	.1841	1649	35.7	3.745	.535	1.762
6	.2111	1642	34	4.091	.625	1.803
8	.2318	1627	44.1	3.73	.535	1.419
10	.2440	1600	65	3.10	.375	0.961
11.68	.2466	1571	149	2.021	.143	.369

TABLE 4.—EVALUATION OF $\int \beta dx - M^* = 3$ AXISYMMETRIC NOZZLES (Continued)

j) $R = 12 R_{th}$, working medium: air, suction 5, $T_{stag} = 300^\circ K$, $T_{wall_{ad}}$

$$\frac{U^*}{\nu^*} = 104.88 \cdot 10^6/m, D^* = 1m$$

$\frac{x}{R_{th}}$	$10^3 \cdot \frac{\theta}{R_{th}}$	Re_θ	$\frac{r}{R_{th}}$	$Re_\theta \sqrt{\frac{\theta}{r}}$	$\beta \theta Re_\theta$	$\beta R_{th} \equiv \beta'$
2.5			convex		< 0	< 0
3	0.0771	3044	59.2	3.47	0.460	1.96
4	.0776	2780	35.7	4.10	.627	2.91
6	.0730	2272	34	3.33	.430	2.59
8	.0678	1904	44.1	2.36	.211	1.63
10	.0639	1676	65	1.612	.068	0.64
11.68	.0618	1574	149	1.01	< 0	< 0

k) $R = 12 R_{th}$, working medium: air, suction 5, $T_{stag} = 300^\circ K$, $T_{wall_{ad}}$

$$\frac{U^*}{\nu^*} = 52.44 \cdot 10^6/m, D^* = 1m$$

$\frac{x}{R_{th}}$	$10^3 \cdot \frac{\theta}{R_{th}}$	Re_θ	$\frac{r}{R_{th}}$	$Re_\theta \sqrt{\frac{\theta}{r}}$	$\beta \theta Re_\theta$	$\beta R_{th} \equiv \beta'$
2.5			convex		< 0	< 0
3	0.109	2155	59.2	2.920	0.333	1.42
4	.110	1965	35.7	3.45	.460	2.13
6	.103	1607	34	2.796	.306	1.845
8	.096	1410	44.1	1.983	.133	1.03
10	.090	1241	65	1.398	.035	0.33
11.68	.087	1165	149	0.852	< 0	< 0

l) $R = 12 R_{th}$, working medium: air, suction 5, $T_{stag} = 300^\circ K$, $T_{wall_{ad}}$

$$\frac{U^*}{\nu^*} = 39.33 \cdot 10^6/m, D^* = 1m$$

$\frac{x}{R_{th}}$	$10^3 \cdot \frac{\theta}{R_{th}}$	Re_θ	$\frac{r}{R_{th}}$	$Re_\theta \sqrt{\frac{\theta}{r}}$	$\beta \theta Re_\theta$	$\beta R_{th} \equiv \beta'$
2.5			convex		< 0	< 0
3	0.126	1863	59.2	2.715	0.287	1.225
4	.127	1702	35.7	3.205	.40	1.855
6	.119	1390	34	2.603	.261	1.513
8	.111	1166	44.1	1.848	.107	0.83
10	.1045	1026	65	1.301	.018	.169
11.68	.101	963	149	0.793	< 0	< 0

TABLE 4.—EVALUATION OF $\int \beta dx - M^* = 3$ AXISYMMETRIC NOZZLES (Continued)

m) $R = 12 R_{th}$, working medium: air, suction 5, $T_{stag} = 300^\circ K$, $T_{wall_{ad}}$

$$\frac{U^*}{\nu^*} = 13.11 \cdot 10^6/m, D^* = 1m$$

$\frac{x}{R_{th}}$	$103 \cdot \frac{\theta}{R_{th}}$	Re_θ	$\frac{r}{R_{th}}$	$Re_\theta \sqrt{\frac{\theta}{r}}$	$\beta \theta Re_\theta$	$\beta R_{th} \equiv \beta'$
2.5			convex		< 0	< 0
3	0.218	1078	59.2	2.065	0.150	0.64
4	.219	983	35.7	2.44	.227	1.05
6	.206	803	34	1.98	.133	0.80
8	.192	673	44.1	1.405	.035	.27
10	.181	592	65	0.99	< 0	< 0
11.68	.175	557	149	.61	< 0	< 0

n) $R = 12 R_{th}$, working medium: air, suction 5, $T_{stag} = 300^\circ K$, $T_{wall_{ad}}$

$$\frac{U^*}{\nu^*} = 6.55 \cdot 10^6/m, D^* = 1m$$

$\frac{x}{R_{th}}$	$103 \cdot \frac{\theta}{R_{th}}$	Re_θ	$\frac{r}{R_{th}}$	$Re_\theta \sqrt{\frac{\theta}{r}}$	$\beta \theta Re_\theta$	$\beta R_{th} \equiv \beta'$
2.5			convex			< 0
3	0.308	761	59.2	1.735	0.088	0.375
4	.310	695	35.7	2.05	.148	.685
6	.292	566	34	1.665	.076	.458
8	.271	476	44.1	1.180	.005	.039
10	.256	419	65	0.830	< 0	< 0
11.68	.247	393	149	.500	< 0	< 0

o) $R = 12 R_{th}$, working medium: air, suction 5, $T_{stag} = 300^\circ K$, $T_{wall_{ad}}$

$$\frac{U^*}{\nu^*} = 26.22 \cdot 10^6/m, D^* = 1m$$

$\frac{x}{R_{th}}$	$103 \cdot \frac{\theta}{R_{th}}$	Re_θ	$\frac{r}{R_{th}}$	$Re_\theta \sqrt{\frac{\theta}{r}}$	$\beta \theta Re_\theta$	$\beta R_{th} \equiv \beta'$
2.5			convex		< 0	< 0
3	0.1541	1522	59.2	2.456	0.231	0.985
4	.1552	1390	35.7	2.898	.329	1.525
6	.1460	1136	34	2.354	.210	1.266
8	.1356	952	44.1	1.669	.076	0.589
10	.1278	838	65	1.175	.005	.047
11.68	.1236	787	149	0.717	< 0	< 0

TABLE 4.—EVALUATION OF $\int \beta dx - M^* = 3$ AXISYMMETRIC NOZZLES (Concluded)

p) $R = 6 R_{th}$, working medium: air, suction 6, $T_{stag} = 300^\circ K$, T_{wallad}

$$\frac{U^*}{\nu^*} = 26.22 \cdot 10^6/m, D^* = 1m$$

$\frac{x}{R_{th}}$	$103 \cdot \frac{\theta}{R_{th}}$	Re_θ	$\frac{r}{R_{th}}$	$Re_\theta \sqrt{\frac{\theta}{r}}$	$\beta \theta Re_\theta$	$\beta R_{th} \equiv \beta'$
1.5			convex		< 0	< 0
2	0.1527	1583	31.3	3.496	0.470	1.944
4	.1843	1565	27.8	4.03	.605	2.098
6	.2120	1569	34.5	3.889	.571	1.717
8	.2318	1569	47.6	3.462	.458	1.259
10.26	.2437	1567	100	2.446	.228	0.597

q) $R = 6 R_{th}$, working medium: air, suction 5, $T_{stag} = 300^\circ K$, T_{wallad}

$$\frac{U^*}{\nu^*} = 26.22 \cdot 10^6/m, D^* = 1m$$

$\frac{x}{R_{th}}$	$103 \cdot \frac{\theta}{R_{th}}$	Re_θ	$\frac{r}{R_{th}}$	$Re_\theta \sqrt{\frac{\theta}{r}}$	$\beta \theta Re_\theta$	$\beta R_{th} \equiv \beta'$
1.5			convex		< 0	< 0
2	0.1450	1504	31.3	3.237	0.405	1.864
4	.1529	1299	27.8	3.04	.356	1.795
6	.1430	1058	34.5	2.15	.168	1.111
8	.1324	896	47.6	1.49	.048	0.405
10.26	.1251	804	100	0.90	< 0	< 0

r) $R = 3 R_{th}$, working medium: air, suction 5, $T_{stag} = 300^\circ K$, T_{wallad}

$$\frac{U^*}{\nu^*} = 26.22 \cdot 10^6/m, D^* = 1m$$

$\frac{x}{R_{th}}$	$103 \cdot \frac{\theta}{R_{th}}$	Re_θ	$\frac{r}{R_{th}}$	$Re_\theta \sqrt{\frac{\theta}{r}}$	$\beta \theta Re_\theta$	$\beta R_{th} \equiv \beta'$
0.8			convex		< 0	< 0
1	0.1240	1407	55.9	2.096	0.157	0.90
2	.1460	1450	24.9	3.511	.479	2.263
4	.1518	1237	25.0	3.048	.36	1.917
6	.1403	1002	36.5	1.964	.13	0.925
8	.1294	850	60.3	1.245	.01	.102
9.55	.1242	790	125	0.787	< 0	< 0

TABLE 5.—EVALUATION OF $\int \beta dx - M^* = 5$ AXISYMMETRIC NOZZLES

a) LARC Q-nozzle, working medium: air, suction 5.1, $T_{stag} = 300^\circ \text{ K}$, $T_{wall_{ad}}$

$$\frac{U^*}{\nu^*} = 26.22 \cdot 10^6/\text{m}, D^* = 1\text{m}$$

$\frac{x}{R_{th}}$	$10^3 \cdot \frac{\theta}{R_{th}}$	Re_θ	$\frac{r}{R_{th}}$	$Re_\theta \sqrt{\frac{\theta}{r}}$	$\beta \theta Re_\theta$	$\beta R_{th} \equiv \beta'$
10			convex		< 0	< 0
12	0.369	1895	207	2.53	0.248	0.355
15	.351	1494	108	2.693	.280	.534
20	.290	1004	153.5	1.38	.030	.103
25	.263	800	192	0.936	< 0	< 0
30	.266	743	222	.813	< 0	< 0
40	.309	795	357	.74	< 0	< 0
49.19	.389	973	435	.92	< 0	< 0

b) LARC Q-nozzle, working medium: air, suction 5.1, $T_{stag} = 300^\circ \text{ K}$, $T_{wall_{ad}}$

$$\frac{U}{\nu^*} = 104.88 \cdot 10^6/\text{m}, D^* = 1\text{m}$$

$\frac{x}{R_{th}}$	$10^3 \cdot \frac{\theta}{R_{th}}$	Re_θ	$\frac{r}{R_{th}}$	$Re_\theta \sqrt{\frac{\theta}{r}}$	$\beta \theta Re_\theta$	$\beta R_{th} \equiv \beta'$
10			convex		< 0	< 0
12	0.185	3790	207	3.583	0.490	0.699
15	.176	2988	108	3.814	.555	1.056
20	.145	2008	153.5	1.952	.128	0.44
25	.132	1600	192	1.327	.02	.095
30	.133	1486	222	1.15	< 0	< 0
40	.155	1590	357	1.045	< 0	< 0
49.19	.195	1946	435	1.303	.015	.04

c) LARC Q-nozzle, working medium: air, suction 5.2, $T_{stag} = 300^\circ \text{ K}$, $T_{wall_{ad}}$

$$\frac{U^*}{\nu^*} = 26.22 \cdot 10^6/\text{m}, D^* = 1\text{m}$$

$\frac{x}{R_{th}}$	$10^3 \cdot \frac{\theta}{R_{th}}$	Re_θ	$\frac{r}{R_{th}}$	$Re_\theta \sqrt{\frac{\theta}{r}}$	$\beta \theta Re_\theta$	$\beta R_{th} \equiv \beta'$
10			convex		< 0	< 0
12	0.4918	2525	207	3.892	0.570	0.459
15	.5595	2382	108	5.422	1.010	.758
20	.6443	2228	153.5	4.565	0.755	.526
25	.6931	2106	192	4.001	.602	.412
30	.7189	2009	222	3.615	.500	.346
40	.757	1949	357	2.838	.309	.209
49.19	.7758	1942	435	2.593	.259	.172

TABLE 5.—EVALUATION OF $\int \beta dx - M^* = 5$ AXISYMMETRIC NOZZLES (Continued)d) LARC Q-nozzle, working medium: air, suction 5.3, $T_{\text{stag}} = 300^\circ \text{ K}$, $T_{\text{wall ad}}$

$$\frac{U^*}{\nu^*} = 26.22 \cdot 10^6/\text{m}, D^* = 1\text{m}$$

$\frac{x}{R_{\text{th}}}$	$10^3 \cdot \frac{\theta}{R_{\text{th}}}$	Re_θ	$\frac{r}{R_{\text{th}}}$	$Re_\theta \sqrt{\frac{\theta}{r}}$	$\beta \theta Re_\theta$	$\beta R_{\text{th}} \equiv \beta'$
10			convex		< 0	< 0
12	0.4072	2091	207	2.933	0.335	0.393
15	.4401	1873	108	3.781	.540	.655
20	.4757	1645	153.5	2.896	.329	.420
25	.4887	1485	192	2.369	.212	.292
30	.4922	1376	222	2.049	.148	.219
40	.5092	1311	357	1.566	.060	.090
49.19	.5184	1298	435	1.417	.037	.055

e) LARC Q-nozzle, working medium: air, suction 5.3, $T_{\text{stag}} = 400^\circ \text{ K}$, $T_{\text{wall ad}}$

$$\frac{U^*}{\nu^*} = 26.22 \cdot 10^6/\text{m}, D^* = 1\text{m}$$

$\frac{x}{R_{\text{th}}}$	$10^3 \cdot \frac{\theta}{R_{\text{th}}}$	Re_θ	$\frac{r}{R_{\text{th}}}$	$Re_\theta \sqrt{\frac{\theta}{r}}$	$\beta \theta Re_\theta$	$\beta R_{\text{th}} \equiv \beta'$
10			convex		< 0	< 0
12	0.3754	2006	207	2.701	0.283	0.376
15	.404	1771	108	3.425	.453	.633
20	.435	1531	153.5	2.577	.254	.381
25	.4453	1367	192	2.082	.153	.251
30	.4486	1261	222	1.793	.096	.17
40	.4654	1200	357	1.370	.028	.05
49.19	.4741	1187	435	1.239	.009	.016

f) LARC Q-nozzle, working medium: air, suction 5.3, $T_{\text{stag}} = 400^\circ \text{ K}$, $T_{\text{wall}} = 300^\circ \text{ K}$

$$\frac{U^*}{\nu^*} = 26.22 \cdot 10^6/\text{m}, D^* = 1\text{m}$$

$\frac{x}{R_{\text{th}}}$	$10^3 \cdot \frac{\theta}{R_{\text{th}}}$	Re_θ	$\frac{r}{R_{\text{th}}}$	$Re_\theta \sqrt{\frac{\theta}{r}}$	$\beta \theta Re_\theta$	$\beta R_{\text{th}} \equiv \beta'$
10			convex		< 0	< 0
12	0.5380	2873	207	4.63	0.780	0.505
15	.577	2530	108	5.85	1.013	.694
20	.605	2129	153.5	4.23	0.663	.515
25	.596	1829	192	3.22	.402	.369
30	.573	1612	222	2.59	.260	.281
40	.544	1403	357	1.73	.088	.115
49.19	.526	1316	435	1.45	.041	.059

TABLE 5.—EVALUATION OF $\int \beta dx - M^* = 5$ AXISYMMETRIC NOZZLES (Concluded)

g) LARC Q-nozzle, working medium: air, no suction, $T_{stag} = 378^\circ \text{K}$, $T_{wall_{ad}}$, $R_{th} = 0.01007\text{m}$

				$\frac{U^*}{\nu^*} = 6.908 \cdot 10^6/\text{m}$			$\frac{U^*}{\nu^*} = 4.934 \cdot 10^6/\text{m}$		
$\frac{x}{R_{th}}$	$10^3 \cdot \frac{\theta}{R_{th}}$	Re_θ	$\frac{r}{R_{th}}$	$Re_\theta \sqrt{\frac{\theta}{r}}$	$\beta \theta Re_\theta$	$\beta R_{th} \equiv \beta'$	$Re_\theta \sqrt{\frac{\theta}{r}}$	$\beta \theta Re_\theta$	βR_{th}
10			convex						
12	4.127	607	207	2.710	1.02	0.407	2.491	0.91	0.363
15	5.250	635	108	4.427	1.91	.573	4.07	1.72	.516
20	7.135	694	153.5	4.732	2.075	.419	4.35	1.87	.378
25	8.864	754	192	5.123	2.29	.343	4.71	2.07	.31
30	10.522	820	222	5.645	2.59	.300	5.19	2.31	.268
40	13.353	955	357	5.841	2.70	.212	5.37	2.42	.19
49.19	15.595	1083	435	6.485	3.07	.182	5.962	2.76	.164

h) LARC rapid expansion nozzle, working medium: air, no suction, $T_{stag} = 378^\circ \text{K}$, $T_{wall_{ad}}$

$$\frac{U^*}{\nu^*} = 6.908 \cdot 10^6/\text{m}, R_{th} = 0.01007\text{m}$$

$\frac{x}{R_{th}}$	$10^3 \cdot \frac{\theta}{R_{th}}$	Re_θ	$\frac{r}{R_{th}}$	$Re_\theta \sqrt{\frac{\theta}{r}}$	$\beta \theta Re_\theta$	$\beta R_{th} \equiv \beta'$
1.5			convex		< 0	< 0
2	1.342	353	51.8	1.797	0.595	1.256
4	2.294	417	50.7	2.805	1.07	1.118
6	3.238	461	57.7	3.453	1.39	0.931
10	5.019	534	78.7	4.264	1.82	.679
15	7.063	615	110	4.928	2.19	.504
20	8.889	693	154	5.265	2.36	.383
30	12.039	850	286	5.515	2.51	.245
38.67	14.267	991	527	5.156	2.30	.163

i) LARC rapid expansion nozzle, working medium: air, suction 5.1, $T_{stag} = 300^\circ \text{K}$, $T_{wall_{ad}}$

$$\frac{U^*}{\nu^*} = 26.22 \cdot 10^6/\text{m}, D^* = 1\text{m}$$

$\frac{x}{R_{th}}$	$10^3 \cdot \frac{\theta}{R_{th}}$	Re_θ	$\frac{r}{R_{th}}$	$Re_\theta \sqrt{\frac{\theta}{r}}$	$\beta \theta Re_\theta$	$\beta R_{th} \equiv \beta'$
1.5			convex		< 0	< 0
2	0.1949	1814	51.8	3.519	0.479	1.355
4	.2761	1807	50.7	4.217	.660	1.323
6	.3106	1611	57.7	3.738	.540	1.079
10	.2949	1157	78.7	2.24	.185	0.542
15	.2440	791	110	1.178	.005	.026
20	.2162	630	154	0.746	< 0	< 0
30	.2611	692	286	.661	< 0	< 0
38.68	.3589	936	527	.772	< 0	< 0

**TABLE 6.—EVALUATION OF $\int \beta dx$ —HIGH MACH NUMBER
AXISYMMETRIC NOZZLES**

a) $M^* = 7$, $R = 30 R_{th}$, working medium: air, suction 7.1, $T_{stag} = 700^\circ K$, $T_{wall ad}$

$$\frac{U^*}{\nu^*} = 26.22 \cdot 10^6/m, D^* = 1m$$

$\frac{x}{R_{th}}$	$103 \cdot \frac{\theta}{R_{th}}$	Re_θ	$\frac{r}{R_{th}}$	$Re_\theta \sqrt{\frac{\theta}{r}}$	$\beta \theta Re_\theta$	$\beta R_{th} \equiv \beta'$
8.5			convex		< 0	< 0
10	0.3314	1913	230	2.296	0.197	0.311
15	.3999	1662	118	3.06	.365	.549
20	.4850	1580	147	2.87	.32	.418
30	.5873	1408	202	2.401	.22	.266
40	.6607	1309	288	1.983	.133	.154
60	.7209	1132	500	1.359	.028	.034
80	.6991	964	820	0.89	< 0	< 0
102.42	.6807	876	2500	.457	< 0	< 0

b) $M^* = 7$, $R = 30 R_{th}$, working medium: air, suction 7.2, $T_{stag} = 700^\circ K$, $T_{wall ad}$

$$\frac{U^*}{\nu^*} = 26.22 \cdot 10^6/m, D^* = 1m$$

$\frac{x}{R_{th}}$	$103 \cdot \frac{\theta}{R_{th}}$	Re_θ	$\frac{r}{R_{th}}$	$Re_\theta \sqrt{\frac{\theta}{r}}$	$\beta \theta Re_\theta$	$\beta R_{th} \equiv \beta'$
8.5			convex		< 0	< 0
10	0.2647	1528	230	1.639	0.071	0.176
15	.3057	1271	118	2.046	.147	.378
20	.3608	1175	147	1.841	.105	.248
30	.4103	983	202	1.401	.035	.087
40	.4555	902	288	1.134	< 0	< 0
60	.4824	757	500	0.744	< 0	< 0
80	.4618	637	820	.478	< 0	< 0
102.42	.4539	584	2500	.249	< 0	< 0

c) $M^* = 7$, $R = 75 R_{th}$, working medium: air, suction 7.1, $T_{stag} = 700^\circ K$, $T_{wall ad}$

$$\frac{U^*}{\nu^*} = 26.22 \cdot 10^6/m, D^* = 1m$$

$\frac{x}{R_{th}}$	$103 \cdot \frac{\theta}{R_{th}}$	Re_θ	$\frac{r}{R_{th}}$	$Re_\theta \sqrt{\frac{\theta}{r}}$	$\beta \theta Re_\theta$	$\beta R_{th} \equiv \beta'$
17			convex		< 0	< 0
20	0.434	1817	221	2.546	0.249	0.316
25	.481	1624	205	2.488	.237	.304
30	.517	1477	217	2.280	.195	.255
40	.616	1397	269	2.114	.161	.187
50	.686	1331	360	1.837	.104	.114
60	.726	1255	450	1.594	.064	.070
70	.732	1160	568	1.317	.020	.024
80	.719	1065	725	1.061	< 0	< 0
90	.707	996	910	0.878	< 0	< 0
111.3	.701	930	2500	.49	< 0	< 0

**TABLE 6.—EVALUATION OF $\int \beta dx$ —HIGH MACH NUMBER
AXISYMMETRIC NOZZLES (Continued)**

d) $M^* = 9$, $R = 200 R_{th}$, working medium: air, suction 9.1, $T_{stag} = 1000^\circ K$, $T_{wall ad}$

$$\frac{U^*}{\nu^*} = 26.22 \cdot 10^6/m, D^* = 1m$$

$\frac{x}{R_{th}}$	$103 \cdot \frac{\theta}{R_{th}}$	Re_θ	$\frac{R_{th}}{r}$	$Re_\theta \sqrt{\frac{\theta}{r}}$	$\beta \theta Re_\theta$	$\beta R_{th} \equiv \beta'$
38			convex		< 0	< 0
50	0.6783	1536	0.00206	1.816	0.100	0.096
60	.7562	1411	.00194	1.709	.083	.078
80	.8974	1282	.00159	1.531	.054	.047
100	.9827	1172	.00115	1.246	.010	.009
120	1.015	1062	.00093	1.032	< 0	< 0
160	1.047	915	.00063	0.743	< 0	< 0
200	1.045	816	.00042	.541	< 0	< 0
230	1.022	756	.00031	.426	< 0	< 0
265.09	1.000	714	.00010	.226	< 0	< 0

e) $M^* = 9$, $R = 200 R_{th}$, working medium: air, suction 9.2, $T_{stag} = 1000^\circ K$, $T_{wall ad}$

$$\frac{U^*}{\nu^*} = 26.22 \cdot 10^6/m, D^* = 1m$$

$\frac{x}{R_{th}}$	$103 \cdot \frac{\theta}{R_{th}}$	Re_θ	$\frac{R_{th}}{r}$	$Re_\theta \sqrt{\frac{\theta}{r}}$	$\beta \theta Re_\theta$	$\beta R_{th} \equiv \beta'$
38			convex		< 0	< 0
50	0.954	2160	0.00206	3.028	0.365	0.177
60	1.084	2022	.00194	2.932	.335	.153
80	1.315	1878	.00159	2.716	.286	.116
100	1.477	1761	.00115	2.295	.198	.076
120	1.579	1651	.00093	2.001	.138	.053
160	1.691	1478	.00063	1.525	.054	.022
200	1.690	1320	.00042	1.112	< 0	< 0
230	1.659	1228	.00031	0.881	< 0	< 0
265.09	1.622	1158	.00010	.467	< 0	< 0

**TABLE 6.—EVALUATION OF $\int \beta dx$ —HIGH MACH NUMBER
AXISYMMETRIC NOZZLES (Continued)**

f) $M^* = 8.93$, $R = 250 R_{th}$, working medium: helium, suction 9.3 He, $T_{stag} = 300^\circ K$, $T_{wall_{ad}}$
 $\frac{U^*}{\nu^*} = 26.22 \cdot 10^6/m$, $D^* = 1m$, $\dot{m}_s/\dot{m}_O = 0.0125$, $\int \beta dx < 0$

$\frac{x}{R_{th}}$	$103 \cdot \frac{\theta}{R_{th}}$	Re_θ	$\frac{r}{R_{th}}$	$Re_\theta \sqrt{\frac{\theta}{r}}$	$\beta \theta Re_\theta$	$\beta R_{th} \equiv \beta'$
30			convex		< 0	< 0
35	0.2877	1156	380	1.006	< 0	< 0
40	.2936	1055	330	0.995	< 0	< 0
50	.3049	914	415	.838	< 0	< 0
60	.3159	829	540	.634	< 0	< 0
70	.3165	752	685	.511	< 0	< 0
80	.3123	687	865	.413	< 0	< 0
100	.3117	616	1300	.302	< 0	< 0

g) $M^* = 8.93$, $R = 250 R_{th}$, working medium: helium, suction 9.4 He, $T_{stag} = 300^\circ K$, $T_{wall_{ad}}$
 $\frac{U^*}{\nu^*} = 26.22 \cdot 10^6/m$, $\dot{m}_s/\dot{m}_O = 0.00625$, $\int \beta dx = 5.1$, $\mu \sim T^{0.675}$

$\frac{x}{R_{th}}$	$103 \cdot \frac{\theta}{R_{th}}$	Re_θ	$\frac{r}{R_{th}}$	$Re_\theta \sqrt{\frac{\theta}{r}}$	$\beta \theta Re_\theta$	$\beta R_{th} \equiv \beta'$
30			convex		< 0	< 0
35	0.5168	2077	380	2.422	0.220	0.205
40	.5368	1929	330	2.460	.232	.224
50	.5782	1734	415	2.047	.145	.145
60	.6055	1589	540	1.683	.080	.083
70	.6198	1472	685	1.400	.035	.038
80	.6212	1366	865	1.158	0	0
100	.6148	1215	1300	0.835	< 0	< 0
122	.6027	1152			< 0	< 0

TABLE 6.—EVALUATION OF $\int \beta dx$ —HIGH MACH NUMBER
AXISYMMETRIC NOZZLES (Concluded)

h) $M^* = 9$, NASA helium nozzle, working medium: helium, suction 9.5 He, $T_{stag} = 300^\circ \text{K}$, $T_{wall_{ad}}$

$$\frac{U^*}{\nu^*} = 26.22 \cdot 10^6/\text{m}, D^* = 1\text{m}, \dot{m}_s/\dot{m}_0 = 0.00847, \int \beta dx = 0.86$$

$$Re_{L_{equ}} = 3.145 \cdot 10^8, \mu \sim T^{0.675}$$

$\frac{x}{R_{th}}$	$10^3 \cdot \frac{\theta}{R_{th}}$	Re_θ	$\frac{r}{R_{th}}$	$Re_\theta \sqrt{\frac{\theta}{r}}$	$\beta \theta Re_\theta$	$\beta R_{th} \equiv \beta'$
10.541	0.2684	1499	225	1.637	0.070	0.174
16.754	.2500	1046	197	1.178	0	0
24.43	.2774	939	268	0.955	< 0	< 0
35.04	.3586	1002	395	.955	< 0	< 0
46.55	.4224	1026	566	.886	< 0	< 0
52.38	.4711	1085	675	.906	< 0	< 0
63.49	.5250	1114	904	.849	< 0	< 0
75.04	.5611	1120	1190	.769	< 0	< 0
86.70	.5841	1117	1570	.681	< 0	< 0
98.67	.6021	1124			< 0	< 0

i) $M^* = 9$, NASA helium nozzle, working medium: helium, suction 9.6 He

$$\frac{U^*}{\nu^*} = 26.22 \cdot 10^6/\text{m}, D^* = 1\text{m}, \dot{m}_s/\dot{m}_0 = 0.0060, \int \beta dx = 5.7$$

$$Re_{L_{equ}} = 3.145 \cdot 10^8, \mu \sim T^{0.675}$$

$\frac{x}{R_{th}}$	$10^3 \cdot \frac{\theta}{R_{th}}$	$\frac{r}{R_{th}}$	Re_θ	$Re_\theta \sqrt{\frac{\theta}{r}}$	$\beta \theta Re_\theta$	βR_{th}	M
10.541	0.3291	225	1837	2.22	0.180	0.298	4.271
16.754	.3395	197	1421	1.865	.110	.228	5.278
24.433	.3778	268	1278	1.517	.053	.110	6.1115
35.039	.4779	395	1335	1.468	.045	.071	6.943
46.546	.5598	566	1360	1.353	.028	.037	7.604
52.376	.6152	675	1416	1.352	.028	.032	7.873
63.487	.6984	904	1483	1.303	.020	.019	8.293
75.036	.7568	1190	1511	1.205	~ 0	0	8.622
86.702	.7976	1570	1526	1.088	< 0	< 0	8.860
98.667	.8296		1548				8.999

TABLE 7.—EVALUATION OF $\int \beta dx - M^* = 4.6$
TWO-DIMENSIONAL JPL NOZZLE

a) Suction 2D-3, $\dot{m}_s/\dot{m}_o = 0.0074$, $T_{stag} = 300^\circ \text{ K}$, $T_{wall_{ad}}$

$$\frac{U^*}{\nu^*} = 26.22 \cdot 10^6/\text{m}, H^* = 1\text{m}, \text{tunnel floor and ceiling}$$

$\frac{x}{0.5H_{th}}$	$10^3 \cdot \frac{\theta}{0.5H_{th}}$	Re_θ	$\frac{r}{0.5H_{th}}$	$Re_\theta \sqrt{\frac{\theta}{r}}$	$\beta \theta Re_\theta$	$\beta (0.5H_{th})$
45			convex		< 0	< 0
50	2.477	2941	1390	3.926	0.585	0.080
70	2.384	2346	652	4.486	.728	.130
90	2.045	1788	603	3.293	.419	.115
120	1.560	1235	830	1.693	.080	.042
160	1.227	914	1317	0.882	< 0	< 0
200	1.125	821	2525	.548	< 0	< 0

b) Suction 2D-3, $\dot{m}_s/\dot{m}_o = 0.0074$, $T_{stag} = 400^\circ \text{ K}$, $T_{wall_{ad}}$

$$\frac{U^*}{\nu^*} = 26.22 \cdot 10^6/\text{m}, H^* = 1\text{m}, \text{tunnel floor and ceiling}$$

$\frac{x}{0.5H_{th}}$	$10^3 \cdot \frac{\theta}{0.5H_{th}}$	Re_θ	$\frac{r}{0.5H_{th}}$	$Re_\theta \sqrt{\frac{\theta}{r}}$	$\beta \theta Re_\theta$	$\beta (0.5H_{th})$
45			convex		< 0	< 0
50	2.260	2793	1390	3.561	0.488	0.077
70	2.171	2174	652	3.967	.590	.125
90	1.842	1627	603	2.844	.314	.105
120	1.397	1111	830	1.441	.041	.026
160	1.112	829	1317	0.762	< 0	< 0
200	1.032	753	2525	.481	< 0	< 0

TABLE 7.—EVALUATION OF $\int \beta dx - M^* = 4.6$
TWO-DIMENSIONAL JPL NOZZLE (Concluded)

c) Suction 2D-1, $\dot{m}_s/\dot{m}_o = 0.0097$, $T_{stag} = 300^\circ \text{ K}$, $T_{wall_{ad}}$

$$\frac{U^*}{\nu^*} = 26.22 \cdot 10^6/\text{m}, H^* = 1\text{m}, \text{tunnel floor and ceiling}$$

$\frac{x}{0.5H_{th}}$	$10^3 \cdot \frac{\theta}{0.5H_{th}}$	Re_θ	$\frac{r}{0.5H_{th}}$	$Re_\theta \sqrt{\frac{\theta}{r}}$	$\beta_\theta Re_\theta$	$\beta (0.5H_{th})$
45			convex		< 0	< 0
50	1.990	2391	1390	2.860	0.319	0.067
70	1.713	1686	652	2.73	.290	.100
90	1.335	1167	603	1.736	.088	.056
120	0.986	781	830	0.851	< 0	< 0
160	.850	633	1317	.509	< 0	< 0
200	.839	613	2525	.353	< 0	< 0

d) Suction 2D-2, $\dot{m}_s/\dot{m}_o = 0.0049$, $T_{stag} = 300^\circ \text{ K}$, $T_{wall_{ad}}$

$$\frac{U^*}{\nu^*} = 26.22 \cdot 10^6/\text{m}, H^* = 1\text{m}, \text{tunnel floor and ceiling}$$

$\frac{x}{0.5H_{th}}$	$10^3 \cdot \frac{\theta}{0.5H_{th}}$	Re_θ	$\frac{r}{0.5H_{th}}$	$Re_\theta \sqrt{\frac{\theta}{r}}$	$\beta_\theta Re_\theta$	$\beta (0.5H_{th})$
45			convex		< 0	< 0
50	3.043	3657	1390	5.411	1.00	0.090
70	3.377	3324	652	7.565	1.66	.148
90	3.285	2872	603	6.703	1.40	.148
120	2.856	2261	830	4.194	0.65	.101
160	2.295	1710	1317	2.257	.189	.048
200	1.951	1425	2525	1.253	.010	.004
230						< 0

TABLE 8.—SUMMARY— $M^* = 3$ AXISYMMETRIC AIR NOZZLES

$$\frac{U^*}{\nu^*} = 26.22 \cdot 10^6/\text{m}, D^* = 1\text{m}, T_{\text{wallad}}$$

Nozzle	Suction no.	$T_{\text{stag}}, ^\circ\text{K}$	\dot{m}_s/\dot{m}_0	$\int \beta dx$
$R = 3 R_{th}$	5	300	0.0049	10.95
$R = 6 R_{th}$	3	300	.0214	8.7
$R = 6 R_{th}$	4	300	.0121	8.7
$R = 6 R_{th}$	5	300	.0052	8.7
$R = 6 R_{th}$	6	300	.0034	13.28
$R = 12 R_{th}$	^a 5	300	.0058	7.06
$R = 12 R_{th}$	6	300	.0036	12.26
$R = 12 R_{th}$	7	300	.0051	9.43
$R = 12 R_{th}$	^a 8	300	.0041	10.94
$R = 12 R_{th}$	^a 9	300	.0075	3.66
$R = 12 R_{th}$	10	300	.0060	7.47

^aEffect of $U^* D^*/\nu^*$ evaluated.

TABLE 9.—SUMMARY— $M^* = 5$ AXISYMMETRIC AIR NOZZLES

$D^* = 1\text{m}$, except for the case of no suction ($R_{th} = 0.01007\text{m}$)

LARC nozzle	Suction no.	$\frac{U^*}{\nu^*}/\text{m}$	$T_{\text{stag}}, ^\circ\text{K}$	$T_{\text{wall}}, ^\circ\text{K}$	\dot{m}_s/\dot{m}_0	$\int \beta dx$
Rapid expansion	No	$6.9 \cdot 10^6$	378	Adiabatic	0	17.9
Rapid expansion	5.1	$26.22 \cdot 10^6$	300	Adiabatic	0.0103	10.05
Q-nozzle	None	$6.9 \cdot 10^6$	378	Adiabatic	0	12.4
Q-nozzle	5.1	$26.2 \cdot 10^6$	300	Adiabatic	0.0113	3.94
Q-nozzle	5.1	$104.9 \cdot 10^6$	300	Adiabatic	.0057	9.37
Q-nozzle	5.2	$26.2 \cdot 10^6$	300	Adiabatic	.0050	14.38
Q-nozzle	5.3	$26.2 \cdot 10^6$	300	Adiabatic	.0075	9.85
Q-nozzle	5.3	$26.2 \cdot 10^6$	400	Adiabatic	.0075	8.35
Q-nozzle	5.3	$26.2 \cdot 10^6$	400	300	.0075	11.90

**TABLE 10.—SUMMARY—HIGH MACH NUMBER
AXISYMMETRIC AIR NOZZLES**

$$\frac{U^*}{\nu^*} = 26.22 \cdot 10^6/\text{m}, D^* = 1\text{m}, T_{\text{wallad}}$$

Mach	Throat curvature	Suction no.	$T_{\text{stag}}, ^\circ\text{K}$	\dot{m}_s/\dot{m}_o	$\int \beta dx$
7.0	$R = 30 R_{\text{th}}$	7.1	700	0.0100	12.40
7.0	$R = 30 R_{\text{th}}$	7.2	700	.0150	5.40
9.0	$R = 200 R_{\text{th}}$	9.1	1000	.0160	3.57
9.0	$R = 200 R_{\text{th}}$	9.2	1000	.0100	11.28
7.0	$R = 75 R_{\text{th}}$	7.1	700	.0103	8.71
7.0	$R = 75 R_{\text{th}}$	7.1a	700	.0091	9.04

TABLE 11.—EFFECT OF U^*/ν^* ON $\int \beta dx$

$M^* = 3, R = 12 R_{\text{th}}, D^* = 1\text{m}, T_{\text{stag}} = 300^\circ\text{K}, T_{\text{wallad}}$
Axisymmetric air nozzle

Suction no.	$\frac{U^*}{\nu^*}/\text{m}$	\dot{m}_s/\dot{m}_o	$\int \beta dx$
5	$104.9 \cdot 10^6$	0.0029	15.71
5	$52.4 \cdot 10^6$.0041	10.94
5	$39.3 \cdot 10^6$.0047	8.82
5	$26.2 \cdot 10^6$.0058	7.06
5	$13.1 \cdot 10^6$.0082	4.40
5	$6.55 \cdot 10^6$.0116	2.37
8	$104.9 \cdot 10^6$.0020	20.92
8	$26.2 \cdot 10^6$.0041	10.94
8	$6.55 \cdot 10^6$.0081	5.01
9	$104.9 \cdot 10^6$.0038	10.41
9	$26.2 \cdot 10^6$.0075	3.66
9	$6.55 \cdot 10^6$.0151	0.74

TABLE 12. - CROSSFLOW STUDY - $M^* = 4.6$ TWO-DIMENSIONAL JPL NOZZLE SIDE WALLS

a) Suction 2D-6, 75% streamline, $T_{\text{stag}} = 400^\circ\text{K}$, $T_{\text{wall ad}}$

$$\frac{U^*}{\nu^*} = 26.22 \cdot 10^6/\text{m}, H^* = 1\text{m}$$

$\frac{x}{R_{\text{th}}}$	Re_θ	$\frac{\theta}{R_{\text{th}}}$	$\frac{\delta}{R_{\text{th}}}$	$\left(\frac{y}{\delta}\right)_{.1}$	$(w_n/U_e)_{\text{max}}$	$Re_{.1\delta w_n}$	$(y/\delta)_{w_n \text{ max}}$
-10	1285	0.000584	0.00720	0.53	0.00885	74	0.156
- 5	1083	.000371	.00389	.81	.00606	56	.206
0	888	.000259	.00264	.91	.00332	27	.243
5	838	.000242	.00252	.84	.00228	17	.254
10	790	.000251	.00280	.89	.00253	20	.285
15	744	.000272	.00328	1.02	.00338	30	.293
20	737	.000314	.00405	1.11	.00462	49	.356
30	626	.000349	.00526	1.18	.00480	53	.365
40	603	.000416	.00695	1.19	.00283	- 34	.414
50	712	.000576	.01031	0.53	-.00025	- 2	.217
60	714	.000651	.01260	1.07	-.00474	- 70	.356
70	688	.000688	.01405	1.11	-.00878	- 137	.410
80	686	.000735	.01561	1.03	-.01191	- 179	.410
90	715	.000810	.01769	1.12	-.01452	- 254	.434
100	775	.000916	.02041	1.11	-.01721	- 330	.408
120	795	.001000	.02327	1.12	-.01848	- 383	.413
140	807	.001056	.02518	1.13	-.01496	- 325	.432
160	826	.001108	.02686	1.14	-.00960	- 219	.453
180	825	.001122	.02750	1.19	-.00335	- 81	.512
200	831	.001137	.02801	0.93	.00161	31	.343
229	850	.001167	.02877	1.17	.00140	34	.534

b) Suction 2D-5, 75% streamline, $T_{\text{stag}} = 400^\circ\text{K}$, $T_{\text{wall ad}}$

$$\frac{U^*}{\nu^*} = 26.22 \cdot 10^6/\text{m}, H^* = 1\text{m}$$

$\frac{x}{R_{\text{th}}}$	Re_θ	$\frac{\theta}{R_{\text{th}}}$	$\frac{\delta}{R_{\text{th}}}$	$\left(\frac{y}{\delta}\right)_{.1}$	$(w_n/U_e)_{\text{max}}$	$Re_{.1\delta w_n}$	$(y/\delta)_{w_n \text{ max}}$
-10	1835	0.000835	0.00941	0.59	0.01545	189	0.170
- 5	1991	.000682	.00704	.86	.01601	283	.227
0	2086	.000609	.00616	1.05	.01493	331	.260
5	2039	.000589	.00608	1.15	.01391	337	.316
10	1875	.000595	.00649	1.16	.01418	336	.296
15	1658	.000607	.00705	1.16	.01580	353	.318
20	1429	.000608	.00773	1.15	.01714	358	.331
30	1020	.000569	.00843	1.20	.01442	261	.380
40	735	.000507	.00851	1.29	.00645	103	.451
50	561	.000454	.00832	1.45	.00052	8	.769
60	500	.000456	.00894	1.14	-.00281	- 31	.358
70	482	.000481	.00984	1.16	-.00482	- 55	.390
80	487	.000522	.01110	1.14	-.00638	- 75	.404
90	514	.000582	.01280	1.12	-.00783	- 99	.450
100	566	.000670	.01499	1.11	-.00957	- 135	.427
120	534	.000671	.01578	1.15	-.00883	- 128	.406
140	498	.000652	.01569	1.15	-.00574	- 79	.408
160	477	.000640	.01562	1.15	-.00290	- 39	.410
180	466	.000633	.01558	1.19	-.00060	- 8	.493
200	460	.000630	.01556	1.12	.00052	10	.411
229	458	.000629	.01555	1.23	.00021	3	.494

**TABLE 12.— CROSSFLOW STUDY— $M^* = 4.6$ TWO-DIMENSIONAL
JPL NOZZLE SIDE WALLS (Continued)**

c) Suction 2D-4, 75% streamline, $T_{stag} = 400^\circ K$, $T_{wall_{ad}}$

$$\frac{U^*}{\nu^*} = 26.22 \cdot 10^6/m, H^* = 1m$$

$\frac{x}{R_{th}}$	Re_θ	$\frac{\theta}{R_{th}}$	$\frac{\delta}{R_{th}}$	$(\frac{y}{\delta})_1$	$(w_n/U_e)_{max}$	$Re \cdot 10\delta_{wn}$	$(y/\delta)_{w_n max}$
-10	2109	0.000959	0.01047	0.61	0.01903	267	0.168
- 5	2311	.000792	.008241	.86	.01997	413	.233
0	2431	.000710	.007221	1.06	.01882	493	.266
5	2409	.000695	.007137	1.17	.01789	518	.314
10	2286	.000726	.007738	1.19	.01885	547	.331
15	2123	.000777	.008785	1.14	.02208	604	.328
20	1952	.000831	.01008	1.11	.02601	684	.349
30	1618	.000903	.01271	1.11	.02831	716	.378
40	1326	.000914	.01469	1.16	.01961	485	.436
50	1091	.000882	.01583	1.26	.00714	176	.566
60	916	.000836	.01628	0.81	-.00487	- 70	.295
70	792	.000791	.01634	1.09	-.01109	-198	.372
80	704	.000755	.01625	1.14	-.01347	-233	.394
90	641	.000726	.01612	1.17	-.01338	-223	.437
100	595	.000704	.01600	1.16	-.01213	-190	.440
120	535	.000673	.01581	1.16	-.00900	-131	.445
140	499	.000653	.01569	1.15	-.00574	- 79	.449
160	478	.000641	.01562	1.15	-.00290	- 39	.451
180	467	.000634	.01558	1.16	-.00060	- 8	.452
200	461	.000631	.01556	1.13	.00081	10	.411
229							

d) Suction 2D-1, 75% streamline, $T_{stag} = 400^\circ K$, $T_{wall_{ad}}$

$$\frac{U^*}{\nu^*} = 26.22 \cdot 10^6/m, H^* = 1m$$

$\frac{x}{R_{th}}$	Re_θ	$\frac{\theta}{R_{th}}$	$\frac{\delta}{R_{th}}$	$(\frac{y}{\delta})_1$	$(w_n/U_e)_{max}$	$Re \cdot 10\delta_{wn}$	$(y/\delta)_{w_n max}$
-10	2422	0.00110	0.01156	0.63	0.02300	368	0.180
- 5	2624	.000899	.009377	.86	.02404	566	.222
0	2653	.000775	.008066	1.07	.02210	653	.278
5	2570	.000742	.007739	1.20	.02042	646	.310
10	2435	.000773	.008264	1.20	.02114	660	.329
15	2280	.000835	.009381	1.18	.02466	745	.341
20	2127	.000906	.010859	1.13	.02932	844	.354
30	1839	.001026	.014147	1.10	.03364	938	.362
40	1580	.001089	.017041	1.13	.02566	716	.451
50	1357	.001098	.019167	1.16	.01165	320	.534
60	1178	.001074	.020466	0.63	-.00516	- 73	.250
70	1039	.001038	.021114	1.25	-.01508	-399	.364
80	933	.001000	.021372	1.10	-.02062	-452	.389
90	853	.000966	.021413	1.14	-.02227	-480	.418
100	794	.000939	.021362	1.15	-.02138	-443	.419
120	715	.000899	.021185	1.16	-.01676	-327	.423
140	668	.000873	.021036	1.17	-.01098	-207	.426
160	640	.000858	.020937	1.18	-.00573	-105	.459
180	624	.000849	.020879	1.20	-.00147	- 26	.490
200	617	.000845	.020849	1.06	.00126	20	.399
229	614	.000843	.020835	1.19	.00056	10	.522

TABLE 12. —CROSSFLOW STUDY— $M^* = 4.6$ TWO-DIMENSIONAL
JPL NOZZLE SIDE WALLS (Continued)

e) Suction 2D-6, 50% streamline, $T_{\text{stag}} = 400^\circ\text{K}$, $T_{\text{wall ad}}$

$$\frac{U^*}{\nu^*} = 26.22 \cdot 10^6/\text{m}, H^* = 1\text{m}$$

$\frac{x}{R_{\text{th}}}$	$Re\theta$	$\frac{\theta}{R_{\text{th}}}$	$\frac{\delta}{R_{\text{th}}}$	$\left(\frac{y}{\delta}\right)_{.1}$	$(w_n/U_e)_{\text{max}}$	$Re \cdot 1\delta w_n$	$(y/\delta)_{w_n \text{ max}}$
80	686	0.000735	0.01561	1.12	—0.00726	—118	0.41
100	775	.000916	.02041	1.10	— .01220	—232	.41
120	795	.001000	.02327	1.10	— .01409	—287	.41
140	807	.001056	.02518	1.12	— .01124	—242	.43
160	826	.001108	.02686	1.16	— .00566	—131	.48
180	825	.001122	.02750	0.75	.00122	19	.28

f) Suction 2D-7, 75% streamline, $T_{\text{stag}} = 400^\circ\text{K}$, $T_{\text{wall ad}}$

$$\frac{U^*}{\nu^*} = 26.22 \cdot 10^6/\text{m}, H^* = 1\text{m}$$

$\frac{x}{R_{\text{th}}}$	$Re\theta$	$\frac{\theta}{R_{\text{th}}}$	$\frac{\delta}{R_{\text{th}}}$	$\left(\frac{y}{\delta}\right)_{.1}$	$(w_n/U_e)_{\text{max}}$	$Re \cdot 1\delta w_n$	$(y/\delta)_{w_n \text{ max}}$
—10	1285	0.000584	0.00720	0.53	0.00885	74	0.156
— 5	1083	.000371	.00389	.81	.00606	56	.206
0	888	.000259	.00264	.91	.00332	27	.243
5	814	.000235	.00245	.85	.00218	16	.261
10	731	.000232	.00261	.90	.00219	16	.275
15	667	.000244	.00296	1.04	.00279	23	.324
20	637	.000271	.00351	1.15	.00361	34	.319
30	519	.000290	.00436	1.19	.00333	31	.367
40	486	.000335	.00562	1.19	.00179	17	.399
50	552	.000446	.00807	0.79	— .00029	— 2	.278
60	526	.000479	.00938	1.13	— .00299	— 35	.409
70	499	.000498	.01026	1.13	— .00503	— 58	.374
80	494	.000530	.01132	1.13	— .00649	— 77	.396
90	510	.000577	.01269	1.14	— .00771	— 99	.403
100	544	.000644	.01445	1.12	— .00894	—122	.399
120	537	.000676	.01583	1.13	— .00871	—124	.404
140	544	.000711	.01704	1.14	— .00662	— 98	.451
160	553	.000742	.01807	1.14	— .00392	— 60	.425
180	550	.000748	.01837	1.18	— .00095	— 15	.488
200							
229							

**TABLE 12.—CROSSFLOW STUDY— $M^* = 4.6$ TWO-DIMENSIONAL
JPL NOZZLE SIDE WALLS (Continued)**

g) Suction 2D-9, 50% streamline, $T_{stag} = 400^\circ K$, $T_{wall_{ad}}$

$$\frac{U^*}{\nu^*} = 26.22 \cdot 10^6/m, H^* = 1m$$

$\frac{x}{R_{th}}$	Re_θ	$\frac{\theta}{R_{th}}$	$\frac{\delta}{R_{th}}$	$\left(\frac{y}{\delta}\right)_{.1}$	$(w_n/U_e)_{max}$	$Re_{.1\delta w_n}$	$(y/\delta)_{w_n max}$
-10	1945	0.000885	0.01002	0.68	0.01254	188	0.160
- 5	1817	.000623	.00689	1.00	.01187	239	.209
0	1584	.000463	.00496	1.25	.00952	202	.257
5	1386	.000400	.00423	1.43	.00738	155	.303
10	1188	.000377	.00420	1.35	.00635	113	.343
15	1043	.000382	.00459	1.22	.00615	94	.349
20	956	.000407	.00526	1.16	.00634	91	.365
30	783	.000437	.00651	1.17	.00499	68	.393
40	713	.000491	.00811	1.22	.00221	32	.394
50	763	.000617	.01104	0.63	-.00029	- 3	.232
60	756	.000689	.01331	1.08	-.00295	- 47	.385
70	744	.000743	.01513	1.10	-.00570	- 95	.381
80	765	.000820	.01733	1.11	-.00858	-154	.369
90	767	.000869	.01901	1.10	-.01117	-206	.404
100	767	.000906	.02038	1.13	-.01274	-248	.440
120	801	.001007	.02343	1.12	-.01412	-295	.437
140	832	.001089	.02596	1.13	-.01182	-265	.444
160	878	.001178	.02845	1.15	-.00625	-152	.450
180	934	.001271	.03092	0.70	.00130	21	.290
200	983	.001347	.03292	1.06	.00727	185	.389
229	1080	.001482	.03624	1.14	.00469	141	.495

h) Suction 2D-10, 25% streamline, $T_{stag} = 400^\circ K$, $T_{wall_{ad}}$

$$\frac{U^*}{\nu^*} = 26.22 \cdot 10^6/m, H^* = 1m$$

$\frac{x}{R_{th}}$	Re_θ	$\frac{\theta}{R_{th}}$	$\frac{\delta}{R_{th}}$	$\left(\frac{y}{\delta}\right)_{.1}$	$(w_n/U_e)_{max}$	$Re_{.1\delta w_n}$	$(y/\delta)_{w_n max}$
-10	2095	0.000953	0.01053	0.58	0.00865	116	0.167
- 5	2074	.000711	.00775	.86	.00936	182	.207
0	1927	.000563	.00601	1.14	.00826	194	.266
5	1751	.000505	.00537	1.30	.00654	158	.298
10	1552	.000493	.00545	1.30	.00511	114	.352
15	1388	.000508	.00601	1.28	.00419	88	.373
20	1282	.000546	.00689	1.26	.00370	75	.372
30	1087	.000607	.00890	1.15	.00325	60	.360
40	999	.000688	.01127	1.13	.00300	55	.398
50	1046	.000847	.01496	1.15	.00190	40	.428
60	1059	.000966	.01831	0.76	-.00110	- 17	.280
70	1054	.001053	.02110	1.03	-.00467	-102	.364
80	1082	.001160	.02417	1.06	-.00812	-194	.371
90	1096	.001241	.02675	1.08	-.01086	-277	.383
100	1102	.001302	.02888	1.08	-.01239	-327	.399
120	1142	.001436	.03306	1.10	-.01282	-371	.465
140	1195	.001563	.03685	1.11	-.01092	-342	.417
160	1268	.001700	.04063	1.13	-.00777	-266	.473
180	1362	.001851	.04451	1.15	-.00401	-151	.518
200	1443	.001976	.04774	0.42	.00044	6	.188
229	1583	.002173	.05253	.98	.00138	52	.463

**TABLE 12.—CROSSFLOW STUDY— $M^* = 4.6$ TWO-DIMENSIONAL
JPL NOZZLE SIDE WALLS (Continued)**

i) Suction 2D-8, 75% streamline, $T_{\text{stag}} = 400^\circ\text{K}$, $T_{\text{wall ad}}$

$$\frac{U^*}{\nu^*} = 26.22 \cdot 10^6/\text{m}, H^* = 1\text{m}$$

$\frac{x}{R_{\text{th}}}$	$Re\theta$	$\frac{\theta}{R_{\text{th}}}$	$\frac{\delta}{R_{\text{th}}}$	$\left(\frac{y}{\delta}\right)_{.1}$	$(w_n/U_e)_{\text{max}}$	$Re \cdot 1\delta w_n$	$(y/\delta)_{w_n \text{ max}}$
-10	1805	0.000821	0.00954	0.58	0.01607	195	0.168
-5	1592	.000546	.00614	.88	.01303	205	.208
0	1311	.000383	.00408	1.19	.00881	146	.274
5	1121	.000324	.00340	1.25	.00574	84	.329
10	943	.000299	.00335	1.14	.00452	54	.334
15	823	.000301	.00362	1.06	.00446	47	.310
20	754	.000321	.00416	1.07	.00499	52	.346
30	607	.000339	.00512	1.12	.00449	46	.375
40	552	.000381	.00633	1.18	.00239	26	.404
50	598	.000484	.00867	0.68	-.00027	-2	.258
60	581	.000530	.01033	1.11	-.00355	-45	.372
70	571	.00570	.01168	1.12	-.00644	-84	.384
80	590	.000633	.01343	1.11	-.00894	-124	.429
90	587	.000665	.01463	1.13	-.01045	-152	.394
100	585	.000692	.01562	1.14	-.01090	-164	.410
120	613	.000771	.01800	1.14	-.01098	-179	.427
140	635	.000830	.01986	1.15	-.00900	-157	.451
160	672	.000902	.02186	1.14	-.00578	-107	.469
180	720	.000979	.02391	1.18	-.00193	-40	.482
200	759	.001039	.02550	1.04	.00162	31	.351
229	835	.001146	.02815	1.15	.00126	30	.500

j) Suction 2D-9, 25% streamline, $T_{\text{stag}} = 400^\circ\text{K}$, $T_{\text{wall ad}}$

$$\frac{U^*}{\nu^*} = 26.22 \cdot 10^6/\text{m}, H^* = 1\text{m}$$

$\frac{x}{R_{\text{th}}}$	$Re\theta$	$\frac{\theta}{R_{\text{th}}}$	$\frac{\delta}{R_{\text{th}}}$	$\left(\frac{y}{\delta}\right)_{.1}$	$(w_n/U_e)_{\text{max}}$	$Re \cdot 1\delta w_n$	$(y/\delta)_{w_n \text{ max}}$
-10	1945	0.000885	0.01002	0.57	0.00786	99	0.160
-5	1817	.000623	.00689	.87	.00794	139	.209
0	1584	.000463	.00498	1.16	.00639	126	.257
5	1386	.000400	.00423	1.30	.00451	86	.303
10	1188	.000377	.00420	1.32	.00314	55	.343
15	1043	.000382	.00459	1.22	.00234	36	.349
20	956	.000407	.00526	1.13	.00197	28	.365
30	783	.000437	.00651	1.12	.00166	22	.344
40	713	.000491	.00811	1.14	.00153	21	.394
50	763	.000617	.01104	1.18	.00087	14	.464
60	756	.000689	.01331	0.97	-.00091	-13	.337
70	744	.000743	.01513	1.09	-.00295	-49	.381
80	765	.000820	.01733	1.10	-.00477	-85	.369
90	767	.000869	.01901	1.10	-.00609	-112	.404
100	767	.000906	.02038	1.12	-.00662	-128	.440
120	801	.001007	.02343	1.12	-.00651	-136	.437
140	832	.001089	.02596	1.13	-.00519	-116	.444
160	878	.001178	.02845	1.14	-.00334	-81	.450
180	934	.001271	.03092	1.19	-.00126	-34	.497
200	983	.001347	.03292	0.90	.00078	17	.350
230	1080	.001482	.03624	1.13	.00086	27	.495

**TABLE 12.—CROSSFLOW STUDY— $M^* = 4.6$ TWO-DIMENSIONAL
JPL NOZZLE SIDE WALLS (Concluded)**

k) Suction 2D-11, 50% streamline, $T_{stag} = 400^\circ K$, $T_{wall_{ad}}$

$$\frac{U^*}{\nu^*} = 26.22 \cdot 10^6/m, H^* = 1m$$

$\frac{x}{R_{th}}$	Re_θ	$\frac{\theta}{R_{th}}$	$\frac{\delta}{R_{th}}$	$\left(\frac{y}{\delta}\right)_{.1}$	$(w_n/U_e)_{max}$	$Re_{.1\delta} w_n$	$(y/\delta)_{w_n max}$
-10	1860	0.000846	0.00972	0.66	0.01191	168	0.165
-5	1678	.000575	.00645	.99	.01076	201	.223
0	1413	.000413	.00444	1.30	.00812	160	.253
5	1217	.000351	.00370	1.45	.00590	110	.303
10	1030	.000327	.00365	1.34	.00483	74	.307
15	900	.000329	.00397	1.21	.00458	60	.323
20	824	.000351	.00457	1.13	.00471	57	.350
30	667	.000372	.00558	1.15	.00354	41	.401
40	606	.000418	.00689	1.23	.00148	18	.418
50	655	.000530	.00949	0.82	-.00033	3	.303
60	641	.000584	.01134	1.11	-.00234	-32	.395
70	629	.000628	.01287	1.12	-.00434	-63	.398
80	649	.000696	.01475	1.12	-.00650	-100	.391
90	648	.000733	.01610	1.12	-.00829	-132	.398
100	645	.000763	.01719	1.12	-.00930	-151	.447
120	674	.000847	.01976	1.11	-.01010	-176	.454
140	698	.000913	.02184	1.13	-.00820	-155	.410
160	738	.000989	.02396	1.16	-.00403	-84	.481
180	789	.001073	.02619	0.88	.00141	24	.342
200	832	.001140	.02795	1.07	.00570	124	.412
229	912	.001252	.03070	1.16	.00304	79	.500

TABLE 13.—SUMMARY— $M^* = 4.6$ TWO-DIMENSIONAL JPL AIR NOZZLE

$$\frac{U^*}{\nu^*} = 26.22 \cdot 10^6/\text{m}, H^* = 1\text{m}, T_{\text{wall ad}}$$

Floor and ceiling walls				
Suction no.	$T_{\text{stag}}, ^\circ\text{K}$	\dot{m}_s/\dot{m}_o	$\int \beta dx$	
2D-1	300	0.0097	4.26	
2D-2	300	.0049	13.48	
2D-3	300	.0074	7.90	
2D-3	400	.0074	7.12	
Side walls				
Streamline,%	Suction no.	$T_{\text{stag}}, ^\circ\text{K}$	$(\text{Re}_{0.1\delta})_{\text{max}}$	$(\text{Re}_{0.1\delta})_{\text{max}}$
75	2D-1	400	940	-480
75	2D-4	400	720	-230
75	2D-5	400	360	-140
75	2D-6	400	80	-390
75	2D-7	400	80	-125
75	^a 2D-8	400	200	-180
50	2D-9	400	240	-300
50	^a 2D-11	400	200	-175
25	2D-10	400	200	-370
25	^a 2D-9	400	140	-140

^aRecommended configuration

**TABLE 14.—CRITICAL HEIGHT OF ISOLATED THREE-DIMENSIONAL
SURFACE ROUGHNESS PARTICLES**

- a) $\frac{U^*}{\nu^*} = 26.22 \cdot 10^6/\text{m}$, $D^* = 1\text{m}$, $Re_{k_{\text{crit}}} = 200$, $T_{\text{wall}_{\text{ad}}}$, axisymmetric air nozzle
 $M^* = 3.009$, $R = 12 R_{\text{th}}$, $T_{\text{stag}} = 300^\circ \text{K}$

Suction 5, $R_{\text{th}} = 0.2440\text{m}$

$\frac{x}{R_{\text{th}}}$	M	$y_{\text{crit}}, \text{mm}$	$\frac{U}{\nu_k} \cdot 10^{-6}/\text{m}$
0	1.000	0.0187	39.52
1	1.381	.0260	31.81
2	1.799	.0351	21.04
4	2.347	.058	10.57
11.68	3.009	.094	4.94

- b) $\frac{U^*}{\nu^*} = 26.22 \cdot 10^6/\text{m}$, $D^* = 1\text{m}$, $Re_{k_{\text{crit}}} = 200$, $T_{\text{wall}_{\text{ad}}}$, axisymmetric air nozzle

$M^* = 5.115$, Q-nozzle, $T_{\text{stag}} = 400^\circ \text{K}$

Suction 5.3, $R_{\text{th}} = 0.09538\text{m}$

$\frac{x}{R_{\text{th}}}$	M	$y_{\text{crit}}, \text{mm}$	$\frac{U}{\nu_k} \cdot 10^{-6}/\text{m}$
0	1.000	0.0100	115.4
2	1.364	.0110	90.4
4	1.905	.0166	57.2
6	2.400	.0273	30.7
8	2.833	.061	11.4
20	4.349	.191	2.44
40	5.0565	.334	1.23

TABLE 14.—CRITICAL HEIGHT OF ISOLATED THREE-DIMENSIONAL
SURFACE ROUGHNESS PARTICLES (Concluded)

c) $\frac{U^*}{\nu^*} = 26.22 \cdot 10^6/\text{m}$, $D^* = 1\text{m}$, $Re_{k_{\text{crit}}} = 200$, $T_{\text{wall}_{\text{ad}}}$, axisymmetric helium nozzle

$M^* = 8.93$, $R = 250 R_{\text{th}}$, $T_{\text{stag}} = 300^\circ \text{K}$

Suction 9.4 He, $R_{\text{th}} = 0.0711\text{m}$

$\frac{x}{R_{\text{th}}}$	M	$y_{\text{crit}}, \text{mm}$	$\frac{U}{\nu_k} \cdot 10^{-6}/\text{m}$
-2	0.528	0.0085	103.5
0	1.000	.0104	114.5
10	1.904	.0213	52.3
20	3.131	.0625	13.23
30	4.661	.194	2.94
40	5.816	.464	1.108
60	7.176	.910	0.431
80	8.046	1.31	.279
122.12	8.93	1.87	.170

d) $\frac{U^*}{\nu^*} = 26.22 \cdot 10^6/\text{m}$, $D^* = 1\text{m}$, $Re_{k_{\text{crit}}} = 200$, $T_{\text{wall}_{\text{ad}}}$, axisymmetric air nozzle

$M^* = 9.066$, $R = 200 R_{\text{th}}$, $T_{\text{stag}} = 1000^\circ \text{K}$

Suction 9.2, $R_{\text{th}} = 0.0272\text{m}$

$\frac{x}{R_{\text{th}}}$	M	$y_{\text{crit}}, \text{mm}$	$\frac{U}{\nu_k} \cdot 10^{-6}/\text{m}$
0	1.000	0.00207	706
10	1.912	.00414	336.1
20	2.965	.01292	78.5
30	4.066	.0362	21.13
40	5.1185	.0935	6.39
60	6.201	.231	2.081
80	6.885	.377	1.179
140	8.100	.807	0.441
265.09	9.066	1.20	.271

TABLE 15.—RATIO $\Delta v_{\perp \max}/v_{\perp \max} = f(\lambda/h)$ FOR LINE AND POINT SINKS

Maximum variation $\Delta v_{\perp \max}$ of the disturbance velocity v_{\perp} in the direction normal to a plane wall, induced by line and point sinks (-e) located on this wall, at the distance h from the wall for different sink spacings λ .

Sinks	λ/h			
	0.5	1	1.5	2
	$\Delta v_{\perp \max}/v_{\perp \max}$			
Line sinks ($n_{\text{sinks}} = \pm\infty$)	0.0001	0.0076	0.0607	0.159
1 row of point sinks ($n_{\text{sinks}} = \pm 20$)	0.0001	0.0245	0.1554	0.349

TABLE 16.—SONIC BOUNDARY LAYER THICKNESS δ_s

a) $M^* = 3$ axisymmetric air nozzle, $R = 12 R_{th}$

$$\frac{U^*}{\nu^*} = 26.22 \cdot 10^6/\text{m}, D^* = 1\text{m}, T_{\text{stag}} = 300^\circ\text{K}, T_{\text{wall ad}}$$

$\frac{x}{R_{th}}$	M	Suct. no. 8 ($\frac{\dot{m}_s}{\dot{m}_0} = 0.0041$)		Suct. no. 5 ($\frac{\dot{m}_s}{\dot{m}_0} = 0.0058$)		Suct. no. 9 ($\frac{\dot{m}_s}{\dot{m}_0} = 0.0075$)	
		$\frac{\delta_s}{R_{th}}$	δ_s, mm	$\frac{\delta_s}{R_{th}}$	δ_s, mm	$\frac{\delta_s}{R_{th}}$	δ_s, mm
1.0	1.381	0.00057	0.139	0.00055	0.134	0.00048	0.117
2.0	1.799	.00052	.127	.00046	.112	.00041	.100
4.0	2.3475	.00061	.149	.00048	.117	.00039	.095
6.0	2.6255	.00064	.156	.00048	.117	.00037	.090
8.0	2.823	.00065	.159	.00047	.115	.00036	.088
10.0	2.953	.00066	.161	.00046	.112	.00036	.088
11.68	3.009	.00066	.161	.00046	.112	.00035	.086

b) $M^* = 5$ axisymmetric Q-nozzle, suction 5.3

$$\frac{U^*}{\nu^*} = 26.22 \cdot 10^6/\text{m}, D^* = 1\text{m}, T_{\text{stag}} = 400^\circ\text{K}, T_{\text{wall ad}}$$

$\frac{x}{R_{th}}$	$\frac{\delta_s}{R_{th}}$	δ_s, mm	M
2.0	0.00077	0.073	1.3644
4.0	.00066	.063	1.9050
6.0	.00080	.076	2.4002
8.0	.00099	.094	2.8332
10.0	.00122	.116	3.2001
15.0	.00173	.165	3.8998
20.0	.00223	.213	4.3491
25.0	.00250	.238	4.6443
30.0	.00272	.259	4.8426
40.0	.00304	.290	5.0445
49.2	.00316	.301	5.1150

TABLE 17.—ISOTHERMAL COMPRESSION OF SUCTION MEDIUM

a) $M^* = 5.115$ axisymmetric LARC Q-nozzle (air), $T_{\text{stag}} = 400^\circ\text{K}$, $T_{\text{wall ad}}$, suction 5.3
 $\frac{U^*}{\nu^*} = 26.22 \cdot 10^6/\text{m}$, $D^* = 1\text{m}$, $\frac{\dot{m}_s}{\dot{m}_o} = 0.0075$, $\int \beta dx = 8.35$ (TG vortex growth factor).

Isothermal compression work $L_{\text{suct isoth}}$ to p_{stag} of suction air at $T = 400^\circ\text{K}$

with 100% efficiency: $\frac{L_{\text{suct isoth}}}{KE_{\text{test section}}} = 0.01259$

$\frac{x}{R_{\text{th}}}$	$\frac{p}{p^*}$	$\frac{d\left(\frac{\dot{m}_s}{\dot{m}_o}\right)}{d\left(\frac{x}{R_{\text{th}}}\right)}$	$\ln\left(\frac{p_{\text{stag}}}{p}\right) \cdot \frac{d\left(\frac{\dot{m}_s}{\dot{m}_o}\right)}{d\left(\frac{x}{R_{\text{th}}}\right)}$	M
-7	602.86	0	0	
-5	594.67	0.000062	$1.00 \cdot 10^{-6}$	0.1536
-2.5	530.85	.000091	$1.18 \cdot 10^{-5}$.4355
0	317.60	.000109	$7.01 \cdot 10^{-5}$	1.000
2.5	166.75	.000121	$1.558 \cdot 10^{-4}$	1.491
5	60.18	.000130	$3.000 \cdot 10^{-4}$	2.160
10	12.224	.000142	$5.539 \cdot 10^{-4}$	3.200
15	4.554	.000149	$7.283 \cdot 10^{-4}$	3.900
20	2.526	.000150	$8.216 \cdot 10^{-4}$	4.349
25	1.747	.000150	$8.769 \cdot 10^{-4}$	4.644
30	1.375	.000150	$9.129 \cdot 10^{-4}$	4.843
35	1.178	.000150	$9.361 \cdot 10^{-4}$	4.973
40	1.0698	.000150	$9.505 \cdot 10^{-4}$	5.056
45	1.016	.000150	$9.582 \cdot 10^{-4}$	
49.19	1.000	.000150	$9.606 \cdot 10^{-4}$	5.115
$-\infty$	604.38 (stag pressure)			

TABLE 17.—ISOTHERMAL COMPRESSION OF SUCTION MEDIUM (Continued)

b) $M^* = 8.93$ axisymmetric helium nozzle, $T_{stag} = 300^\circ K$, $T_{wall_{ad}}$, suction 9.4 He, $R = 250R_{th}$

$$\frac{U^*}{\nu^*} = 26.22 \cdot 10^6 / m, D^* = 1m, \frac{\dot{m}_s}{\dot{m}_o} = 0.00625, \int \beta dx = 5.1 \text{ (TG vortex growth factor).}$$

Isothermal compression work $L_{suct_{isoth}}$ to p_{stag} of suction helium at $T = 300^\circ K$

$$\text{with 100\% efficiency: } \frac{L_{suct_{isoth}}}{KE_{test \text{ section}}} = 0.0163$$

$\frac{x}{R_{th}}$	M	$\frac{p}{p^*}$	$\frac{d\left(\frac{\dot{m}_s}{\dot{m}_o}\right)}{d\left(\frac{x}{R_{th}}\right)}$	$\ln\left(\frac{p_{stag}}{p_i}\right) \cdot \frac{d\left(\frac{\dot{m}_s}{\dot{m}_o}\right)}{d\left(\frac{x}{R_{th}}\right)}$
-7	0.012	4099.6	0	0
-3.5	.289	3828.8	0.00003125	$2.14 \cdot 10^{-6}$
-2	.528	3286.6	.000050625	$1.119 \cdot 10^{-5}$
0	1.000	1998.3	.000050625	$3.64 \cdot 10^{-5}$
5	1.414	1145.6	.000050625	$6.45 \cdot 10^{-5}$
10	1.904	566.96	.000050625	$1.002 \cdot 10^{-4}$
20	3.131	108.67	.000050625	$1.838 \cdot 10^{-4}$
30	4.661	20.81	.000050625	$2.675 \cdot 10^{-4}$
40	5.816	7.651	.000050625	$3.181 \cdot 10^{-4}$
60	7.176	2.8576	.000050625	$3.68 \cdot 10^{-4}$
90	8.361	1.3747	.000050625	$4.05 \cdot 10^{-4}$
122.19	8.93	1.000	.000050625	$4.211 \cdot 10^{-4}$

c) $M^* = 9$ axisymmetric NASA helium nozzle, $T_{stag} = 300^\circ K$, $T_{wall_{ad}}$, suction 9.6 He, $D^* = 1m$

$$\frac{U^*}{\nu^*} = 26.22 \cdot 10^6 / m, \frac{\dot{m}_s}{\dot{m}_o} = 0.0060, \int \beta dx = 5.7 \text{ (TG vortices), } Re_{Lequ} = 3.145 \cdot 10^8.$$

Isothermal compression work $L_{suct_{isoth}}$ to p_{stag} of suction helium at $T = 300^\circ K$

$$\text{with 100\% efficiency: } \frac{L_{suct_{isoth}}}{KE_{test \text{ section}}} = 0.0159$$

$\frac{x}{R_{th}}$	M	$\frac{p}{p^*}$	$\frac{d\left(\frac{\dot{m}_s}{\dot{m}_o}\right)}{d\left(\frac{x}{R_{th}}\right)}$	$\ln\left(\frac{p_{stag}}{p_i}\right) \cdot \frac{d\left(\frac{\dot{m}_s}{\dot{m}_o}\right)}{d\left(\frac{x}{R_{th}}\right)}$
-7	0.012	4257.8	0	0
-3.5	.289	3980	0.0000315	$2.15 \cdot 10^{-6}$
-2	.528	3413.2	.0000389	$8.60 \cdot 10^{-6}$
0	1.000	2052.6	.0000510	$3.72 \cdot 10^{-5}$
1.604	1.649	850.53	.0000552	$8.89 \cdot 10^{-5}$
5.036	2.823	166.36	.0000770	$2.497 \cdot 10^{-4}$
10.541	4.271	31.67	.0001029	$5.043 \cdot 10^{-4}$
20.56	5.723	8.561	.0000966	$5.998 \cdot 10^{-4}$
35.04	6.943	3.4694	.0000657	$4.671 \cdot 10^{-4}$
52.38	7.873	1.9065	.0000448	$3.455 \cdot 10^{-4}$
75.04	8.622	1.2306	.0000392	$3.194 \cdot 10^{-4}$
98.67	8.999	1.0000	.0000357	$2.983 \cdot 10^{-4}$

TABLE 17.—ISOTHERMAL COMPRESSION OF SUCTION MEDIUM (Concluded)

d) $M^* = 9$ axisymmetric NASA helium nozzle, $T_{stag} = 300^\circ\text{K}$, $T_{wall_{ad}}$, suction 9.6 He, $\frac{U^*}{v^*} = 26.22 \cdot 10^6/\text{m}$, $D^* = 1\text{m}$, $\frac{\dot{m}_s}{\dot{m}_o} = 0.0060$

Isothermal compression at 100% efficiency of the suction helium at $T = T_{stag} = 300^\circ\text{K}$ from p to p' :

$\frac{x}{R_{th}}$	$= 0.0391 \cdot P_{stag}$		$= 0.1998 \cdot P_{stag}$		$= 0.482 \cdot P_{stag}$		$= P_{stag}$
	$\frac{p'}{p}$	$\ln\left(\frac{p'}{p}\right) \cdot \frac{d\left(\frac{\dot{m}_s}{\dot{m}_o}\right)}{d\left(\frac{x}{R_{th}}\right)}$	$\frac{p'}{p}$	$\ln\left(\frac{p'}{p}\right) \cdot \frac{d\left(\frac{\dot{m}_s}{\dot{m}_o}\right)}{d\left(\frac{x}{R_{th}}\right)}$	$\frac{p'}{p}$	$\ln\left(\frac{p'}{p}\right) \cdot \frac{d\left(\frac{\dot{m}_s}{\dot{m}_o}\right)}{d\left(\frac{x}{R_{th}}\right)}$	
-3.5							
-2							
0							
1.604							
5.036	1.000	0	1.000	0	1.000	0	
10.541	5.253	$1.707 \cdot 10^{-4}$	5.1126	$1.256 \cdot 10^{-4}$	2.4134	$4.863 \cdot 10^{-5}$	
20.56	19.432	$2.866 \cdot 10^{-4}$	26.86	$3.386 \cdot 10^{-4}$	12.34	$1.935 \cdot 10^{-4}$	
35.04	47.95	$2.542 \cdot 10^{-4}$	99.35	$4.442 \cdot 10^{-4}$	64.81	$4.292 \cdot 10^{-4}$	
52.38	87.26	$2.002 \cdot 10^{-4}$	245.15	$3.614 \cdot 10^{-4}$	239.8	$5.293 \cdot 10^{-4}$	
75.04	135.19	$1.923 \cdot 10^{-4}$	446.1	$2.733 \cdot 10^{-4}$	591.6	$4.192 \cdot 10^{-4}$	
98.67	166.36	$1.826 \cdot 10^{-4}$	691.15	$2.563 \cdot 10^{-4}$	1076.6	$3.128 \cdot 10^{-4}$	
			850.5	$2.408 \cdot 10^{-4}$	1668.0	$2.908 \cdot 10^{-4}$	
					2052.6	$2.723 \cdot 10^{-4}$	
$\frac{L_{suct, isoth}}{KE_{test section}} =$	0.0082		0.0120		0.0141		0.0159

TABLE B-1.—COORDINATES OF LONGITUDINAL SLOT RODS

Slot a $a/b = 2, g/2b = 0.1$		Slot b $a/b = 2, g/2b = 0.1$		Slot c $a/b = 2, g/2b = 0.1$		Slot d $a/b = 1.5, g/2b = 0.1$		Slot e $a/b = 2.15, g/2b = 0.1$	
x/b	y/b	x/b	y/b	x/b	y/b	x/b	y/b	x/b	y/b
2.0	0	2.0	0	2.0	0	1.5	0	2.15	0
1.998	0.044	1.998	0.025	1.998	0.025	1.4985	0.040	2.14	0.070
1.995	.070	1.995	.040	1.995	.042	1.4963	.0625	2.13	.100
1.99	.099	1.99	.060	1.99	.065	1.4925	.088	2.1	.180
1.98	.141	1.98	.107	1.98	.125	1.485	.127	2.05	.292
1.95	.230	1.95	.202	1.95	.254	1.4625	.204	2.0	.380
1.9	.350	1.9	.330	1.9	.395	1.425	.312	1.9	.517
1.8	.503	1.8	.518	1.8	.585	1.35	.456	1.8	.619
1.7	.605	1.7	.643	1.7	.686	1.275	.566	1.7	.695
1.6	.683	1.6	.725	1.6	.750	1.2	.639	1.6	.755
1.4	.785	1.4	.826	1.4	.837	1.05	.750	1.4	.837
1.2	.855	1.2	.882	1.2	.886	0.9	.827	1.2	.886
1.0	.905	1.0	.920	1.0	.921	.75	.882	1.0	.921
0.8	.938	0.8	.946	0.8	.946	.6	.917	0.8	.946
.6	.961	.6	.964	.6	.964	.45	.947	.6	.964
.4	.978	.4	.978	.4	.978	.3	.971	.4	.978
.2	.991	.2	.990	.2	.990	.15	.987	.2	.990
0	1.000	0	1.000	0	1.000	0	1.000	0	1.000

TABLE D-1.—ASYMPTOTIC SUCTION PROFILES (ADIABATIC WALL)

Air						Helium					
Mach 2			Mach 3			Mach 5			Mach 9		
y/δ	u/U_e	y/δ	y/δ	u/U_e	y/δ	y/δ	u/U_e	y/δ	y/δ	u/U_e	u/U_e
0	0	0	0	0	0	0	0	0	0	0	0
0.0239	0.0822	0.0242	0.0329	0.0717	0.0329	0.0229	0.0796	0.0229	0.0296	0.0586	0.0895
.0478	.1579	.0484	.0658	.1385	.0658	.0458	.1532	.0458	.0591	.1140	.1344
.0716	.2277	.0726	.0988	.2008	.0988	.0686	.2216	.0686	.0887	.1664	.1953
.0955	.2922	.0968	.1317	.2591	.1317	.0915	.2853	.0915	.1182	.2160	.2525
.1194	.3518	.1210	.1646	.3138	.1646	.1144	.3447	.1144	.1478	.2631	.3063
.1443	.4070	.1452	.1975	.3650	.1975	.1373	.4003	.1373	.1774	.3078	.3570
.1671	.4580	.1694	.2304	.4130	.2304	.1602	.4523	.1602	.2069	.3504	.4049
.1910	.5052	.1936	.2634	.4580	.2634	.1830	.5009	.1830	.2365	.3908	.4502
.2149	.5488	.2178	.2963	.5003	.2963	.2059	.5465	.2059	.2661	.4294	.4929
.2388	.5891	.2420	.3292	.5400	.3292	.2288	.5891	.2288	.2956	.4661	.5333
.2665	.6607	.2904	.3950	.6120	.3950	.2745	.6662	.2745	.3547	.5343	.6074
.3343	.7214	.3388	.4609	.6751	.4609	.3203	.7334	.3203	.4139	.5961	.6735
.3820	.7726	.3872	.5267	.7302	.5267	.3661	.7914	.3661	.4730	.6521	.7320
.4298	.8156	.4356	.5925	.7780	.5925	.4118	.8410	.4118	.5321	.7025	.7837
.4775	.8514	.4840	.6584	.8191	.6584	.4576	.8826	.4576	.5912	.7479	.8288
.5731	.9052	.5808	.7901	.8837	.7901	.5491	.9439	.5491	.7095	.8245	.9011
.6686	.9408	.6776	.9217	.9286	.9217	.6406	.9791	.6406	.8277	.8840	.9512
.7641	.9638	.7744	.9876	.9582	.9876	.7321	.9886	.7321	.9460	.9283	.9817
.8596	.9782	.8712	1.0534	.9767	1.0534	.8236	.9943	.8236	1.0051	.9593	.9906
.9551	.9871	.9680	1.1192	.9875	1.1192	.9152	.9974	.9152	1.0642	.9792	.9959
1.0506	.9924	1.0648	1.1851	.9935	1.1851	.9609	.9988	.9609	1.1233	.9858	.9986
1.1461	.9956	1.1616	1.2509	.9967	1.2509	1.0067	.9995	1.0067	1.1825	.9906	.9996
1.3371	.9985	1.3552		.9992		1.0982		1.0982		.9962	
						1.1897		1.1897		.9987	
$H_i = 2.12$			$H_i = 2.20$			$H_i = 2.31$			$H_i = 2.28$		
									$H_i = 2.32$		

TABLE E-1.—TABLE INDEX

Nozzle type	Medium	M*	Nozzle		Suction no.	Table no.	
Axisymmetric	Air	3	R = 3 R _{th}		5	2b, 4r, 8	
			R = 6 R _{th}		3 4 5 6	1a, 8 1a, 8 1a, 2a, 4q, 8 1a, 2a, 4p, 8	
			R = 12 R _{th}		^a 5 6 7 ^a 8 ^a 9 10	1b, 2c, 4j, 4k, 4l, 4m, 4n, 4o, 8, 11, 14a, 16a 1b, 2d, 4i, 8 1b, 2d, 4h, 8 1b, 2e, 4e, 4f, 4g, 8, 11, 16a 1b, 2e, 4b, 4c, 4d, 8, 11, 16a 2f, 4a, 8	
		5	LARC Q		None ^a 5.1 5.2 ^b 5.3	1c, 2l, 5g, 9 1c, 2k, 5a, 5b, 9 1c, 2g, 5c, 9 1c, 2h, 2i, 2j, 5d, 5e, 5f, 9, 14b, 16b, 17a	
			LARC rapid expansion		None 5.1	1d, 2m, 5h, 9 1d, 2n, 5i, 9	
		7	R = 30 R _{th}		7.1 7.2	1e, 2p, 6a, 10 1e, 2r, 6b, 10	
			R = 75 R _{th}		7.1a 7.1	1f, 2o, 10 1f, 2q, 6c, 10	
		9	R = 200 R _{th}		9.1 9.2	1g, 2t, 6d, 10 1g, 2s, 6e, 10, 14d	
		Helium	9	R = 250 R _{th}		9.3 He 9.4 He	1h, 2v, 6f 1h, 2u, 6g, 14c, 17b
				NASA He		9.5 He 9.6 He	1i, 2w, 6h 1i, 2x, 6i, 17c, 17d
Two-dimensional	Air	4.6	Floor/ceiling		2D-1 2D-2 ^b 2D-3	1j, 3c, 7c, 13 1j, 3c, 7d, 13 1j, 3a, 3b, 7a, 7b, 13	
			Side	75% streamline	2D-1 2D-4 2D-5 2D-6 2D-7 2D-8	12d, 13 12c, 13 12b, 13 12a, 13 3g, 12f, 13 3f, 12i, 13	
					50% streamline	2D-6 2D-9 2D-11	12e 3d, 12g, 13 3i, 12k, 13
				25% streamline		2D-9 2D-10	3e, 12h, 13 3h, 12j, 13

^aEffect of $\frac{U^*D^*}{\nu^*}$ evaluated^bEffect of T_{stag} or wall cooling evaluated

TABLE E-2.—FIGURE INDEX

Nozzle type	Medium	M*	Nozzle	Suction no.	Figure no.	
Axisymmetric	Air	3	R = 3 R _{th}	5	3a, 4a, 12a, 17, 23a	
			R = 6 R _{th}	3 4 5 6	3a, 17 3a, 17 3a, 4a, 5a, 11a, 12b, 17, 23a 3a, 4a, 12c, 17, 23a	
			R = 12 R _{th}	^a 5 6 7 ^a 8 ^a 9 10	3a, 4b, 5b, 11b, 12d, 12h, 12k, 17, 23b, 28a, 29a, 37a 3a, 4b, 12e, 17, 23b 3a, 4b, 5c, 12f, 17, 23b 3a, 4b, 5d, 12i, 12k, 17, 23b, 37a 3a, 4b, 5e, 12j, 12k, 17, 23b, 37a 3a, 4b, 5f, 12g, 17, 23b	
		5	LARC Q	None ^a 5.1 5.2 ^b 5.3	3b, 6c, 11e, 13c, 17, 23d 3b, 4c, 6d, 13d, 17, 23d 3b, 4c, 6e, 13e, 17, 23d 3b, 4c, 6f, 6g, 6h, 11f, 11g, 13f, 17, 28a, 29b, 37a	
			LARC rapid expansion	None 5.1	3b, 6a, 11c, 13a, 17, 23c 3b, 4d, 6b, 11d, 13b, 17, 23c	
		7	R = 30 R _{th}	7.1 7.2	3c, 4e, 7a, 14a, 17, 23e, 37b 3c, 4e, 7b, 14b, 17, 23e	
			R = 75 R _{th}	7.1a 7.1	3c, 4e, 14c, 17, 23e 3c, 4e, 7c, 14d, 17, 23e	
		9	R = 200 R _{th}	9.1 9.2	3d, 4f, 8a, 15a, 23f, 37b 3d, 4f, 8b, 11h, 15b, 23f, 28b	
		Helium	9	R = 250 R _{th}	9.3 He 9.4 He	3e, 3f 3e, 3f, 28b, 30, 31b, 37b, 37c
				NASA He	9.5 He 9.6 He	3e, 3f 3e, 3f, 9, 11i, 28b, 30, 31a, 37b, 37c
Two-dimensional	Air	4.6	Floor/ceiling	2D-1 2D-2 ^b 2D-3	3g, 4g, 10a, 16a, 17, 23g 3g, 4g, 10b, 16b, 17, 23g, 37a 3g, 4g, 10c, 10d, 11j, 16c, 17, 23g, 37a	
			Side	75% streamline	2D-1 2D-4 2D-5 2D-6 2D-7 2D-8	18, 19a, 21a 18, 19a, 21b 18, 19a, 21c 18, 19a, 21d 4h, 10i, 18, 19a, 20e, 21e, 23h, 37a 4h, 10j, 18, 19a, 19b, 20f, 21f, 22, 23h, 37a
				50% streamline	2D-6 2D-9 2D-11	18, 19a, 21d 4h, 10g, 18, 19b, 20c, 23h, 37a 4h, 10h, 18, 19b, 20d, 22, 23h
				25% streamline	2D-9 2D-10	4h, 10e, 18, 19b, 20a, 22, 23h 4h, 10f, 18, 19b, 20b, 22, 23h

^aEffect of $\frac{U^* D^*}{\nu^*}$ evaluated^bEffect of T_{stag} or wall cooling evaluated

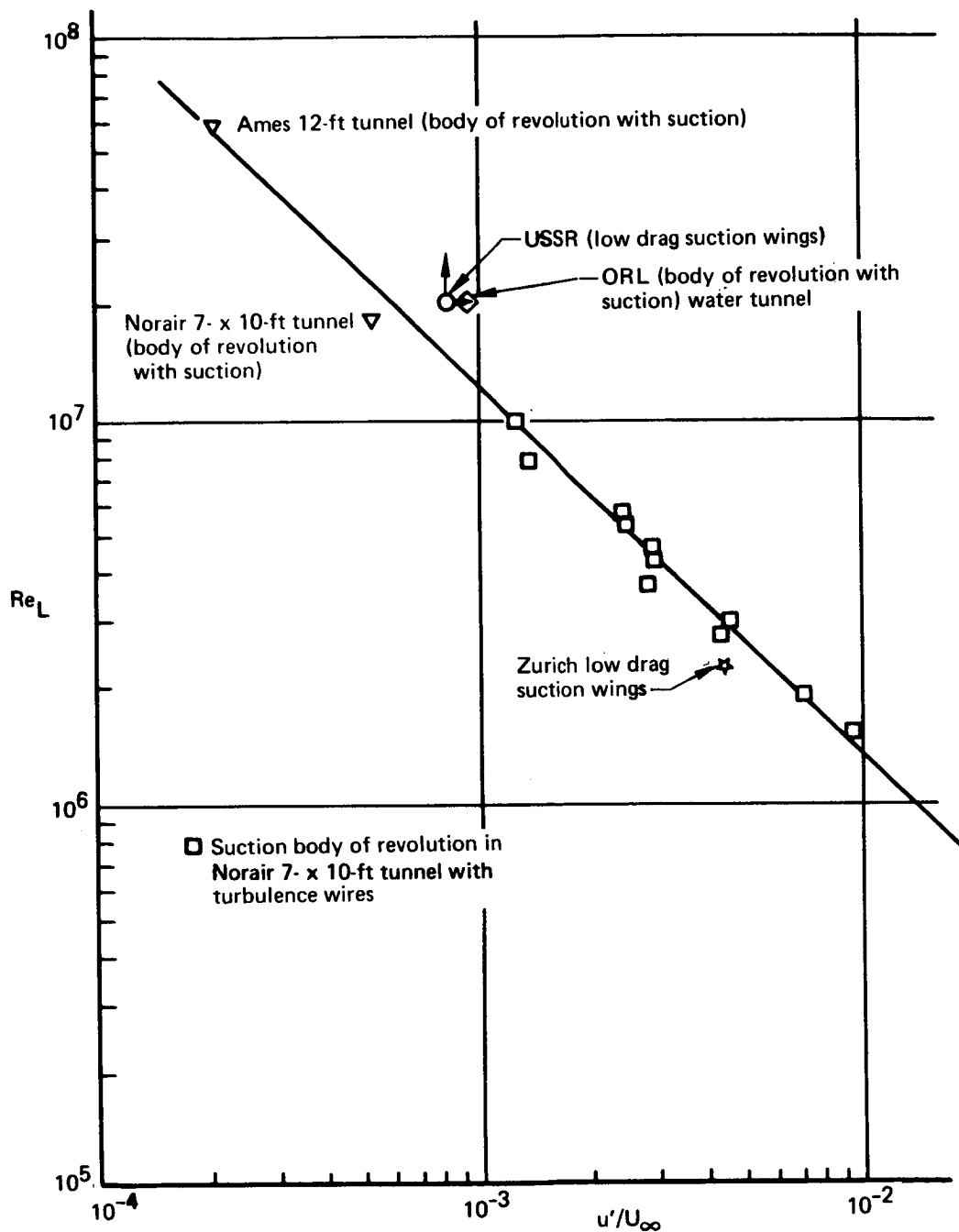


FIGURE 1.—MAXIMUM LENGTH REYNOLDS NUMBER WITH FULL LAMINAR FLOW VERSUS EXTERNAL TURBULENCE LEVEL

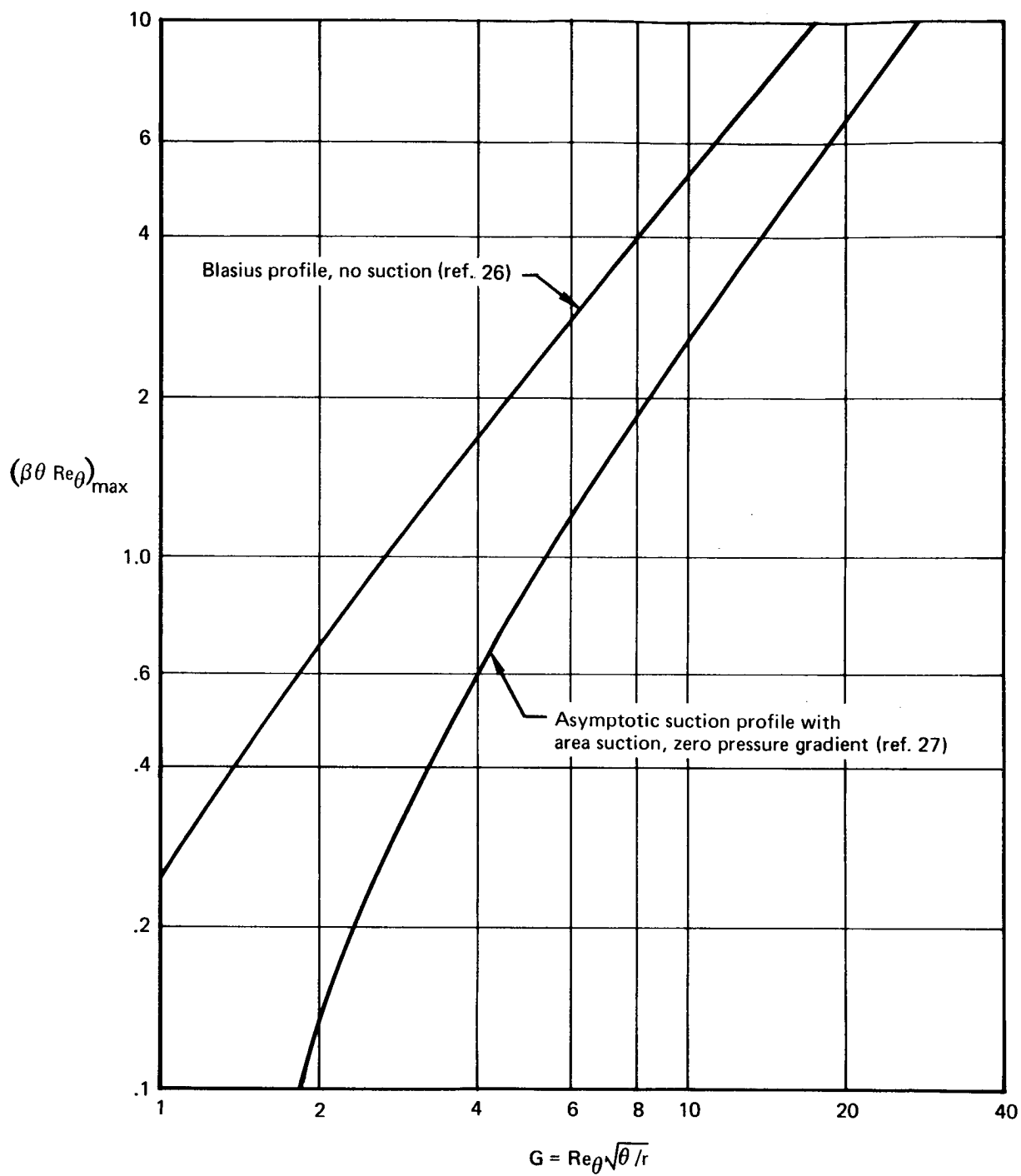
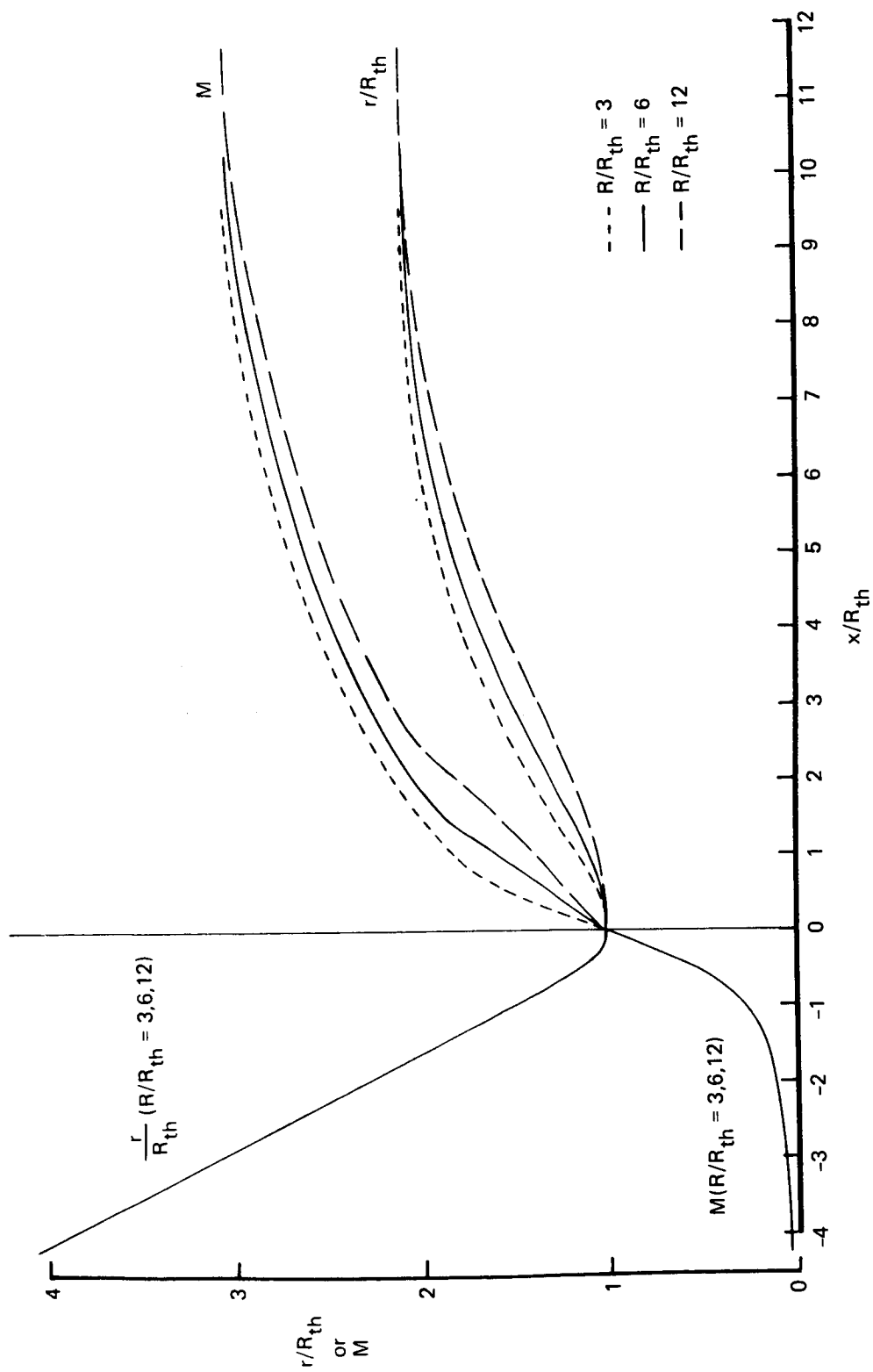
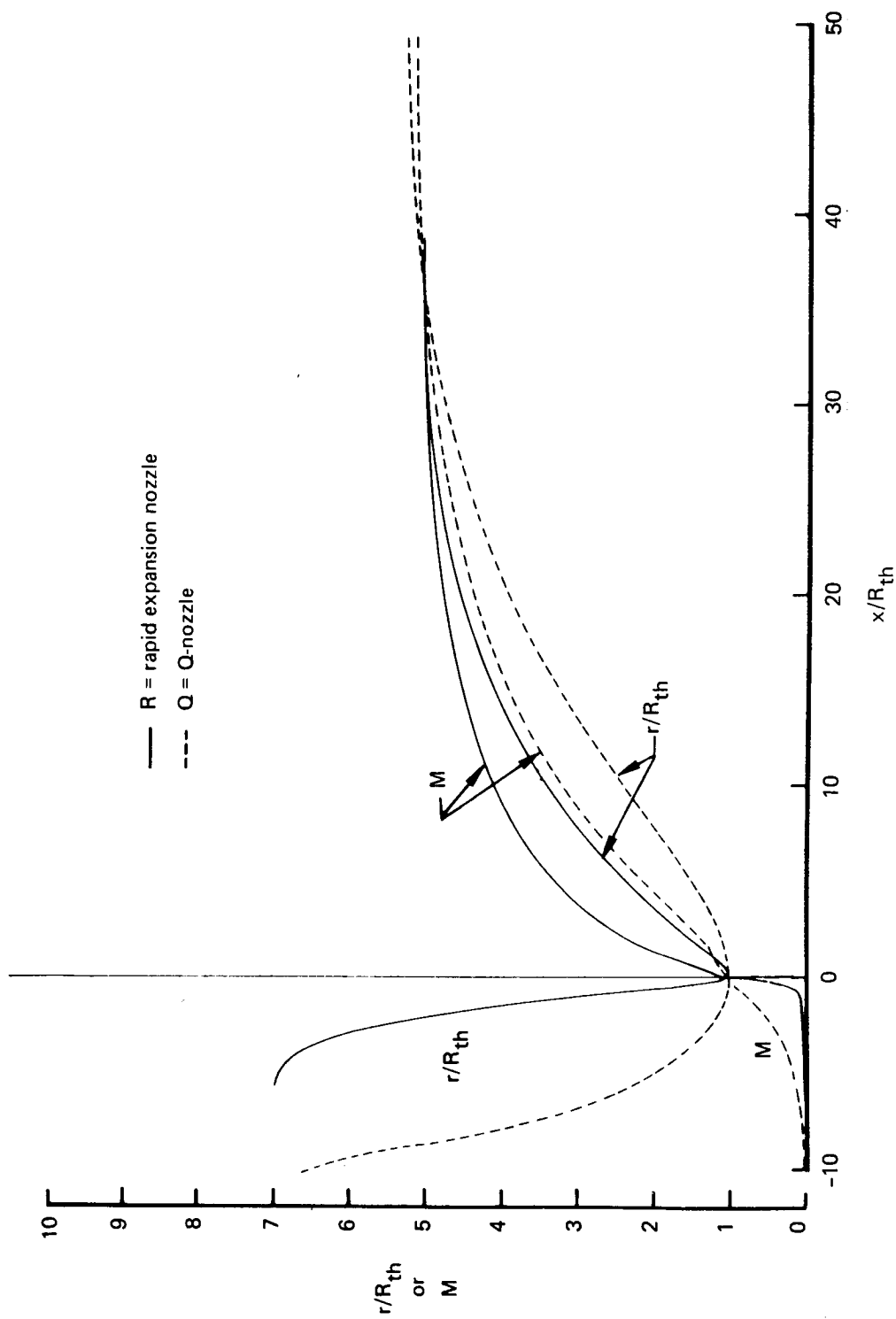


FIGURE 2.—TG BOUNDARY LAYER INSTABILITY



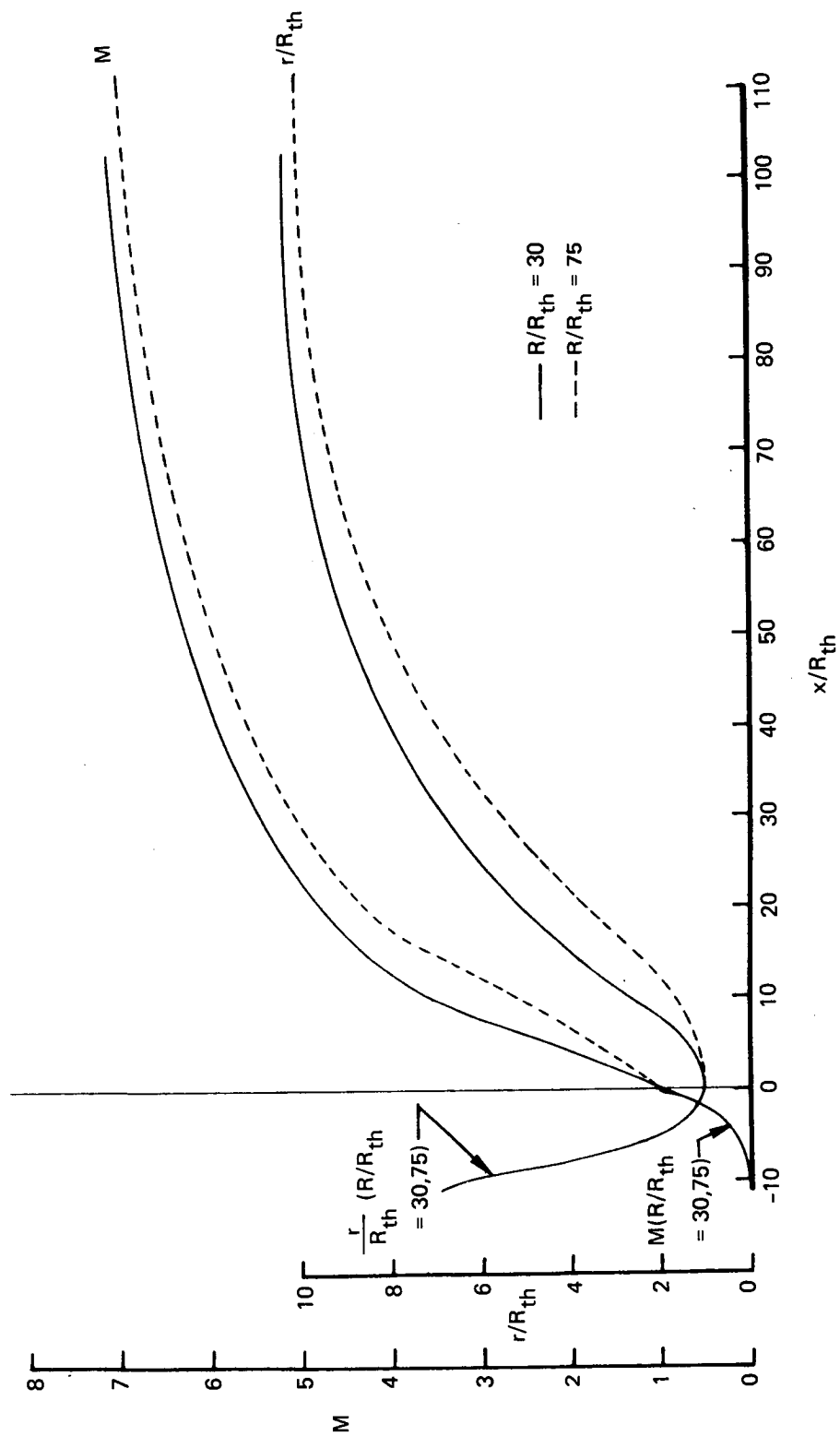
a) $M^* = 3$ axisymmetric air nozzle

FIGURE 3.—COORDINATES AND STREAMWISE MACH NUMBER VARIATION



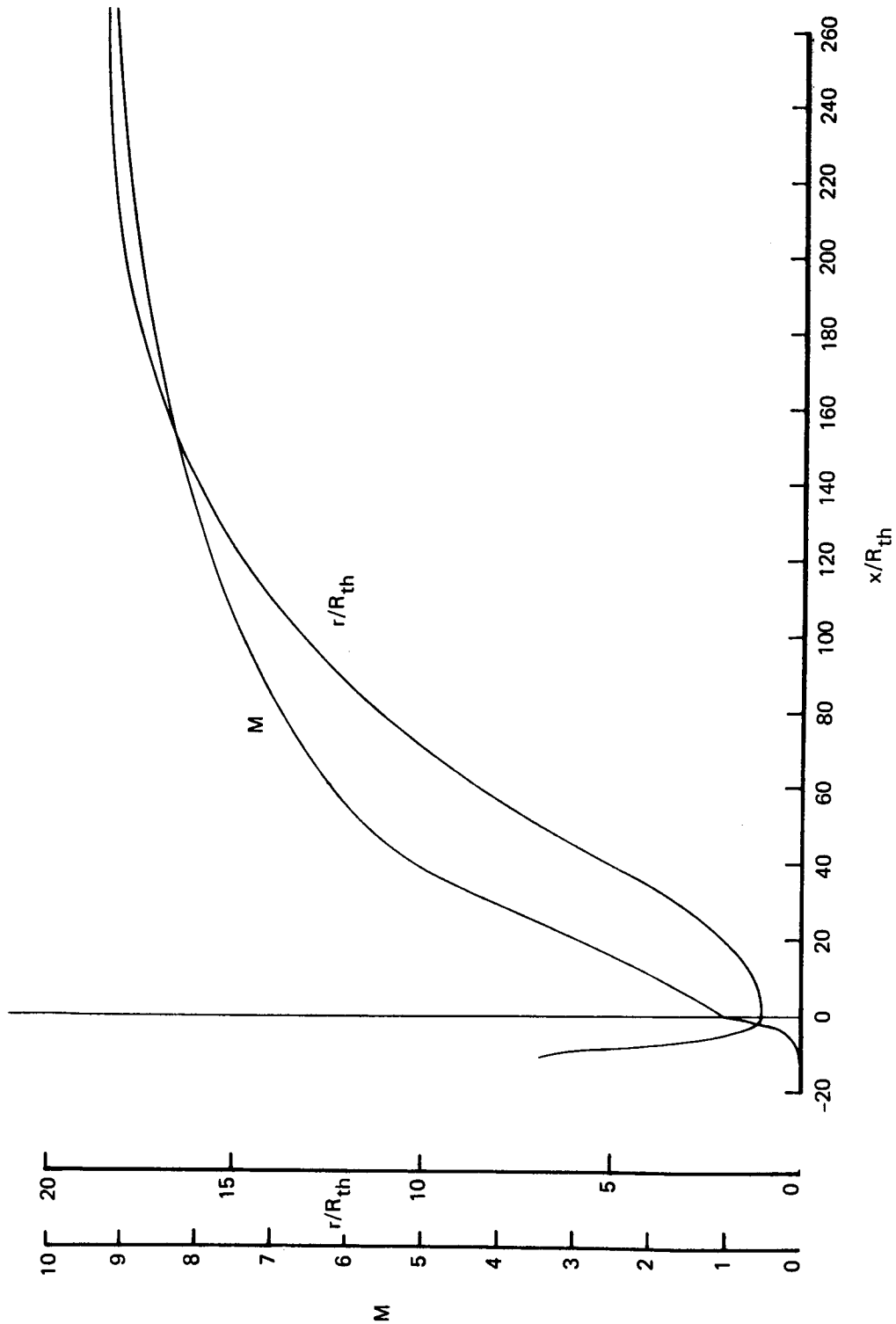
b) $M^* = 5$ axisymmetric air nozzle

FIGURE 3.—COORDINATES AND STREAMWISE MACH NUMBER VARIATION (Continued)



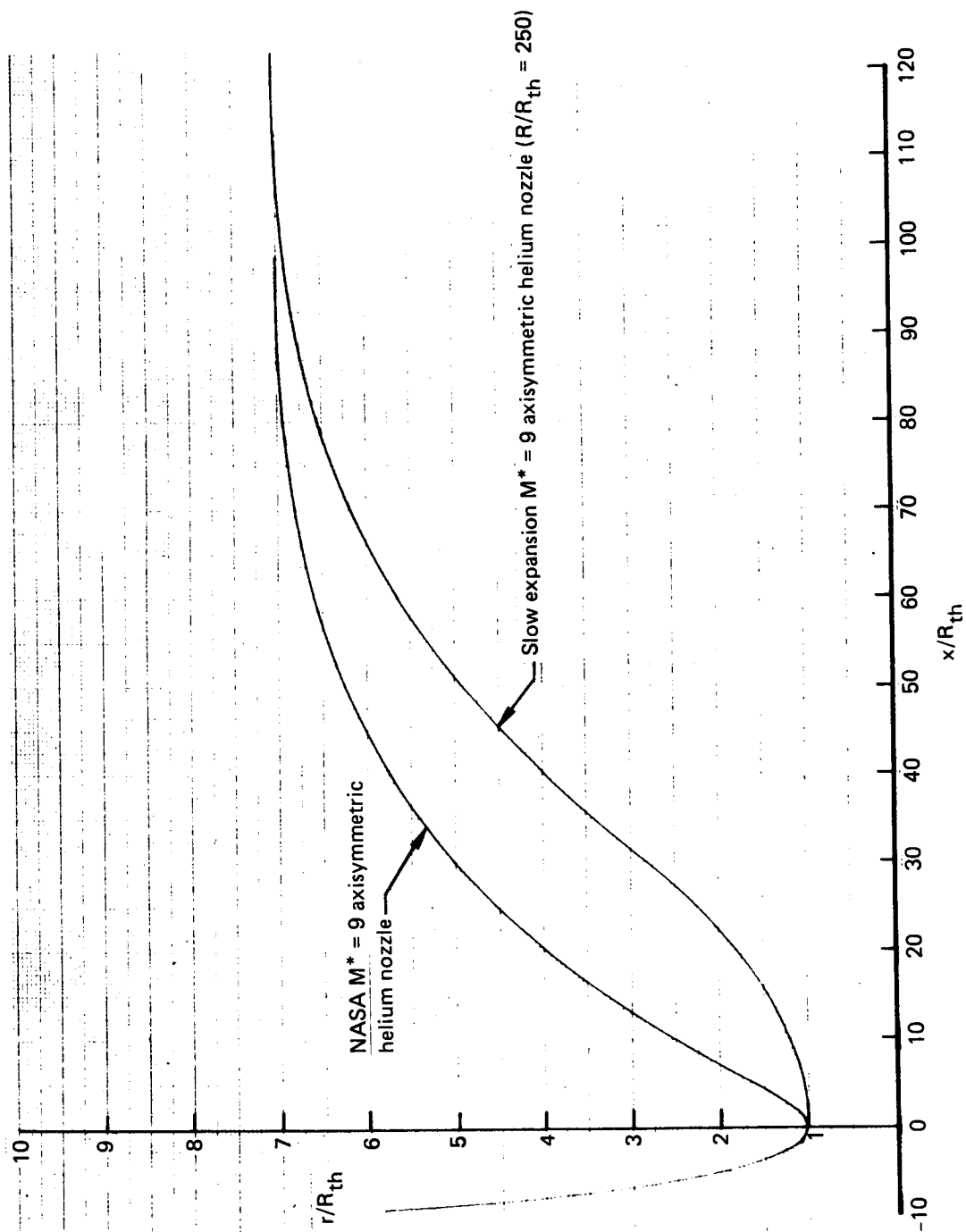
c) $M^* = 7$ axisymmetric air nozzles

FIGURE 3.—COORDINATES AND STREAMWISE MACH NUMBER VARIATION (Continued)



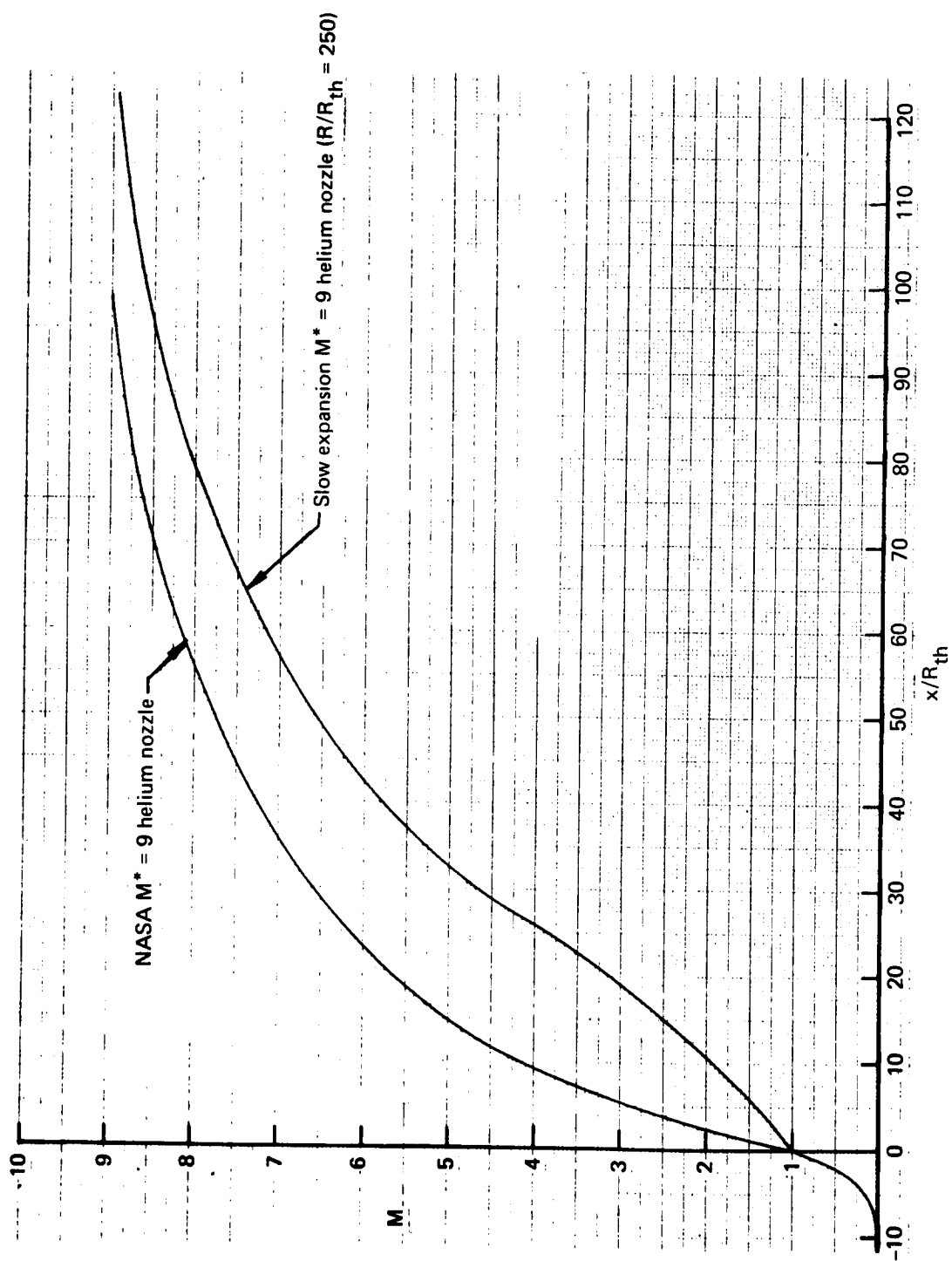
d) $M^* = 9$ axisymmetric air nozzle, $R/R_{th} = 200$

FIGURE 3.—COORDINATES AND STREAMWISE MACH NUMBER VARIATION (Continued)



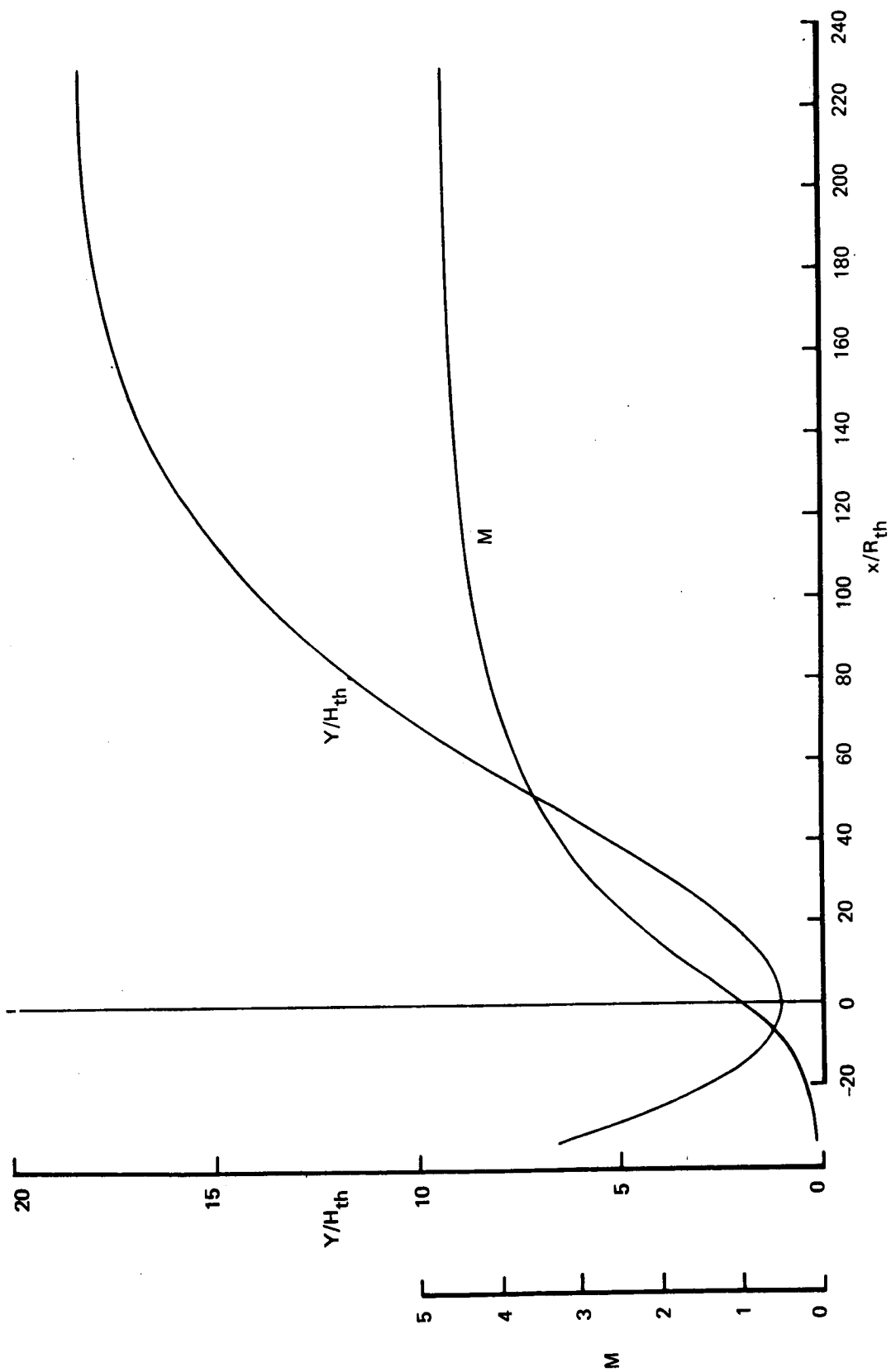
e) $M^* = 9$ axisymmetric helium nozzle contours

FIGURE 3.—COORDINATES AND STREAMWISE MACH NUMBER VARIATION (Continued)



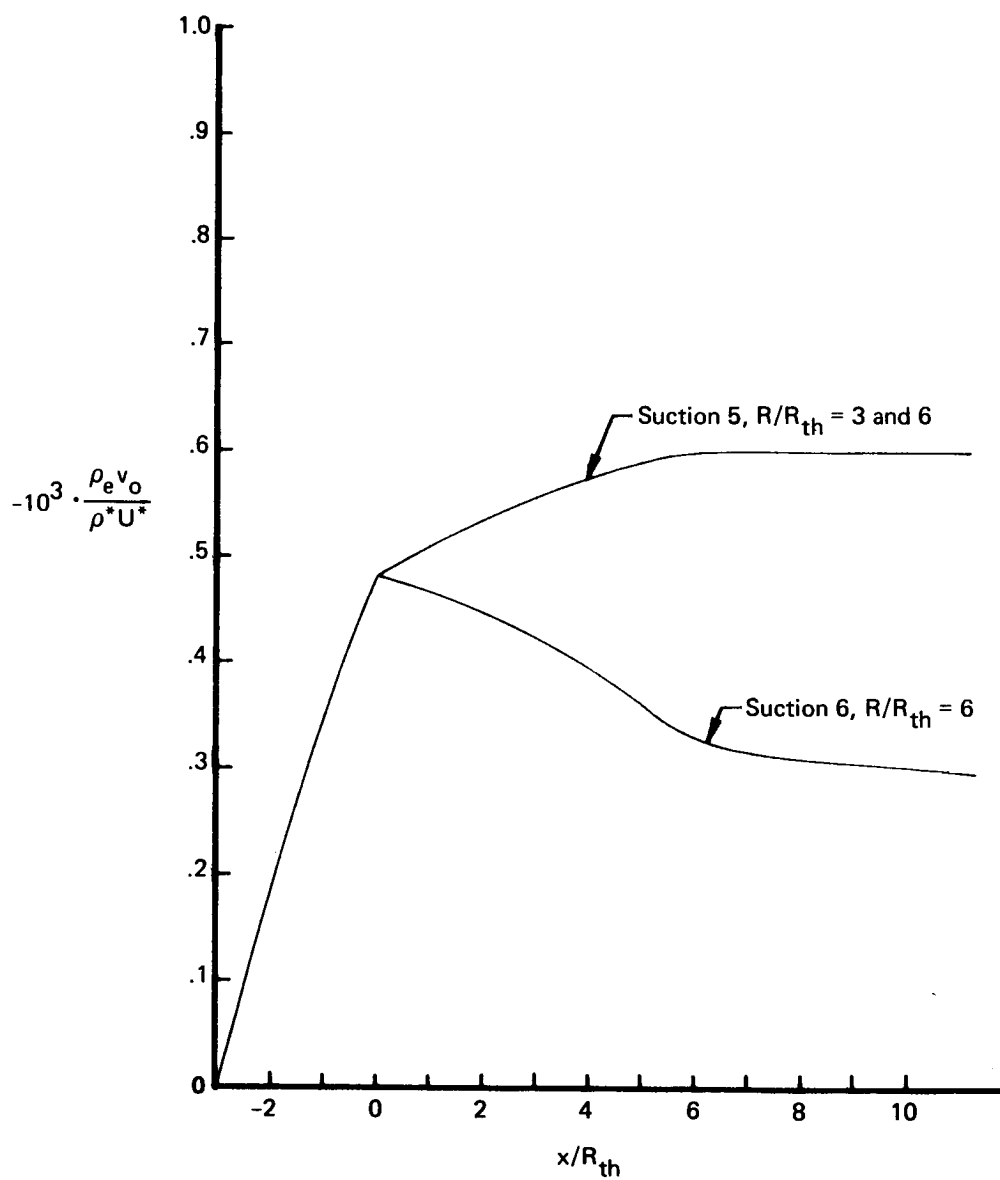
f) $M^* = 9$ axisymmetric helium nozzle Mach number variation

FIGURE 3.—COORDINATES AND STREAMWISE MACH NUMBER VARIATION (Continued)



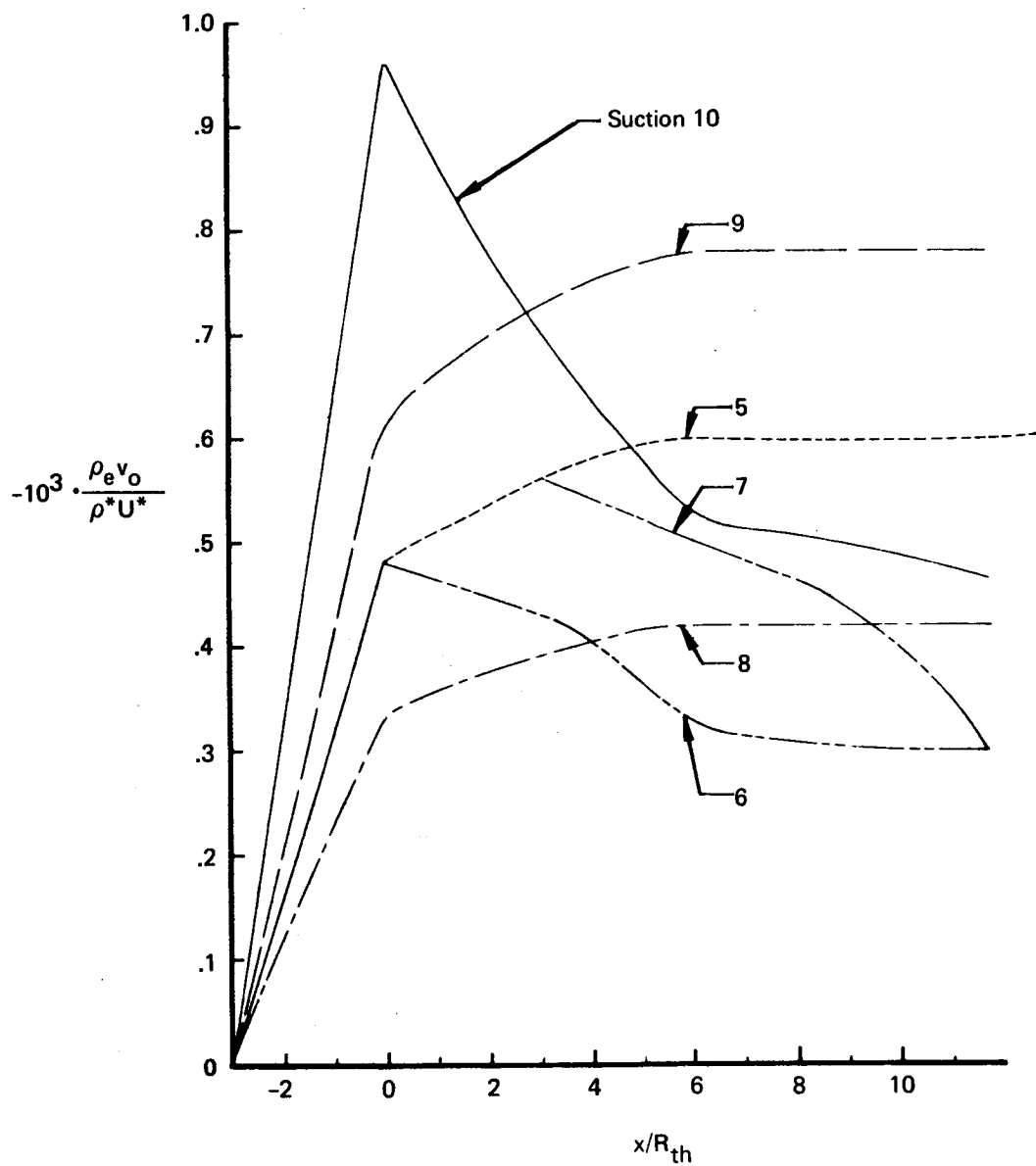
g) $M^* = 4.6$ two-dimensional JPL nozzle (air)

FIGURE 3.—COORDINATES AND STREAMWISE MACH NUMBER VARIATION (Concluded)



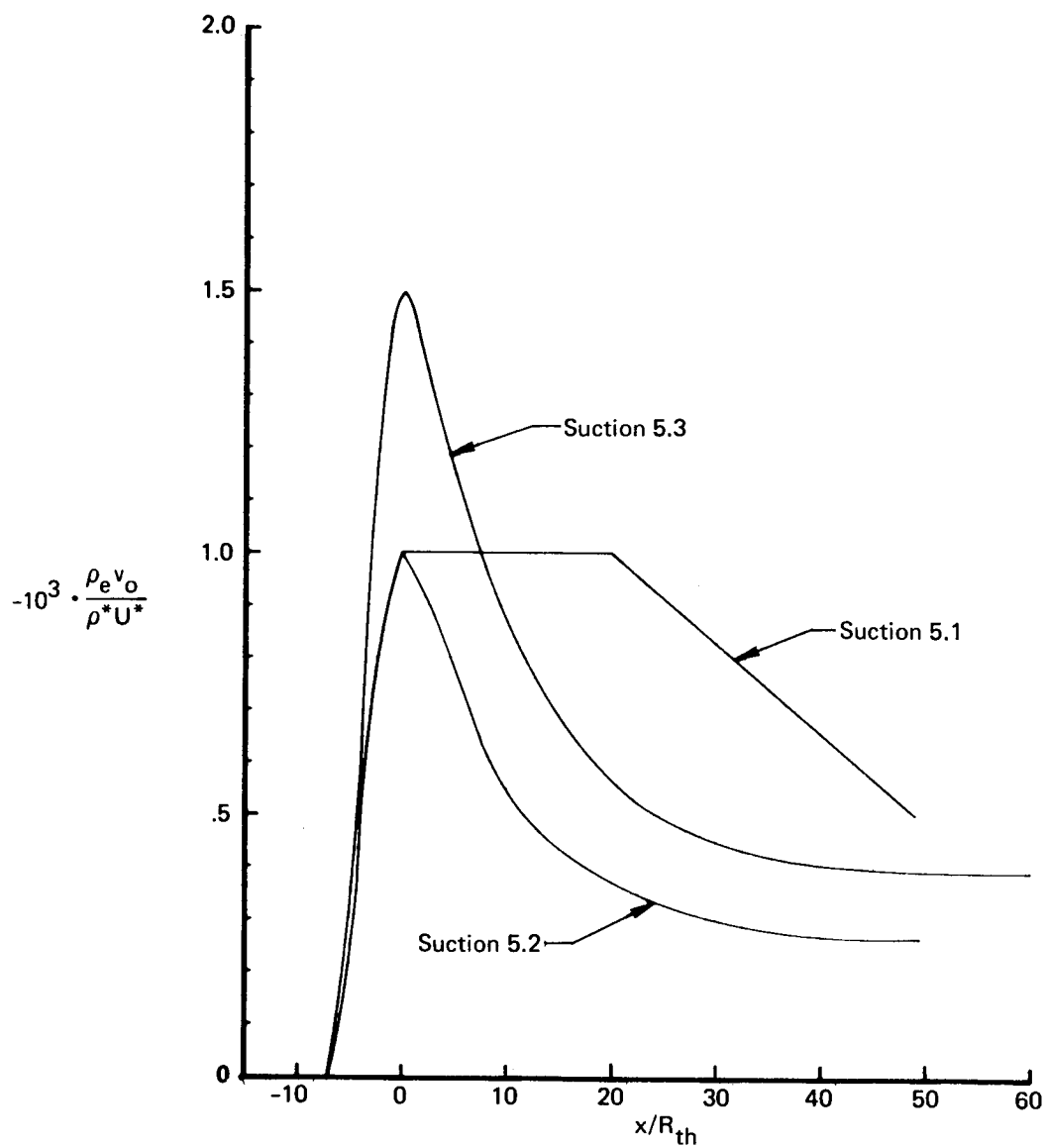
a) $M^* = 3$ axisymmetric nozzles, $T_{stag} = 300^\circ \text{ K}$, $T_{wall_{ad}}$, $U^*/\nu^* = 26.22 \cdot 10^6/\text{m}$, $D^* = 1\text{m}$

FIGURE 4.—STREAMWISE SUCTION MASS FLOW DISTRIBUTIONS



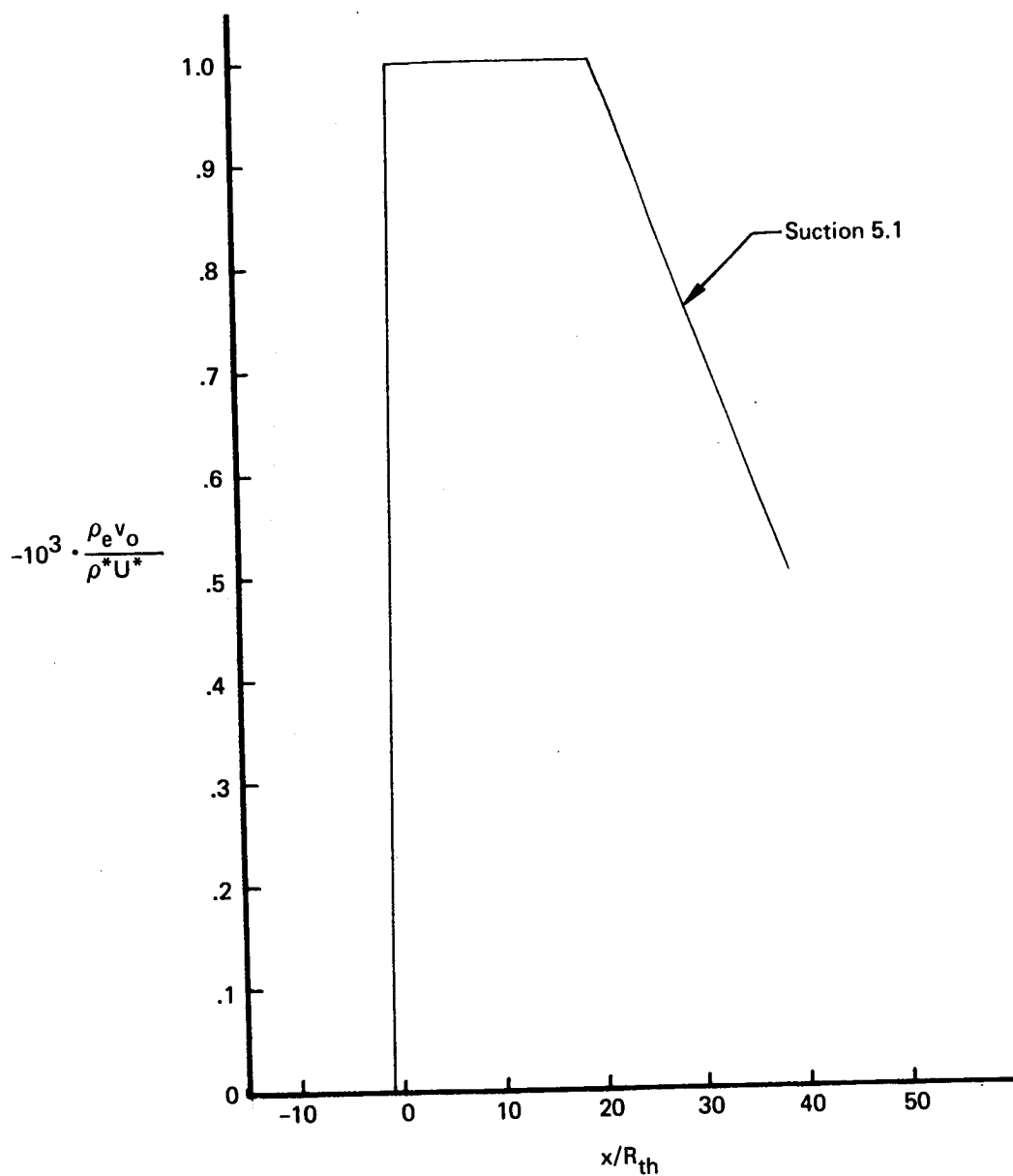
b) $M^* = 3$ axisymmetric nozzle, $R/R_{th} = 12$, $T_{stag} = 300^\circ \text{ K}$, $T_{wall_{ad}}$, $U^*/\nu^* = 26.22 \cdot 10^6/\text{m}$, $D^* = 1\text{ m}$

FIGURE 4.—STREAMWISE SUCTION MASS FLOW DISTRIBUTIONS (Continued)



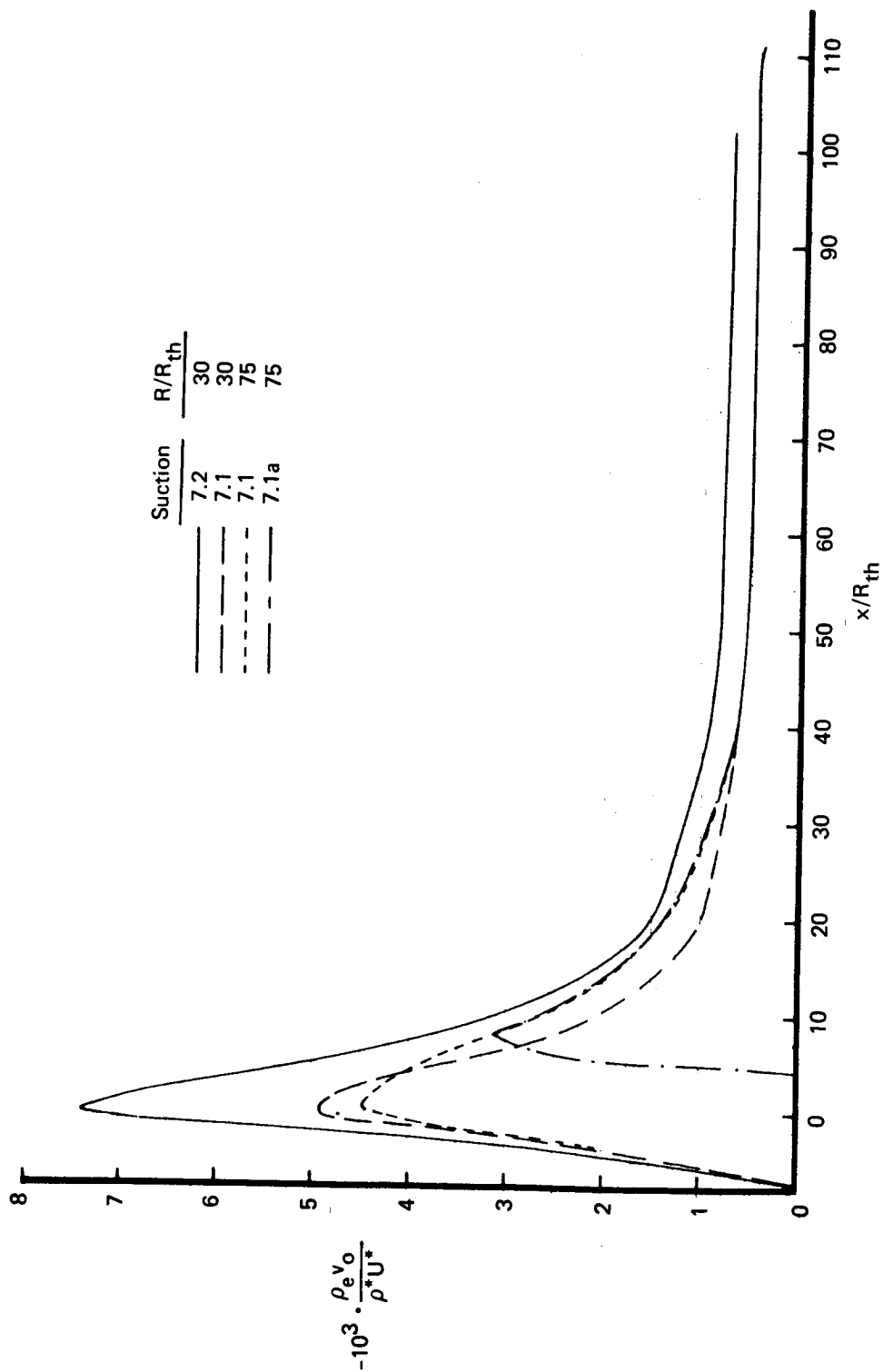
c) $M^* = 5$ LARC axisymmetric Q-nozzle, $U^*/\nu^* = 26.22 \cdot 10^6/m$, $D^* = 1m$

FIGURE 4.—STREAMWISE SUCTION MASS FLOW DISTRIBUTIONS (Continued)



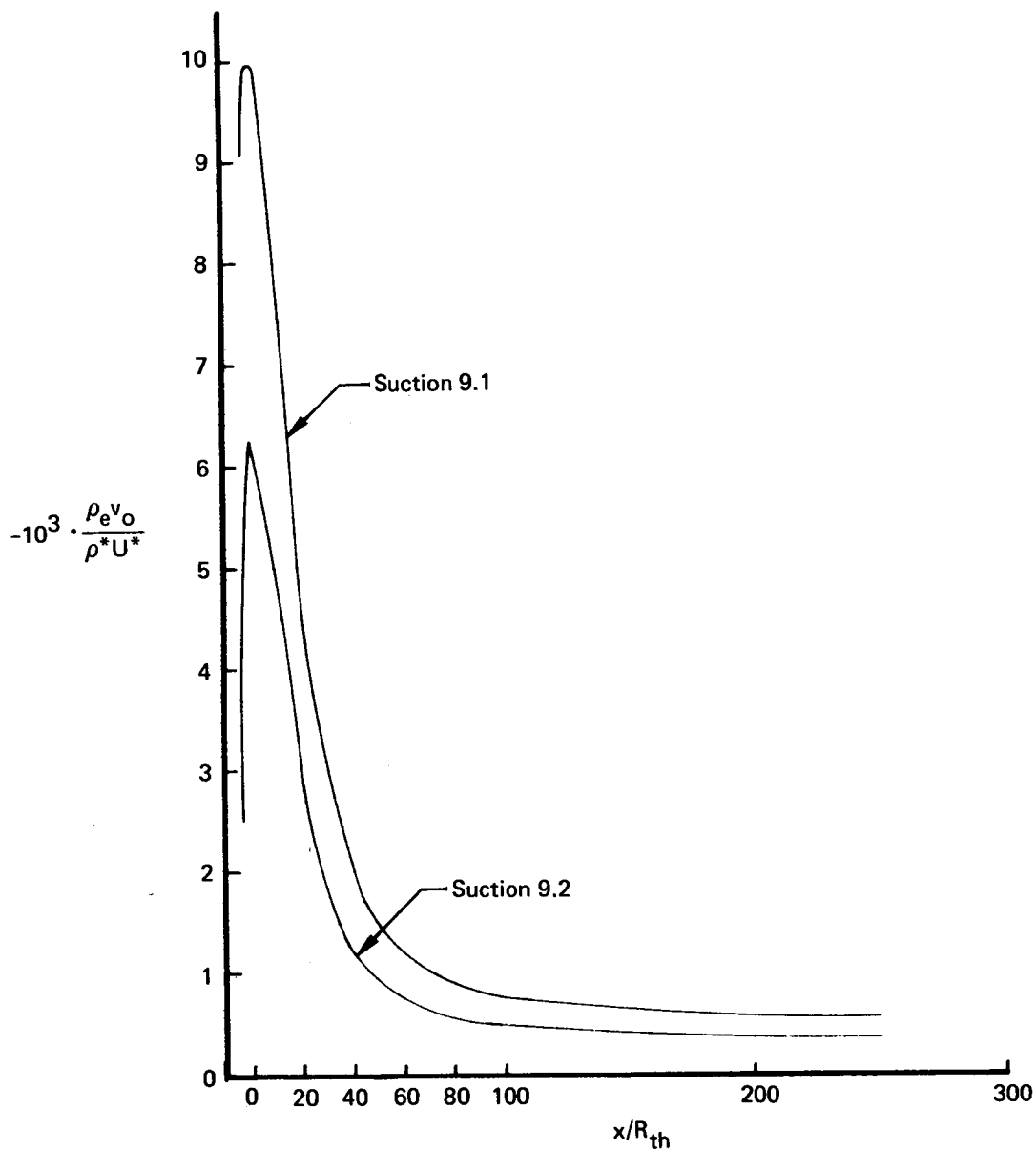
d) $M^* = 5$ rapid expansion axisymmetric nozzle, $T_{stag} = 300^\circ \text{ K}$, $T_{wall_{ad}}$, $U^*/p^* = 26.22 \cdot 10^6/\text{m}$, $D^* = 1\text{ m}$

FIGURE 4.—STREAMWISE SUCTION MASS FLOW DISTRIBUTIONS (Continued)



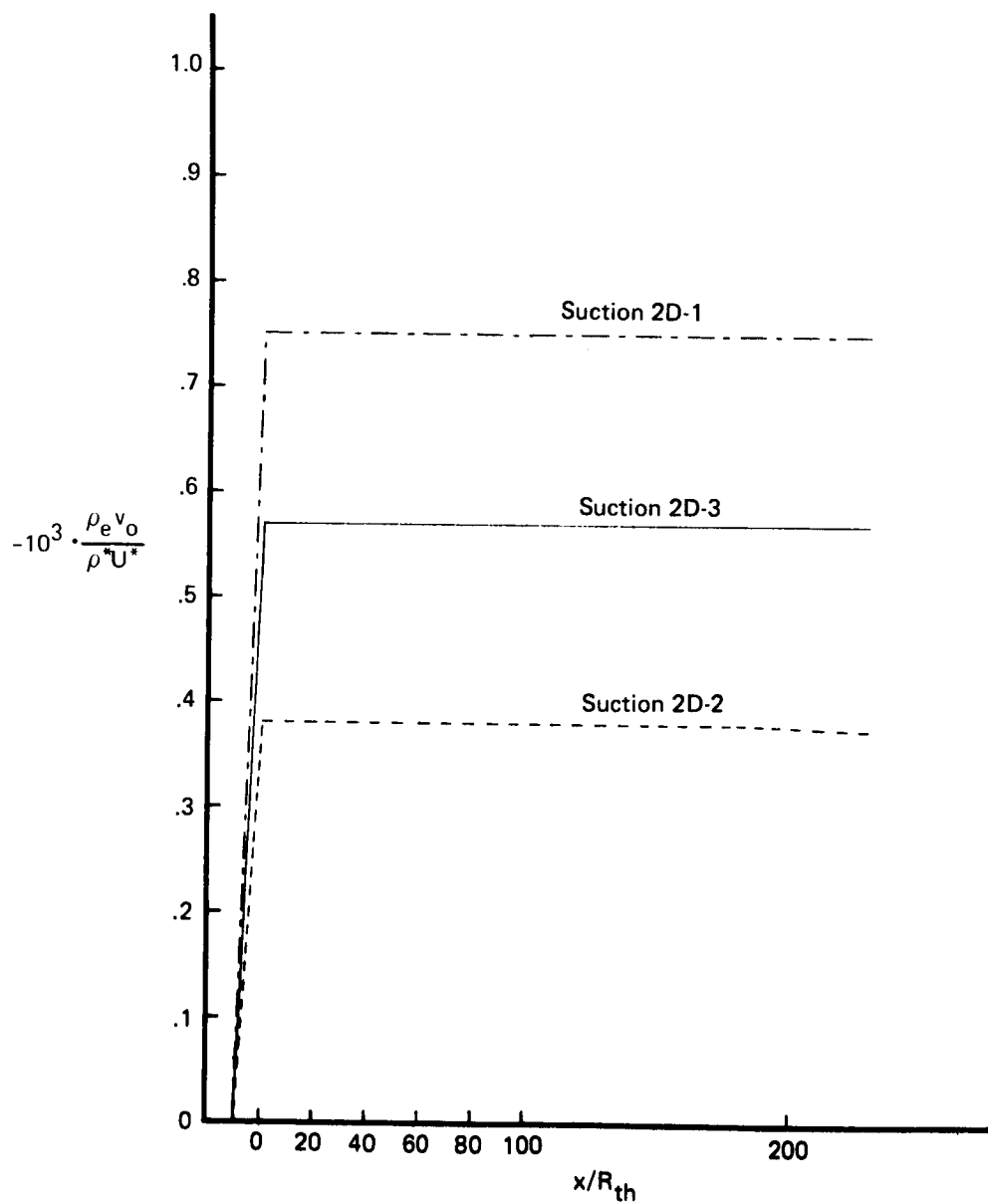
e) $M^* = 7$ axisymmetric nozzle, $T_{stag} = 700^\circ \text{ K}$, $T_{wall_{ad}} = 26.22 \cdot 10^6 / M$, $D^* = 1 \text{ m}$

FIGURE 4.—STREAMWISE SUCTION MASS FLOW DISTRIBUTIONS (Continued)



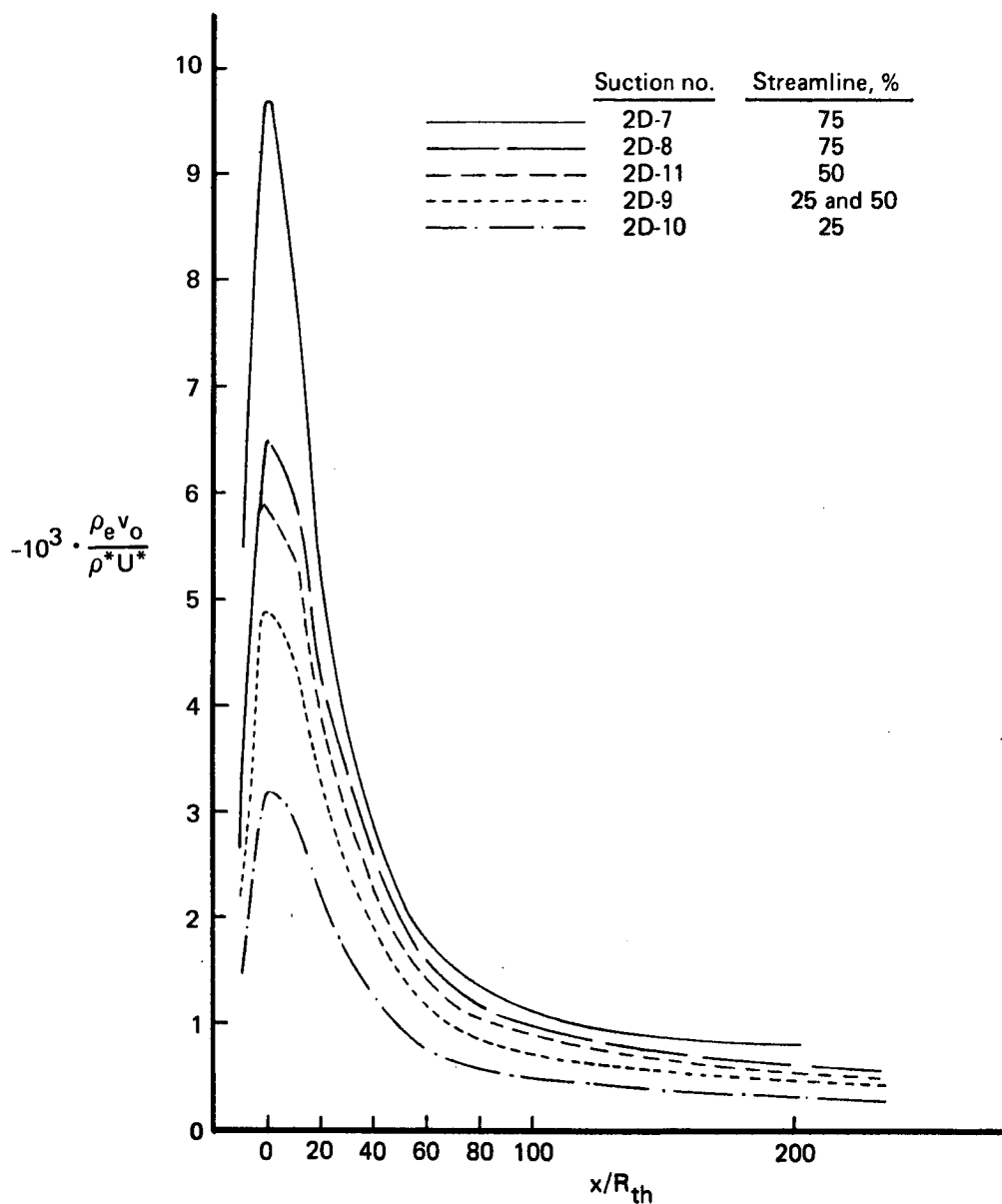
f) $M^* = 9$ axisymmetric nozzle, $R = 200 R_{th}$, $T_{stag} = 1000^\circ \text{ K}$, $T_{wall_{ad}}$, $U^*/\nu^* = 26.22 \cdot 10^6/\text{m}$, $D^* = 1\text{ m}$

FIGURE 4.—STREAMWISE SUCTION MASS FLOW DISTRIBUTIONS (Continued)



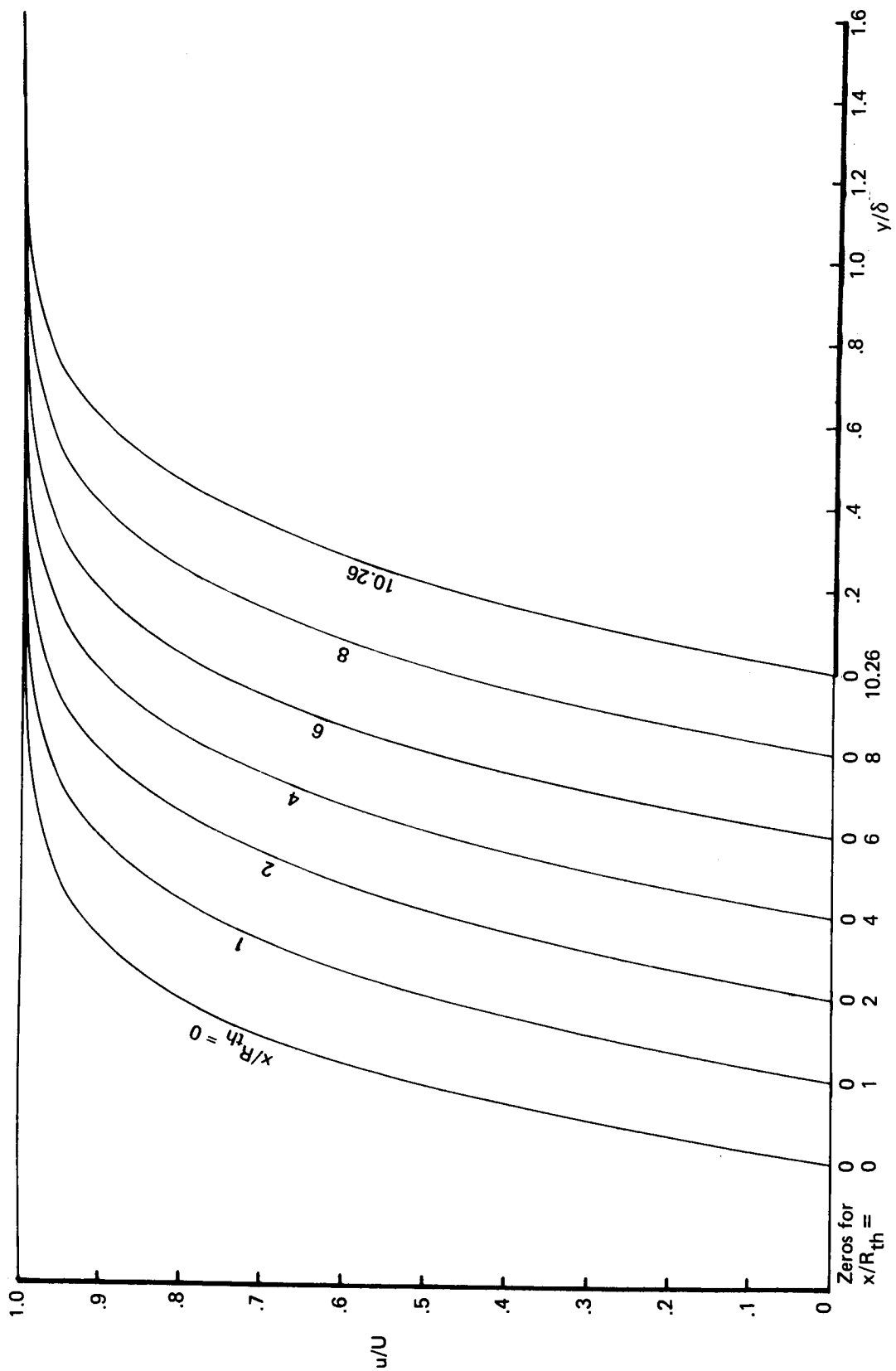
g) $M^* = 4.6$ two-dimensional JPL nozzle, floor and ceiling walls, $T_{wall,ad} U^*/\nu^* = 26.22 \cdot 10^6/m$, $H^* = 1m$

FIGURE 4.—STREAMWISE SUCTION MASS FLOW DISTRIBUTIONS (Continued)



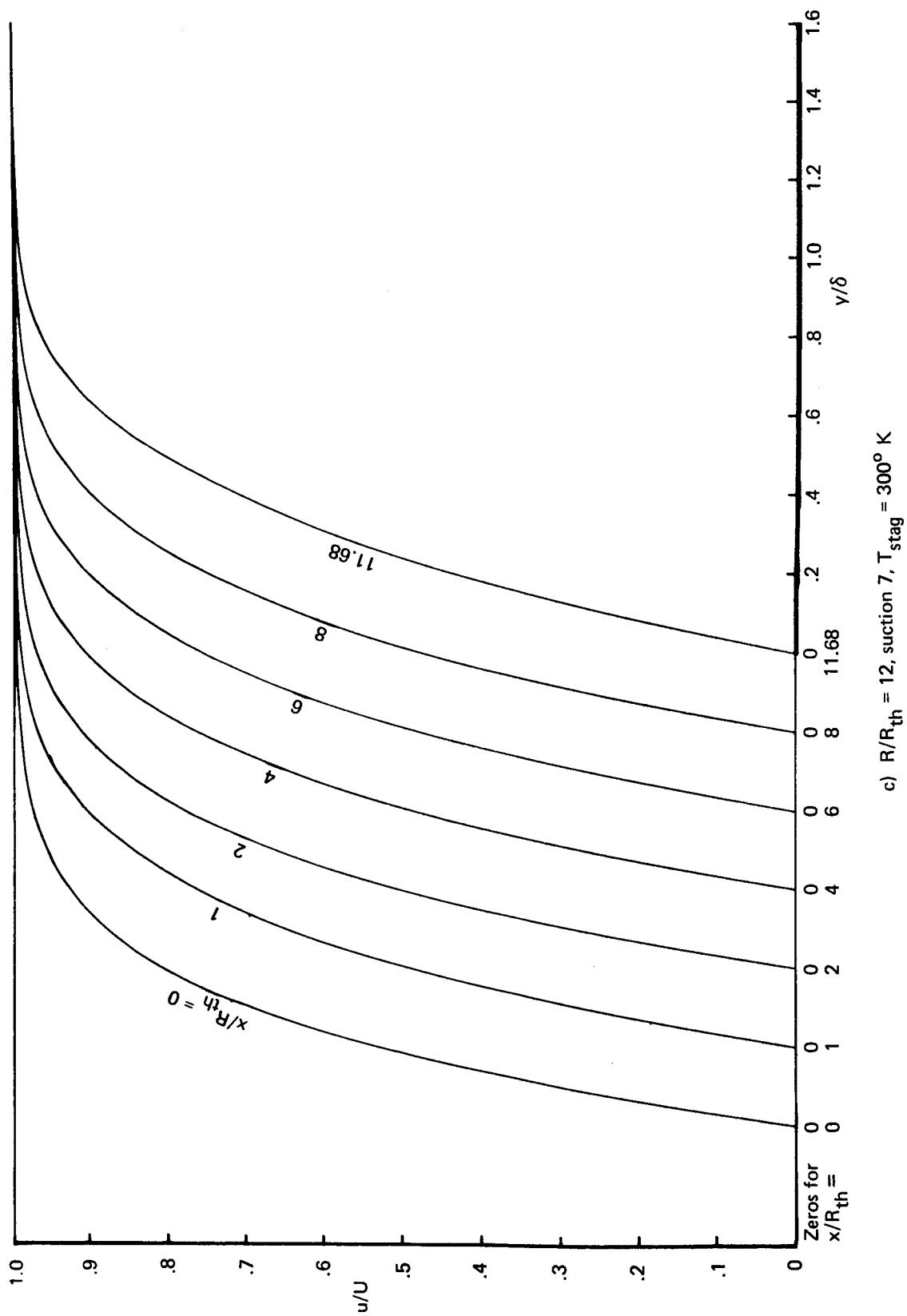
h) $M^* = 4.6$ two-dimensional JPL nozzle, side walls, $T_{\text{stag}} = 400^\circ \text{ K}$, $T_{\text{wall ad}} = 26.22 \cdot 10^6 / \text{m}$, $U^* / \nu^* = 26.22 \cdot 10^6 / \text{m}$, $H^* = 1 \text{ m}$

FIGURE 4.—STREAMWISE SUCTION MASS FLOW DISTRIBUTIONS (Concluded)



a) $R/R_{th} = 6$, suction 5, $T_{stag} = 300^\circ K$

FIGURE 5.—NOZZLE WALL BOUNDARY LAYER VELOCITY PROFILES— $M^* = 3$ AXISYMMETRIC AIR NOZZLES

FIGURE 5.—NOZZLE WALL BOUNDARY LAYER VELOCITY PROFILES— $M^* = 3$ AXISYMMETRIC AIR NOZZLES (Continued)

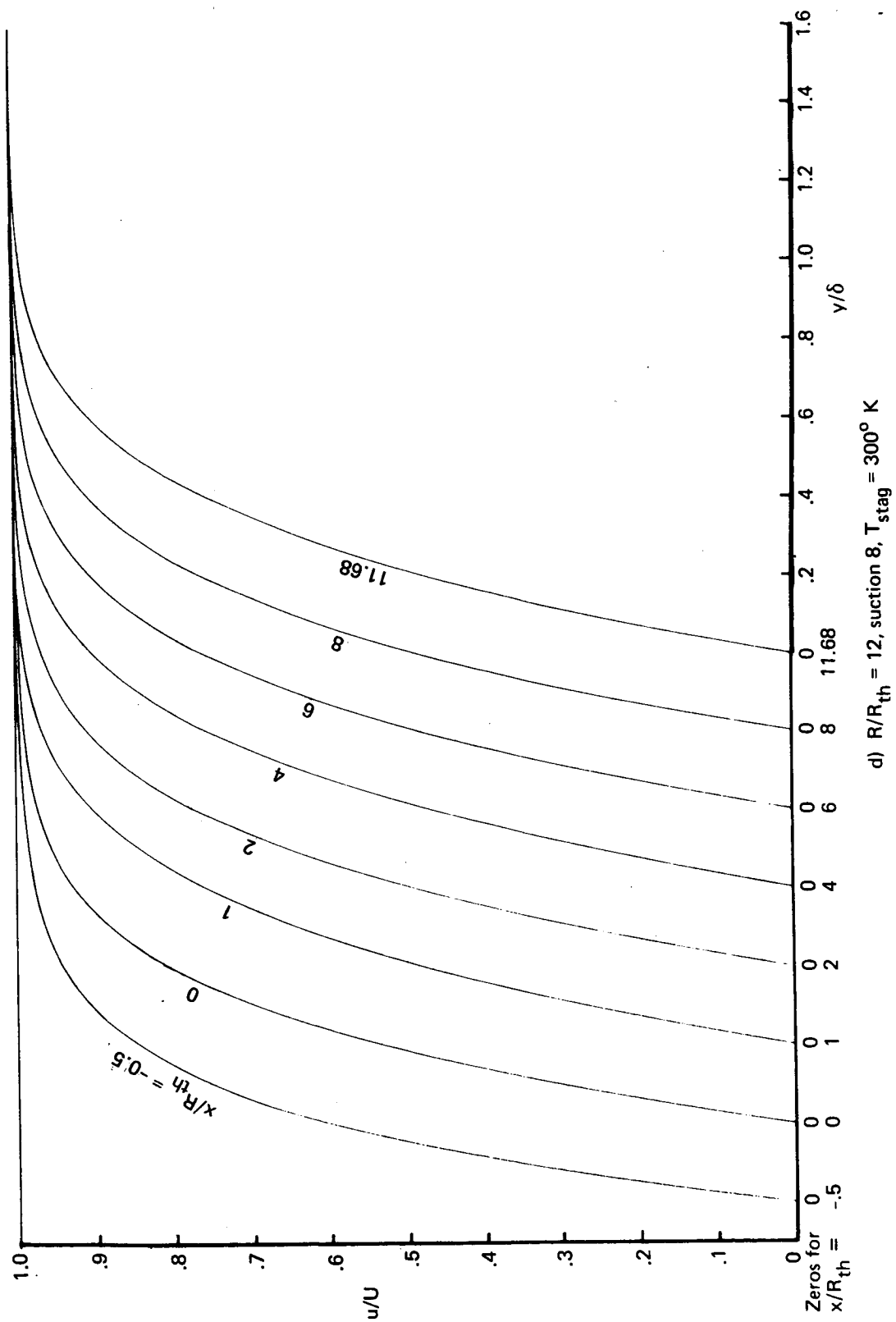


FIGURE 5.—NOZZLE WALL BOUNDARY LAYER VELOCITY PROFILES— $M^* = 3$ AXISYMMETRIC AIR NOZZLES (Continued)

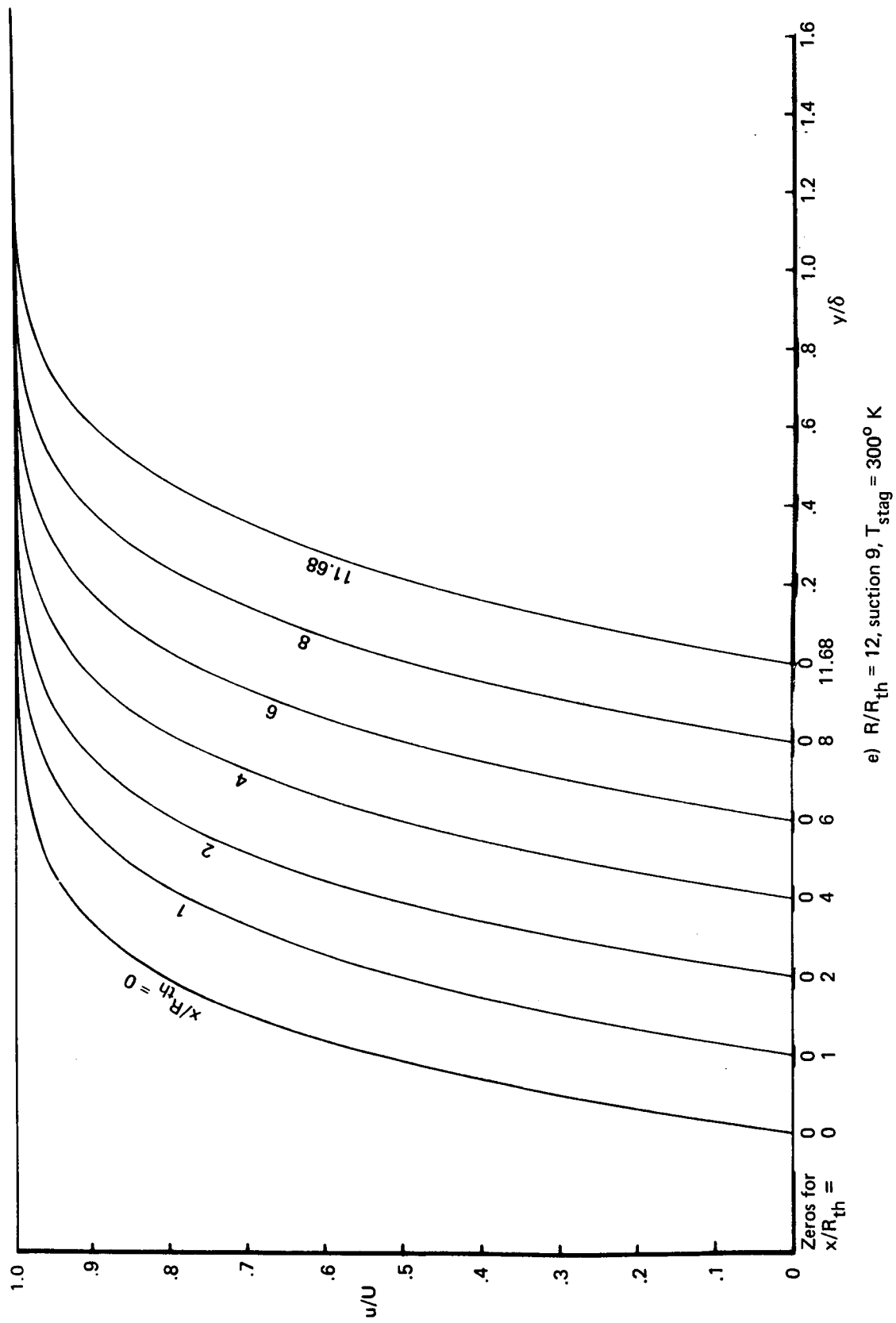


FIGURE 5.—NOZZLE WALL BOUNDARY LAYER VELOCITY PROFILES— $M^* = 3$ AXISYMMETRIC AIR NOZZLES (Continued)

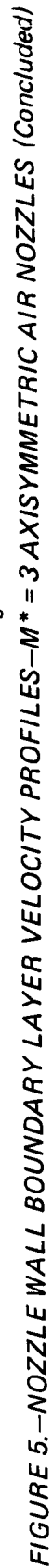
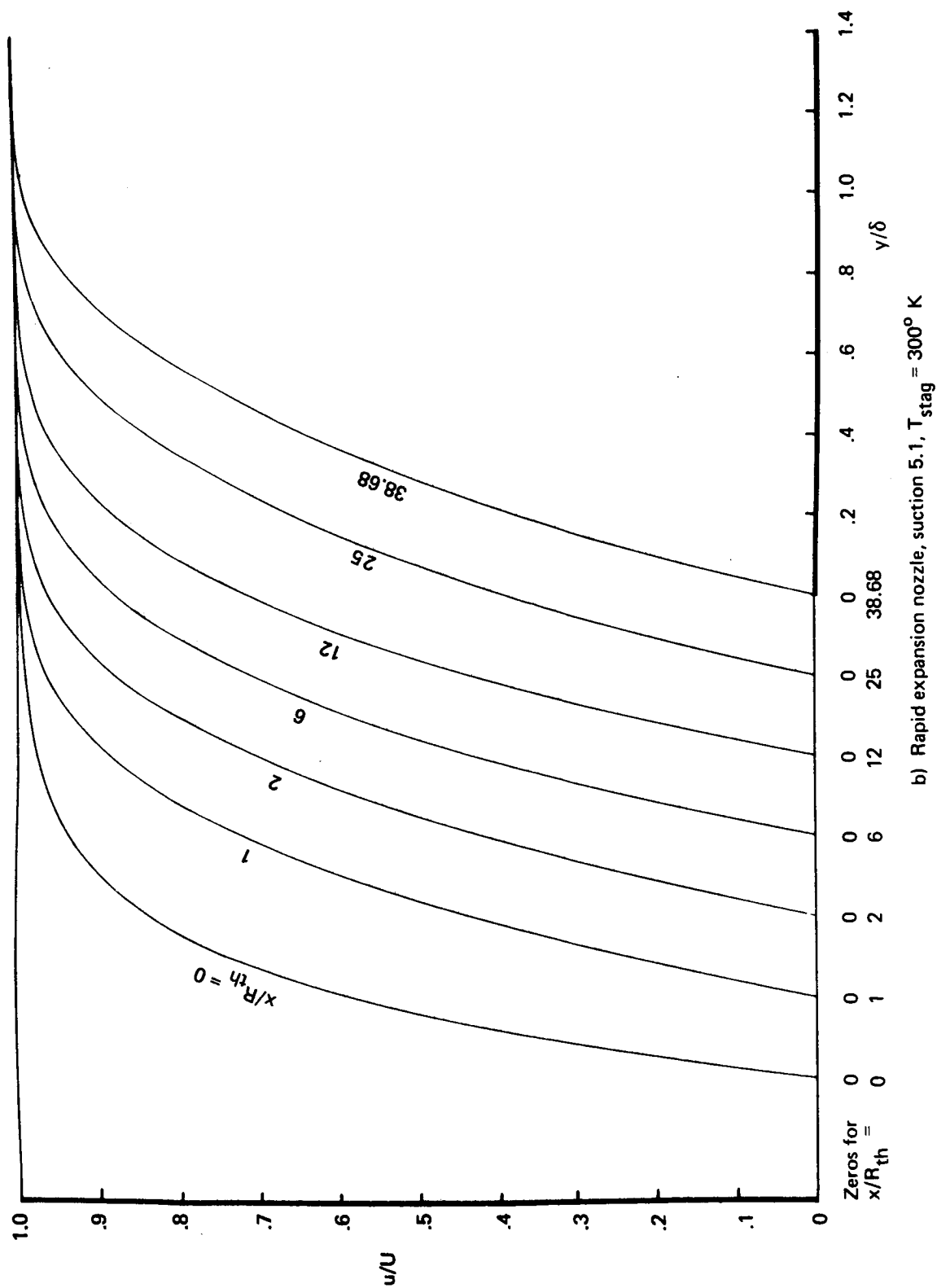
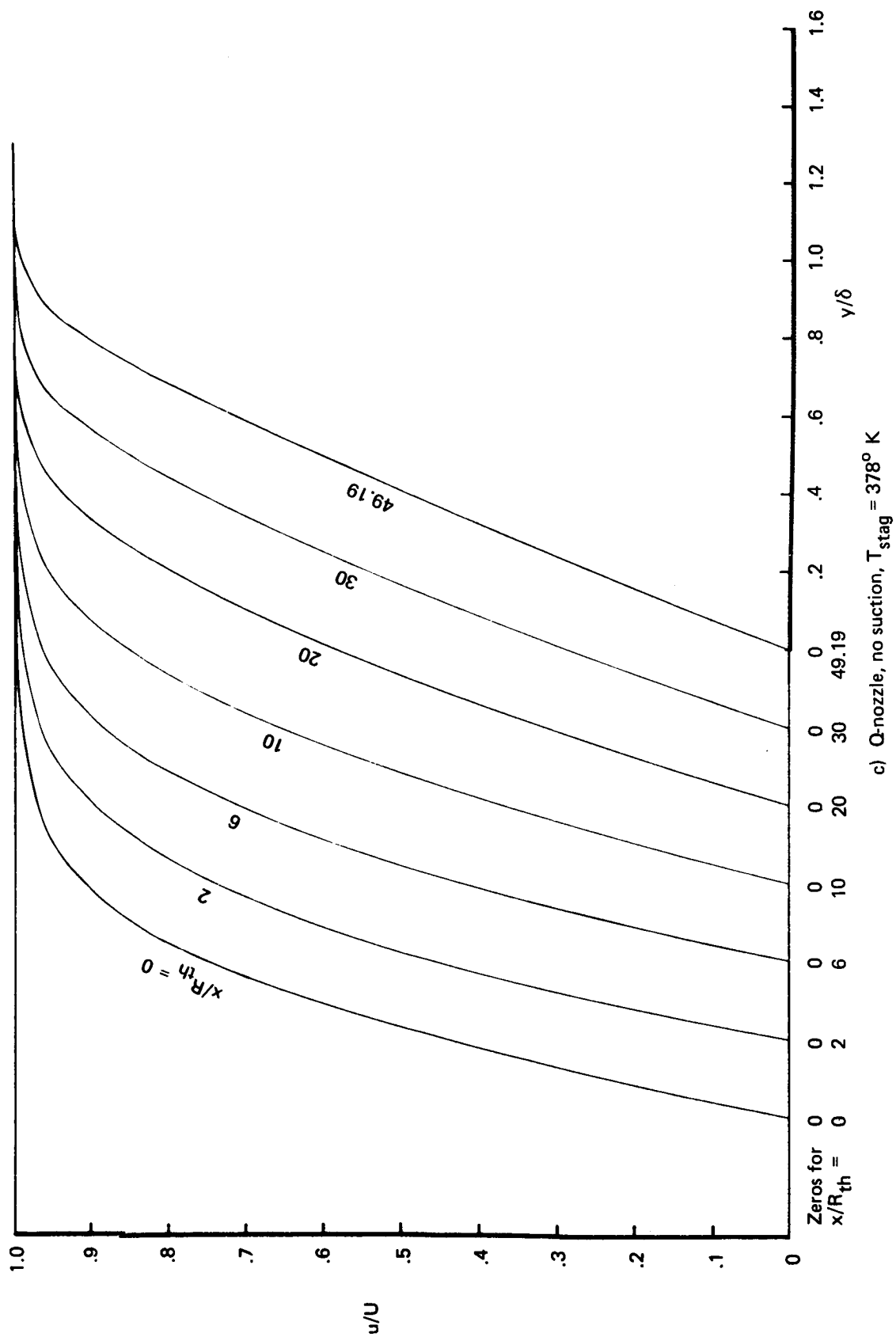


FIGURE 6.—NOZZLE WALL BOUNDARY LAYER VELOCITY PROFILES— $M^* = 5$ AXISYMMETRIC AIR NOZZLES



FIGURE 6.—NOZZLE WALL BOUNDARY LAYER VELOCITY PROFILES— $M^* = 5$ AXISYMMETRIC AIR NOZZLES (Continued)

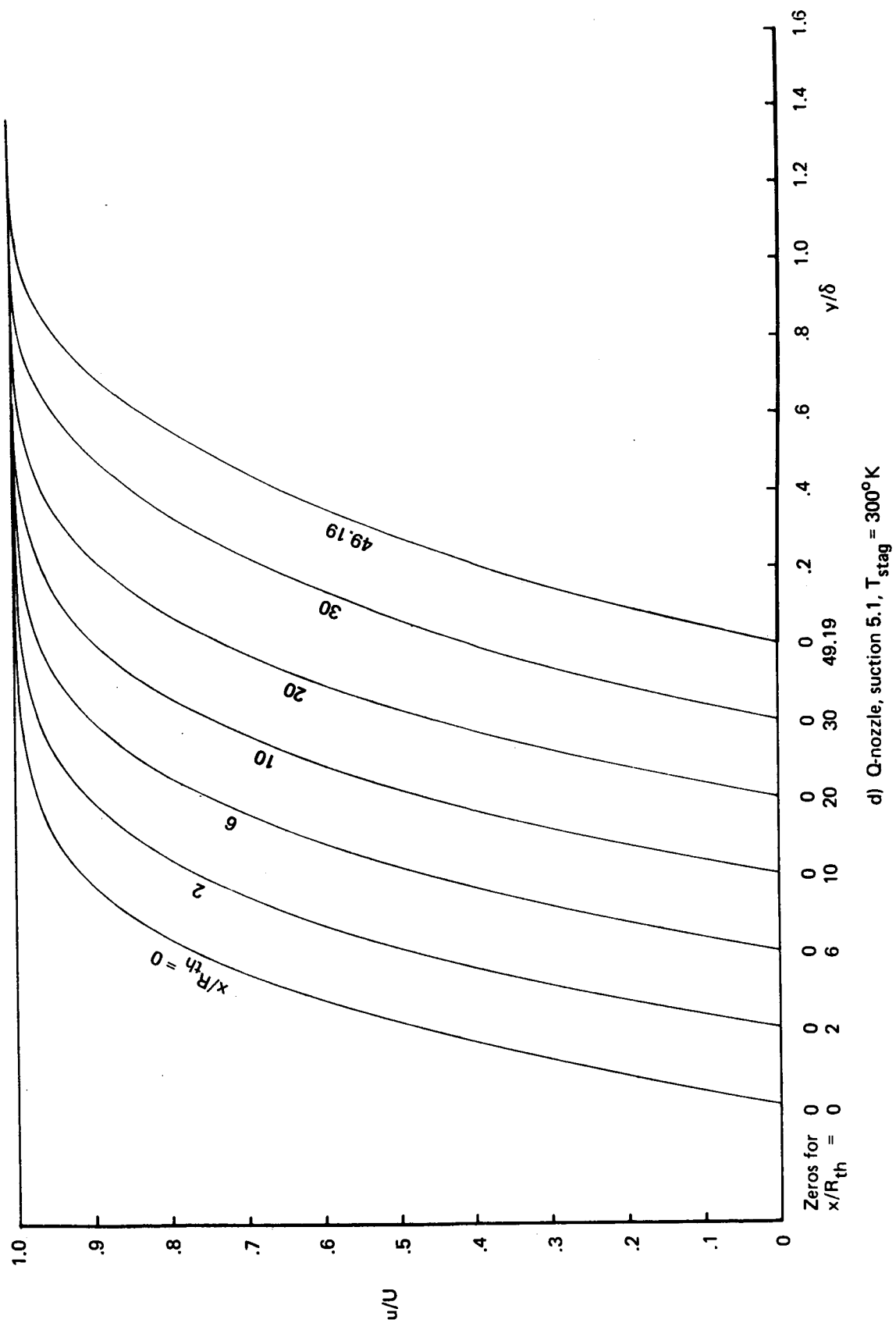
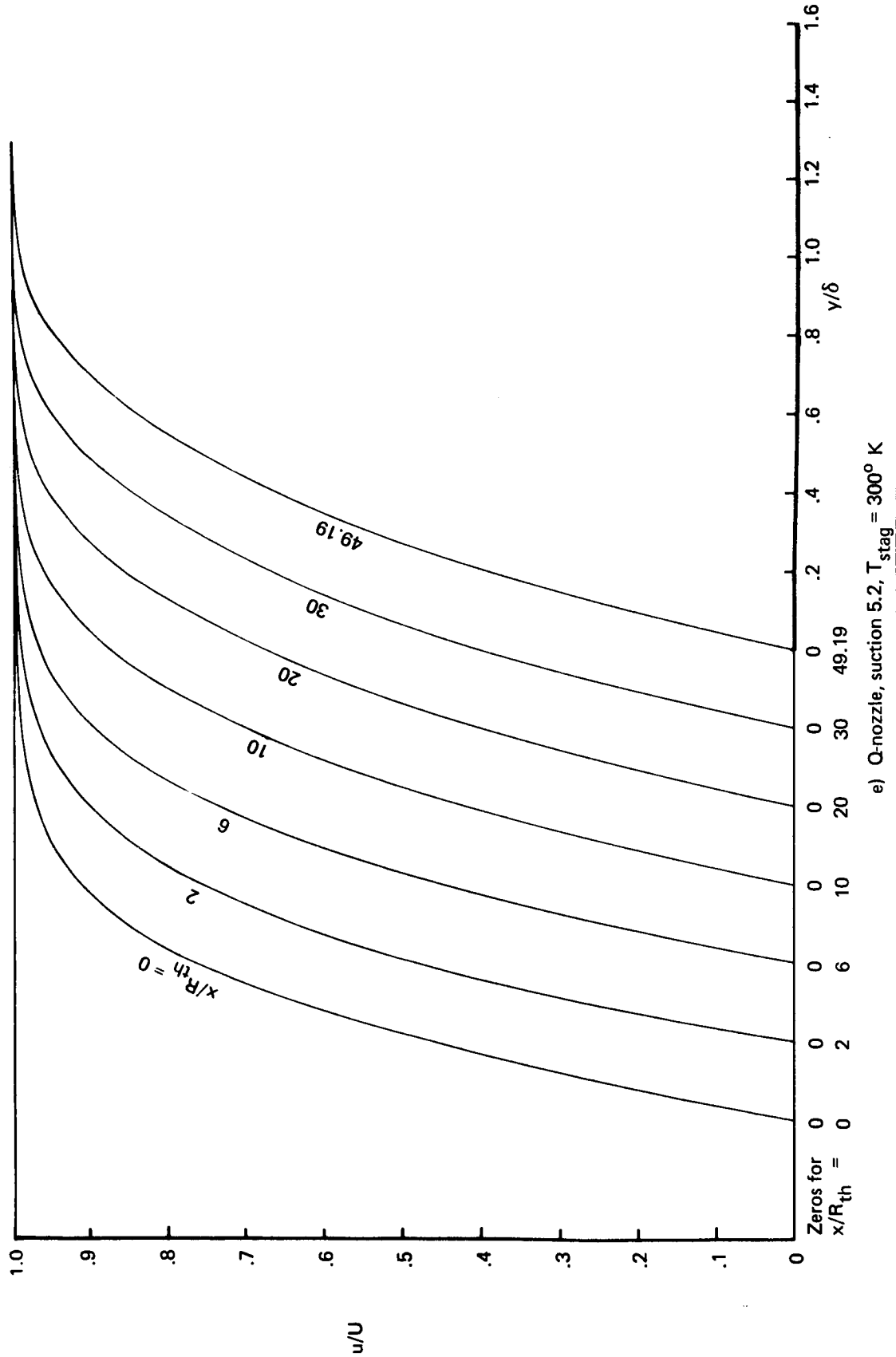


FIGURE 6.—NOZZLE WALL BOUNDARY LAYER VELOCITY PROFILES— $M^* = 5$ AXISYMMETRIC AIR NOZZLES (Continued)

FIGURE 6.—NOZZLE WALL BOUNDARY LAYER VELOCITY PROFILES— $M^* = 5$ AXISYMMETRIC AIR NOZZLES (Continued)

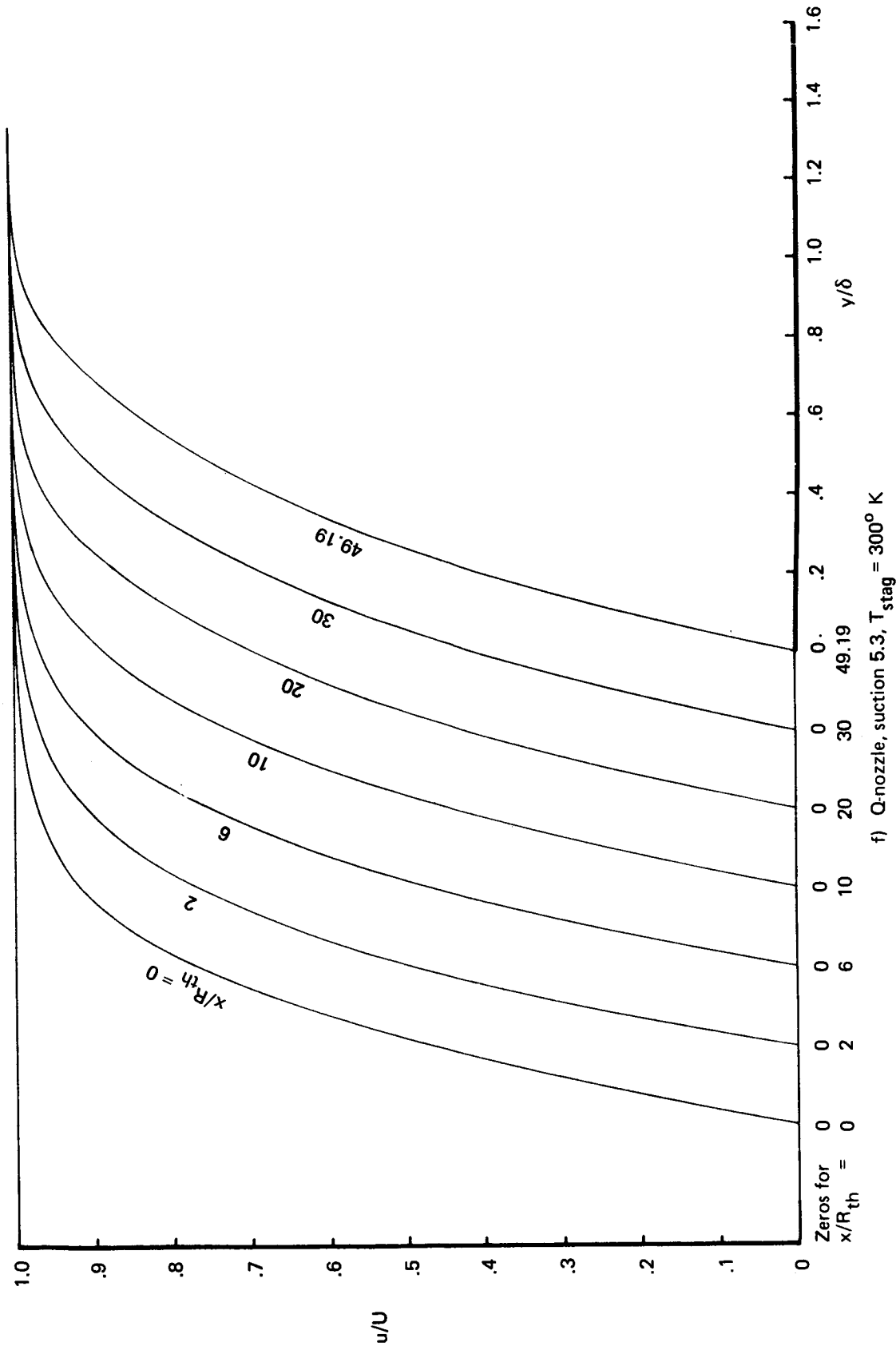


FIGURE 6.—NOZZLE WALL BOUNDARY LAYER VELOCITY PROFILES— $M^* = 5$ AXISYMMETRIC AIR NOZZLES (Continued)

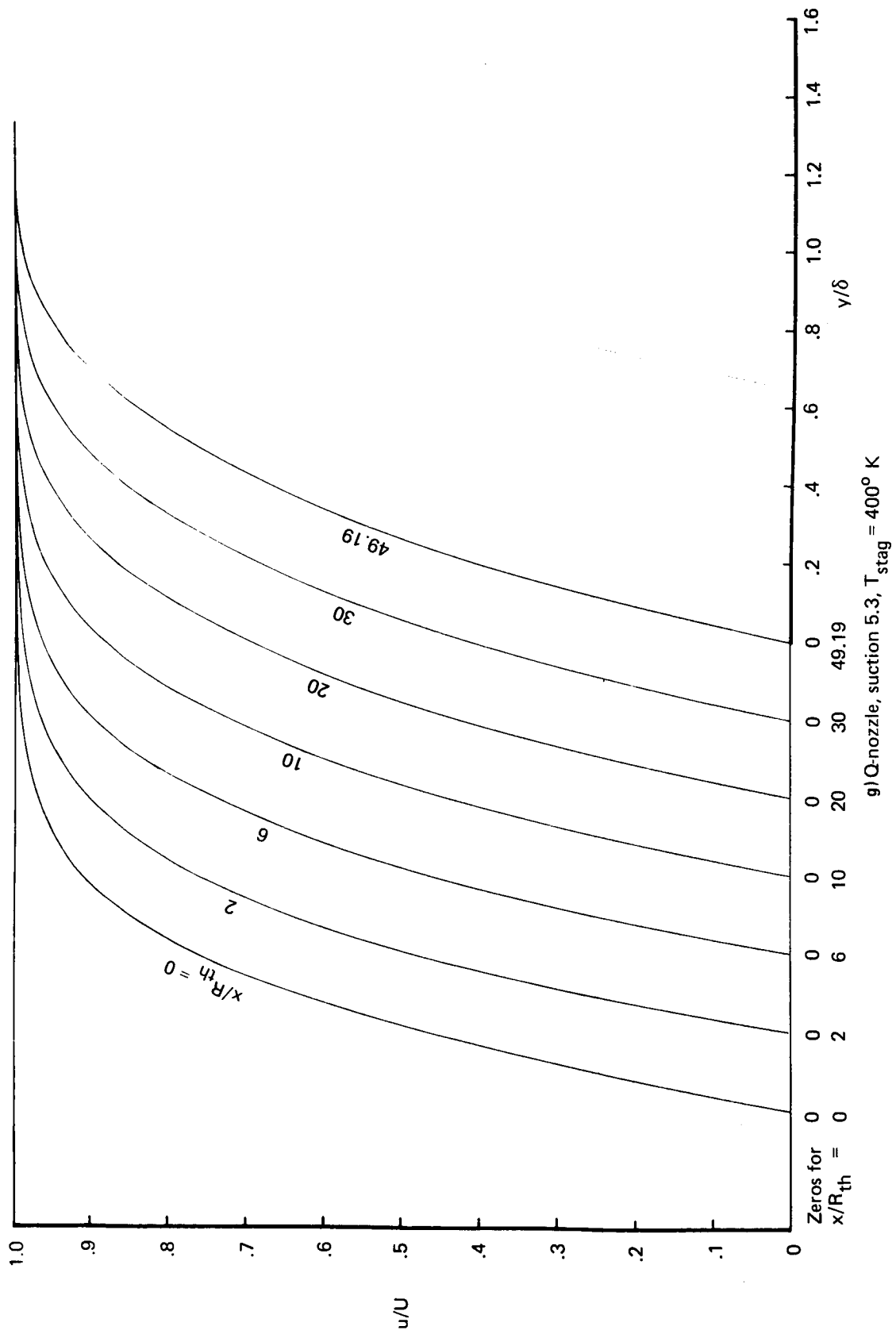


FIGURE 6.—NOZZLE WALL BOUNDARY LAYER VELOCITY PROFILES— $M^* = 5$ AXISYMMETRIC AIR NOZZLES (Continued)

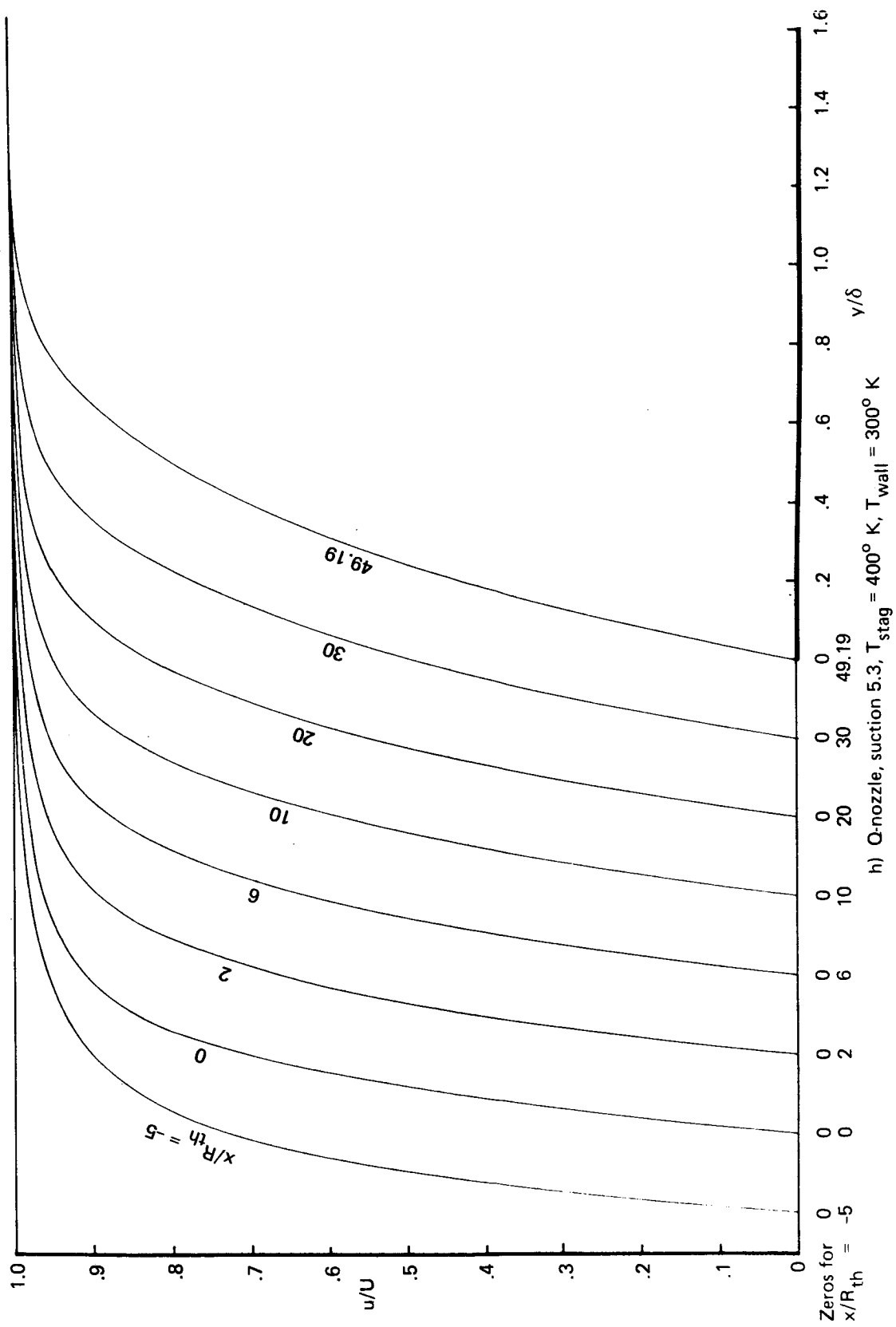


FIGURE 6.—NOZZLE WALL BOUNDARY LAYER VELOCITY PROFILES— $M^* = 5$ AXISYMMETRIC AIR NOZZLES (Concluded)

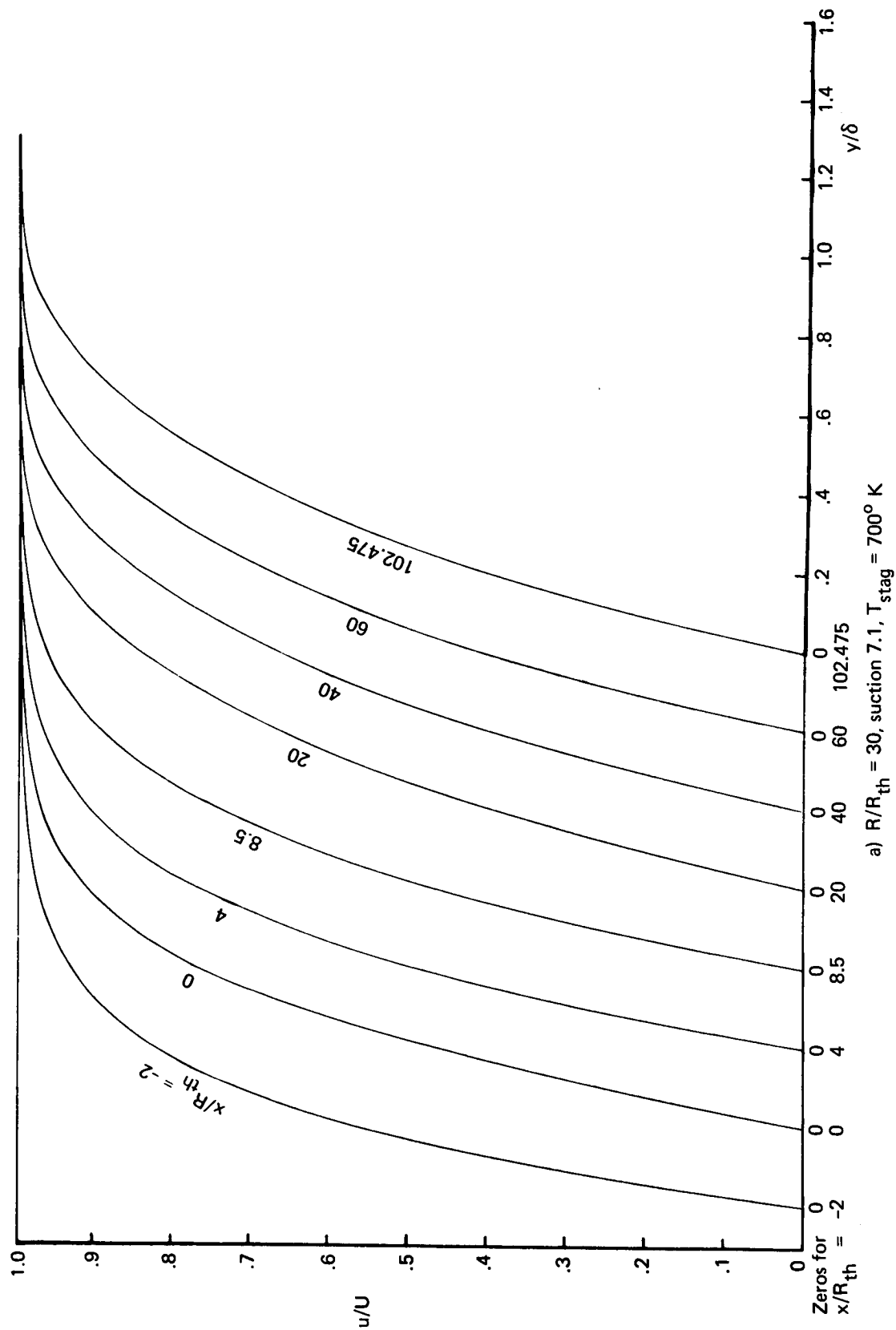


FIGURE 7.—NOZZLE WALL BOUNDARY LAYER VELOCITY PROFILES— $M^* = 7$ AXISYMMETRIC AIR NOZZLES

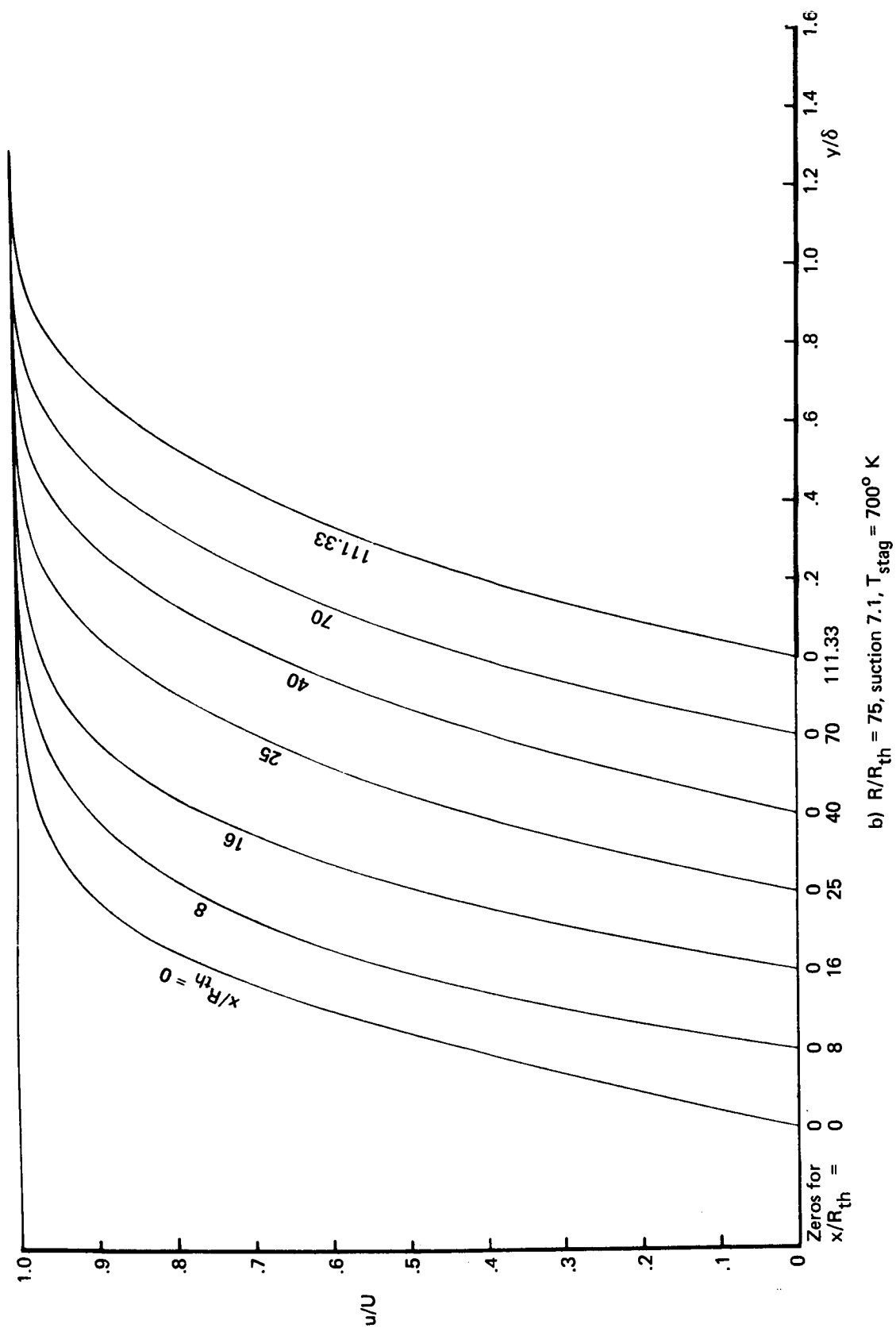
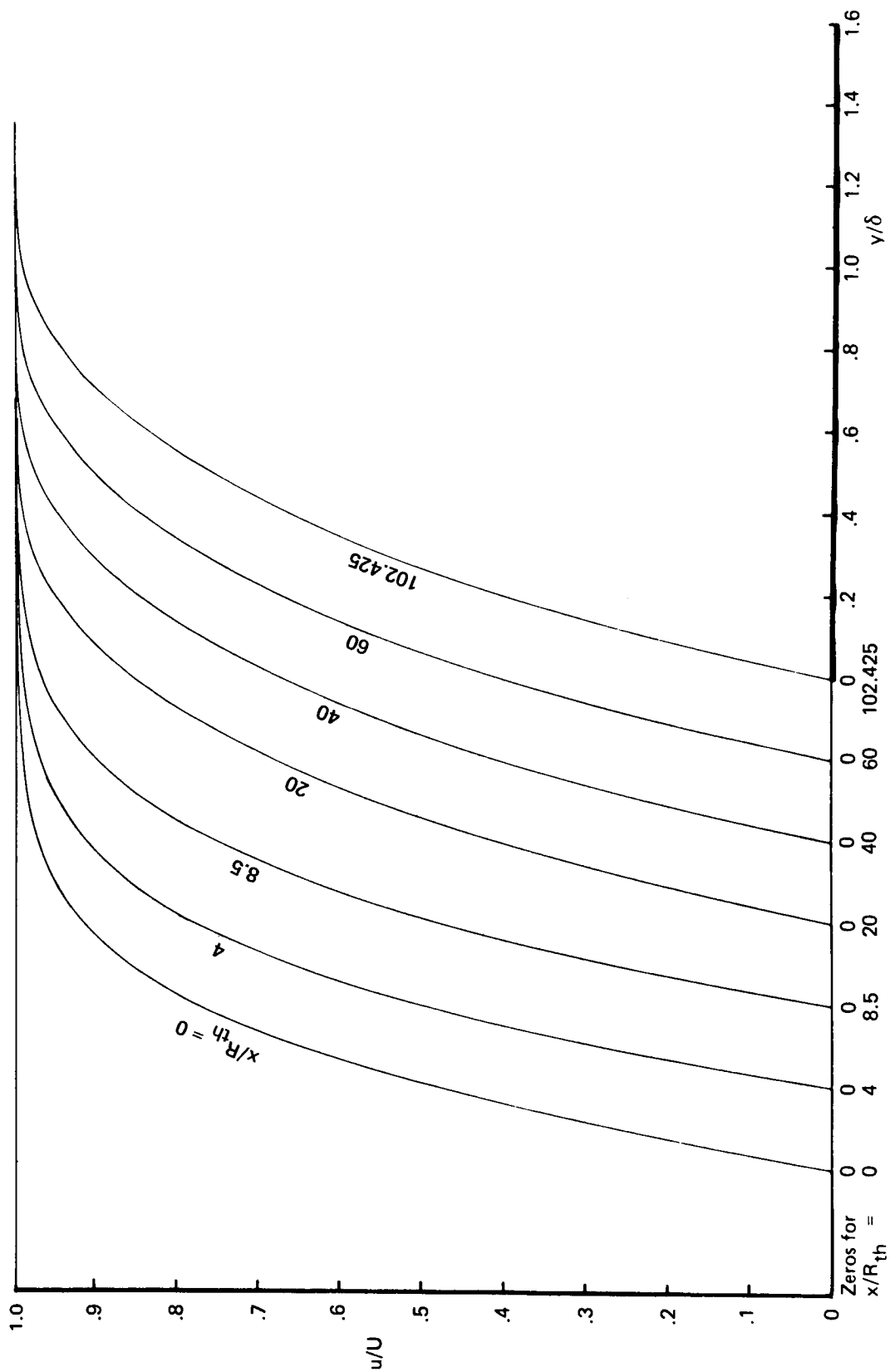


FIGURE 7.—NOZZLE WALL BOUNDARY LAYER VELOCITY PROFILES— $M^* = 7$ AXISYMMETRIC AIR NOZZLES (Continued)



c) $R/R_{th} = 30$, suction 7.2, $T_{stag} = 700^\circ K$

FIGURE 7.—NOZZLE WALL BOUNDARY LAYER VELOCITY PROFILES— $M^* = 7$ AXISYMMETRIC AIR NOZZLES (Concluded)

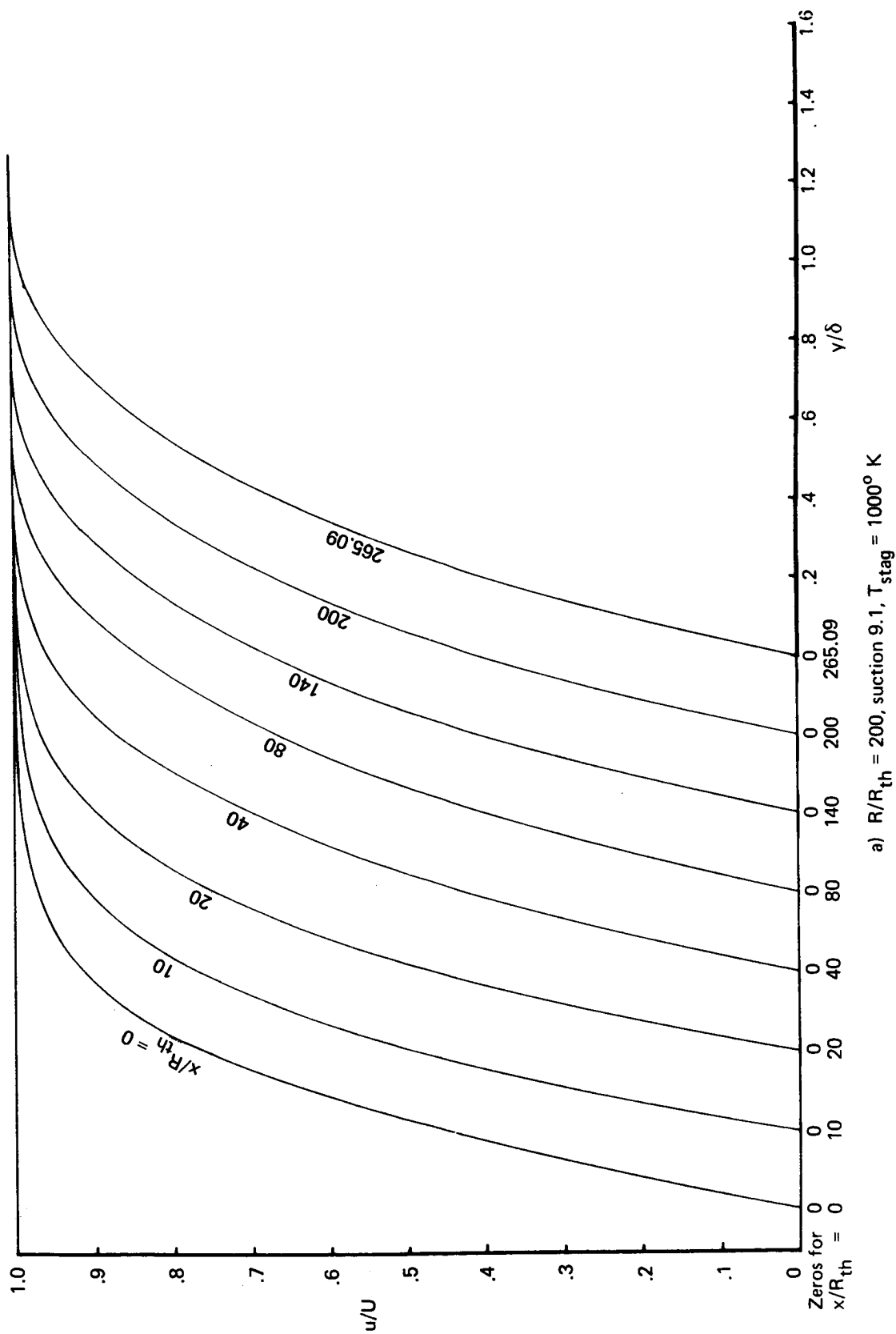


FIGURE 8.—NOZZLE WALL BOUNDARY LAYER VELOCITY PROFILES— $M^* = 9$ AXISYMMETRIC AIR NOZZLES

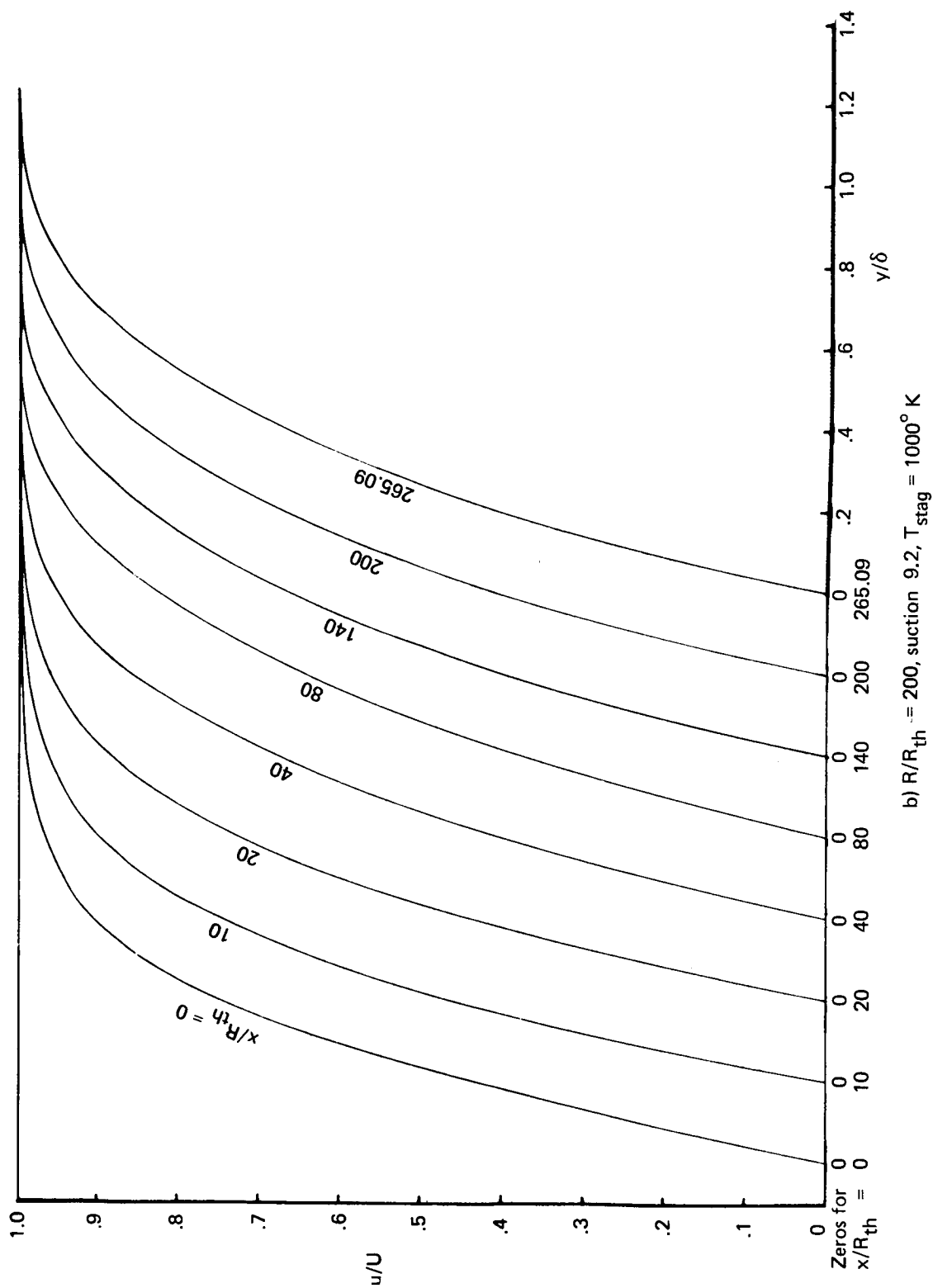


FIGURE 8.—NOZZLE WALL BOUNDARY LAYER VELOCITY PROFILES— $M^* = 9$ AXISYMMETRIC AIR NOZZLES (Concluded)

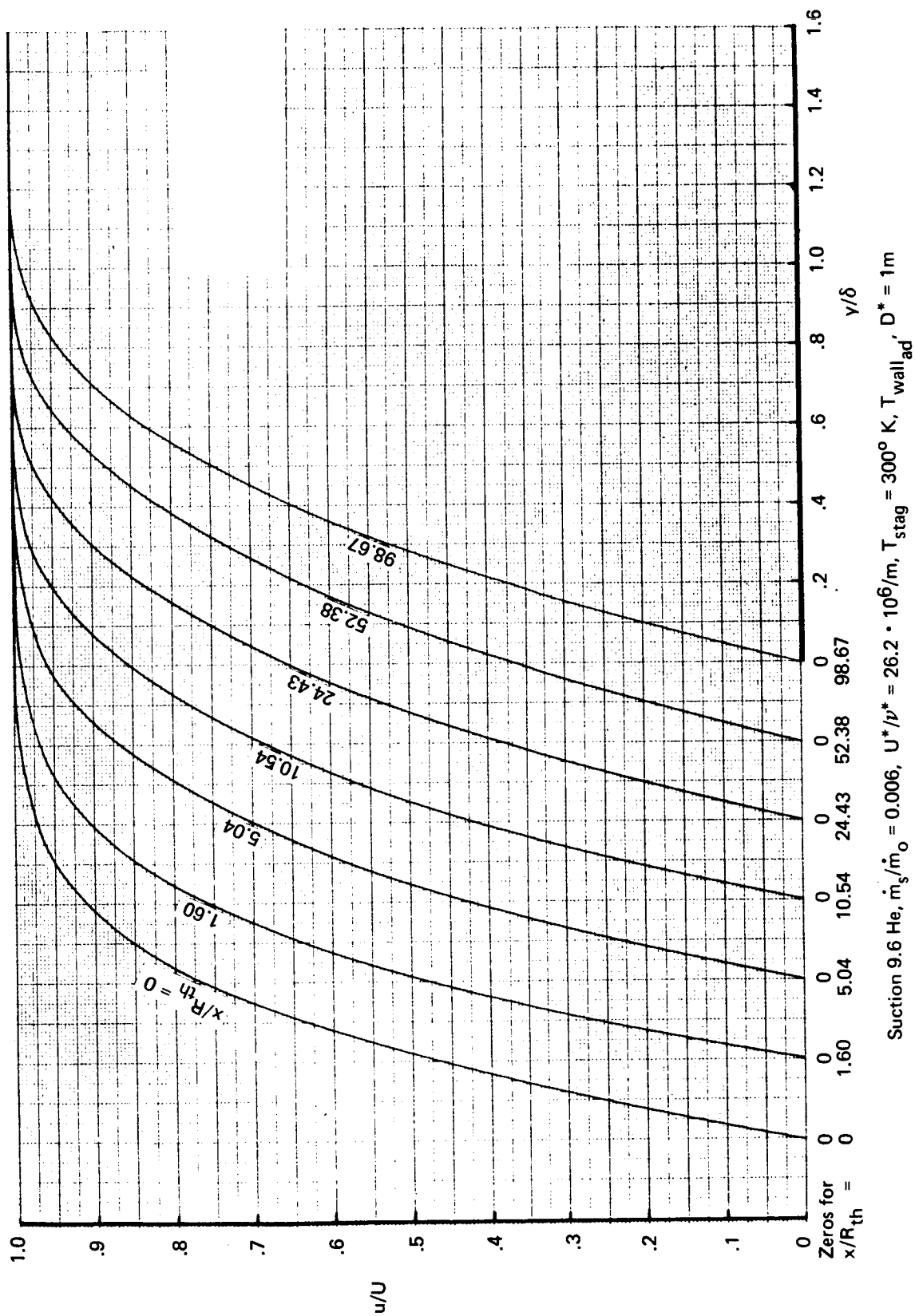
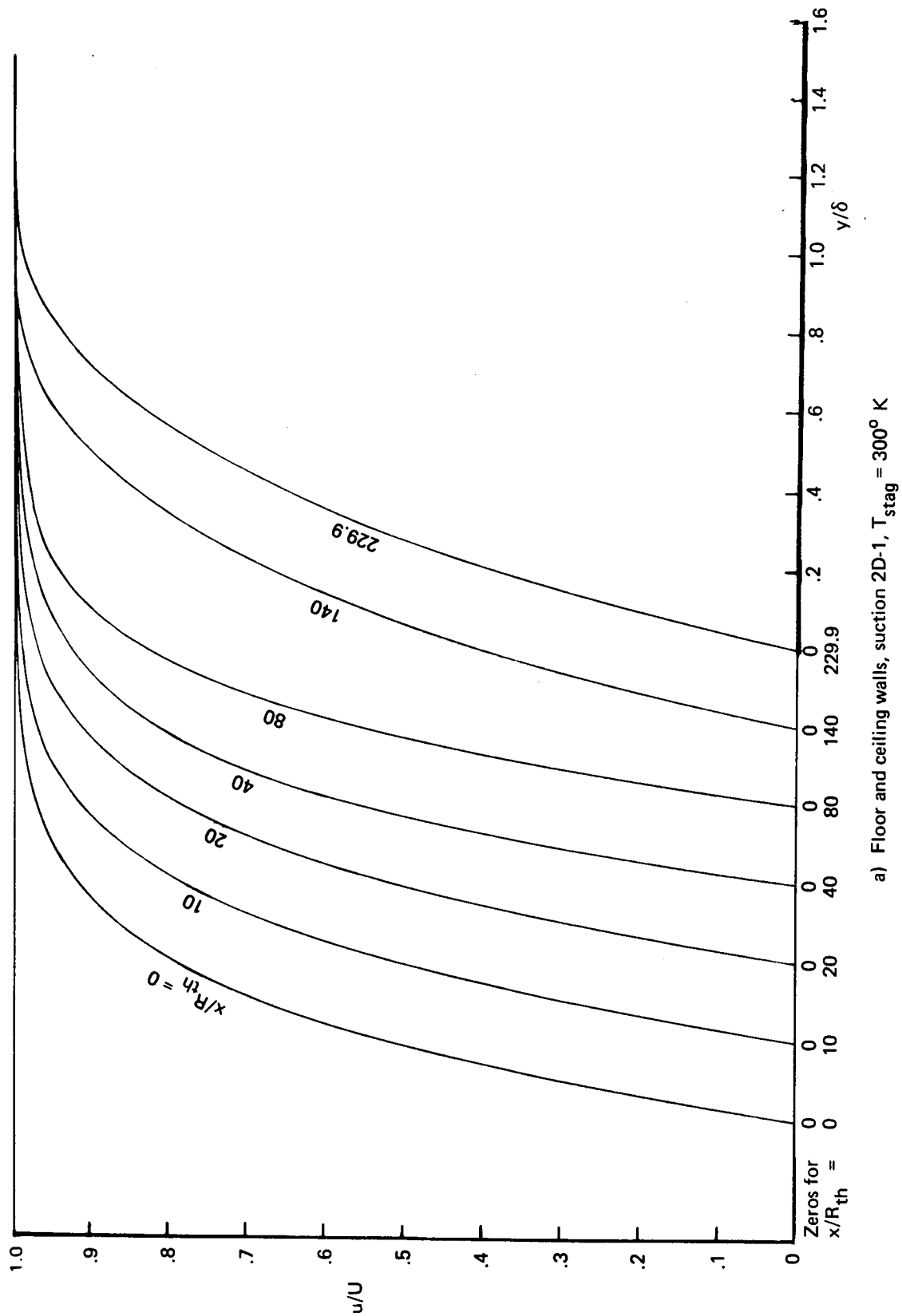
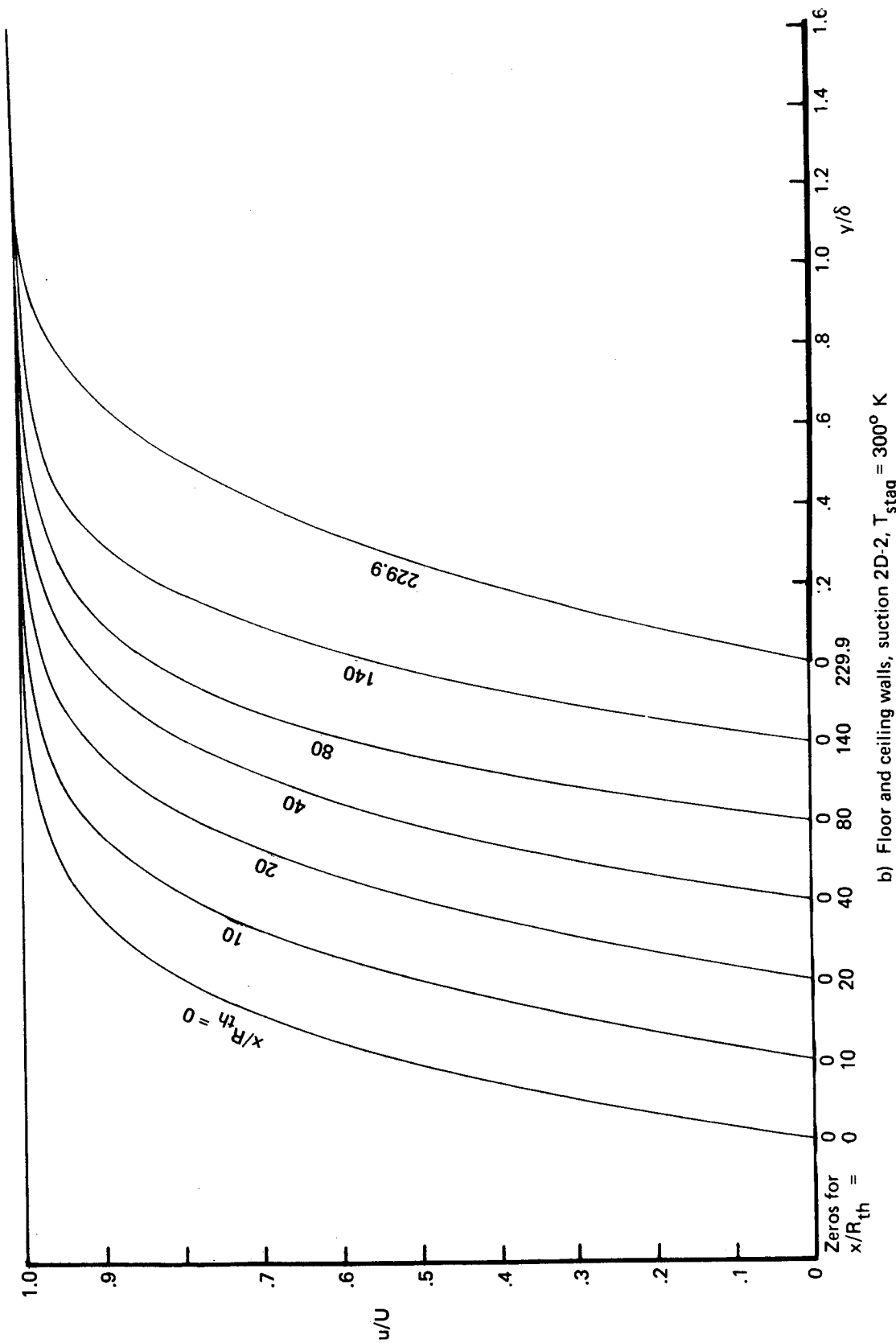


FIGURE 9.—NOZZLE WALL BOUNDARY LAYER VELOCITY PROFILES— $M^* = 9$ NASA AXISYMMETRIC HELIUM NOZZLE



a) Floor and ceiling walls, suction 2D-1, $T_{stag} = 300^\circ K$

FIGURE 10.—NOZZLE WALL BOUNDARY LAYER VELOCITY PROFILES— $M^* = 4.6$ TWO-DIMENSIONAL JPL NOZZLE



b) Floor and ceiling walls, suction 2D-2, $T_{stag} = 300^\circ K$

FIGURE 10.—NOZZLE WALL BOUNDARY LAYER VELOCITY PROFILES—
 $M^* = 4.6$ TWO-DIMENSIONAL JPL NOZZLE (Continued)

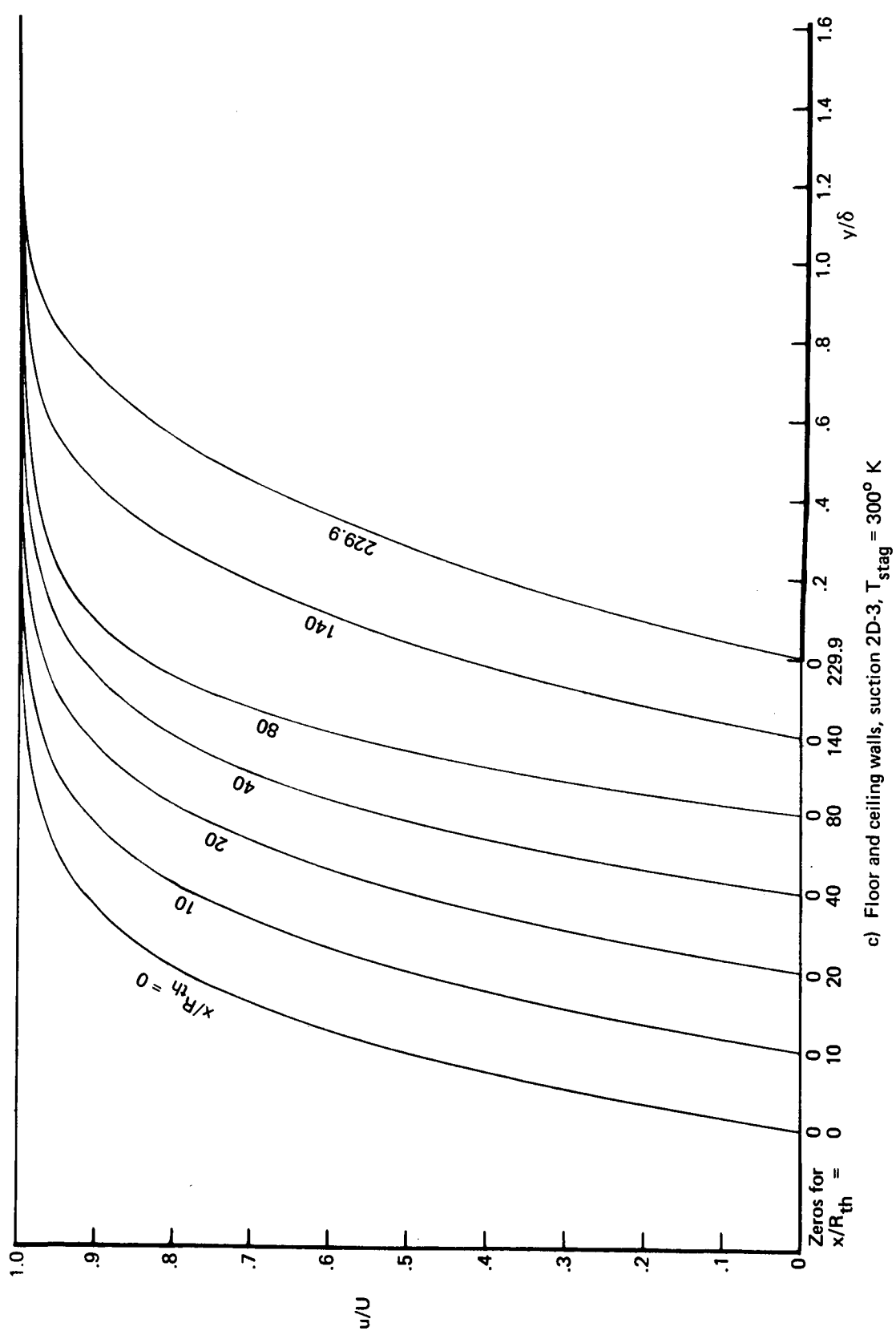
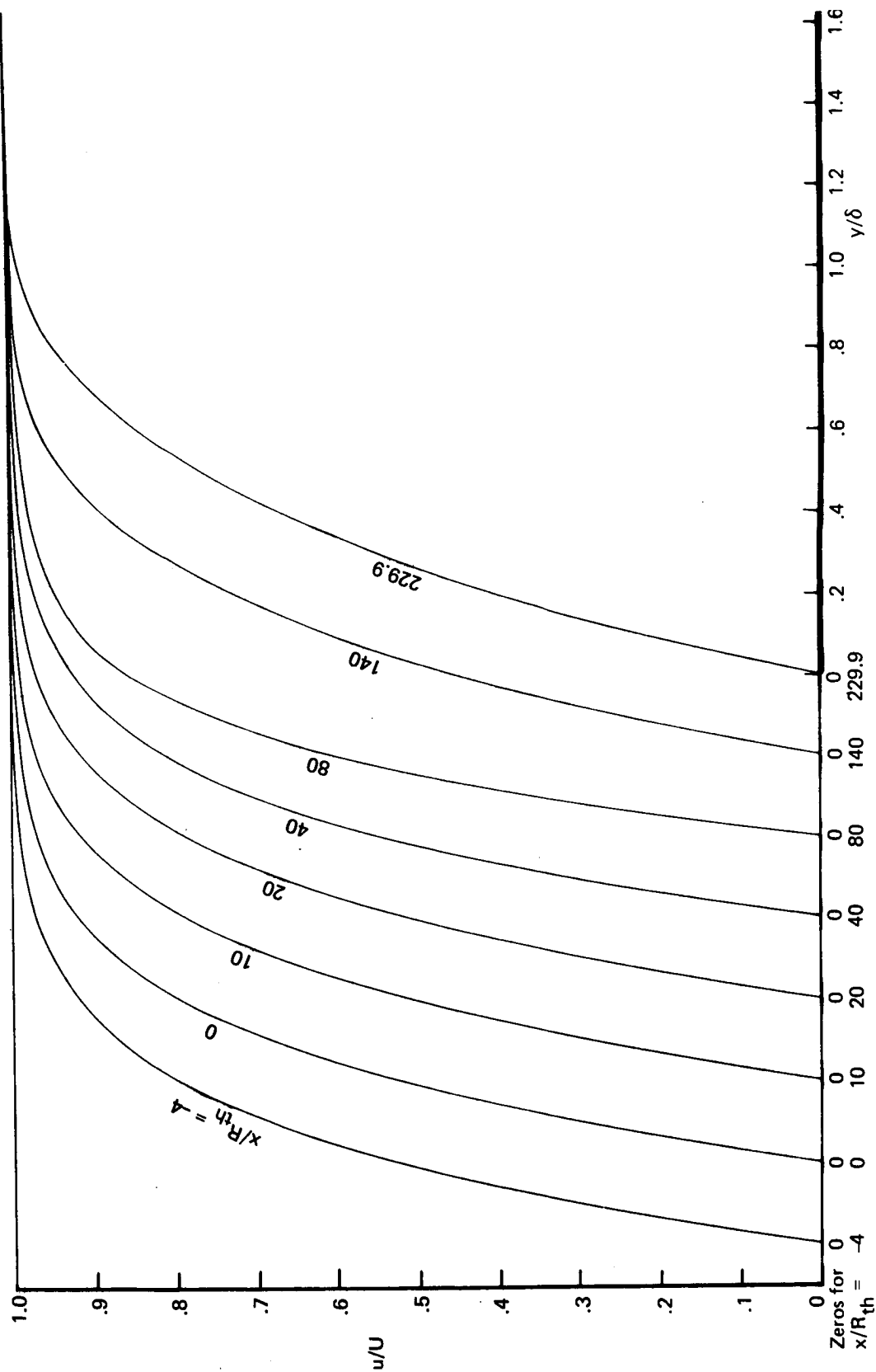


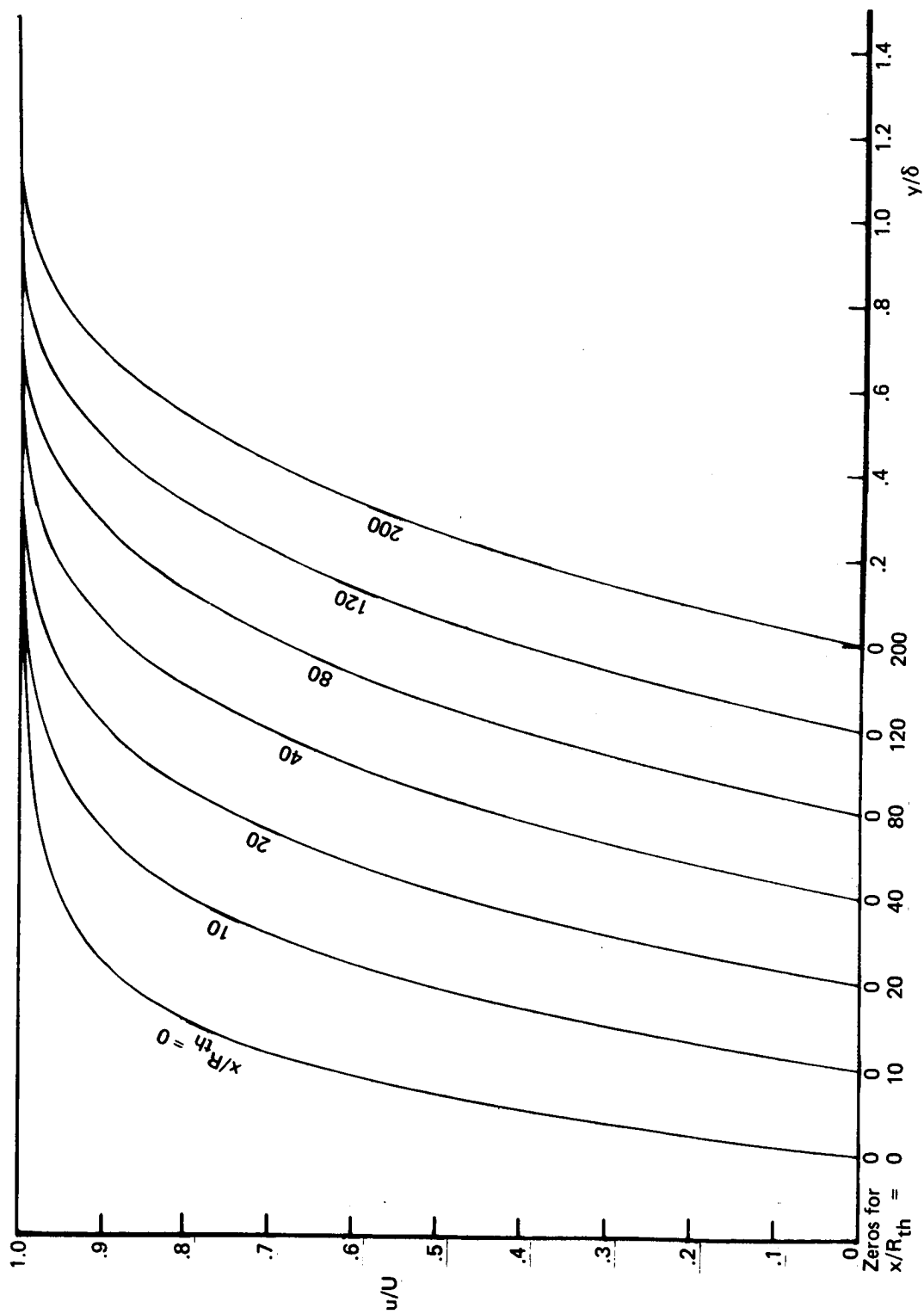
FIGURE 10.—NOZZLE WALL BOUNDARY LAYER VELOCITY PROFILES—
 $M^* = 4.6$ TWO-DIMENSIONAL JPL NOZZLE (Continued)



d) Floor and ceiling walls, suction 2D-3, $T_{stag} = 400^\circ K$

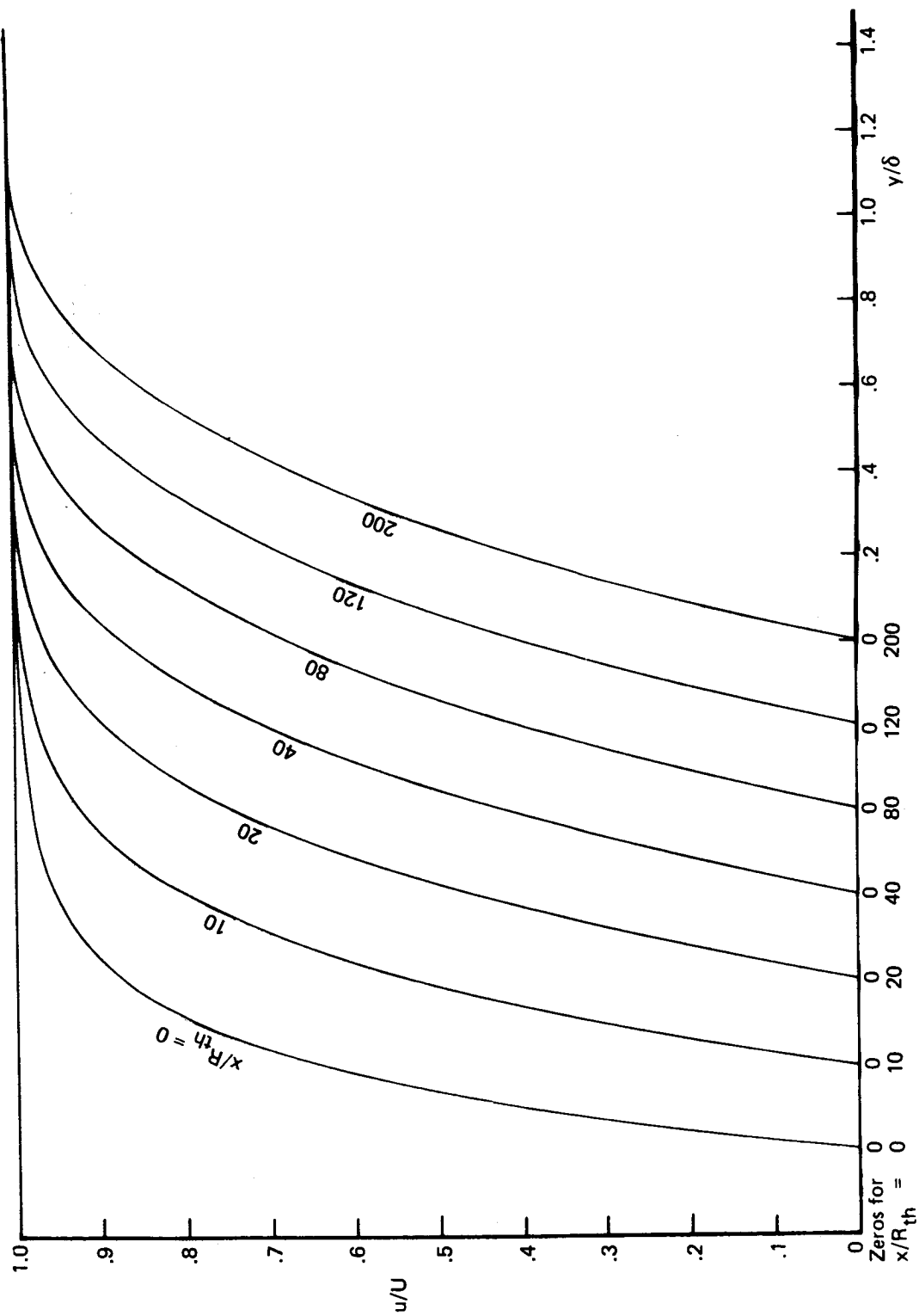
FIGURE 10.—NOZZLE WALL BOUNDARY LAYER VELOCITY PROFILES—

$M^* = 4.6$ TWO-DIMENSIONAL JPL NOZZLE (Continued)



e) Side walls, 25% streamline, section 2D-9

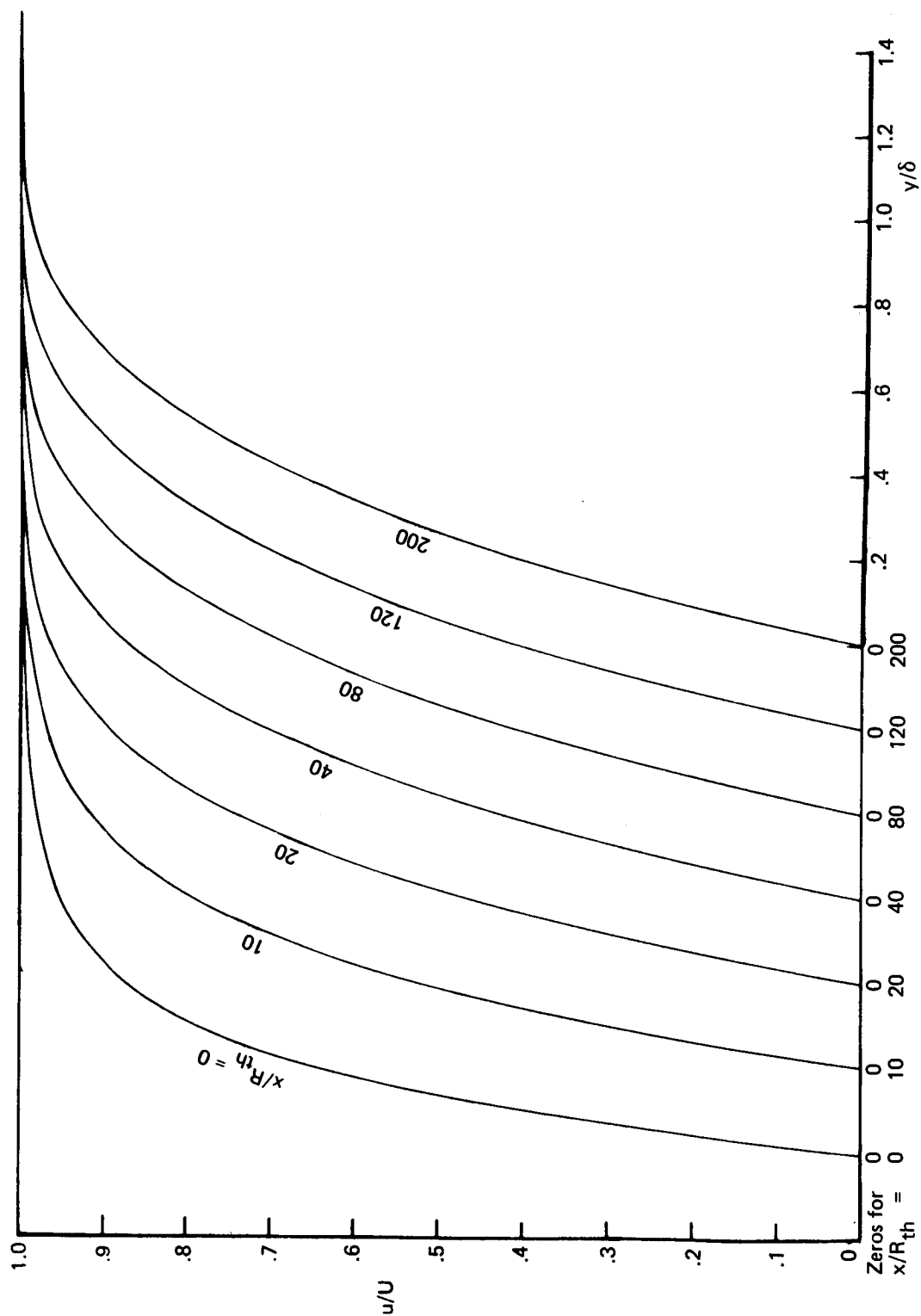
FIGURE 10.—NOZZLE WALL BOUNDARY LAYER VELOCITY PROFILES—
 $M^* = 4.6$ TWO-DIMENSIONAL JPL NOZZLE (Continued)



f) Side walls, 25% streamline, suction 2D-10

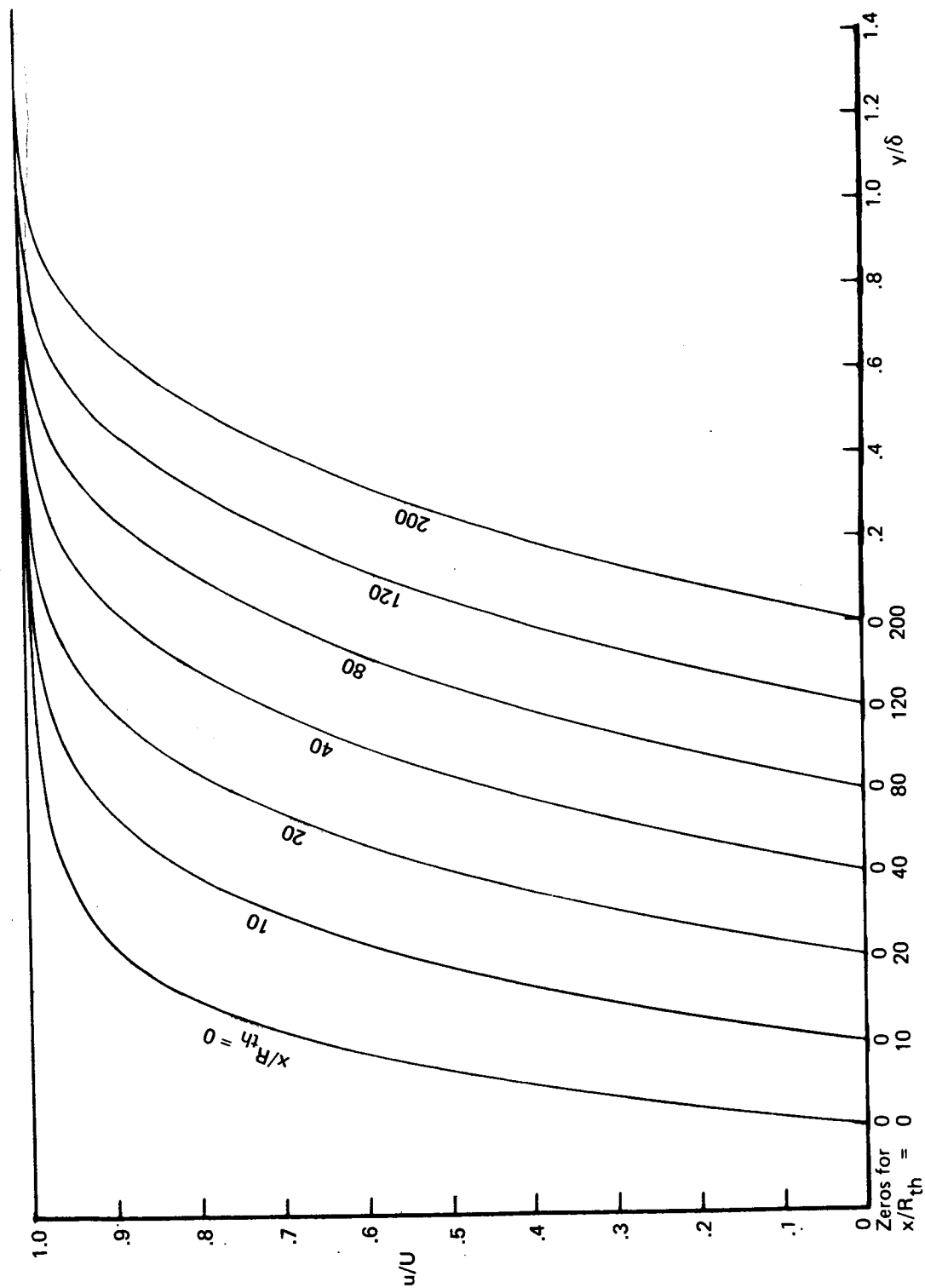
FIGURE 10.—NOZZLE WALL BOUNDARY LAYER VELOCITY PROFILES—

$M^* = 4.6$ TWO-DIMENSIONAL JPL NOZZLE (Continued)



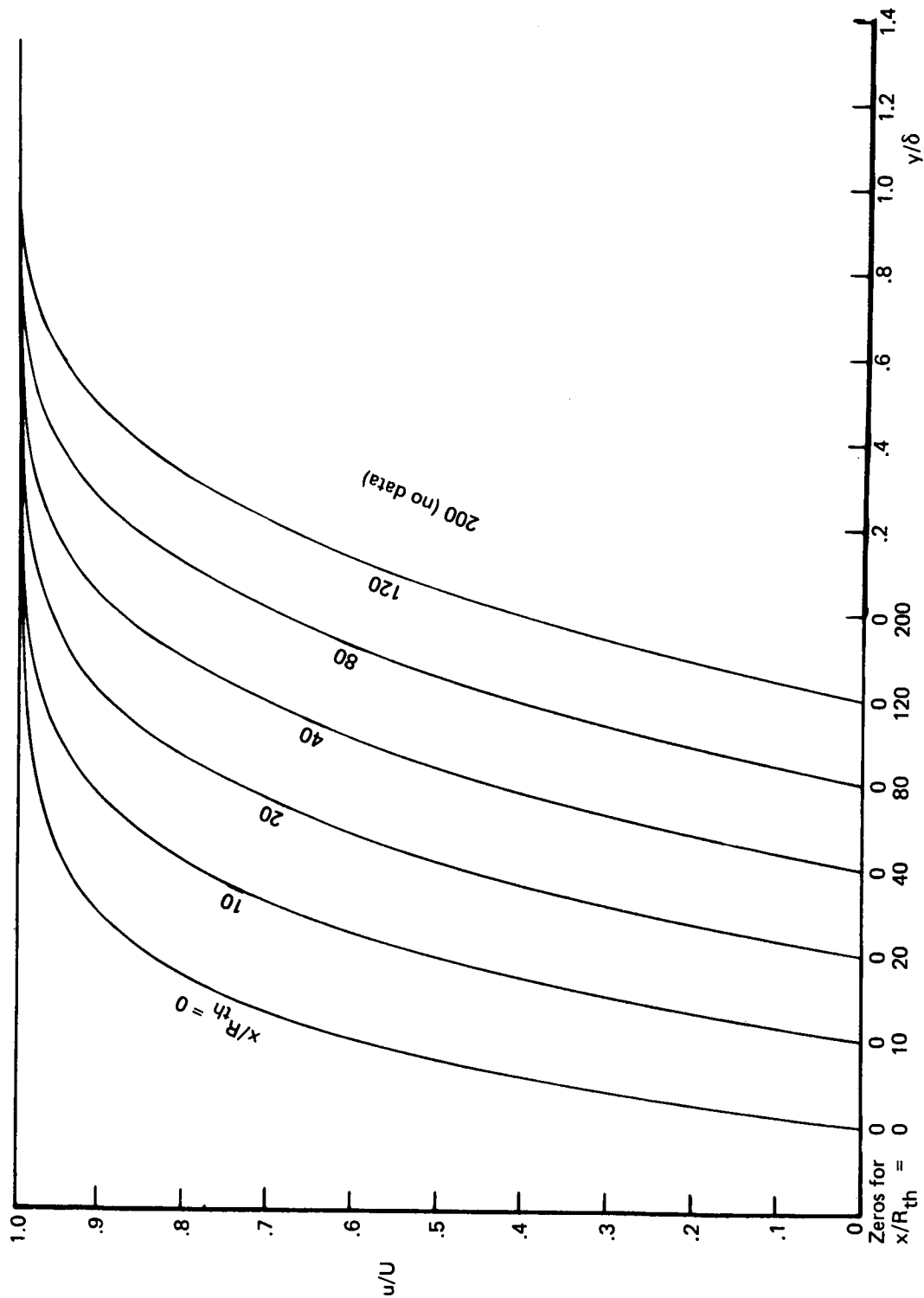
g) Side walls, 50% streamline, suction 2D-9

FIGURE 10.—NOZZLE WALL BOUNDARY LAYER VELOCITY PROFILES—
 $M^* = 4.6$ TWO-DIMENSIONAL JPL NOZZLE (Continued)



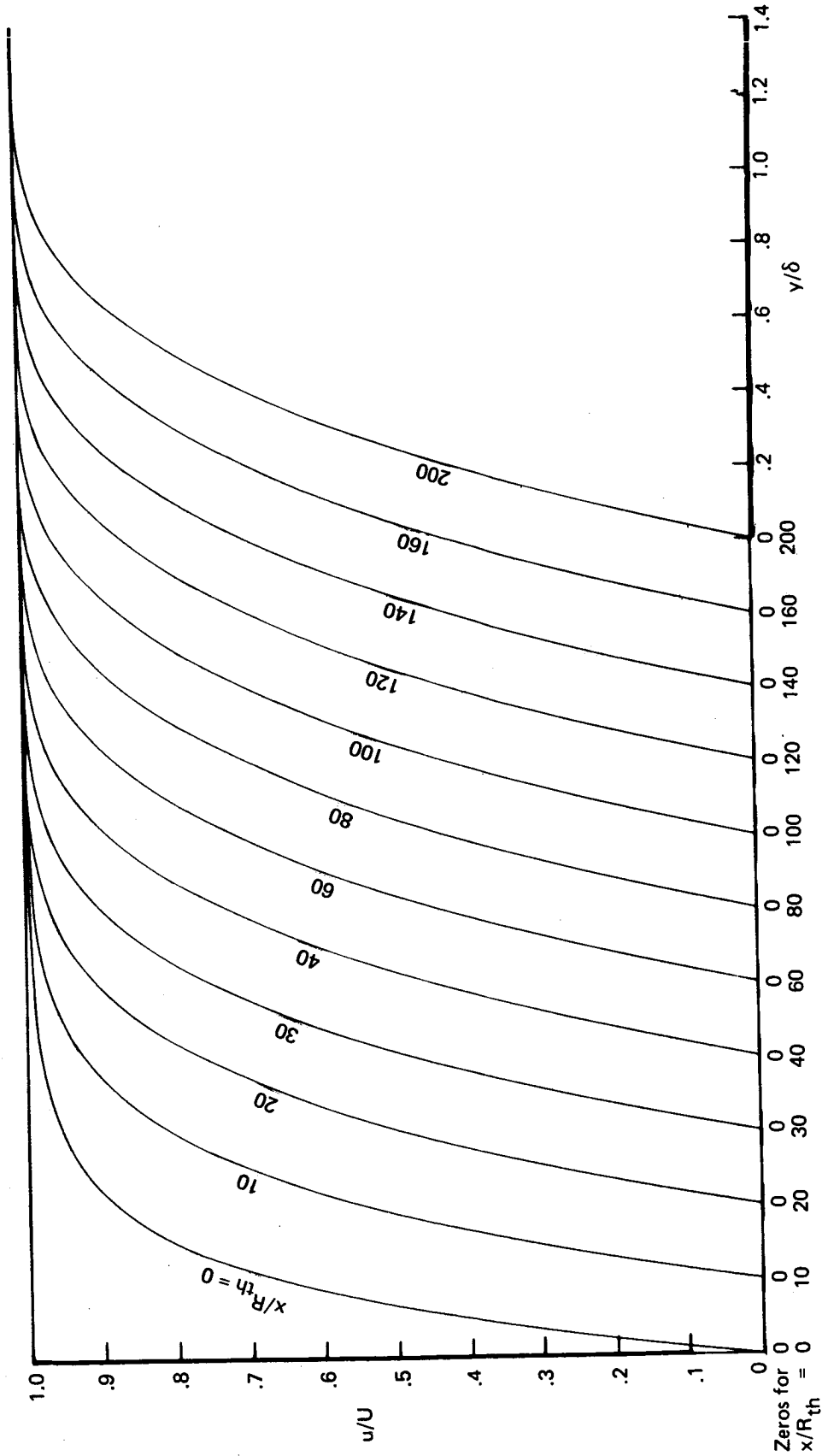
h) Side walls, 50% streamline, suction 2D-11

FIGURE 10.—NOZZLE WALL BOUNDARY LAYER VELOCITY PROFILES—
 $M^* = 4.6$ TWO-DIMENSIONAL JPL NOZZLE (Continued)



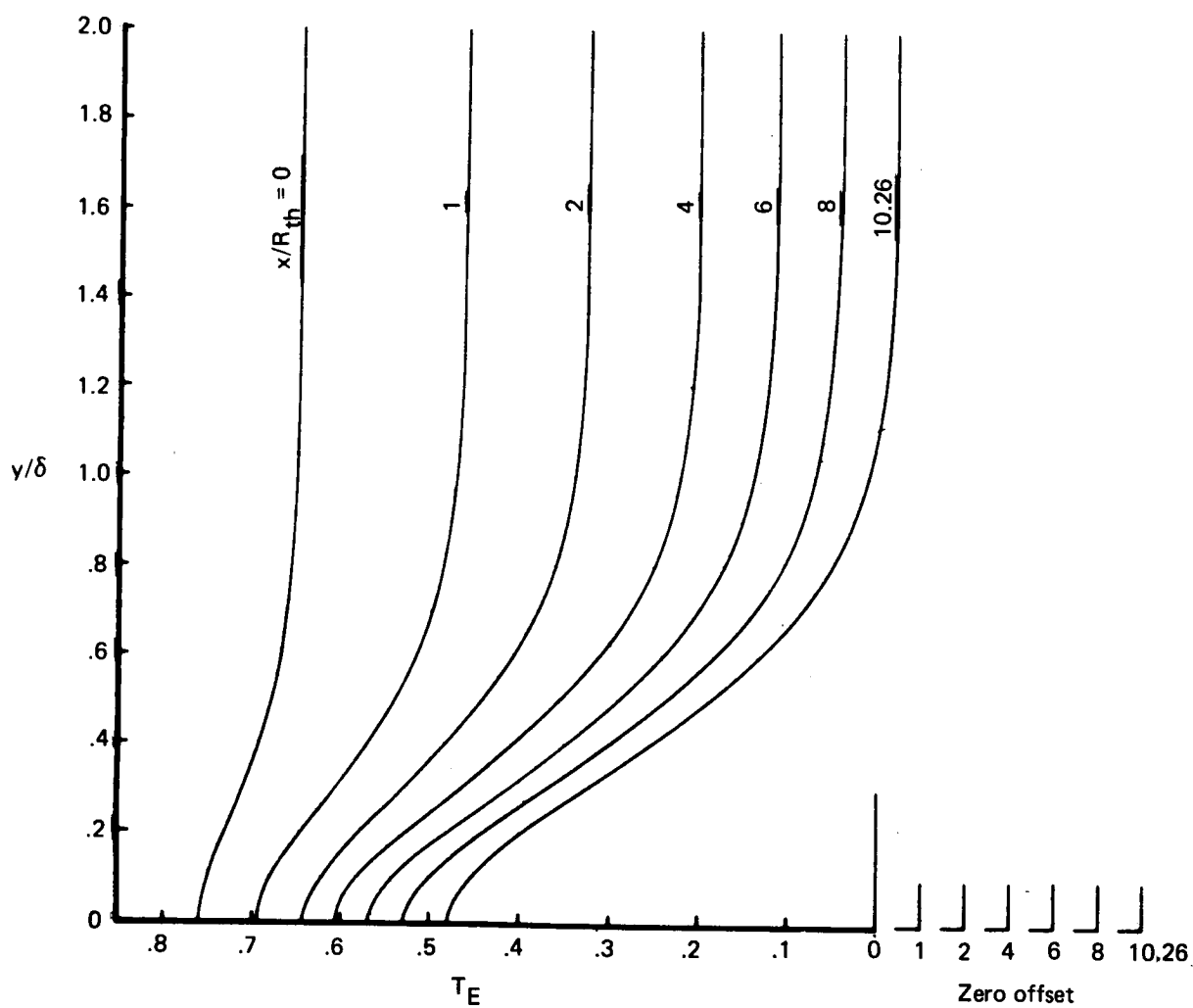
i) Side walls, 75% streamline, section 2D-7

FIGURE 10.—NOZZLE WALL BOUNDARY LAYER VELOCITY PROFILES—
 $M^* = 4.6$ TWO-DIMENSIONAL JPL NOZZLE (Continued)



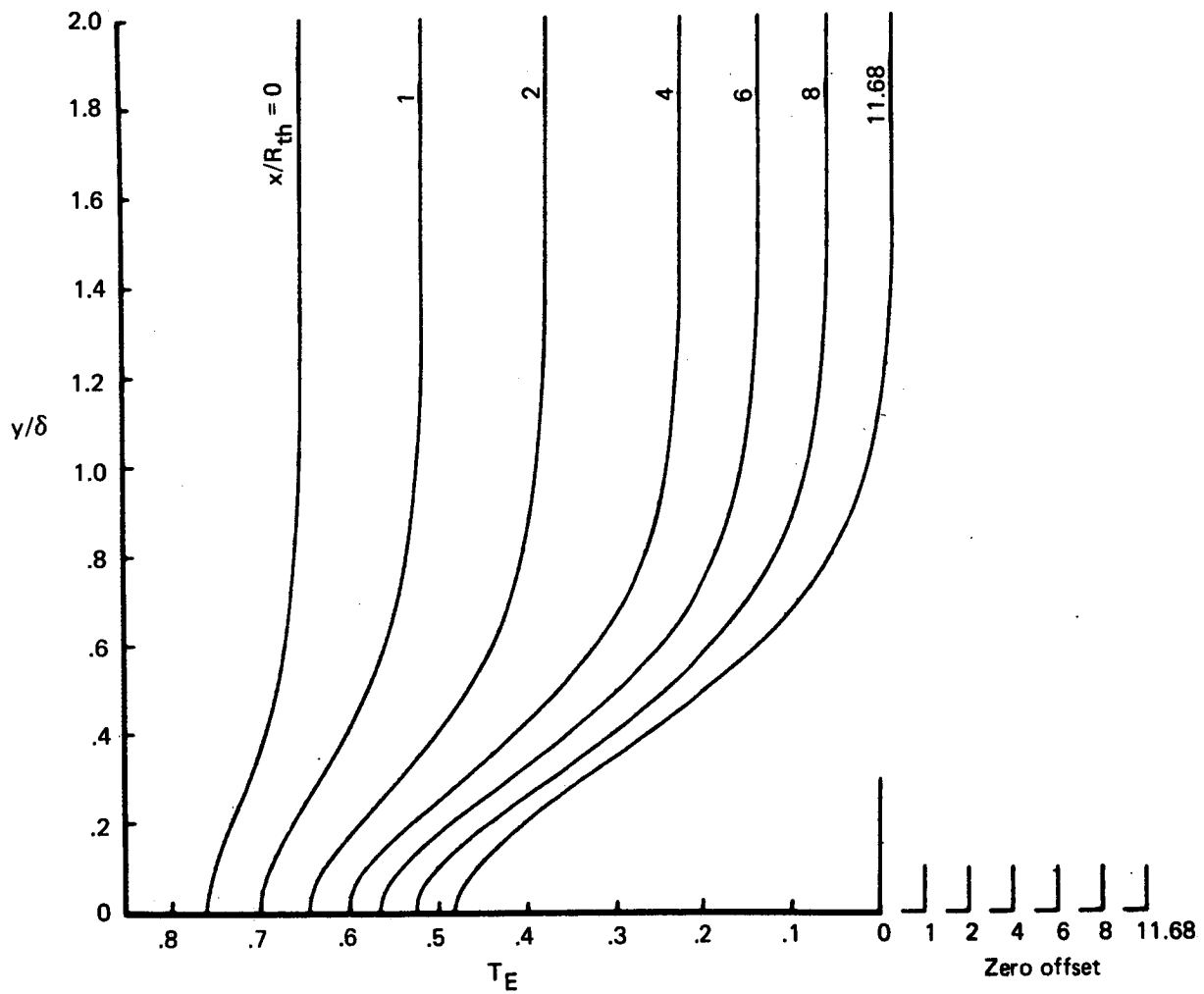
j) Side walls, 75% streamline, section 2D-8

FIGURE 10.—NOZZLE WALL BOUNDARY LAYER VELOCITY PROFILES—
 $M^* = 4.6$ TWO-DIMENSIONAL JPL NOZZLE (Concluded)



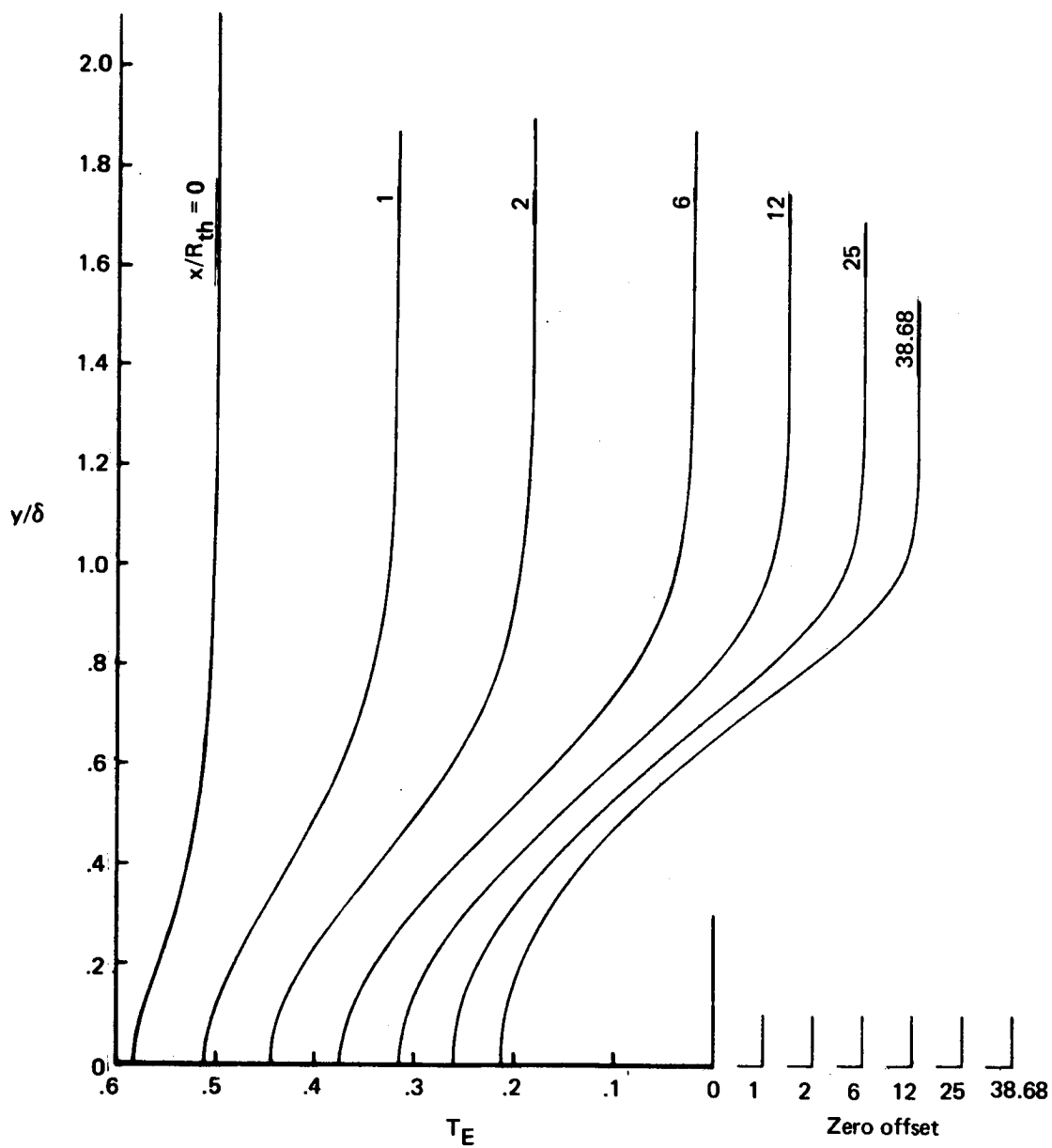
a) $M^* = 3$, $R/R_{th} = 6$, suction 5, $T_{stag} = 300^\circ \text{ K}$

FIGURE 11.—NOZZLE WALL BOUNDARY LAYER TEMPERATURE PROFILES



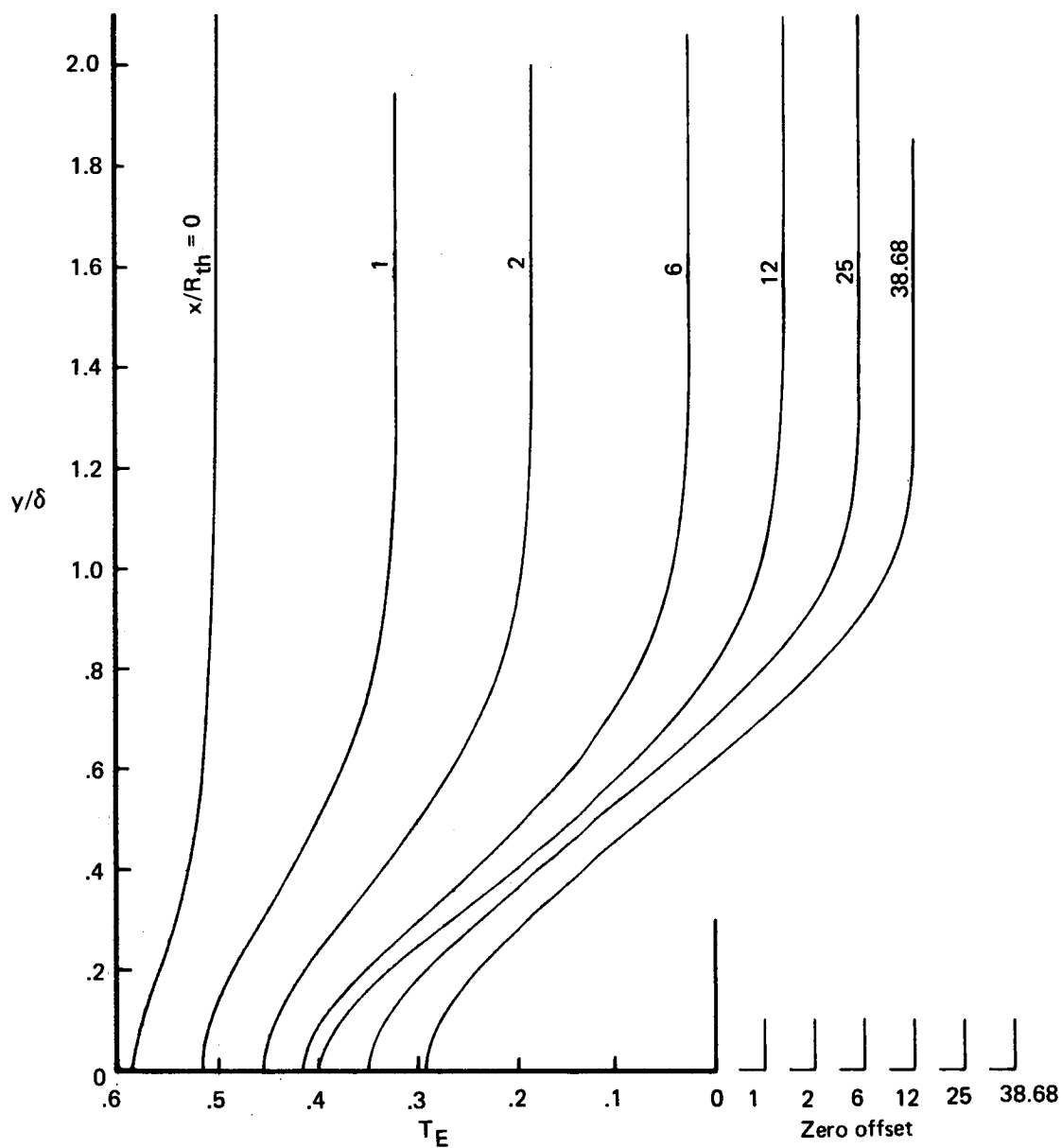
b) $M^* = 3$, $R/R_{th} = 12$, suction 5, $T_{stag} = 300^\circ \text{ K}$

FIGURE 11.—NOZZLE WALL BOUNDARY LAYER TEMPERATURE PROFILES (Continued)



c) $M^* = 5$ rapid expansion nozzle, no suction, $T_{stag} = 378^\circ \text{ K}$, $T_{wall_{ad}}$

FIGURE 11.—NOZZLE WALL BOUNDARY LAYER TEMPERATURE PROFILES (Continued)



d) $M^* = 5$ rapid expansion nozzle, suction 5.1, $T_{stag} = 300^\circ \text{ K}$, $T_{wall_{ad}}$

FIGURE 11.—NOZZLE WALL BOUNDARY LAYER TEMPERATURE PROFILES (Continued)

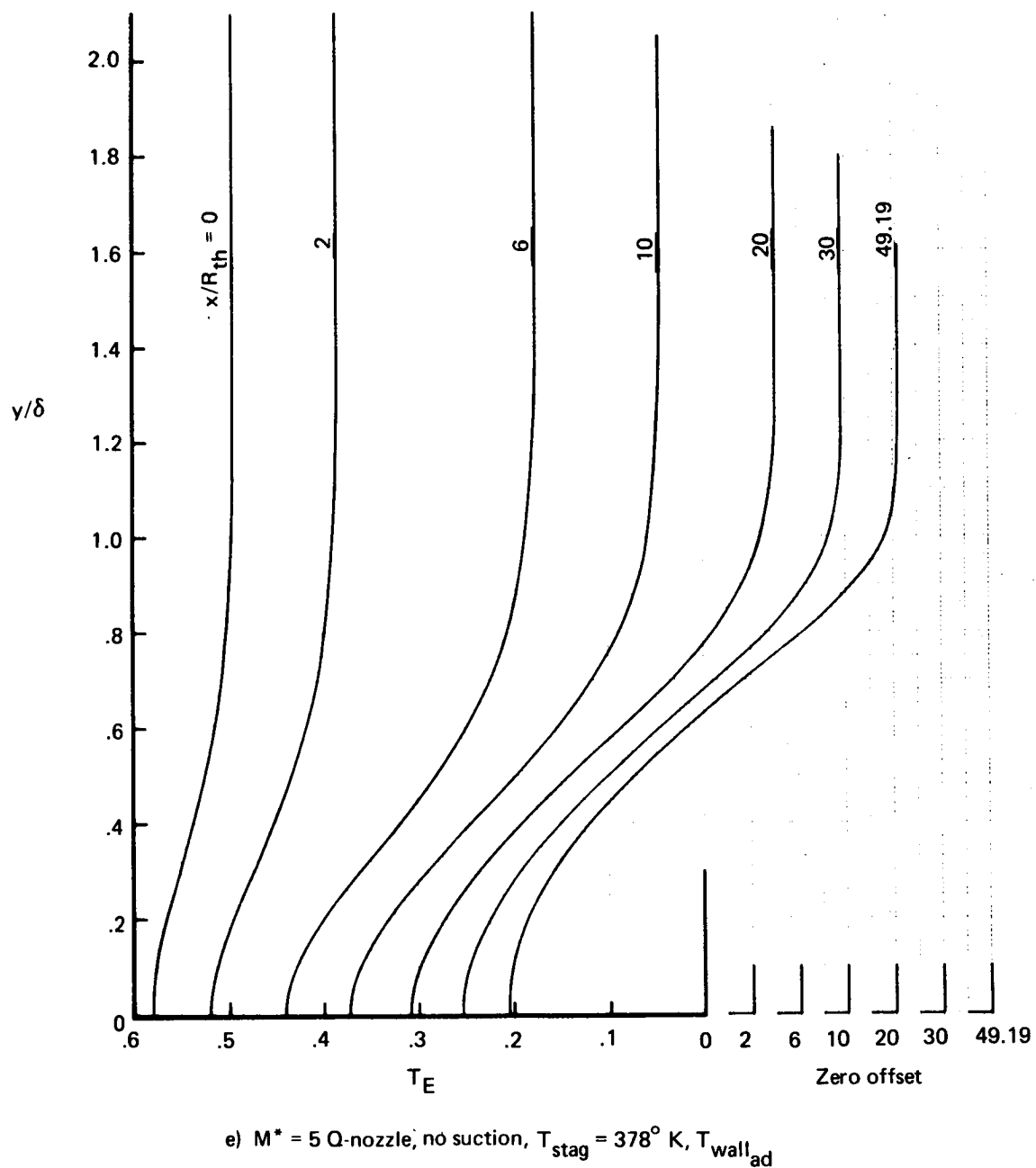
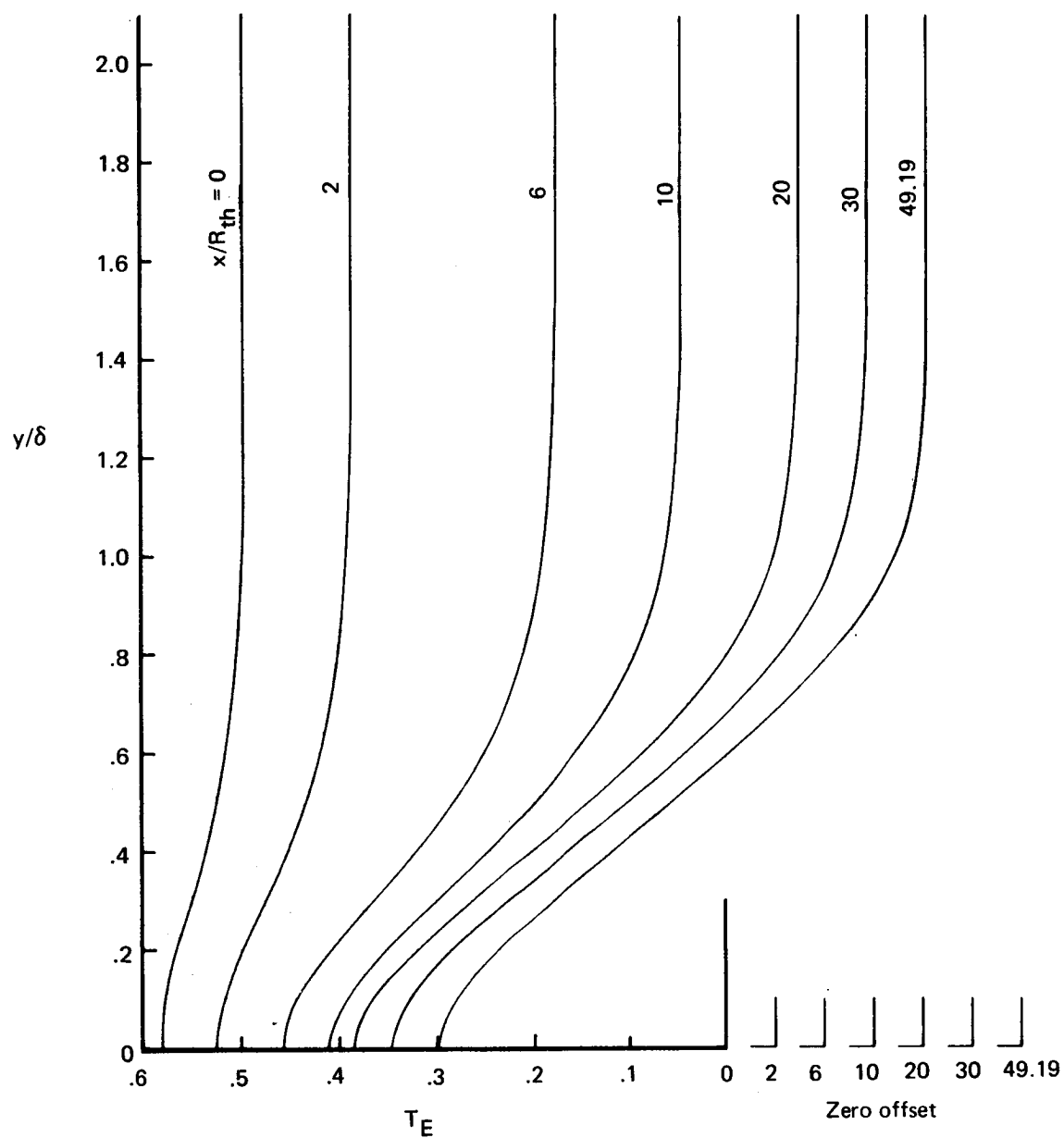
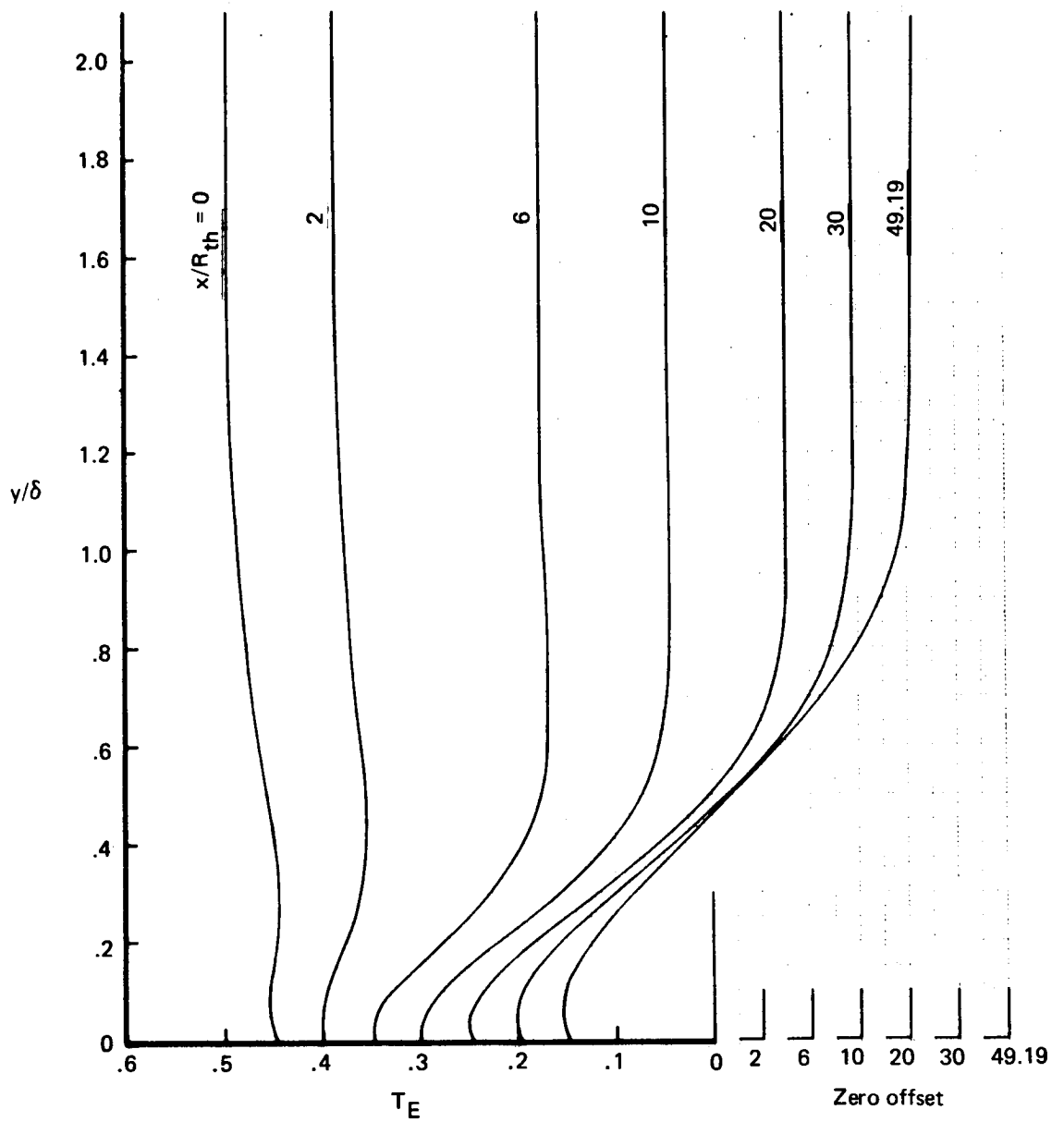


FIGURE 11.—NOZZLE WALL BOUNDARY LAYER TEMPERATURE PROFILES (Continued)



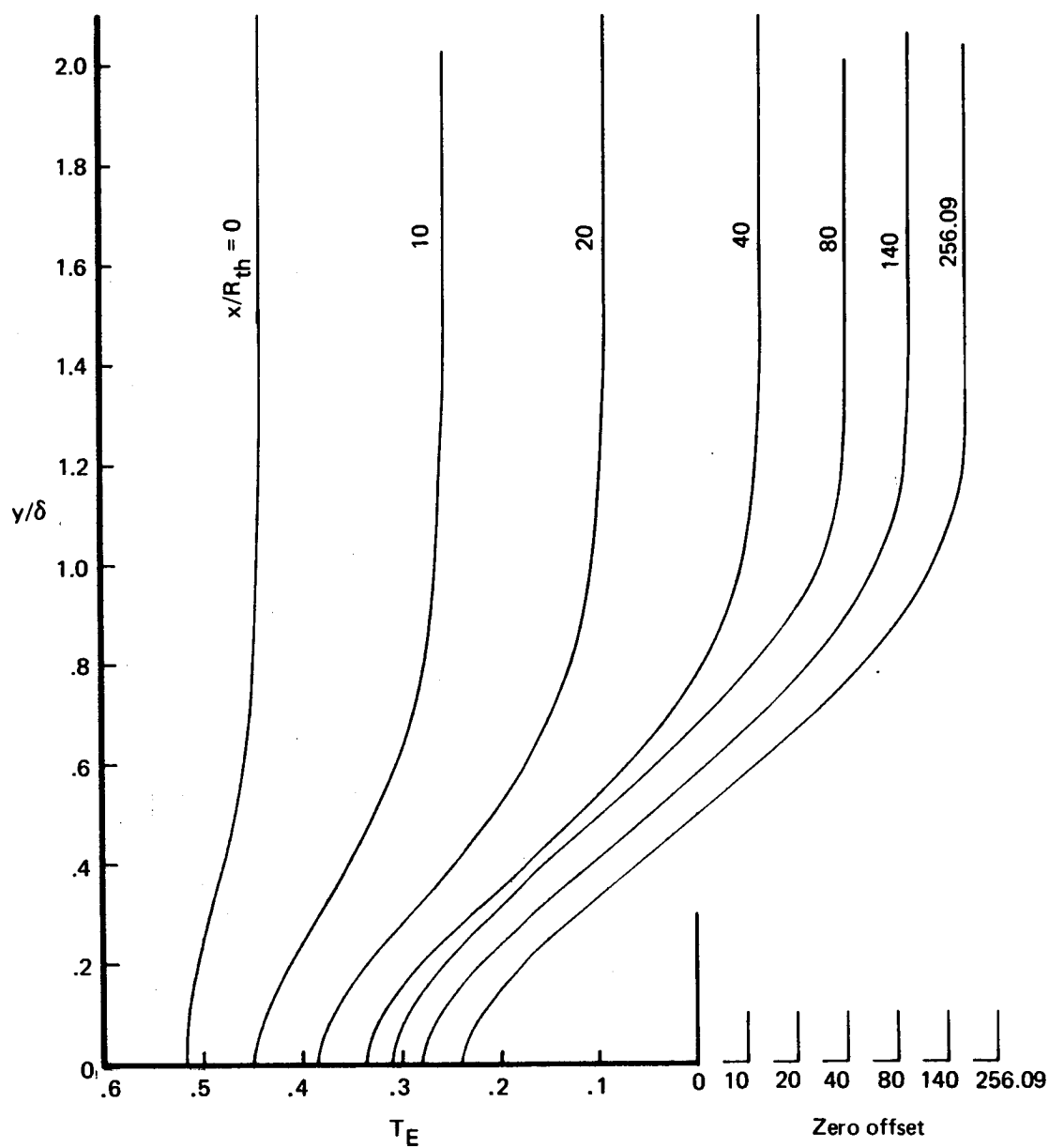
f) $M^* = 5$ Q-nozzle, suction 5.3, $T_{stag} = 400^\circ \text{ K}$, $T_{wall_{ad}}$

FIGURE 11.—NOZZLE WALL BOUNDARY LAYER TEMPERATURE PROFILES (Continued)



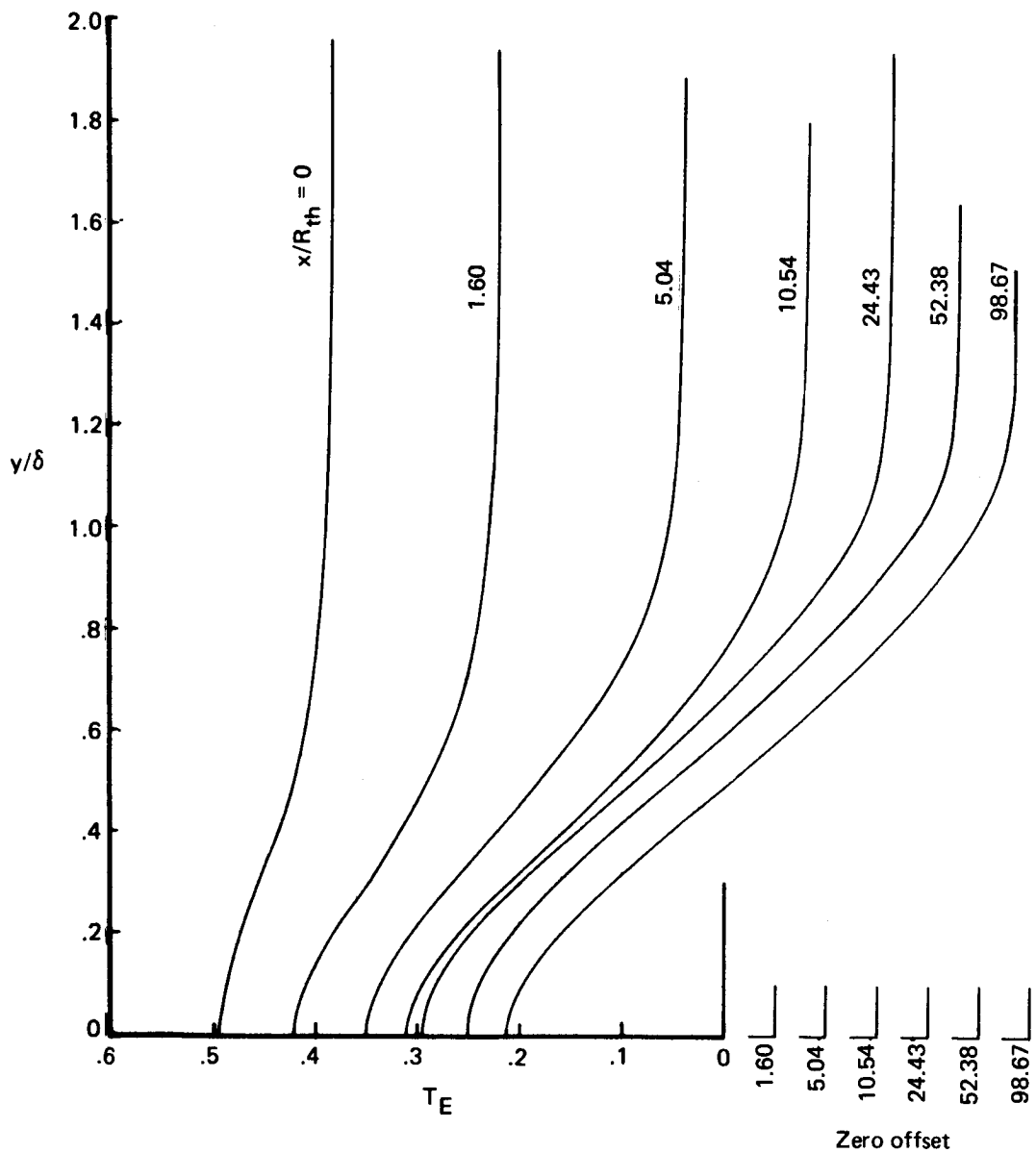
g) $M^* = 5$ Q-nozzle, suction 5.3, $T_{stag} = 400^\circ \text{ K}$, $T_{wall} = 300^\circ \text{ K}$

FIGURE 11.—NOZZLE WALL BOUNDARY LAYER TEMPERATURE PROFILES (Continued)



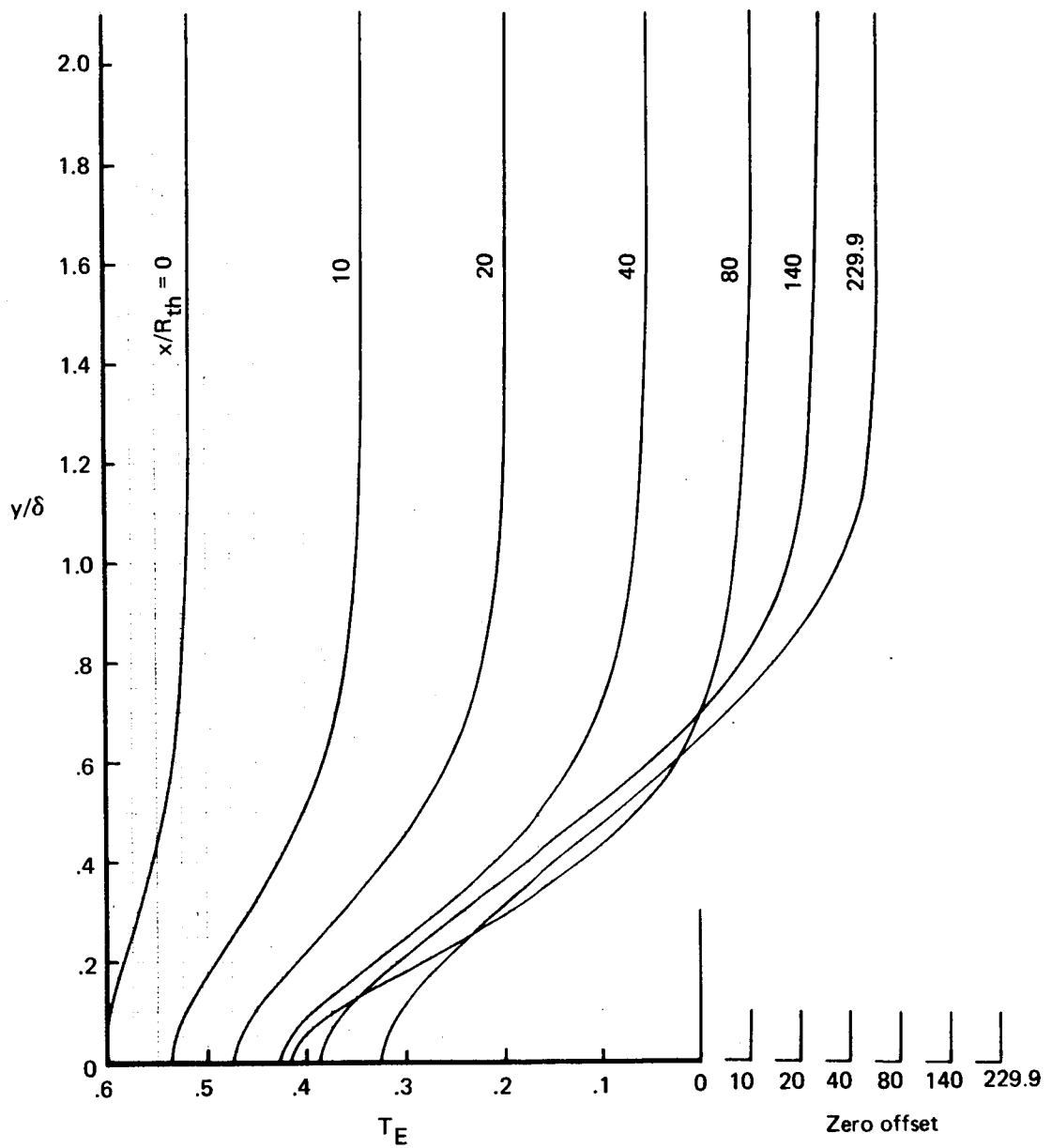
h) $M^* = 9$, $R/R_{th} = 200$, suction 9.2, $T_{stag} = 1000^\circ \text{ K}$

FIGURE 11.—NOZZLE WALL BOUNDARY LAYER TEMPERATURE PROFILES (Continued)



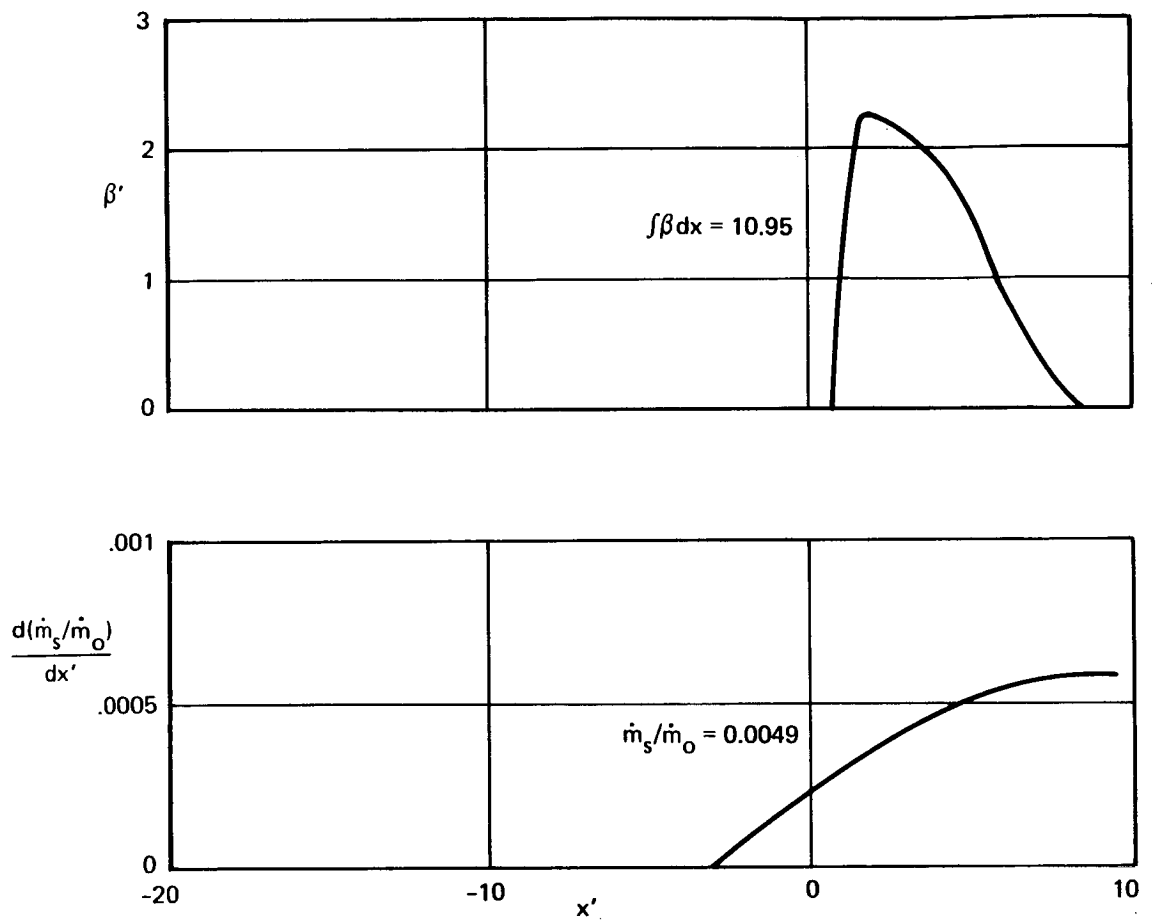
i) $M^* = 9$ NASA axisymmetric helium nozzle, suction 9.6 He, $T_{stag} = 300^\circ \text{ K}$, $T_{wall_{ad}}$

FIGURE 11.—NOZZLE WALL BOUNDARY LAYER TEMPERATURE PROFILES (Continued)



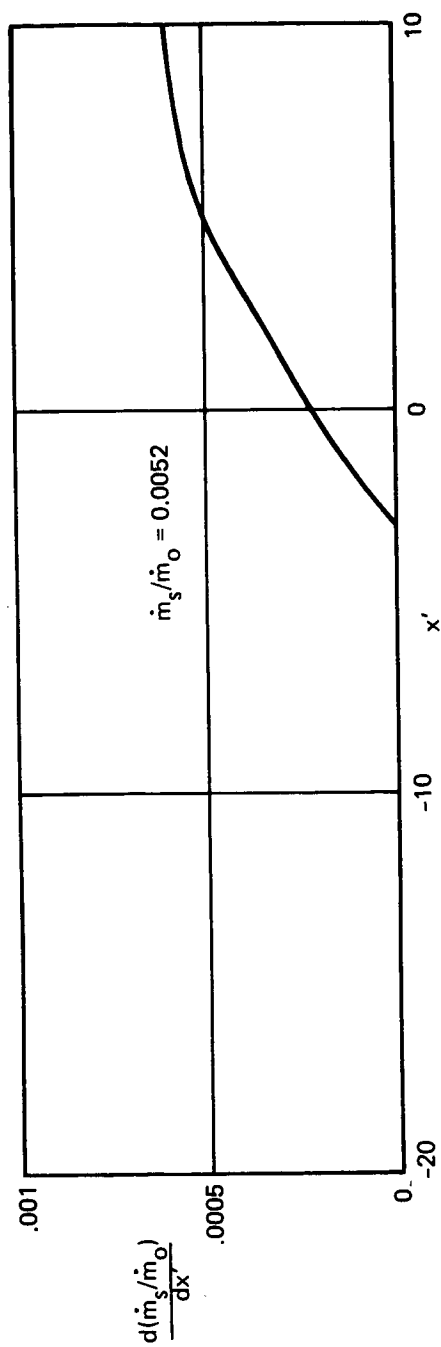
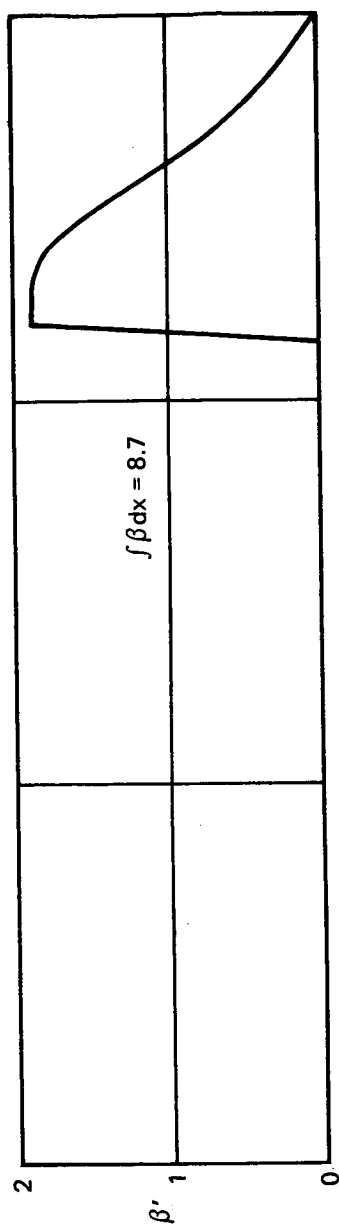
j) $M^* = 4.6$ JPL nozzle, suction 2D-3, $T_{stag} = 400^\circ \text{ K}$, floor and ceiling

FIGURE 11.—NOZZLE WALL BOUNDARY LAYER TEMPERATURE PROFILES (Concluded)



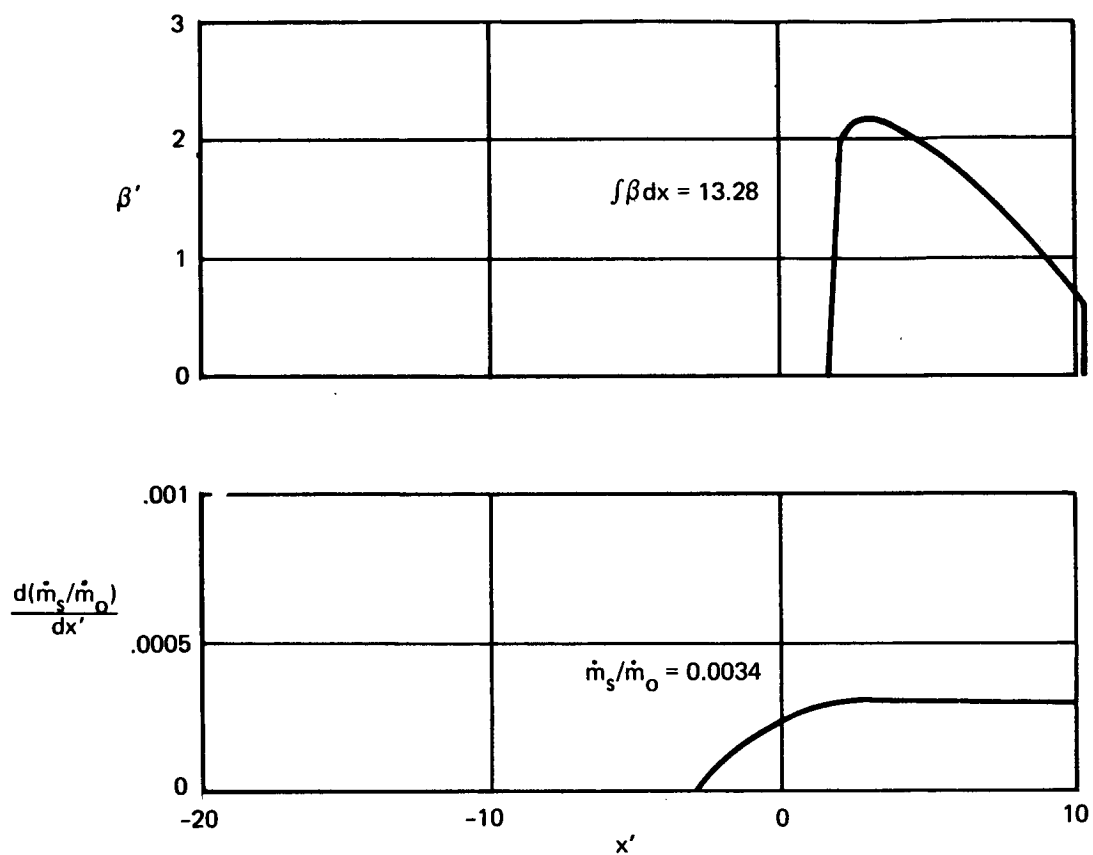
a) $R/R_{th} = 3$, suction 5, $U^*/\nu^* = 26.2 \cdot 10^6/m$, $D^* = 1m$, $T_{stag} = 300^\circ K$, $T_{wall_{ad}}$

FIGURE 12.—TAYLOR-GOERTLER INSTABILITY— $M^* = 3$ AXISYMMETRIC AIR NOZZLES



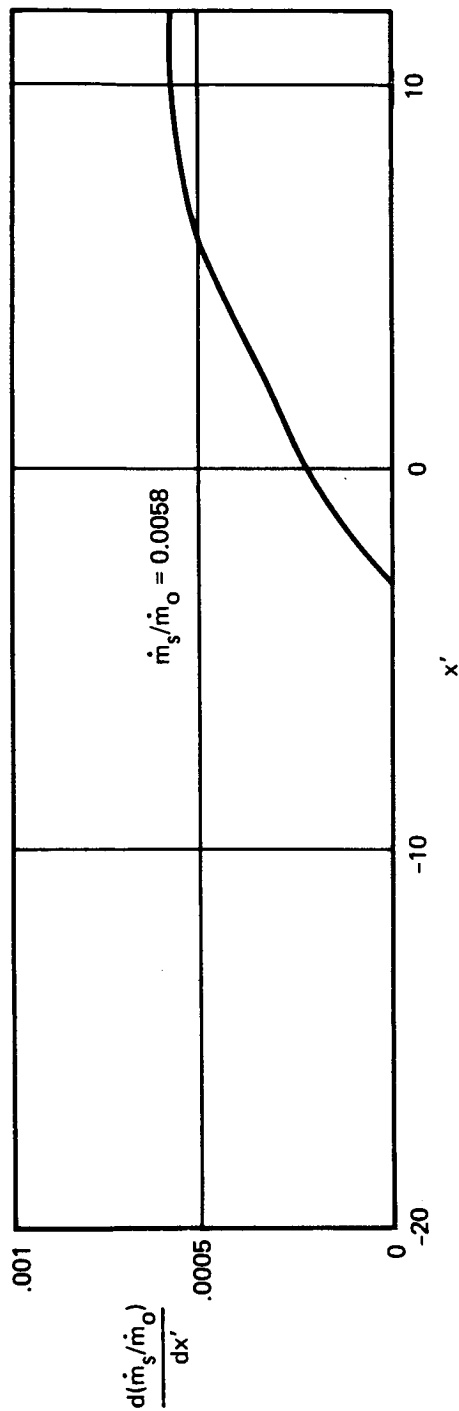
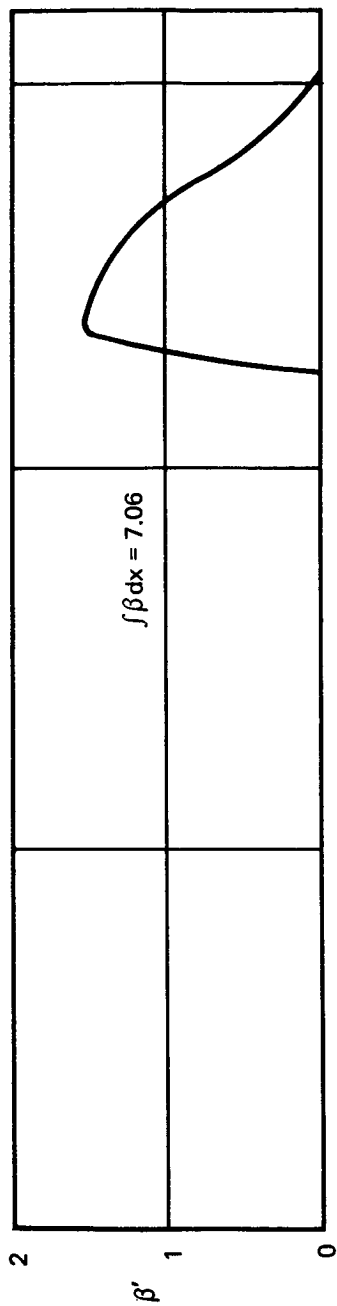
b) $R/R_{th} = 6$, suction 5, $U^*/\nu^* = 26.2 \cdot 10^6/m$, $D^* = 1m$, $T_{stag} = 300^\circ K$, $T_{wall_{ad}}$

FIGURE 12.—TAYLOR-GOERTLER INSTABILITY— $M^* = 3$ AXISYMMETRIC AIR NOZZLES (Continued)



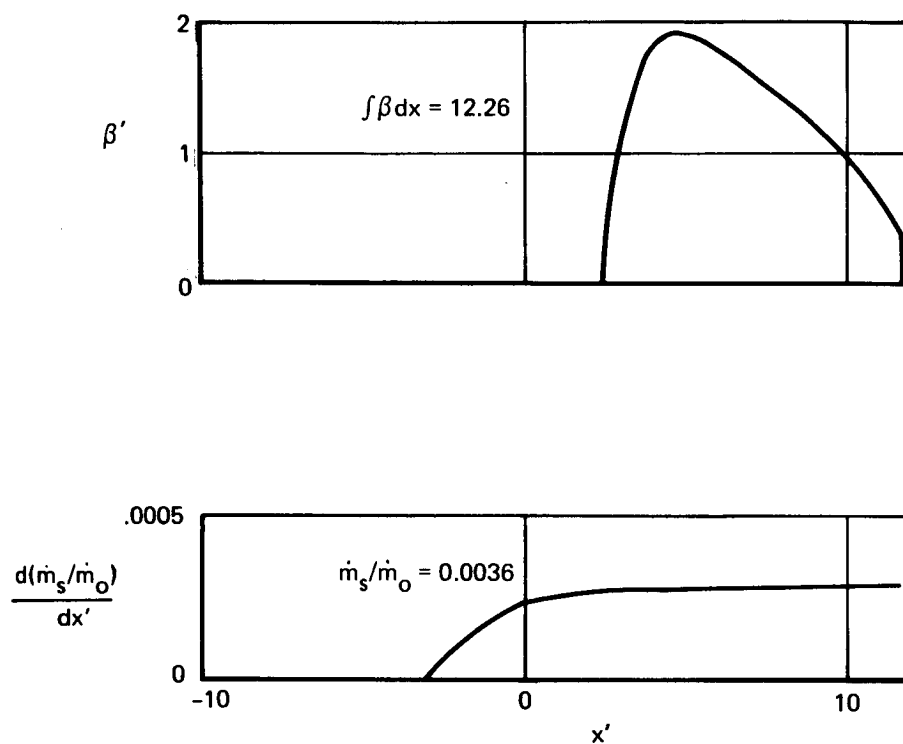
c) $R/R_{th} = 6$, suction 6, $U^*/\nu^* = 26.2 \cdot 10^6/m$, $D^* = 1m$, $T_{stag} = 300^\circ K$, $T_{wall_{ad}}$

FIGURE 12.—TAYLOR-GOERTLER INSTABILITY— $M^* = 3$ AXISYMMETRIC AIR NOZZLES
(Continued)



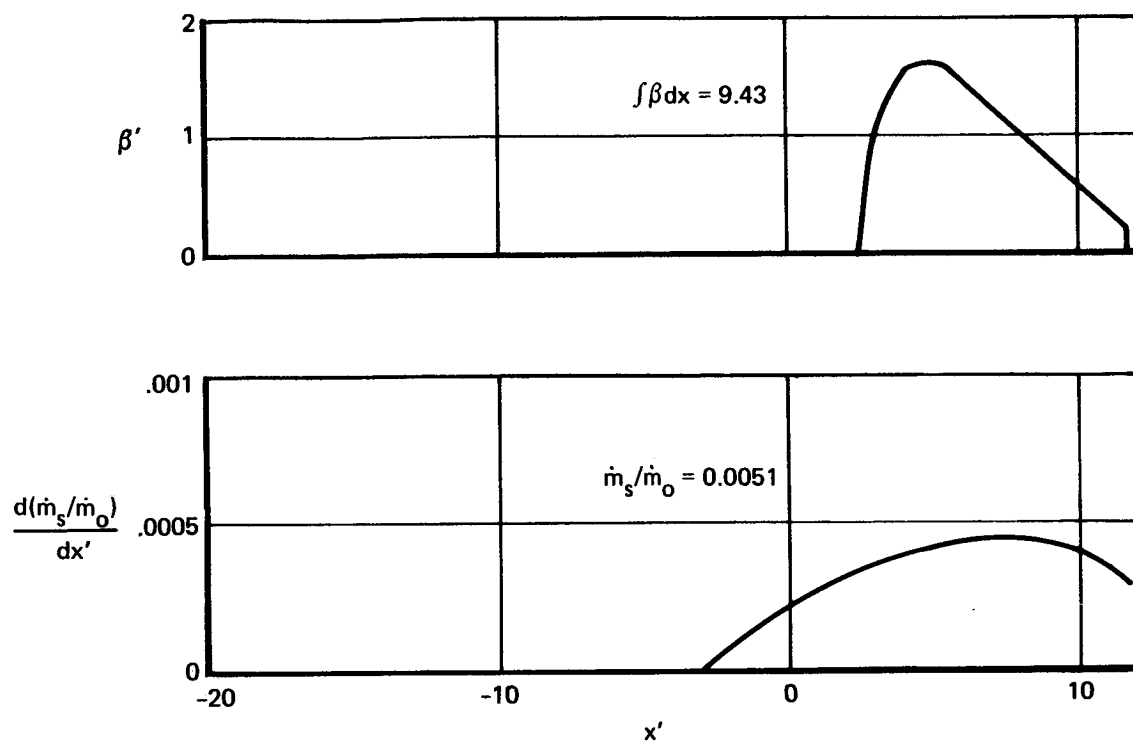
d) $R/R_{th} = 12$, suction 5, $U^*/\nu^* = 26.2 \cdot 10^6/m$, $D^* = 1m$, $T_{stag} = 300^\circ K$, $T_{wall_{ad}}$

FIGURE 12.—TAYLOR-GOERTLER INSTABILITY— $M^* = 3$ AXISYMMETRIC AIR NOZZLES (Continued)



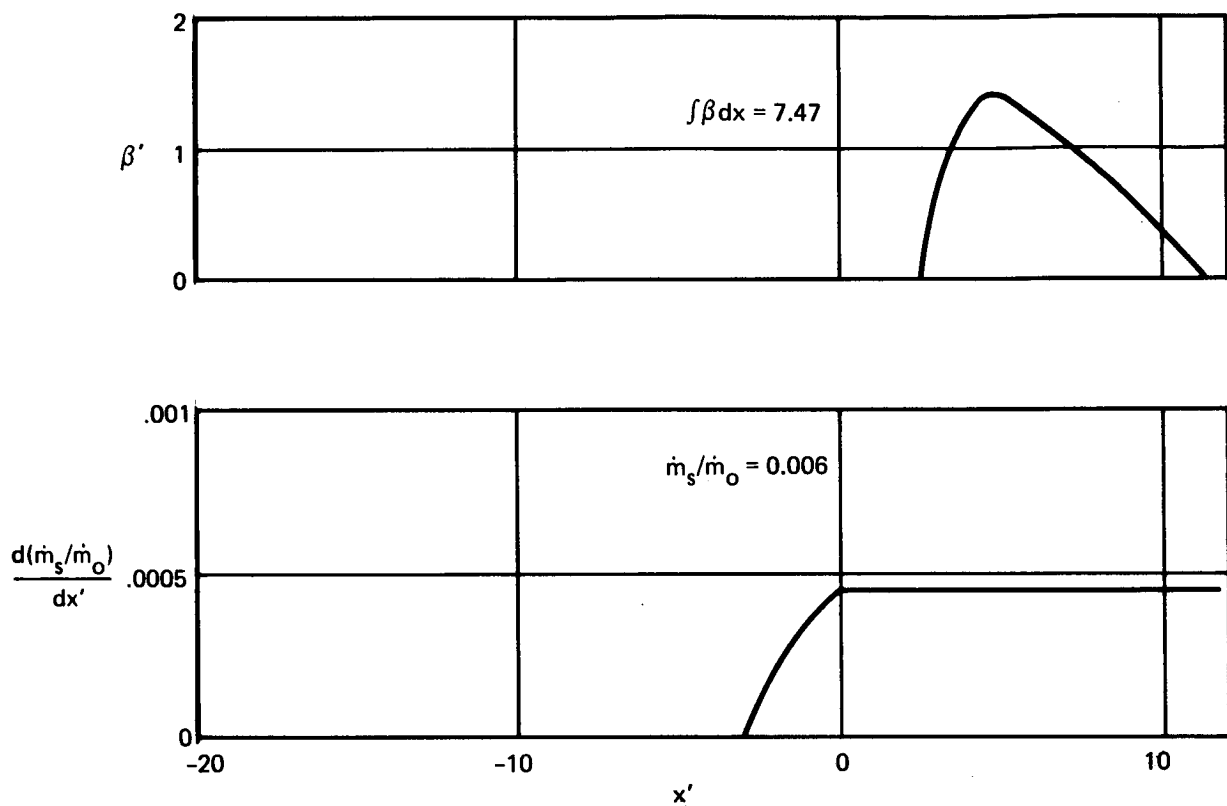
e) $R/R_{th} = 12$, suction 6, $U^*/\nu^* = 26.2 \cdot 10^6/m$, $D^* = 1m$, $T_{stag} = 300^u K$, $T_{wall_{ad}}$

FIGURE 12.—TAYLOR-GOERTLER INSTABILITY— $M^* = 3$ AXISYMMETRIC AIR NOZZLES
(Continued)



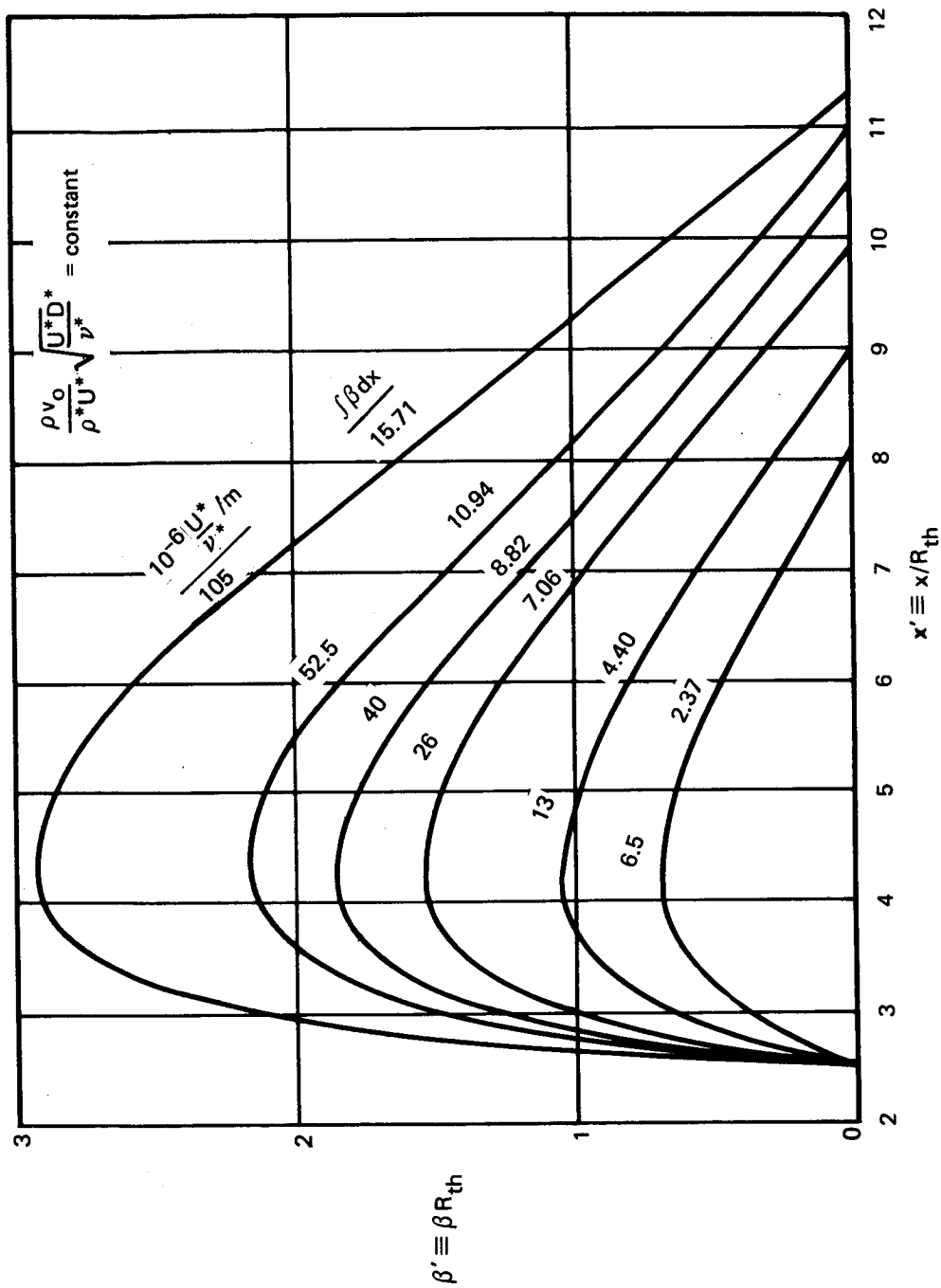
f) $R/R_{th} = 12$, suction 7, $U^*/\nu^* = 26.2 \cdot 10^6/m$, $D^* = 1m$, $T_{stag} = 300^\circ K$, $T_{wall_{ad}}$

FIGURE 12.—TAYLOR-GOERTLER INSTABILITY— $M^* = 3$ AXISYMMETRIC AIR NOZZLES
(Continued)



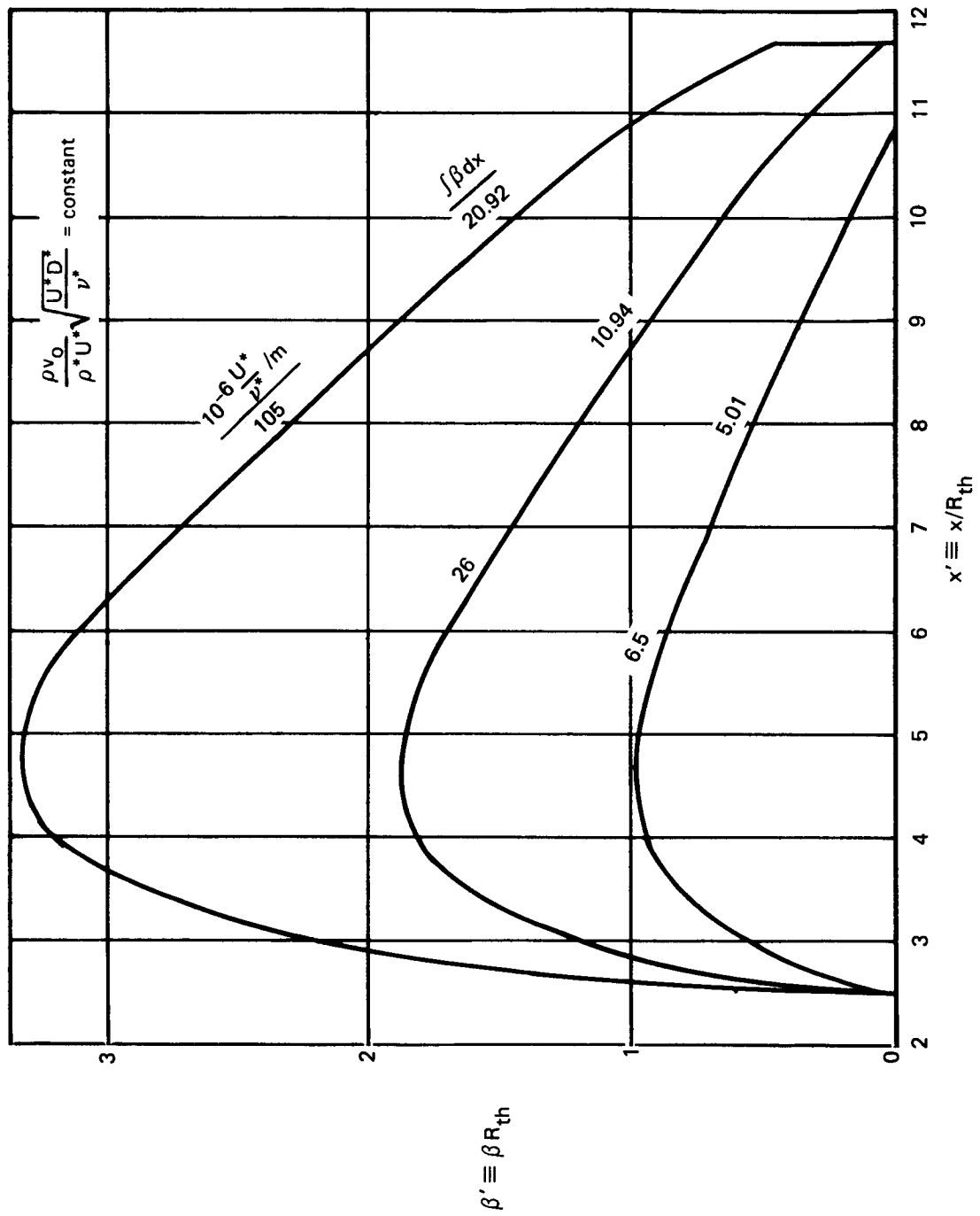
g) $R/R_{th} = 12$, suction 10, $U^*/\nu^* = 26.2 \cdot 10^6/m$, $D^* = 1m$, $T_{stag} = 300^\circ K$, $T_{wall_{ad}}$

FIGURE 12.—TAYLOR-GOERTLER INSTABILITY— $M^* = 3$ AXISYMMETRIC AIR NOZZLES
(Continued)



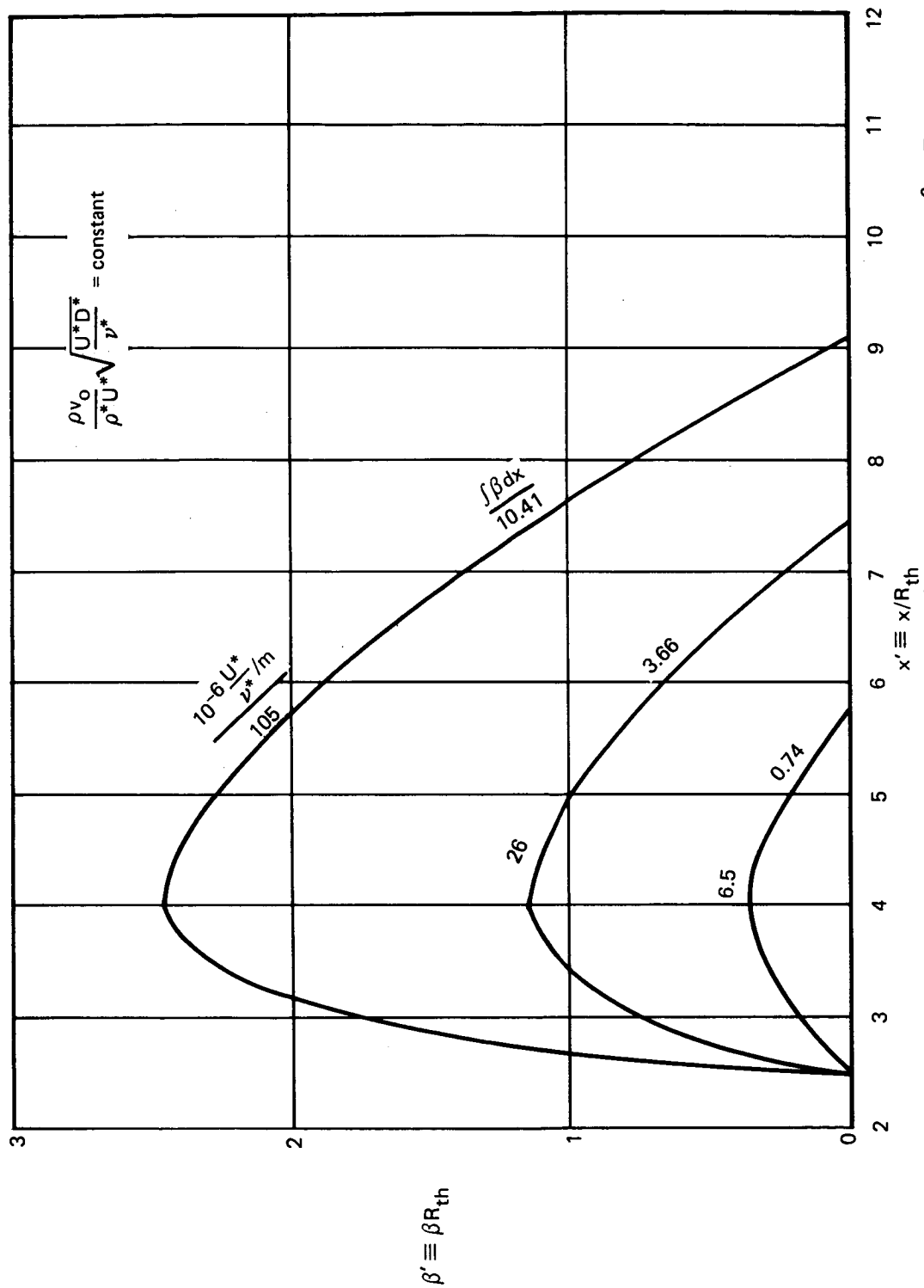
h) Influence of unit length Reynolds number, $R/R_{th} = 12$, section 5, $D^* = 1\text{m}$, $T_{stag} = 300^\circ\text{K}$, $T_{wall,ad}$

FIGURE 12.—TAYLOR-GOERTLER INSTABILITY— $M^* = 3$ AXISYMMETRIC AIR NOZZLES (Continued)



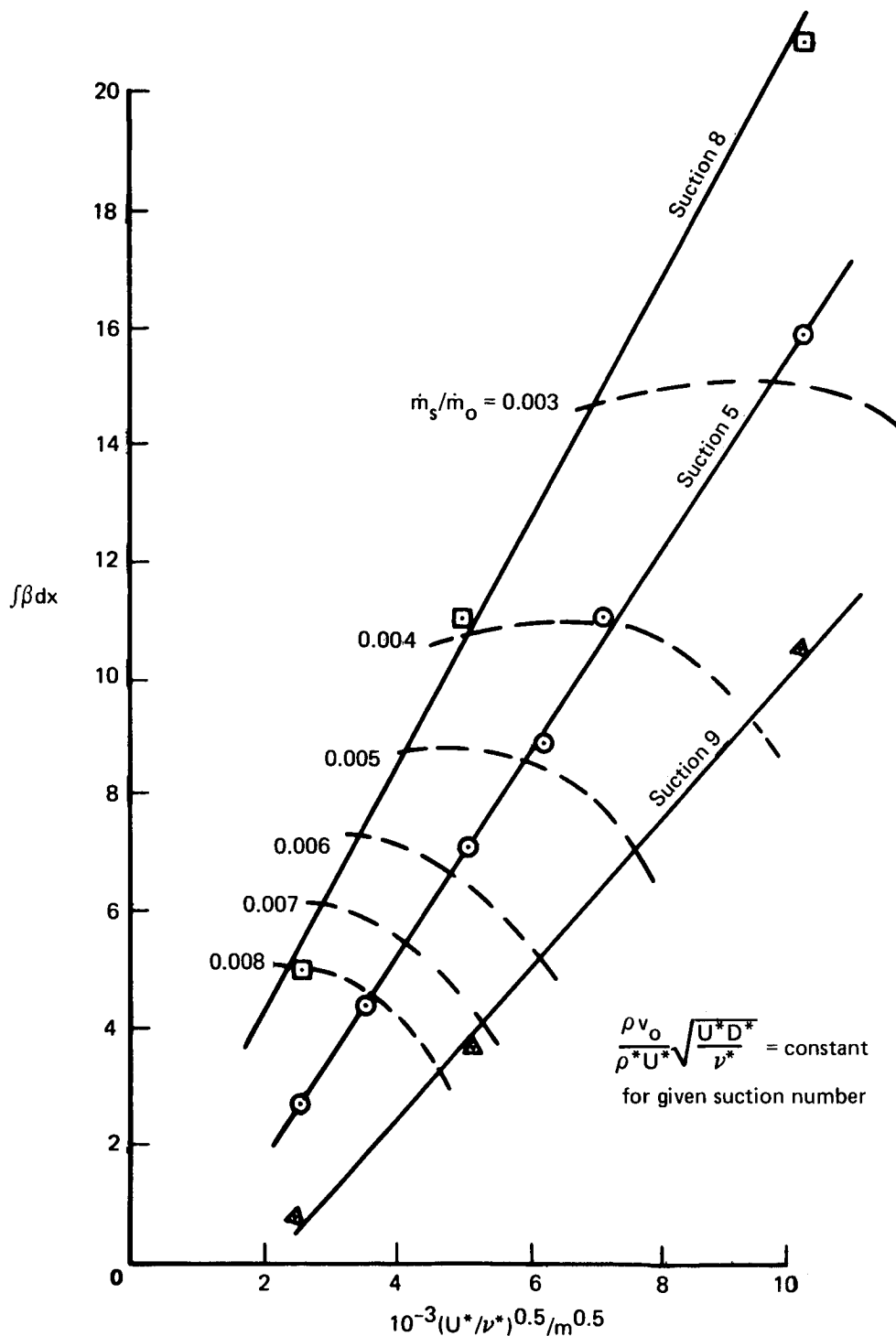
i) Influence of unit length Reynolds number, $R/R_{th} = 12$, suction 8, $D^* = 1m$, $T_{stag} = 300^\circ K$, $T_{wall,ad}$

FIGURE 12.— TAYLOR-GOERTLER INSTABILITY— $M^* = 3$ AXISYMMETRIC AIR NOZZLES (Continued)



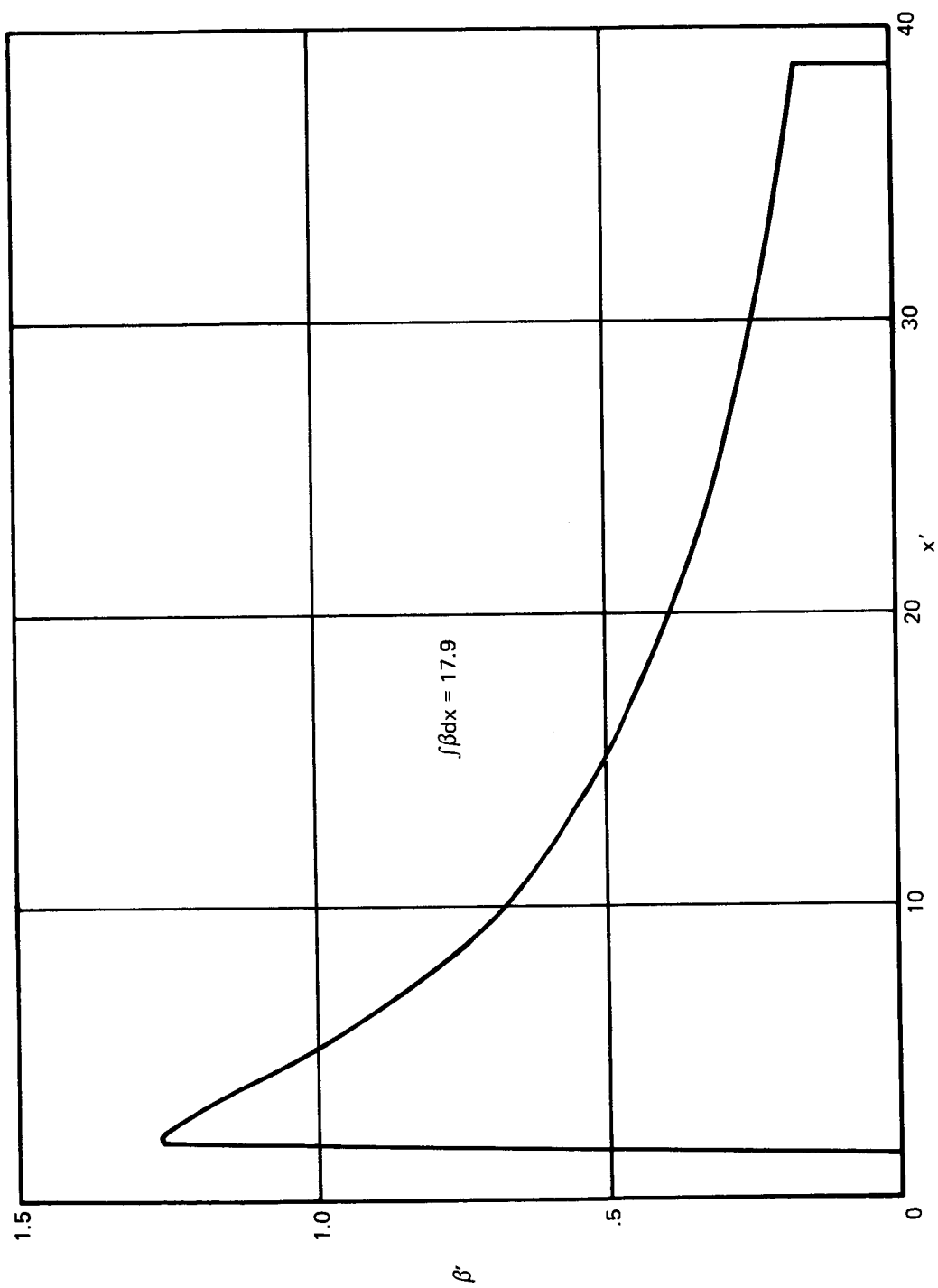
j) Influence of unit length Reynolds number, $R/R_{th} = 12$, suction 9, $D^* = 1m$, $T_{stag} = 300^\circ K$, $T_{wall,ad}$

FIGURE 12.—TAYLOR-GOERTLER INSTABILITY— $M^* = 3$ AXISYMMETRIC AIR NOZZLES (Continued)



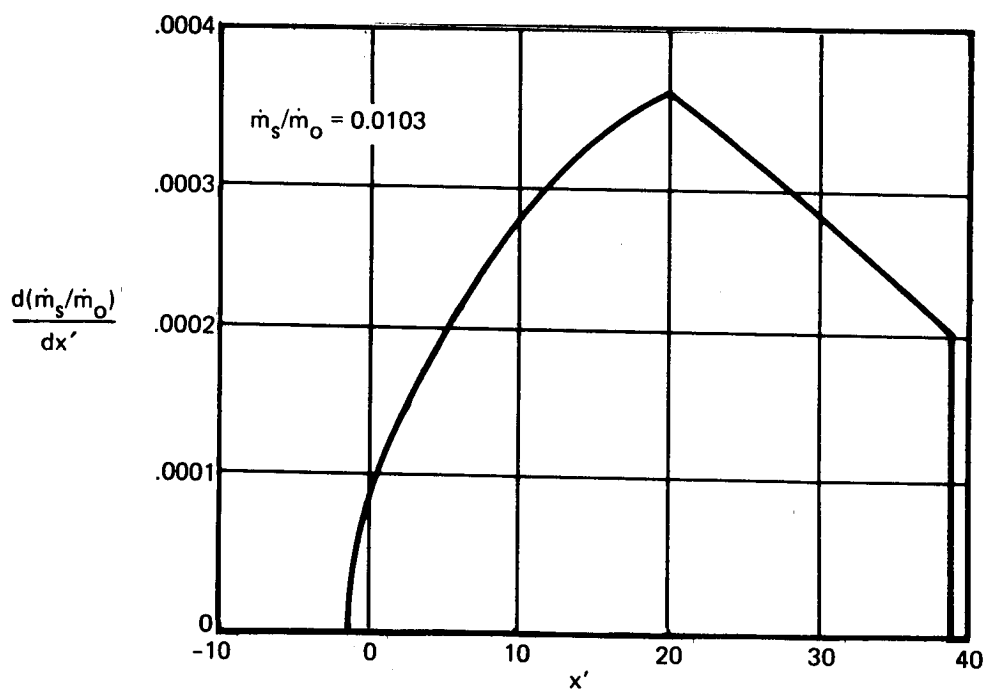
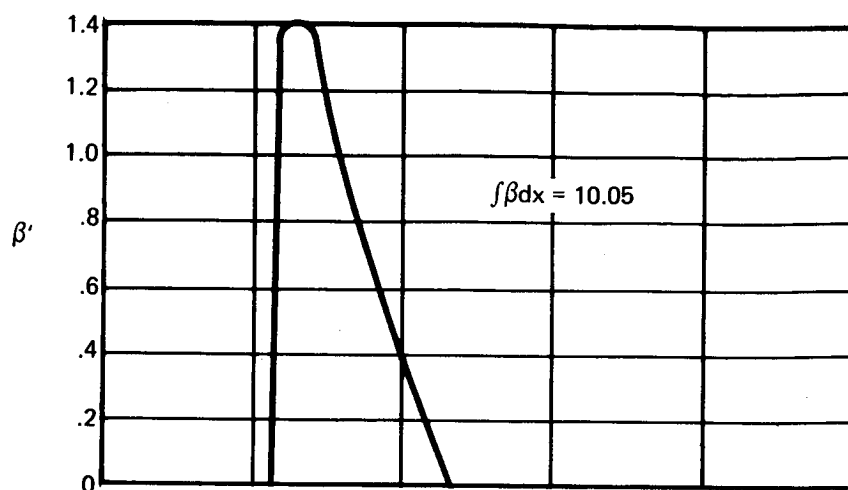
k) Influence of unit length Reynolds number and suction rate on $\int \beta dx$, $R/R_{th} = 12$, $D^* = 1m$

FIGURE 12.- TAYLOR-GOERTLER INSTABILITY- $M^* = 3$ AXISYMMETRIC AIR NOZZLES
(Concluded)



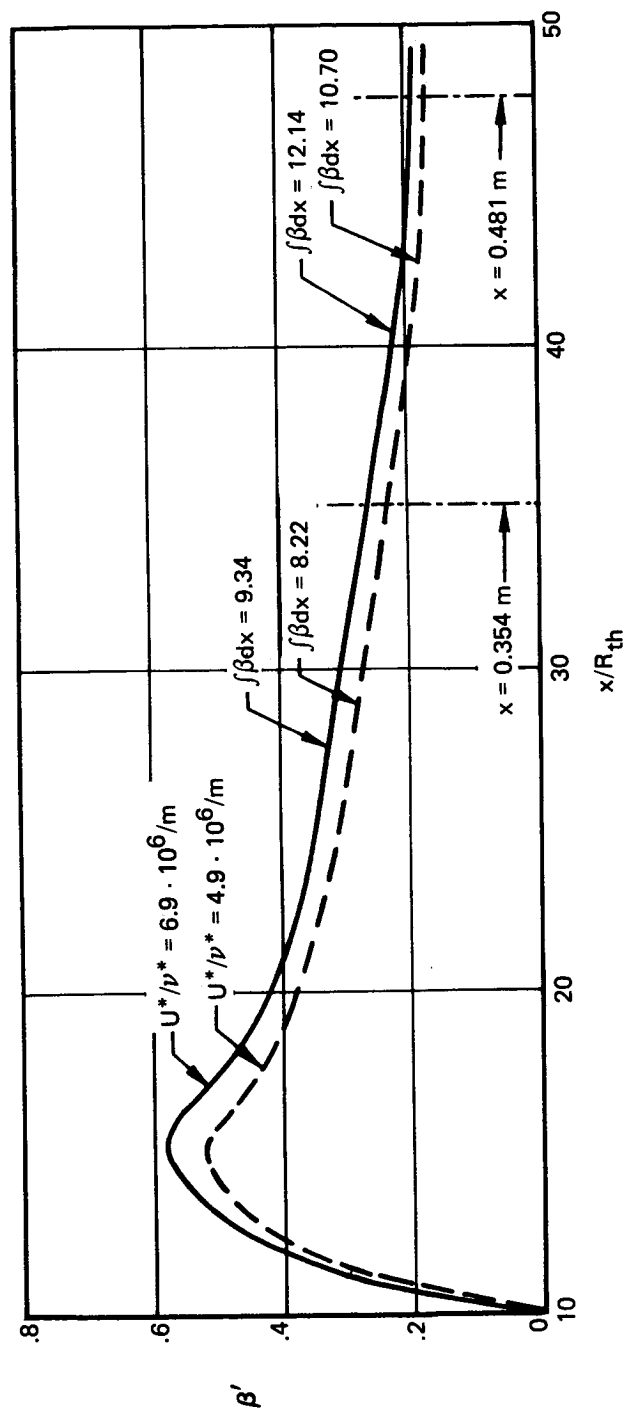
a) Rapid expansion nozzle, no suction, $U^*/\nu = 6.9 \cdot 10^6/\text{m}$, $R_{th} = 0.01007 \text{ m}$, $T_{stag} = 378^\circ \text{ K}$, $T_{wall_{ad}}$

FIGURE 13.—TAYLOR-GOERTLER INSTABILITY— $M^* = 5$ AXISYMMETRIC AIR NOZZLES



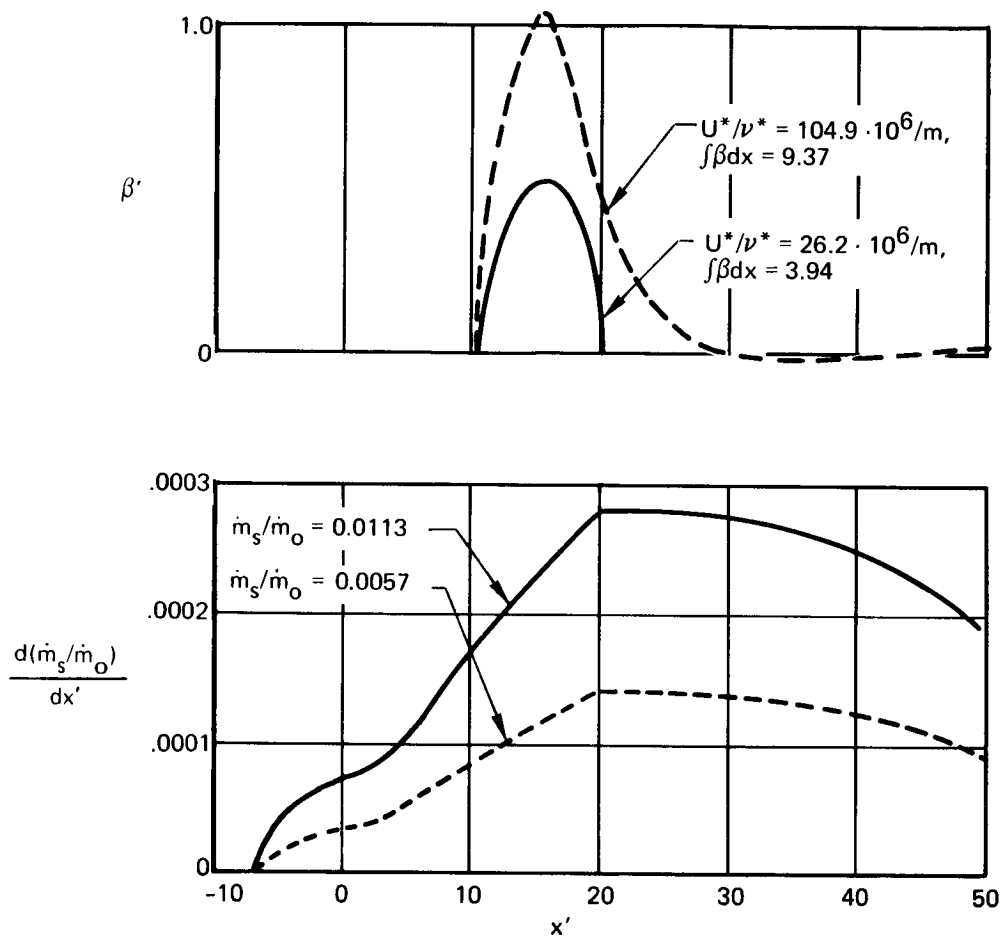
b) LARC rapid expansion nozzle, suction 5.1, $U^*/\nu^* = 26.2 \cdot 10^6 \text{ m}$, $D^* = 1 \text{ m}$, $T_{\text{stag}} = 300^\circ \text{ K}$, $T_{\text{wall ad}}$

FIGURE 13.—TAYLOR-GOERTLER INSTABILITY— $M^* = 5$ AXISYMMETRIC AIR NOZZLES (Continued)



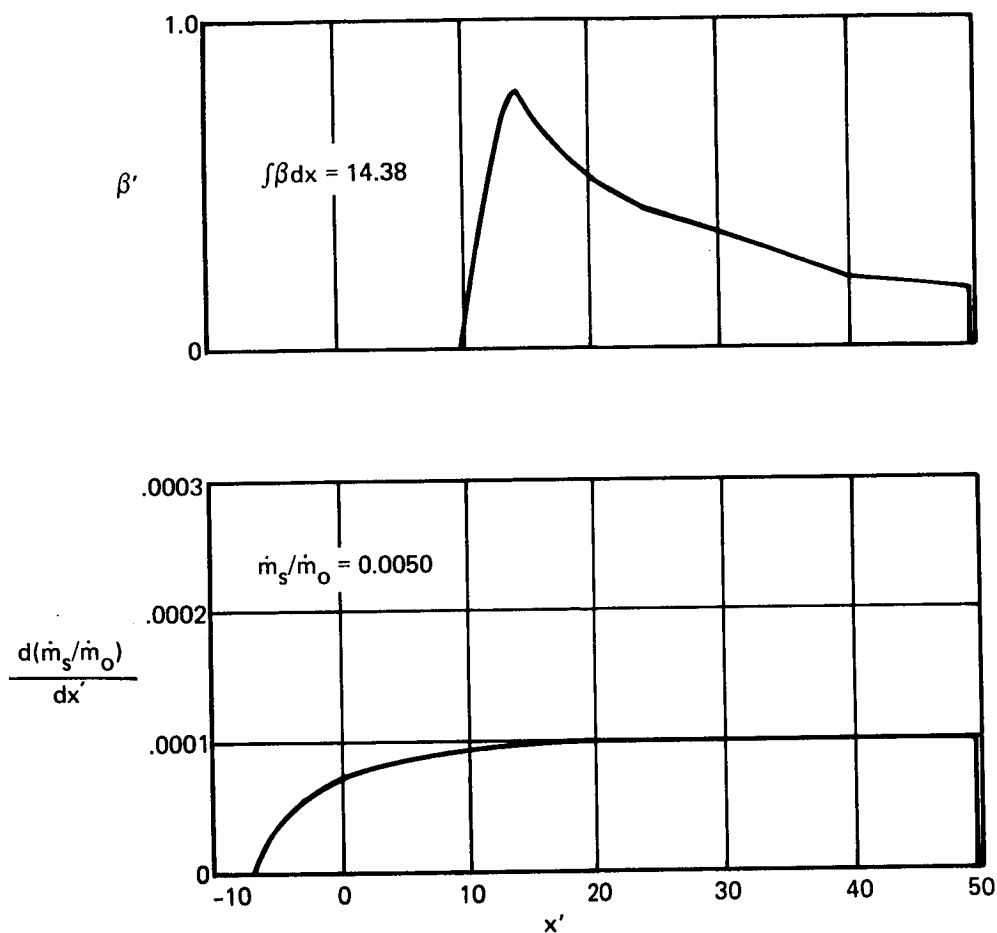
c) Q-nozzle, no suction, $R_{th} = 0.01007 \text{ m}$, $T_{stag} = 378^\circ \text{ K}$, $T_{wall_{ad}}$

FIGURE 13.—TAYLOR-GOERTLER INSTABILITY— $M^* = 5$ AXISYMMETRIC AIR NOZZLES (Continued)



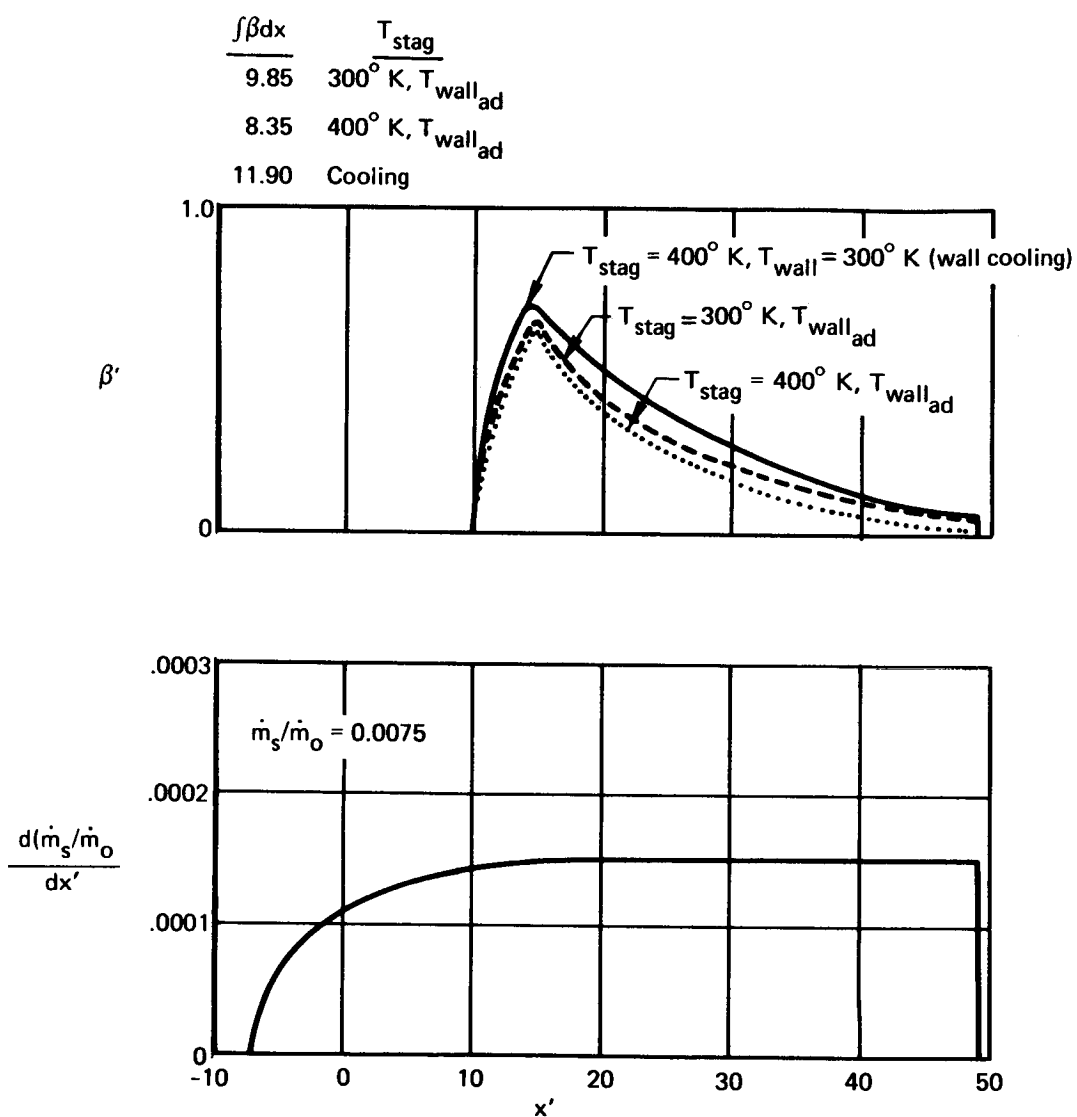
d) LARC Q-nozzle, suction 5.1, $T_{\text{stag}} = 300^\circ \text{ K}$, $T_{\text{wall}_{\text{ad}}}$

FIGURE 13.—TAYLOR-GOERTLER INSTABILITY— $M^* = 5$ AXISYMMETRIC AIR NOZZLES (Continued)



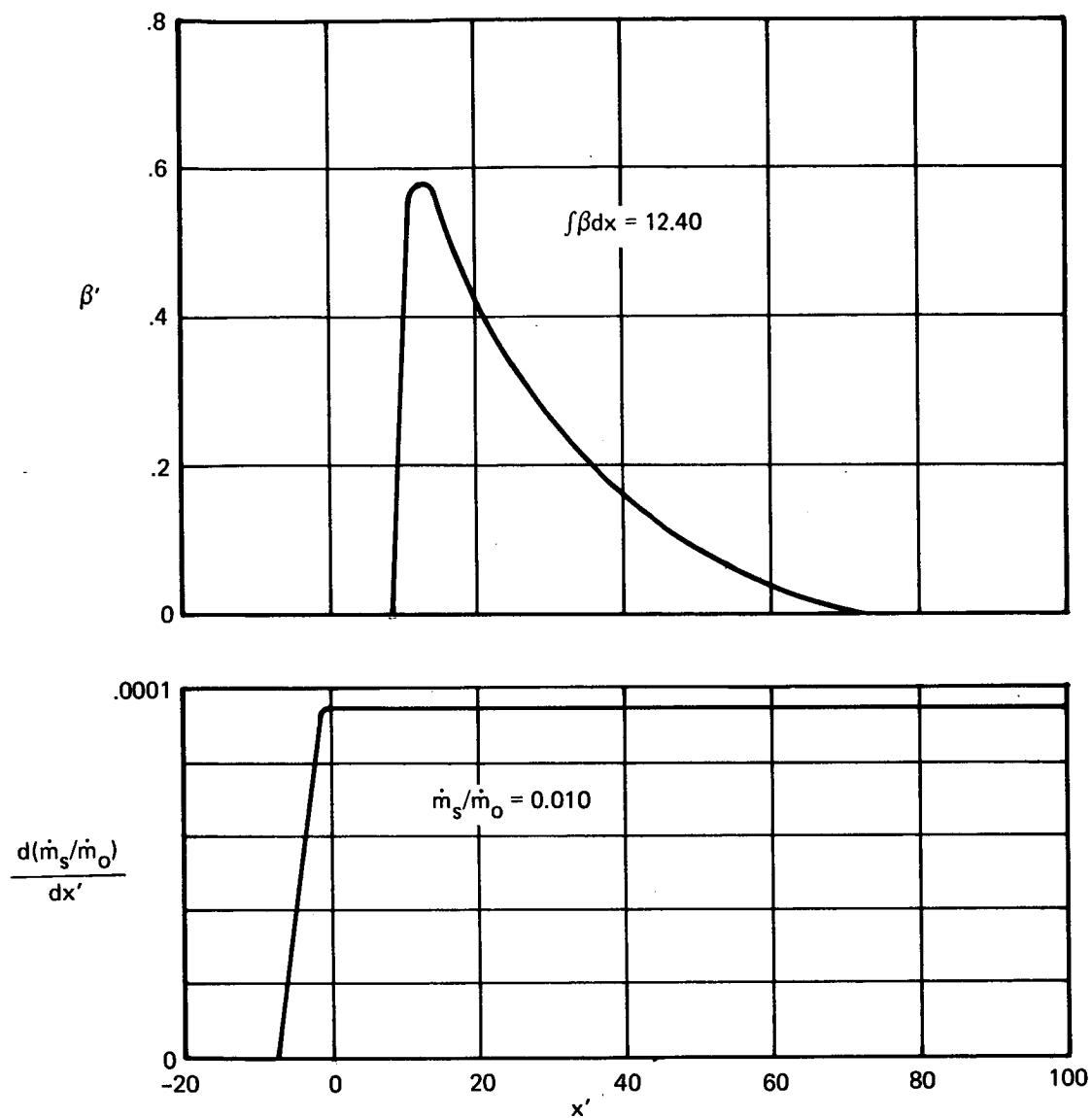
e) LARC nozzle, suction 5.2, $T_{\text{stag}} = 300^\circ \text{ K}$, $T_{\text{wall}_{\text{ad}}}$, $U^*/\nu^* = 26.2 \cdot 10^6/\text{m}$, $D^* = 1 \text{ m}$

FIGURE 13.—TAYLOR-GOERTLER INSTABILITY— $M^* = 5$ AXISYMMETRIC AIR NOZZLES (Continued)



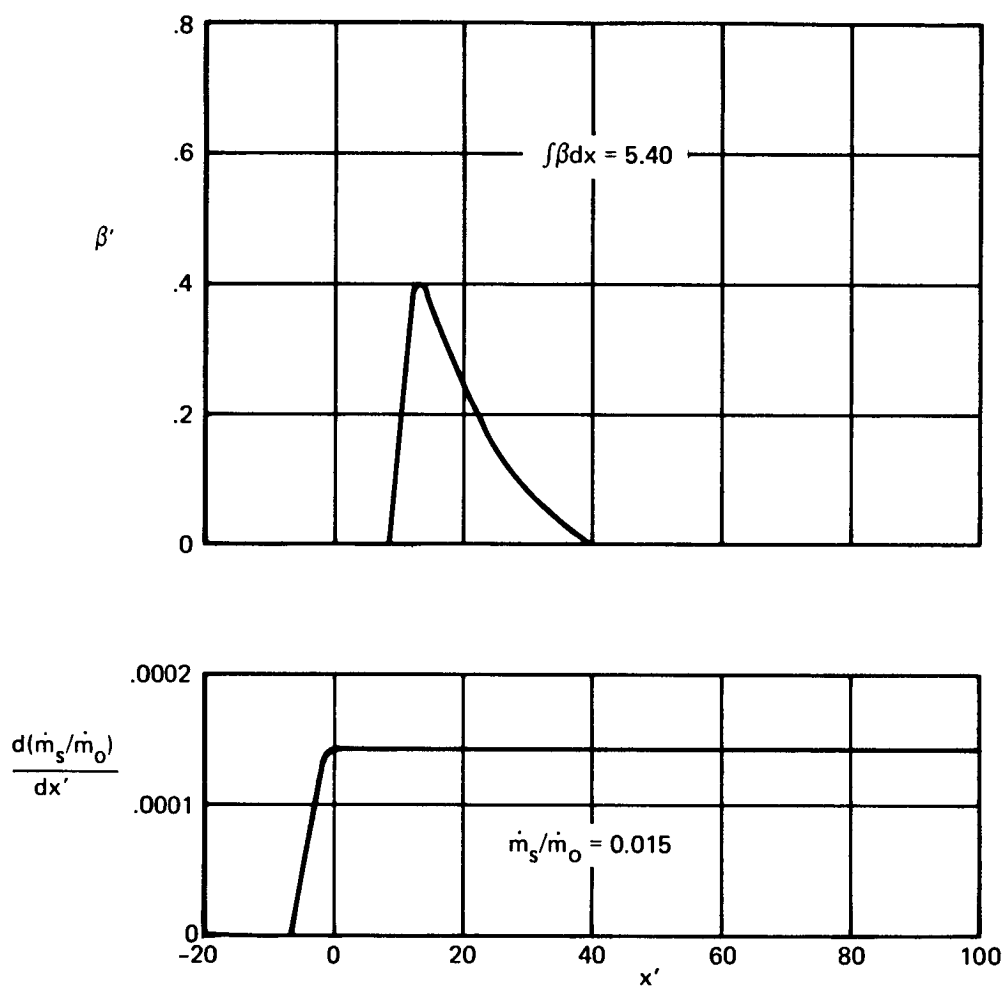
f) LARC Q-nozzle, suction 5.3

FIGURE 13.—TAYLOR-GOERTLER INSTABILITY— $M^* = 5$ AXISYMMETRIC AIR NOZZLES (Concluded)



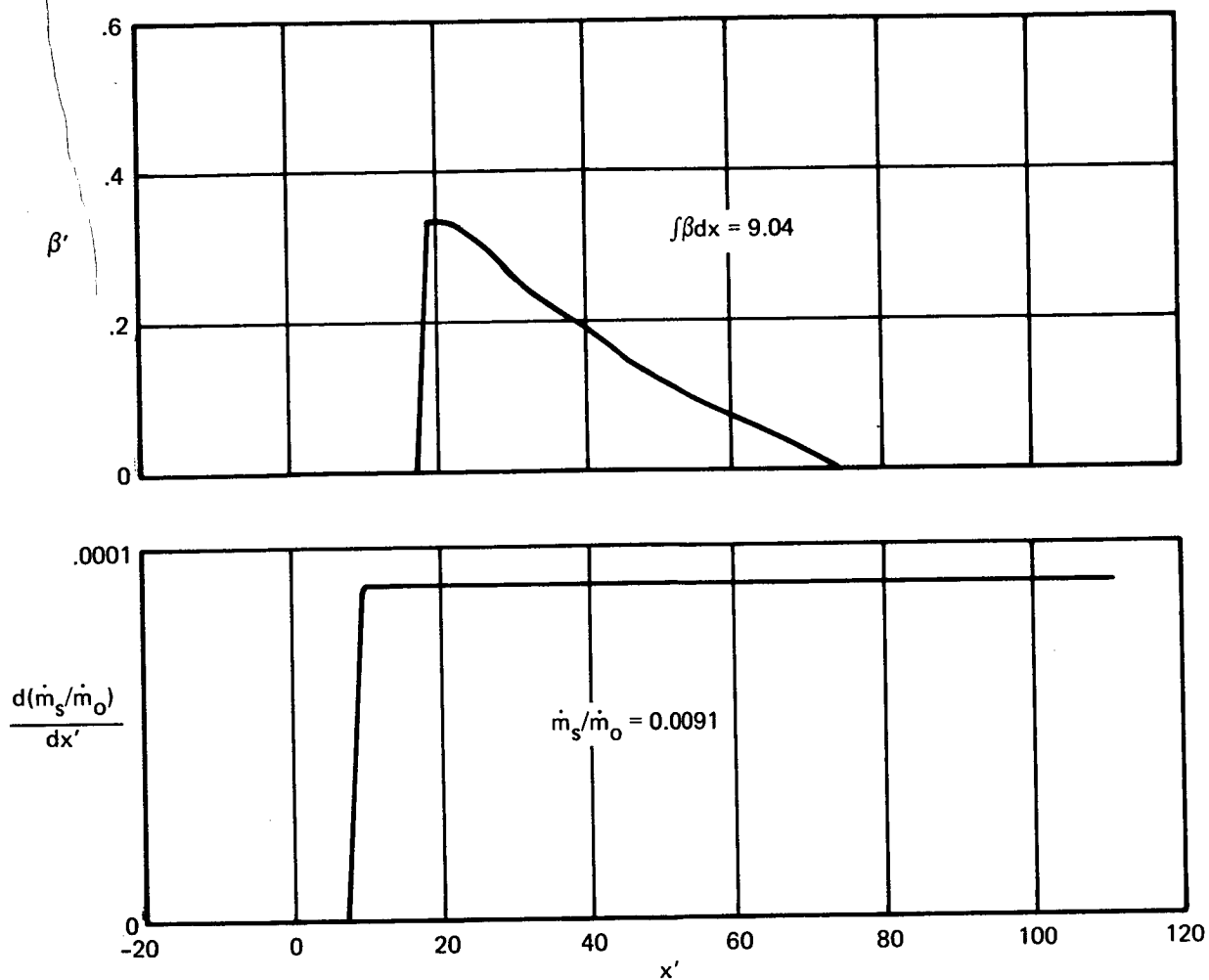
a) $R/R_{th} = 30$, suction 7.1, $U^*/\nu^* = 26.2 \cdot 10^6/m$, $D^* = 1$ m, $T_{stag} = 700^\circ$ K, $T_{wall_{ad}}$

FIGURE 14.—TAYLOR-GOERTLER INSTABILITY— $M^* = 7$ AXISYMMETRIC AIR NOZZLES



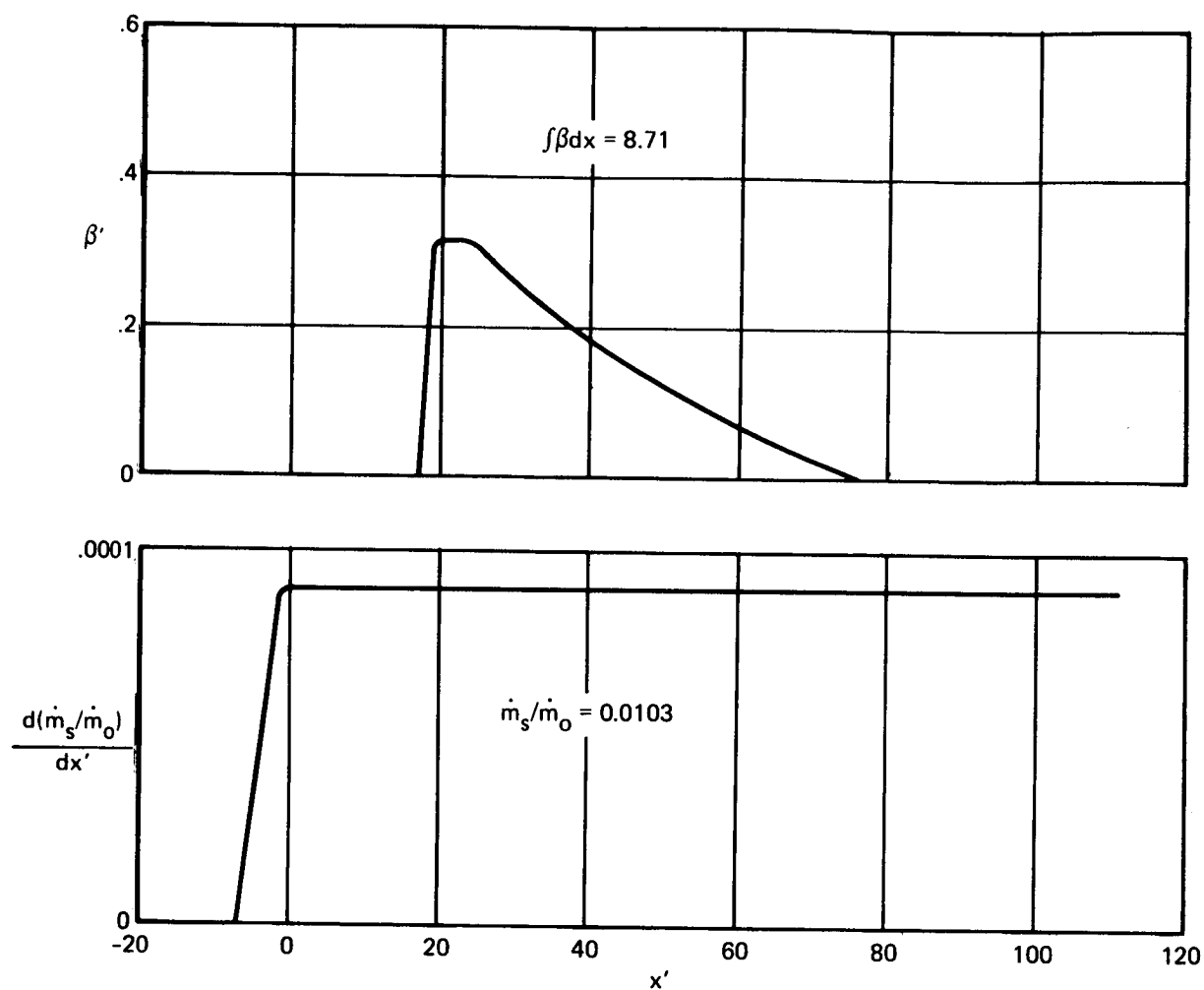
b) $R/R_{th} = 30$, suction 7.2, $U^*/\nu^* = 26.2 \cdot 10^6/m$, $D^* = 1$ m, $T_{stag} = 700^\circ$ K, $T_{wall_{ad}}$

FIGURE 14.—TAYLOR-GOERTLER INSTABILITY— $M^* = 7$ AXISYMMETRIC AIR NOZZLES (Continued)



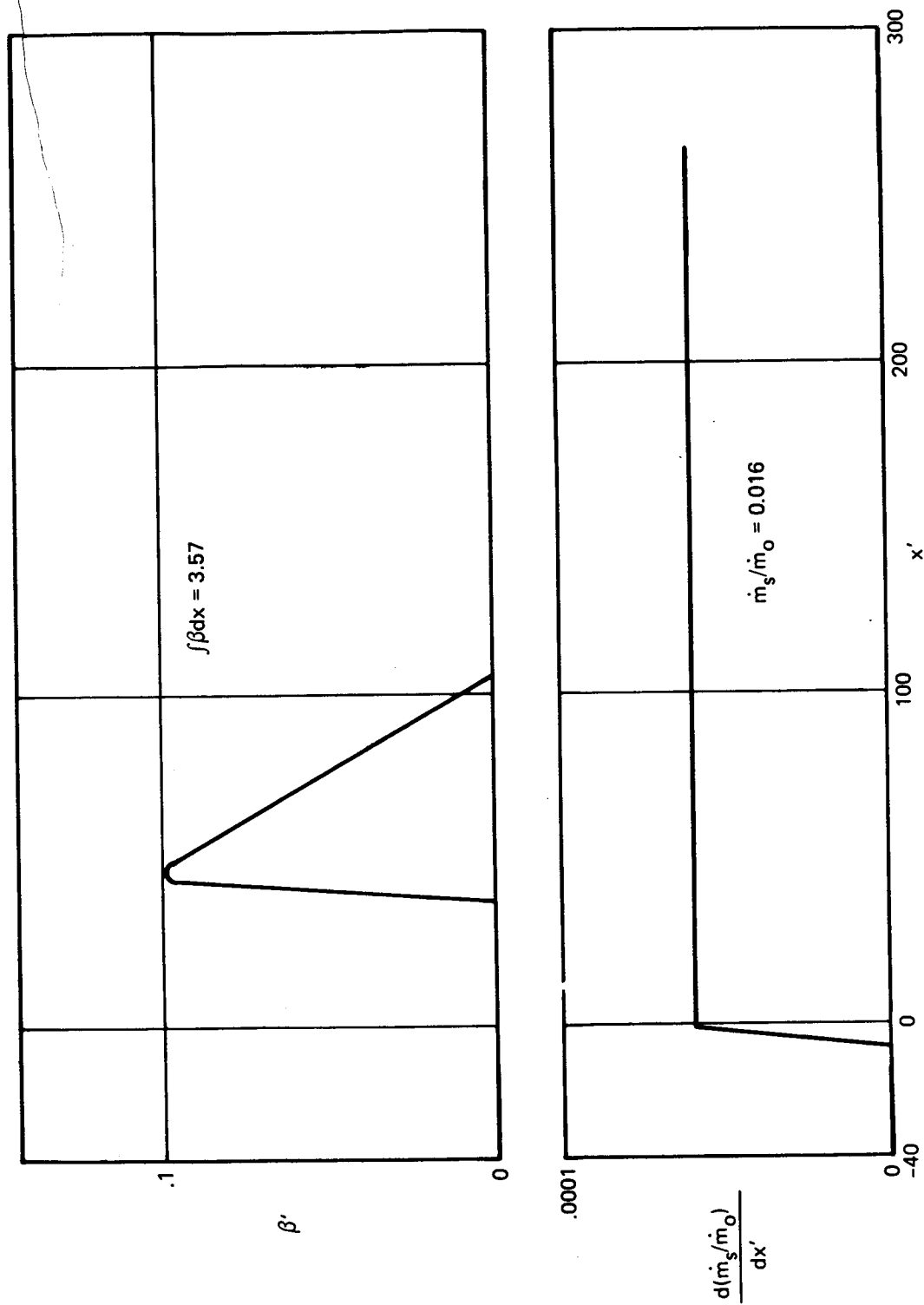
c) $R/R_{th} = 75$, suction 7.1a, $U^*/\nu^* = 26.2 \cdot 10^6/m$, $D^* = 1$ m, $T_{stag} = 700^\circ$ K, $T_{wall_{ad}}$

FIGURE 14.—TAYLOR-GOERTLER INSTABILITY— $M^* = 7$ AXISYMMETRIC AIR NOZZLES (Continued)



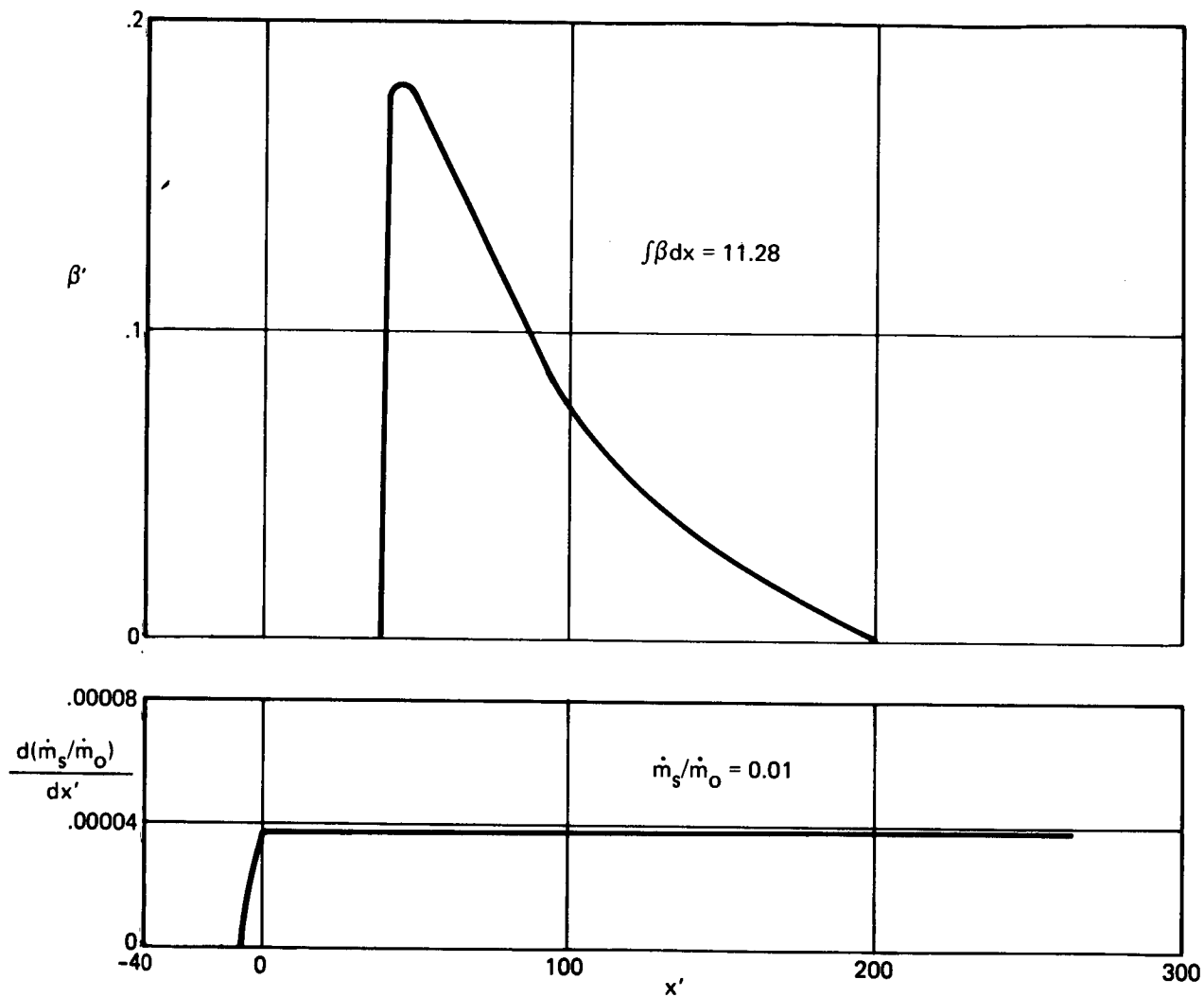
d) $R/R_{th} = 75$, suction 7.1, $U^*/\nu^* = 26.2 \cdot 10^6/m$, $D^* = 1$ m, $T_{stag} = 700^\circ$ K, $T_{wall_{ad}}$

FIGURE 14.—TAYLOR-GOERTLER INSTABILITY— $M^* = 7$ AXISYMMETRIC AIR NOZZLES (Concluded)



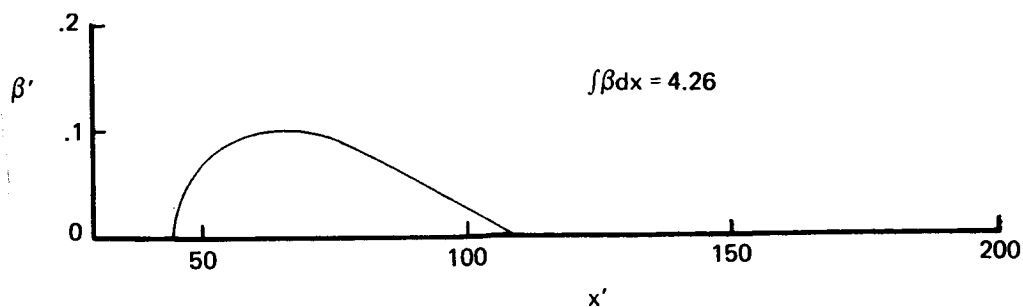
a) $R/R_{th} = 200$, suction 9.1, $U^*/\nu^* = 26.2 \cdot 10^6/m$, $D^* = 1$ m, $T_{stag} = 1000^\circ$ K, $T_{wall_{ad}}$

FIGURE 15. — TAYLOR-GOERTLER INSTABILITY — $M^* = 9$ AXISYMMETRIC AIR NOZZLE

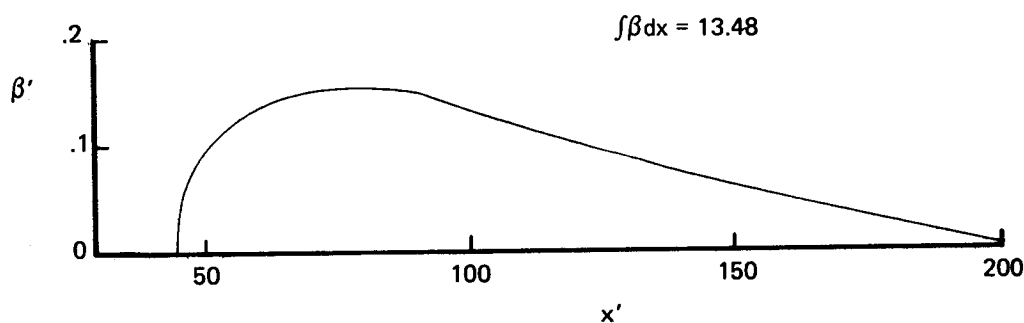


b) $R/R_{th} = 200$, suction 9.2, $U^*/\nu^* = 26.2 \cdot 10^6/m$, $D^* = 1$ m, $T_{stag} = 1000^\circ$ K, $T_{wall_{ad}}$

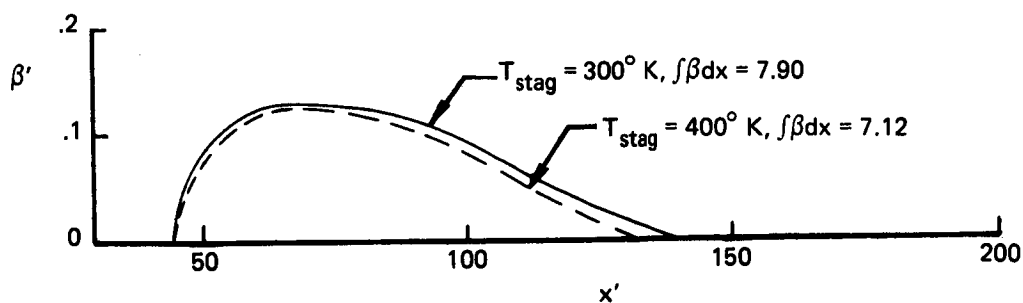
FIGURE 15.—TAYLOR-GOERTLER INSTABILITY— $M^* = 9$ AXISYMMETRIC AIR NOZZLE (Concluded)



a) Floor and ceiling walls, suction 2D-1, $\dot{m}_s/\dot{m}_0 = 0.0097$, $U^*/\nu^* = 26.22 \cdot 10^6/\text{m}$, $H^* = 1 \text{ m}$, $T_{\text{stag}} = 300^\circ \text{ K}$, $T_{\text{wall ad}}$

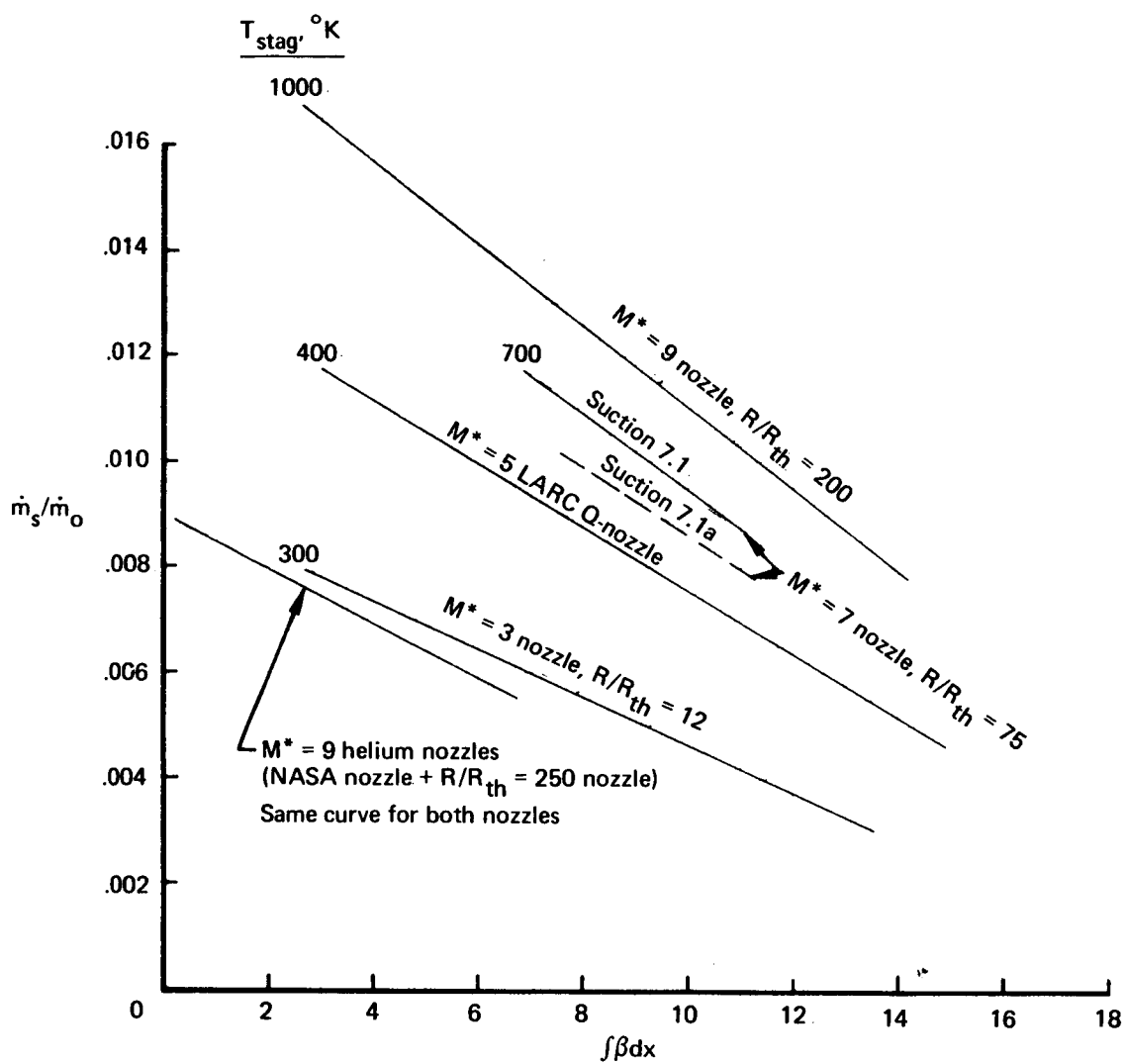


b) Floor and ceiling walls, suction 2D-2, $\dot{m}_s/\dot{m}_0 = 0.0049$, $U^*/\nu^* = 26.22 \cdot 10^6/\text{m}$, $H^* = 1 \text{ m}$, $T_{\text{stag}} = 300^\circ \text{ K}$, $T_{\text{wall ad}}$



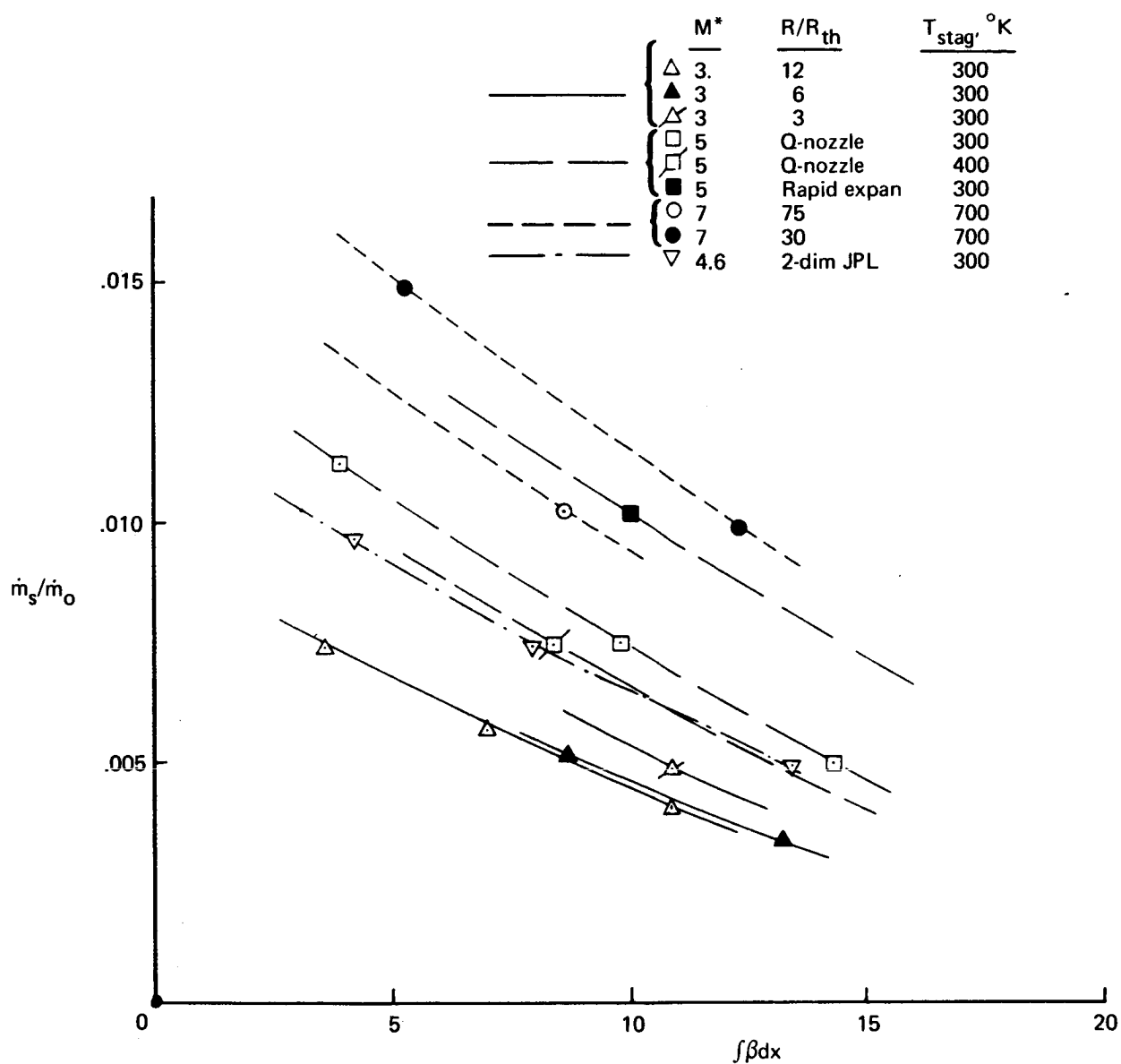
c) Floor and ceiling walls, suction 2D-3, $\dot{m}_s/\dot{m}_0 = 0.0074$, $U^*/\nu^* = 26.22 \cdot 10^6/\text{m}$, $H^* = 1 \text{ m}$, $T_{\text{stag}} = 300^\circ \text{ K}$, $T_{\text{wall ad}}$

FIGURE 16.—TAYLOR-GOERTLER INSTABILITY— $M^* = 4.6$ TWO-DIMENSIONAL JPL NOZZLE



a) Axisymmetric air and helium nozzles, $U^*/\nu^* = 26.22 \cdot 10^6/m$, $D^* = 1$ m, $T_{wall_{ad}}$

FIGURE 17.—TAYLOR-GOERTLER INSTABILITY SUMMARY



b) Axisymmetric and two-dimensional air nozzles, $U^*/\nu^* = 26.22 \cdot 10^6/m$, $T_{wall_{ad}}$

FIGURE 17.—TAYLOR-GOERTLER INSTABILITY SUMMARY (Concluded)

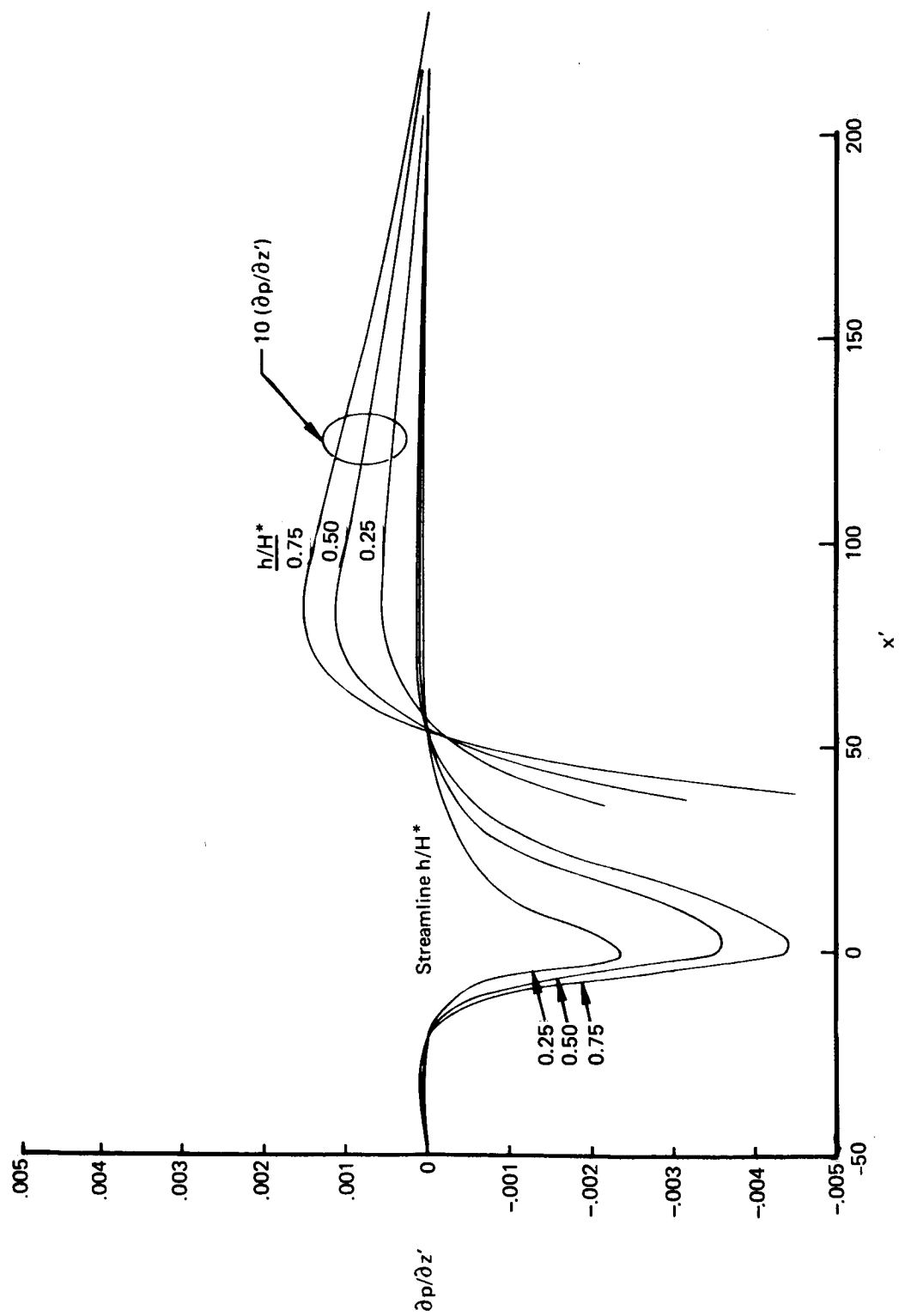
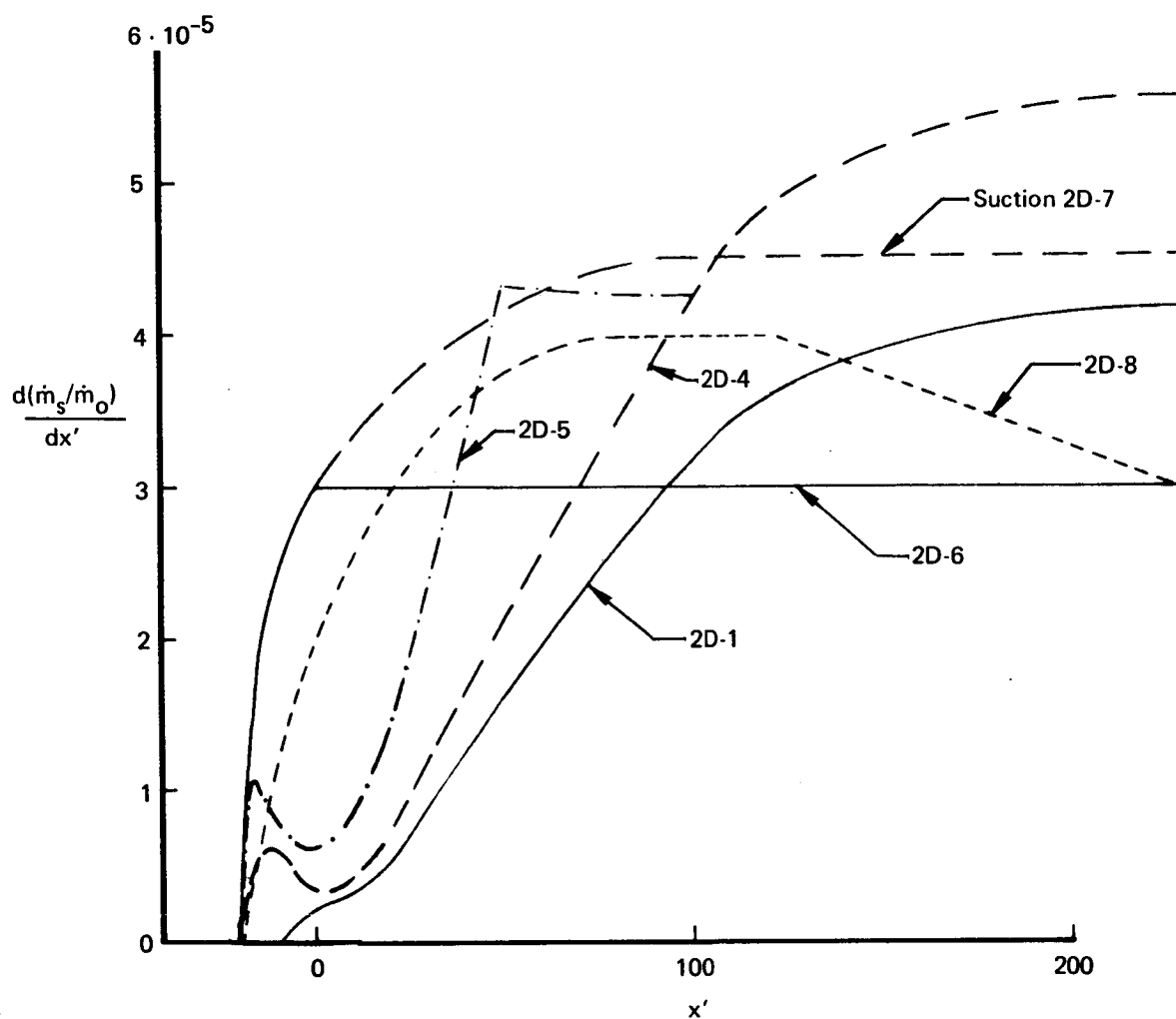


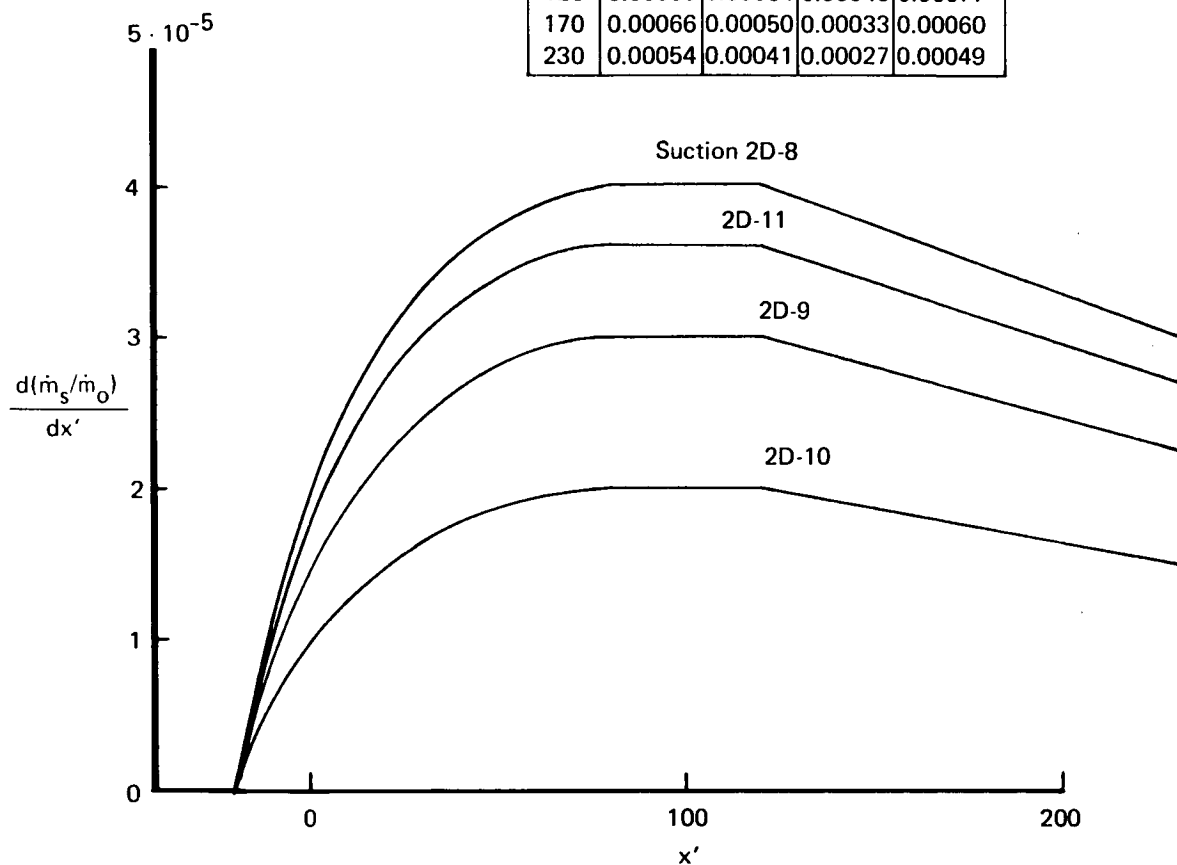
FIGURE 18.—PRESSURE GRADIENTS— $M^* = 4.6$ TWO-DIMENSIONAL JPL NOZZLE SIDE WALLS



a) Suction 2D1-2D8, $U^*/\nu^* = 26.22 \cdot 10^6/\text{m}$, $H^* = 1 \text{ m}$, $T_{\text{stag}} = 400^\circ \text{ K}$, $T_{\text{wall ad}}$

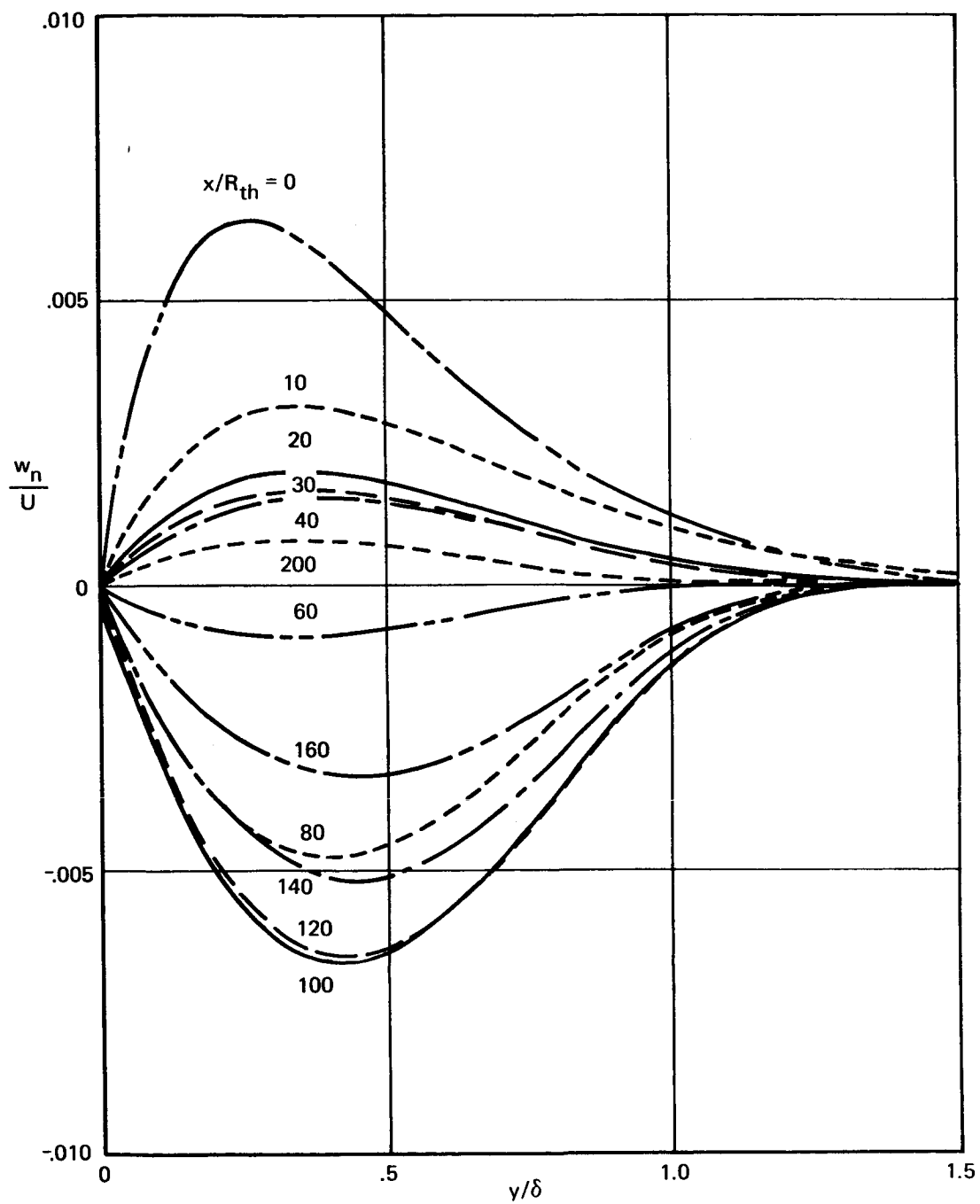
FIGURE 19.—SUCTION MASS FLOW DISTRIBUTIONS— $M^* = 4.6$ TWO-DIMENSIONAL JPL NOZZLE SIDE WALLS

x'	$-\rho_e v_o / \rho^* U^*$			
	2D-8	2D-9	2D-10	2D-11
-20	0	0	0	0
-15	0.00120	0.00090	0.00060	0.00108
0	0.00650	0.00488	0.00325	0.00585
10	0.00600	0.00450	0.00300	0.00540
20	0.00424	0.00318	0.00212	0.00382
50	0.00174	0.00131	0.00087	0.00157
80	0.00114	0.00086	0.00057	0.00103
120	0.00085	0.00064	0.00043	0.00077
170	0.00066	0.00050	0.00033	0.00060
230	0.00054	0.00041	0.00027	0.00049



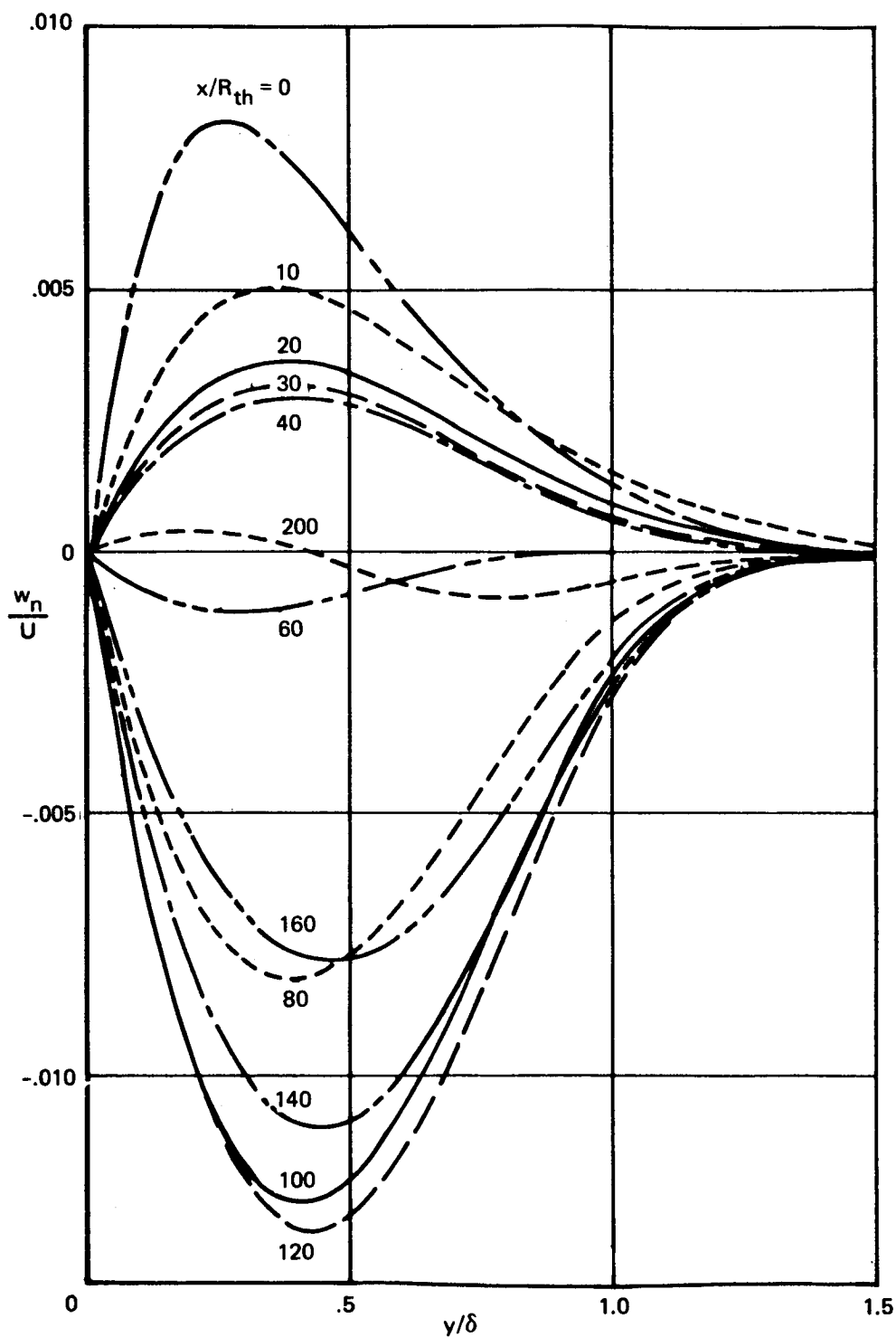
b) Suction 2D8-2D11, $U^*/\nu^* = 26.22 \cdot 10^6/\text{m}$, $H^* = 1 \text{ m}$, $T_{\text{stag}} = 400^\circ \text{ K}$, $T_{\text{wall ad}}$

FIGURE 19.—SUCTION MASS FLOW DISTRIBUTIONS— $M^* = 4.6$ TWO-DIMENSIONAL JPL NOZZLE SIDE WALLS (Concluded)



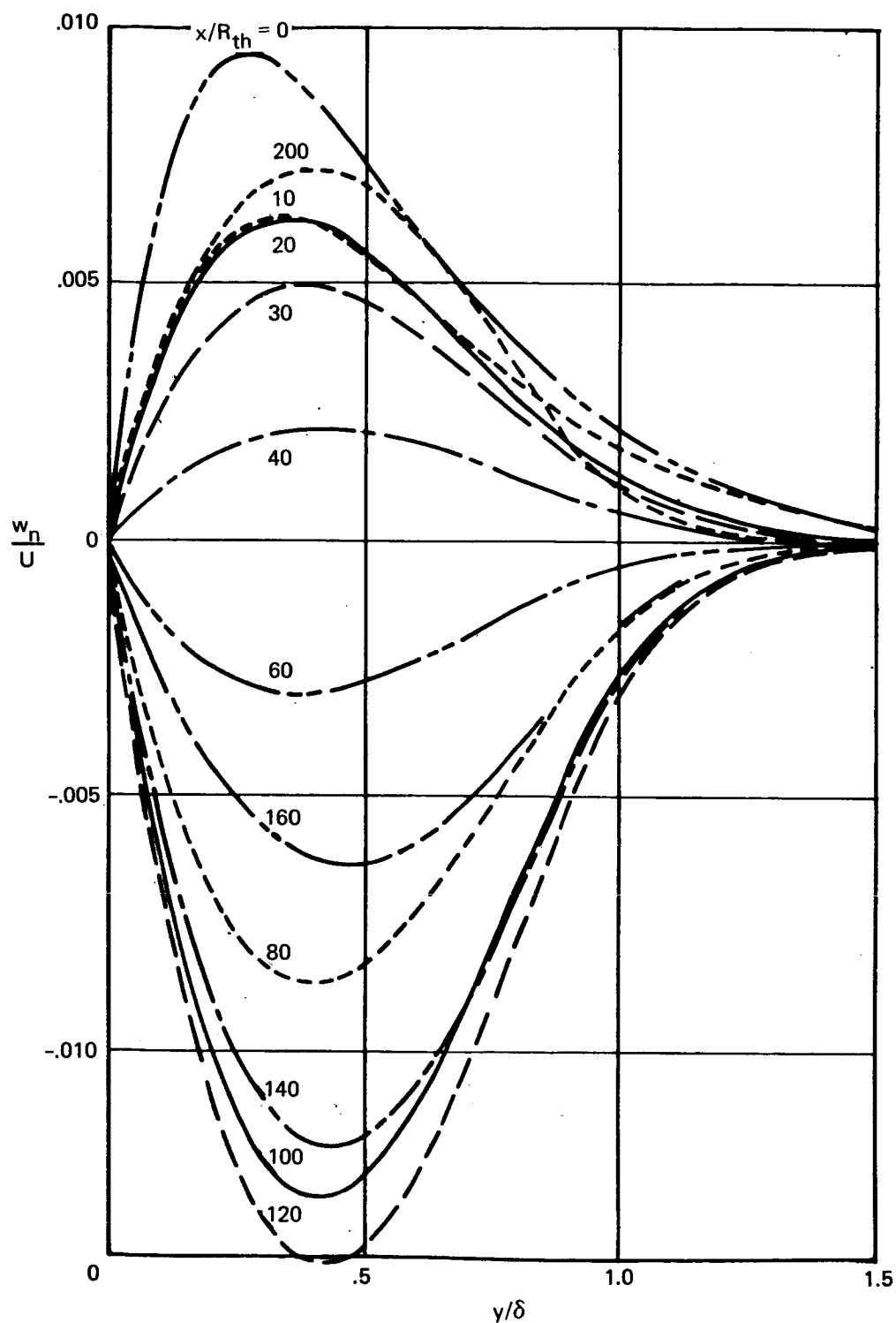
a) 25% streamline, suction 2D-9

FIGURE 20.—BOUNDARY LAYER CROSSFLOW VELOCITY PROFILES—
 $M^* = 4.6$ TWO-DIMENSIONAL JPL NOZZLE SIDE WALLS



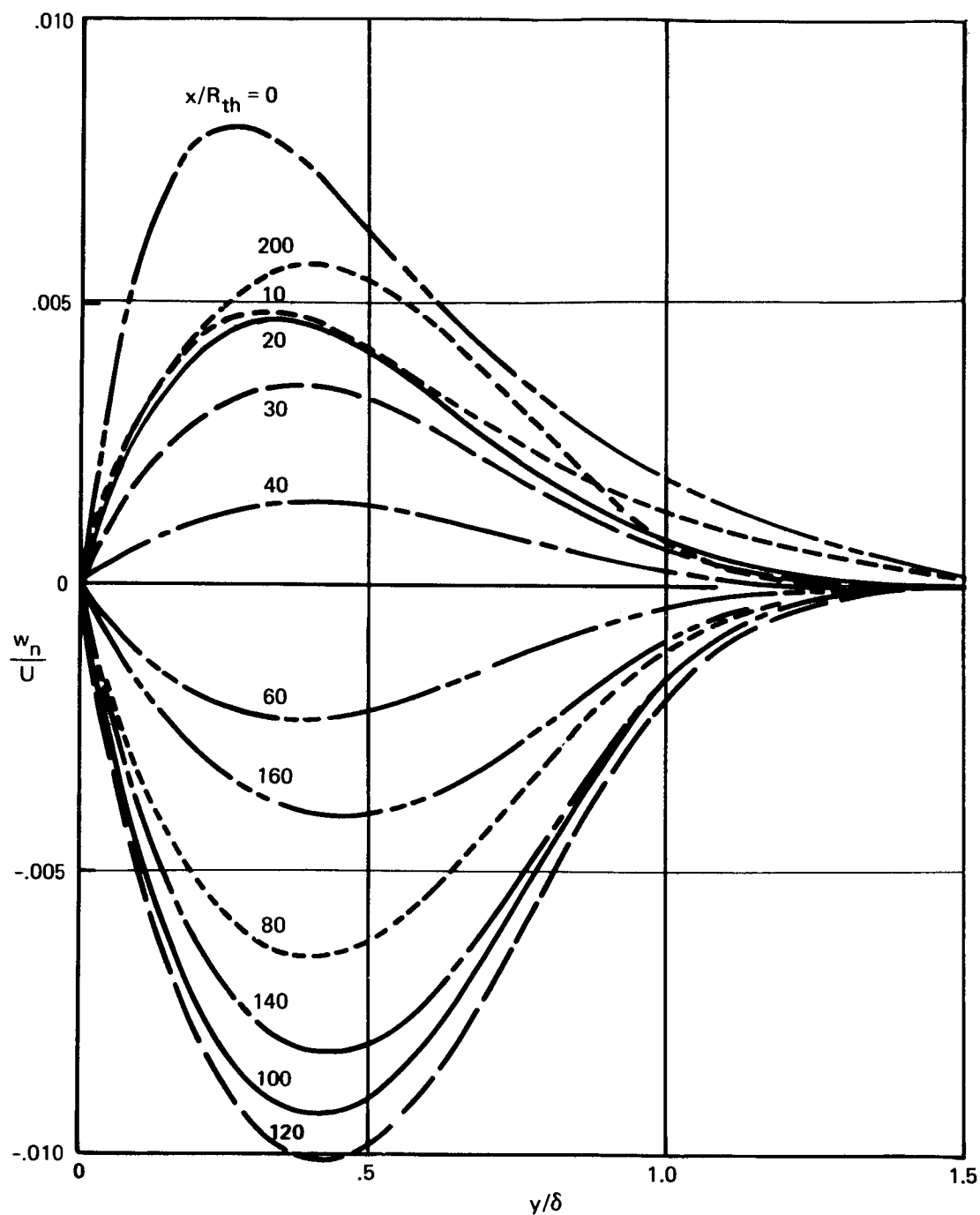
b) 25% streamline, suction 2D-10

FIGURE 20.—BOUNDARY LAYER CROSSFLOW VELOCITY PROFILES—
 $M^* = 4.6$ TWO-DIMENSIONAL JPL NOZZLE SIDE WALLS (Continued)



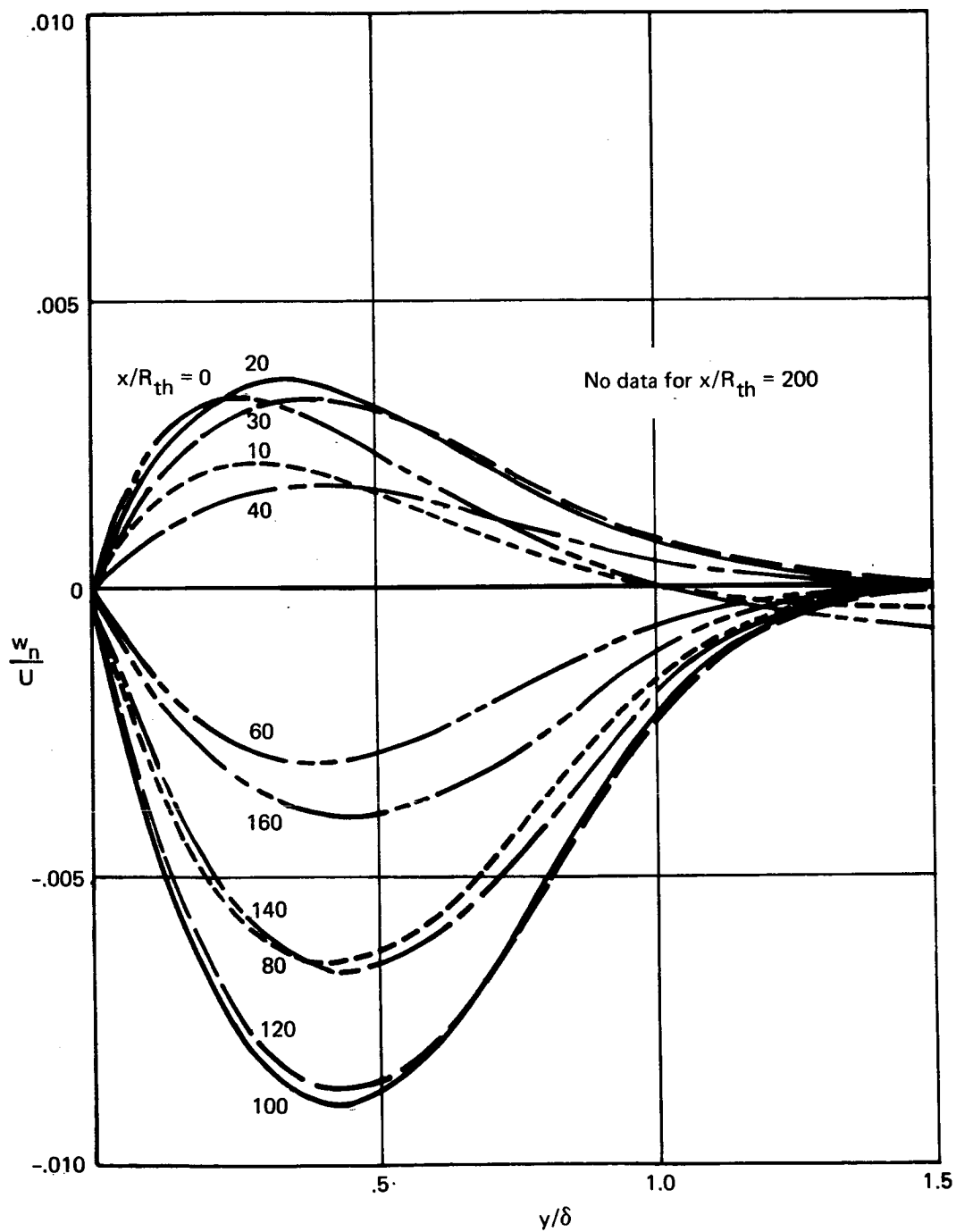
c) 50% streamline, suction 2D-9

FIGURE 20.—BOUNDARY LAYER CROSSFLOW VELOCITY PROFILES—
 $M^* = 4.6$ TWO-DIMENSIONAL JPL NOZZLE SIDE WALLS (Continued)



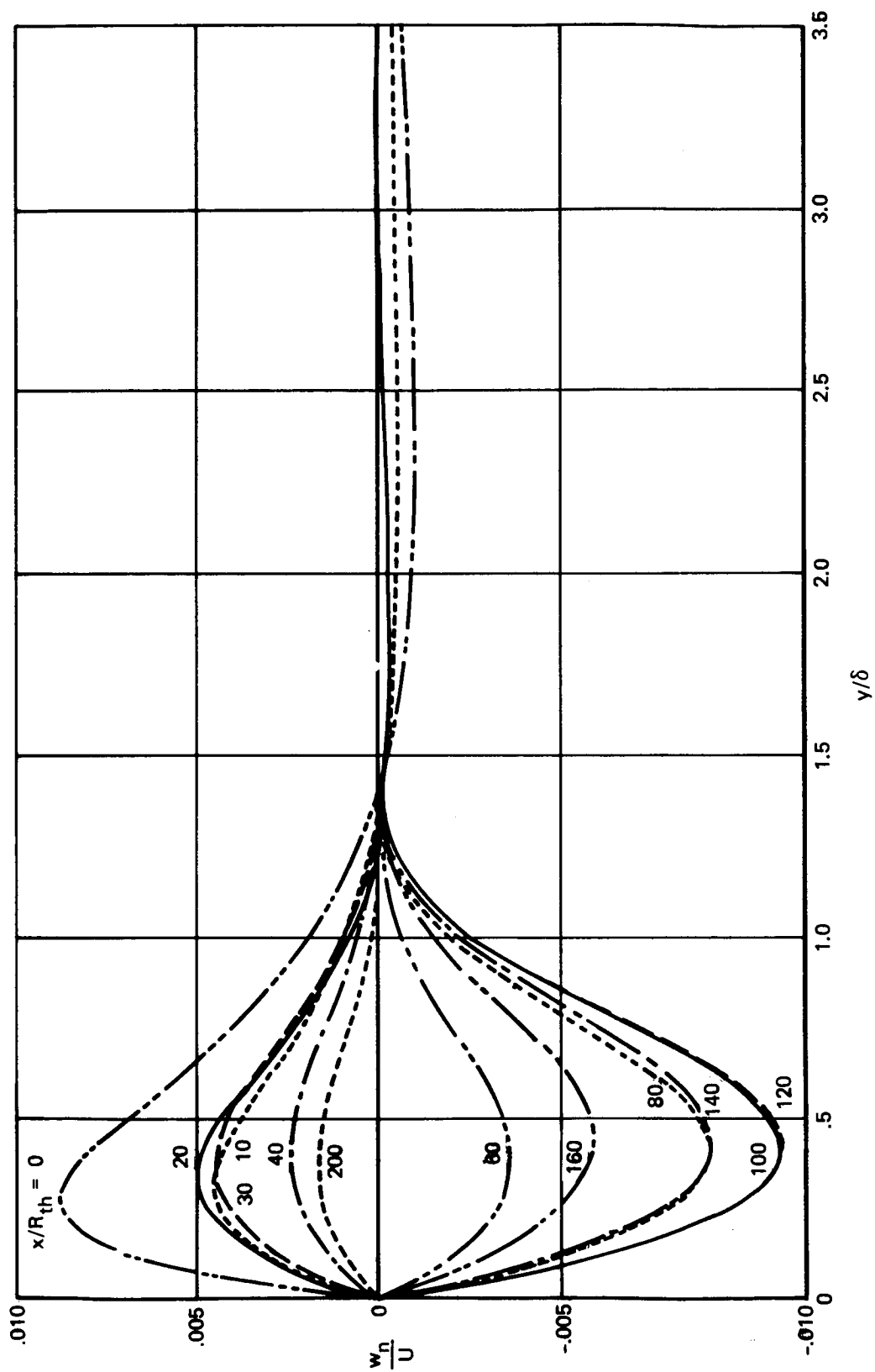
d) 50% streamline, suction 2D-11

FIGURE 20.—BOUNDARY LAYER CROSSFLOW VELOCITY PROFILES—
 $M^* = 4.6$ TWO-DIMENSIONAL JPL NOZZLE SIDE WALLS (Continued)



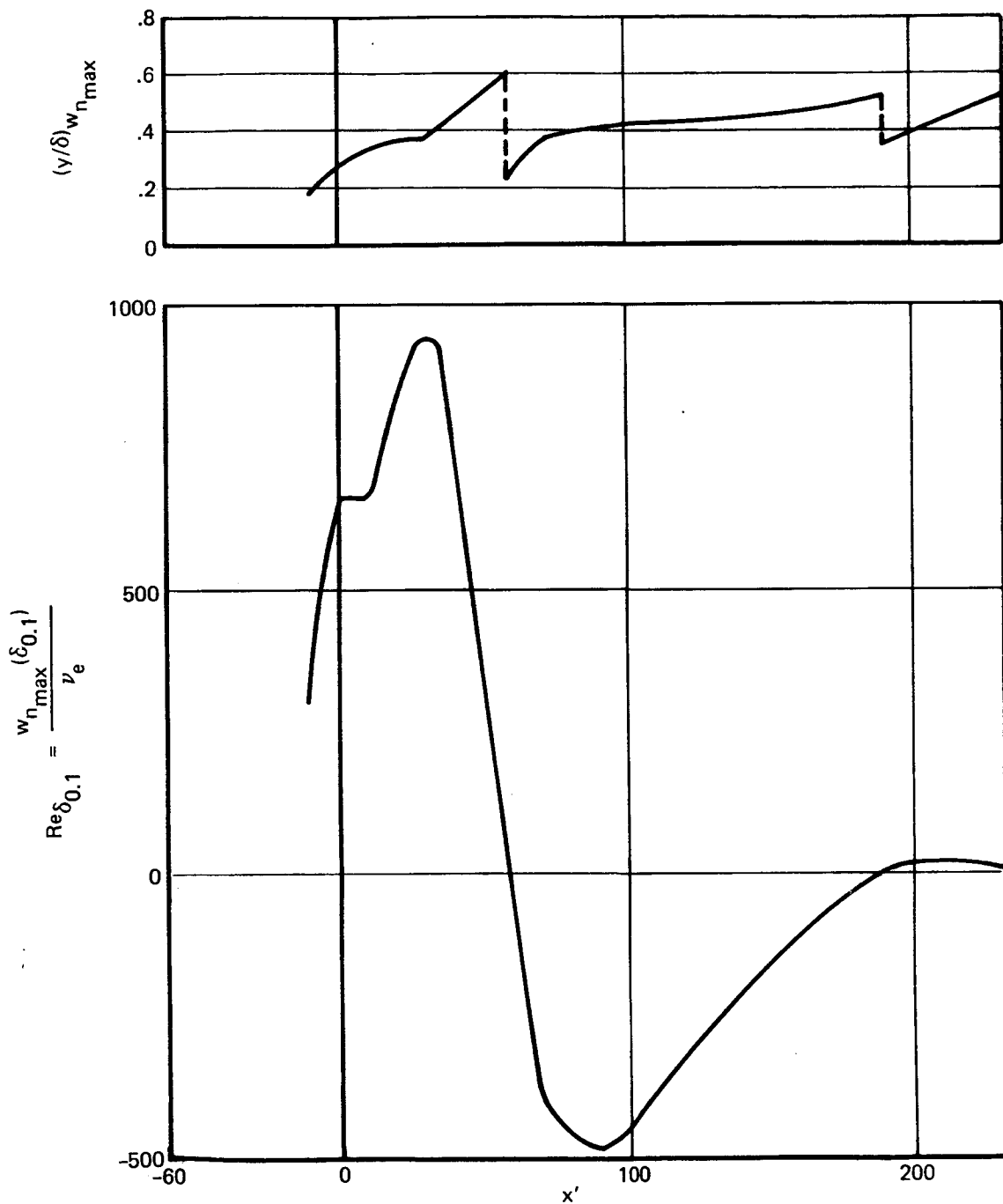
e) 75% streamline, suction 2D-7

FIGURE 20.—BOUNDARY LAYER CROSSFLOW VELOCITY PROFILES—
 $M^* = 4.6$ TWO-DIMENSIONAL JPL NOZZLE SIDE WALLS (Continued)



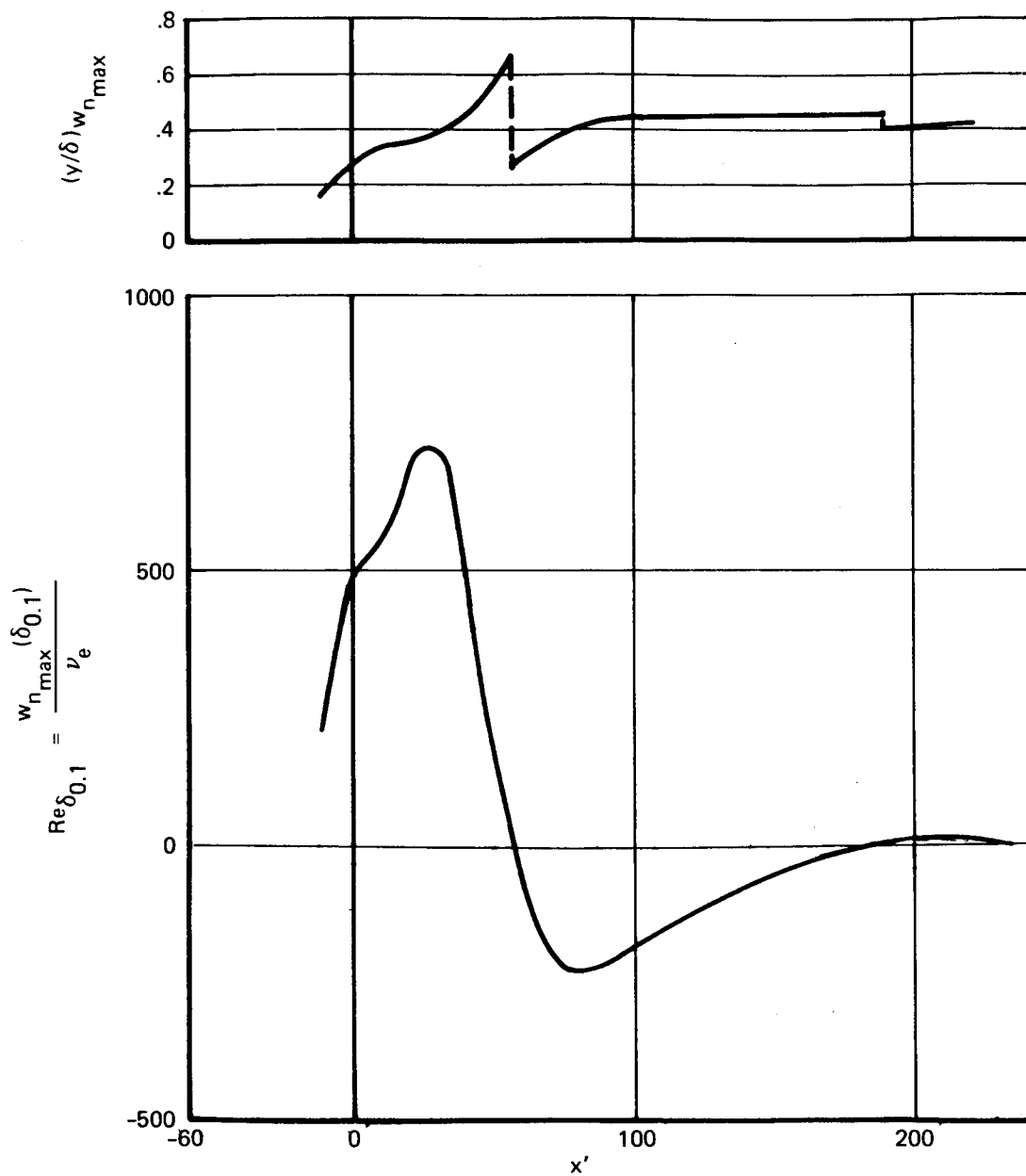
f) 75% streamline, suction 2D-8

FIGURE 20.—BOUNDARY LAYER CROSSFLOW VELOCITY PROFILES—
 $M^* = 4.6$ TWO-DIMENSIONAL JPL NOZZLE SIDE WALLS (Concluded)



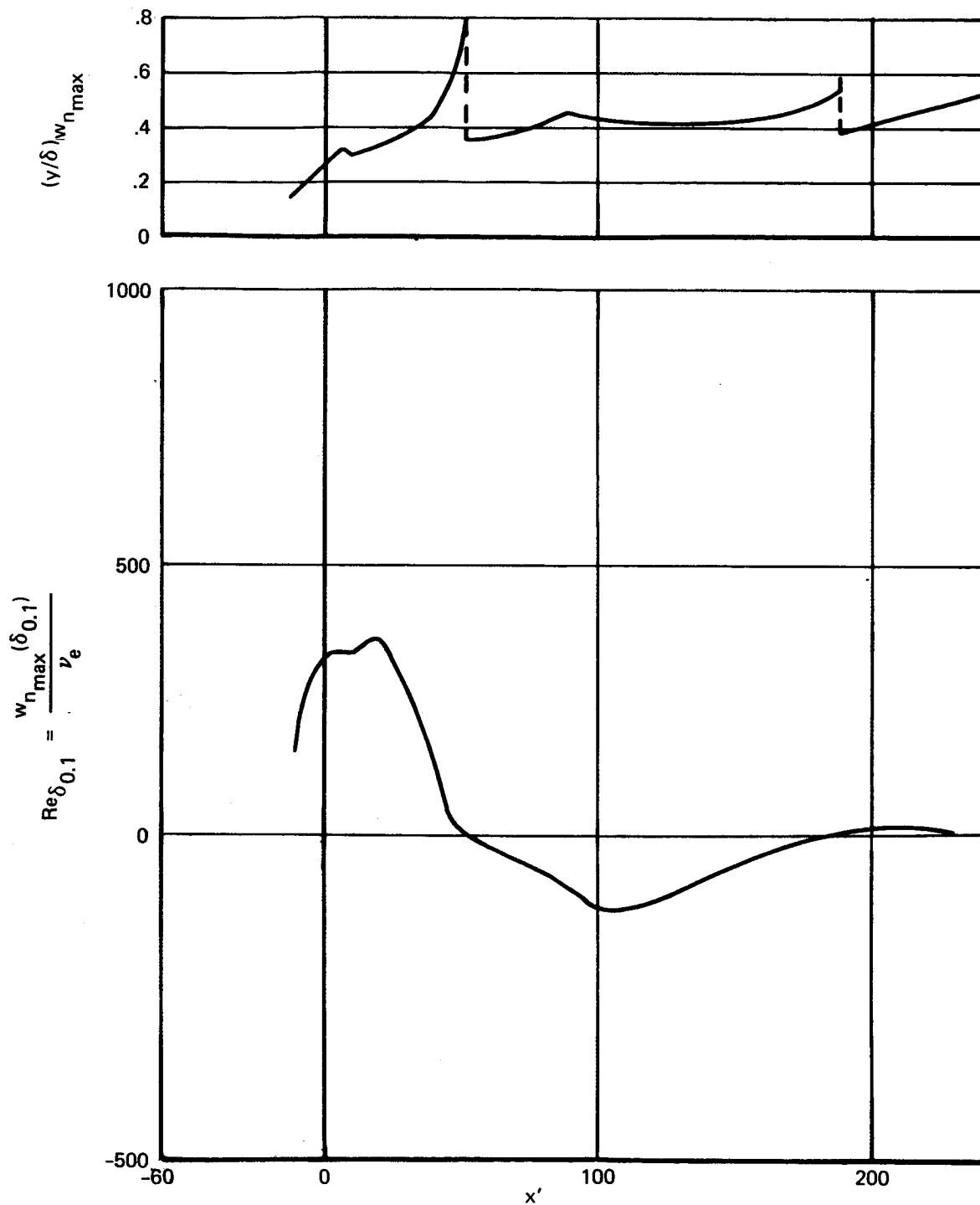
a) 75% streamline, suction 2D-1, $U^*/\nu^* = 26.22 \cdot 10^6/\text{m}$, $H^* = 1\text{m}$, $T_{\text{stag}} = 400^\circ \text{K}$, $T_{\text{wall ad}}$

FIGURE 21.—BOUNDARY LAYER CROSSFLOW REYNOLDS NUMBER AND $(y/\delta)w_{\eta_{\max}}$ —
 $M^* = 4.6$ TWO-DIMENSIONAL JPL NOZZLE SIDE WALLS



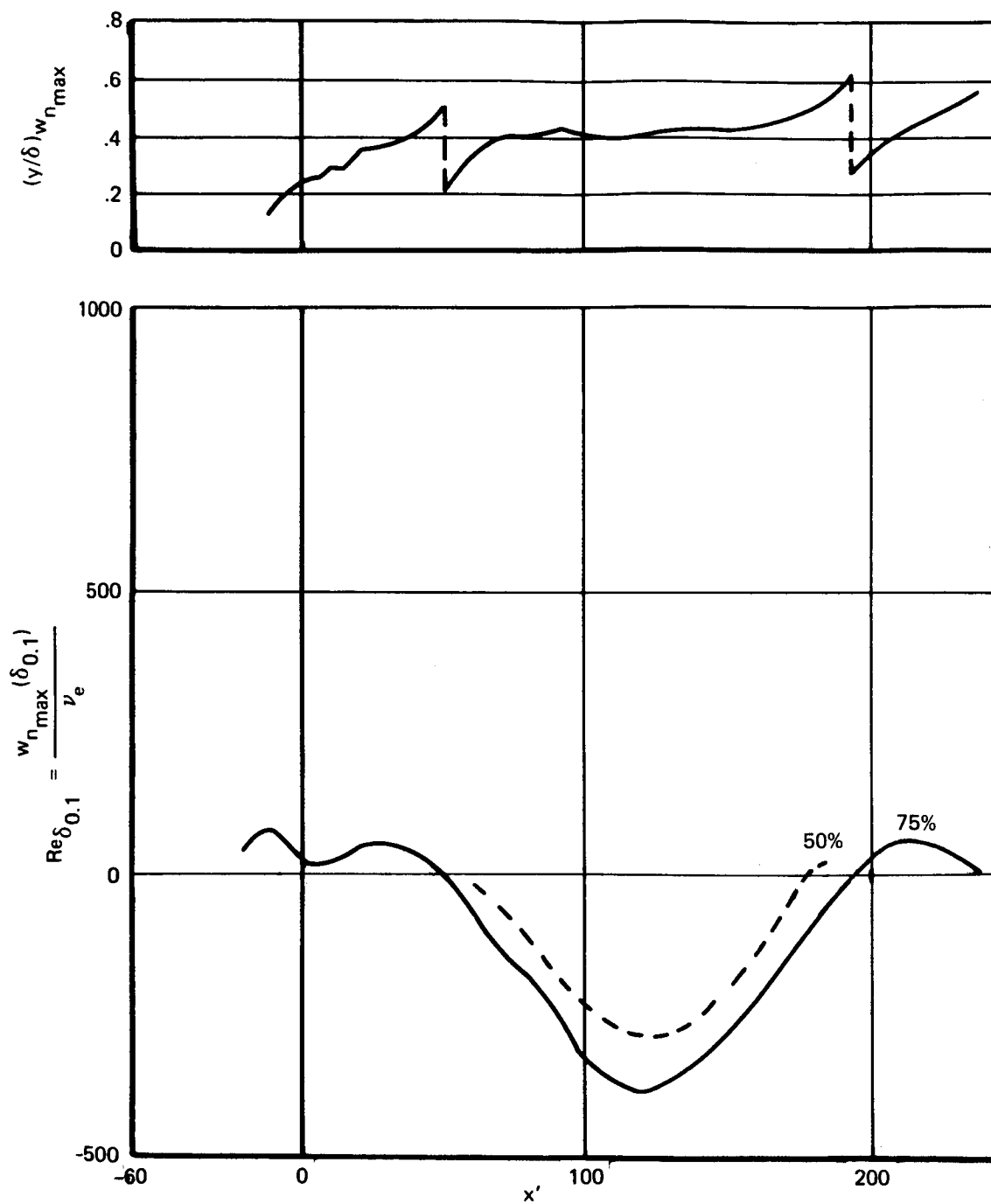
b) 75% streamline, suction 2D-4, $U^*/\nu^* = 26.22 \cdot 10^6/m$, $H^* = 1m$, $T_{stag} = 400^\circ K$, $T_{wall_{ad}}$

FIGURE 21.—BOUNDARY LAYER CROSSFLOW REYNOLDS NUMBERS AND $(y/\delta)w_{n\max}$ —
 $M^* = 4.6$ TWO-DIMENSIONAL JPL NOZZLE SIDE WALLS (Continued)



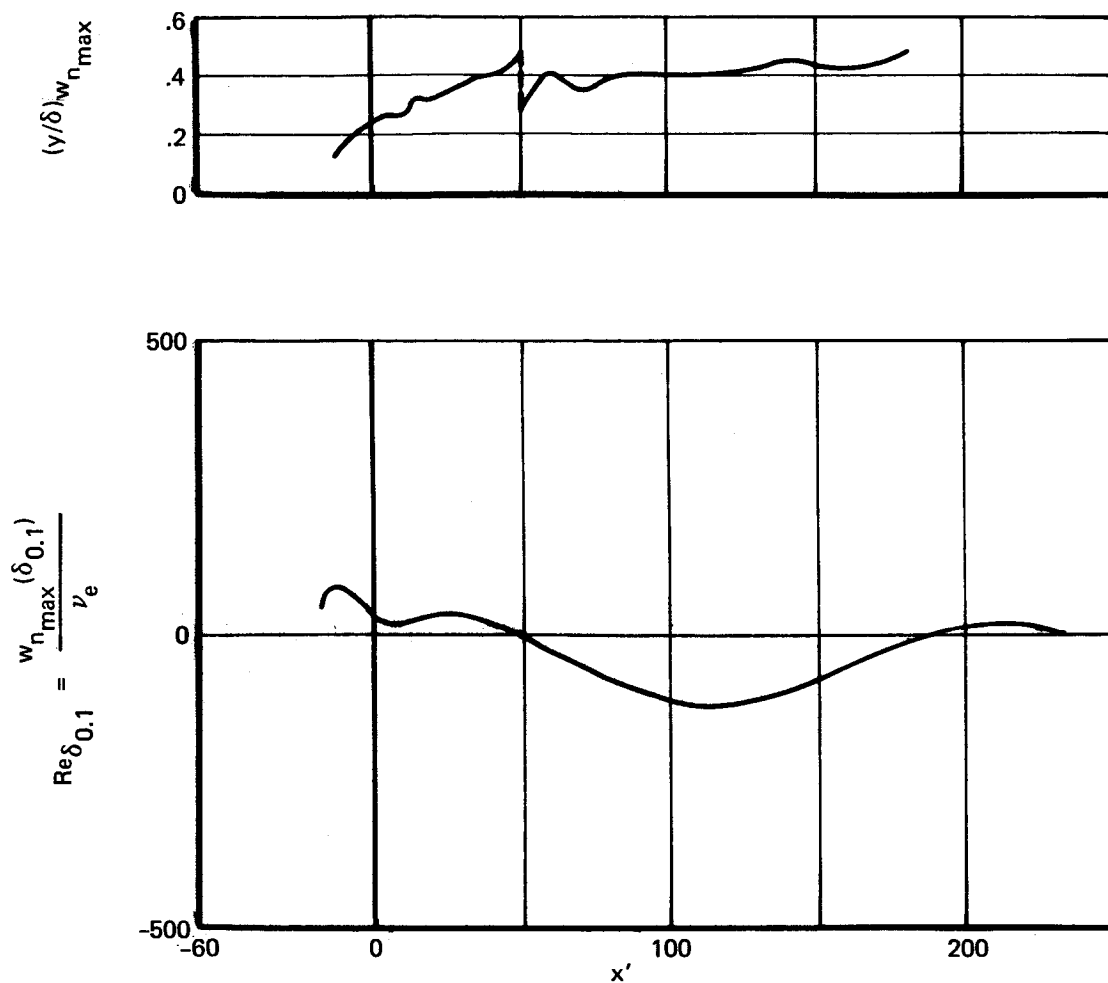
c) 75% streamline, suction 2D-5, $|U^*/\nu^* = 26.22 \cdot 10^6/\text{m}$, $H^* = 1\text{m}$, $T_{\text{stag}} = 400^\circ \text{K}$, $T_{\text{wall ad}}$

FIGURE 21.—BOUNDARY LAYER CROSSFLOW REYNOLDS NUMBER AND $(y/\delta)_{w_{\eta_{\max}}}$ —
 $M^* = 4.6$ TWO-DIMENSIONAL JPL NOZZLE SIDE WALLS (Continued)



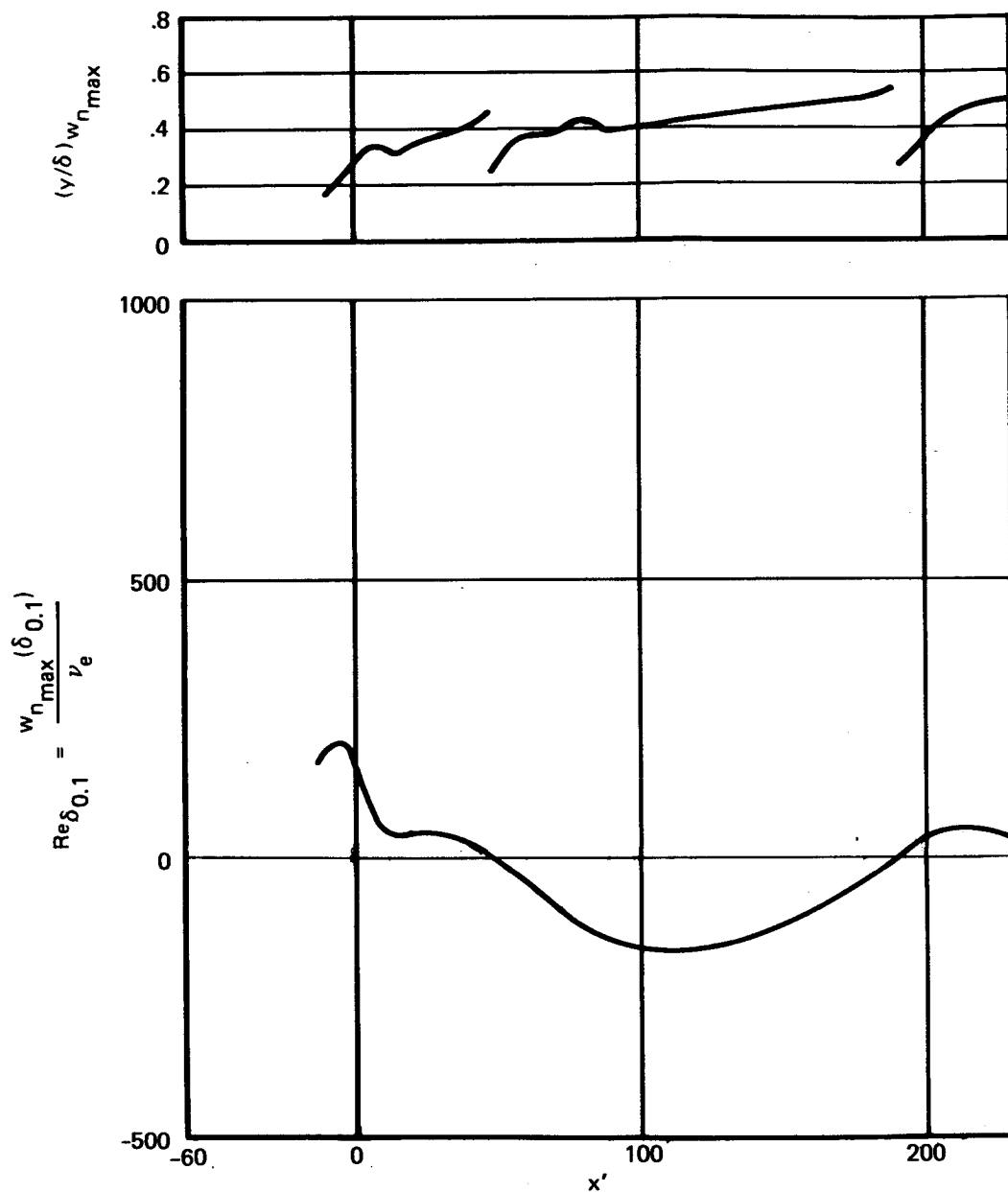
d) 50% and 75% streamlines, suction 2D-6, $u^*/\nu^* = 26.22 \cdot 10^6/m$, $H^* = 1m$; $T_{stag} = 400^\circ K$, $T_{wall_{ad}}$

FIGURE 21.—BOUNDARY LAYER CROSSFLOW REYNOLDS NUMBER AND $(y/\delta)w_{n_{max}}$ —
 $M^* = 4.6$ TWO-DIMENSIONAL JPL NOZZLE SIDE WALLS (Continued)



e) 75% streamline, suction 2D-7, $U^*/\nu^* = 26.22 \cdot 10^6/\text{m}$, $H^* = 1\text{m}$, $T_{\text{stag}} = 400^\circ \text{K}$, T_{wallad}

FIGURE 21.—BOUNDARY LAYER CROSSFLOW REYNOLDS NUMBER AND $(y/\delta)_{w_{n_{\max}}}$ —
 $M^* = 4.6$ TWO-DIMENSIONAL JPL NOZZLE SIDE WALLS (Continued)



f) 75% streamline, suction 2D-8,, $U^*/\nu^* = 26.22 \cdot 10^6/m$, $H^* = 1m$, $T_{stag} = 400^{\circ} K$, $T_{wall_{ad}}$

**FIGURE 21.—BOUNDARY LAYER CROSSFLOW REYNOLDS NUMBER AND $(y/\delta) w_{n_{max}}$
 $M^* = 4.6$ TWO-DIMENSIONAL JPL NOZZLE SIDE WALLS (Concluded)**

	Streamline, %	Suction no.
—	75	2D-8
- - -	50	2D-11
- · - · -	25	2D-9

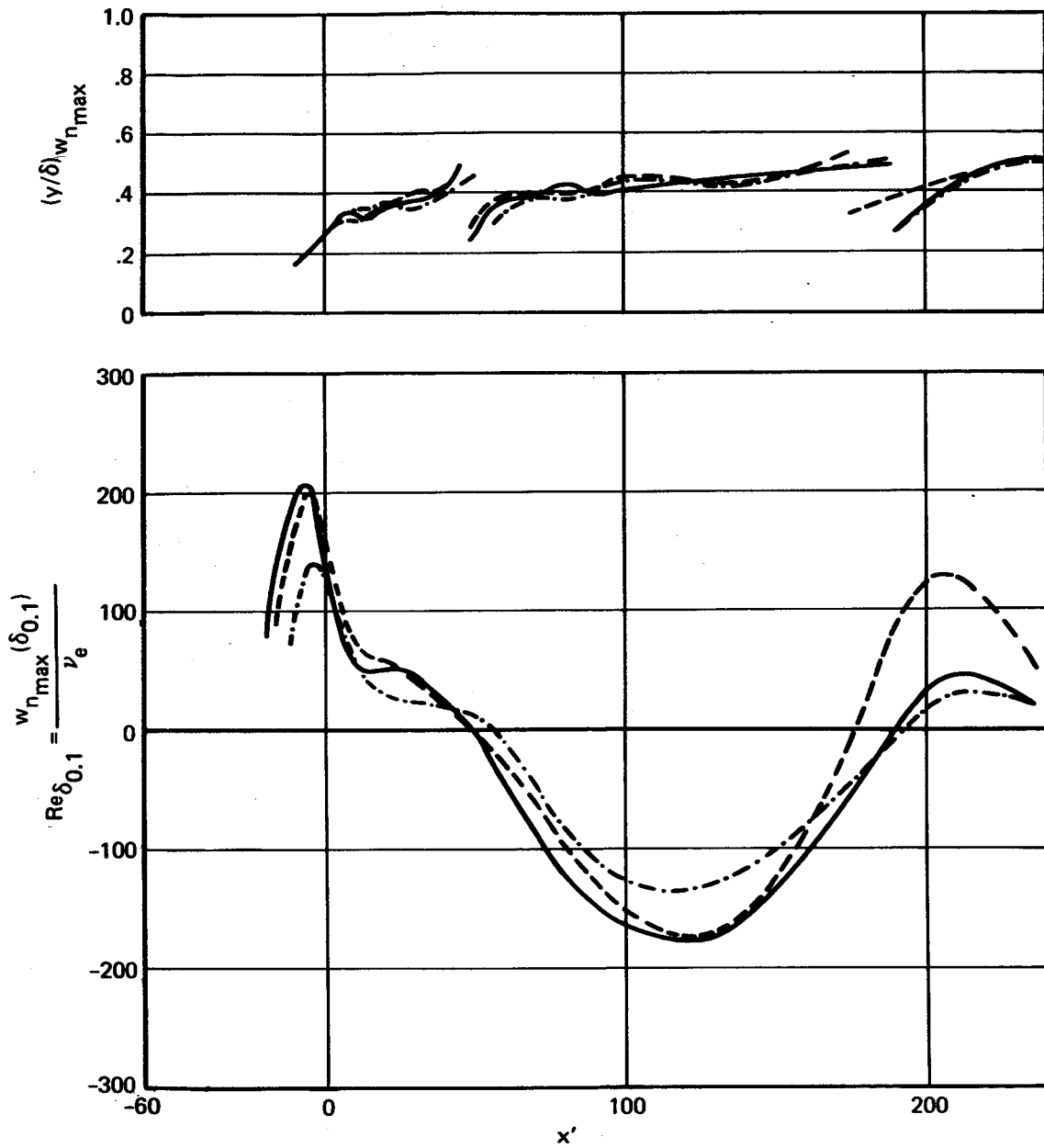
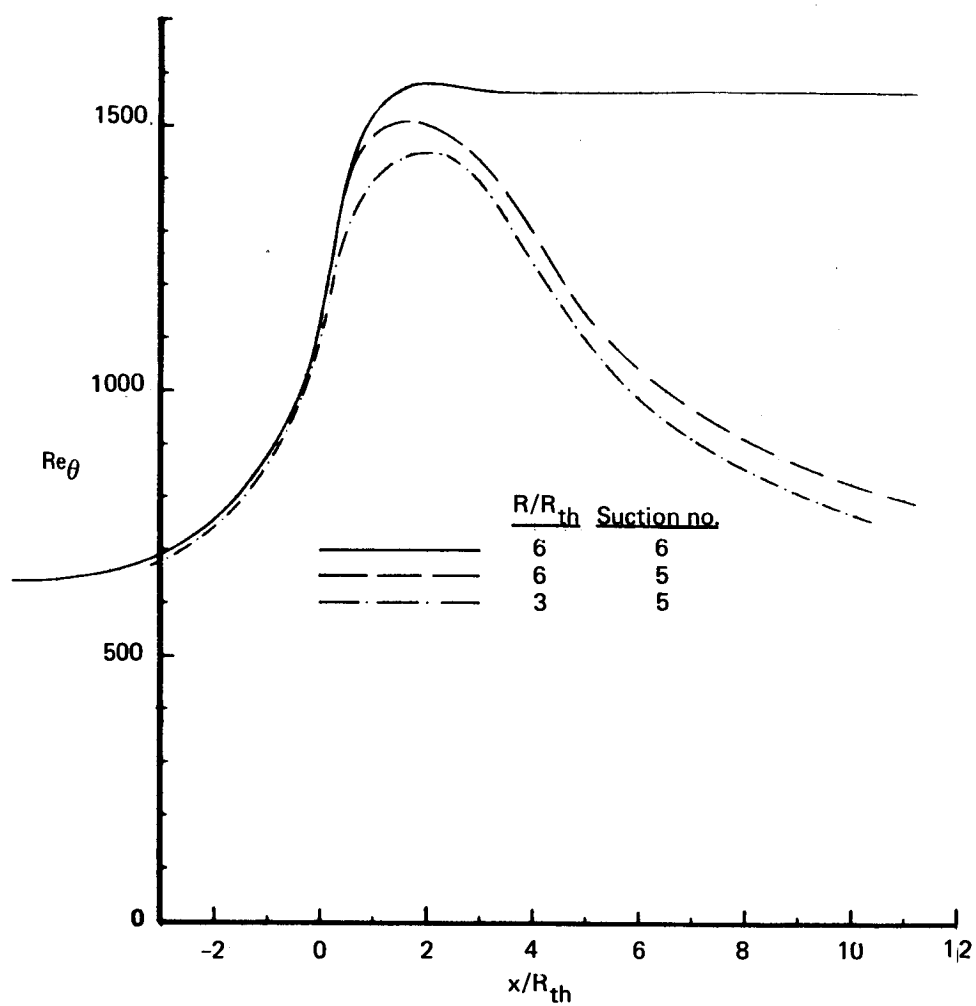
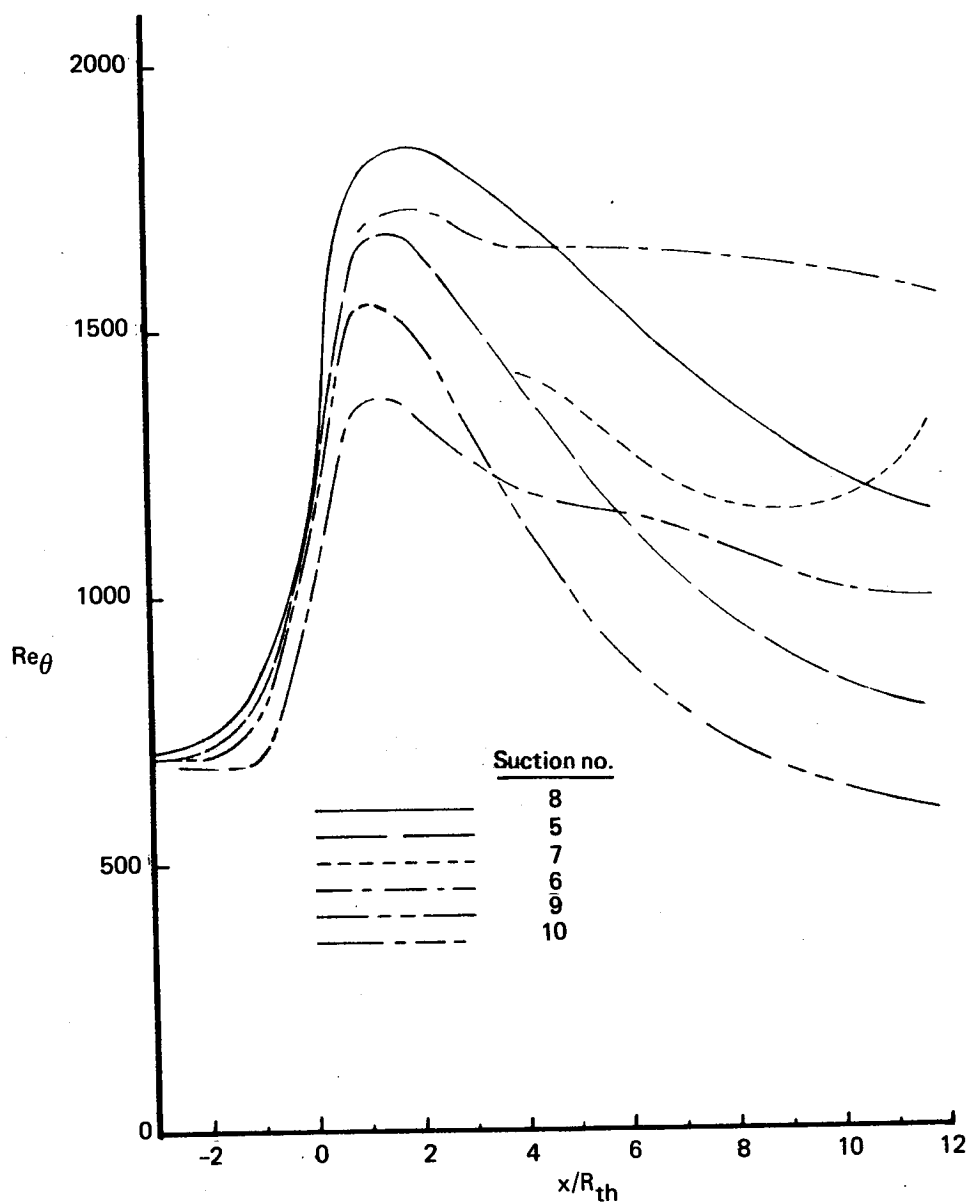


FIGURE 22.—CROSSFLOW STUDY SUMMARY—RECOMMENDED CONFIGURATION



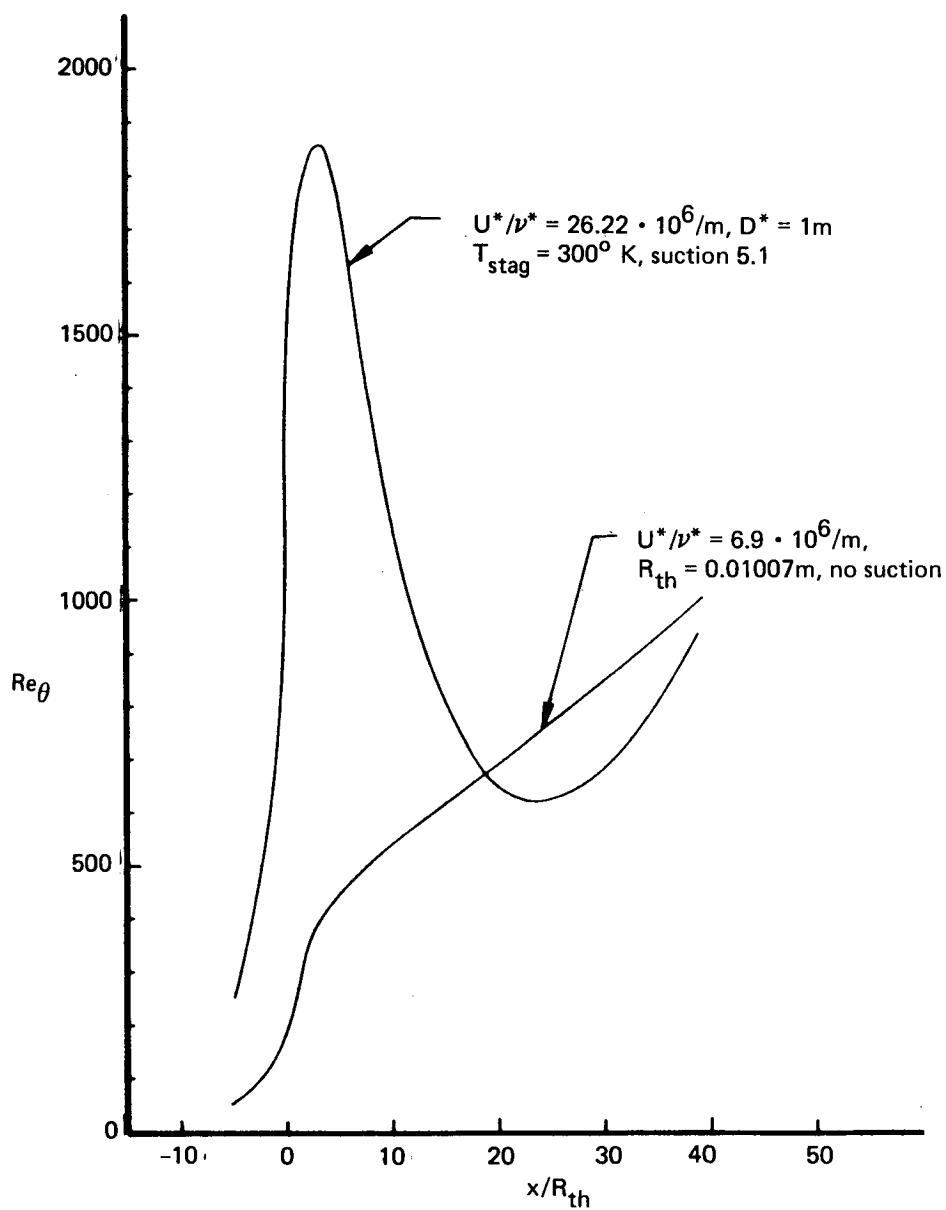
a) $M^* = 3$ axisymmetric nozzle, $U^*/\nu^* = 26.22 \cdot 10^6/m$, $D^* = 1m$, $T_{stag} = 300^\circ K$, $T_{wall_{ad}}$

FIGURE 23.—VARIATIONS OF Re_θ IN SUPERSONIC AIR NOZZLES



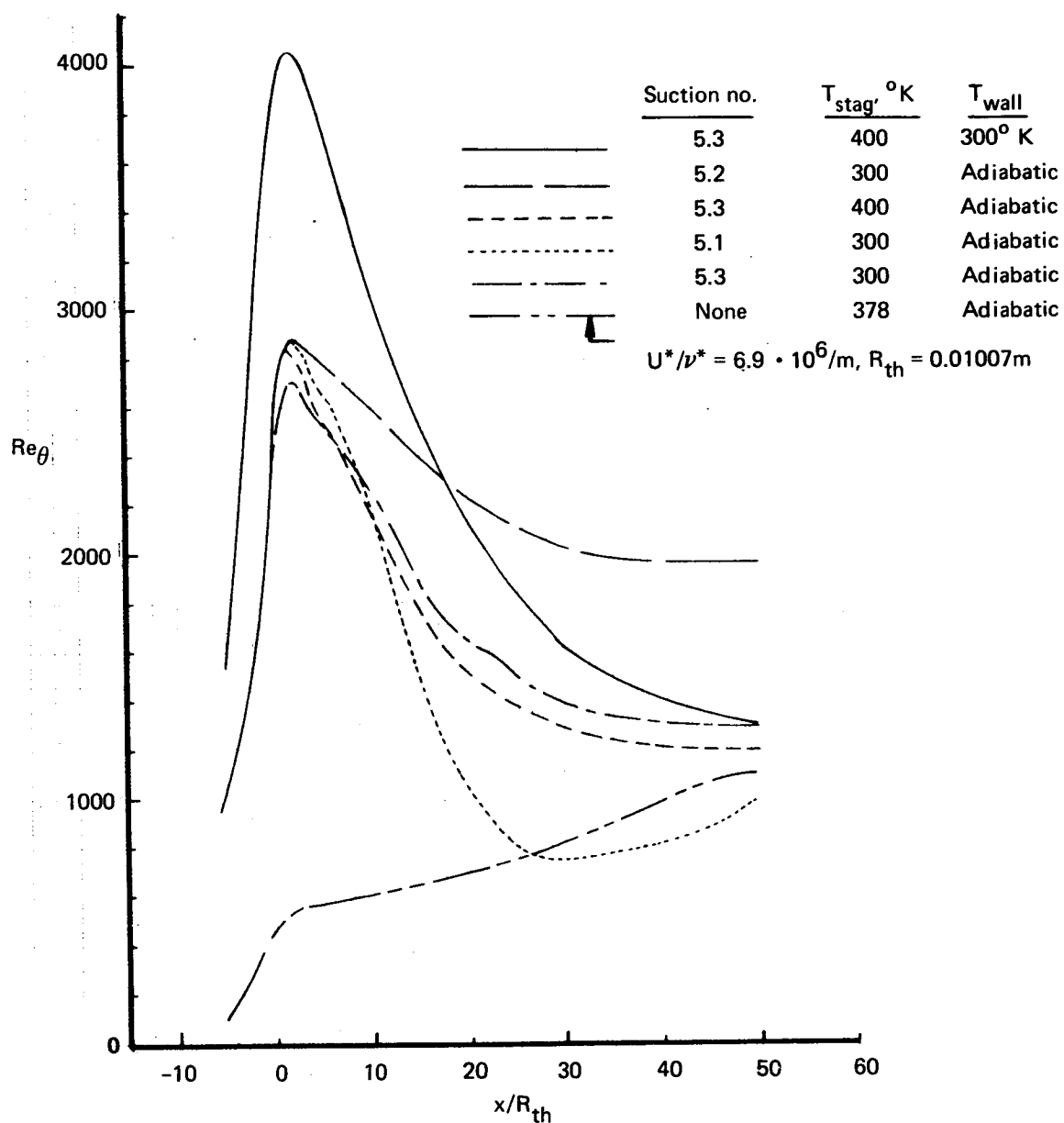
b) $M^* = 3$ axisymmetric nozzle, $R/R_{th} = 12$, $U^*/\nu^* = 26.22 \cdot 10^6/m$, $D^* = 1m$, $T_{stag} = 300^\circ K$, $T_{wall_{ad}}$

FIGURE 23.—VARIATIONS OF Re_θ IN SUPERSONIC AIR NOZZLES (Continued)



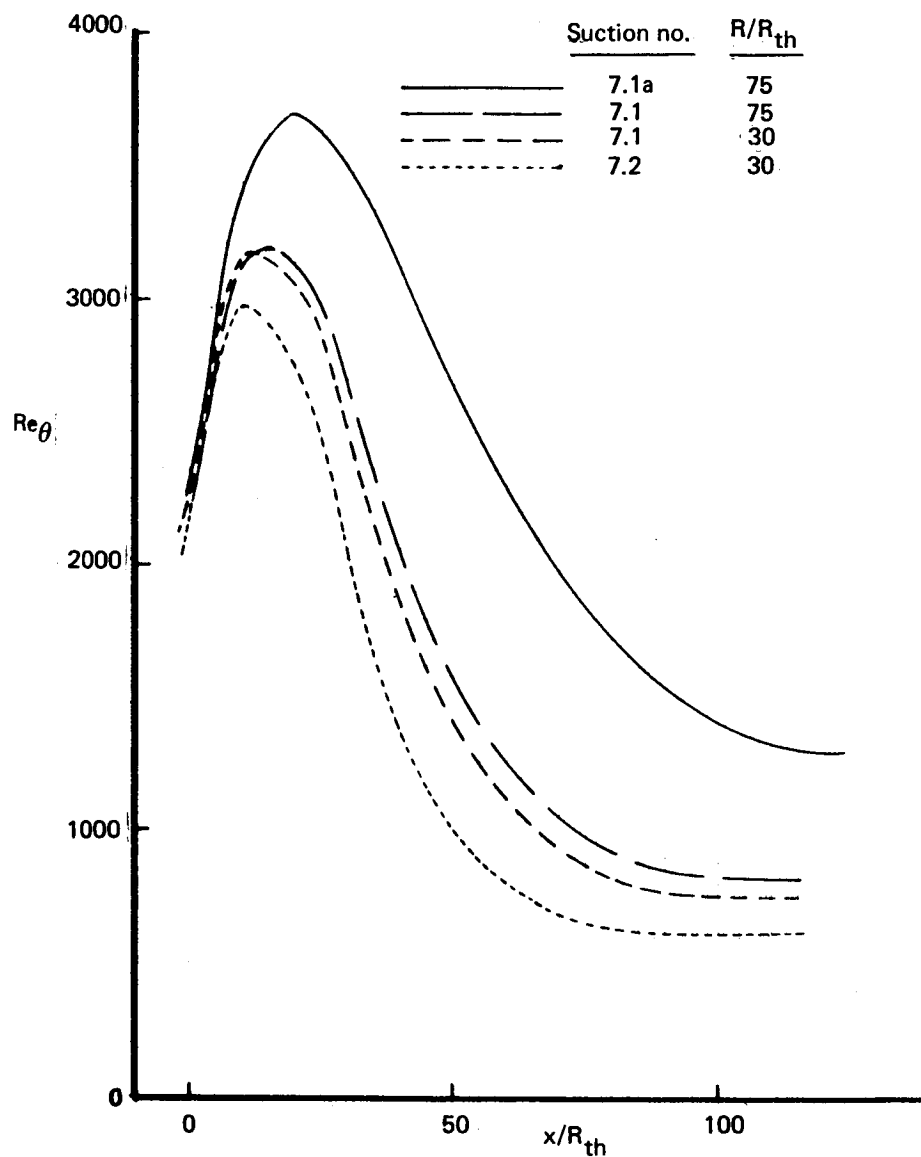
c) $M^* = 5$ rapid expansion axisymmetric nozzle, $T_{\text{wall ad}}$

FIGURE 23.—VARIATIONS OF Re_θ IN SUPERSONIC AIR NOZZLES (Continued)



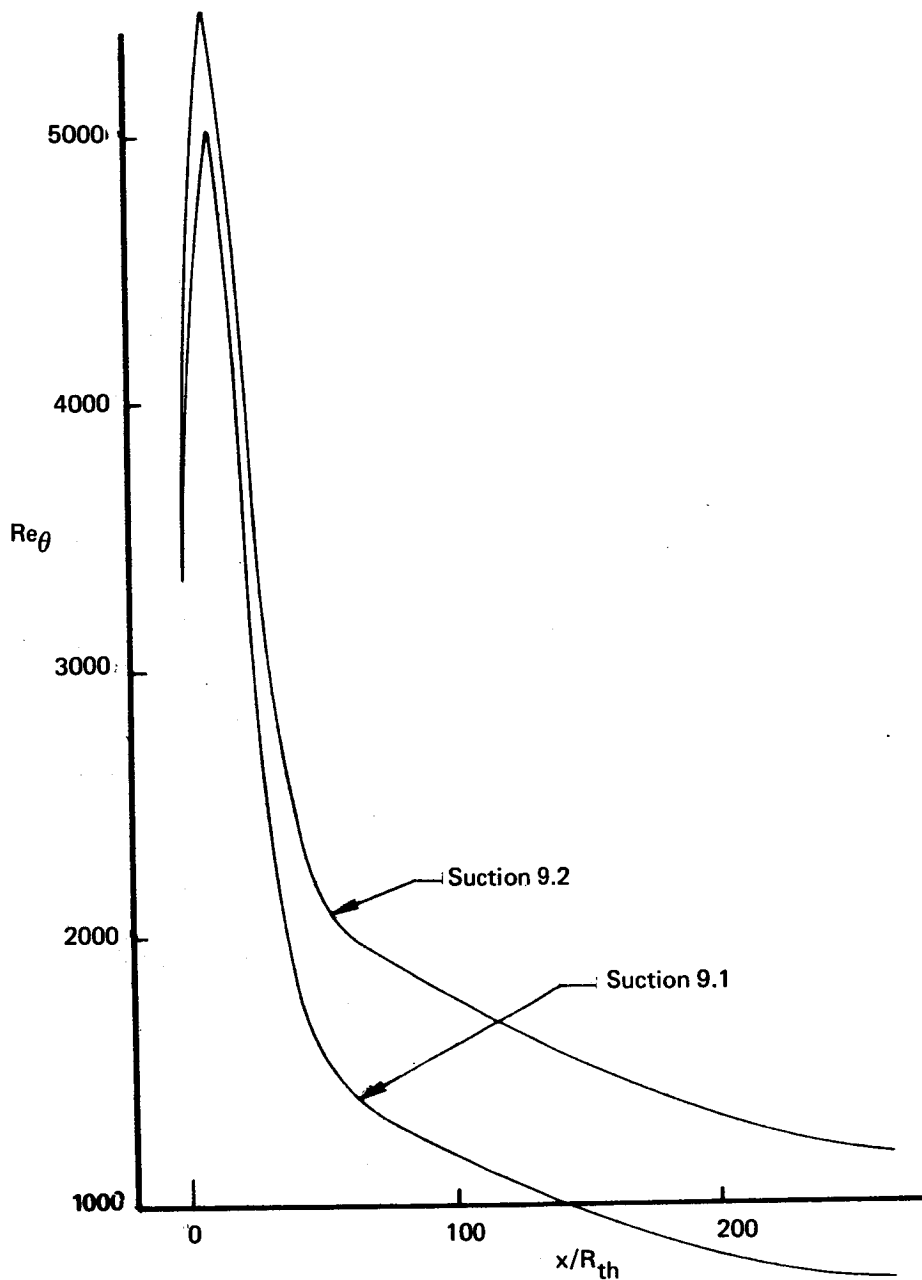
d) $M^* = 5$ LARC axisymmetric Q-nozzle, $U^*/\nu^* = 26.22 \cdot 10^6/m$, $D^* = 1m$

FIGURE 23.—VARIATIONS OF Re_θ IN SUPERSONIC AIR NOZZLES (Continued)



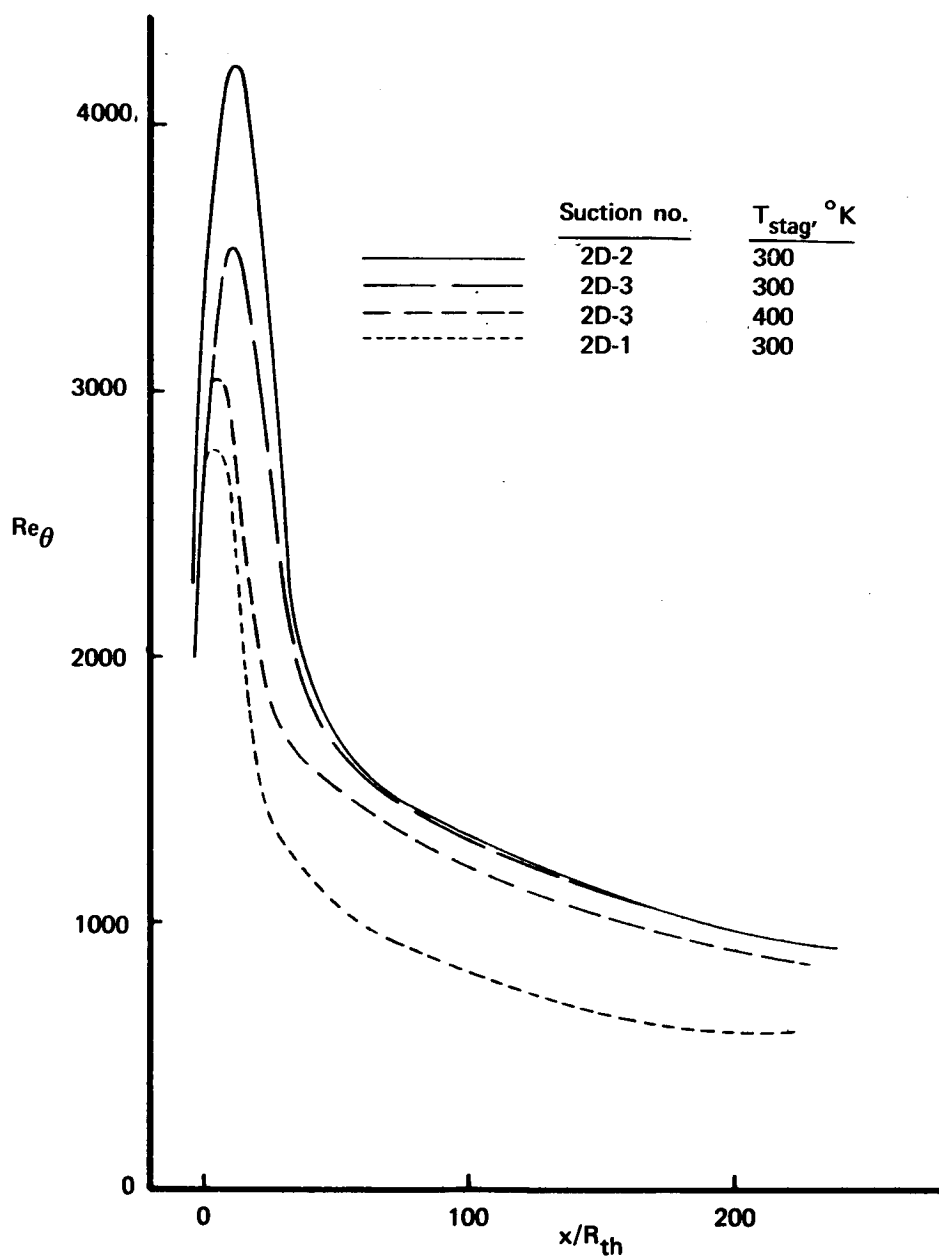
e) $M^* = 7$ axisymmetric nozzle, $U^*/\nu^* = 26.22 \cdot 10^6/m$, $D^* = 1m$, $T_{stag} = 700^\circ K$, $T_{wall_{ad}}$

FIGURE 23.—VARIATIONS OF Re_θ IN SUPERSONIC AIR NOZZLES (Continued)



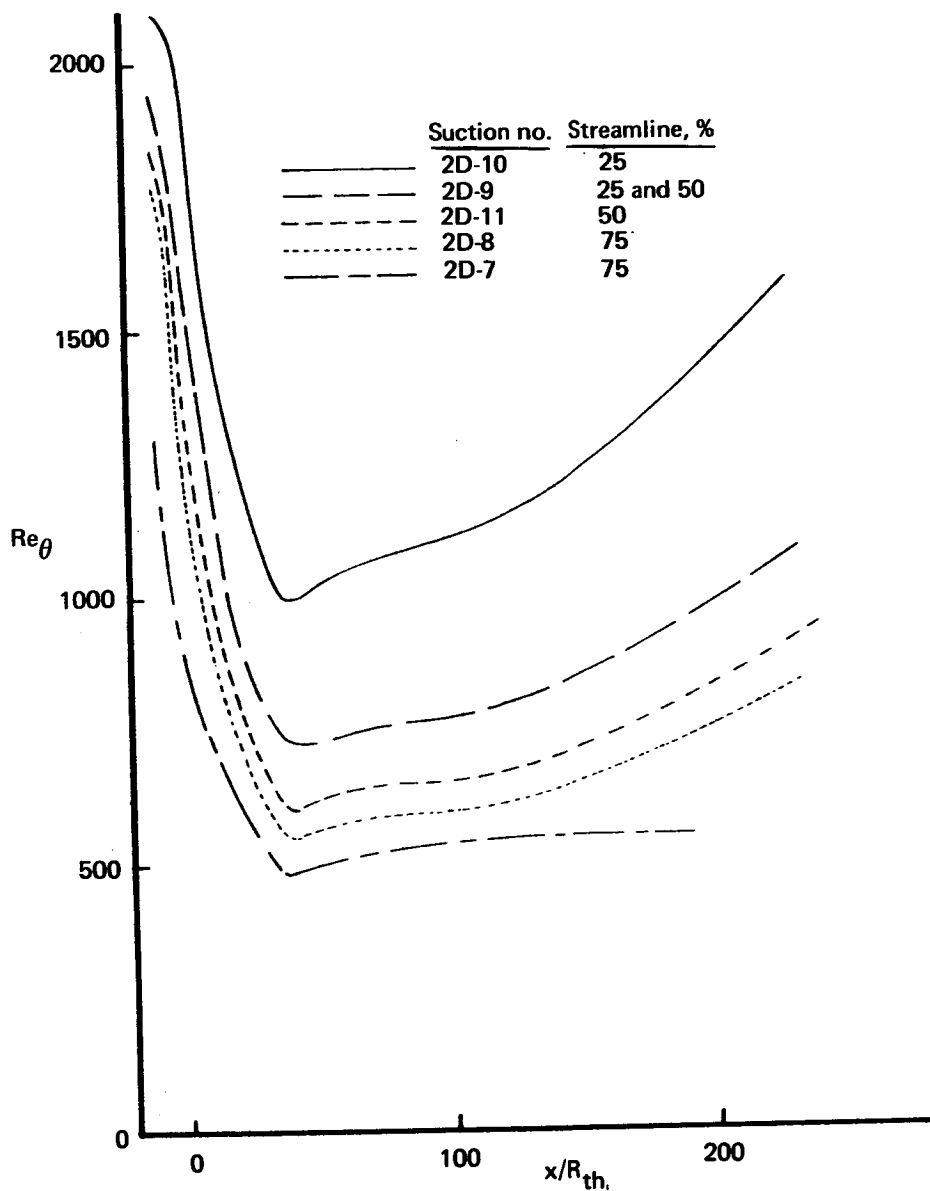
f) $M^* = 9$ axisymmetric nozzle, $R/R_{th} = 200$, $U^*/\nu^* = 26.22 \cdot 10^6/m$, $D^* = 1m$, $T_{stag} = 1000^\circ K$, $T_{wall_{ad}}$

FIGURE 23.—VARIATIONS OF Re_θ IN SUPERSONIC AIR NOZZLES (Continued)



g) $M^* = 4.6$ two-dimensional JPL nozzle, floor and ceiling walls, $|U^*/\nu^*| = 26.22 \cdot 10^6/m$, $H^* = 1m$, T_{wallad}

FIGURE 23.—VARIATIONS OF Re_θ IN SUPERSONIC AIR NOZZLES (Continued)



h) $M^* = 4.6$ two-dimensional JPL nozzle, side walls, $U^*/\nu^* = 26.22 \cdot 10^6/\text{m}$, $H^* = 1\text{m}$, $T_{\text{stag}} = 400^\circ\text{K}$, $T_{\text{wall ad}}$

FIGURE 23.—VARIATIONS OF Re_θ IN SUPERSONIC AIR NOZZLES (Concluded)

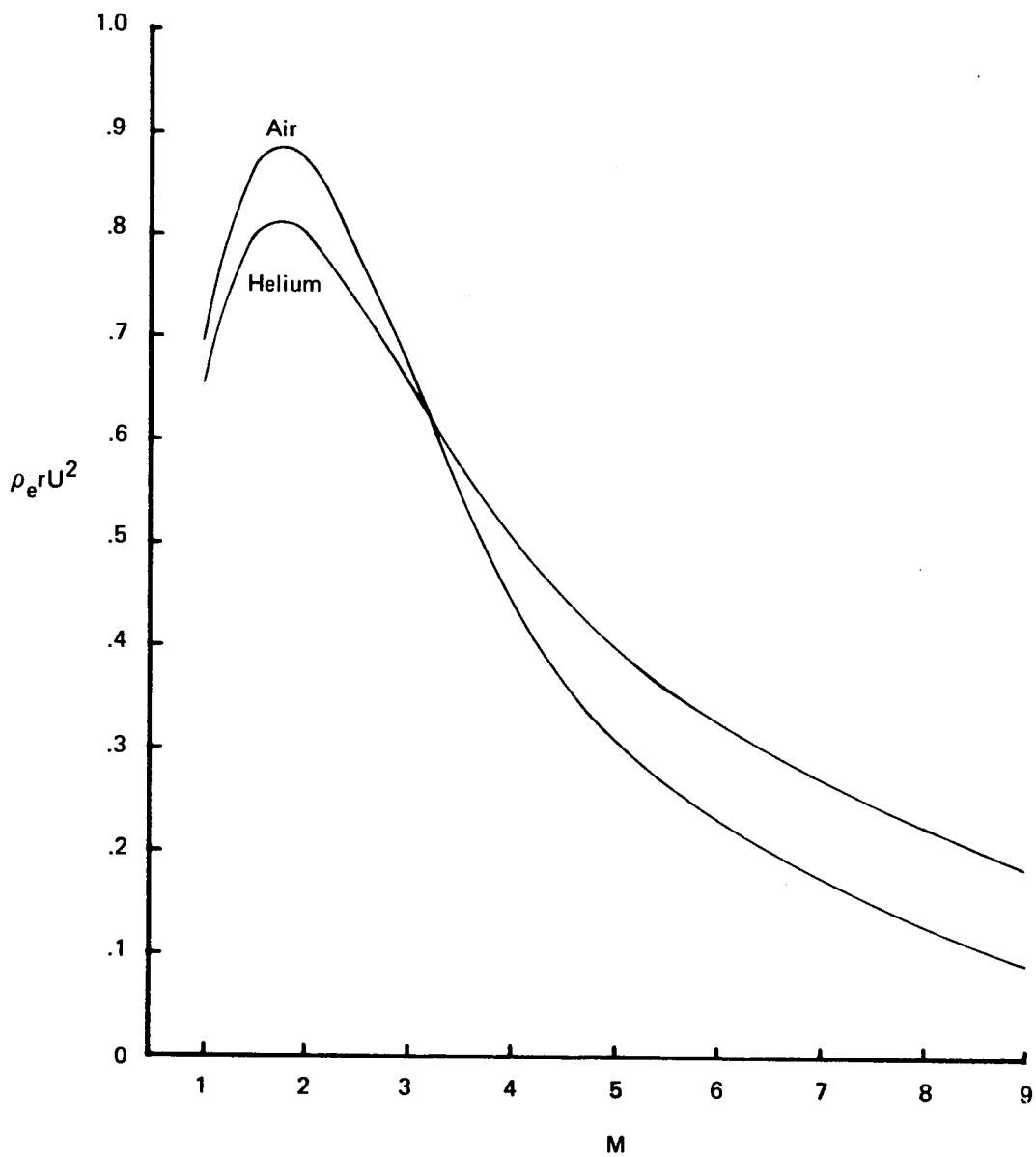
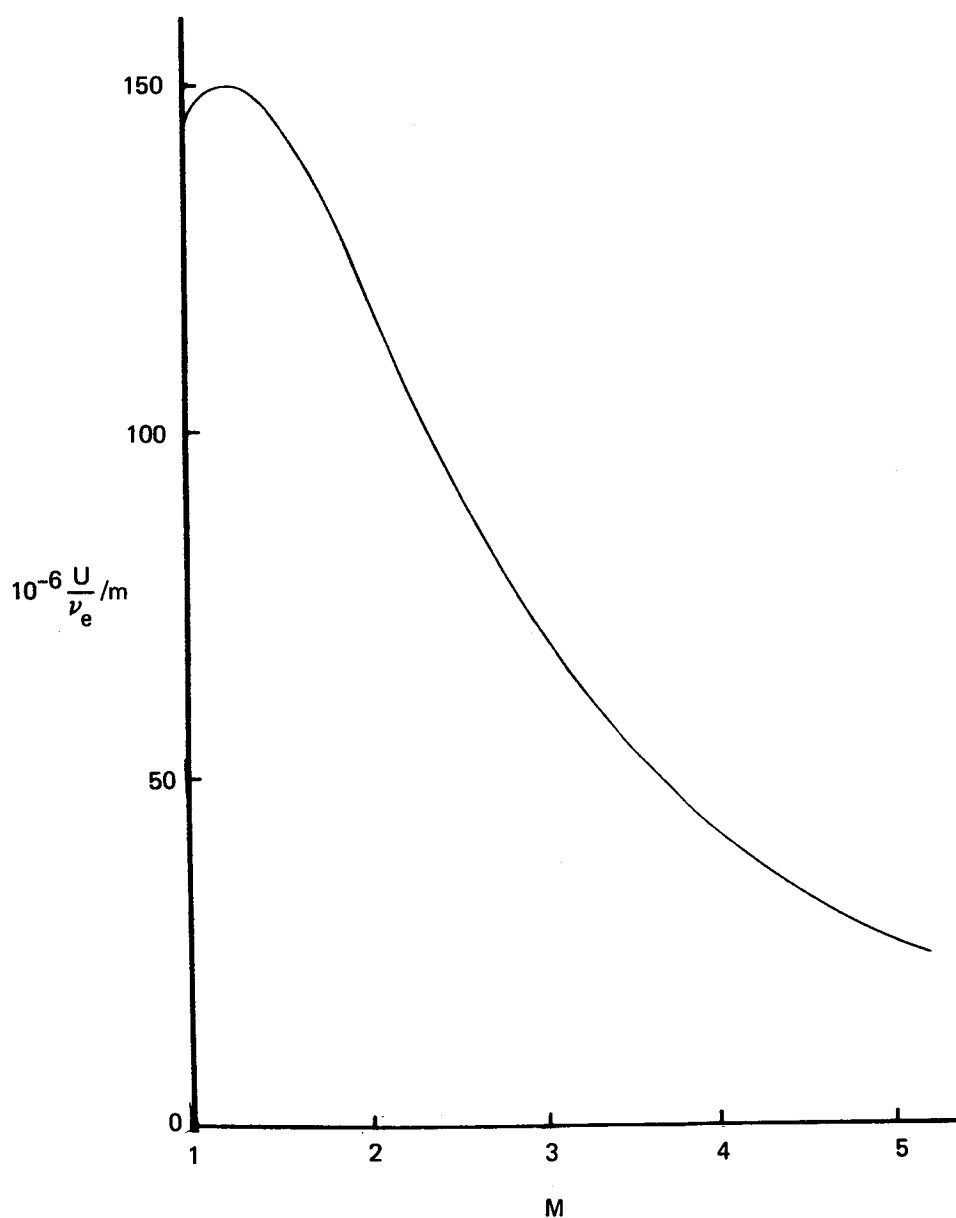
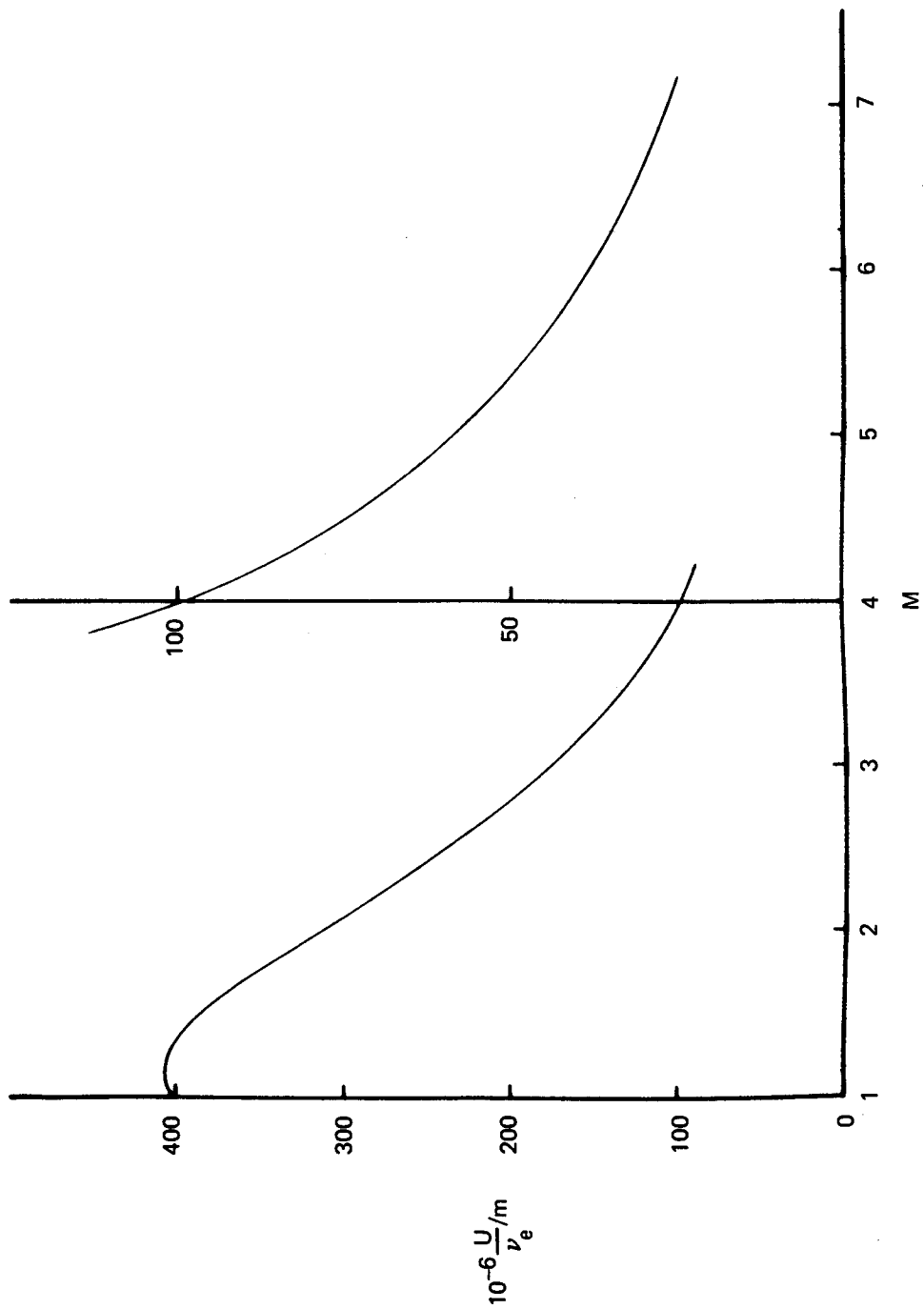


FIGURE 24.—VARIATION OF $\rho_e r U^2$ WITH LOCAL MACH NUMBER IN SUPERSONIC HELIUM AND AIR NOZZLES



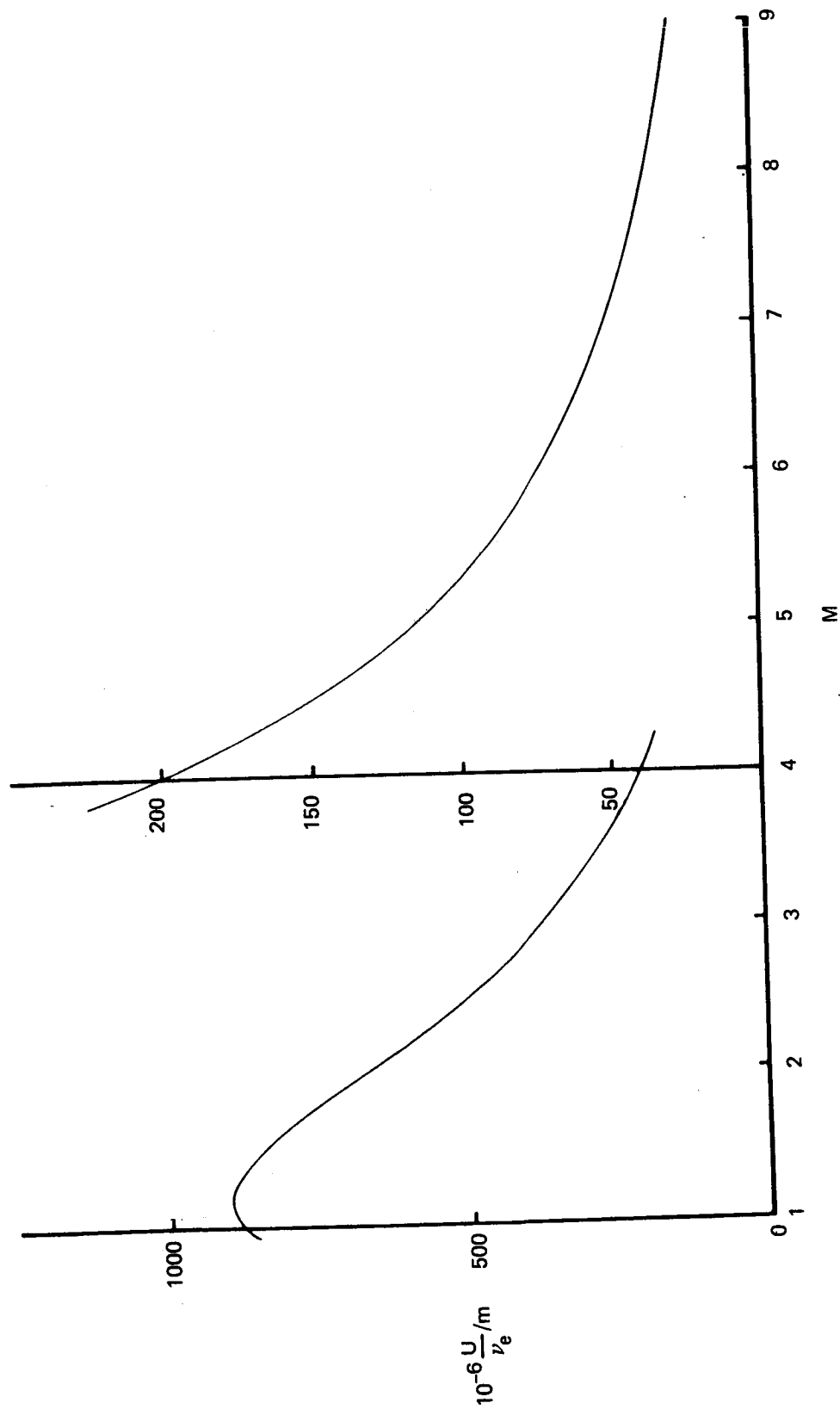
a) $M^* = 5$, $U^*/\nu^* = 26.22 \cdot 10^6 / m$, $T_{stag} = 400^\circ K$

FIGURE 25.—VARIATION OF LOCAL UNIT LENGTH REYNOLDS NUMBER IN SUPERSONIC AIR NOZZLES



b) $M^* = 7$, $U^*/\nu^* = 26.22 \cdot 10^6/m$, $T_{stag} = 700^\circ K$

FIGURE 25.— VARIATION OF LOCAL UNIT LENGTH REYNOLDS NUMBER IN SUPERSONIC AIR NOZZLES (Continued)



c) $M^* = 9$, $U^*/\nu^* = 26.22 \cdot 10^6/m$, $T_{stag} = 1000^\circ K$

FIGURE 25.— VARIATION OF LOCAL UNIT LENGTH REYNOLDS NUMBER IN SUPERSONIC AIR NOZZLES (Concluded)

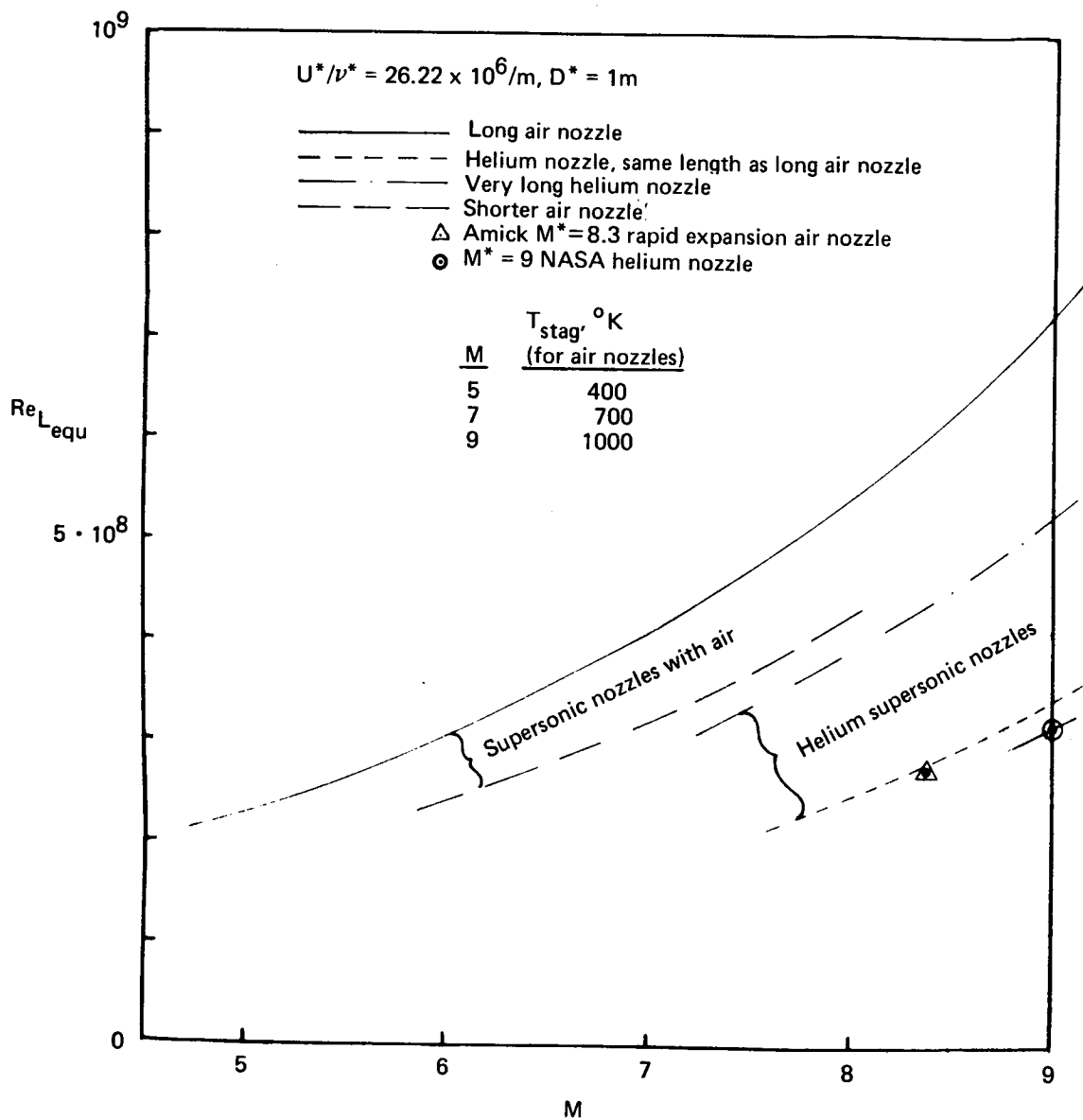


FIGURE 26.—EQUIVALENT LENGTH REYNOLDS NUMBERS
FOR VARIOUS WIND TUNNEL NOZZLES

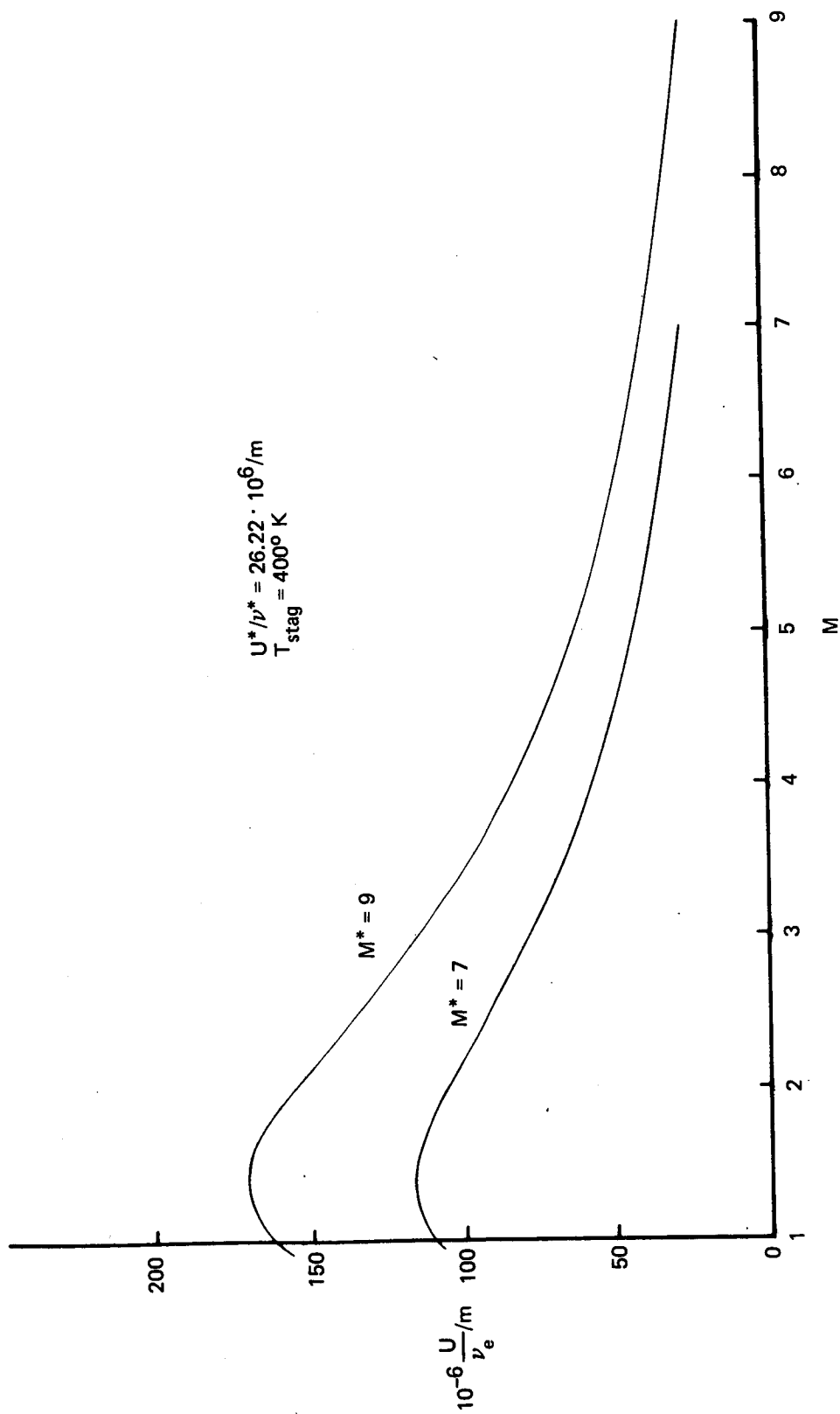
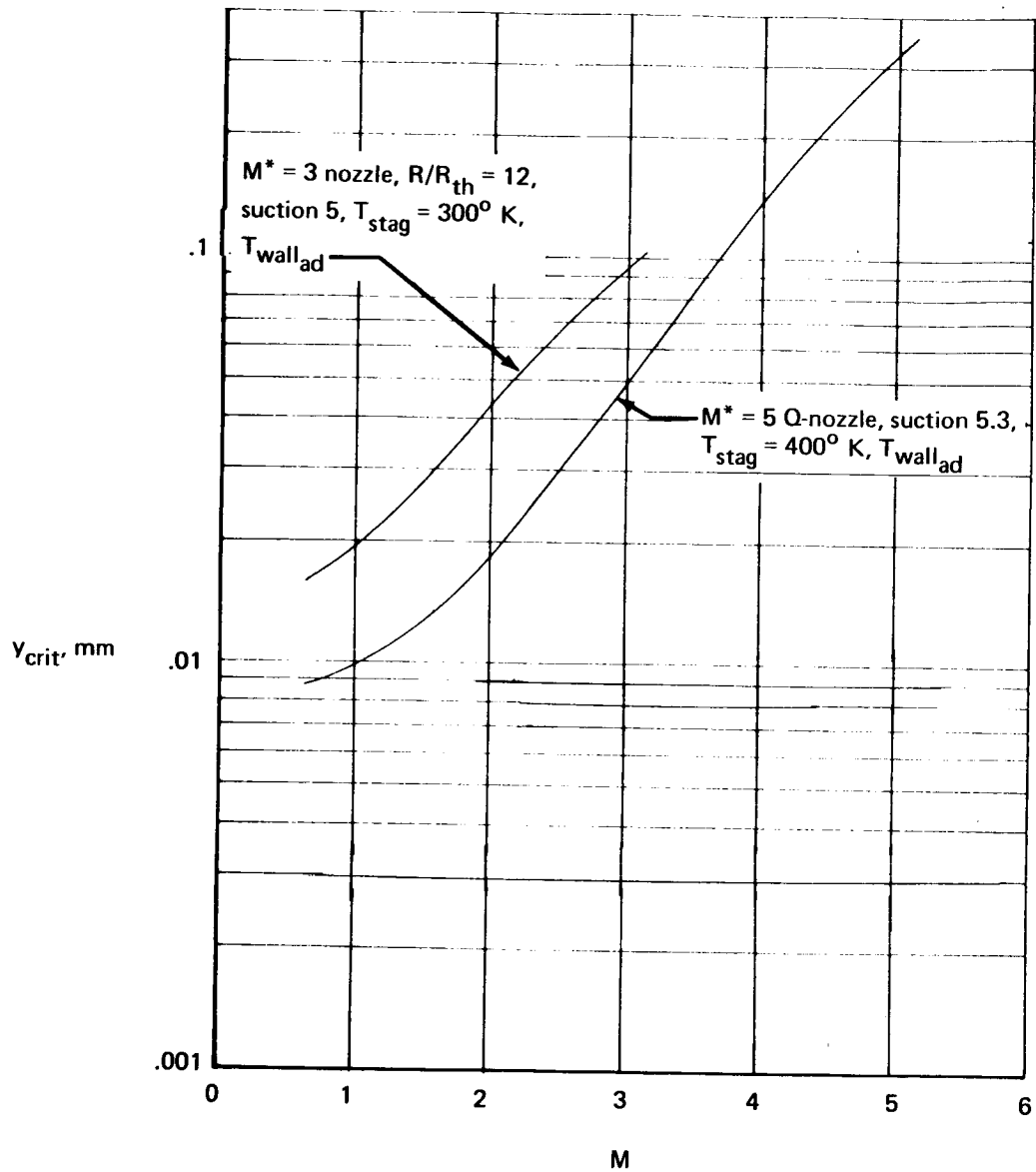
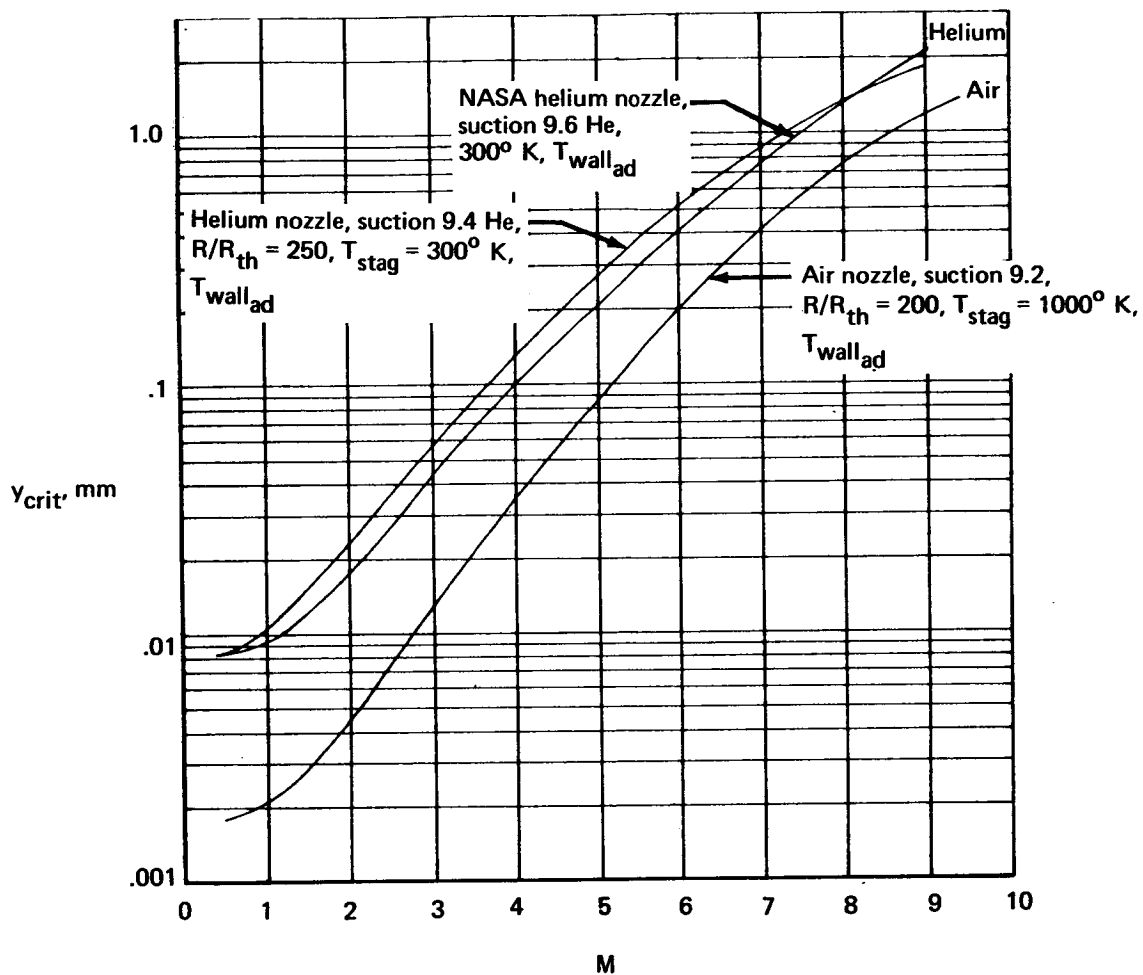


FIGURE 27.— VARIATION OF LOCAL UNIT LENGTH REYNOLDS NUMBER IN SUPERSONIC HELIUM NOZZLES



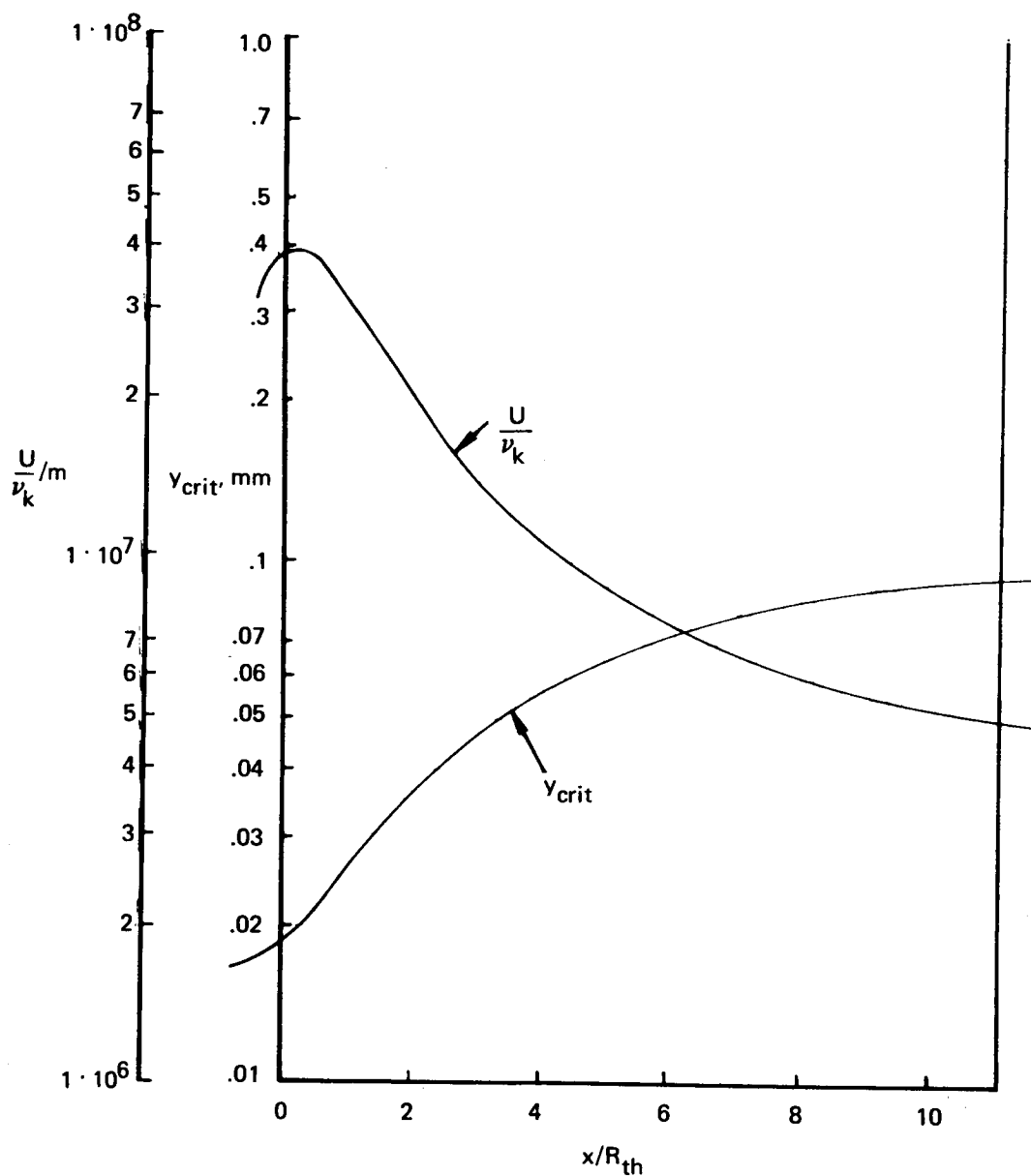
a) $M^* = 3$ and 5 axisymmetric air nozzles,
 $U^*/\nu^* = 26.22 \cdot 10^6/\text{m}$, $D^* = 1\text{ m}$

FIGURE 28.—CRITICAL ROUGHNESS HEIGHT ($Re_k = 200$)



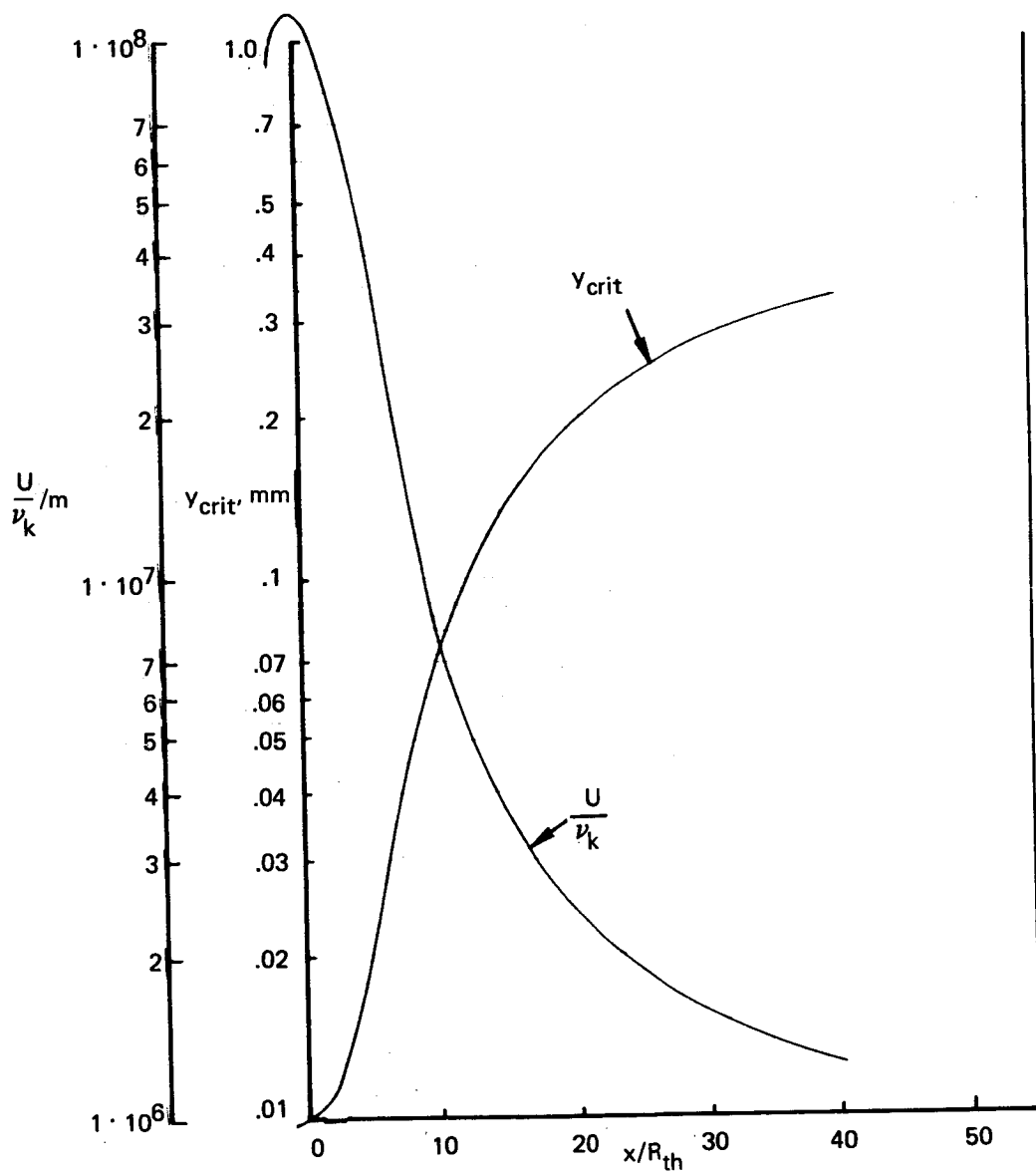
b) $M^* = 9$ axisymmetric nozzles,
 $U^*/\nu^* = 26.22 \cdot 10^6/\text{m}$, $D^* = 1\text{m}$

FIGURE 28.—CRITICAL ROUGHNESS HEIGHT ($Re_k = 200$) (Concluded)



a) $M^* = 3$ axisymmetric air nozzle, $(R/R_{th} = 12)$, $Re_{k_{crit}} = 200$, suction 5,
 $U^*/\nu^* = 26.22 \cdot 10^6/m$, $D^* = 1m$, $R_{th} = 0.244 m$, $T_{stag} = 300^\circ K$, $T_{wall_{ad}}$

FIGURE 29.—CRITICAL ROUGHNESS HEIGHT AND UNIT LENGTH REYNOLDS NUMBER



b) $M^* = 5.115$ LARC Q-axisymmetric air nozzle, $Re_{k,crit} = 200$, suction 5.3,
 $U^*/\nu^* = 26.22 \cdot 10^6/m$, $D^* = 1m$, $R_{th} = 0.0954 m$, $T_{stag} = 400^\circ K$, $T_{wall,ad}$

FIGURE 29.—CRITICAL ROUGHNESS HEIGHT AND UNIT LENGTH REYNOLDS NUMBER (Concluded)

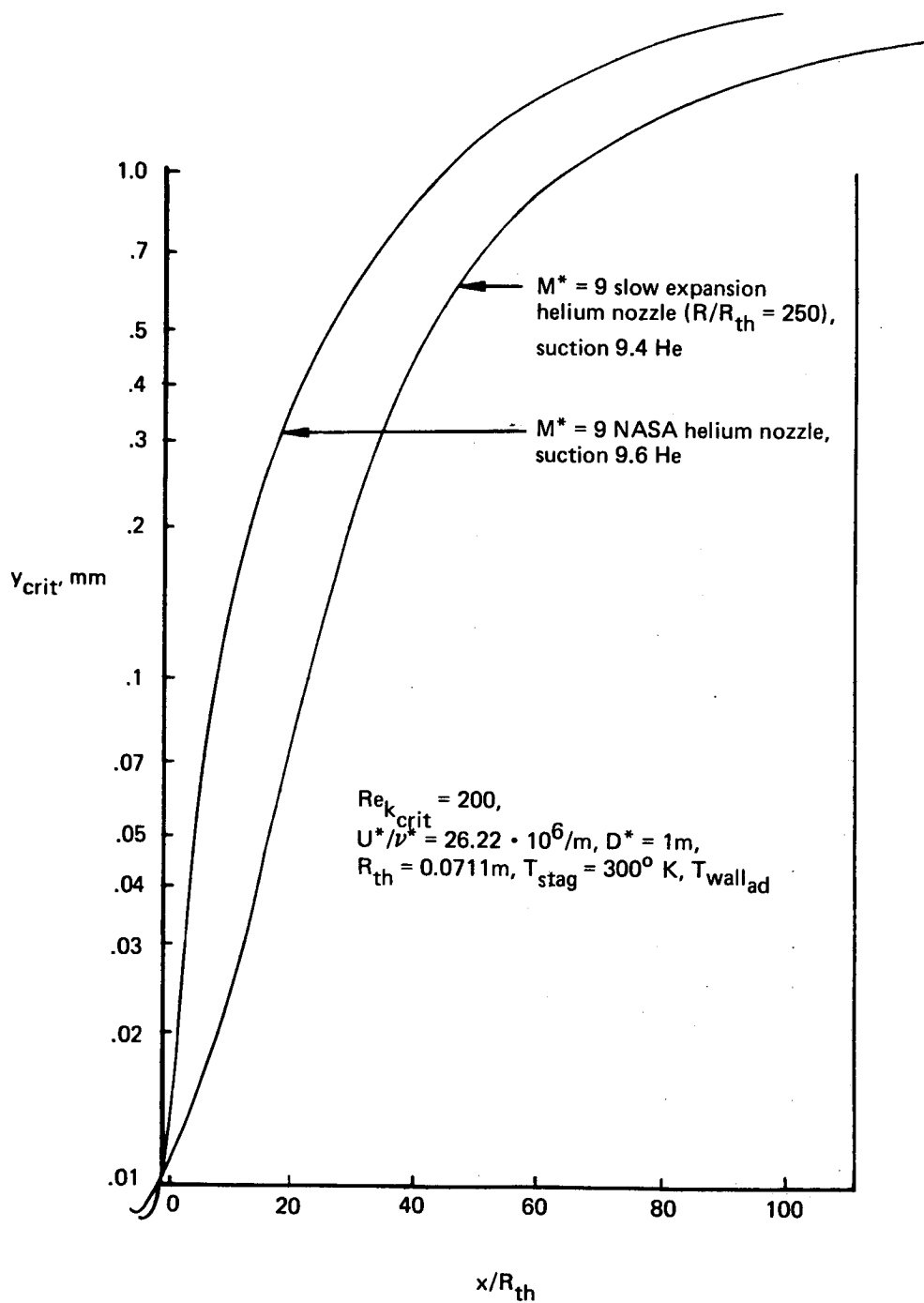
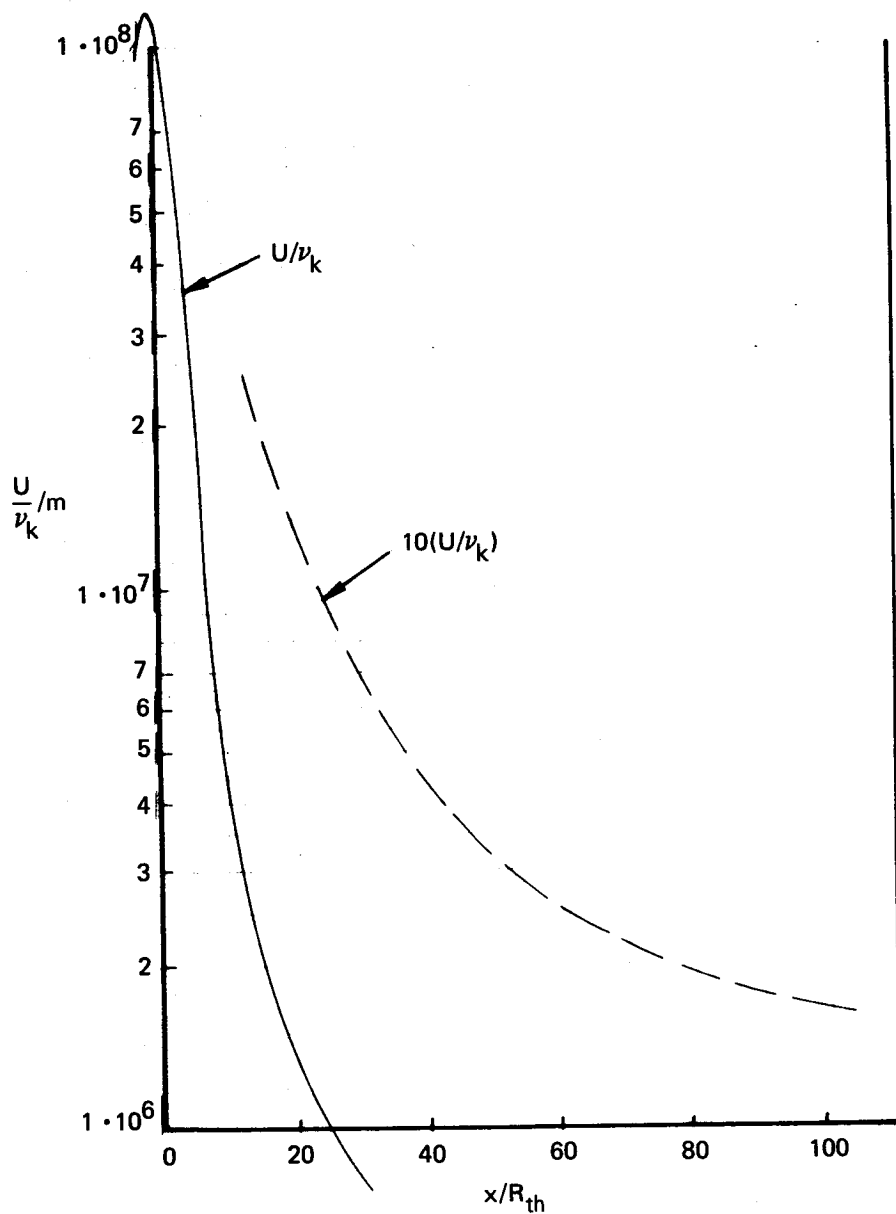
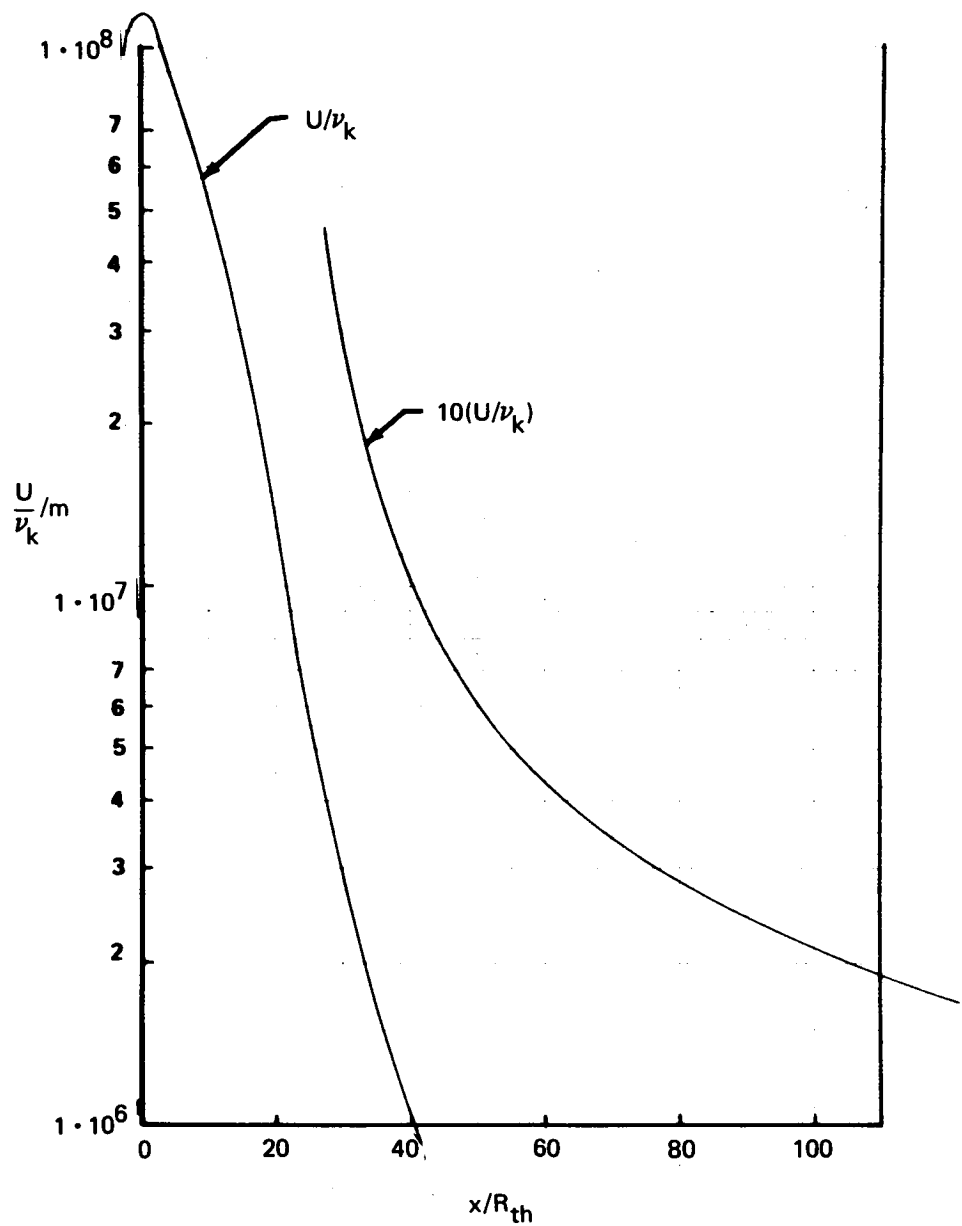


FIGURE 30.—CRITICAL SURFACE ROUGHNESS HEIGHT, IN $M^* = 9$,
 AXISYMMETRIC HELIUM NOZZLES



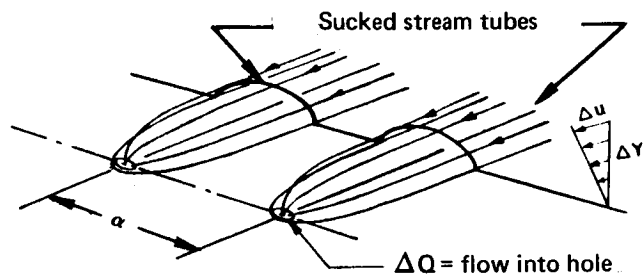
a) $M^* = 9$ NASA axisymmetric helium nozzle, $Re_{k_{crit}} = 200$, suction 9.6 He,
 $U^*/\nu^* = 26.22 \cdot 10^6/m$, $D^* = 1m$, $R_{th} = 0.0711$ m, $T_{stag} = 300^\circ$ K, $T_{wall_{ad}}$

FIGURE 31.—UNIT LENGTH REYNOLDS NUMBER, U/ν_k



b) $M^* = 9$ slow expansion axisymmetric helium nozzle ($R/R_{th} = 250$), $Re_{k_{crit}} = 200$, suction 9.4 He
 $U^*/\nu^* = 26.22 \cdot 10^6/m$, $D^* = 1m$ $R_{th} = 0.0711 m$, $T_{stag} = 300^\circ K$, $T_{wall_{ad}}$

FIGURE 31.—UNIT LENGTH REYNOLDS NUMBER, U/ν_k (Concluded)



$$h = \text{"average" height of intercepted layer} = \sqrt{2 \frac{\Delta Q}{\alpha} / \frac{\Delta u}{\Delta y}}$$

$$u = \text{"average" velocity of intercepted layer} = \frac{\Delta Q}{\alpha h}$$

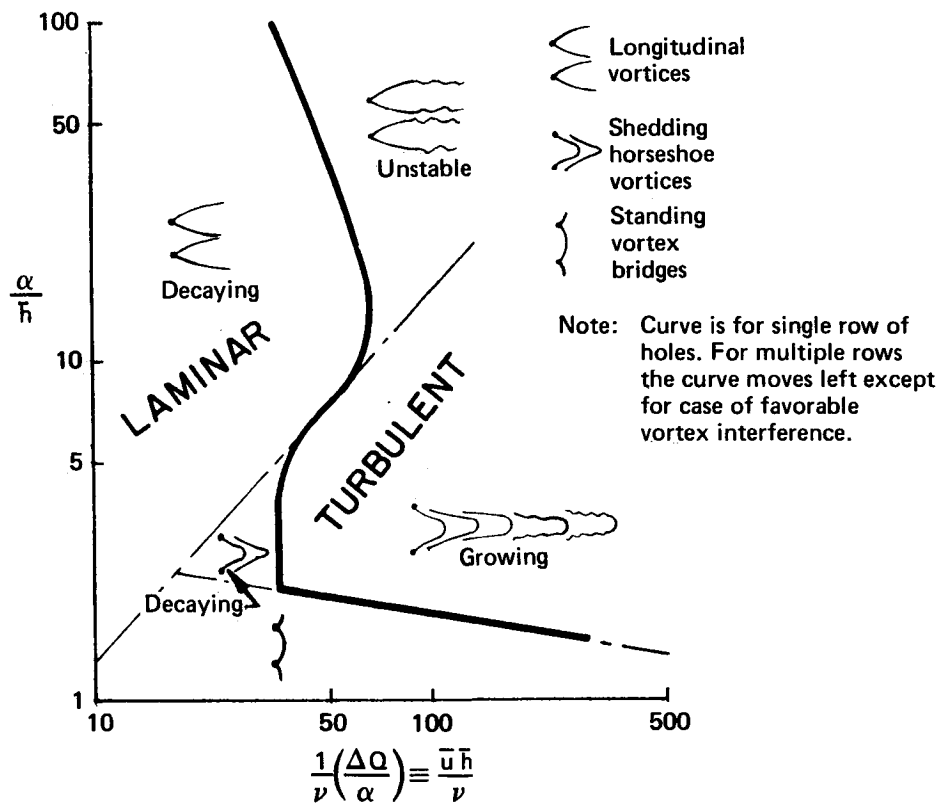


FIGURE 32.—CRITICAL SUCTION FOR LAMINAR FLOW (Ref. 45)

$Re_{\theta_{alT}}$ = Reynolds number based on momentum thickness at start of transition on attachment line

$$v_o^* = v_o / \sqrt{\nu \left(\frac{\partial u}{\partial s} \right)_{al}}$$

$-v_o$ = suction velocity

$\left(\frac{\partial}{\partial s} \right)_{al}$ = directional derivative at attachment line in a direction normal to leading edge and along surface

u = potential flow velocity component normal to leading edge and along surface

w = spanwise potential flow velocity component

z = spanwise length along attachment line

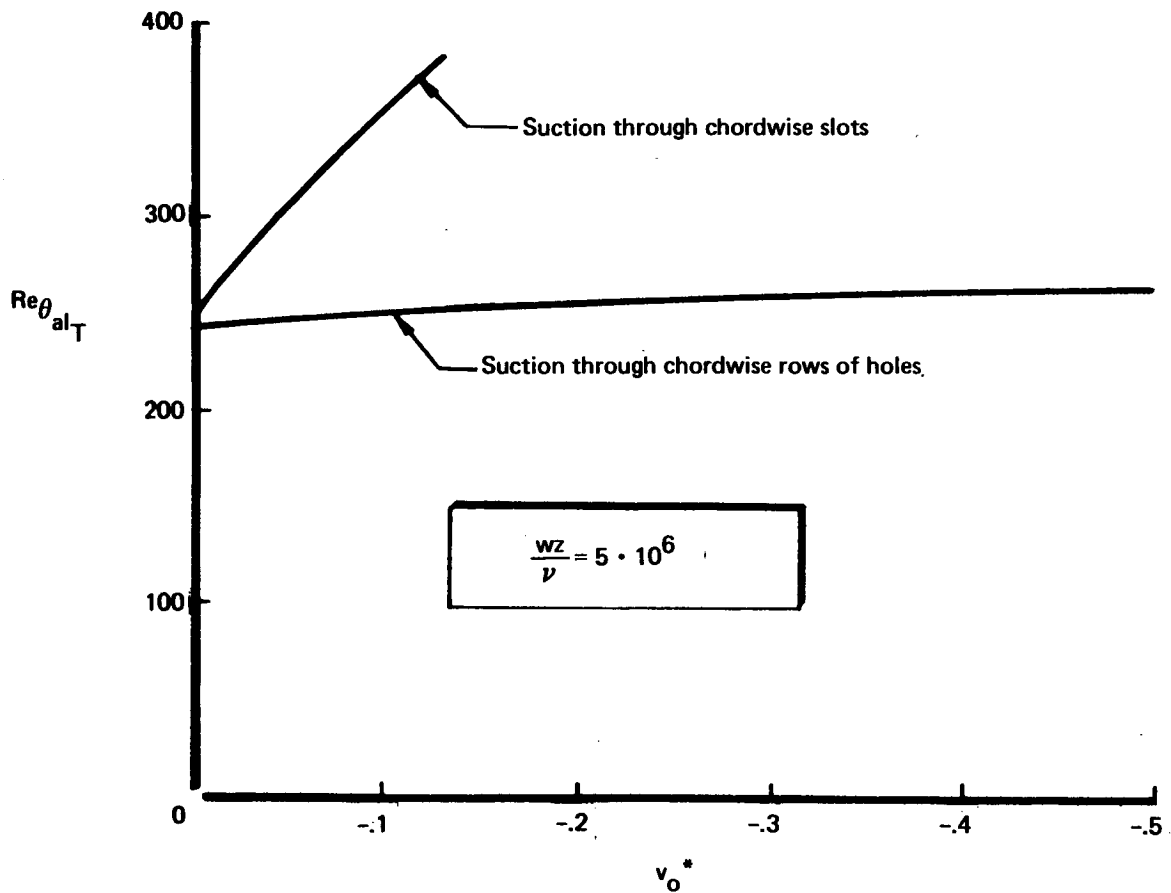
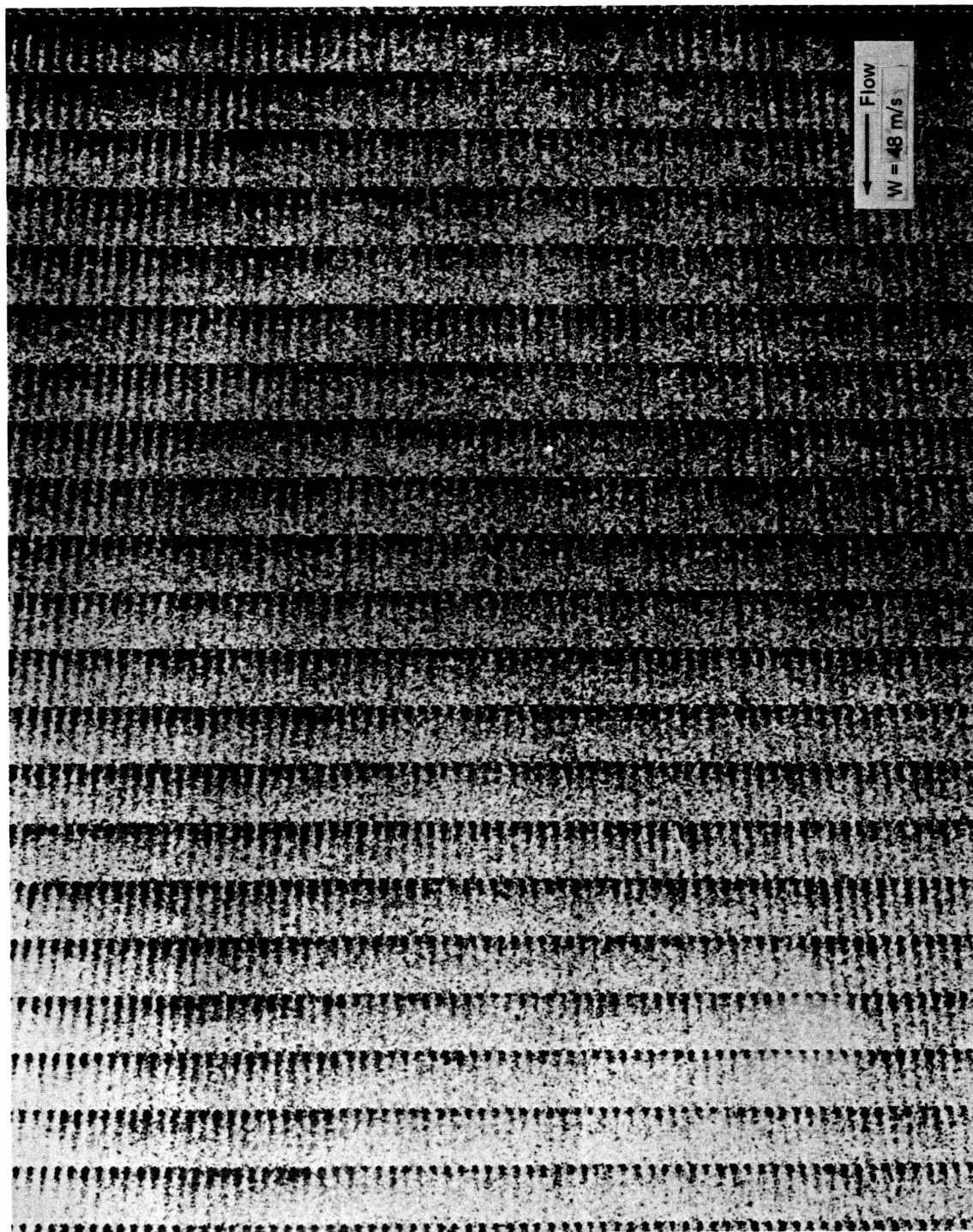


FIGURE 33.—EFFECT OF SUCTION ON TRANSITION AT THE ATTACHMENT LINE OF A 45° SWEEP BLUNT-NOSED WING IN NORAIR 7-BY 10-FT TUNNEL



Note: Suction through chordwise rows of holes located at the attachment line

*FIGURE 34.—NAPHTHALENE SPRAY SUBLIMATION AT THE FRONT ATTACHMENT LINE
OF A 45° SWEEP BLUNT-NOSED WING*

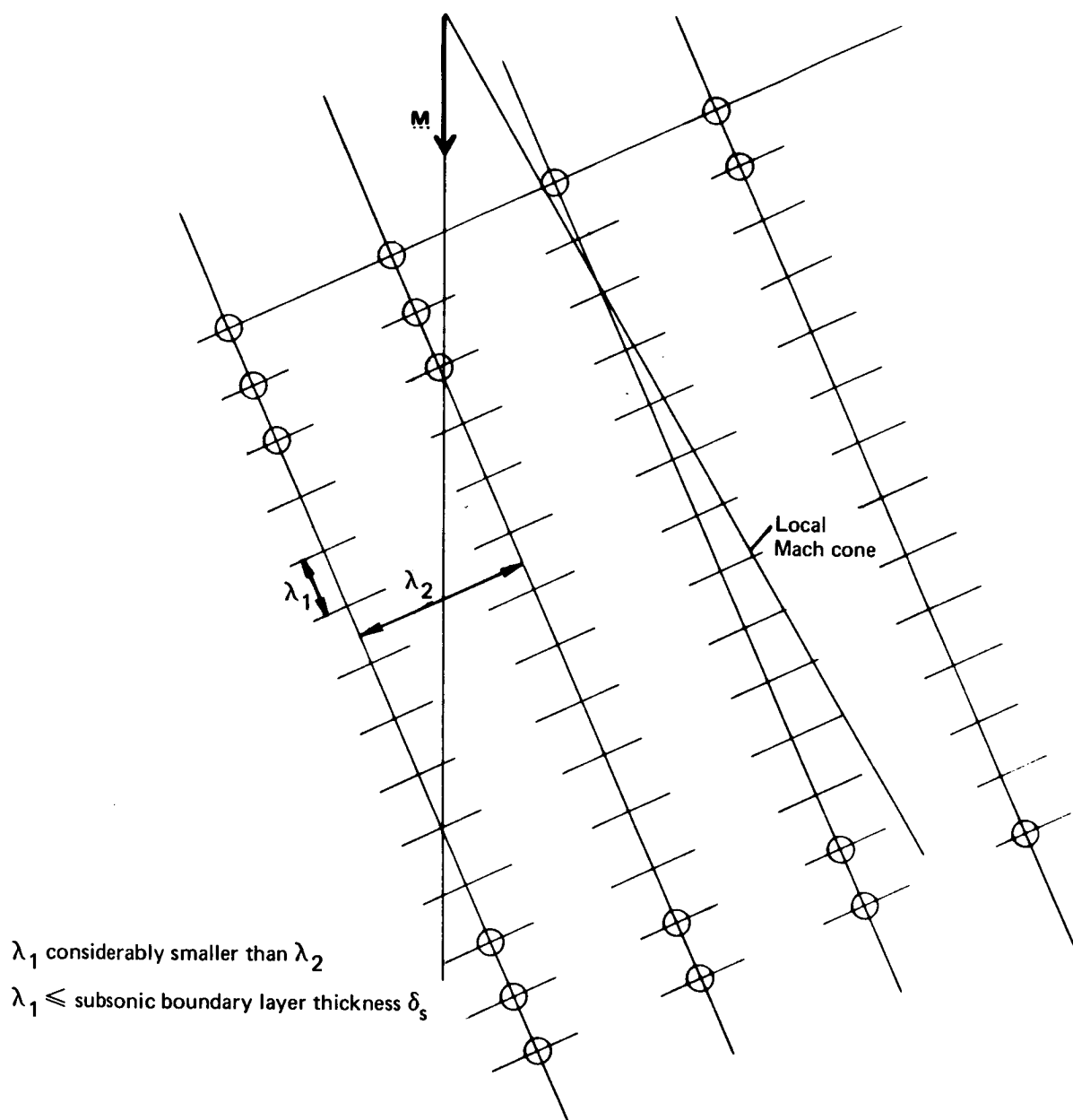


FIGURE 35.—ROWS OF CLOSELY SPACED SUCTION HOLES SWEEPED BEHIND THE LOCAL MACH ANGLE (SCHEMATIC)

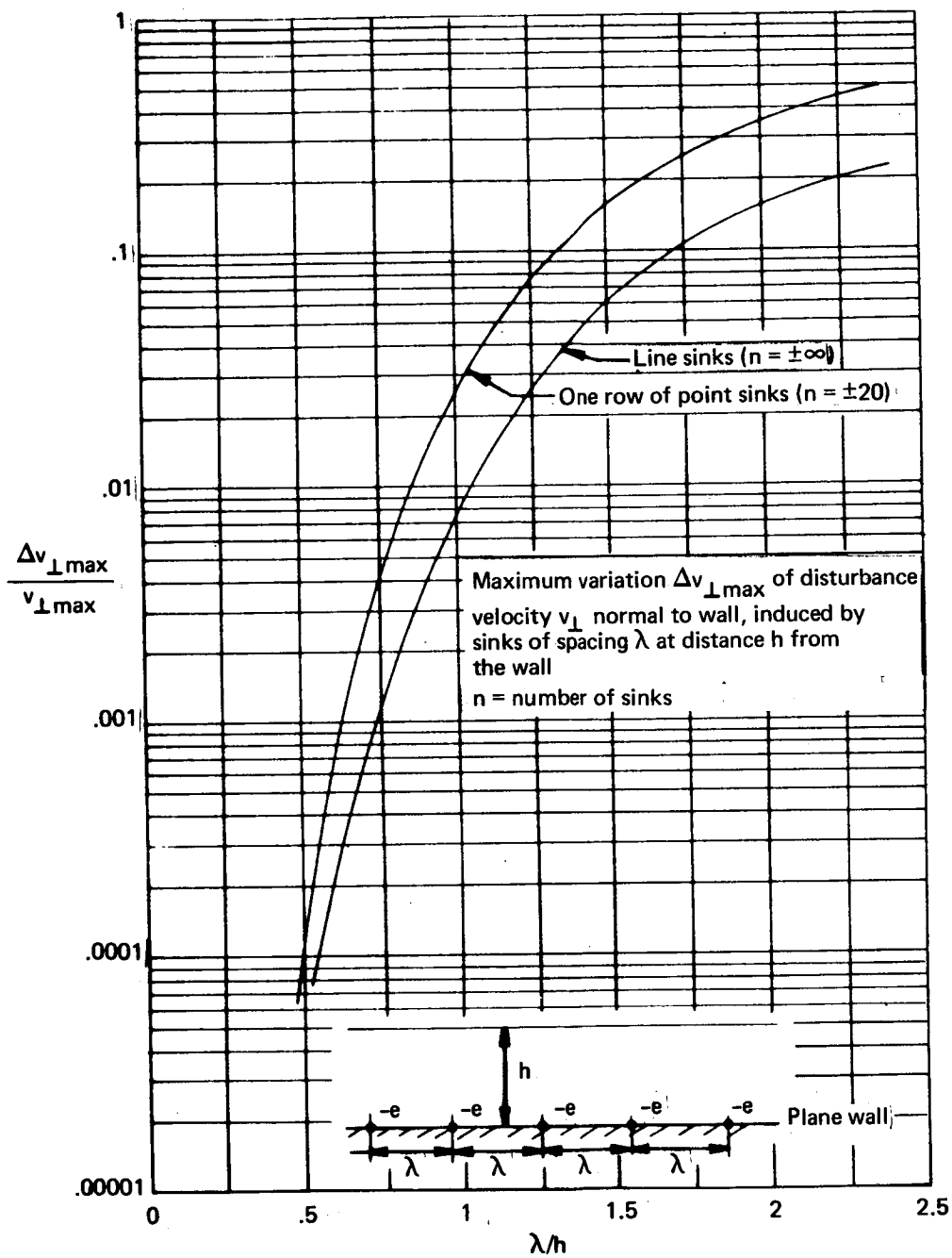
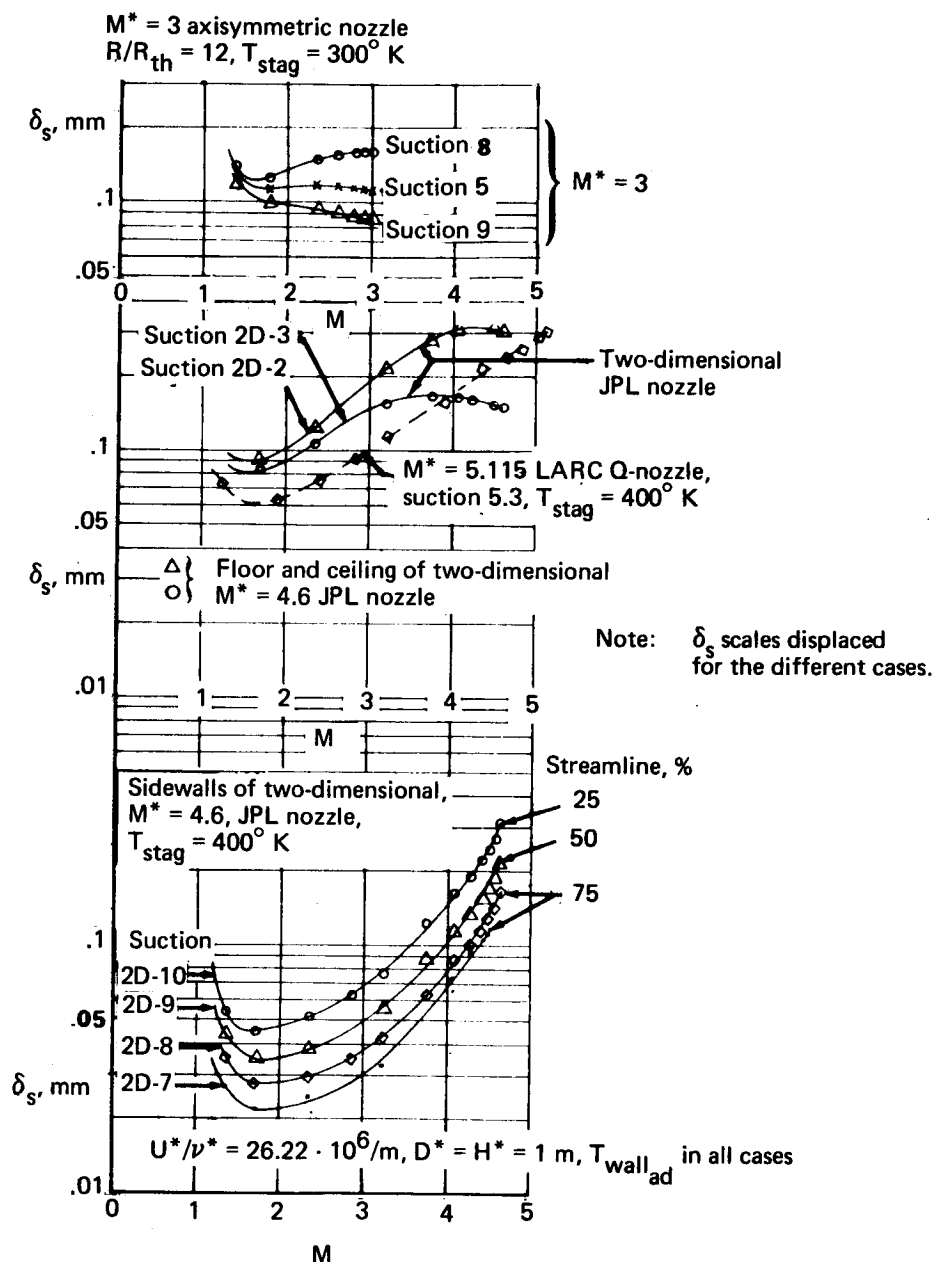
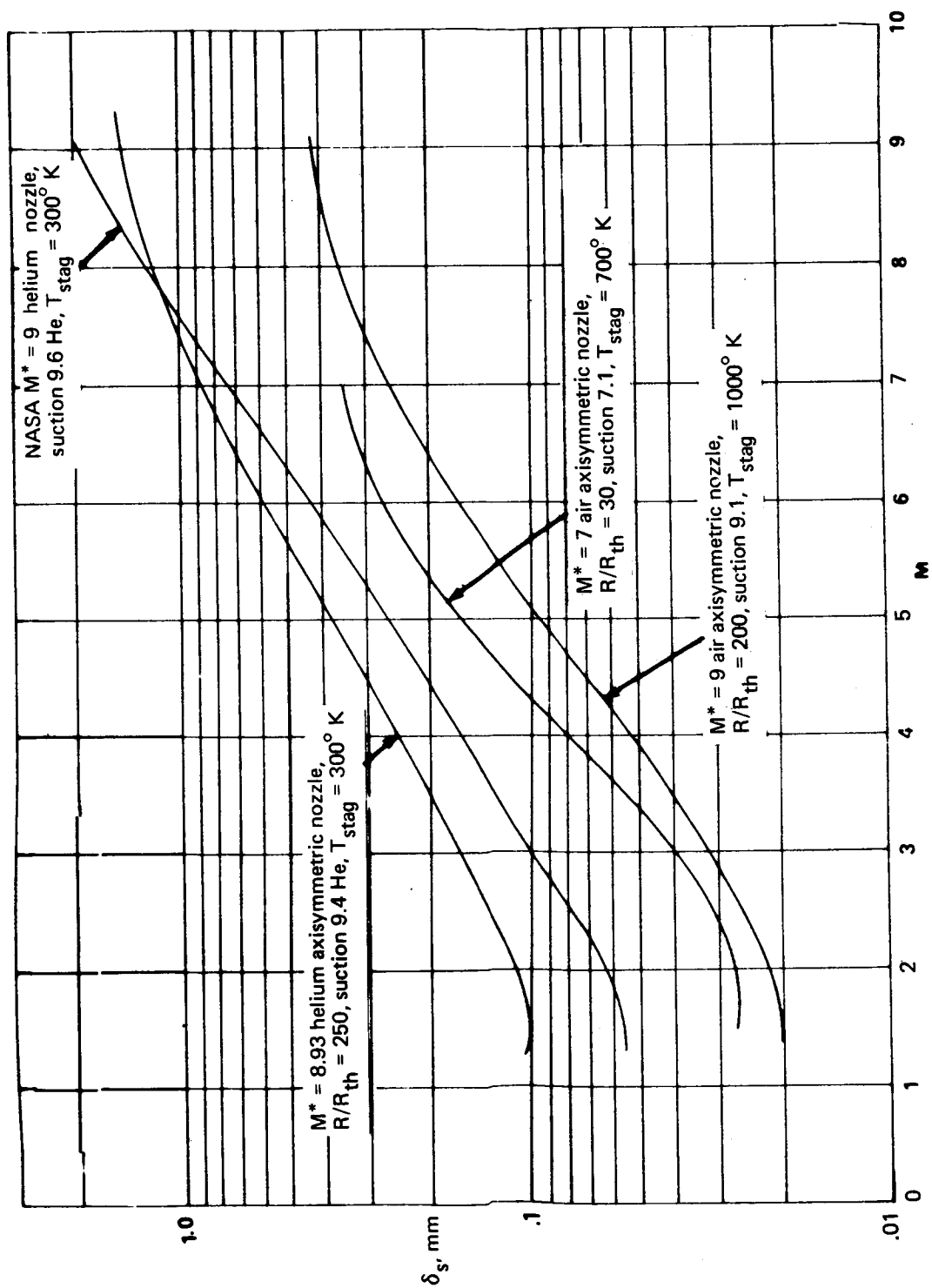


FIGURE 36.—RATIO $\Delta v_{\perp \max}/v_{\perp \max} = f(\lambda/h)$ FOR LINE AND POINT SINKS



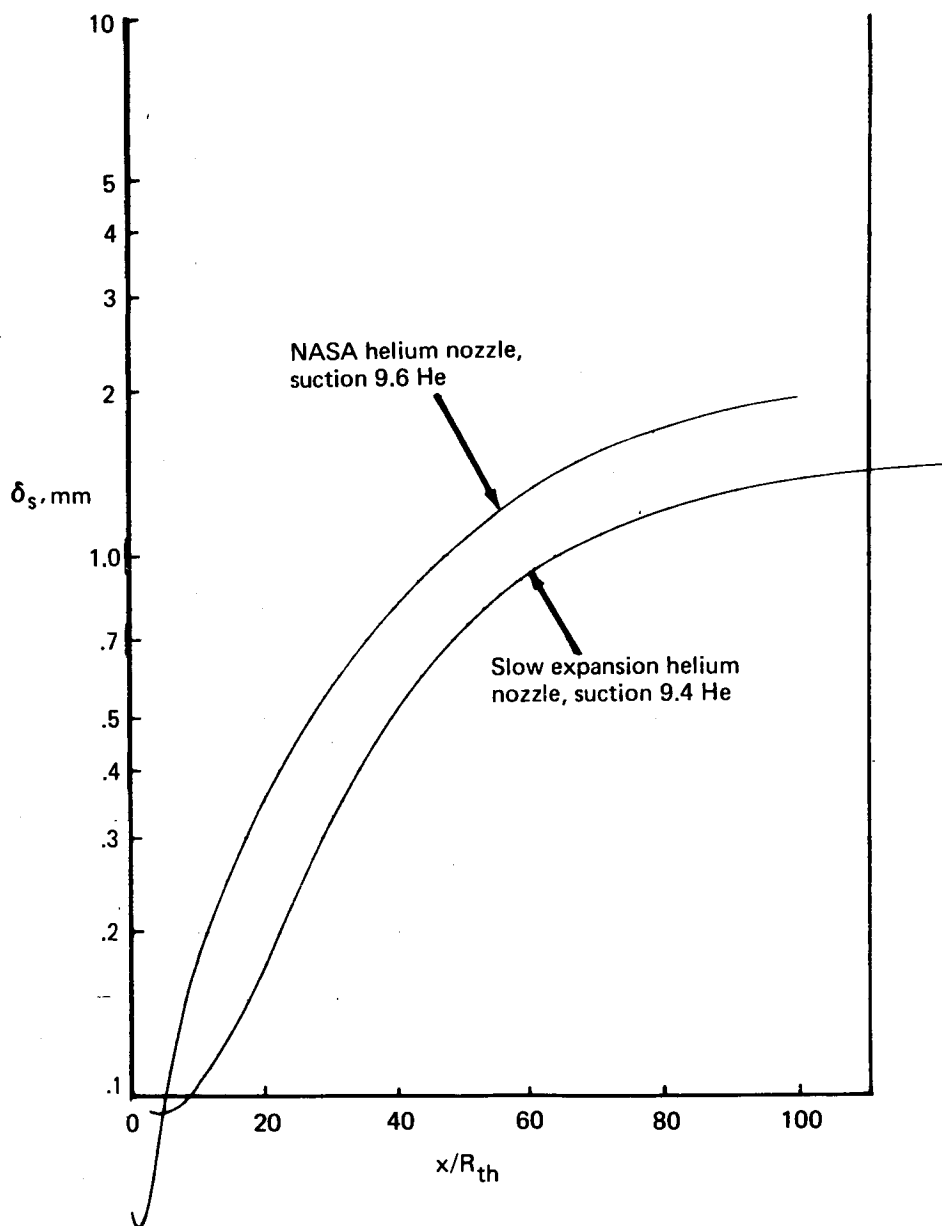
a) Low supersonic Mach axisymmetric and two-dimensional air nozzles

FIGURE 37.—THICKNESS δ_s OF SUBSONIC PART OF THE NOZZLE WALL BOUNDARY LAYER



b) High supersonic Mach axisymmetric air and helium nozzles, $U^*/\rho^* = 26.22 \cdot 10^6/m$, $D^* = 1 m$, $T_{wall_{ad}}$

FIGURE 37.—THICKNESS δ_s OF SUBSONIC PART OF THE NOZZLE WALL BOUNDARY LAYER (Continued)



c) $M^* = 9$ axisymmetric helium nozzles, $U^*/\nu^* = 26.22 \times 10^6/\text{m}$, $D^* = 1 \text{ m}$,
 $R_{th} = 0.0711 \text{ m}$, $T_{stag} = 300^\circ\text{K}$, $T_{wall_{ad}}$

FIGURE 37.—THICKNESS δ_s OF SUBSONIC PART OF THE NOZZLE WALL BOUNDARY LAYER (Concluded)

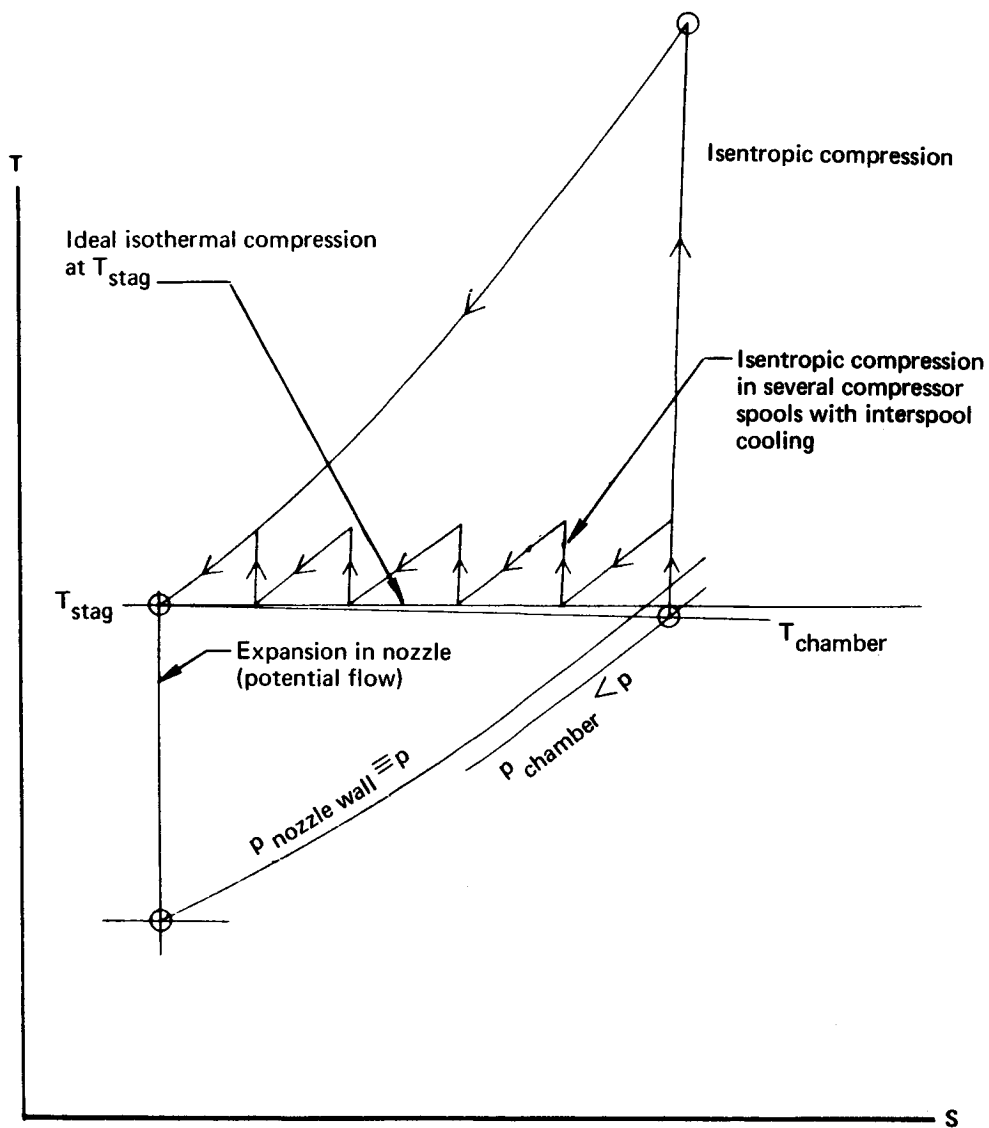


FIGURE 38.—TS DIAGRAM OF SUCTION COMPRESSOR CYCLE

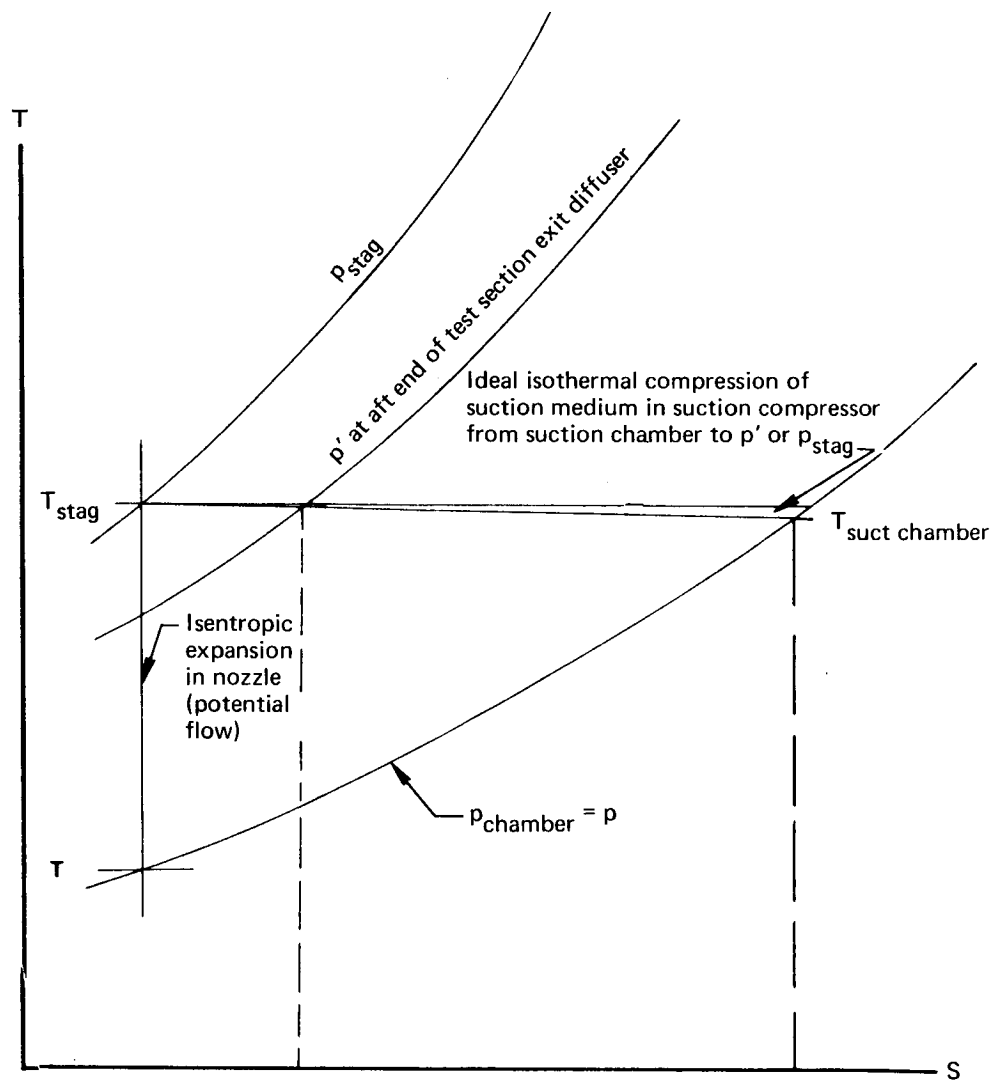
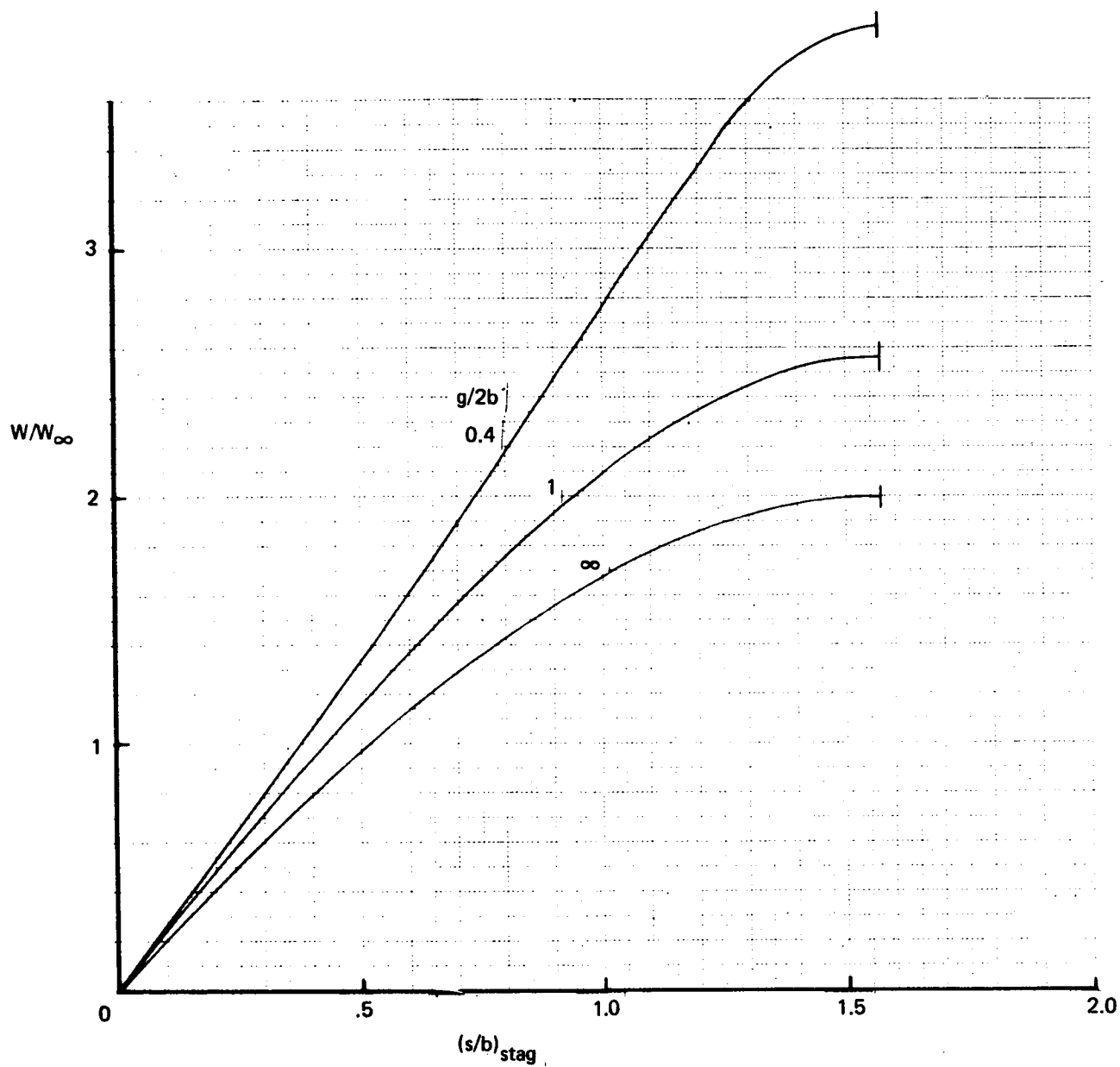
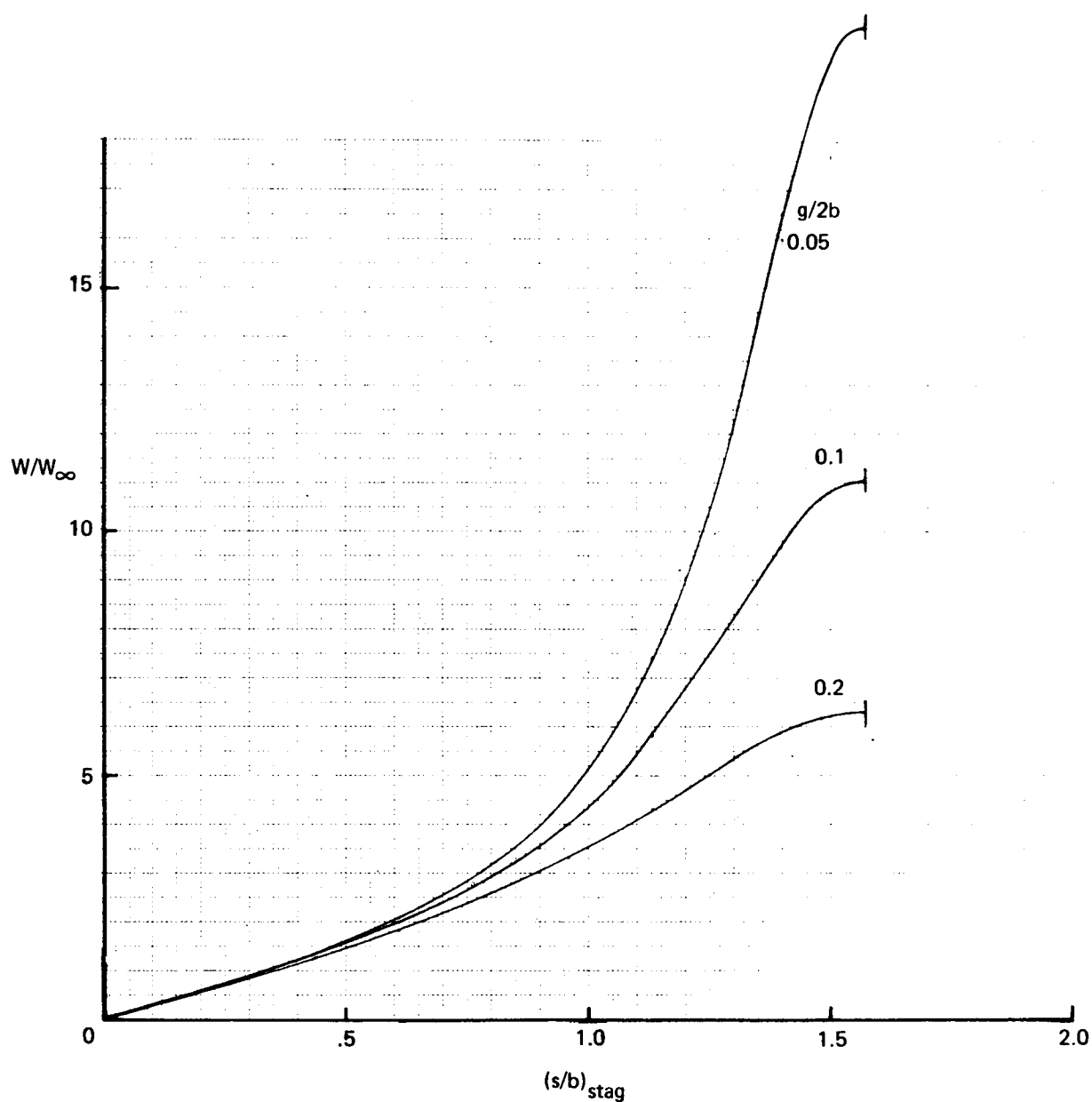


FIGURE 39.—TS DIAGRAM OF IDEAL ISOTHERMAL COMPRESSION OF SUCTION MEDIUM



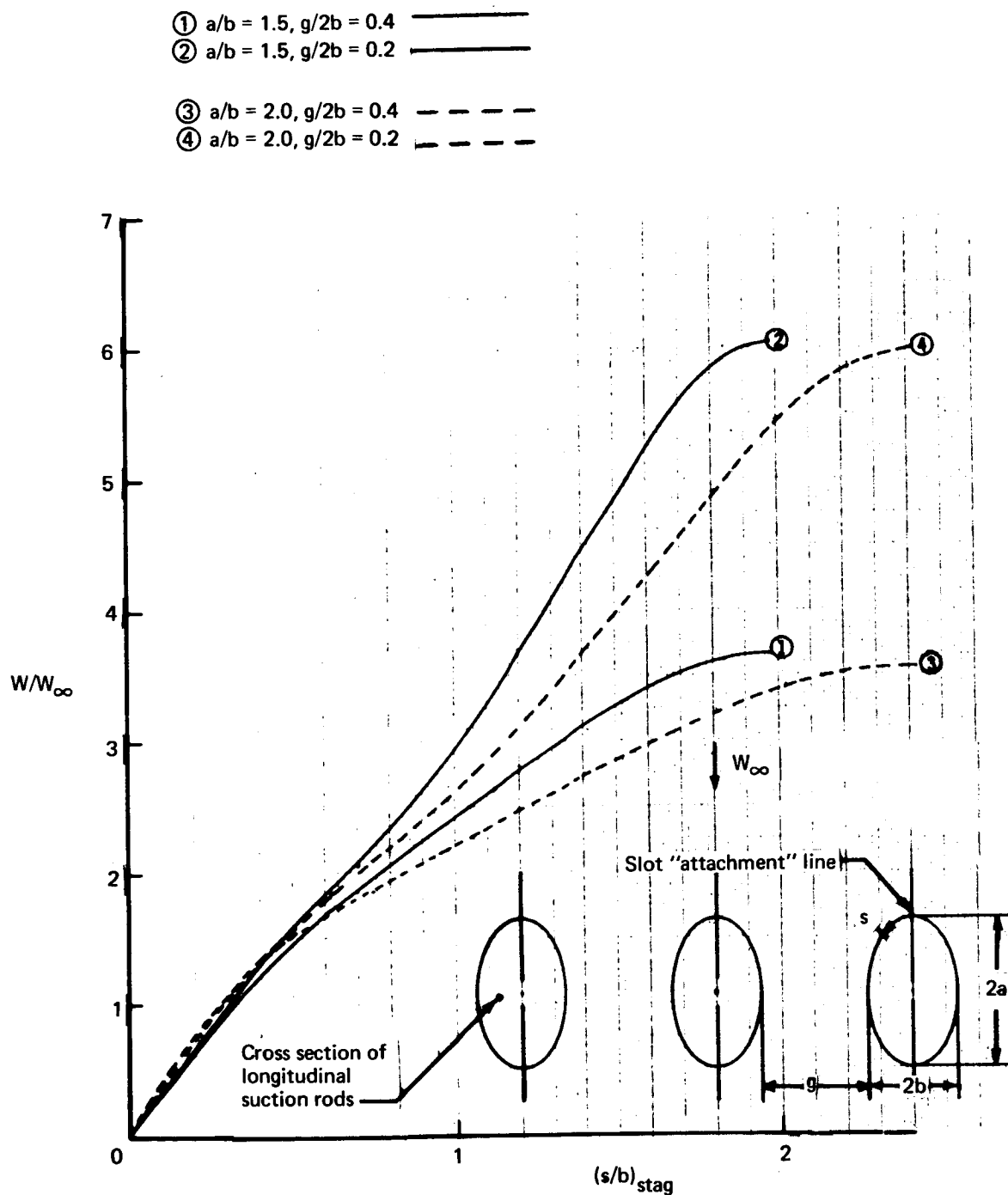
a) $g/2b \geq 0.4$, $a/b = 1$

FIGURE B-1.—CROSSFLOW VELOCITY RATIO ON CIRCULAR RODS FOR DIFFERENT SLOT WIDTH RATIOS, $g/2b$



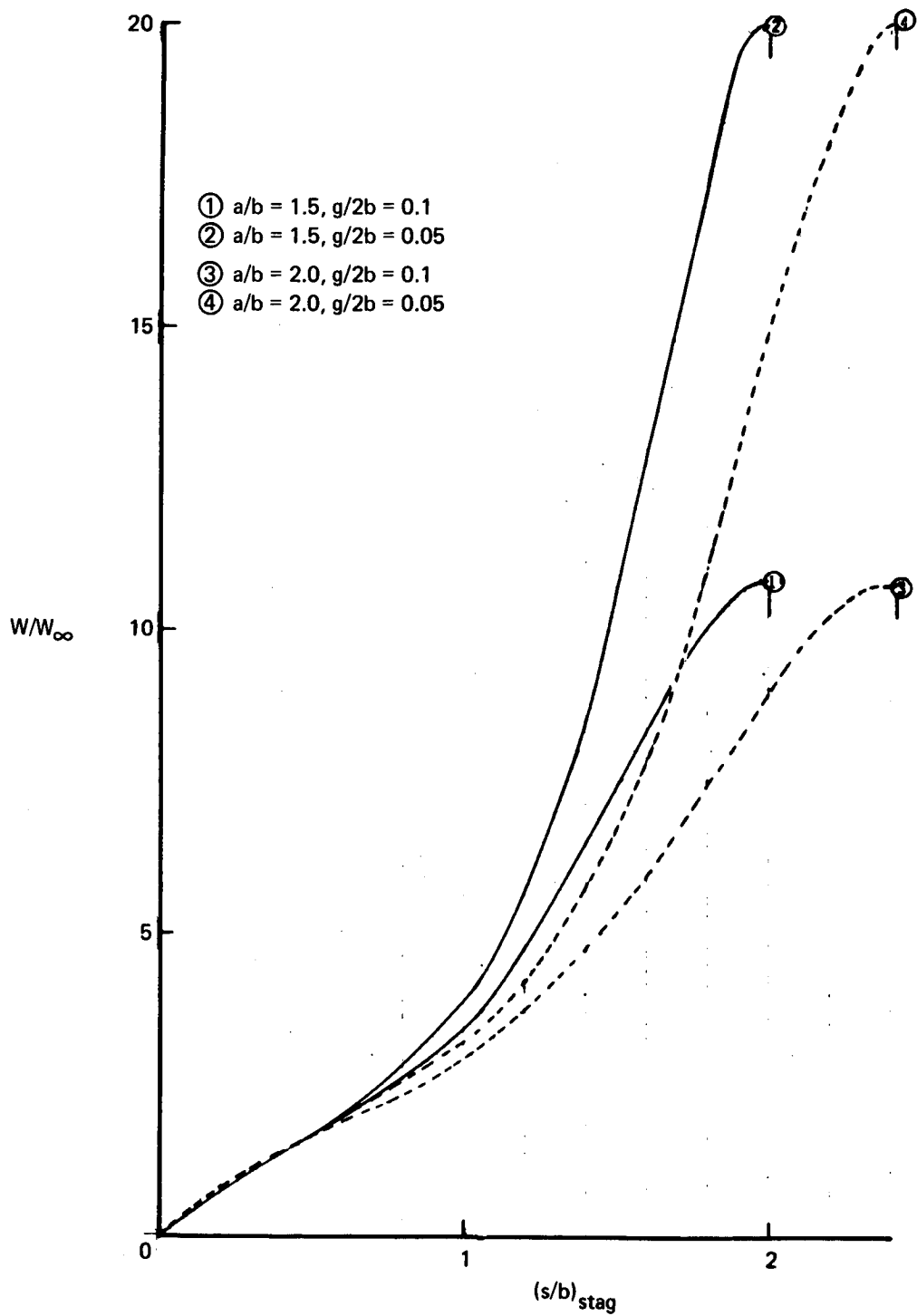
b) $g/2b = 0.05 - 0.2$, $a/b = 1$

FIGURE B-1.—CROSSFLOW VELOCITY RATIO ON CIRCULAR RODS FOR DIFFERENT SLOT WIDTH RATIOS, $g/2b$ (Concluded)



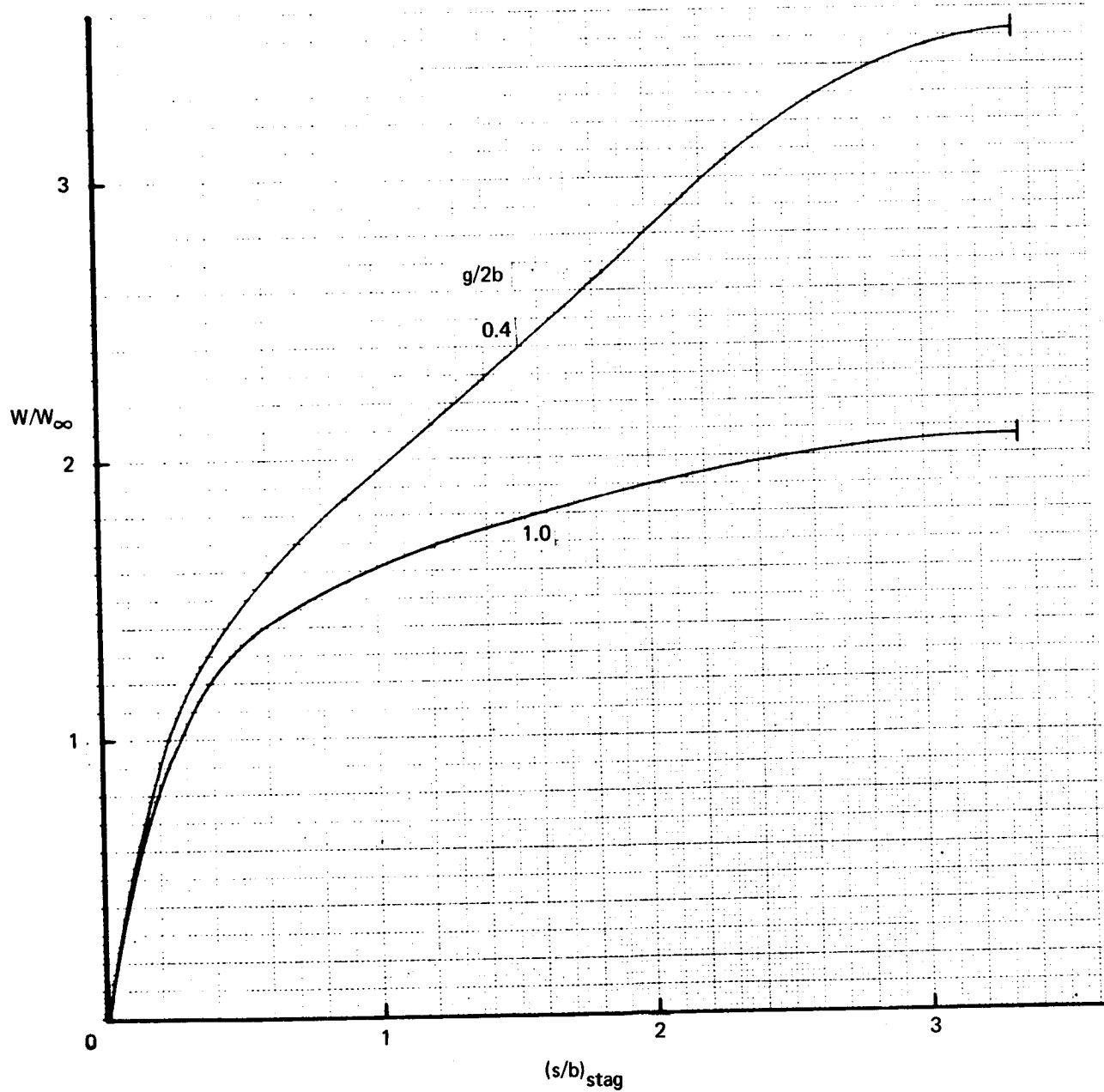
a) $g/2b = 0.2$ and 0.4 , $a/b = 1.5$ and 2.0

FIGURE B-2.—CROSSFLOW VELOCITY RATIO ON ELLIPTICAL RODS OF DIFFERENT AXIS RATIOS, a/b , AND SLOT WIDTH RATIOS, $g/2b$



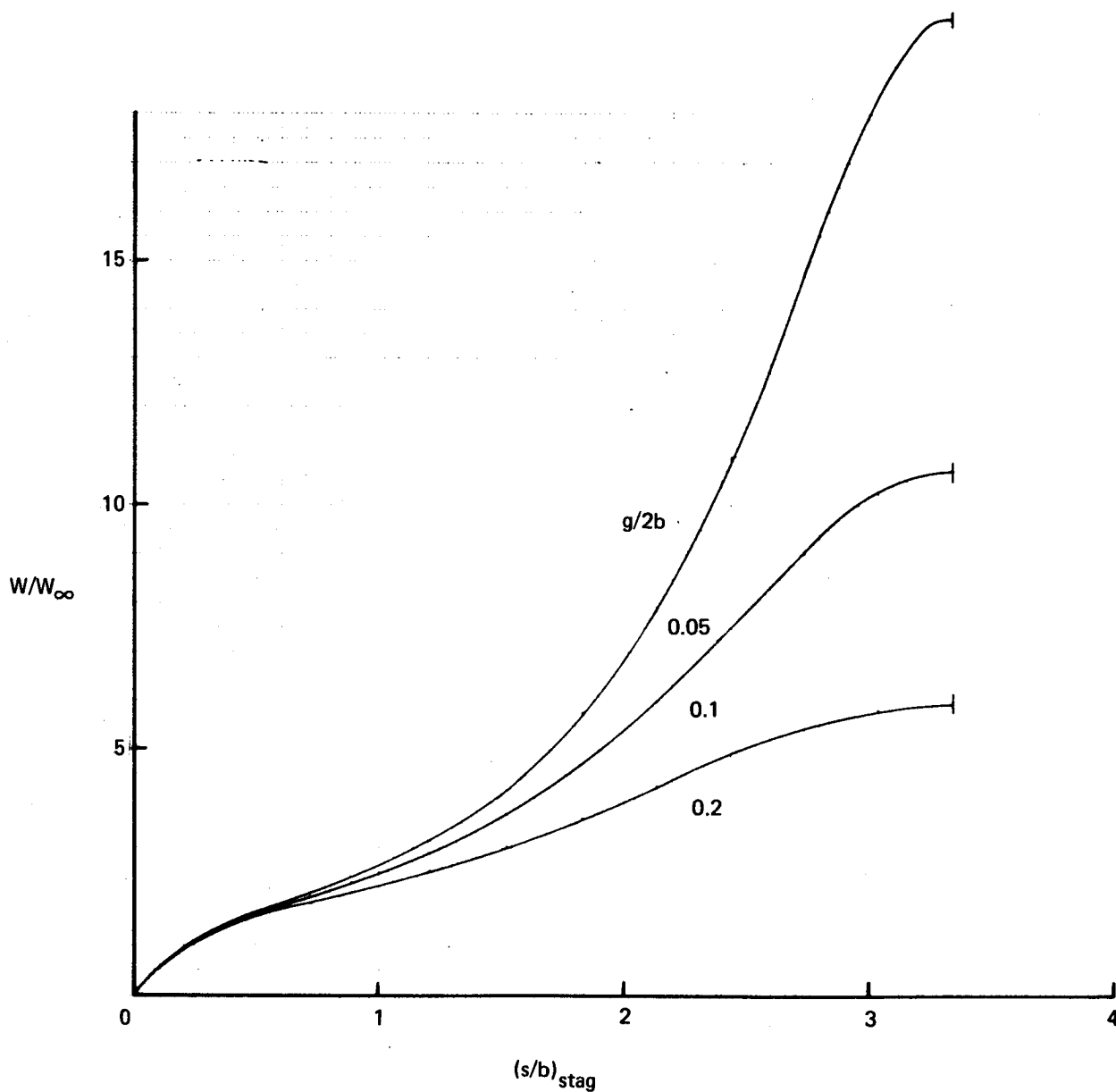
b) $g/2b = 0.05$ and 0.1 , $a/b = 1.5$ and 2.0

FIGURE B-2.—CROSSFLOW VELOCITY RATIO ON ELLIPTICAL RODS OF DIFFERENT AXIS RATIOS, a/b , AND SLOT WIDTH RATIOS, $g/2b$ (Continued)



c) $g/2b = 0.4$ and 1.0 , $a/b = 3.0$

FIGURE B-2.—CROSSFLOW VELOCITY RATIO ON ELLIPTICAL RODS OF DIFFERENT AXIS RATIOS, a/b , AND SLOT WIDTH RATIOS, $g/2b$ (Continued)



d) $g/2b = 0.05, 0.2$, and 0.1 , $a/b = 3.0$

FIGURE B-2.—CROSSFLOW VELOCITY RATIO ON ELLIPTICAL RODS OF DIFFERENT AXIS RATIOS, a/b , AND SLOT WIDTH RATIOS, $g/2b$ (Concluded)

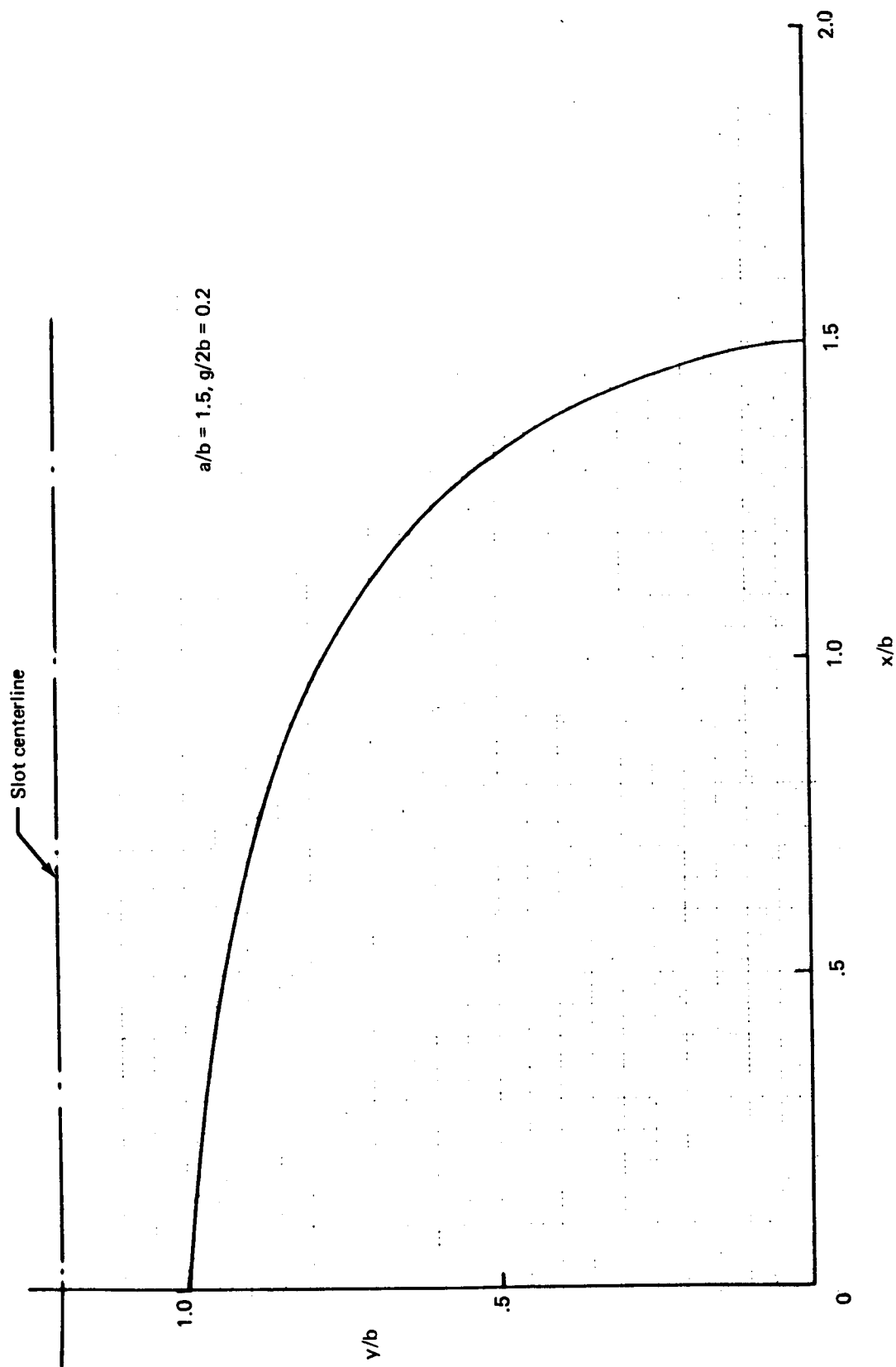


FIGURE B-3.—CONTOUR OF LONGITUDINAL SUCTION ROD @

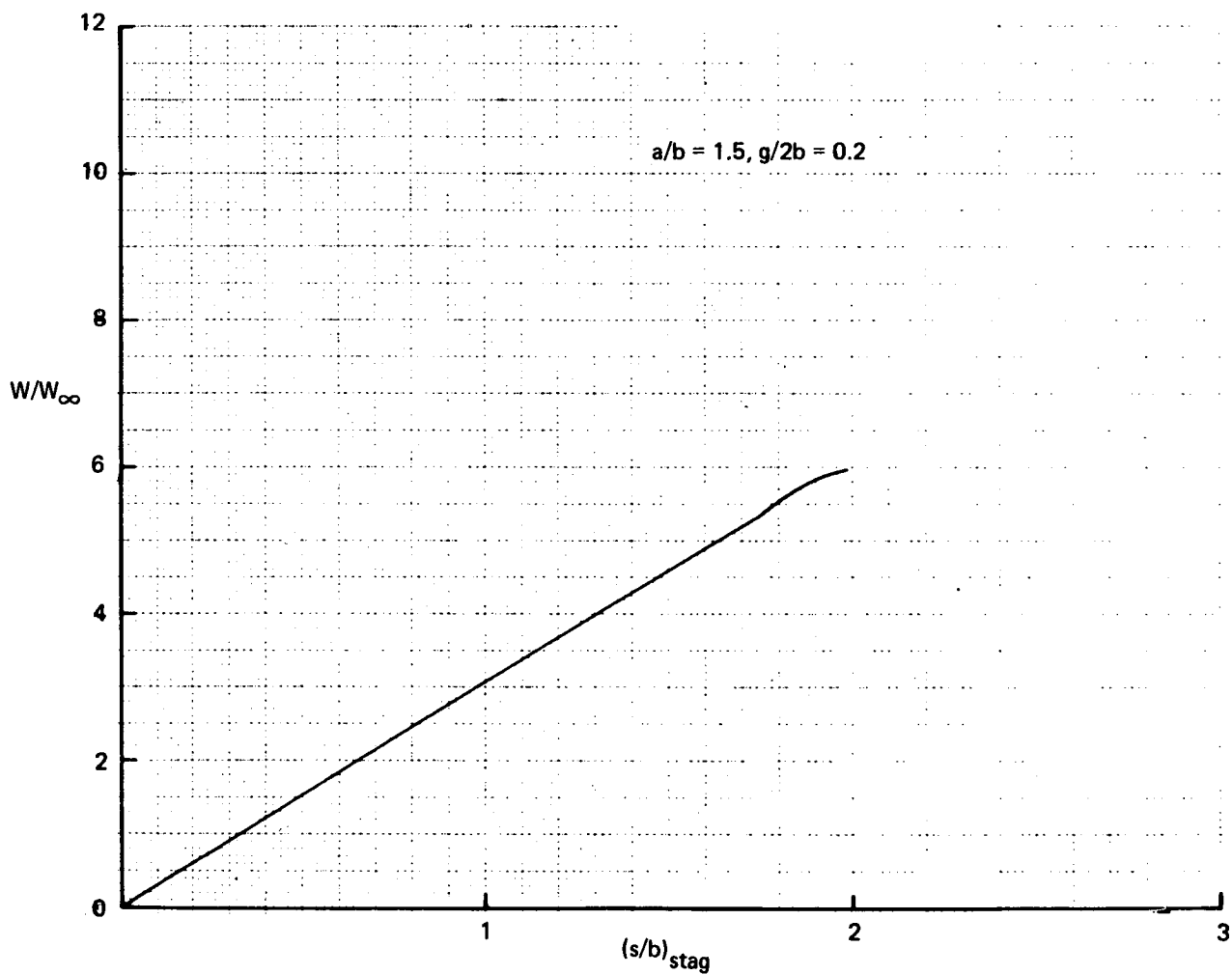


FIGURE B-4. —CROSSFLOW VELOCITY RATIO FOR LONGITUDINAL SUCTION ROD (d)

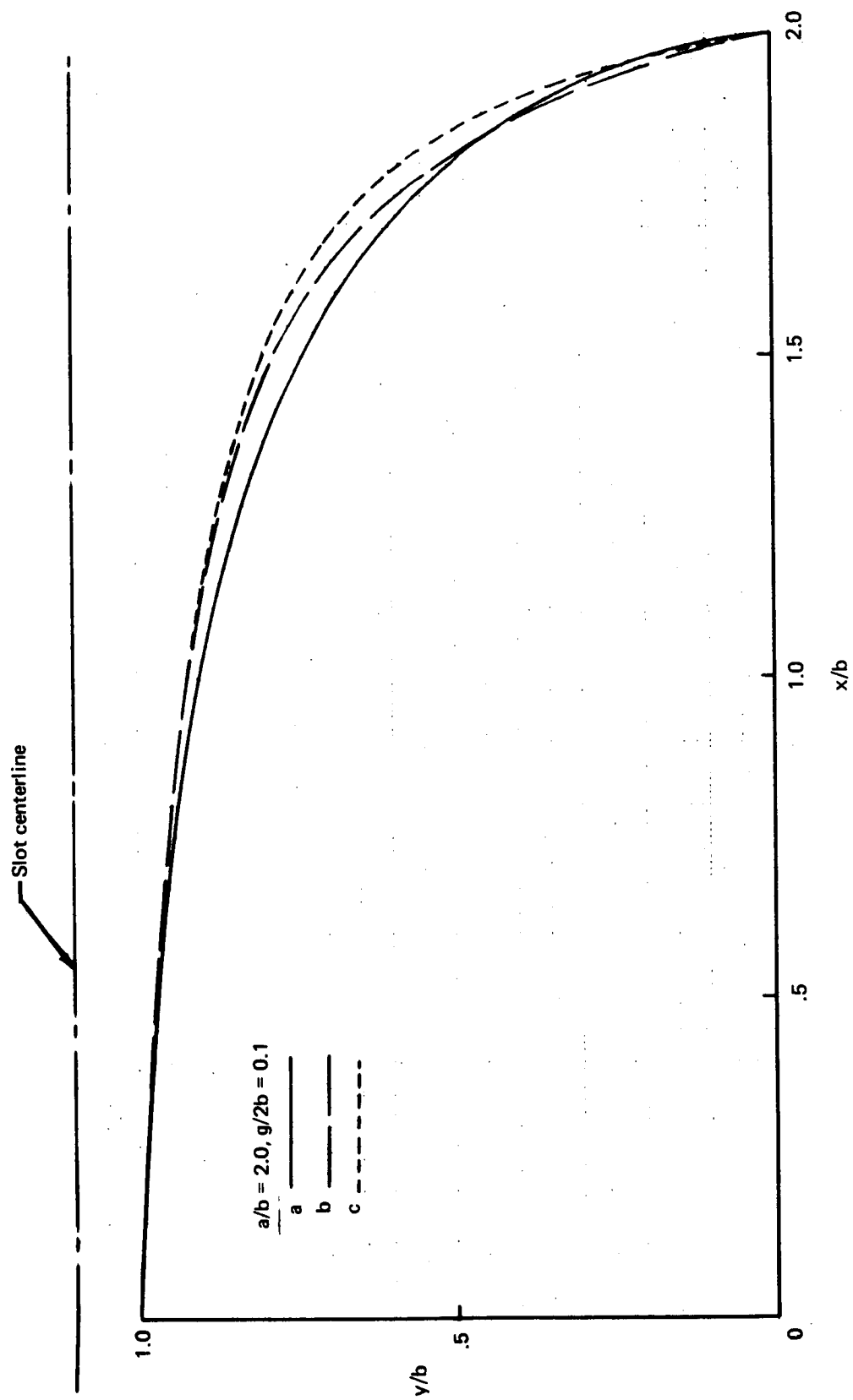


FIGURE B-5. —CONTOURS OF LONGITUDINAL SUCTION RODS (a), (b), (c)

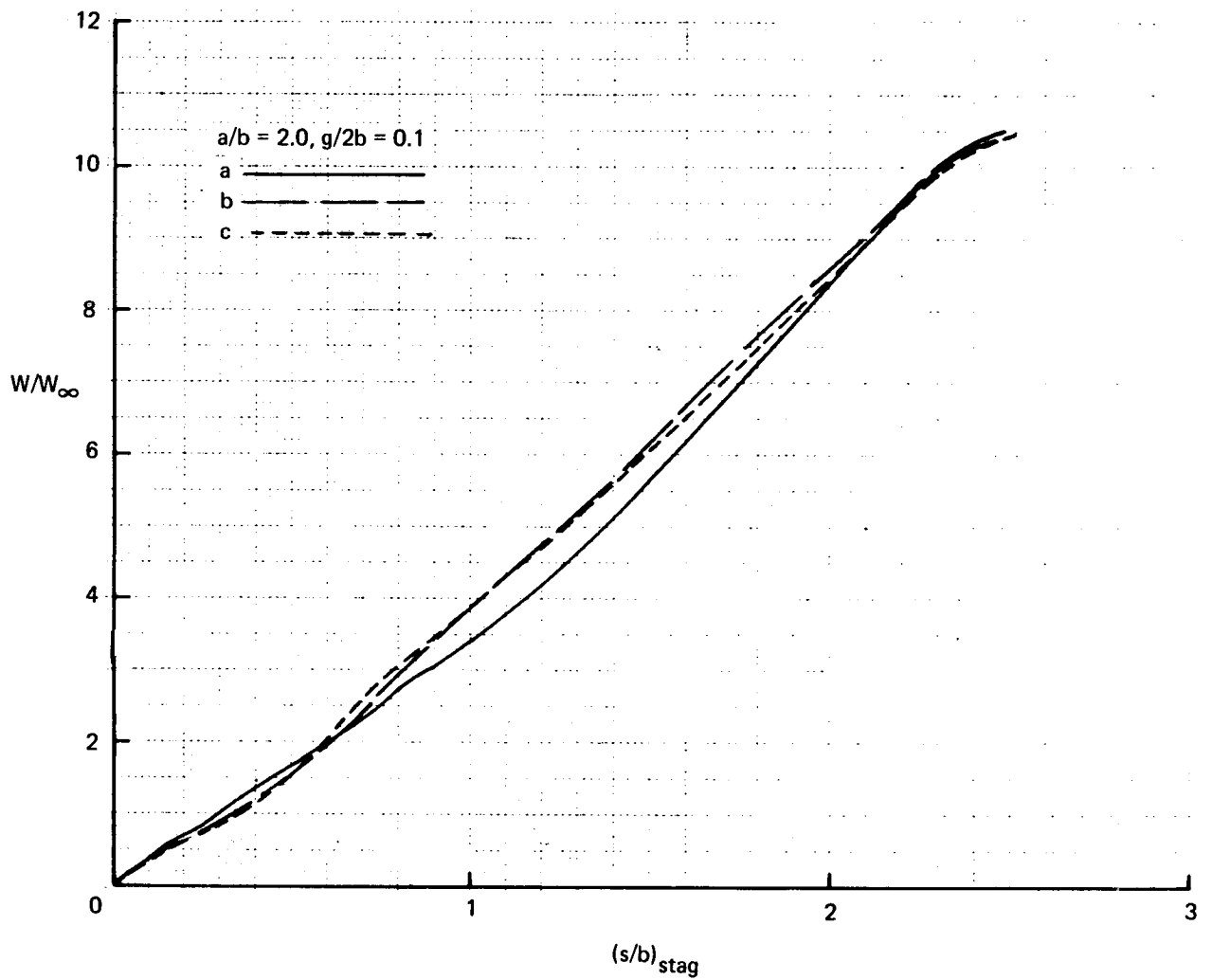


FIGURE B-6.—CROSSFLOW VELOCITY RATIO FOR LONGITUDINAL SUCTION RODS (a), (b), (c)

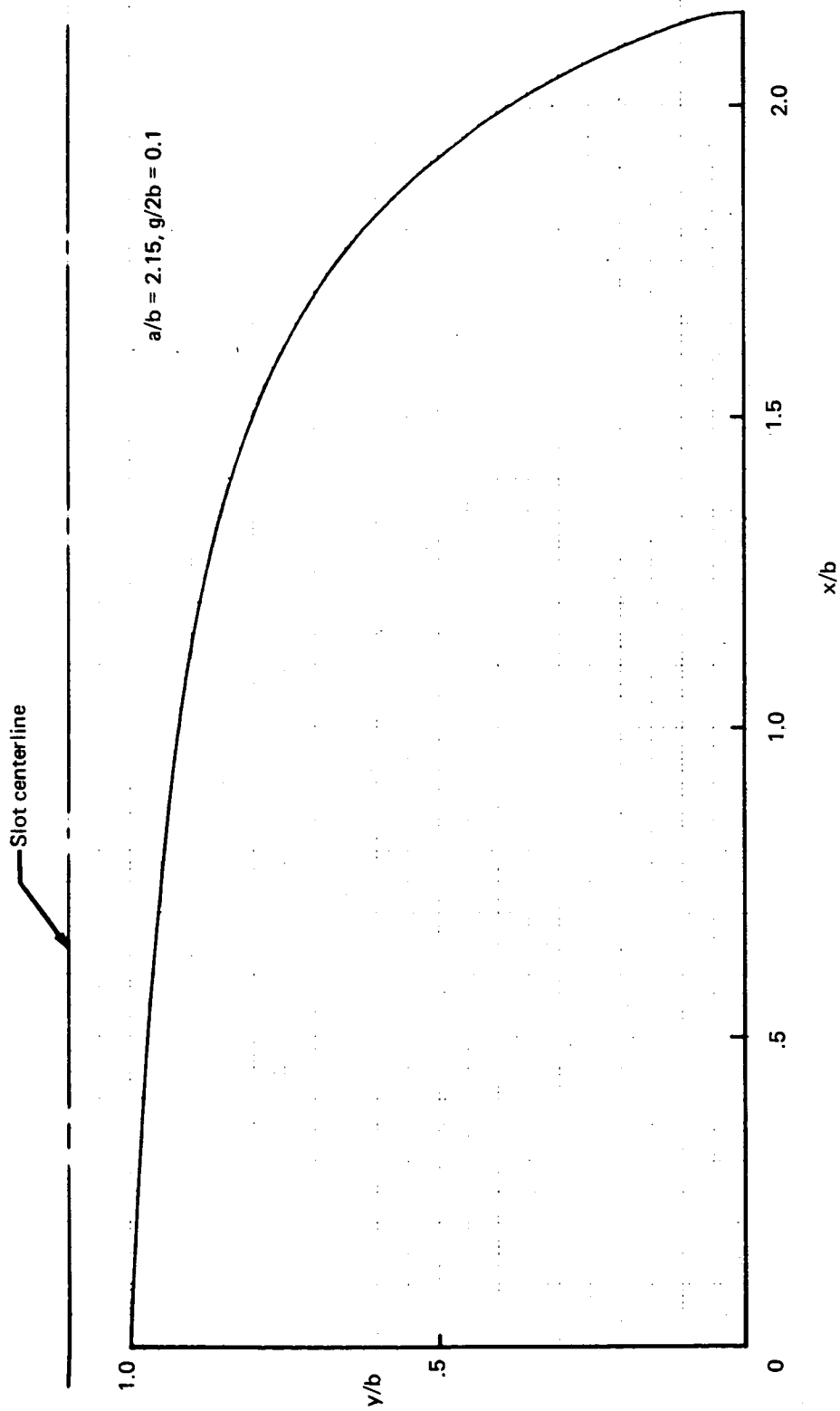


FIGURE B-7. —CONTOUR OF LONGITUDINAL SUCTION ROD ©

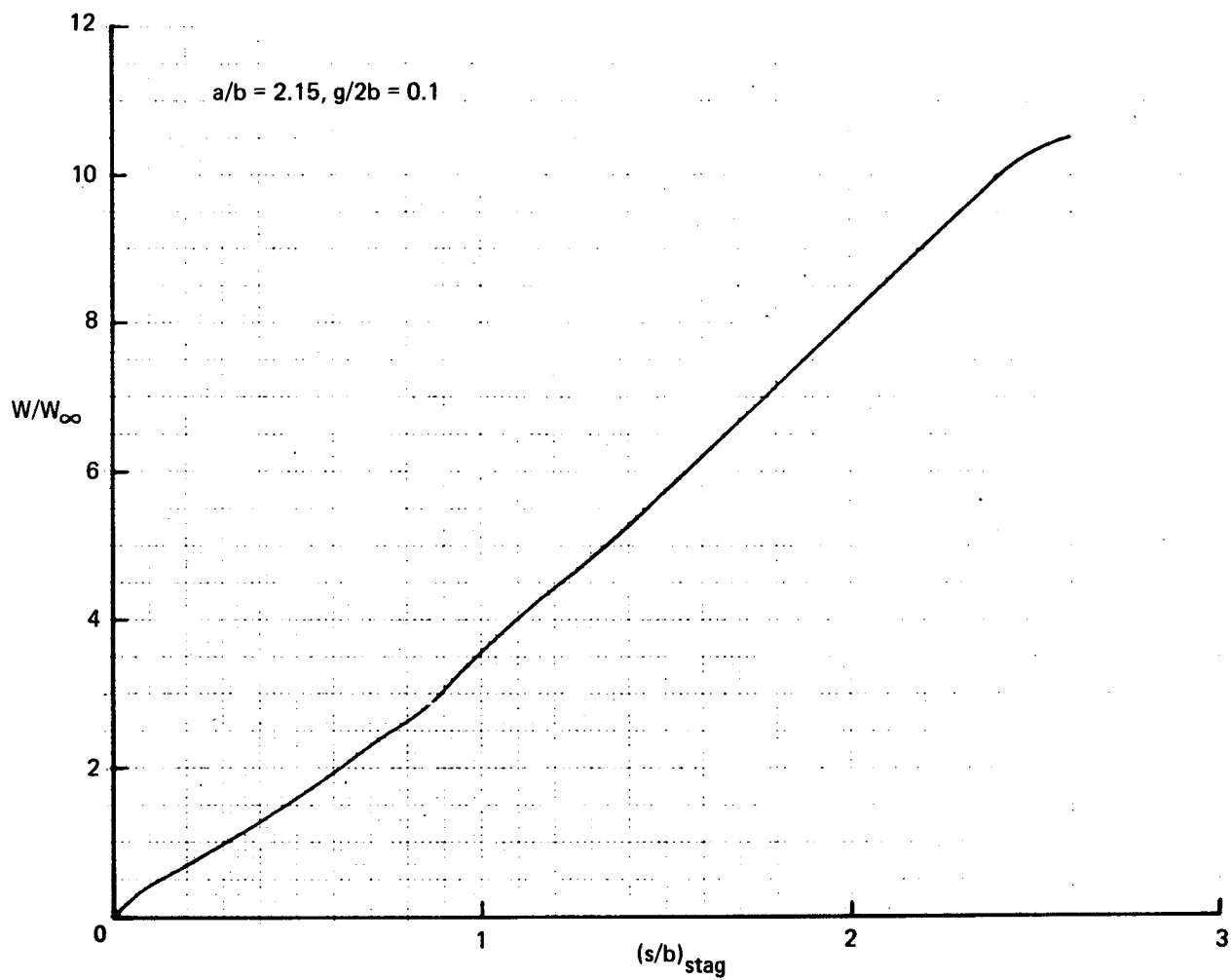


FIGURE B-8.—CROSSFLOW VELOCITY RATIO FOR LONGITUDINAL SUCTION ROD ©

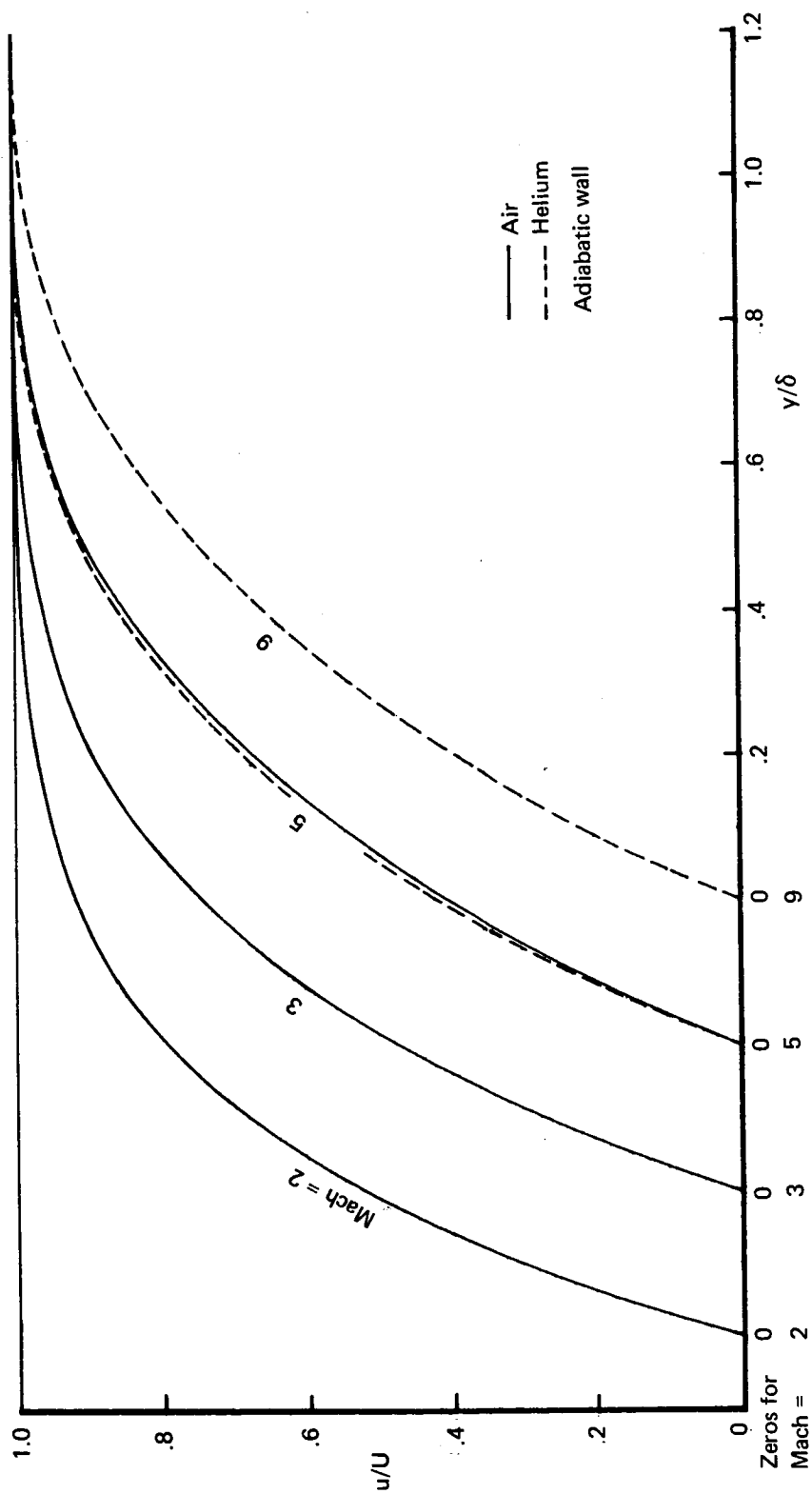


FIGURE D-1.—ASYMPTOTIC SUCTION PROFILES